LIÈGE université
School of Engineering

The Fluid Dynamics of Speleothem Growth

Thesis submitted in partial fulfillment of the requirements
for the degree of Doctor of Philosophy (PhD) in Engineering Science

by

Justine PARMENTIER

Supervisor: Tristan GILET

Co-supervisor: Vincent E. TERRAPON

DOCTORAL COLLEGE IN AEROSPACE AND MECHANICS

JANUARY 2024

EXAMINATION COMMITTEE

Prof. Dominique Toye (president)
University of Liège (Liège, Belgium)

Prof. Tristan Gilet (supervisor)
University of Liège (Liège, Belgium)

Prof. Vincent Terrapon (co-supervisor)
University of Liège (Liège, Belgium)

Dr. Sophie Verheyden
Geological Survey of Belgium (Brussels, Belgium)

Prof. Hanneke Gelderblom
Eindhoven University of Technology (Eindhoven, Netherlands)

Prof. Benoît Scheid
Université Libre de Bruxelles (Brussels, Belgium)

ABSTRACT

Beyond their outstanding beauty, stalagmites found in karstic caves may serve as proxies to help improve our understanding of palaeoclimatology. The study of stalagmite laminae completed with isotope dating may reveal particularly useful, just as dendrochronology or the analysis of sediment cores. While other proxies provide information on, e.g., past greenhouse gas concentration, stalagmite growth is in essence related to the past hydrology and soil coverage above the caves. Stalagmite growth stems from the precipitation and accumulation of calcium ions into calcite in the residual film of water left by the successive drops impacting the stalagmites, each incoming drop being responsible for the renewal of both these ions and of the liquid film. Nevertheless, in previous models of stalagmite growth, little attention has been given to the aerodynamics and hydrodynamics of drops falling from the cave ceiling onto the stalagmites, at the very origin of stalagmite growth. In this work combining field and lab experimentation, as well as physical and numerical modelling, we propose to analyse all elements of fluid mechanics involved from the moment the drop leaves the stalactite tip until it reaches the stalagmite top. We can divide the drop trajectory into distinct main steps: first, the drop falls freely into the air. Second, the drop impacts the thin film covering the stalagmite, usually at velocities that have been shown sufficient to generate splash, accompanied with the formation of a crown and the ejection of secondary droplets. Simultaneously, the ion contents of both drop and film are mixed together and redistributed in the film. Finally, the film left by the series of drops is depleted through gravity-driven drainage while the ions in solution precipitate.

Our first focus is to model the free fall of drops in caves. In previous models of stalagmite growth, it was commonly accepted that drops fall along a straight vertical line from the stalactite, thereby feeding the film from one central point. Through high-speed imaging of drops impacting stalagmites from several caves, we however observe that the impact point position of the drops is scattered, sometimes over several centimetres. We demonstrate that this dispersal has no external cause and must, therefore, be self-induced. Through Langevin-like equations describing the position and velocity of the drop free fall in response to gravity and aerodynamic forces, we rationalize the observed dependence of the impact point dispersal on the falling height travelled by the drops. We finally show that the impact point dispersal of the drops sets some constraints on the average stalagmite width.

We then move onto lab experiments to study in detail the mixing occurring during the impact between a drop and a film of similar radius and thickness as in caves, respectively. The impact out-

come, mostly dictated by the retraction phase following the crown developing during the impact, varies as a function of the film thickness and drop impact velocity. We investigate how the film thickness is affected by this impact dynamics, as well as how the ions would be redistributed in the film following the impact. We recorded high-speed top and side view movies of impacts on films of controlled thickness. By using two different colours for the drop and the film and applying a colorimetry technique based on Beer-Lambert law in the top view movies, we are able to assess the mixing between the drop and the film. We also measured the film thickness right after impact in all points from the impact position up to the unperturbed film free surface, and deduce how much liquid would be added following one impact. We then further relate all these parameters to four regimes that we identified based on the crown geometry measured from the side movies.

Afterward, we perform an analysis of the residual film filling and drainage dynamics by directly measuring the time evolution of the film thickness on various stalagmites in actual caves. We complete these measurements with lab experiments conducted on an actual stalagmite. Three phases are considered: the filling of the film starting from a dry stalagmite surface, the stationary state of this film reached after a certain number of drop impacts, and the sole drainage of the film in response to an interruption of the drop inflow. The experimental measurements show that the drop dripping period and stalagmite shape are the most important parameters influencing the filling, stationary state and drainage dynamics of the film. Instead of only considering the average width of the stalagmites, in this third part we attempt to rationalise how the particular shape of the stalagmite affects the drainage of the film. A numerical resolution of Reynolds lubrication equation expressed in a curvilinear system of coordinates allows to model the filling of a thin film on a stalagmite of general shape, as well as the sole drainage following an interrupted inflow of drops. Using a set of parameters corresponding to the stalagmites studied in lab and in caves, we are able to faithfully reproduce the drainage on the stalagmites from our dataset. From this analysis, we also conclude that the drainage is either driven by the film thickness gradients on very flattened or even horizontal stalagmite surfaces, while it depends on the stalagmite inclination in the case of convex stalagmites. Both stalagmite shapes are commonly found in caves. The film drainage has been omitted in previous stalagmite growth models and the film thickness was considered constant over the entire stalagmite, at least over an average on many drop impacts. Nevertheless, the results from our analysis show that these hypotheses are not always valid.

Finally, we gather ingredients from the former studies in order to model the complete process of a drop addition into a thin film over a stalagmite of arbitrary shape, accompanied with the gravity-driven drainage of this film and the precipitation of the ions brought by the drop into the film. In addition to the drainage equation previously developed, we estimate the evolution over time and space of the ion concentration in the film by using an advection-reaction equation, in a limiting regime with no diffusion. An equation describing the stalagmite shape variation as a consequence of the ion precipitation completes the model. We are therefore able to simulate a diversity of stalagmite shapes in response to variable entry parameters such as, e.g., the amount of ions contained within the drops impacting the film. Our results emphasise how the dripping period of the drops, along with the drainage and precipitation timescales, interact with one another to produce different types of stalagmites. The addition of drop and thin film physics explored in this work to existing models of stalagmite growth should help improve the robustness and accuracy of palaeoclimate reconstruction.

RÉSUMÉ

Façonnées par les siècles, les stalagmites qui décorent le sol des grottes karstiques ne sont pas juste d'époustouflantes créations de la Nature. Elles peuvent en effet aider à améliorer notre compréhension de la paléoclimatologie. L'étude des différentes lamines constituant les stalagmites, couplée à la datation isotopique, peut se révéler particulièrement utile. D'autres techniques de datation permettant de mieux appréhender les mystères de la paléoclimatologie incluent la dendrochronologie, l'analyse sédimentaire ou encore l'analyse de carottes glaciaires. Ces dernières, par exemple, fournissent d'importants renseignements sur l'historique des gaz à effet de serre dans une région donnée, tandis que les variations visibles entre les lamines des stalagmites sont par essence liées aux écoulements locaux passés et à la couverture naturellement présente au-dessus des grottes. Les modèles de croissance de stalagmite existants ne considèrent pas l'aérodynamique et l'hydrodynamique des gouttes tombant du plafond des grottes sur les stalagmites. Ces gouttes sont pourtant essentielles à la croissance des stalagmites, puisque ce sont elles qui apportent les ions calcium à l'origine du processus de croissance. Les ions en solution dans le film mince d'eau recouvrant les stalagmites précipitent progressivement pour former de la calcite qui s'accumule petit à petit, permettant à la stalagmite de grandir par ce biais. Chacune des centaines de milliers de gouttes tombant sur une même stalagmite est donc responsable du renouvellement des ions calcium en solution, ainsi que du film mince d'eau sur la stalagmite.

À travers ce travail qui combine des mesures expérimentales prises sur terrain et en laboratoire, complétées par de la modélisation physique et numérique, nous proposons d'analyser chacune des parties importantes de la trajectoire d'une goutte dans une grotte. Depuis son détachement au bout de la stalactite surplombant la stalagmite sur laquelle elle finit par atterrir, une goutte tombant dans une grotte n'a pas une vie que l'on pourrait qualifier de long fleuve tranquille. Cette goutte tombe librement dans l'air depuis des hauteurs sous plafond qui peuvent parfois atteindre 20 ou 30 m. Parcourir une telle distance permet à la goutte d'atteindre une vitesse suffisante pour générer du splash, ainsi que l'éjection de nombreuses gouttelettes, lors de son impact avec le film mince d'eau recouvrant la stalagmite sur laquelle elle s'écrase. Au cours de chaque impact, les ions en provenance de la goutte et du film se mélangent entre eux et sont redistribués dans le film. Parallèlement aux impacts de gouttes qui le remplissent progressivement, le film se déplète par drainage le long des parois de la stalagmite tandis que les ions en solution précipitent.

Nous commençons par nous pencher sur la chute libre des gouttes dans les grottes. Les modèles de croissance des stalagmites précédemment établis ont pour habitude de considérer que chaque

goutte tombe en parfaite ligne droite depuis la stalactite, remplissant ainsi le film mince d'eau en un unique point central sur la stalagmite. Nous observons pourtant à travers de nombreuses vidéos à imagerie rapide enregistrées en grottes, que la position du point d'impact de la goutte est dispersée et s'étale parfois même sur plusieurs centimètres. Nous démontrons à l'aide de divers arguments que cette dispersion ne peut pas être expliquée par un facteur extérieur à la goutte, et doit dès lors être induite par la chute de la goutte elle-même. Plus particulièrement, c'est l'interaction entre la goutte et l'air au travers duquel elle tombe qui est responsable de la dispersion du point d'impact. À travers des équations de type Langevin décrivant la position et la vitesse d'une goutte en chute libre soumise à la résistance aérodynamique de l'air, nous expliquons la dispersion du point d'impact observée en fonction de leur hauteur de chute. Finalement, nous relions cette dispersion à la taille moyenne des stalagmites.

La deuxième partie de ce travail porte sur le mélange entre la goutte et le film au moment de l'impact. L'impact d'une goutte sur un film mince s'accompagne de la formation d'une couronne qui croît au cours du temps, et finit par se déchirer ou se rétracter vers son centre. L'issue finale de l'impact dépend fortement de cette phase de rétraction, elle-même tributaire des conditions d'impact, à savoir l'épaisseur initiale du film et la vitesse de chute de la goutte. Nous nous intéressons à la façon dont l'épaisseur du film est modifiée à la suite d'un impact, ainsi qu'à la redistribution des ions en solution, découlant des variations d'épaisseur du film. Pour ce faire, nous utilisons à nouveau l'imagerie rapide, cette fois afin d'enregistrer des vues de haut et de profil d'impacts de gouttes sur des films d'épaisseur semblable à celles observées en grottes. Grâce à une technique de colorimétrie basée sur la loi de Beer-Lambert, en colorant la goutte et le film de deux façons différentes nous sommes en mesure d'estimer le niveau de mélange entre ceux-ci sur les vues de haut. Nous parvenons également à mesurer l'épaisseur du film en tout point à la suite de l'impact, du centre de l'impact au bord du film. De là, nous pouvons déduire la quantité de liquide ajoutée au film à la suite d'un impact. Toutes les mesures effectuées peuvent finalement être reliées aux divers régimes d'impact que nous identifions à l'aide des vues de profil.

Nous nous attardons ensuite sur l'équilibre existant entre le remplissage et la déplétion par drainage du film d'eau résiduel recouvrant les stalagmites. Nous récoltons des données d'évolutions temporelles d'épaisseurs de films sur de vraies stalagmites, en grottes ainsi qu'en laboratoire. Nous considérons trois phases durant ces expériences : le remplissage progressif du film par des impacts de gouttes successifs, l'état stationnaire du film atteint après un certain nombre d'impacts et le drainage seul résultant de l'interruption des impacts de gouttes. Nos mesures révèlent que les paramètres affectant le plus l'épaisseur du film sont la fréquence de chute des gouttes et la forme de la stalagmite. C'est pourquoi, dans cette troisième partie, nous ne considérons plus seulement la taille moyenne des stalagmites, mais également leur aspect géométrique. Partant de l'équation de lubrification de Reynolds que nous exprimons dans un système curviligne, nous sommes en mesure de modéliser l'évolution d'un film mince sur une stalagmite de forme quelconque non seulement en réponse à un apport intermittent de gouttes, mais aussi lorsque le drainage seul opère. Nous pouvons résoudre les équations que nous obtenons par le biais d'outils numériques et reproduire fidèlement le drainage observé sur les stalagmites de notre jeu de données à l'aide de paramètres d'entrée adéquats. L'analyse menée nous permet de plus de conclure que le drainage dépend principalement des gradients d'épaisseur sur les stalagmites aux profils plans, voire horizontaux, tandis qu'il est conditionné par l'inclinaison de la stalagmite lorsque celle-ci présente un profil plutôt convexe. Ces deux types de stalagmites sont fréquemment rencontrés en grottes. Bien que le drainage ait été omis des modèles de croissance de stalagmite existants et que ces derniers considéraient le film d'épaisseur parfaitement constante sur toute la surface de la stalagmite, nous montrons à travers cette étude que ces hypothèses ne sont pas toujours valables.

Pour clôturer ce travail, nous ajoutons à notre modèle de drainage un ingrédient capital : la précipitation des ions calcium en calcite. Le but de cette dernière partie est de modéliser la croissance des stalagmites en incluant les différents impacts successifs des gouttes qui amènent des ions calcium en solution, le drainage du film opérant entre deux impacts ainsi que la façon dont la concentration en ions dans le film varie en réponse au drainage du film et à la précipitation des ions grâce à une équation d'advection-réaction négligeant la diffusion des ions. Nous complétons ce modèle à l'aide d'une dernière équation décrivant la nouvelle forme prise par la stalagmite à la suite de la précipitation des ions en solution. La croissance des stalagmites dans divers régimes peut ainsi être étudiée. Celle-ci est tantôt dominée par le drainage du film qui répartit les ions avant que ceux-ci ne précipitent, tantôt uniquement présente là où la goutte a impacté la stalagmite. Un autre paramètre important qui influe la croissance de la stalagmite est la concentration des ions amenés dans chaque goutte qui impacte le film. À l'aide du modèle que nous avons développé, nous sommes en mesure de produire différentes formes de stalagmites en réponse aux derniers paramètres évoqués.

Ce travail décrit comment la physique des gouttes et du film peut être prise en compte dans les modèles existants de croissance de stalagmite. Nous espérons que les éléments de réponse que nous amenons aideront à améliorer la reconstruction paléoclimatique basée sur les lamines de stalagmites en termes de précision et de robustesse.

x

ACKNOWLEDGEMENTS

CONTENTS

IV   **Drop impact on thin film**   55

V   **Drainage of a thin film**   97

VI Growth model — 187

VII Conclusion — 239

FIGURES

TABLES

How to read this manuscript

All the documents (manuscript PDF, auxiliary sheet, research articles, supplemental material and videos) can be found in the Orbi repository relative to this manuscript.

🔴 This manuscript contains 8 separately readable chapters, with the exception of Ch. VI (*Growth Model*) for which we advise to first read Chs. I, IV and V.

🔴 Chapters alone are referenced by an uppercase roman letter, figures (and tables) by the chapter in arabic, followed by the internal figure (table) number, also in arabic. *Example: the first chapter is Ch. I, and the second figure of the third chapter is Fig. 3.2.*

🔴 Sections are internally numbered, the chapter being precised if needed. *Example: the fourth section of the fifth chapter is simply Sec. 4.*

🔴 The Appendix relative to a specific chapter can be found at the end of this one.

🔴 Short versions of the general nomenclature and measurements relative to the visited caves are provided in the auxiliary sheet.

🔴 For readers in a hurry, a *Highlights* section is available at the beginning of each chapter, and a technical *Summary* at the end (after the Appendix). It differs from the conclusion relative to the chapter, which is oriented toward the interpretation of the results.

Since the dawn of time, caves have been a source of timeless fascination [121]. Although they were first used as simple natural shelters, nowadays they are the theater of curious relics from the past. From bearing the oldest known cave paintings made by Neanderthals about 64000 years ago [113] to becoming today's unskippable touristic exhibitions, ideal setups for speleology aficionados and even decors of escape games, caves have silently witnessed the evolution not only of mankind, but also of its environment. Caves were actually there long before us, and have survived all types of major climate change events, from frequent glaciation periods to rapid warmings, or even variations in the atmosphere state [76]. The calcareous concretions found inside caves, commonly known as speleothems, are of greatest interest for palaeoclimate studies and reconstruction [219]. Stalagmites, in particular, can reveal good palaeoclimate proxies, just like sediments, ice cores, rocks, fossils or tree rings [76]. They can provide useful information up to thousands of years ago. Understanding their growth may thus help gain insight into the past and future evolution of local climate.

But if the story ends there, it does not start inside the cave. Water originating far upstream as a combination of rainfall, evapotranspiration and runoff makes its way through the ground and the vessels of the cave ceiling to reach stalagmites after a long and tremendous journey. Inside the caves, it appears under the form of drops hanging from the ceiling. Without these drops, there would not be stalagmites. Yet, in previously proposed mathematical models of stalagmite growth, the physical phenomena accompanying the drops were often omitted [20, 70]. Far from the idea behind Plato's Allegory of the Cave, in this work we only aim at exploring the various physical processes involved in the drop-stalagmite interactions within the caves, and assess whether or not they should be taken into account. Although the framework of this thesis is to improve stalagmite growth modelling, most chapters focus on fundamental aspects of the drop physics through experimentation and theoretical work, sometimes completed by direct in situ measurements. In this introduction, we start by reviewing the specific interest of stalagmites in the context of palaeoclimatology reconstruction. We then continue by examining the entire trajectory of the drop until it reaches the stalagmite, a trajectory that can be divided into several distinct steps detailed afterward. From there, we further describe the content of the thesis and its chapters.

1. Stalagmites as palaeoclimate proxies

Over the last decades, an increasing number of proofs have contributed to the consensus regarding the role played by human activities on climate forcing [119]. However, climate change itself is not a novel phenomenon. The Earth has experienced a large number of glaciation periods, interrupted by interglacial or warming events, for instance during the Quaternary [231]. The Quaternary is the

latest period of the Cenozoic, i.e., the current geological era[1], which starts from the penultimate mass extinction event (the Cretaceous–Paleogene extinction event, which includes the extinction of most non-avian dinosaurs), about 66 Ma ago[2] [40]. The Quaternary can be further divided into two epochs: the Pleistocene, covering the most recent alternation of aforementioned repeated glaciations, spanning from 2.58 Ma to 11 700 a ago, and the subsequent Holocene, which continues until today [231]. Although these epochs cover long geological times, climate records have only been monitored since the late nineteenth century. In particular, surface temperatures have been recorded since the 1880s [126], while the monitoring of carbon dioxide atmospheric concentrations started in the late 1950s [134]. Without delving into the historical Quaternary climate events that occurred at much larger scales than the climate records at our disposal, it is therefore not possible to develop a clear comprehension of contemporary climate. Long-term data, which are essential for climate modelling, are only accessible through climate proxies.

The beginning of precise surface temperature monitoring is not purposeless. Even before modern evidence of climate change, a number of observations and discoveries sparked the interest of scientists for Quaternary climate study [231]. The second half of the eighteenth century witnessed the birth of vertebrae palaeontology, which accompanied the discovery of mastodon fossil remains [61]. Additionally, evidence of boulders and piles of rocks being displaced by ice, as well as the presence of in-land glacier deposits, stemmed across Europe and, later, North America [231]. From there arose the premises of the theory on the alternation of glaciation and interglacial events, simultaneously to the theory of evolution [10]. However, the causes of these glaciation events remained unsolved at that time. Although explaining accurately these events is still an ongoing field of research, a commonly accepted theory is that of Milankovitch [165], who hypothesised that the changes in the relative position of the Earth with respect to the Sun are key to triggering glaciation and warming events [165]. He investigated how the solar radiation reaching the surface of the Earth is affected by changes in the orbital movements of the Earth, comprising the eccentricity (the shape of the orbit), the obliquity (the tilt in the angle made by the axis of rotation and orbital plane) and the precession (the direction of the axis of rotation). Owing to these changes in solar radiation intercepted by the surface of the Earth, cooler summers may decrease snow melt, ultimately contributing to the long-term growth of ice sheets through snow accumulation at specific latitudes [231]. Milankovitch calculated that glaciation events should occur roughly every 41 000 a, which corresponds to the obliquity cycle period and was later confirmed by an analysis of deep-sea sediment cores revealing the same periodicity [109]. However, about 800 ka ago, the cycle of glaciation events lengthened to 100 ka, aligning with the eccentricity cycle period, while reasons behind this transition remain elusive. The significance of climate proxies is revealed through this example, which holds global importance, but it is also evidenced by many other examples from the literature which focus on smaller timescales or local palaeoclimatology studies [76, 231].

Figure 1.1: Examples of proxies used for palaeoclimatology. *Left.* The skeleton of marine corals is used in palaeoceanography. *Right.* Tree rings are used in dendrochronology.

---

[1]The Cenozoic itself, with other eras, is part of the Phanerozoic, the current eon, which has started 538.8 Ma ago. An eon represents the largest geologic time, the second largest one being the era, followed by periods (e.g., the Quaternary) and epochs.

[2]The symbol a (annum) is only used in this chapter, so as to be consistent with the literature, while y (year) will be used in the rest of the manuscript.

The term palaeoclimatology refers to the study of ancient climates through the use of various proxies, i.e., preserved materials serving as ancient climate archives. These archives can either be physical, chemical or biological, and spans various geological times [76]. Proxies can provide information on various parameters and environmental conditions, such as the atmosphere temperature, the air mass trajectories, the carbon cycle, the ocean water salinity, the ocean stratification, the sea level, the water mass circulation, or the intensity of rainfall [76]. These measurements are often indirect and require a precise calibration of actual variables such as the temperature or isotopic composition [225]. Palaeoclimatology is a general term which can become environment or proxy-specific. For instance, palaeobotany refers to the statistical analysis of pollen data [207]. Pollen spores falling to the bottom of lake basins and peatlands can be preserved in sedimentary layers. If these sedimentary cores are well-dated and with the unique features displayed by pollen spores, palaeobotany allows to reconstruct Quaternary vegetation history [207, 231], proving, e.g., that an ensemble of plants which used to grow together no longer do, or documenting the invasion and spreading of some past species [205, 226]. Palaeoceanography is another large subdomain of palaeoclimatology, and involves the study of, e.g., the isotopic composition of phytoplankton, coral skeletons (see Fig. 1.1), mollusk shells, or algae [193]. Dating techniques are of the upmost importance for these types of proxies, and more generally for studies conducted on the Quaternary [231]. They allow to estimate, with more or less precision, the age of a material sample. Most widely used dating techniques include, but are not limited to, (i) radioactive nuclide methods, which infer the decay or buildup of radioactive isotopes within the material from concentration analysis, including radiocarbon dating [213], (ii) radiative dosimetry methods, which are based on the analysis of material radiation damage through, e.g., thermoluminescence [6], and (iii) qualitative and comparative methods, such as, for instance, lichenometry, a novel technique used to estimate the age of rock surfaces by measurement of incremental growth of lichens at the surface [118]. These methods can provide information from 10 to 10^7 a ago, none of them being able to accurately span the entire time range [231]. They are therefore complementary and allow to cover almost the entire Quaternary. Radiocarbon isotopes, e.g., can trace back measurements from up to 50 ka ago in organic material and proxies containing carbonates.

Among qualitative and comparative dating methods, dendrochronology deals with the study of tree rings, which are another form of annual increments (see Fig. 1.1) [91]. Recently, dendrochronology helped unveil the cause of fall of the ancient Hittite empire, which is related to the Late Bronze Age collapse and led to anarchy, uprisings, civil wars, famines and outbreaks of diseases in neighbouring sovereign nations around 1200 b.c.[3] [158]. The Hittite Empire was rival to Egypt but had disappeared for unknown reasons, until its collapse was recently correlated with a severe drought that lasted for a few years in a central area of the Empire, revealed by the annual growth of local tree rings and their moisture content, measured through radiocarbon dating [158]. Other examples of environmental proxies of annual resolution include speleothems, and most specifically stalagmites found in karstic caves. Speleothems present a number of physical and chemical characteristics which can be related to past climate evolution. The main interest of speleothems, by contrast with proxies such as tree rings, lies in their potential for continuous growth through thousands or even tens of thousands of years [35, 91]. Numerous studies have explored the relation between annually laminated layers of growth of stalagmites and local palaeoclimate history. One of the earliest indications of paleoclimate variations recorded by speleothems originates from Devil's Hole (USA), where records going back to 500 ka have been observed. The periodicity of 100 ka exhibited by these speleothems, similar to the eccentricity cycle period of the Earth, could be correlated with marine and ice proxies, thereby challenging the traditional orbital

---

[3]The abbreviations *b.c.* and *a.d.* refer to "before Christ" and "anno domini", i.e., "from the birth year of the Christ", respectively.

theory of climate change. Other examples of the implications of speleothems for palaeoclimate reconstruction include, e.g., records of the variations in monsoon activity, as exemplified by stalagmites from China caves [228]. We represent in Fig. 1.2 records of oxygen isotope variations, δ^{18}O, obtained by Wang et al. [228] from several stalagmites, juxtaposed to each other (note that the ordinate axis direction has been inverted for comparison with the other curve in the graph). The stalagmites all come from caves found within areas dominated by monsoon seasons. Additionally, the summer solar irradiance in the Northern Hemisphere is represented in Fig. 1.2 for the same period, i.e., the past 2.25 ka. Both curves from Fig. 1.2 are approximately in phase (they actually are in phase opposition), such that the oxygen isotope variations in stalagmites seem correlated with the local solar irradiance. More recently, speleothem records could also be related to past fire frequency and intensity, and thereby to antecedent climatic conditions leading to fire events in Yonderup cave (Australia) [164], by comparison with well-documented recent wildfire events.

With such implications of speleothem records as proxies for palaeoclimate reconstruction, it is necessary to get a clear understanding of both their formation and relation to their direct environment. For instance, the partial fractures damaging the outer wall base of stalagmites, a common phenomenon in mid-latitude caves, was previously attributed to lateral flows of ice formerly present in caves, while recent work seems to prove otherwise [204]. The thermoelastic stresses within the expanding ice body would reach values equating and even exceeding the tensile strength of stalagmite, causing a vertical uplift of the stalagmite through interface stress jump and suggesting a connection between glacial climate variability and corresponding glaciation cycles of the Pleistocene [204]. Additionally, we note that, despite the apparent synchronicity between the oxygen isotope variations and solar irradiance in Fig. 1.2, disparities in the relative amplitudes of both curves remain present. The oxygen isotope variations also display peaks and troughs uncorrelated to the monsoon signal. In this work, we thus propose to investigate some physical processes related to stalagmite growth in karstic caves that have not been clearly comprehended yet, or at least not in the particular context of stalagmites. Before diving into these various processes in Sec. 1.3, we review a few fundamental aspects of these speleothems in the next section.
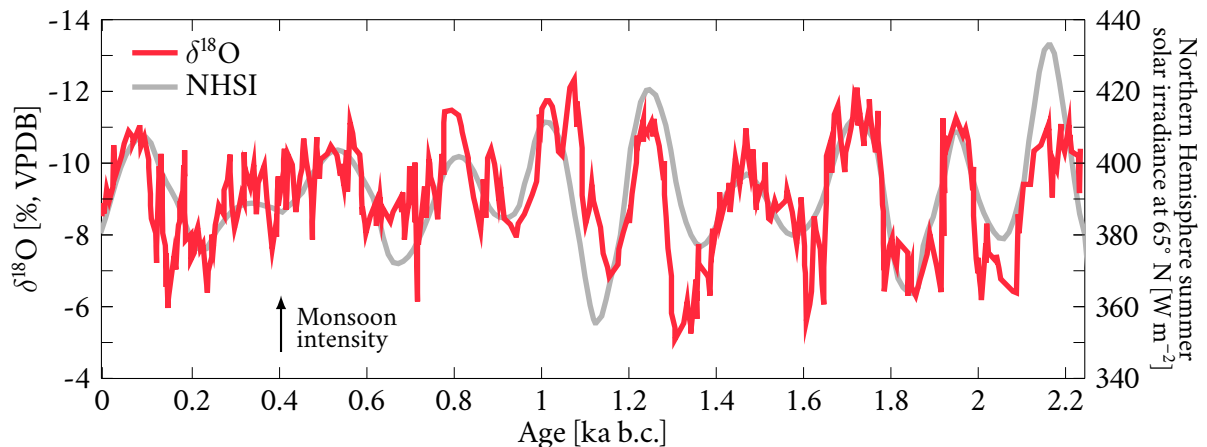
Figure 1.2: Ensemble of oxygen isotope records[4] from stalagmites in Hulu Cave, northeastern China (26° N, 105° E) (from ∼20 ka b.c. to ∼50 ka b.c.), and various stalagmites from Sanbao Cave, central China (32° N, 110° E) (rest of the graph), represented by the red line, juxtaposed to each other. The variations in the oxygen concentration, δ^{18}O, is plotted against the age of the stalagmites. The Hulu δ^{18}O record were plotted 1.6 % more negative to account for the higher values at Hulu Cave compared to Sanbao Cave. Northern Hemisphere summer solar irradiance (NHSI, up to July 21) at 65° N is represented by the gray line. Isotopic values are plotted inversely, such that monsoon intensity (indicating the percentage of summer rainfall in the annual rainfall total) increases upward, as indicated by the arrow. Adapted from Wang et al. [228], Fig. 1 a, and Bradley [35], Fig. 8.5. Note that the original δ^{18}O graph was drawn with different colours, in correspondence with the 9 stalagmites analysed by Wang et al., which is not reproduced here.

---

[4]*Vienna Pee Dee Belemnite* reference scale for Carbon stable isotopes analysis.

● continuous carbonate rocks	● discontinuous evaporite rocks
● discontinuous carbonate rocks	● mixed carbonate and evaporite rocks
● continuous evaporite rocks	⊥⊥ permaforst boundary
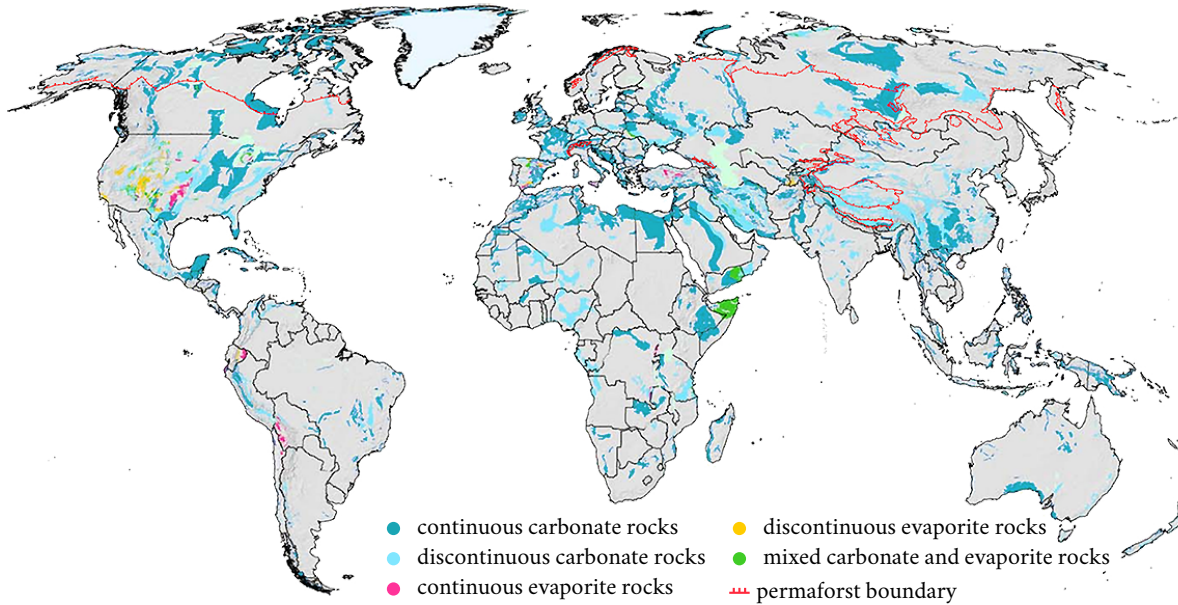
Figure 1.3: World karst aquifer map, adapted from Goldscheider et al. [102], showing already existing karst aquifers, and karstifiable carbonate and evaporite rocks that represent potential karst aquifers.

1.1 Karstic caves and speleothem growth

Stalagmites, and more generally speleothems, are found in caves formed within karst landforms. The erosion of the landscape over the surface of the Earth results from a combination of chemical weathering and mechanical transport, such as, e.g., soil creep or landslides [76]. In limestone (calcium carbonate sedimentary rock), dolomite (calcium carbonate containing magnesium) and gypsum (calcium sulfate dihydrate), chemical removal of rock masses by dissolution dominates mechanical transport and leads to the formation of karst[5]. The various forms of karst represent between 15 % and 20 % of the land areas on Earth, and are constituted mostly of calcium carbonate rocks [102, 231]. The map from Fig. 1.3 represents the world distribution of karst aquifers already formed (carbonate rocks), and possibly currently under development (evaporite rocks) [102]. Limestone itself can differ depending on the form of the $CaCO_3$ crystal, the most widespread forms being calcite, which is also the most stable form, and aragonite [143].

The development of karst therefore mainly results from the dissolution of soluble carbonate rocks, which can lead to both surface and subsurface features and yield different karst landforms. Surface features of karst may result from, e.g., the attack of rainfall on structural weaknesses of the exposed rocks, leading to the formation of crevices, a famous example being the Burren pavements from Ireland [76]. Subsurface karst features, on the other hand, result from water infiltration and drainage from the water recharge to discharge point [89], and the accompanied subsurface rock dissolution. This dissolution leads to the formation below the soil surface of open conduits or cavities ranging from a few millimetres to several kilometres in length, and up to tens of metres high, [89], i.e., caves. The presence of caves is one of the distinctive features of karst, compared to other landforms. Only a small portion of existing caves is currently explored, the vast majority of them being undiscovered or simply not accessible by humans [76]. Another important aspect of karst landforms is that, given that they form and evolve over several millions of years, most of them have been exposed to the alternation of glaciation and warming events from the Pleistocene.

---

[5]*Karst* is a germanized form of *Kras*, the original name of a carbonate plateau located north-east of the Adriatic Sea, near Trieste (Italy). The exact area covered by *Kras* remains the subject of ongoing discussions [231].

Speleothems formed within karstic caves, and particularly stalagmites, are therefore of great interest for palaeoclimate reconstruction. In particular [56], (i) they have a worldwide presence and are widely distributed (see Fig. 1.3), (ii) they are often well-preserved given the little variability of environmental conditions (temperature, atmosphere composition) inside caves, (iii) they can be precisely dated, and (iv) they contain a variety of palaeoclimate indicators. Speleothems can be found in many geometric forms, although they result from the same chemical reactions. In the following, we start by detailing the chemistry leading to speleothem formation and review a few existing types of speleothems found inside of a cave in Sec. 1.2. While all cave formations exhibit interesting features, from there we only focus on stalagmites, which are more useful for palaeoclimate reconstruction. We then describe how cross-sectional cuts of stalagmites are used as palaeoclimate proxies in Sec. 1.5, with a particular emphasis on the dating techniques and palaeoclimate indicators generally used in reconstruction studies.

1.2 Chemistry and mechanisms of speleothem formation

The chemical reactions leading to calcite dissolution or precipitation in karst systems have been long well established. While dissolution occurs in limestone bedrocks, yielding, among others, cave formation, precipitation often occurs within caves and is responsible for, e.g., the emergence of stalagmites [35]. As aforementioned, the aragonite form of calcium carbonate is a less commonly used proxy for palaeoclimate reconstruction than its calcite counterpart [141], primarily because the aragonite form is metastable and may yield recrystallisation over existing speleothems. Calcite also constitutes about 90 % of karstic concretions [143]. Hence, only calcite formation is considered here. Without detailing all the elementary reactions at play, we recall that, like most carbonate compounds, calcite can be dissolved into an acid medium [174], yielding the reaction

$$CaCO_{3,(s)} + 2H^+ \leftrightarrows Ca^{2+} + H_2O + CO_{2,(aq)}, \tag{1.1}$$
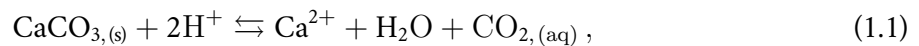
with $CaCO_{3,(s)}$ the calcite form of calcium carbonate and $CO_{2,(aq)}$ the dissolved carbon dioxide. Note that the former reaction is a combination of three different attacks from the system H_2O-CO_2
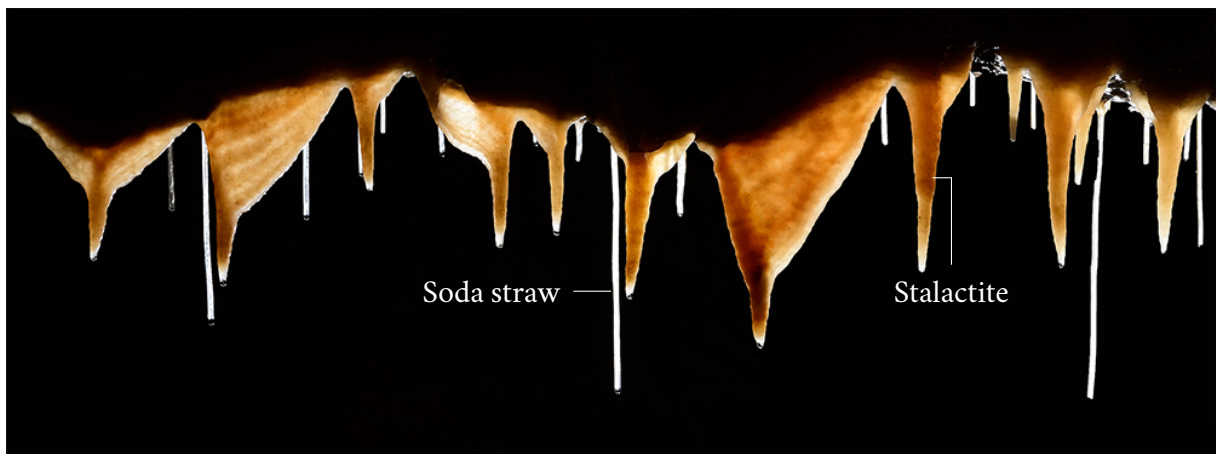
Figure 1.4: Group of soda straws and stalactites hanging from the ceiling of Han-sur-Lesse cave (Belgium). Soda straws are very thin concretions formed by accumulation of calcite rings around drops hanging from the cave ceiling. Stalactites accumulate thicker deposit layers around the central cavity when other drops flow along the ceiling until they reach the outer wall of the stalagmite, thereby precipitating on the outside of this wall and allowing the stalactite to thicken. The ceiling shape of the photograph illustrates well how the drop trajectories inside and outside the drips may enlarge stalactites. Some stalactites from the photograph even show features similar to flowstones (see Fig. 1.6 (a)). The length of the labeled soda straw in the photograph is about 15 cm to 20 cm. Courtesy of P. Crochet [58].
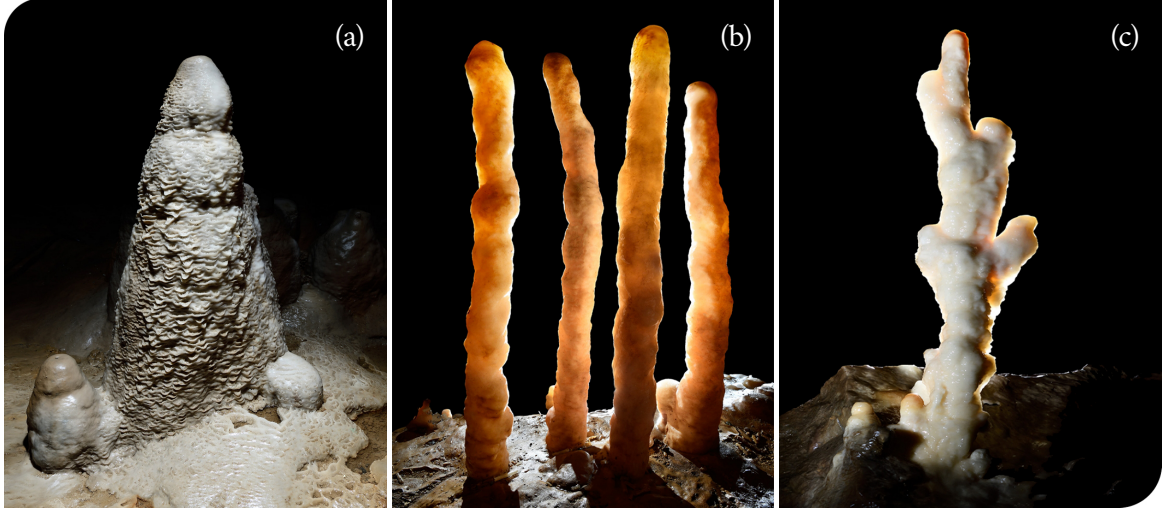
Figure 1.5: Stalagmite examples. (a) A large, human-size stalagmite from Han-sur-Lesse cave (Belgium) with micro-gours forming on the outer wall and rimstones around the base. (b) Four very similar stalagmites, approximately 40 cm to 60 cm tall, from Père Noël cave (Belgium). (c) A stalagmite constituted by a series of tiny stalagmite portions that have only grown for a short time, stacked on one another. The ensemble may result from a group of close dripstones either not active at the same time or that have been sequentially active before drying out for good. The resulting concretion comes from Père Noël cave (Belgium) and should be about 60 cm to 80 cm tall. Courtesy of P. Crochet [58].

to the calcite surface [70]. We come back in Sec. 1.3 to the possibility of having ions and compounds in solution at the surface of stalagmites. Simultaneously, the carbon dioxide CO_2 is converted into bicarbonate ions HCO_3^- as [174]

$$CO_{2,\,(aq)} + H_2O \underset{k^+}{\overset{k^-}{\leftrightarrows}} H^+ + HCO_3^- \,. \tag{1.2}$$
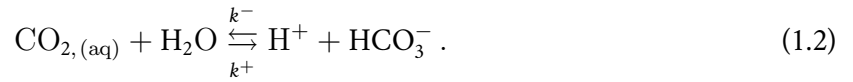
In a lack of dissolved carbon dioxide $CO_{2,\,(aq)}$, the bicarbonate ions quickly reform with the protons in solution, promoting the reverse reaction. The global reaction of dissolution ($\rightarrow$) and precipitation ($\leftarrow$) of calcite into calcium ions is thus given by [174]

$$CaCO_{3,\,(s)} + CO_{2,(aq)} + H_2O \leftrightarrows Ca^{2+} + 2HCO_3^- \,, \tag{1.3}$$
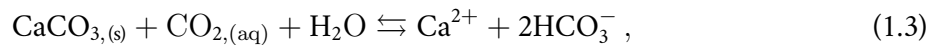
The above reaction is dominated by the amount of dissolved carbon dioxide in the solution. If the partial pressure in CO_2 is larger in the environment surrounding the solution, dissolved $CO_{2,\,(aq)}$ will enter the solution and promote the direct reaction, i.e., the dissolution of calcite into calcium ions. Conversely, if the dissolved $CO_{2,\,(aq)}$ inside the solution has a sufficient concentration, the carbon dioxide will degas toward the outside of the solution and cause precipitation [174]. The processes have very close kinetics of reaction, which is why they can both be found in karst. In Eq. (1.2), the direct reaction rate is denoted k^+ and the reverse one k^-, both depending on the solution temperature, pH, and dissolved excess ion concentrations. At 25 °C and pH $\lesssim$ 8, e.g., we have $k^+ \simeq 3 \times 10^{-3}\,\mathrm{s}^{-1}$ and $k^- \simeq 2 \times 10^{-3}\,\mathrm{s}^{-1}$ [216]. Dissolution usually occurring in the limestone right above the caves in closed system conditions continues inside the stalactites hanging from the ceiling of the caves [35, 76]. On the other hand, for open systems such as stalagmites, the partial pressure in $CO_{2,\,(aq)}$ is often larger than in the cave, in the vicinity of the stalagmite. Hence, degassing of carbon dioxide from the film toward the cave atmosphere is at the origin of calcite precipitation forming stalagmites [35, 76].

Figure 1.6: Drip- & flowstones. (a) Draperies are sheetlike flowstones, here from Han-sur-Lesse cave (Belgium), measuring roughly 2 m to 3 m in length. (b) Helictites, here from Aven d'Orgnac (France), either grow in a non-vertical direction or change their growth direction over time. The helictites in the photograph are about 5 cm to 10 cm long. Courtesy of P. Crochet [58].
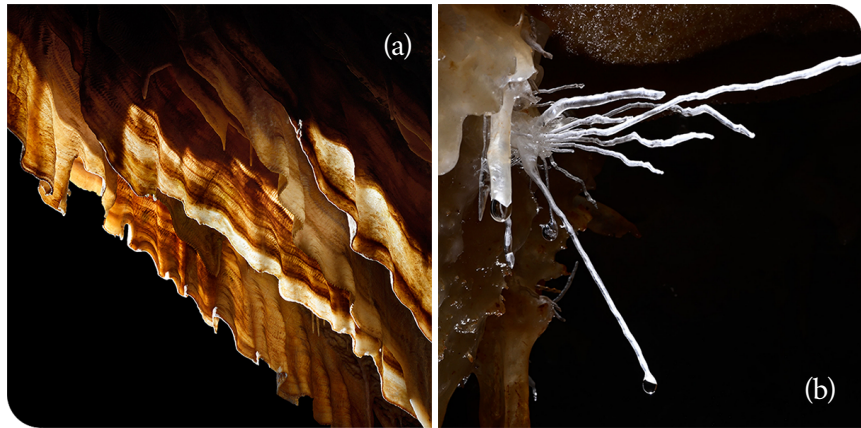
Dissolution and precipitation are thus responsible for the formation of all types of speleothems inside karstic caves. Speleothems can grow downward from the ceiling, upward from the floor or along cave walls. Drops of water can hang from cave ceilings and, instead of falling, remain attached long enough for calcite rings to form due to precipitation directly on the area surrounding the drops. The accumulation of calcite rings leads to the formation of soda straws [56], as illustrated in Fig. 1.4. If precipitation leads to further accumulation on the sides of the soda straw, additional external layers of calcite may yield the formation of wider stalactites [56], as shown in Fig. 1.4, which are nonetheless still hollow. Flowstones are large formations of calcite deposits usually found close to cave walls [111], which can reach sizes of the order of several metres, as illustrated by Fig. 1.6 (a) showing draperies, a particular flowstone. Rimstones are similar formations found on the floor, often looking like staircases and presenting micro-gours at their surface, i.e., an array of tiny basins of the order of the centimetre [111] (see Fig. 1.5 (a)). On the floor of caves, stalagmites grow by accumulation of calcite layers deposited on top of each other. Examples of stalagmites are shown in Fig. 1.5 (a-c). Stalagmites present a large variety of shapes themselves, to which we come back further in the text. When a stalactite and an underlying stalagmite join each other, they may form a complete column. Other varieties of speleothems are found in caves and are not limited to calcite-based formations, including, e.g., helictites, i.e., speleothems that change their growth axis because of capillary forces acting during the precipitation [35, 231] (see Fig. 1.6 (b)), aragonite crystals (see Fig. 1.7), networks of pearls or pisolithes (see Figs. 1.8 (a-b)), coloured concretions due to bacterial activity [105] (see Fig. 1.8 (b)), and many more.

Hence, stalagmites are not the only speleothems presenting a clear sequence of growth. However, stalactites grow faster and are formed both around a central conduit and by accumulation on the already existing outer wall by non-trivial processes, making them more difficult to interpret [56]. Other types of concretions, e.g., helictites, involve additional processes to the calcite precipitation, so that they are not well suited for interpreting past signals either. Stalagmites often present a clear chronological

Figure 1.7: Aragonite crystal needles from Clamouse cave. Aragonite is a metastable form of calcite at cave temperatures. The droplets in the photograph have a diameter measuring between roughly 2 mm and 8 mm. Courtesy of P. Crochet [58].

Figure 1.8: Drop impacts on a deep reservoir covering a network of pisolithes in caves. Pisolithes are grain-like calcite formations resembling pearls, with a diameter comprised between a few millimetres and about 3 cm. (a) Pisolithes in the bottom of a small basin covered by sand. The drop impact on the liquid layer covering the basin is accompanied by a growing crown. (b) Large network of blue pisolithes found in a Southern France cave, exhibiting a surprising blue colour. Two drop impacts producing central jets can be seen impacting the water surface. See Ch. IV on drop impacts. Courtesy of P. Crochet [58] ((a) and (b)).

axis growing upward and an annually sequenced, high-resolution stratification, making them ideal for palaeoclimate reconstruction. To achieve this reconstruction, dating techniques must be used to identify and calibrate specific periods in the temporal signal obtained from the stalagmite cross-sectional cut [76]. We first review in the next section the exact physical processes at play that allow, in addition to the calcite precipitation, the emergence of stalagmites. We then come back to the dating of the yearly deposited layers of calcite forming stalagmites, along with their implications for palaeoclimate reconstruction, in Sec. 1.5.

1.3 Narrative of a drop in a cave

Ions precipitating and leading to stalagmite growth are found in solution within a thin residual film covering the stalagmite, which is fed by drops infiltrating the karst then dripping from the ceiling of caves. Figure 1.9 depicts the trajectory followed by a drop until it falls onto a stalagmite. Rainfall are responsible for renewing the water both above and below the ground. Once rainfall drops approach the ground, they can be partially captured by the canopy of trees and plants. Splash often occurs when drops impact plant leaves and twigs [144, 145], hence quantifying exactly the amount of water actually reaching the ground can reveal tricky. Some drops also directly land on the ground or flow along the sides of the trees, while runoff and evapotranspiration from the soil and plants tend to diminish the quantity of water penetrating underground [83]. Although we cannot estimate exactly the amount of water that actually reaches the interior of the cave, it can be safely assumed that underground water recharge varies seasonally and regionally, as rainfall do [56, 231].

As water drops travel through the atmosphere, encounter vegetation then infiltrate the soil, they are progressively loaded with various ions and chemical species [35, 56], including dissolved CO_2, as well as Ca^{2+} and HCO_3^- ions. Finally, when water reaches the ceiling of the cave, it can flow through the end tip of stalactites [56]. Once the weight of the drop becomes sufficient, the drop drips from the stalactite tip and falls, until it often encounters a stalagmite located beneath the stalactite. The precipitation allowing the stalagmite to grow comes from the ions carried by the drop.
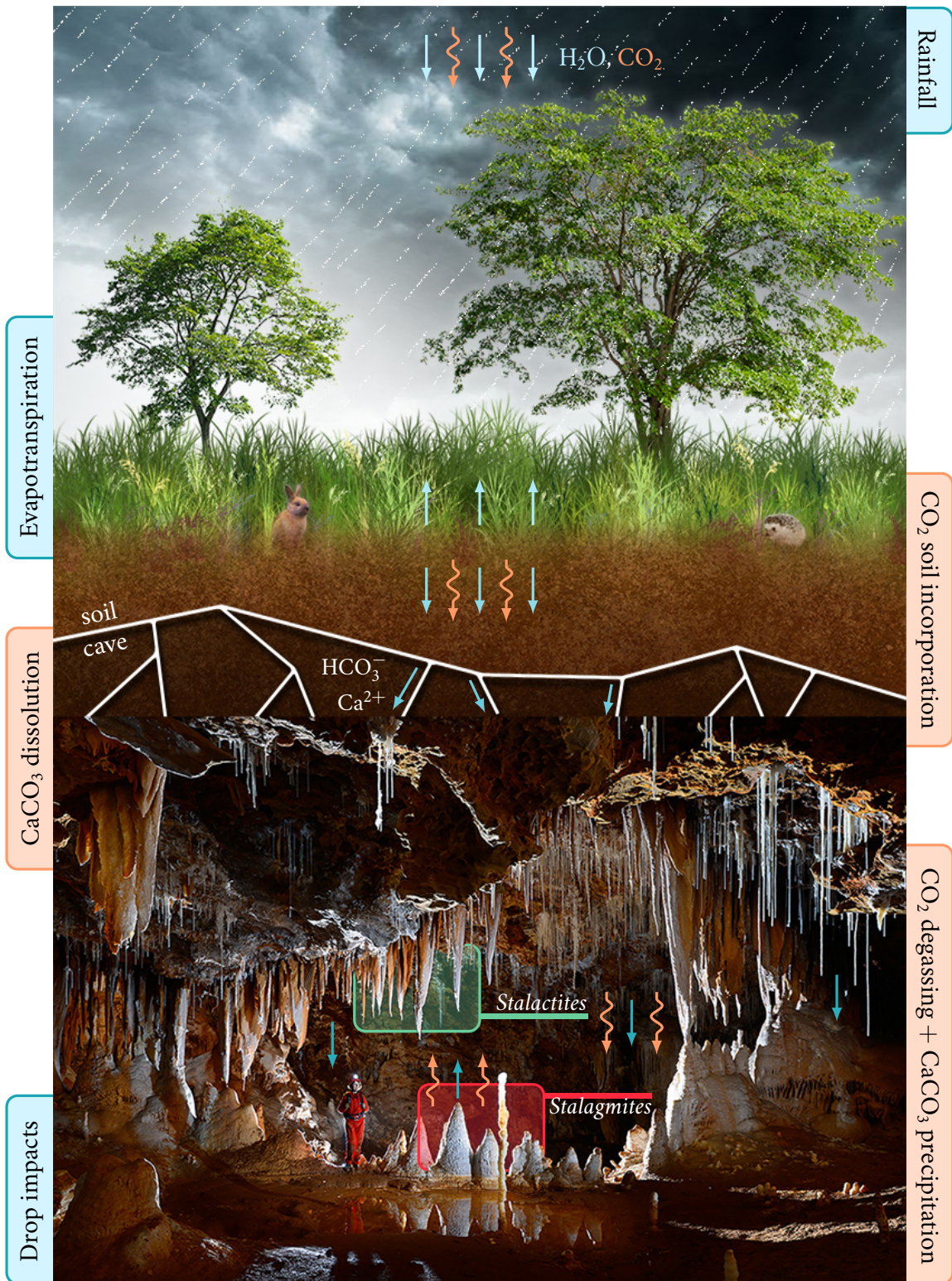
Figure 1.9: Complete trajectory of a drop, from rainfall to the impact on a stalagmite. The water-related processes are described in blue, while the processes associated with stalagmite growth because of the ion precipitation are drawn in orange. Blue arrows indicate the water trajectory. Downward orange arrows indicate ion loading or ion incorporation through the soil. Upward orange arrows indicate precipitation/carbon dioxide degassing. The bottom photograph was taken by P. Crochet in Clamouse cave [58]. The group of large stalactites is called "the Jaw".

Each drop falling from the above stalactite and impacting this film brings in new calcium and bicarbonate ions. The stalagmite growth rate depends on the concentration of these ions [18], which is set by the dissolution of limestone upstream [70]. The calcium ions precipitate in the film as long as the partial pressure p_{CO_2} of the cave is sufficiently low, or that the partial pressure p_{CO_2} in the drop is sufficiently large [21, 68, 195]. The amount of dissolved CO_2 gained from the vegetation and soil above the cave by the drops can become very large compared to the partial pressure in CO_2 in the cave atmosphere [70]. The partial pressure in CO_2 in the soil can even reach 10 % of the soil atmosphere content [230]. The growth rate also depends on the dripping rate at which the water within the film lying on the stalagmite is partially renewed. This rate varies with both inter-annual and seasonal changes of recharge and weather events [95, 99]. Dripping rates are higher during the rainy season [98], at least when the groundwater path upstream of the stalactite is sufficiently short [161]. If the soil layer thickness above the cave is large, it will act as a reservoir that can sustain more uniform dripping periods for longer periods of time [96]. The stalagmite growth rate also depends on the temperature in the vicinity of the stalagmite [70], and on the plant and microorganisms in the soil above the cave, which directly influence the carbon content of the drops [56]. It is also possible for drops to induce precipitation at higher altitudes where no vegetation is present above the surface, since stalagmites were also found in mountains subjected to year-long glaciation, although they present smaller growth rates [56, 70].

Finally, the growth rate depends on the thickness h of the liquid film, which typically ranges between 50 μm and 300 μm [172]. The film likely results from a balance of the incoming flow rate that drips from the associated stalactite [60] and the gravity-induced drainage along the sides of the stalagmite, although there is currently no dedicated hydrodynamic model that rationalizes this assumption [20]. By contrast, a model that couples equations of chemical kinetics and thin-film hydrodynamics has already been proposed to describe the growth and shape of stalactites [196, 197]. A complete model of the dissolution/precipitation kinetics of calcite coupled to the ion transport by molecular diffusion within a thin water film was proposed and validated experimentally by Buhmann and Dreybrodt [41, 42]. These authors then suggested a numerical model [68, 70] to estimate the vertical, time-averaged, growth rate of a stalagmite. The model was also compared to ice and deep-sea core data by Kaufmann [133], who used temperature variations along with changes in precipitation and soil coverage to derive stalagmite stratigraphies reflecting paleoclimate variations over long periods of time ($> 300\,000$ a). Although Dreybrodt's model yields a good approximation of the average vertical growth rate (though once the film thickness is arbitrarily adjusted), it fails at capturing the horizontal heterogeneity of the lamina thickness, caused e.g. by stalagmite roughness and curvature [20]. Therefore, it cannot reproduce the wide variety of stalagmite shapes and sizes observed in a cave. Consequently, only cylindrical, regular stalagmites (as shown in, e.g., Fig. 1.5 (b)) were used so far as paleoclimate proxies because of their apparent regularity [17]. We come back to a more detailed description of Dreybrodt's model in the following section, before reviewing the analysis of the laminae formed by the stalagmites in Sec. 1.5.

1.4 Existing model of stalagmite growth

The model developed by Dreybrodt et al. [41, 42, 70] focuses on regular stalagmites, i.e., stalagmites forming a column of more or less constant diameter, of diameter comprised between 3 cm and 10 cm. The model is based on an idea already proposed by Franke [90], that when a drop impacts the ground below the stalactite, it spreads out radially and subsequently yields the apparition of a thin disc of calcite through ion precipitation in the liquid left by the drop. The precipitation would be the greatest at the centre and would cause the calcite disk to be thicker toward the centre than the outer edges. This process would then be repeated for many drops, increasing the stalag-

mite height by building up a "series of dome-shaped layered hoods one above the other", to quote Franke [90]. The stalagmite would then keep the same shape as long as the parameters determining its growth remain constant [70].

Following this, in Dreybrodt's model a few assumptions are made. (i) The model only considers axisymmetric stalagmites and approximates the stalagmite surface as an n-points polygon. An example is depicted in Fig. 1.10 (a). (ii) Once equilibrium is attained, the stalagmite is supposedly subjected to the same vertical growth rate in all points. The growth rate allowing to calculate the next stalagmite shape is then defined perpendicularly to the stalagmite surface. (iii) The drop bringing in new ions would always land at the centre of the apex of the stalagmite, on a film with constant and uniform thickness, denoted h, empirically measured as $100\,\mu$m [70]. (iv) In all points of the stalagmite surface denoted η at a given time, the subsequent stalagmite surface is obtained by adding a vertical growth increment $\Delta\eta$, mitigated by an arbitrary function decreasing with the distance to the impact point. This growth rate function is defined in point i of the surface as follows:

$$\Delta\eta_i = \Delta\eta_{\text{Drey}}^{\text{max}} \exp\left(-\frac{|P_0 P_i|}{\lambda}\right), \quad |P_0 P_i| = \sum_{j=1}^{i} \left|P_{j-1} P_j\right|, \tag{1.4}$$

with λ a constant defined as the stalagmite radius and $|P_0 P_i|$ the distance from point P_0 to point P_i. The increment $\Delta\eta_{\text{Drey}}^{\text{max}}$ is the maximum increment at the dripping point position, i.e., in η_0, corresponding to $\Delta\eta_{\text{Drey}}^{\text{max}} = 0.1\,\text{cm}/(\Delta t)$, with Δt the time needed for the stalagmite to grow by 0.1 cm (we attribute the specific name of $\Delta\eta_{\text{Drey}}^{\text{max}}$ to the maximum growth rate at the centre as we come back to this parameter in Ch. VI). An equilibrium and a constant radius of λ would then be reached after the stalagmite has grown from the floor by a height equivalent to twice its diameter, under constant conditions of growth. This equilibrium shape would then grow up by translation along the stalagmite axis, which is always oriented upward. As emphasised by Eq. (1.4), the growth rate decreases with increasing distance from the central dripping point as a monotonic function, until it reaches a null value after a certain distance.

Growth rates are computed according to the method already described by Curl [60]. Drops of volume V_{d} and containing ions in a concentration c_{d} fall periodically on the stalagmite and are separated by a time t_0. If a drop falls into the film of thickness h and of initial excess ion concentration c[6] lying on the stalagmite, according to Dreybrodt [70], either part of the film or all of it should be replaced by the drop. After the drop addition to the film, the newly formed film should thus end up with a new ion concentration c', obtained as

$$c' = (1 - \phi)c + \phi\, c_{\text{d}}, \tag{1.5}$$

where ϕ is a mixing coefficient between the drop and the film (see Ch. IV for details). In Dreybrodt's model, a linear approximation of the calcite deposition is further made by using Fick's law. It is assumed that the precipitation flux, or the change in excess ion concentration in film, c, is proportional to $-\alpha c$, with α a fitting parameter having the dimensions of a length per unit time [70]. Hence, the change in excess ion saturation should evolve over time as

$$\partial_t c = -\frac{\alpha c}{h}, \tag{1.6}$$

---

[6]The excess ion concentration is defined as $c = \left(\left[\text{Ca}^{2+}\right]_{\text{sat}} - \left[\text{Ca}^{2+}\right]\right)$, where $\left[\text{Ca}^{2+}\right]$ is the concentration of the calcium ions in solution, and $\left[\text{Ca}^{2+}\right]_{\text{sat}}$ is the saturation calcium ion concentration. Details are provided in Ch. VI, although the parameter c is defined differently within that chapter than in the present section.
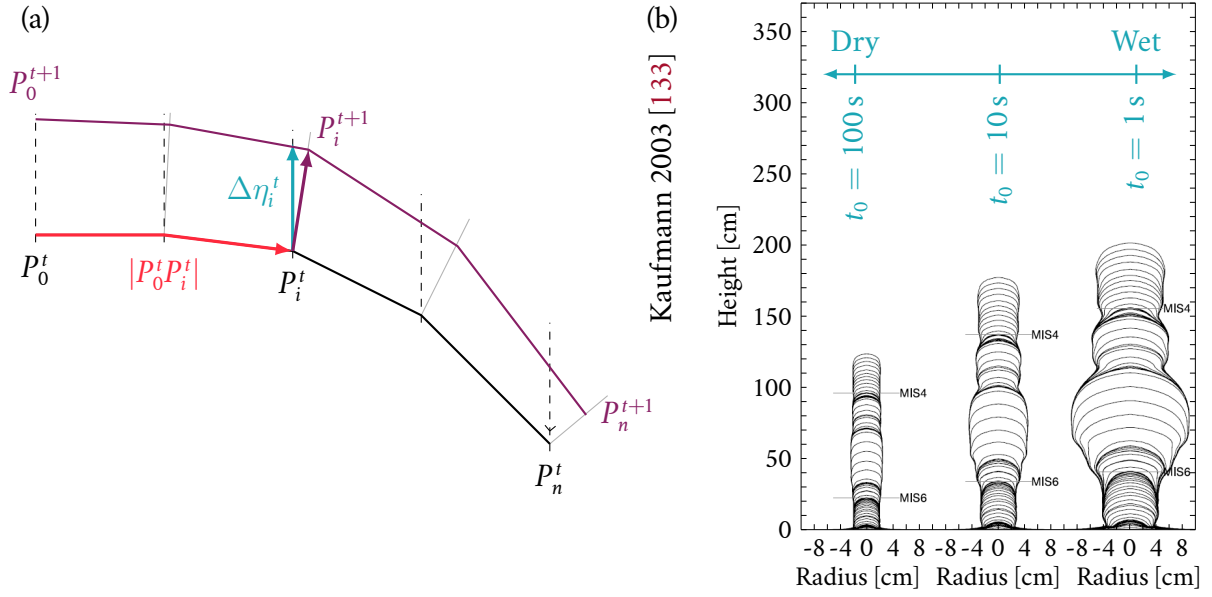
Figure 1.10: Dreybrodt's model illustrations. (a) Evolution of the stalagmite surface at successive times t and $(t+1)$ from Dreybrodt's model [70]. The points P_i^t show the stalagmite geometric surface at times t and $t+1$ (black and mauve polygons). The dashed lines correspond to the verticals drawn from each point P_i^t. The gray lines correspond to the perpendicular lines to $P_{i-1}^t P_i^t$. The vertical increment $\Delta\eta_i^t$ comes from Eq. (1.4). Drawing is copied from Fig. 10.3, p. 259 in [70]. (b) Example of the evolution over time of stalagmite shapes created using Dreybrodt's model, by varying the dripping period in between the drops. The time span in between successive lines is 1000 y. Adapted from Kaufmann 2003 [133] (Fig. 13).

which admits a time exponential solution for the excess concentration c, with a decay time denoted $t_{\mathrm{p}} = h/\alpha$ that we will detail in Ch. VI. Combining these results and averaging the excess ion concentration over time yields

$$\partial_t \langle c \rangle = \frac{\alpha \phi c_{\mathrm{d}}}{t_0} \frac{\left[1 - \exp\left(-\dfrac{t_0}{t_{\mathrm{p}}}\right)\right]}{\left[1 - (1-\phi)\exp\left(-\dfrac{t_0}{t_{\mathrm{p}}}\right)\right]} , \tag{1.7}$$

where $\langle \cdot \rangle$ designates the time average over the dripping period t_0. Depending on the ratio between t_0, the time period between two drops, and t_{p}, the decay time of excess ion concentration relative to Eq. (1.6), different regimes appear, denoted: (i) low flow, such that $t_0 \gg t_{\mathrm{p}}$, and (ii) high flow, for which $t_0 \ll t_{\mathrm{p}}$. In the low flow regime, the supersaturation excess tends to zero before a new drop arrives, while in the high flow regime, the supersaturation excess remains close to c_{d}. Dreybrodt further considers that, away from the stalagmite, the solution should have lost its supersaturation, i.e., all the ions should have precipitated into the film over a radius of deposition called r_{sm}, the stalagmite radius. The amount of ions brought by the drops precipitating over the dripping period t_0 should correspond to the average growth over this radius, i.e.,

$$\frac{V_{\mathrm{d}} c_{\mathrm{d}}}{t_0} = \partial_t \langle c \rangle \, \pi r_{\mathrm{sm}}^2 . \tag{1.8}$$

In the low flow regime, the stalagmite radius should become

$$r_{\mathrm{sm}} = \sqrt{\frac{V_{\mathrm{d}}}{h \phi \pi}} , \tag{1.9}$$

13

such that the radius decreases for increasing h, i.e., for a thicker film. In the high flow regime,

$$r_{\text{sm}} = \sqrt{\frac{V_{\text{d}}}{\pi \alpha t_0}} \,.$$ (1.10)

Hence, in this regime, the stalagmite radius would decrease with increasing dripping period, i.e., with decreasing drop inflow. On the other hand, it increases with increasing fit parameter describing how fast the ions precipitate in the film, α. A larger α would correspond to a faster precipitation of the ions in solution.

The above model was later used by Kaufmann [133], along with the inclusion of the effect of the temperature on, e.g., p_{CO_2} and, therefore, α (see Ch. VI), to reproduce stratigraphies of stalagmites with variable parameters. This is illustrated by Fig. 1.10 (b) for a variable dripping period between the drops, t_0, assuming a common temperature variation for the three stalagmites presented in the figure. Temperature records were derived from an ice core from Greenland over two glaciation cycles, while other parameters in the model were kept constant, except for t_0 which was set to 100 s (low flow), 10 s and 1 s (high flow) in Fig. 1.10 (b), respectively. The resulting shapes obtained by Kaufmann depict how the aforementioned stalagmite radius from Eqs. (1.9) and (1.10) evolves with the dripping period of the drops, t_0. The dripping period also affects the growth rate over time as layers become thicker with decreasing t_0.

We note that some physical processes observed to occur in caves are not captured by the model presented above, or that some simplifying hypotheses were made but may prove inadequate. We list the issues that we are able to identify hereafter:

- First, the drops are assumed to always land at the apex of the stalagmite, which is contradicted by empirical observations.

- The thickness of the film is assumed to remain constant over the entire stalagmite in the model. The model produces curved stalagmite surfaces, as shown in Fig. 1.10, which resemble actual stalagmites. However, this suggests that the film could experience gradients caused by, e.g., gravity-driven drainage, which should further be affected by the local surface curvature and film thickness.

- Gradients appearing in the film should further be responsible for variations in the ion distribution, while the only parameter affecting this concentration in the model is the inclusion of the successive drops into the film, as shown by Eq. (1.5). In reality, the ions being displaced in the film away from the drop inclusion position at the apex precipitate at the same time as they are being carried away, which could lead to a decrease in c departing from the apex. The growth from Eq. (1.4) also assumes that the vertical growth is constant along the stalagmite while the growth perpendicular to the local surface decreases exponentially with the distance from the apex of the stalagmite. Although the combinations of these effects may yield a similar effect as having both h and c vary with the distance to the apex of the stalagmite, there is no physical argument supporting the exponential profile considered in Eq. (1.4). Depending on the time needed for the ions to precipitate with respect to the time needed for the film to flow away from the apex of the stalagmite, various regimes of growth could occur.

- To the best of our understanding, the mixing parameter is arbitrarily set to a constant value in the simulations such as the ones shown in Fig. 1.10 (b), and no physical argument is presented to evaluate ϕ in the model derived by Dreybrodt [70], nor in the simulations made by Kaufmann [133] where no mention of ϕ is made. However, several questions naturally arise when considering the mixing occurring during the impact of a drop on a thin film: if the drop experiences splash upon impact, how much liquid can be ejected away? Among these

ejections, which part originates from the impacting drop, and which part belongs to the initial film? Do these parameters depend on impact conditions such as the drop radius, the film thickness, or the drop impact speed? Lastly, are there other relevant parameters affecting this mixing? Without answering these queries, there is no physical rationale permitting to assign a value to ϕ.

- The drops are also considered not to produce any movement in the film that could potentially lead to a new distribution of ions into the film following a drop inclusion in the model. However, as a drop impacts a thin film such as found in caves, it may experience splash and yield liquid ejection away from the stalagmite [227, 235].

- In the low flow regime approximation yielding the stalagmite radius from Eq. (1.9), the radius is only set by the amount of ions brought into the film. This approximation considers that the decay time of the excess ion concentration, t_p, is sufficiently shorter than the dripping period between two drops, t_0, for the ions to have entirely precipitated before a new drop is brought into the film. At constant drop concentration c_d, the amount of ions that precipitate in between two drops should indeed increase with the drop volume and decrease with the film thickness. However, according to Eq. (1.9), the stalagmite radius would decrease with increasing mixing factor between the drop and the film, ϕ, and reach a maximum value at $\phi = 1$. In the low flow regime, if all the ions have precipitated between two successive drops, $c = 0$ right before a new drop is added into the film according to Eq. (1.5), such that a value of $\phi = 1$ should yield the maximum possible amount of ions that may precipitate into the film. Not finding that the radius increases in this case is therefore counterintuitive, or at least indicates that some physical processes are not taken into account to conclude whether these ions should yield a larger radius or a thicker layer of newly precipitated ions. Note that this discussion can be made based on Eqs. (1.7) and (1.8) and thus does not depend on the regime considered.

- In the high flow regime such that $t_0 \ll t_p$, the concentration of ions in solution should reach a steady-state because of the balance between the ions that precipitate in between two drop inclusions into the film, and the ions brought by the succesive drops. However, Eq. (1.10) suggests that r_{sm} could continuously keep increasing for decreasing dripping periods, and even reach infinite values. The continuous inflow should be constrained by other limits.

- While the stratigraphies presented in Fig. 1.10 (b) are based on actual palaeoclimate records, they cannot be compared to stalagmite cuts that would correspond to the parameters used. It is therefore difficult to asses the validity of the model regarding the effect of, e.g., the dripping period on stalagmite growth.

- Finally, we can also point out that the case where the film would eventually dry out is not considered here. Even by setting $\phi = 0$, because the drainage and evaporation of the film are not taken into account, it is not possible to model the particular case where the dripping period of the drops is long enough for the film to disappear in between impacts, while this should clearly be the case for a stalagmite being only fed by one drop over several days [133].

In the light of these observations, we note that some important physical processes are not taken into account: (i) the aerodynamics of drops freely falling in caves, (ii) the interaction between the drop and the residual film lying on the stalagmite as the drop impacts the film, (iii) the effect of gravity-driven drainage on the film thickness evolution with time and space in between drop impacts, and (iv) the comparison between the inflow of drops, i.e., their dripping period, with the drainage of the film and precipitation of the ions in solution. We come back to these processes in Sec. 2. The next section focuses on the annual growth of stalagmite laminae and the associated dating techniques.

1.5 Properties and analysis of annually laminated stalagmites

In order to reconstruct palaeoclimate history from annually resolved proxies such as laminated stalagmites, it is important to precisely date sections of the proxy, in this case of laminae from the stalagmite cross-sectional cut [35, 231]. Speleothems such as stalagmites provide the opportunity to use different dating methods, including, but not limited to laminae visual identification, radioactive nuclide dating which can be based on, e.g., the decay of ^{234}U into ^{230}Th, or even thermoluminescence [19]. The ^{234}U into ^{230}Th dating is a widely used technique and allows to date samples back to about 500 ka. In addition to the precise dating of specific stalagmite portions, the most common indicators inferred from stalagmites are the variations in oxygen and carbon isotopes found within the stalagmite [220]. Isotopes are chemical elements having identical atomic number but different atomic masses, i.e., a different number of neutrons. In particular, the ^{18}O isotope, resp. ^{13}C, is one of the stable isotopes of oxygen, resp. carbon, and represents approximately 0.1995 % of the Earth's oxygen, resp. 1.11 % of the Earth's carbon [56, 134]. Measurements of δ^{18}O and δ^{13}C are collected from stalagmite samples by isotope ratio mass spectrometry. Once the sample is prepared, the extent to which the ions are deflected by the magnetic field inside the mass spectrometer depends on their mass-to-charge ratio, such that the ratios of heavy to light isotopes, i.e., of ^{18}O/^{16}O for instance, can be deduced from the sample. The measurements are then expressed as δ^{18}O, the variations with respect to a standard variation. In other words, δ^{18}O does not represent the absolute variation between the contents in ^{18}O and ^{16}O within the stalagmite; δ^{18}O rather corresponds to the relative difference between ^{18}O/^{16}O from the sample and the standard value of ^{18}O/^{16}O [56], therefore expressed in percents. Examples of the δ^{18}O signals from several stalagmites juxtaposed to each other are represented in Fig. 1.2 from Sec. 1. The isotopic variations in δ^{18}O are usually used for temperature and rainfall pattern reconstruction, while the variations in δ^{13}C contain information regarding the vegetation, soil and ecosystems above the cave at a specific period.

Relating, e.g., δ^{18}O to rainfall history is possible because of isotope fractionation, a process where isotopes are separated or distributed differently during physical or chemical processes because of their relative weight. Lighter isotopes, for instance ^{16}O, tend to participate preferentially in some processes such as evaporation or precipitation. During evaporation, the lighter oxygen isotopes tending to evaporate more easily leave behind them a larger proportion of water molecules containing ^{18}O. Regarding carbon isotopes, photosynthesis, e.g., favors the use of ^{12}C rather than ^{13}C isotopes. It is therefore not surprising for δ^{13}C measurements from palaeoclimate proxies to yield precious information on, e.g., past vegetation. During the precipitation of calcite, the calcite and water isotopically exchange at equilibrium as

$$1/3\,\mathrm{CaC^{18}O_3} + \mathrm{H_2^{16}O} \leftrightarrow 1/3\,\mathrm{CaC^{16}O_3} + \mathrm{H_2^{18}O}\,. \qquad (1.11)$$
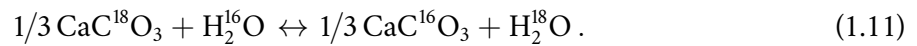
This relation was shown to only depend on temperature [78]. However, because isotope fractionation can be sensitive to various processes, it is sometimes not possible to deduce, from a given stalagmite sample, the exact processes at the origin of the isotope fractionation. The δ^{18}O signal should a priori matches the δ^{18}O composition of local rainfall [170], which is usually known and depends, among others, on the surface temperature. Additionally, isotope fractionation of ^{18}O during calcite precipitation depends on the cave temperature, as shown by Eq. (1.11) above. The combination of these two effects should yield a linear relation of ^{18}O with the past temperature through a stalagmite. [3] However, depending on the thickness of the soil layer above the cave, i.e., the water reservoir feeding the stalagmite, it can become tedious to interpret δ^{18}O variations collected from stalagmite signals [56, 76]. This interpretation requires the knowledge of details about seasonal and inter-annual variability, i.e., about growth rate variations, laminae thicknesses, mineral com-

position of the stalagmite and possible presence of trace elements [219], and the comparison of the signal from the stalagmite with other well-recorded signals from other proxies found in the same area [56, 76]. Similarly, the composition of ^{13}C in the stalagmite depends on the atmospheric carbon dioxide, the karst layer through which water infiltrates when loading in ions, and the carbon dioxide produced within the soil about the cave [170]. Interpreting δ^{13}C variations from stalagmites for paleoclimate reconstruction thus also faces challenges, including the effects of vegetation and soil processes, potential kinetic effects during calcite formation,
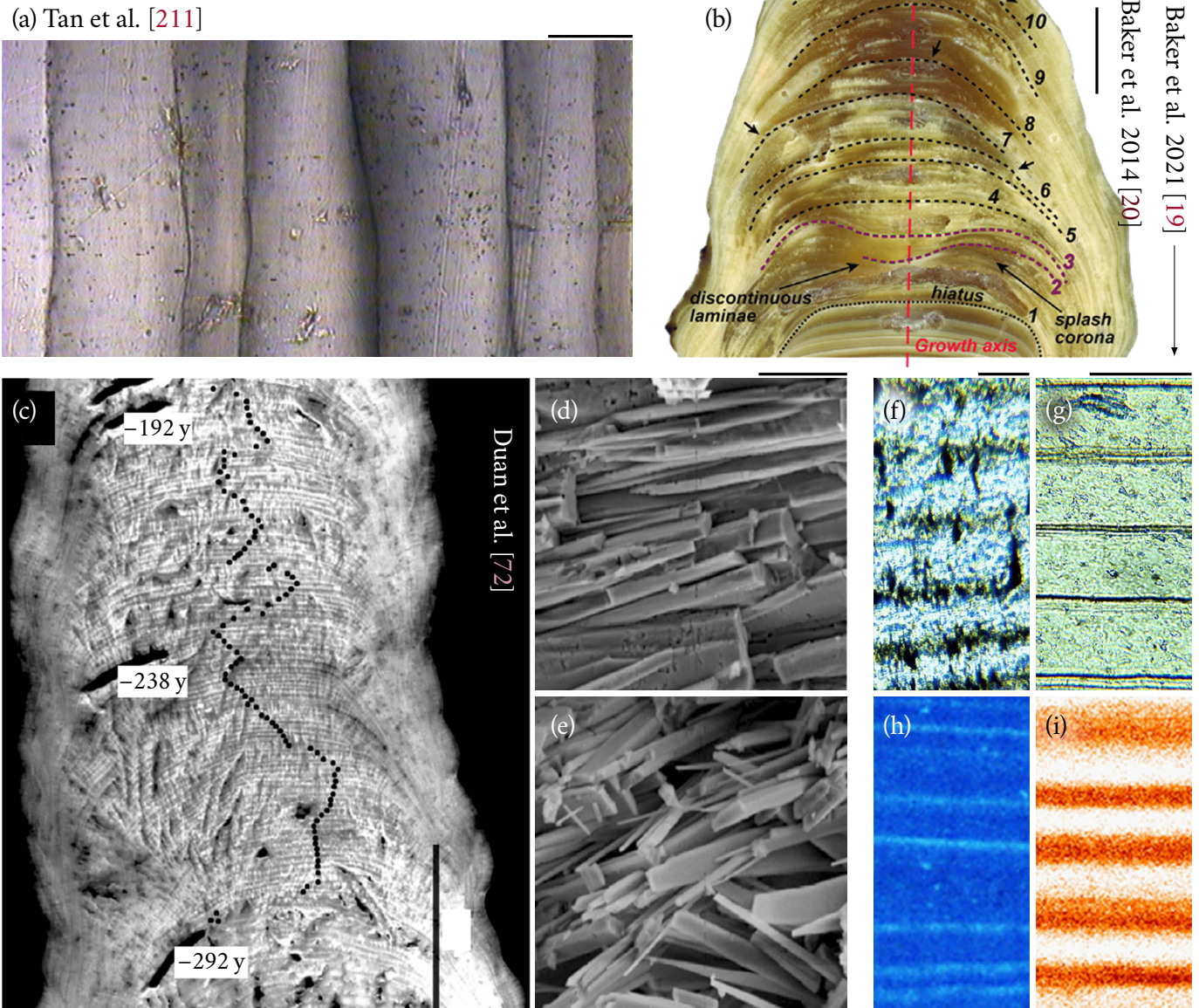
Figure 1.11: Examples of laminae visible in stalagmite cuts, adapted from the literature. (a) Close-up photograph of a stalagmite cut exhibiting laminae of variable thickness. The axis of growth is directly horizontally. The scale bar is 100 μm. Adapted from Tan et al. [211]. (b) Evolution of the laminae displayed by a stalagmite cut. A hiatus, corresponding to a period of absence of growth, is visible at the bottom of the photograph. The scale bar is 1 cm. Adapted from Baker et al. [20]. (c-e) Photograph of a stalagmite cross-sectional cut (c), and scanning electron microscopy pictures of a portion of stalagmite displaying a high grain density calcite (d), and another portion corresponding to a low-grain density calcite (e). The scale bars are 2 cm (c), and 20 μm (d-e). Adapted from Duan et al. [72]. (f-i) Examples of different types of laminae: (f) visible laminae, (g) organic-based laminae, (h) chemical laminae revealed by UV fluorescence, (i) laminae based on Sr traces. The scale bars are all 100 μm (f-i). Adapted from Baker et al. [19].

17

and variations in the isotopic composition of carbon in the source materials [170]. Evaporation, fast precipitation, an interruption during the growth, known as hiatus, or even microorganism activity can also affect the isotope fractionation of both ^{18}O and ^{13}C.

Possible solutions to these issues involve the analysis of the fluid inclusions found within the stalagmite sample, i.e., local trapping of tiny amounts of the water in which the stalagmite calcite has precipitated at a given time in the past [65]. However, analysing sub-microliter volumes of water without inducing artificial isotope fractionation may prove challenging [56, 76]. Another widely used technique consists in performing a Hendy test on some lamina within the stalagmite sample [110]. Isotope fractionation equilibrium conditions are verified if the CO_2 degassing is sufficiently low and there is no evaporation of the film. Hence, over a particular lamina, these equilibrium conditions should yield a progressive change in δ^{13}C from the stalagmite apex toward the outer wall of the stalagmite because of the progressive precipitation, while the δ^{18}O should remain constant because the film thickness should remain sufficiently large to act as a reservoir of ^{18}O [110]. However, there is no dedicated model describing the evolution of the film thickness with the distance to the stalagmite apex. Therefore, if isotope fractionation equilibrium conditions are maintained along a specific lamina, the signal in δ^{13}C and δ^{18}O along this lamina should not present any covariance, and there should not be any enrichment of δ^{18}O so as to validate the absence of film evaporation [110]. Evaporation of thin films as found in caves, which is one of the physical processes involved in the isotope fractionation of ^{18}O and ^{13}C, is dependent of the film thickness [92] as long as the pressure in the film overcomes the disjoining pressure (see Appendix B.5 from Ch. V). Hence, the drainage of the film should also affect ^{18}O and ^{13}C through this process [92]. The limitations of the Hendy test lie within the difficulty to ensure that measurements are performed along one and only one lamina, or the interpretation of the covariance between δ^{13}C and δ^{18}O which may still results from actual paleoclimate variability. The most reliable technique to asses potential out-of-equilibrium conditions of the isotope fractionation consists in verifying whether signals from several contemporary stalagmites from the same area are related to one another [56, 76], but this technique would imply the collection of several samples while caves should remain as unperturbed as possible.

Hence, all these potential effects point out to the importance of measuring the thickness of the laminae constituting the stalagmites as precisely as possible, and to be able to clearly asses the processes that may induce physical isotope fractionation of ^{18}O and ^{13}C. A few examples coming from the literature are shown in Fig. 1.11 and represent the variability presented along one lamina. Figure 1.11 (a) presents a close-up optical view of a stalagmite cut such that the growth axis is oriented horizontally, from left to right. Tan et al. [211] have shown that measuring the successive laminae thicknesses along different routes parallel to the growth axis (i.e., along different horizontal sections in Fig. 1.11 (a)) yields a variability of the in-between lamina thickness measurements, which is visible in Fig. 1.11 (a). This effect is also clearly visible in Fig. 1.11 (b) where a stalagmite cut presented by Baker et al. [20] shows laminae of variable thickness and shape as the stalagmite grows upward. Baker et al. [20] emphasised the lack of constraints existing on the estimation of the film thickness that lead to calcite precipitation for a particular lamina. They tried to infer this thickness from the global curvature of the various visible laminae in the stalagmite cut from Fig. 1.11 (b) by approximating the thickness of the film, h, as constant and equal to V_d/A_{dome} over a dome of surface area $A_{dome} \approx 2\pi r_{dome}^2$, with r_{dome} the dome radius and V_d the drop volume. They conducted lab measurements on domes of various curvature radii and obtained a decreasing film thickness with decreasing dome curvature radius r_d to approximate the film thickness on each of the laminae from Fig. 1.11 (b) in attempting to reconstruct local paleaoclimate variations [20]. As we will show in Ch. V, this estimation can actually be improved.
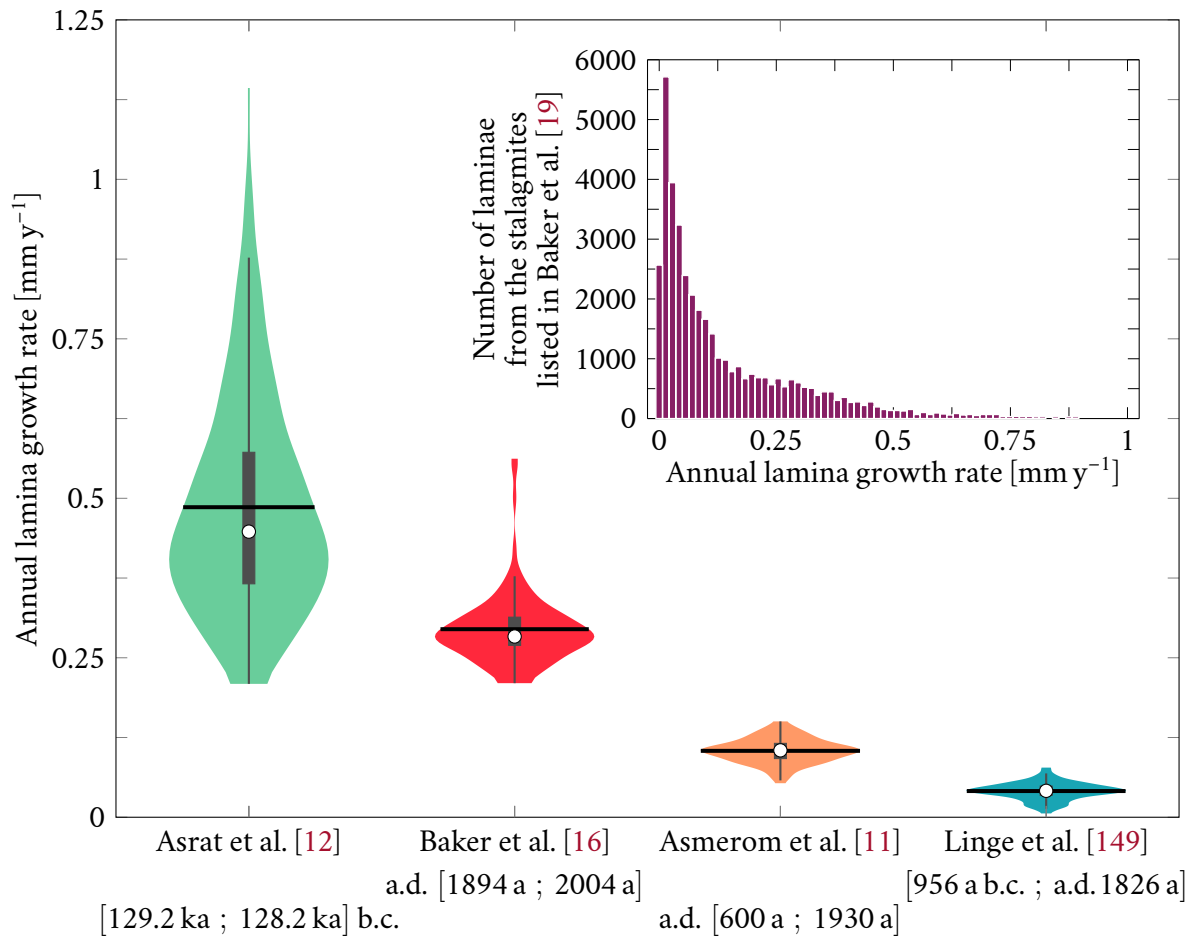
Figure 1.12: Examples of annual lamina growth rates from the literature. The main graph represents violin plots (a violin plot is the combination of a kernel density plot showing the distribution shape of the data (coloured area), and of a usual box plot, which includes the median (white dot ○), the interquartile range (gray box), and the rest of the distribution from which the outliers have been removed (gray line), to which we further added the mean (**thick** black line)). From left to right, the violin plots show data of annual lamina growth rate, i.e., lamina thickness measured over the course of a year, adapted from Fig. 5 in Asrat et al. [12] (green), Fig. 5 in Baker et al. [16] (red), Fig. 1 in Asmerom et al. [11] (orange), and Fig. 5 in Linge et al. [149] (blue), respectively. The inset is adapted from Fig. 5 in Baker et al. [19], and represents a histogram of the number of laminae corresponding to a given annual lamina growth rate, which is approximated as a log-normal distribution by the authors. The data come from an ensemble of 39 time-series of stalagmite laminae analysed in the articles reviewed and presented by Baker et al. [19].

Figures 1.11 (c), (d) and (e) correspond to the same stalagmite cross-sectional cut analysed by Duan et al. [72]. Due to the aforementioned seasonal variability that may exist in δ^{18}O and δ^{13}C signals, the calcite may present variable porosity at different times, depending on the conditions of precipitation. Lamina hue therefore appears lighter or darker depending on whether the stalagmite is fed during a drier or wetter season, respectively [72]. This is particularly visible in the laminae shown in the stalagmite cut from Fig. 1.11 (c). A more compact calcite layer, resp. a less compact one, as shown by scanning electron microscopy in Fig. 1.11 (d), resp. Fig. 1.11 (e), is therefore less porous, resp. more porous. Although laminae can be defined as the annually deposited layers of calcite on the stalagmite, other definitions of laminae in stalagmites may exist due to the recent advances in, e.g., the identification of annual variability of trace elements such as Sr or Mg [219]. In Figs. 1.11 (f)-(i), we represent examples from Baker et al. [19] of the other types of laminae appearing in stalagmites, or laminae obtained through unconventional dating methods for speleothem growth. In Fig. 1.11 (f), physical, i.e., visible, laminae are formed from the aforementioned calcite porosity variability. In Fig. 1.11 (g), the annual variability in organic matter concentration is represented, which may reflect the seasonal transport of soil-derived material [19]. The organic

matter variability may also appear through UV fluorescence, as shown in Fig. 1.11 (h). Finally, annual variations in trace elements, Sr in the case of Fig. 1.11 (i), are known as chemical laminae [19]. It can further be noted that a same stalagmite may present different types of laminae, e.g., both physical and chemical laminae can be measured from the same sample (see, e.g., Figs. 1.11 (f-i)).

In Fig. 1.12, we represent the annual growth rate evolution of physical laminae coming from samples analysed in the literature. The times covered by the samples are indicated below the graph and come from different geological times. The shortest record is the one from Baker et al. [16] (red), which only spans a century while the other records span $\lesssim$ 1000 a. Without detailing the specific conditions relative to each stalagmite, we note in Fig. 1.12 that the annual growth rate of stalagmite laminae (expressed per year y^{-1} and not per annum a^{-1}) is comprised between about $10\,\mu m\,y^{-1}$ and $1000\,\mu m\,y^{-1}$. The four stalagmites illustrated present different distributions. Each distribution is represented under the form of a violin plot, which corresponds to a combination of a usual box plot and a kernel density plot, allowing to represent the exact distribution shape of the data (see caption of Fig. 1.12 for details). The mean is also added to the violin plots. We note that the stalagmites with the larger average growth rates also present a larger variability of growth rates over the entire record, as exemplified by the shapes of the violin plots relative to the stalagmite from Asrat et al. [12] (green) and the one from Baker et al. [16] (red). The distribution from Asrat et al. [12] (green) is also very skewed, which is also indicated by the difference between the mean and median values of the annual growth rate. The distribution from Baker et al. [16] (red), on the other hand, only presents a few outliers. Regarding the distributions of Asmerom et al. [11] and Linge et al. [149], they both present a smaller average annual growth rate, with no identified outliers.

The inset shows a histogram from Baker et al. [20], who reviewed and compiled the annual growth rates measurements of all the laminae from 39 stalagmites analysed in the literature. The ordinate axis thus represents the number of laminae corresponding to a specific annual growth rate, all stalagmites considered. The mean annual growth rate from this distribution is $163\,\mu m\,y^{-1}$, while the median is $93\,\mu m\,y^{-1}$ [19]. It is not surprising to obtain such different values since large annual growth rates are less commonly observed. Large annual growth rates seem to correspond to values above $250\,\mu m\,y^{-1}$. If we assume that all the ions from the drops feeding the film on the stalagmite further precipitate completely, for 100 000 drops impacting the stalagmite per day (which corresponds to a dripping period slightly inferior to 1 s), such a large growth rate would correspond to a growth per drop of 6.8×10^{-12} m, which seems plausible with respect to the values of lamina growth observed in Fig. 1.12. From empirical values observed in caves (see Ch. II), a dripping period of 1 s corresponds to a large inflow. By contrast, an inflow of one drop per day would yield a growth per drop of 6.8×10^{-7} m, which seems aberrant given that it would lead an almost visible new layer of calcite at every drop. Hence, we can infer from these data that large growth rates should be associated with short dripping periods, in accordance with the conclusions from Dreybrodt's model. Depending on the conditions at play, the location of the cave or the geological time spanned by the record, the annual lamina growth of the stalagmites presented in Fig. 1.12 indicates that very different distributions of annual lamina growth rates can be obtained, illustrating once again the complexity of palaeoclimate reconstruction.

2. Outline of the thesis and contributions

In the light of the difficulties arising during the analysis of annually resolved stalagmites and shortcomings of existing models of stalagmite growth, in this work we propose to gain a better comprehension of the aerodynamics and hydrodynamics at play when drops impact stalagmites. Following our description of Sec. 1.3, we may divide the physical processes involving the drop and the residual film lying on the stalagmite into distinct steps. We will omit the upstream path of the

drop before it reaches the cave ceiling in our analysis, although it appears clear from Sec. 1.5 that the water isotope enrichment in the soil above the cave encompasses non-trivial and poorly characterised processes. We will exclusively focus on the drop trajectory once it has reached the tip of a stalactite, which is illustrated by Fig. 1.13 and can be chronologically described as follows: (i) the drop detaches from the stalactite tip and falls through cave air, (ii) the drop impacts the thin film of residual liquid covering the top surface of the stalagmite, (iii) the film flows away from the stalagmite centre because of the gravity-induced drainage and, simultaneously, (iv) the ions in solution precipitate to form calcite, thereby allowing the stalagmite to grow progressively. Other processes at play involve but are not limited to: the diffusion of ions into the film, either in a parallel ($\sim$ horizontal) or perpendicular ($\sim$ vertical) direction to the stalagmite surface, or the evaporation of the film.

These processes present a distinctive feature: the timescale at which they take place. We denote these timescales as depicted in Fig. 1.13. They are also summarised in Tab. 1.0, and recalled in Tab. 1.2 from the auxiliary sheet. Under constant environmental conditions, the drops regularly fall from the stalactites [90]. Two drops are separated by the dripping period, defined as t_0. The dripping period varies by several orders of magnitude, ranging approximately in $[10^{-1} ; 10^7]$ s, i.e., from less than a second to several months [133]. The drop impact on the thin film covering the stalagmite occurs during a short time called t_i, which can be approximated as $2R_d/u_d$, where R_d designates the drop radius and u_d its falling velocity after the drop has fallen over a distance z (see Fig. 1.13). Without even calculating precisely this timescale, it appears quite clear that the impact time should be shorter than one second. As it will be demonstrated in Chs. III and IV, t_i actually is of the order of a few milliseconds. The drainage timescale, on the other hand, is more difficult to evaluate, and so is the ion precipitation timescale. We denote by t_d the typical timescale needed for the ions located in the film to spread out over a given distance. For instance, we could define the drainage timescale as the time needed for the ions to travel a distance corresponding to the radius of the stalagmite top surface. Similarly, the precipitation timescale can be seen as corresponding to the time needed for a certain quantity of ions to have fully precipitated into calcite, cancelling the excess ion concentration in the film. We denote this timescale t_p. Because the hygrometry in most caves is relatively high (see Ch. V for more details), the evaporation can be disregarded at first order. The diffusion time of ions in solution can be approximated by ℓ^2/D, with ℓ the characteristic length of the direction considered, and $D \sim 10^{-9}$ m^2 s^{-1} the molecular diffusion coefficient order of magnitude of most species found in solution in caves [45]. The diffusion over a length scale of the order of the film thickness of about 100 µm [20, 70, 133] yields a diffusion time of approximately 10 s. On the other hand, for ions to cover a horizontal length of the order of a few centimetres, e.g., if a distance of about 5 cm is taken over the stalagmite, this time becomes of the order of three weeks. Hence, horizontal diffusion may be safely neglected. Vertical diffusion will be discussed in the chapters focusing on drainage and precipitation as the three timescales have the potential to be of the same order of magnitude. Additionally, given the eventuality that some timescales might be of the same order, we expect several regimes of stalagmite growth to arise when comparing them. Hence, among these processes, we note that the dripping period t_0, the drainage timescale t_d and precipitation timescale t_p, in particular, should be compared. We gather all these timescales in Tab. 1.0, along with other timescales that will be discussed throughout the following chapters and that we will not comment for now. The auxiliary sheet also comprises the general nomenclature and summarises the timescales presented here (see beginning of the chapter, p. xxii, for details).

The outline of the thesis follows the aforementioned trajectory of the drop linearly, and can be read in Fig. 1.13. Aiming at getting a better comprehension of processes involving drop impacts

and film thickness variability in caves, we directly conducted experimental measurements in caves when possible. We therefore start by presenting the field campaigns that have been carried out in the scope of this work in Ch. II. The next chapter, Ch. III, focuses on the first part of the drop journey in cave, i.e., its free fall from the stalactite tip until the drop reaches the underlying stalagmite top. We then investigate the mixing occurring between the impacting drop and the film lying on the stalagmite at impact in Ch. IV. The gravity-driven drainage of the film is the subject covered in Ch. V. Measurements from caves were obtained for Chs. III and V, while in Ch. IV, we conducted lab experiments. In both Chs. III and V, the experimental measurements are also completed by physical and numerical modelling of the physical processes studied in these chapters. Finally, in Ch. VI, we propose to model stalagmite growth by combining the ion precipitation process to the results obtained from the previous chapter on drainage and the mixing results from Ch. IV. We further add results from Ch. III at the end of Ch. VI. Conclusions and perspectives are then presented in Chs. VII and VIII, respectively. The main research chapters are therefore Chs. III, IV, V and VI, of which we detail the respective contributions hereafter.

In Ch. III, we reveal the key features of drops impacting thin films lying on stalagmites through high-speed imaging, which had until then not been explored. We also propose a theoretical model to describe the trajectory of the freely falling drops, which allows us to compute both the terminal velocity and position of the drops as they impact the stalagmite. We are able to validate this modelling with the experimental data collected from the analysis of the high-speed movies. In this chapter, we also measure the average radius of stalagmites from various caves, and show that this radius is set by the distribution of the impact point position of the drops. We obtain a good correlation between the results of our modelling and the radii measurements.

In Ch. IV, we conduct lab experiments of drops impacting thin films in a similar range of thicknesses as in caves, using once again high-speed imaging. We infer the mixing occurring between the drop and the film upon impact from the videos, by using a colorimetry algorithm that we developed. The total ejected volume at impact, as well as the proportion of the drop entering the film at impact, can also be measured. We are thus able to solve one of the issues arising in the previously existing models of stalagmite growth (see Sec. 1.4). The mixing occurring between the drop and the film is indeed

Figure 1.13: Structure of the thesis according to the evolution of a drop in a cave. The studied stalagmites are described in Ch. II. Drop detachment and free fall are part of Ch. III. The mixing occurring during the impact of a drop on a thin film is treated in Ch. IV. The gravity-induced drainage of this thin film is extensively discussed in Ch. V. Finally, a model of stalagmite growth is presented in Ch. VI. The timescales defined in the picture can be found in Tab. 1.0.

t_0

Chapter III
Drop detachment and free fall

$2R_d$

u_d

z

Chapter II
Stalagmite description

Chapter IV
Drop impact on thin film and mixing

t_i

Chapter V
Thin film gravity-driven drainage

t_d

Chapter VI
Calcium ion precipitation and stalagmite growth

CO_2

Ca^{2+}

$t_\rightarrow$ $t_\downarrow$

t_p

22
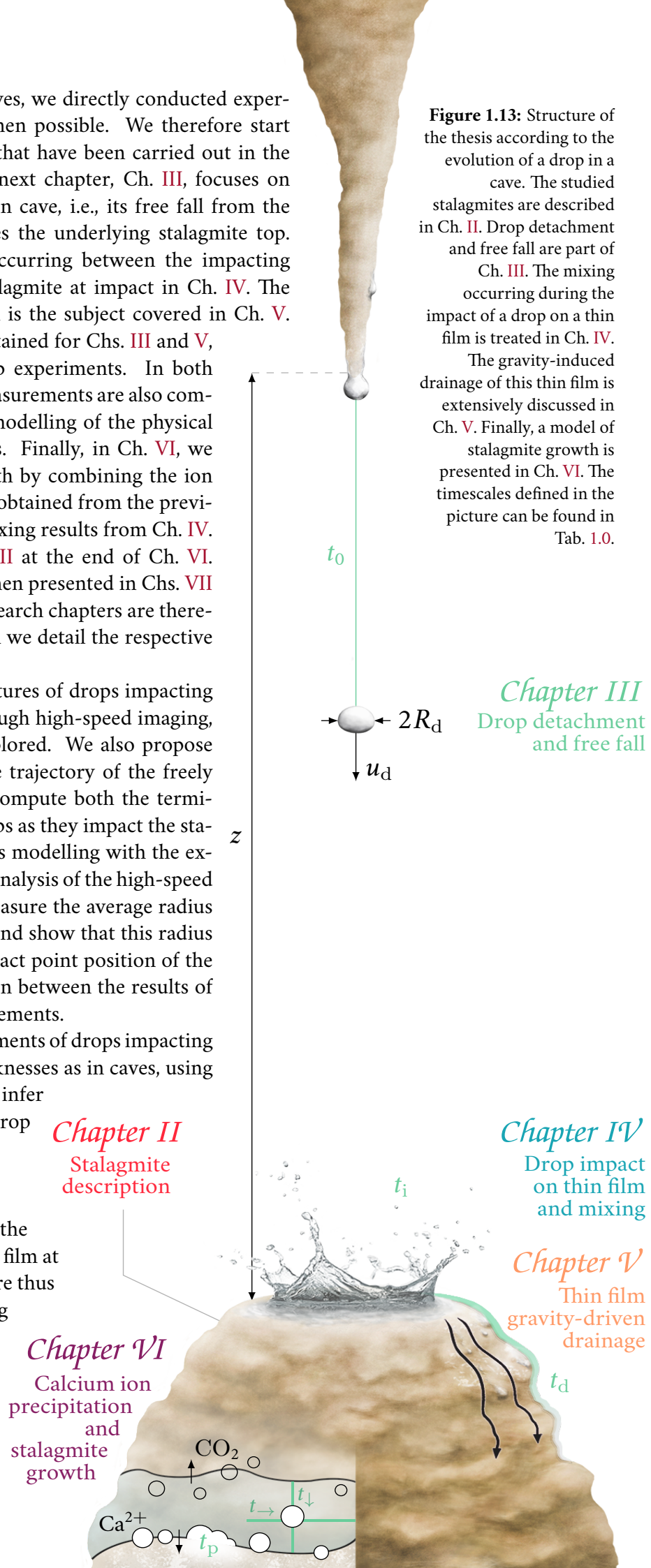
an important parameter in assessing the quantity of ions actually ending up in the solution in the film on top of the stalagmite and subsequently precipitating. In this chapter, we also show that stalagmites presenting a hollow centre and having a concave shape do not result from the splash of drops at impact, to which their particular shape has been attributed [84].

In Ch. V, we once again collect measurements in caves, this time to estimate the evolution in time and space of the thickness of the residual film lying on stalagmites, that we complete by lab measurements conducted on an actual stalagmite. A physical model of the film drainage is also obtained, allowing us to conclude that the drainage is either driven by the film thickness gradients on very flattened or even horizontal stalagmite surfaces, or that it depends on the stalagmite inclination in the case of convex stalagmites. Both these stalagmite shapes can be witnessed in the examples of Fig. 2.1 from Ch. II (see also Figs. 1.5 and 1.11 (b)). The film drainage has been omitted in previous stalagmite growth models, and the film thickness was considered to remain constant over the entire stalagmite. We show that this is not the case in Ch. V, and that, even over a time average of drop impacts, assuming the film as having a constant thickness at first order might not be a valid approximation. The analysis from Baker et al. [20], e.g., could be improved in the light of the drainage modelling proposed in Ch. V.

Finally, in Ch. VI, we include elements from Chs. IV and V, along with ion precipitation, into a coupled system of equations describing the growth of stalagmites over time and space. Solving this system numerically allows observing the response of the stalagmite shape to entry parameter variations. In particular, in this chapter, we show that the stalagmite growth, under constant conditions, is mostly influenced by the ion drop content which may further precipitate, but also by the comparison between two timescale ratios: the ratio of the dripping period t_0 over the drainage timescale t_d, and the ratio of the drainage timescale t_d and the ion precipitation timescale t_p. Hence, we add an additional parameter to the previously existing models of stalagmite growth described in Sec. 1.4, which only compared the dripping period of the drops to the ion precipitation timescale.

Variable	Symbol	Value/Range	Chapter
dripping period	t_0	$[0.1\,;10^7]\,\mathrm{s}$	III, IV, V and VI
drop impact	t_i	$[1\,;5]\,\mathrm{ms}$	IV
capillary effects	t_c	$15\,\mathrm{ms}$	IV
drainage	t_d	$12\,\mathrm{s}$	V
precipitation	t_p	$[20\,;2\times10^4]\,\mathrm{s}$	VI
viscous vertical diffusion	t_ν	$[5\,;280]\,\mathrm{ms}$	IV
viscous horizontal diffusion	$t_{\nu,\mathrm{d}}$	$6\,\mathrm{s}$	IV
molecular vertical diffusion	$t_\downarrow$	$10\,\mathrm{s}$	IV, V and VI
molecular horizontal diffusion	$t_\rightarrow$	$\sim\mathrm{days}$	IV, V and VI

Table 1.0: Summary of the imescales relative to all the physical processes accompanying the impact of a drop in a cave: physical process associated with the timescale, symbol used, order of magnitude and related chapter(s). The processes include the dripping of the drop, t_0, drop impact, t_i, capillary effects, t_c, gravity-driven drainage of the film, t_d, precipitation of the ions in solution, t_p, viscous vertical and horizontal diffusion, t_ν and $t_{\nu,\mathrm{d}}$, molecular vertical and horizontal diffusion, $t_\downarrow$ and $t_\rightarrow$. Some of the timescales presented in this table refer to ideas and analyses conveyed in the subsequent chapters. The summary of the timescales can also be found in Tab. 1.2 from the auxiliary sheet (see beginning of the chapter, p. xxii, for details).

Finally, it should be emphasized that the work conducted in this thesis also provides novel insight into several drop physics-related phenomena in situations that do not only appear in caves. For instance, the mixing between a drop and a thin film could have implications in, e.g., the rain-induced dispersal of pathogens between neighbouring plants [144, 145]. The drainage of a thin film is also involved in other geophysical processes than stalagmite growth, e.g., in sedimentary flows [167]. But more importantly, in the general context of palaeoclimate reconstruction, we hope that getting a better understanding of the interaction between the drop impacts, the film evolution and the ion precipitation will allow refining stalagmite growth modelling and help decipher the origins of isotope fractionation in stalagmite samples analysed in the future. This work has also led to the publication of peer-reviewed articles that are listed in

Because we are concerned with the fluid dynamics-related processes involved in stalagmite growth, we visited several caves in order to take measurements directly on stalagmites. We describe hereafter the stalagmites used for the studies conducted in Chs. III and V, respectively, with some overlaps existing between the two datasets. We only focus here on the physical features of the stalagmites that should directly affect the aspect of the laminae formed afterward, i.e., their average sizes and shapes. In each case, the experimental techniques used and their potential drawbacks are discussed in the corresponding Chapters.

1. Generalities

As aforementioned, the laminae formed throughout the entire life of a stalagmite, only revealed in the stalagmite cross-sectional cut, have different features that possibly change over time. The successive laminae usually present seasonal or yearly colour gradients that may be attributed to the dripping period variability of the drops feeding the stalagmite [96, 97]. The colour changes usually help distinguish the laminae from one another [231]. But the outline of the successive laminae can also differ over time (Fig. 1.11). Tan et al. [211] further pointed out that the thickness of a particular lamina could also vary depending on its horizontal position (Fig. 1.11 (a)), while Duan et al. [72] showed that the porosity, or calcite grain density distribution, could change throughout a particular lamina (Figs. 1.11 (d) and (e)). More particularly, the stalagmite in Fig. 1.11 (b) presented laminae with curvatures oriented both upward and downward, shifting from one another as time went by. We can qualify the outline of these laminae as either flattened out, convex or concave-looking. From there, we can further classify the stalagmites in the same manner based on the sole appearance of their summit, without considering the shapes of the former laminae lying below the current visible profile of each stalagmite.

Examples of stalagmites with these typical shapes are shown in Fig. 2.1. Flat stalagmites such as the one in Fig. 2.1 (b) have a very horizontal and smooth summit. Regarding the two other types, we refer to convex and concave shapes in a similar manner as in the case of polygons, i.e., a convex-looking stalagmite has an upward curved profile such that all points of the surface can be connected without getting out of the stalagmite, as seen in Fig. 2.1 (a). On the other hand, concave stalagmites such as the one in Figs. 2.1 (c) i and ii have a dimpled summit that can be filled with water with a sufficient amount of drops. An explanation advanced in some cases regarding the apparition of this dimple is the splash that would only occur during certain drop impacts [20]. From there, the resulting ion deposition would only cover the outer edge of the stalagmite top surface, and not

the centre. But given the large falling heights of the drops and the thin residual films commonly found on top of stalagmites, in most cases splash is promoted during drop impact in caves [227]. In the same manner, if the variability in the dripping period of the drops has been related to changes in the stalagmite average width [133], no relevant parameter can explain, for instance, why some stalagmites have a flat top surface while some others have an almost rounded top, as it can be seen by comparing Figs. 2.1 (a) and (b).
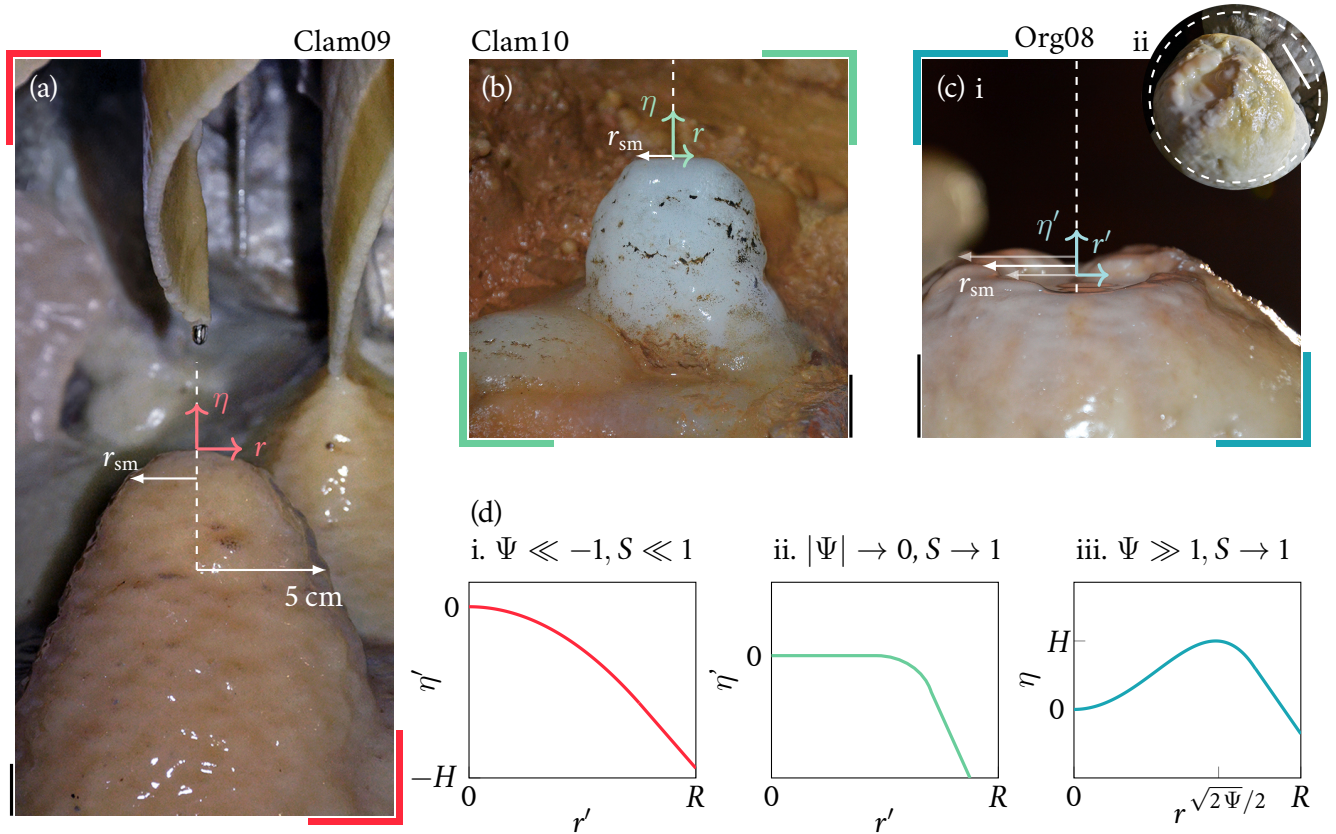
Figure 2.1: Examples of stalagmite shapes found in caves and corresponding graphical representations. The average top radius r_{sm} is drawn in white in each picture, starting from the stalagmite axis of symmetry represented by a dashed line (see Sec. 3.1). In each picture, the axes (r, η) relate to Eq. (2.1) and show the position from which we measured Ψ and S in each case. The domain limit of 5 cm is also shown in (a) (see Sec. 3.2). The scale bars are 2 cm, except in (c) ii where it is 5 cm. (a) Clam09 has a convex profile with an average top radius $r_{\mathrm{sm}} = 2.4$ cm. The profile of Clam09 can be represented as in (d) i with $\Psi = -192$ and $S = 2 \times 10^{-4}$. (b) Clam10 has a flat top of radius $r_{\mathrm{sm}} = 2.8$ cm, with $\Psi = -0.8$ and $S = 1.5$. Its graphical representation is shown in (d) ii. (c) Org08 presents a central dimple filled with water, which can be approximated as a concave profile. The height of the dimple is about 1 cm. The characteristic radius $r_{\mathrm{sm}} = 2.5$ cm corresponds to the average of the outer and inner radii of the rim surrounding the dimple, as indicated by the arrows around r_{sm} in the profile view of (c) i. In (c) ii, a top view of Org08 shows how imprecise it could be to define a radius r_{sm} corresponding to the mid-line of the outer rim contouring the dimple. The corresponding shape is represented in (d) iii, with $\Psi = 26$ and $S = 0.6$. (d) Graphical representation of the profiles defined by Eq. (2.1).

Both Chs. III and V are articulated around data collected directly from cave environments. In the next Section, we present the field campaigns that we conducted in order to gather these measurements, constituted of high-speed movies of drop impacts, photographs of stalagmites and thickness measurements of the residual film lying on top of the stalagmites. In Sec. 3, we describe the physical aspects of the stalagmites from our datasets. In Subsec. 3.1, we only focus on the average size of the stalagmites, while in Subsec. 3.2, we consider in more detail the large variability displayed by stalagmite shapes. To conclude this Chapter, we compile some important measurements in two tables, one relative to Ch. III (Tab. 2.1), the other relative to Ch. V (Tab. 2.2). A condensed version of these two tables is also provided in the auxiliary sheet.

2. In situ measurements

In total, three field measurement campaigns were conducted in karstic caves located in Southern France. First, in March 2015 in Aven d'Orgnac[1], where some preliminary measurements to Ch. III, were made. Then, in June 2016, a more systematic and larger dataset, which is used in Ch. III, was obtained in Aven d'Orgnac, Clamouse cave and La Salamandre cave by T. Gilet, S. Lejeune, J.-C. Maréchal and M. Maréchal [172]. A few complementary pictures were also provided by F. Bourges from Bétharram, Gargas and Niaux caves and Gouffre d'Esparros. Finally, in March 2022, additional measurements relative to the study conducted in Ch. V were taken in Aven d'Orgnac and Clamouse cave by J. Parmentier and K. Bulthuis. The Aven d'Orgnac, Clamouse cave and La Salamandre cave are located in Ardèche, Hérault and Gard, respectively, which are neighbouring departments. The other four caves are all located close to the Pyrenees.

Before diving into the description of our measurements, we recall that measurements relative to Ch. III are reported in Tab. 2.1, and those relative to Ch. V in Tab. 2.2. The following items are common to both tables: we specify the cave in which the measurements relative to a particular stalagmite were taken, as well as the position of the stalagmite based on the most common name attributed to the rooms and distinctive concretions from each visited cave. We attributed a name and number to each stalagmite based on their cave of origin, the number having no particular meaning. For instance, the first stalagmite on which we conducted measurements in Clamouse cave is labelled Clam01. Several stalagmites were common to both datasets, hence we kept the same numbering in both Tabs. 2.1 and 2.2. We also attributed a specific colour and symbol to each stalagmite from Tab. 2.1, both of which will be reported in the graphs relative to Ch. III. We proceeded in the same manner for Tab. 2.2 and Ch. V. It should be noted that, if symbols are simply there to identify the stalagmites, the colours have a particular meaning and differ for both Chs. III and V. In the case of Ch. III, the colour simply indicates the cave of origin while in Ch. V, the colour is related to the shape of the stalagmite.

All the visited caves present a large variability of ceiling heights, numerous types of active and inactive concretions and other peculiarities such as the ones presented in Sec. 1.2. A remarkable concretion is the *Pomme de Pin* stalagmite from Salle de Joly in Aven d'Orgnac, that we illustrate in Fig. 2.2. Although this iconic stalagmite is 11 m tall, it is still smaller than the 25 m to 30 m ceiling of Salle de Joly. Due to its height, we could unfortunately not include this

Figure 2.2: The majestic *Pomme de Pin* stalagmite from Aven d'Orgnac, with a total height of 11 m. Courtesy of P. Crochet [58].

---

[1]The aperture visible in the ceiling of Fig. 2.2 is what gives it its "Aven" denomination, in opposition to caves having side natural entrances or no natural entrance at all.

stalagmite into our datasets. Nevertheless, during the first two campaigns from 2015 and 2016, a total of 65 shorter stalagmites were used to conduct measurements (at most 2 m tall). In this case, we were interested in assessing whether the trajectories followed by the drops landing on these stalagmites had any effect on subsequent stalagmite growth. Hence, we measured the falling heights of these drops and took still pictures of the stalagmites so as to be able to measure their average top radius r_{sm}, which was done according to Sec. 3.1. Out of this dataset, we also recorded high-speed videos of drop impacts on 14 of these stalagmites. More information regarding the analysis of these movies is provided in Ch. III. The measurements relative to these 14 stalagmites are the measurements reported in Tab. 2.1. The falling height z was measured for all individuals by laser telemetry. For large falling heights (up to 26 m), uncertainty in the measurements might reach 50 cm, owing to the very irregular ceiling, and the difficulty to precisely point at the emitting stalactite. However, because this uncertainty remains smaller than 5 %, we did not report it in the tables nor in the graphs. In addition, we timed the estimated dripping period t_0 of the drops falling on each stalagmite. We do not report the measurements relative to the stalagmites for which we only had still pictures as they do not appear anywhere but in one graph from Ch. III. The raw data are nevertheless available in the Supplemental Material[3] of Parmentier et al. [172].

During the 2022 field measurement campaign, our goal was to assess the thickness variations of the residual film lying on top of the stalagmite in response to stalagmite shapes and other parameters, such as the dripping period of the drops. We thus measured the film thickness as a function of time in a precise location on a total of 14 different stalagmites, some of which having already been considered in the study of Ch. III. Additionally, a stalagmite from Aven d'Orgnac was used for the lab measurements, to which we refer as Lab01. We either stopped the inflow of the drops and measured the response of the film thickness afterward, or, starting from a dry stalagmite, we measured the progressive filling of the film after a certain amount of drops had fallen onto the stalagmite. The measurements were performed using two techniques thoroughly described in Ch. V. Additionally, we collected information on the surroundings of the selected stalagmites: dripping period t_0 and falling height z of the drops, and temperature T and relative humidity RH in a close vicinity of the stalagmite. The dripping period of t_0 corresponds to the average $\pm$ s.d. made over at least 30 measurements for dripping periods $t_0 \lesssim 2$ min, but only over about 10 measurements for $t_0 > 2$ min. Temperature and relative humidity measurements were obtained thanks to a hygro-thermometer. Getting a significant amount of film thickness measurements required at least 1 h to 2 h, hence RH and T for a given stalagmite correspond to the average $\pm$ s.d. of about 15 measurements taken over this time span. We also took photographs of the stalagmites from different angles (side and top views) in order to describe their physical aspects, this time according to Sec. 3.2. From these photographs, we measured the shape and scale factor Ψ and S, respectively, associated with each stalagmite. All the measurements relative to this last field trip are reported in Tab. 2.2. We also report in Tab. 2.2 the stalagmite radius r_{sm} obtained according to Sec. 3.1, in addition to Ψ and S. The type of measurements that we were able to take is indicated as well, i.e., thickness measurements during the filling of the film and/or during sole drainage using either the mass-based or distance-based technique (see Ch. V). In the particular case of Lab01, we only used the laser sensor (see Ch. V). Finally, we note that the parameter t_0^{drain} comes from a fit on the drainage curves obtained for each stalagmite and will be detailed in Ch. V.

---

[2]Available in the Orbi entry relative to this manuscript, or the Royal Society's website. See PDF version for direct hyperlinks.

3. Stalagmite geometry

In both Chs. III and V, we will include the physical aspect of actual stalagmites into our measurements. For the sake of simplicity, we limit our study to axisymmetric, candlestick-like stalagmites. We tried to select the studied stalagmites according to this criterion, i.e., no stalagmite from the datasets should have been exposed to former, now inactive drips that may have enlarged its overall size and could affect the measurements. We also only selected stalagmites that were active and only fed by one drip at the time of the measurement campaign. Our analysis of the drop free fall from Ch. III will mostly be concerned with the position at which the drops impact the stalagmite, such that there is no need to consider the geometrical variations of the studied stalagmites but only their average size. The drainage of the film, however, could likely be influenced by the local slope of the stalagmite top surface, hence we will need a more detailed description of the studied stalagmite shapes in Ch. V.

3.1 Average top radius

In a first approach, we only focus on the average size of the stalagmites, without considering the intricate details of their geometry. Nevertheless, we still need to acknowledge that stalagmites do not all look the same. We consider the three aforementioned profiles illustrated in Fig. 2.1: flat, convex and concave. Defining a characteristic radius for flat and concave stalagmite is rather straightforward. Flat stalagmites indeed exhibit a horizontal and smooth summit with an easily identifiable radius r_{sm}. Concave stalagmites can also be characterized by a radius r_{sm} corresponding to the size of their dimple. We measure both the outer and inner radii surrounding the rim around the dimple and take the average of these two measurements as our average top radius r_{sm}.

In the case of convex stalagmites, attempting to proceed in the same manner can prove arbitrary. However, we note that, among our dataset, the top part of convex stalagmites is often surrounded by an outer wall with a more or less constant angle, as illustrated by the stalagmite from Fig. 2.1 (a) and in Fig. 2.3 below. We tried to measure the radius corresponding to the transition between the very curved top part of the stalagmite and this uniformly inclined wall. This transition usually occurs about 1 cm to 3 cm below the apex of the stalagmite. Hence, this radius corresponds to the top of convex stalagmites and should be more or less equivalent to our two other characteristic radius definitions (flat and concave). In Fig. 2.3, we illustrate the average radii of the three stalagmite types schematically. In practice, we used the average of several measurements and, whenever possible, measured the radius from different angles (side and top view) to average out the small irregularities at the stalagmite surface.
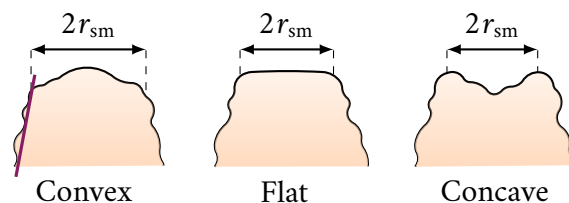
Figure 2.3: Schematic radius r_{sm} for each stalagmite type. The purple line over the convex stalagmite schematic shows the more or less uniform outer wall inclination often displayed by these stalagmites.

3.2 Shape variability formalism

Because all the studied stalagmites can be considered as axisymmetric, it is possible to describe their shape as a function of the sole radial coordinate r (in cm) taken from the stalagmite axis, as

shown in Fig. 2.1 for each stalagmite type. We designate by η the stalagmite height (in cm) starting from either the centre of the apex of convex and flat stalagmites, or from the centre of the dimple of concave stalagmites, as shown in Fig. 2.1. A simple representation for concave stalagmites, i.e., the most complex of the precited shapes, is to assimilate them to fourth-order polynomials with no odd powers in order to reproduce the change in concavity between the centre and the outer wall of the stalagmite. By adjusting the coefficients of such polynomials, we could also easily represent convex and flat stalagmite profiles. We consider all the stalagmite profiles over a unique domain limit starting from the stalagmite axis of symmetry illustrated in Fig. 2.1, i.e., we only look at them for $|r| \leq 5$ cm. Few stalagmites from our datasets present an apex or top surface with a larger radius (see Tab. 2.2). For Clam09 shown in Fig. 2.1 (a), e.g., we measure $\eta = -5.23$ cm at a radius $r = 5$ cm. Hence, it is a priori not necessary to take into account the entire stalagmite outer wall. Moreover, some stalagmites may be really small and not even reach a radius of 5 cm at their basis, such as, e.g. Clam10 which is presented in Fig. 2.1 (b). Taking a too large domain size would thus not allow to capture its shape very precisely. We will further verify that restricting ourselves to this truncated domain is an adequate assumption in Ch. V.
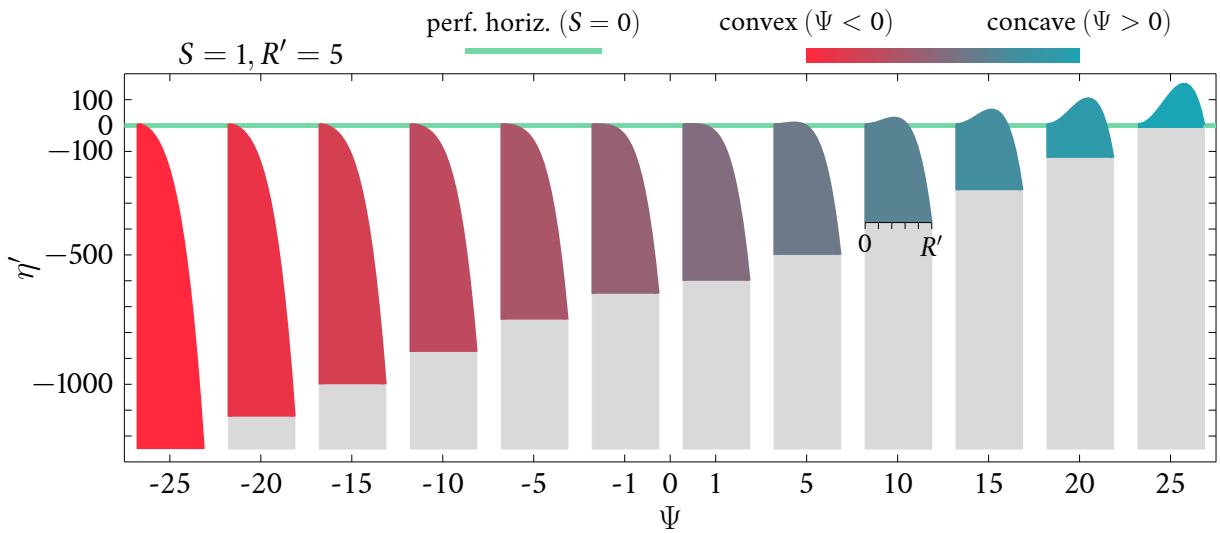
Figure 2.4: Examples of shapes obtained by Eq. (2.1) for variable Ψ, at a fixed value of $S = 1$. The graph shows the nondimensional stalagmite height η' produced by the equation on a domain of radius $R' = 5$. The colour indicates the general shape as described per Fig. 2.1: more convex shapes are drawn in red and more concave ones in blue. Flat stalagmites are associated with in-between colours for $|\Psi| \lesssim 1$. Perfectly horizontal stalagmites correspond to the green line for $S = 0$.

In Ch. V, we will also cover into more detail the decoupling in the characteristic vertical and horizontal length scales that we use to nondimensionalize our variables. In order to describe the stalagmites in a uniform manner, we nondimensionalize the stalagmite height η by using the typical film thickness order of magnitude of 100 μm. For the radial coordinate r, we use a length of 1 cm. Hence, we now write as $\eta' = \eta/100$ μm and $r' = r/1$ cm our nondimensional coordinates. Using the following fourth-order polynomial:

$$\eta'(r'\,;S,\Psi) = S\,(r')^2\left(\Psi - (r')^2\right)\,, \quad r' \leq R'\,, \quad S > 0\,, \tag{2.1}$$

we describe all three shapes by simply tuning what we denote (i) the shape parameter Ψ, and (ii) the scale S, a coefficient related to the size of the stalagmite. The radius $R = 5$ cm represents the truncation of the physical domain, corresponding to a nondimensional radius $R' = 5$. A negative Ψ yields a parabolic shape while a positive Ψ induces a small protuberance at a distance $r' = \sqrt{2\Psi}/2$

from the centre, representative of the change in concavity. We are thus able to reproduce the shape of both convex and concave stalagmites. Using $S = 0$ would lead to a perfectly horizontal profile, although in practice $S \to 0$ suffices since the case $S = 0$ induces an indeterminate stalagmite size. In Fig. 2.4, we show examples of the shapes obtained with Eq. (2.1) for variable Ψ, at a given scale $S = 1$. We represent 12 profiles $\eta'(r')$ produced by varying Ψ from -25 to 25. We further note in Fig. 2.4 that small values of $|\Psi|$ yield profiles with a very flattened top. We thus consider our stalagmites as flat if they correspond to $|\Psi| \leq 1$ without considering their sign. On the other hand, we can consider our stalagmites to be convex, resp. concave, whenever $\Psi < -1$, resp. $\Psi > 1$.

In order to find the values of Ψ and S that correspond to the stalagmites from our dataset, we use side photographs that we took of each stalagmite from various angles. We then contour the stalagmite outline to gather n pairs of dimensional data points $(\hat{r}, \hat{\eta})$ (in cm), with the axes positioned as illustrated in Fig. 2.1 for each stalagmite type. We nondimensionalize our results as described above, with $100\,\mu\text{m}$ for $\hat{\eta}$ and $1\,\text{cm}$ for $\hat{r}$, before proceeding to adjust Eq. (2.1). We can express the relation between our data points as

$$\hat{\eta}_i \approx S\Psi\hat{r}_i^2 - S\hat{r}_i^4, \quad 0 \leq i < n-1. \tag{2.2}$$

Next, we define the following vector of experimental data points: $\boldsymbol{\eta} = \begin{bmatrix} \hat{\eta}_0 & \cdots & \hat{\eta}_{n-1} \end{bmatrix} \in \mathbb{R}^{(1 \times n)}$, and the design matrix

$$\mathbf{R} = \begin{bmatrix} \hat{r}_0^2 & \cdots & \hat{r}_{n-1}^2 \\ \hat{r}_0^4 & \cdots & \hat{r}_{n-1}^4 \end{bmatrix} \in \mathbb{R}^{(2 \times n)}.$$

We designate by $\boldsymbol{\beta} = \begin{bmatrix} S\Psi & -S \end{bmatrix} \in \mathbb{R}^{(1 \times 2)}$ the parameter vector. In the least square sense, we find by means of the normal equations that this parameter vector is given by

$$\boldsymbol{\beta} = \boldsymbol{\eta}\,\mathbf{R}^T \left(\mathbf{R}\mathbf{R}^T \right)^{-1}. \tag{2.3}$$

In Figs. 2.1 (d) i-iii, we additionally show the general representation of the stalagmite profiles from Figs. 2.1 (a-c), respectively, i.e., Eq. (2.1). We note that Clam09 has a very large negative shape factor $\Psi = -192 \ll -1$, associated with a small scale $S = 10^{-4}$. By contrast, Org08 is concave and corresponds to a shape factor $\Psi = 26 \gg 1$, with a scaling $S = 0.6$ close to unity. Regarding Clam10, we obtain $\Psi = -0.8$, as expected for a flat stalagmite, for a scaling $\Psi = 1.5$ close to unity as well. To be more precise, we could not consider stalagmites as axisymmetric and take into account all the little bumps visible at their surface. Nevertheless, they all present both variable sizes and shapes, as indicated by the large span of Ψ and S values, and not making these assumptions would increase the number of parameters describing the stalagmite profiles. With the domain of fixed radius $R = 5\,\text{cm}$ (or $R' = 5$) over which we consider the stalagmites, and with the relative simplicity of the equations presented in this section, we are now able to easily describe the stalagmites from our dataset with a common formalism.

Cave	Room / Concr.	Name	Sb.	Nb. videos	Date	z [m]	h [μm]	r_{sm} [cm]
Clamouse	*Salle à Manger*	Clam01	●	50	06.16.16	8.70	50	4.5
	Cimetière	Clam02	■	50	06.16.16	1.20	125	2.7
	Cimetière	Clam03	◆	10	06.16.16	0.29	90	2.4
	Below Cimetière	Clam04	▼	49	06.16.16	15.60	60	5.7
Orgnac	Tour de Pise *(SJ)*	Org01	●	56	03.24.15 – 06.13.16	23.80	255	6.7
	Pomme de Pin *(SJ)*	Org02	■	27	03.25.15 – 06.13.16	20.10	130	5.0
	Near *Salle Glory (SJ)*	Org03	◆	50	06.14.16	2.55	300	3.7
	Near *Salle Petit (SJ)*	Org04	▼	48	06.14.16	3.85	170	2.8
	Blocs Cyclopéens *(SJ)*	Org05	▲	50	06.14.16	21.50	90	6.8
	Cône d'Éboulis *(SJ)*	Org06	▶	42	06.14.16	25.20	60	8.5
	Salle Glory	Org07	◀	7	03.25.15	4.50	–	3.7
La Salamandre	Pomme de Pin	Sal01	●	43	06.15.16	25.60	40	6.7
	Cierges	Sal02	■	50	06.15.16	21.60	60	6.9
	Grands Massifs	Sal03	◆	50	06.15.16	16.00	110	5.8

Table 2.1: Cave measurements database: high-speed movies (Ch. III). *From left to right* – Cave in which high-speed videos of drop impacts on stalagmites were recorded. – Most usual name of the *room*/closest neighbouring concretion where the stalagmite is found (*SJ* stands for *Salle Joly*). – Name that we attributed to the stalagmite. – Symbol associated with each stalagmite in the graphs presented in Ch. III (the colours indicate the corresponding cave). – Number of high-speed videos analyzed for each filmed stalagmite. – Date(s) at which videos were recorded. – Falling height z between the top of the stalagmite and the tip of its corresponding stalactite. – Residual film thickness h on top of the stalagmites. – Stalagmite average top radius r_{sm} estimated as defined in Sec. 3.1.
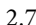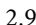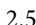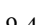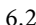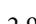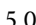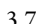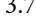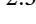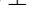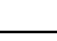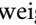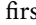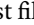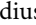
Cave	Room/Concr.	Name	Type	z [m]	t_0 [s]	RH [%]	T [°C]	Sb.	r_{sm} [cm]	Ψ	S	t_0^{drain} [s]	Meas.
Clamouse	Cimetière	Clam02	▭	1.2	31.4 ± 3.6	91.8 ± 0.8	15.7 ± 0.1	●	2.7 ± 0.3	1.2	0.04	16.9	● ■
	Cimetière	Clam05	▭	2	53.3 ± 0.5	91.1 ± 1.3	15.2 ± 0.1	◆	2.9 ± 0.6	2	0.5	19.5	● ■
	Below Cimetière	Clam06	▭	2.9	4.9 ± 0.4	90.0 ± 4.7	16.4 ± 0.1	▼	2.5 ± 0.2	-168	0.05	–	●
	Salle à Manger	Clam07	⌒	7.6	3.0 ± 0.9	95.8 ± 1.2	16.0 ± 0.1	●	9.4 ± 0.5	-375	10^{-4}	7.8	● ◨
	Salle à Manger	Clam08	▭	8.2	59.6 ± 1.3	86.5 ± 0.8	17.1 ± 0.1	▲	6.2 ± 0.3	-0.6	1	–	●
	Near Excentriques	Clam09	⌒	0.05	1.1 ± 0.0	92.0 ± 1.0	16.7 ± 0.1	■	2.9 ± 0.1	-192	2×10^{-4}	14.1	● ■
	Near *Couloir Blanc*	Clam10	▭	6.4	767.1 ± 26.3	91.8 ± 0.4	15.8 ± 0.1	▶	2.0 ± 0.2	-0.8	1.5	247	■
Orgnac	Pomme de Pin (*SJ*)	Org02	▭	20.1	10.5 ± 0.5	92.1 ± 0.6	13.1 ± 0.1	■	5.0 ± 0.9	0.5	2×10^{-3}	–	●
	Near *Salle Glory* (*SJ*)	Org03	∿	2.6	6.5 ± 0.5	78.6 ± 0.5	14.7 ± 0.1	●	3.7 ± 0.8	21.5	0.8	6.9	● ■
	Near *Salle Petit* (*SJ*)	Org04	∿	3.9	88.3 ± 3.5	88.3 ± 1.6	12.3 ± 0.2	■	2.8 ± 0.2	12	1.4	5.6	■
	Salle Glory	Org07	∿	4.7	201.8 ± 2.4	94.2 ± 0.8	12.3 ± 0.1	◆	3.7 ± 0.4	16	5	–	●
	Near *Salle Petit* (*SJ*)	Org08	∿	5.6	88.3 ± 1.8	88.4 ± 1.4	12.3 ± 0.2	▼	2.5 ± 0.2	26	0.6	100	● ■
	Pomme de Pin (*SJ*)	Org09	⌒	22.7	2.9 ± 0.9	95.3 ± 0.5	11.7 ± 0.1	◆	7.0 ± 0.2	-88	2×10^{-4}	16.7	● ■
	Cône d'Éboulis (*SJ*)	Org10	⌒	25.5	6.2 ± 0.4	93.4 ± 0.8	12.4 ± 0.5	▼	7.6 ± 0.4	-9.7	5×10^{-3}	22.7	● ■
Orgnac	*μfluidics Lab*	Lab01	⌒	0.05	–	–	–	●	7.5 ± 0.6	-120	2×10^{-3}	–	● ■

Table 2.2: Cave measurements database: drainage (Ch. V). *From left to right* – Cave from which the stalagmite comes. – Most usual name of the *room*/closest neighbouring concretion where the stalagmite is found (*SJ* stands for *Salle Joly*). – Name that we attributed to the stalagmite. – Estimated shape of the stalagmite profile (flat, convex, concave). – Falling height of the drops impacting the stalagmite, z. – Dripping period of the drops, t_0. – Air relative humidity in the vicinity of the stalagmite averaged during the measurements, RH. – Air temperature in the vicinity of the stalagmite averaged during the measurements, T. – Symbol associated with each stalagmite in the graphs presented in Ch. V (the colours indicate the corresponding shape, except for the lab stalagmite which is identified by the orange colour). – Stalagmite average radius estimated as defined in Sec. 3.1. – Shape parameter Ψ of the stalagmite profile, defined by Eq. (2.1). – Scale S of the stalagmite profile, defined by Eq. (2.1). – Estimated time of the first film thickness measurement, t_0^{drain}, used with Eq. (5.65), as described in Sec. 5.4.3. – Type of measurements taken with the stalagmite: filling ● and/or drainage ■, using either the weighing technique ⌒, the dial gauge ● or the optical sensor ●.

Highlights (Ch. III)

🫧 In Ch. III (see next page), we present findings coming mostly from high-speed imaging of drop impacts on stalagmites recorded in caves, completed by a few lab experiments. The methodology is reviewed in Sec. 1.

🫧 Observations from caves regarding the drop detachment from the stalactite tip and the impact on the stalagmite top are summarised in Sec. 2. A noteworthy feature of drops impacting stalagmites in caves is the non-negligible scattering exhibited in the impact point position of these drops. We postulate that the scattering comes from the drops deviating from their initial vertical trajectory during their fall. We show that this deviation has no external cause and must, therefore, be self-induced.

🫧 In Sec. 3, we model the drop free fall into the air by a simple application of Newton's second law. The particularity of our modelling lies in the inclusion of a randomly-oriented lift component in the aerodynamic force acting on the drop. Two Langevin-like relations describe the position and velocity of the drop in Subsec. 3.2, allowing us to characterise the scattering in the drop impact point position as a function of the falling height of the drop.

🫧 In Sec. 4, we show that there exists a relation between the scattering observed in the drop impact point position and the average width of stalagmites measured in the previous chapter and reported in Tab. 2.1.

As aforementioned, drops have been assumed to always land on the apex of the stalagmite in models describing stalagmite growth [20, 189, 190]. As we will show in this chapter, this is not always the case. We thus investigate how the aerodynamics of falling drops could actually set some constraints on the average stalagmite width. We report high-speed imaging measurements of radius, velocity and impact point position of drops falling on stalagmites from several different caves, as well as in a more controlled lab setting. We then show that these measurements are correlated to the height of fall of the drops and we propose a theoretical model to rationalise this fact. We finally relate the distribution of the drop impact point position to the average width of stalagmites, that we measured according to Ch. II. Further discussion regarding the implications of our findings on modelling stalagmite growth are discussed in the subsequent chapters.

1. Imaging from caves

To investigate and attempt to model the free fall of drops in caves, what better starting point is there than direct field observations of drops falling on actual stalagmites? Given the length and time scales at play though, monitoring closely the entire fall of a drop in a cave would prove technically complicated. Drops are indeed millimetric objects falling over possibly several metres for less than a few seconds. We recorded instead high-speed side view movies of (i) drops dripping from 2 stalactites, and (ii) drops impacting various stalagmites, using a Phantom Miro M110 colour camera (5400 fps). A total of 582 high-speed movies on 14 stalagmites were recorded, then analysed using image processing tools. Still side and top view photographs of 65 stalagmites were also taken, including the ones for which high-speed movies are available. The stalagmites come from 7 different caves from the South of France and are thoroughly described in Ch. II. In particular, the stalagmites for which high-speed movies were recorded are Clam01–Clam04 from the Clamouse cave, Org01–Org07 from the Aven d'Orgnac and Sal01–Sal03 from the Salamandre cave (see Tab. 2.1). The high-speed movies were recorded by setting the tripod holding the camera in place next to the stalagmite (or stalactite tip) such that the entire stalagmite top part and first few centimetres of the stalagmite body were visible, with minimum bank angle. Front lighting was ensured by a powerful LED lamp while the recording of the movies was started manually through a computer. Hence, all videos relative to one stalagmite were obtained in identical conditions. As explained in Ch. II, stalagmites used for taking measurements relative to Chs. III and V can all be considered as axisymmetric and related to only one active drip. Since both the drops and the

stalactite from which they originate are relatively axisymmetric too, we may assume that the two-dimensional distribution of the horizontal impact point position of the drops is also axisymmetric. Hence, only looking at the drop impacts in one vertical plane should be enough to characterise the entire distribution, as long as there is a sufficient amount of drop impacts recorded per stalagmite. On average, 42 videos were taken for each stalagmite (details are provided in Tab. 2.1). The main sources of error in the measurements resulting from image analysis in these videos should thus be the poorly lit cave environment and the resolution of the videos (640 × 480 px for a field of view of roughly 15 × 20 cm^2).

Additional measurements made for all individual stalagmites include the falling height of the drops z and stalagmite average top radius r_{sm}. Although stalagmites can be classified according to their shape (flat, convex or concave), only the average width of the stalagmites will be considered in the present chapter. Examples are provided in Sec. 3.1 from Ch. II for each type of stalagmite shape. Regarding the subset of stalagmites for which high-speed videos were recorded, we also measured in each video the drop radius R_d and vertical impact velocity u_d. The drop vertical and horizontal radii were measured in each frame (from $\sim$ 30 to 80 frames depending on the stalagmite and drop velocity), then the average from all frames was taken for each video. As shown in Fig. 3.5 (b) from Sec. 3.1, the field of view in the movies only shows the last $\sim$ 10 cm of the drop fall. The impact velocity u_d was obtained by taking the difference in vertical positions of the drop in the first frame in which it appears, and in the last frame before it impacts the stalagmite, then by dividing this distance by the time spent between both frames.

Finally, we also measured the horizontal impact point dispersal in the position of the drops. Since the analysed stalagmites can all be viewed as axisymmetric, we simply measured the horizontal distance x between the axis of symmetry of the stalagmite top and the impact position of each drop, as shown in Fig. 3.4 (a) from Sec. 2.2. An example of resulting distribution of x is shown in Fig. 3.4 (b) for Sal01. The distribution of x can be approximated not only as axisymmetric but also as Gaussian. We verified this latter assumption by performing a Kolmogorov-Smirnov statistical test for the distributions obtained on all our stalagmites, with a 5 % significance level. We thus consider that the distribution of x is entirely characterised by its standard deviation, and we denote this parameter Δ:

$$\Delta = \text{s.d.}(x).$$

Since the distribution is Gaussian, the error made in the measurement of Δ was estimated as follows, using a significance level of 1 %: $N\Delta^2/\varsigma^2 \sim \chi^2_{N-1}$, where N is the sample size, ς is the actual standard deviation of the entire population of drops impacting a stalagmite and χ^2_{N-1} is the chi-squared distribution with $N - 1$ degrees of freedom. Values of R_d, u_d and Δ are reported in the Supplemental Material[1] of Parmentier et al [172].

A complementary set of free fall measurements (R_d, $u_d(z)$ and $\Delta(z)$) was performed in a laboratory setting that offers more controlled conditions. Water drops of 2.32-mm radius were pushed out of a 2-mm diameter tube thanks to a syringe pump (WPI, AL-1000) at a flow rate of 200 μL/min. The release height was varied between 15 cm and 400 cm, which determined the impact velocity of the drop on the substrate. To prevent any parasitic air currents that could interfere with the drops, the splash column was isolated by a rigid plastic tube of diameter equal to 20 cm, which was sufficient to neglect the aerodynamic interaction of the falling drop with the tube.

---

[1]Available in the Orbi entry relative to this manuscript, or the Royal Society's website. See PDF version for direct hyperlinks.

2. Drops travelling through cave air

From its formation at the tip of a stalactite to its disintegration on top of the stalagmite underneath, the trajectory followed by a drop in a cave is not as simple as it seems. We describe it point by point in the present section, starting from the dripping of the drop in Sec. 2.1, then we continue with the drop impact in Sec. 2.2.

2.1 Dripping from the stalactite tip

We show in Fig. 3.1 a sequence from a high-speed movie taken in Aven d'Orgnac, during which a drop detaches from a stalactite tip of outer radius equal to $r_{st} = 2.2$ mm. When water reaches the tip of the stalactite, it forms a growing pendant drop (Figs. 3.1 (a-c)). Once the drop becomes sufficiently heavy, surface tension can no longer hold it still, and the drop falls [8, 238] (Figs. 3.1 (d-i)). The drop radius measurements described in the former section and reported in the Supplemental Material[1] of Parmentier et al. [172] suggest that R_d is fairly constant in cave, with a value for all drops of 2.63 ± 0.18 mm (average ± s.d. in all the radii related to all the stalagmites), and close to the capillary length of water $\lambda_c = \sqrt{\gamma/\rho g} = 2.73$ mm, with $\gamma \simeq 70$ mN m^{-1} the water surface tension. The mass of the pendant growing drop of equivalent radius R_d is $m_d = 4/3\pi\rho R_d^3$ and its weight is $m_d g$, with g the gravitational acceleration. The maximum drop weight that can be balanced by surface tension forces is of the order of $2\pi\gamma r_{st}$. Because the stalactite is formed by the drop
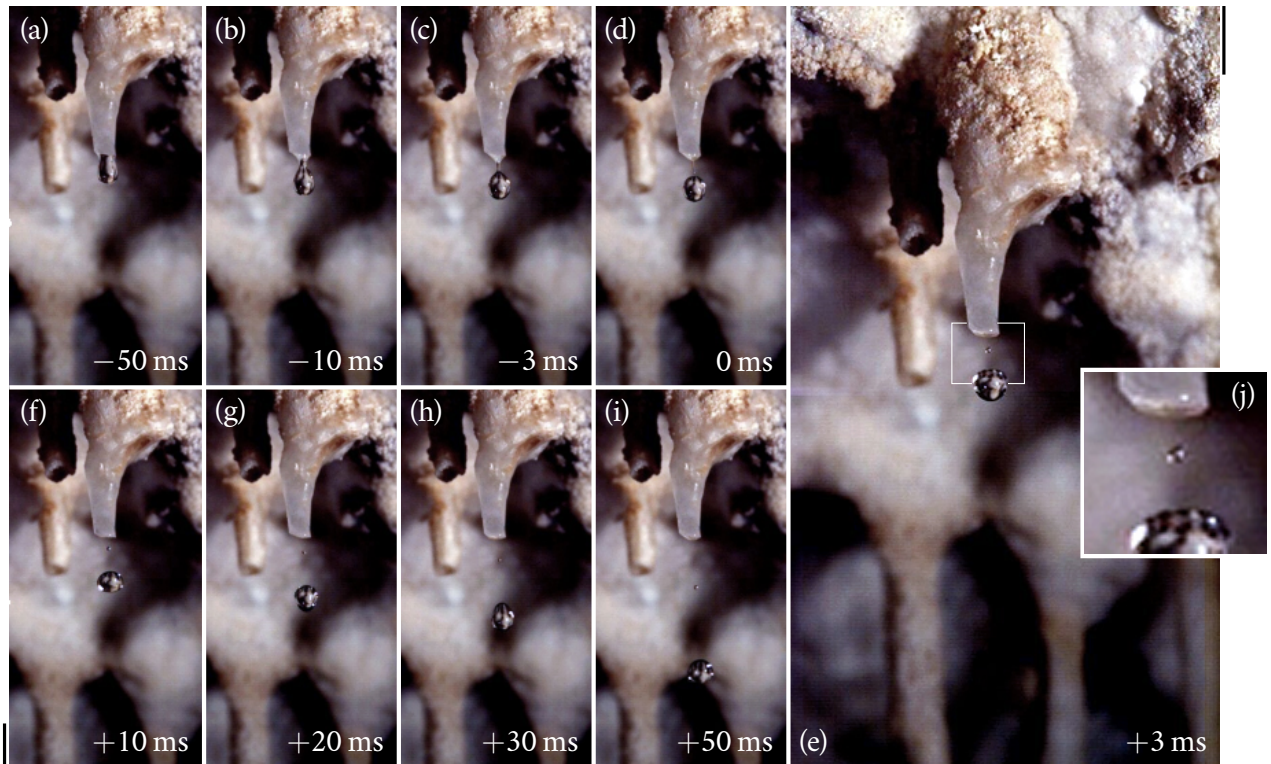
Figure 3.1: Evolution of a growing pendant drop (a), forming a neck (b), detaching (c) and falling from a stalactite tip (d) in Orgnac cave, salle de Joly. The sequence shows the drop from (a) at most 50 ms before it detaches in (d), to (i) at least 50 ms after. The most pronounced shape variations of the drop appearing on the first few centimetres of its trajectory can be seen in the photographs (e-i). A satellite droplet formed because of the detachment of the main drop can also be seen in (e-i) and is emphasised in (j), with a radius of 500 μm. The stalactite tip radius is equal to 2.2 mm and the drop formed has a radius $R_d = 2.68$ mm. The left scale bar refers to pictures (a-d) and (f-i), and the right one to picture (e) only. Both scale bars are 1 cm.

itself, the tip radius of the stalactite should approximately match the drop equivalent radius, i.e., $r_{\mathrm{st}} = kR_{\mathrm{d}}$ where k is a proportionality constant. With $k = 2/3$ of the order of unity, the drop radius R_{d} would be estimated as $\sqrt{3k\gamma/2\rho g} = \lambda_{\mathrm{c}}$, which corresponds to our measurements. The parameters involved can be considered as more or less constant in the temperature and pressure ranges encountered in caves (see Ch. II). Hence, R_{d} should also be fairly constant from one stalactite to another and in between different drops falling from a given stalactite [59].

The size of the drop, R_{d}, can still slightly depend on the water flow rate feeding the stalactite [98]. This flow rate is inversely proportional to the dripping period t_0 separating two successive dripping events from the same stalactite, which is observed to vary seasonally, possibly from less than a second to several months, i.e., $t_0 \in [10^{-1}, 10^7]$ s. When $t_0 \lesssim 1$ s, the drop volume decreases and satellite droplets of significant volume form [98]. This phenomenon differs from what we observe in Fig. 3.1 (j), where a tiny satellite droplet of about $500\,\mu$m radius appears right after the drop has started to fall. Its presence results from instabilities appearing when the neck of the pendant drop pinches off during the drop detachment from the stalactite [238]. The volume of this satellite droplet is almost 200 times smaller than the main drop volume and is thus negligible, by contrast with the regime where $t_0 \lesssim 1$ s. Nevertheless, the drop formation from stalactites always remains in the periodic dripping regime (contrary to jetting or chaotic dripping) since the capillary time of the drop $t_{\mathrm{c}} = \sqrt{4\rho R_{\mathrm{d}}^3/(3\gamma)} \simeq 15$ ms is always smaller than t_0 [52] (see Chs. I and IV).
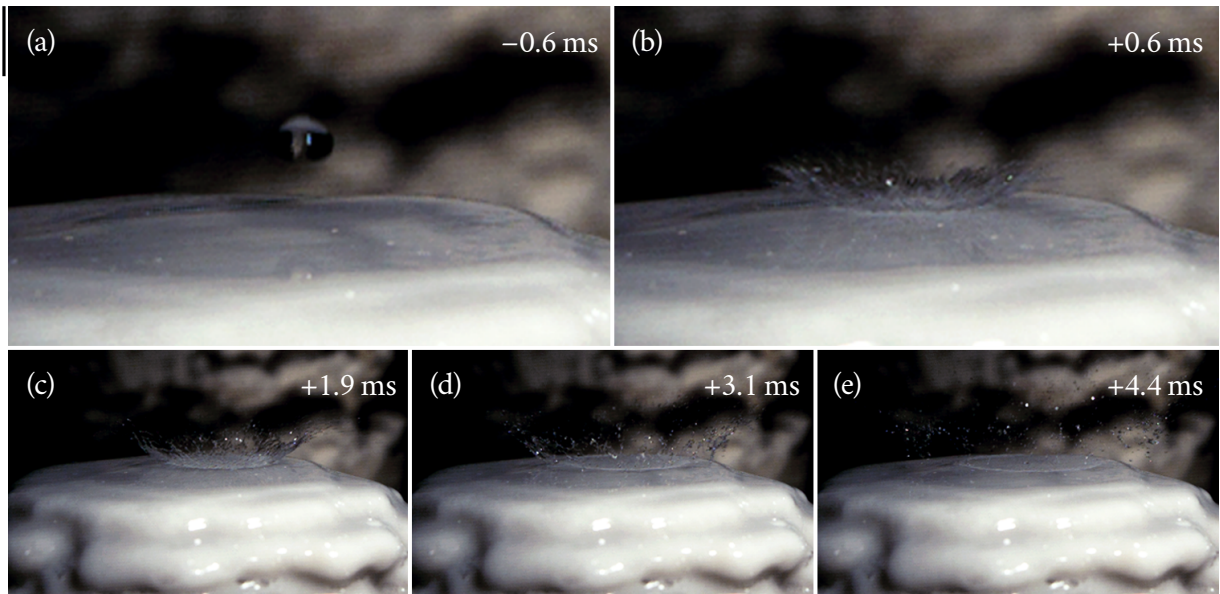
Figure 3.2: Time sequence of the impact of a drop on stalagmite Org02, with crown formation and fragmentation. (a) The flattened drop right before the impact. (b) Formation of the crown after the drop has started to crush on the stalagmite. (c) The crown grows and is accompanied by the formation and ejection of secondary jets destabilising into droplets. (d) Fragmentation of the crown. (e) The puddle left by the drop in the film has reached a value $r_{\mathrm{c}} = 2.1$ cm (see Sec. 2.1 from Ch. IV). The impacting drop has a radius $R_{\mathrm{d}} = 2.68$ mm and velocity $9.28\,\mathrm{m\,s^{-1}}$. All frames (a-e) are separated by 1.25 ms. The upper left scale bar relative to (a-b) is 5 mm while the bottom right one refers to (c-e) and is 2 cm.

During the first few centimetres of fall, the drop detaching from the stalactite is also subjected to strong shape variations and mostly alternates between oblate (horizontal radius > vertical radius) and prolate (horiz. < vert.) shapes [4, 24], as it can be seen in Fig. 3.1 (f-i). These internal oscillations result from the elongated shape of the drop upon detachment from the stalactite and the effect of surface tension, which causes the drop to recover to a more spherical shape [238]. Secondary modes of oscillations are also present [26] but cannot be easily seen in the photographs from Fig. 3.1. These modes correspond to the first spherical harmonics ℓ obtained by linear analysis

for a free drop and have the following Rayleigh frequency [142, 209, 238]:

$$\sqrt{\frac{\gamma}{3\pi m_{\mathrm{d}}}\ell(\ell+2)(\ell-1)} \, . \tag{3.1}$$

The damping time of these modes is given by

$$\frac{2R_{\mathrm{d}}^2}{\nu(2\ell+1)(\ell-1)} \, , \tag{3.2}$$

where $\nu \simeq 10^{-6} \, \mathrm{m^2 \, s^{-1}}$ is the water kinematic viscosity. Modes $\ell = 2, 3$ and 4 are associated with frequencies of 29 Hz, 55 Hz and 86 Hz, respectively. The corresponding damping times are 2.26 s, 810 ms and 420 ms, respectively. These times correspond to a fall of about 14.4 m for $\ell = 2$, 2.9 m for $\ell = 3$, and 90 cm for $\ell = 4$ (see Sec. 3.1). Due to the large cave ceilings, most drops landing on stalagmites should no longer be subjected to internal oscillations for $\ell \gtrsim 4$. The second and third modes, however, were still visible in our videos for short falling heights, as in the case of, e.g., Clam03 ($z = 30$ cm). Nevertheless, it is expected that neither of these oscillations affect the fall trajectory nor the impact of the drop. Moreover, the drop equivalent radius was estimated by considering both the vertical and horizontal radii of the drop and the oscillations should not affect the measurements either. After these internal modes of oscillations are damped, the drop is flattened out in response to aerodynamic forces and remains oblate for the rest of its fall.
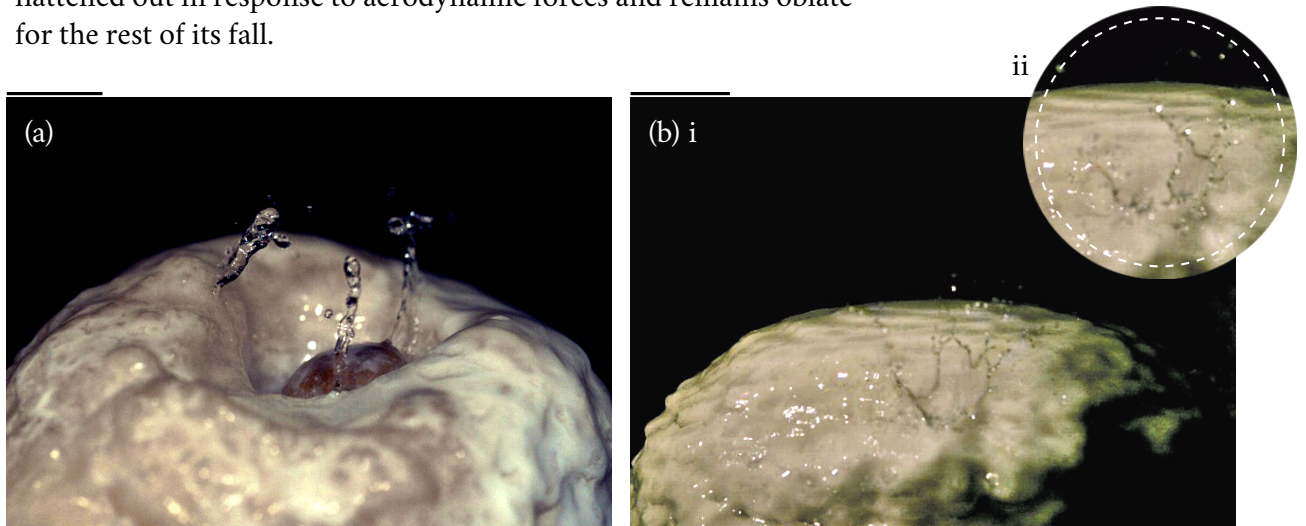
Figure 3.3: Two instances of non-traditional drop impacts on stalagmites. (a) Drop impact in a splash-cup stalagmite (Org07), with a small pisolite inside. The photograph was taken 15 ms after the initial impact. The scale bar is 1 cm. (b) Liquid sheet detaching from the surrounding wall of a convex stalagmite (Org01). The rim of the sheet was enhanced to be more visible in both photographs, which were respectively taken 10.2 ms (i) and 13.8 ms (ii) after the beginning of the impact. The scale bar is 5 cm.

2.2 Impacting the stalagmite top

The fall of the drop is eventually hindered by the stalagmite underneath the stalactite from which the drop originates, this stalagmite being usually covered by a thin residual film of water. Figure 3.2 depicts the impact of a drop on the flat top of Org02 at different times. Due to its long fall ($z = 19.4$ m), the incoming drop of radius $R_{\mathrm{d}} \simeq 2.61$ mm is slightly flattened (Fig. 3.2 (a)). It impacts the stalagmite at a velocity $u_{\mathrm{d}} \simeq 9.39 \, \mathrm{m \, s^{-1}}$. The impact is accompanied by the formation of an inclined crown growing over time (Figs. 3.2 (b)). Secondary jets destabilising into droplets are ejected from the edge of the crown (Fig. 3.2 (c)). The crown then fragments into many droplets

without retracting (Fig. 3.2 (d)). Finally, the rim surrounding the liquid puddle left by the crushed drop into the film reaches its maximum visible extension of radius $r_c \simeq 2.1$ cm (Fig. 3.2 (e)). A comprehensive study of highly-accelerated drop impacts on thin films is provided in Ch. IV, with r_c defined more precisely in Sec. 2.1 from Ch. IV. On the other hand, the drop impact on a concave stalagmite looks different, as shown in Fig. 3.3 (a) on Org07. Instead of forming a circular crown, the crushed drop is deflected during its spreading by the curved stalagmite top, and, in the case presented in Fig. 3.3 (a), by the presence of a small pisolite. The liquid is ejected away in a few preferential directions constrained by the shape of the stalagmite. Secondary jets and droplets also form but are much larger and slower than in the case of a flat stalagmite. In Fig. 3.3 (b), a drop impacts the side of the convex stalagmite Org01. Although impacts on the very top of convex stalagmites resemble those from Fig. 3.2, in this case we note the formation of a liquid sheet in a preferential direction too, in a similar manner as those observed on inclined substrate edges [144]. We observe the liquid sheet forming and growing at a certain angle from the stalagmite outer wall in Fig. 3.3 (b) i, then detaching and fragmenting into secondary droplets away from the stalagmite in Fig. 3.3 (b) ii.

It is also observed that drops in caves do not fall along vertical straight lines. Indeed, drops originating from a single punctiform stalactite impact the underlying stalagmite at different positions, sometimes scattered over several centimetres. Figure 3.4 (a) shows a collage of five drops coming from one stalactite but landing on different spots on the same stalagmite (Sal01), up to 13.2 cm apart. In Fig. 3.4 (b), we show the complete histogram of the distance between the impact point position of the drops that fell on Sal01, and the axis of symmetry of this stalagmite, defined as x in Sec. 1. We also remind in Fig. 3.4 (b) the introduction of the parameter Δ as the standard deviation of this distribution; in this case, we obtain $\Delta = 3.75$ cm. Although the drops all detached from the same point in the same conditions, they experienced different falls. This dispersal may
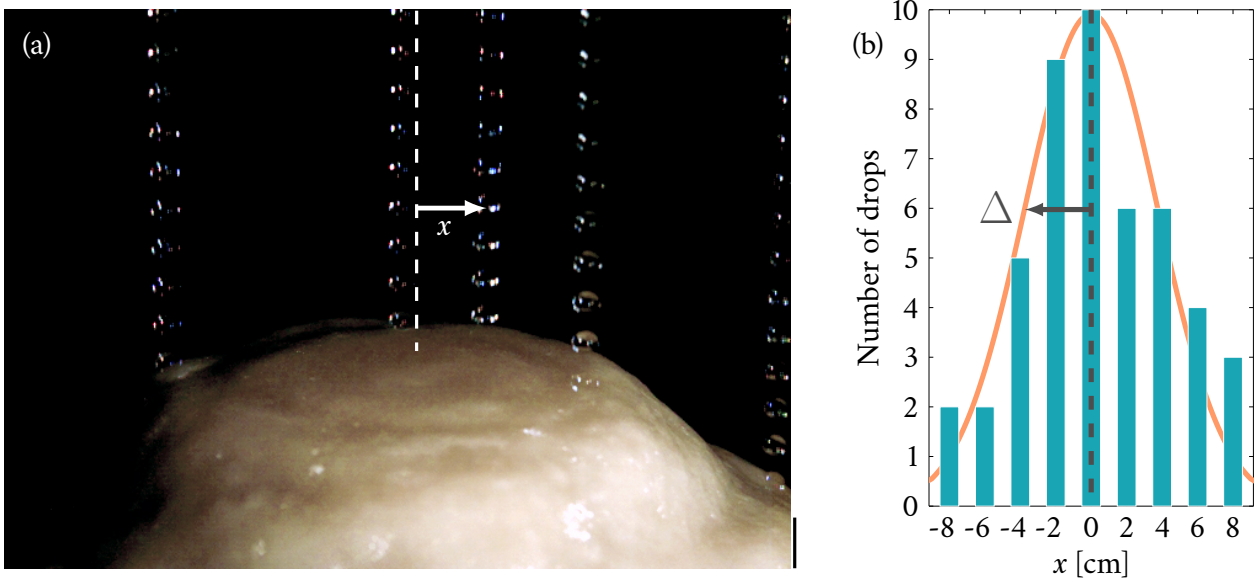
Figure 3.4: Dispersal in the drop horizontal impact point position. (a) Drops coming from the same stalactite fall in different locations on the stalagmite Sal01, from La Salamandre cave. The image was obtained by superposing frames showing the trajectories followed by five drops landing on this stalagmite. For each drop, the frames used are all separated by 740 μs, from the moment the drop appears in the field of view up to right before impact. The scale bar is 1 cm. (b) Histogram showing the entire distribution of the distance between the impact point position of the drop and the axis of symmetry of the stalagmite, x, for the 43 drop impacts that were recorded on Sal01 (blue bars). The orange line represents the corresponding probability density function drawn with the standard deviation Δ of the distribution (if this distribution was normalized). With a falling height of $z = 25.6$ m, the value of Δ obtained for this stalagmite is 3.75 cm, with an average stalagmite radius $r_{sm} = 5.5$ cm.

set some constraints on the overall stalagmite shape and width, which we will attempt to model in the following Section. As seen above, depending on the position on which the drop lands and stalagmite curvature, the impact itself can take various forms. The impact variability can in turn affect the local subsequent stalagmite growth. We will only focus on the drop free fall and impact point position rather than on the complete drop impact in this Chapter. Ensuing the observations from this Section, our primary goal is to model the scattering witnessed in the impact point position of the drops, which we will complete by an estimation of the drop velocity at the end of its fall, and verify whether we can relate it to the average stalagmite radius.

3.   Drop velocity and impact point dispersal

In this Section, we model the entire drop trajectory according to our observations. This allows us to derive (i) a relation between the drop impacting velocity, u_d, and the drop falling height, z, in Sec. 3.1, and (ii) a relation between the scattering observed in the drop impact point position, Δ, and the drop falling height, z, in Sec. 3.2. We also compare our modelling to the experimental measurements of u_d and Δ, obtained according to the methodology described in Sec. 1.

In Fig. 3.5 (a), the impact velocity u_d of the analysed drops (average $\pm$ s.d. in all videos relative to one stalagmite) is represented as a function of their falling height z. Data obtained in caves and in a lab setting are in good agreement with each other. The velocity u_d increases non-linearly with the falling height z, and seems to reach a saturation value for large falling heights ($z > 20$ m). In Fig. 3.7 (a), we show the measured standard deviation Δ of the impact position distribution (s.d. in all the measurements relative to one stalagmite) as a function of the falling height z. The impact point dispersal Δ increases almost linearly with z. Again, data obtained in caves and more controlled lab conditions overlap. Figures 3.5 (b) and 3.7 (b) remind how u_d and Δ were measured (see Sec. 1). Based on our observations, we reckon that the scattering in the impact position cannot be attributed to a factor specific to caves. For example, while the small irregularities at the surface of the stalactite might give the drop some initial horizontal momentum when this latter detaches, such momentum would be systematic and would not lead to a Gaussian dispersal. The local wind originating from the venting of the cave might also induce some additional drift to the drop. However, such a contribution seems negligible. For example, a maximum airflow rate of the order of 160 000 m^3 d^{-1} was measured at the open-air entrance of the first room (Salle de Joly) of the Aven d'Orgnac [34]. Because the cave cross-section is about 2500 m^2, the background air speed should be of $\sim$ 0.7 mm s^{-1}. A drop falling at more than 8 m s^{-1} takes less than 4 s to achieve a 30-m fall and would be deviated at most by 3 mm due to background air currents. Hence, these latter cannot explain the scattering in the drop impact point. Moreover, the same distribution is observed in all the caves and in the lab, where the drop fall is protected from parasitic air currents. The apparent random deviation in drop trajectory must therefore be self-induced.

We propose to model the influence of these aerodynamic forces – reflecting the randomly-oriented vortices – on the trajectory of the falling drop through a Langevin-like equation. The drop position is $\mathbf{X} = \mathbf{x} + z\mathbf{e}_z$, where $\mathbf{x} = (x, y)$ is the horizontal position vector, and $\mathbf{e}_z$ is a vertical unit vector oriented upward with respect to the downward drop trajectory (the vertical position z differs from the drop falling height and is only used in this paragraph). The velocity and acceleration of the drop are given by $\dot{\mathbf{X}} = \dot{\mathbf{x}} + u\mathbf{e}_z$ and $\ddot{\mathbf{X}} = \ddot{\mathbf{x}} + \dot{u}\mathbf{e}_z$, respectively, with $u = \dot{z}$. The motion of a falling drop of mass m_d satisfies Newton's second law:

$$m_\mathrm{d}\ddot{\mathbf{X}} = -m_\mathrm{d}g\mathbf{e}_z + \mathbf{F}, \tag{3.3}$$

where $m_\mathrm{d}g$ is the weight and $\mathbf{F}$ is the aerodynamic force. This latter comprises the drag, opposed

to the drop motion, and an additional lift component in a plane perpendicular to the drop motion:

$$\mathbf{F} = -C_{\mathrm{D}}\frac{\rho_{\mathrm{a}}A\left|\dot{\mathbf{X}}\right|}{2}\dot{\mathbf{X}} - C_{\mathrm{L}}\frac{\rho_{\mathrm{a}}A\left|\dot{\mathbf{X}}\right|}{2}\mathbf{E}\times\dot{\mathbf{X}}, \tag{3.4}$$

where $\rho_{\mathrm{a}} \simeq 1.2\,\mathrm{kg\,m^{-3}}$ is the air density, A is the cross-sectional area of the drop perpendicular to its motion direction, $\mathbf{E}$ is a unit vector of random direction in the plane perpendicular to $\dot{\mathbf{X}}$ and C_{D} and C_{L} are the drag and lift coefficients, respectively. The lift appearing in the former equation is caused by the loss of symmetry in the wake of the falling drop, as explained in more detail in Sec. 3.2.

3.1 Drop velocity

Since the drop is axisymmetric (axis $\mathbf{e}_z$) and its motion is mostly vertical ($C_{\mathrm{L}} \ll C_{\mathrm{D}}$, which will be verified later), we expect both $|\dot{\mathbf{x}}| \ll u \Rightarrow |\dot{\mathbf{X}}| \simeq u$ and $(\mathbf{e}_z \times \mathbf{E}) \cdot \dot{\mathbf{X}} \ll \mathbf{e}_z \cdot \dot{\mathbf{X}}$. Consequently, the vertical component of the lift is negligible in comparison to the vertical component of the drag, and the vertical projections of Eqs. (3.3) and (3.4) become:

$$\dot{u} = g - \frac{C_{\mathrm{D}}\rho_{\mathrm{a}}Au^2}{2m_{\mathrm{d}}}. \tag{3.5}$$

The drag coefficient C_{D} depends on the Reynolds number of the drop in the air $\mathrm{Re} = 2R_{\mathrm{d}}\rho_{\mathrm{a}}u/\mu_{\mathrm{a}}$, where $\mu_{\mathrm{a}} \simeq 18 \times 10^{-6}\,\mathrm{Pa\,s}$ is the dynamic viscosity of air. This dependence is here approximated by [73]

$$C_{\mathrm{D}} = \begin{cases} \dfrac{24}{\mathrm{Re}}(1 + c_1\mathrm{Re}^{2/3}) & \text{for } \mathrm{Re} < \mathrm{Re}_{\mathrm{c}}, \\[2mm] 0.45 & \text{for } \mathrm{Re} \geq \mathrm{Re}_{\mathrm{c}}, \end{cases} \tag{3.6}$$

which is valid for at least $\mathrm{Re} < 10^5$. For a hard sphere, $\mathrm{Re}_{\mathrm{c}} \simeq 1000$ and $c_1 \simeq 0.175$. However, the drops are flattened in response to aerodynamic forces (see Figs. 3.1 (f) and 3.2 (a)). Their deformation is resisted by surface tension, so dimensional analysis [181] suggests that the effective horizontal surface A is

$$A = \pi R_{\mathrm{d}}^2 + 2\pi c_2\frac{\rho_{\mathrm{a}}R_{\mathrm{d}}^3u^2}{\gamma}, \tag{3.7}$$

with c_2 to be determined. Moreover, as the drop is liquid, it might not satisfy the same no-slip condition as a hard sphere. However, since tangential stresses remain continuous at the water/air interface, the ratio of characteristic velocity in the water vs. in the air should be of the order of the ratio between dynamic viscosity in the air vs. in the water: $U_{\mathrm{w}}/U_{\mathrm{a}} \simeq U_{\mathrm{w}}/u_{\mathrm{d}} \sim \mu_{\mathrm{a}}/\mu$. Because the water viscosity is around a hundred times larger than the air viscosity, recirculation velocities inside the drop should not overcome a hundredth of the vertical translation velocity of the drop. Consequently, the no-slip condition should apply in first approximation and the falling drop should experience the same drag force as a hard sphere.

Time integration of Eq. (3.5) gives the relation between the falling height of the drop z and its impacting velocity u_{d} as

$$z = \int_0^{u_{\mathrm{d}}} \frac{u\,\mathrm{d}u}{g - \dfrac{C_{\mathrm{D}}\rho_{\mathrm{a}}Au^2}{2m_{\mathrm{d}}}}. \tag{3.8}$$

This relation is compared to the corresponding experimental results in Fig. 3.5. A least-square fit on velocity data (both from caves and lab) gives $c_1 = 0.198$ and $c_2 = 0.029$. The terminal veloc-

ity $u_\infty \simeq 10.51 \, \mathrm{m \, s^{-1}}$ is reached by the drop when

$$m_\mathrm{d} g = \frac{1}{2} C_{\mathrm{D},\infty} \rho_\mathrm{a} A_\infty u_\infty^2 \,, \tag{3.9}$$

where $C_{\mathrm{D},\infty}$ and A_∞ are obtained by substituting $u = u_\infty$ in Eqs. (3.6) and (3.7), respectively. This terminal velocity, associated with the fairly constant size of cave drops, yields an upper bound on the Reynolds number of Re $\sim$ 3500, which is still within the range of validity of Eq. (3.6). While the drag-induced deformation of the drop significantly affects its falling velocity, we note that it is not sufficiently large to induce some in-flight fragmentation, as experienced for example by large raindrops [182]. Indeed, the criterion for such fragmentation is $\rho_\mathrm{a} R_\mathrm{d} u_\mathrm{d}^2 / \gamma > 15$. Given the size constraint on drops originating from stalactites, satisfying this criterion would require the falling velocity to reach $17 \, \mathrm{m \, s^{-1}}$, which is well beyond the terminal velocity $u_\infty = 10.51 \, \mathrm{m \, s^{-1}}$.
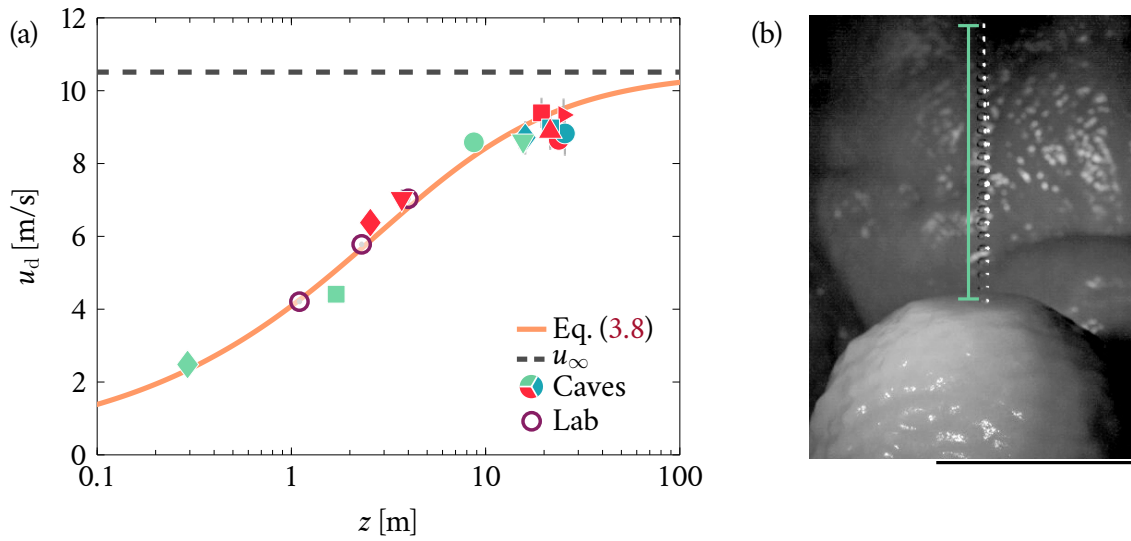
Figure 3.5: (a) Impact velocity u_d of the drop as a function of the falling height z, measured in both cave and lab settings (symbols), compared to the prediction given by Eq. (3.8) (solid line in orange) for parameters $c_1 = 0.198$ and $c_2 = 0.029$, with a drop radius $R_\mathrm{d} = 2.64$ mm. It should be noted that some error bars are not visible. The dashed line shows the terminal velocity $u_\infty = 10.51 \, \mathrm{m \, s^{-1}}$ that drops may reach based on these experimental data. Hollow symbols ∘ represent lab data corresponding to a drop radius similar to the drop radius measured in caves. Solid symbols (in red ●, green ● and blue ●) represent cave data, each marker corresponding to a stalagmite from Tab. 2.1 for which high-speed videos were recorded. (b) Example of impact velocity measured on a video relative to Clam01 (symbol ●). Images are obtained by superposition of frames separated by $740 \, \mu$s until the end of the drop fall. The distance between the positions of the drop when it first appears in the field of view and right before it impacts the stalagmite (represented by the green line) is 14.1 cm. Both positions are separated by 16.3 ms (88 frames at a rate of $5400 \, \mathrm{fr \, s^{-1}}$), hence the final velocity of this drop is approximately equal to $8.65 \, \mathrm{m \, s^{-1}}$. The corresponding velocity given by Eq. 3.8 is $8.18 \, \mathrm{m \, s^{-1}}$ for $z = 8.7$ m and $R_\mathrm{d} = 2.63$ mm. The scale bar is 10 cm.

3.2 Drop horizontal deflection

The vortex-induced vibrations of the trajectory of a sphere falling into air is a complex phenomenon. Although the drop is actually deformable, in this section we will neglect the oscillations of the drop shape and assume that it is a rigid sphere of constant volume. During the fall of the drop, the first vortices appear in its downstream wake at Re $\simeq 212$, namely after a distance of $z \simeq 1.3$ cm. Before that, the flow is perfectly axisymmetric and no lift force is exerted on the sphere. This is illustrated by Fig. 3.6 (a) adapted from Bouchet et al. [33], in which we observe that the lift coefficient C_L in a

plane perpendicular to the sphere trajectory increases from 0 with the Reynolds number. The first emitted vortices are non-axisymmetric and in counter-rotation with one another. They randomly develop around a longitudinal plane of symmetry containing the sphere center. A lift force varying in magnitude and whose direction is contained within the symmetry plane also appears above Re $\simeq$ 212 [79]. A second Hopf bifurcation appears at about Re $\simeq$ 273, as shown in Fig. 3.6 (a), in which case vortices become periodically emitted, the plane of symmetry selected by the former bifurcation being preserved [33, 79]. An example is shown in Fig. 3.6 (b) with experimental photographs adapted from Johnson and Patel [124], obtained at Re = 300. The sequence shows an entire period of vortex emission in the very near wake of the sphere. Moreover, the vortices take the shape of large-amplitude hairpins aligned in the same direction, leading to a lift force constant in direction but whose magnitude oscillates around a non-zero mean[2] [79].

As the Reynolds number further increases to 320, a secondary frequency of trajectory vibration appears but is three times smaller than the primary frequency [33]. The wake becomes irregular but the planar symmetry is still conserved up to Re = 355, corresponding to a distance z = 3.8 cm. Beyond this value, the wake becomes fully three-dimensional and chaotic [79]. Two examples of instantaneous lift coefficient C_{L} evolving with time in a plane perpendicular to the flow direction are shown in Fig. 3.6 (c), for Re = 3700 (Fig. 3.6 (c) i) and Re = 10 000 (Fig. 3.6 (c) ii). Both are adapted from simulations obtained by Yun et al. [237]. We observe that the lift coefficient indeed varies in a random manner in sign and in amplitude. The break of symmetry in the wake past the drop is thus responsible for the apparition of the lift force in Eq (3.4), and the trajectory followed by the drop appears to vary randomly. Falling heights typically found in caves are usually much greater than a few centimetres, thus the landing point of the drops is always scattered.

We assume that two successive vortex shedding events are separated by a time T, which is related to the Strouhal number of the flow defined by

$$\mathrm{St} = \frac{2R_{\mathrm{d}}}{u_{\mathrm{d}}T}.$$

(3.10)

On average, the time T separating two vortex emissions decreases with increasing Reynolds number. There is currently no analytical model that relates the Strouhal number St to Re for falling spheres. In the particular regime of Re $\gtrsim$ 273, the Strouhal number associated with the vortex emission is St = 0.127 [79]. Additionally, experimental data [2] suggest that St increases with Re, typically during the first 5 m of fall, up to approximately 0.9. Then St decreases with increasing Re but, in the range covered in caves, remains larger than 0.5. The St(Re) experimental data of Achenbach et al. [2] are here approximated by a cubic polynomial in the range Re < 3500.

We also hypothesise that the vortices emitted from a falling drop do not interact with the trajectory of the next drop. This is most likely true if the dripping period t_0 between two drops is larger than the time over which vortices fade away by viscous dissipation. By comparing the inertial and laminar viscous dissipation terms in the mechanical energy budget derived from Navier-Stokes momentum equation, this time might be estimated as $\rho_{\mathrm{a}}R_{\mathrm{d}}^2/(4\mu_{\mathrm{a}}) \simeq 1 \times 10^{-1}$ s. In the visited caves, the smallest dripping period t_0 relative to stalagmites for which high-speed videos were recorded was of the order of 2 s (see Tab. 2.1). Hence, in the present case, we may consider that the passage of a drop does not affect the trajectory of subsequent ones.

---

[2]The hairpin pattern is not visible in Fig. 3.6 (b).
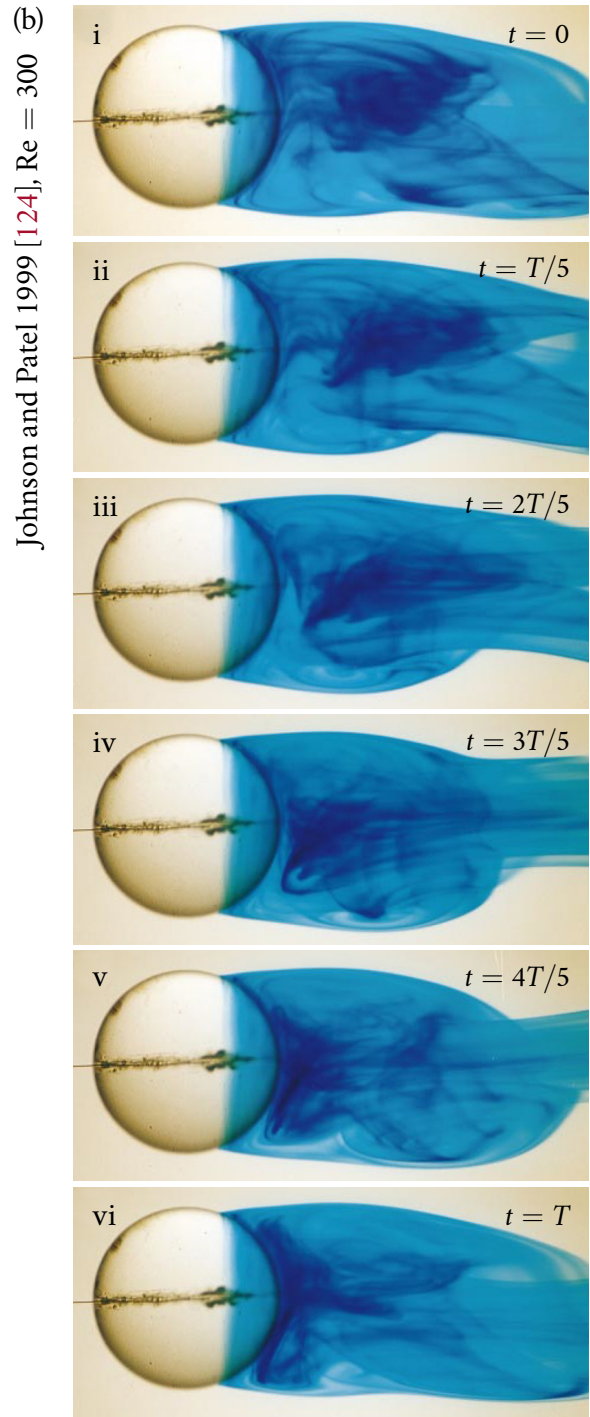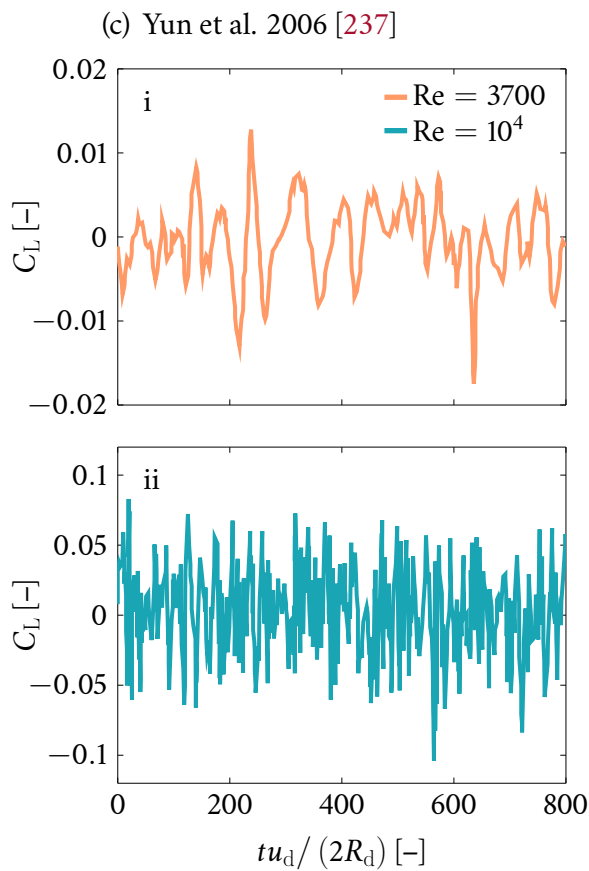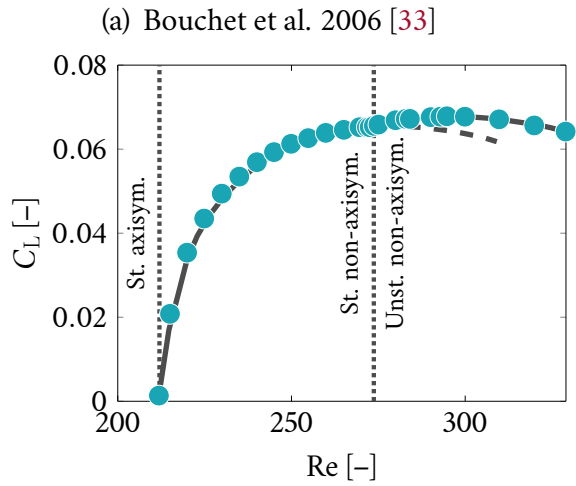
Figure 3.6: Evolution of the lift acting on a sphere with time and Reynolds number. (a) Graph adapted from Bouchet et al. 2006 [33], Fig. 11 – The lift coefficient C_L develops from an originally null value as Re increases above 212. Markers come from simulations. Regimes separated by dotted lines are respectively referred to as *steady axisymmetric*, *steady non-axisymmetric* and *unsteady non-axisymmetric* by the authors. The dashed line starting from the second Hopf bifurcation (at Re = 273) corresponds to an extrapolation of the subcritical regime. (b) Photographs adapted from Johnson and Patel 1999 [124], Fig. 41 – Complete sequence of vortex emission in the periodic regime, at Re = 300, for an entire period T. The blue dye shows the near wake of the sphere obtained experimentally. Photographs are all separated by $T/5$. (c) Graphs adapted from Yun et al. 2006 [237], Fig. 5 – Instantaneous lift coefficient measured in a plane perpendicular to the main flow direction, from simulations performed at Re = 3700 (i, orange) and Re = 10 000 (ii, blue). The legend in i refers to both i and ii curves.

The impact point dispersal Δ is estimated as a function of the falling height z, by considering the horizontal projection of Newton's second law of motion from Eq. (3.3):

$$m_{\mathrm{d}}\ddot{\mathbf{x}} = -\frac{1}{2}C_{\mathrm{D}}\rho_{\mathrm{a}}Au\dot{\mathbf{x}} + \frac{1}{2}C_{\mathrm{L}}\rho_{\mathrm{a}}Au^2\boldsymbol{e}, \tag{3.11}$$

where $\boldsymbol{e} = \mathbf{E} \times \mathbf{e}_z$ is a vector of random horizontal direction that is almost unitary since the drop velocity is almost vertical. We neglect the drop deformation, which is here a second-order term, thus the cross-sectional area A is now approximated by πR_{d}^2. No exact relation between the lift coefficient C_{L} and the Reynolds number Re could be found in the literature over the entire range of Re values covered by the falling drop, i.e., up to Re $\sim$ 3500. However, the instant lift coefficient has been computed from numerical simulations at peculiar Re by several authors, as reported in Tab. 3.1. All coefficients presented in this table correspond to the root mean square value computed over a time period during which at least a few tens of vortices were shed. An example is presented in Fig. 3.6 (c) ii, in which we note that the absolute value of C_{L} is bounded by about 0.1, which verifies our hypothesis that $C_{\mathrm{L}} \ll C_{\mathrm{D}}$. In Tab. 3.1, it can further be observed that the lift coefficient remains of constant order of magnitude (except at Re = 3700, where the shear layer separates laminarly from the sphere whereas turbulence occurs within this layer [186, 237], see Fig. 3.6 (c) i). The average value of all the lift coefficients presented in Tab. 3.1 is $C_{\mathrm{L}} = 0.067$. Equation (3.11) can be made dimensionless by defining $\tau = t/T$, $\boldsymbol{x} = \mathbf{x}/(uT)$ and $\dot{\boldsymbol{x}} = \dot{\mathbf{x}}/u$:

$$\ddot{\boldsymbol{x}} = -c_{\mathrm{D}}\dot{\boldsymbol{x}} + c_{\mathrm{L}}\boldsymbol{e}, \tag{3.12}$$

where $c_{\mathrm{D}} = (3\rho_{\mathrm{a}}/4\rho)(C_{\mathrm{D}}/\mathrm{St})$ and $c_{\mathrm{L}} = (3\rho_{\mathrm{a}}/4\rho)(C_{\mathrm{L}}/\mathrm{St})$.
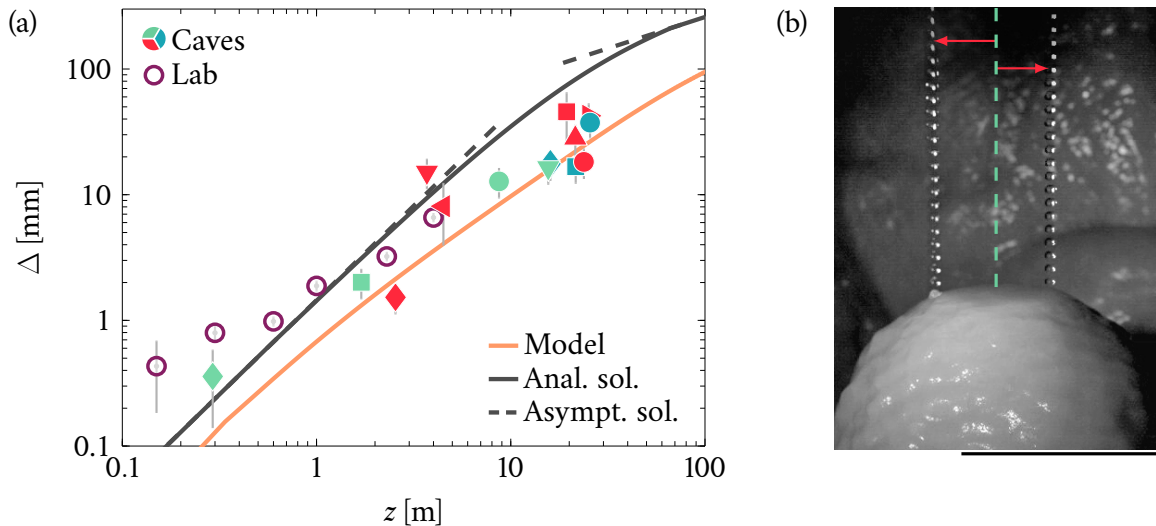
Figure 3.7: (a) Standard deviation Δ of the distribution of the impact point position as a function of the falling height z. The orange solid curve is obtained by solving numerically the recurrence relations from Eqs. (3.13) and (3.14) and by varying the parameters u, T, Re, St and C_{D} at each vortex emission. The lift coefficient C_{L} is set to 0.067, as an average across Reynolds numbers of the root-mean-square values found in the literature (see Tab. 3.1). Hollow symbols ∘ correspond to data obtained in a lab setting for drops of radius $R_{\mathrm{d}} = 2.32$ mm. All the solid symbols (in red ●, green ● and blue ●) represent experimental measurements obtained in caves with high-speed videos (see Tab. 2.1 for symbol correspondence). The solid black line shows the analytical solution obtained at constant drop velocity in Eqs. (3.19)–(3.21), while the dashed lines represent the asymptotic solutions of this analytical solution in the regimes for which $nc_{\mathrm{D}} \ll 1$ (left) and $nc_{\mathrm{D}} \gg 1$ (right). (b) Examples of drop impact point positions deviating from the axis of symmetry of the stalagmites (corresponding to the green dashed line). Images are obtained by superposition of frames separated by $740\,\mu$s until the end of the drop fall. Measurements are shown in the case of Clam01 (symbol ●), with the two distances represented by the red arrows equal to 3.2 cm (left) and 2.7 cm (right). The scale bar is 10 cm.

The horizontal position and velocity of the drop can be obtained by first integrating Eq. (3.12) over one period T between two successive shedding events denoted $(n-1)$ and n, respectively, i.e., for $\tau \in [n-1; n]$. We assume that the lift component of the aerodynamic force remains constant in magnitude and direction over this shedding period. The horizontal position $\boldsymbol{x}_n$ and velocity $\dot{\boldsymbol{x}}_n$ after the nth shedding event are therefore related to the position $\boldsymbol{x}_{n-1}$ and velocity $\dot{\boldsymbol{x}}_{n-1}$ at the $(n-1)^{\text{th}}$ shedding event through the following Langevin-like recurrence relations, where we define $\alpha = \exp(-c_{\text{D}})$:

$$\boldsymbol{x}_n = \boldsymbol{x}_{n-1} + \frac{(1-\alpha)}{c_{\text{D}}}\dot{\boldsymbol{x}}_{n-1} + \frac{c_{\text{L}}}{c_{\text{D}}^2}(\alpha - 1 + c_{\text{D}})\,\boldsymbol{e}, \tag{3.13}$$

$$\dot{\boldsymbol{x}}_n = \alpha\dot{\boldsymbol{x}}_{n-1} + \frac{c_{\text{L}}}{c_{\text{D}}}(1-\alpha)\,\boldsymbol{e}. \tag{3.14}$$

The dimensional standard deviation of the horizontal position is by definition

$$\Delta = \sqrt{\langle \mathbf{x}_n \cdot \mathbf{x}_n \rangle} = uT\sqrt{\langle \boldsymbol{x}_n \cdot \boldsymbol{x}_n \rangle}, \tag{3.15}$$

where $\langle \ldots \rangle$ denotes an ensemble average over many falling drops. It is calculated based on the non-dimensional standard deviation $\sqrt{\langle \boldsymbol{x}_n \cdot \boldsymbol{x}_n \rangle}$, obtained by multiplying and averaging Eqs. (3.13) and (3.14):

$$\langle \boldsymbol{x}_n \cdot \boldsymbol{x}_n \rangle = \langle \boldsymbol{x}_{n-1} \cdot \boldsymbol{x}_{n-1} \rangle + \frac{(1-\alpha)^2}{c_{\text{D}}^2}\langle \dot{\boldsymbol{x}}_{n-1} \cdot \dot{\boldsymbol{x}}_{n-1} \rangle + 2\frac{(1-\alpha)}{c_{\text{D}}}\langle \boldsymbol{x}_{n-1} \cdot \dot{\boldsymbol{x}}_{n-1} \rangle$$
$$+ \frac{c_{\text{L}}^2}{c_{\text{D}}^4}(\alpha - 1 + c_{\text{D}})^2, \tag{3.16}$$

$$\langle \dot{\boldsymbol{x}}_n \cdot \dot{\boldsymbol{x}}_n \rangle = \alpha^2 \langle \dot{\boldsymbol{x}}_{n-1} \cdot \dot{\boldsymbol{x}}_{n-1} \rangle + \frac{c_{\text{L}}^2}{c_{\text{D}}^2}(1-\alpha)^2, \tag{3.17}$$

$$\langle \boldsymbol{x}_n \cdot \dot{\boldsymbol{x}}_n \rangle = \alpha\langle \boldsymbol{x}_{n-1} \cdot \dot{\boldsymbol{x}}_{n-1} \rangle + \frac{\alpha(1-\alpha)}{c_{\text{D}}}\langle \dot{\boldsymbol{x}}_{n-1} \cdot \dot{\boldsymbol{x}}_{n-1} \rangle + \frac{c_{\text{L}}^2}{c_{\text{D}}^3}(1-\alpha)(\alpha - 1 + c_{\text{D}}). \tag{3.18}$$

Since the lift direction $\boldsymbol{e}$ is assumed to be random and uncorrelated with the drop horizontal position and velocity, both $\langle \boldsymbol{x}_n \cdot \boldsymbol{e} \rangle$ and $\langle \dot{\boldsymbol{x}}_n \cdot \boldsymbol{e} \rangle$ vanish, and $\langle \boldsymbol{e} \cdot \boldsymbol{e} \rangle = 1$.

These coupled recurrence relations can be solved numerically from rest initial conditions to find Δ. We consider that the velocity $u(z)$ increases at each vortex emission n according to Eq. (3.8), and that Re, St and C_{D} vary accordingly, which is why Eqs. (3.16)–(3.18) cannot be integrated analytically. Nevertheless, an analytical solution at constant u is presented hereafter. Solving the recurrence relations with the average value $C_{\text{L}} = 0.067$ yields the numerical solution $\Delta(z)$ shown in Fig. 3.7. The model captures very well the measurements $\Delta(z)$, without any fitting parameter. The root mean square error (RMSE) in all the measurements is 7.8 mm, the main contribution to this error coming from the measurements obtained at large falling height z. Although this error seems larger than the measurements made at small falling height z, by taking the root mean square error for $z \leq 4$ m (the height reachable in lab), we only have RMSE $= 3.7$ mm while for $z > 4$ m, we obtain RMSE $= 8.9$ mm. For the smaller falling heights, we actually obtain $\Delta(z \leq 4\,\text{m}) = 3.4$ mm on average, which is of the same order as the RMSE made on these measurements, the radius of the drop R_{d}, and the maximum deviation that a drop subjected to parasitic air currents can possibly sustain (see discussion on page 41). Hence, with all these contributions it is not possible to state whether the error comes from the model failing at capturing the impact point dispersal for small z or if the deviation observed between the measurements and the model comes from external factors, or even from errors in the image analysis process.

Regarding the measurements at mid and large falling height ($z > 4\,\text{m}$), on average the relative error between the prediction and the actual value of Δ is of about 24 %, which indicates that there might be other second-order effects to take into account to better capture the free fall of the drop. These effects may include but should not be limited to: (i) the background air currents, (ii) the deformability and internal oscillations of the drop [238], (iii) the recirculation velocity field inside the drop, (iv) the possible initial shift that could appear because of irregularities around the stalactite tip/lab dripping tube surface, (v) the Magnus effect if the drop is subjected to an initial rotational speed [39], and (vi) the variability in the dripping period of the drop, especially the seasonal variability in caves that leads to drop volume variations [98].

Authors	Re [–]	C_L^{rms} [–]
Bagchi 2003 [14]	107	0.091
Bagchi 2003 [14]	261	0.058
Johnson 1999 [124]	211–250	0–0.062
Bouchet 2006 [33]	212–330	0–0.068
Plouhmans 2002 [173]	300	0.060
Plouhmans 2002 [173]	500	0.058
Bagchi 2003 [14]	609	0.081
Plouhmans 2002 [173]	1000	0.167
Yun 2006 [237]	3700	0.006
Jones 2008 [125]	10 000	0.033
Yun 2006 [237]	10 000	0.046

Table 3.1: Root mean square value of the lift coefficient C_L^{rms} around a sphere, obtained by several authors at various Reynolds numbers Re. The value of C_L^{rms} corresponds to the average made on at least a few tens of vortices shed in the wake past the sphere.

3.2.1 Analytical prediction at constant fall velocity

Since Re, St, and then c_D and c_L directly depend on the increasing fall velocity u, the recurrence relations of Eqs. (3.16)–(3.18) can only be solved numerically. We may nevertheless seek for an analytical solution by imposing a constant velocity u_d, i.e., constant c_D and c_L. The solution to Eqs. (3.16)–(3.18) starting from initial rest conditions $\boldsymbol{x_0} = \boldsymbol{0}$ and $\dot{\boldsymbol{x}}_0 = \boldsymbol{0}$ is

$$\langle \dot{\boldsymbol{x}}_n \cdot \dot{\boldsymbol{x}}_n \rangle = \frac{c_L^2}{c_D^2} \frac{1-\alpha}{1+\alpha} \left(1 - \alpha^{2n} \right), \tag{3.19}$$

$$\langle \boldsymbol{x}_n \cdot \dot{\boldsymbol{x}}_n \rangle = \frac{c_L^2}{c_D^3} \frac{1-\alpha^n}{1+\alpha} \left[(\alpha - 1)(1 + \alpha^n) + c_D (1 + \alpha) \right], \tag{3.20}$$

$$\langle \boldsymbol{x}_n \cdot \boldsymbol{x}_n \rangle = \frac{n c_L^2}{c_D^2} + \frac{c_L^2}{c_D^4} \frac{(1-\alpha)(1-\alpha^{2n})}{1+\alpha} - \frac{2c_L^2}{c_D^3} \left(1 - \alpha^n \right). \tag{3.21}$$

The resulting curve at constant parameters is shown in Fig. 3.7 with $R_d = 2.63\,\text{mm}$, $u_d = 10.5\,\text{m s}^{-1}$ the limit terminal velocity, $T = 2.5\,\text{ms}$ the vortex shedding period reached above $z \simeq 1\,\text{m}$ (which

corresponds to a peak frequency of 400 Hz), St $= 0.2$ the Strouhal number, $C_D = 0.45$ as for a hard sphere, and $C_L = 0.067$. We note that the general trend followed by both the model and the measurements is well captured by this approximation at constant u_d. Due to our choice of parameters and particularly the fact that we used the terminal velocity, the analytical prediction is with no surprise larger than the measurements overall, with a RMSE of 3.4 cm.

3.2.2 Asymptotic regimes

In the limit case where $nc_D \ll 1$, or $\alpha^n \to 1$, the drop does not have a velocity sufficient to generate significant drag, which can therefore be neglected. This approximately corresponds to a falling height $z \lesssim 0.5$ cm. In this case, the leading term in Eq. (3.21) becomes proportional to $c_L^2 n^3/3$. As $nc_D \gg 1$, or $\alpha^n \ll 1$, corresponding here to $z \gtrsim 25$ m, the leading order becomes $\sim c_L^2 n/c_D^2$. These two asymptotes are represented by the dashed lines in Fig. 3.7. Between the two asymptotic regions, which corresponds to the range of values covered experimentally, $\langle \mathbf{x}_n \cdot \mathbf{x}_n \rangle$ is thus in an intermediate regime that can be approximated as proportional to n^2. Therefore, from Eq. (3.15), Δ increases linearly with n. Considering St, T and v as constant during the whole drop trajectory, n can be estimated proportional to z, hence Δ is more or less proportional to z too in the range covered in cave and in lab, as observed in Fig. 3.7.

3.2.3 Timing of the drop movement

From Eq. (3.8), we can additionally compute the time t_{fall} taken by a drop to complete a fall of length z. This time is represented in Fig. 3.8 (a), in which we observe that t_{fall} increases monotonously with z, with two different slopes. In the region where $z \lesssim 10$ m, it is known from Fig. 3.5 that the impact velocity of the drop u_d increases with z. Around $z \simeq 10$ m, the concavity in the curve of u_d changes before it approaches the terminal velocity u_∞ for large falling heights. It is thus not surprising to observe the change of slope in the curve $t_{\text{fall}}(z)$ around $z \simeq 10$ m as well. Below this value, t_{fall} approximately follows a curve $\sim z^{1/2}$ while for $z \gtrsim 10$ m, we have $t_{\text{fall}} \sim z$, as illustrated in Fig. 3.8 (a). A drop of radius $R_d = 2.63$ mm falls over 1 m during approximately 440 ms, while a 10-m fall for this drop takes about 1.75 s.
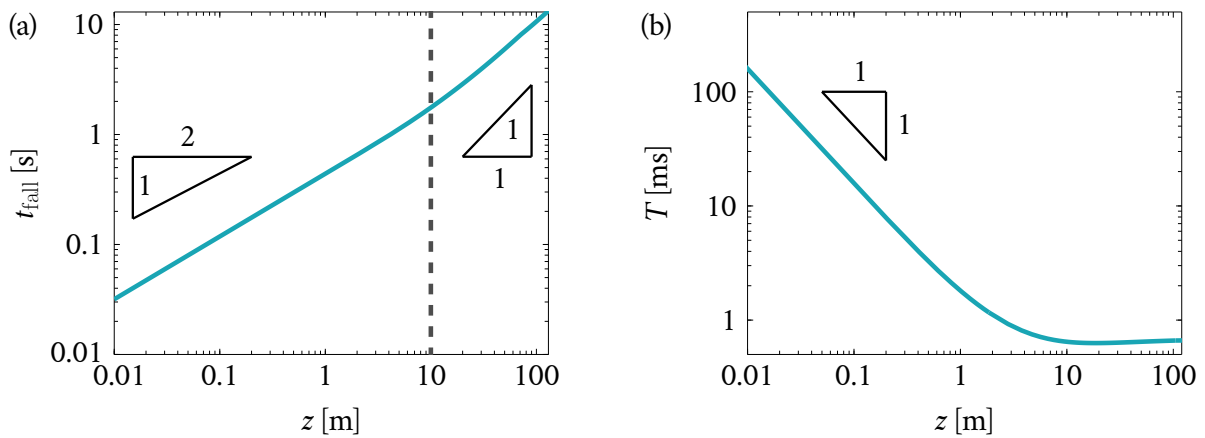
Figure 3.8: (a) Time t_{fall} taken by the drop to complete a fall of height z with the two asymptotic regimes $t_{\text{fall}} \sim z^{1/2}$ ($z < 10$ m) and $t_{\text{fall}} \sim z$ ($z > 10$ m). The time t_{fall} was computed using Eq. (3.8). The dashed line shows the value $z = 10$ m above which the velocity of the drop u_d becomes close to u_∞. (b) Time period T between two successive vortex shedding emissions, with asymptotic regime $T \sim z^{-1}$ ($z < 10$ m), obtained using Eqs. (3.8) and (3.10), with data from Achenbach et al. [2].

Additionally, in Fig. 3.8 (b), we represent the time period T between two vortex shedding events as a function of the drop falling height z. The curve was obtained by using Eq. (3.10) and the approximate evolution of St(Re) from Achenbach et al. [2], as well as the instantaneous velocity of the drop. We observe that T decreases as a/z up to $z \gtrsim 10$ m, value upon which it reaches a stationary value $T \simeq 0.7$ ms. This is consistent with the observation that both u_d and St have also reached a limit value.

4. Link with stalagmite width

The scattering observed in the impact point position of the drops can sometimes compare to stalagmite sizes, with the largest value measured in the visited caves being $\Delta = 4.6$ cm. The impact point dispersal can be solely related to the falling height of the drops. We report in this section our findings regarding the link that may exist between the dispersal observed and the average width of stalagmites originating from one drip.

4.1 Relation to the impact point dispersal observed

As described in Ch. 3.1, we measured the stalagmite radius r_sm taken as an average along the entire stalagmite body of 65 stalagmites from 7 different caves, as well as the falling height z associated with them. In Fig. 3.9 (a), we present the measured radius r_sm as a function of the dispersal Δ. The values used for Δ either come from measurements[1] or from the model developed
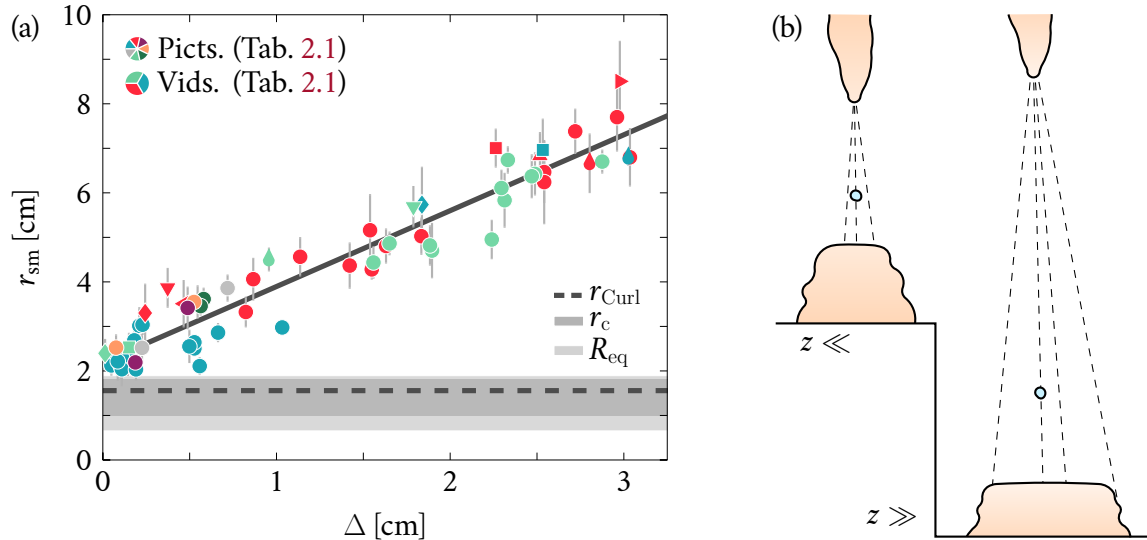
Figure 3.9: (a) Average stalagmite radius r_sm as a function of the impact point dispersal Δ, either measured from the high-speed videos or computed using Eqs. (3.16)–(3.18). Each symbol (in grey ●, light green ●, dark green ●, orange ●, purple ●, red ● and blue ●) represents a single stalagmite, with one colour per cave (see Tab. 2.1 and Supplemental Material from Parmentier et al. [172][1]). Markers which differ from dots relate to the stalagmites for which high-speed videos were recorded (see Tab. 2.1 for symbols correspondence, where the actual dot symbol relative to some stalagmites was here replaced by a drop shape ●). The solid line shows the linear regression from Eq. (3.22). The dashed horizontal line corresponds to the radius derived by Curl [60] (for $R_\mathrm{d} = 2.63$ mm and $\delta = 100$ μm). The two grey filled areas represent the intervals of values reached by the maximum extension of the crown radius during the drop impact in the film, r_c, and the equivalent red spot radius left by the drop in the film after the impact, R_eq, in lab experiments, the larger one corresponding to R_eq and the darker one to r_c (see Ch. IV for definitions). (b) Illustration of the effect of the dispersal in the impact point position of the drop: on the left, z is small and there is almost no dispersal, leading to smaller stalagmites, by contrast with the large dispersal generating a larger stalagmite radius on the right.

in the former section providing the relation $\Delta(z)$ (see Eqs. (3.16) to (3.18)). There is a significant correlation between the stalagmite radius $r_{\rm sm}$ and Δ. A linear regression with a coefficient of determination of $R^2 = 0.86$ indeed yields

$$r_{\rm sm}(\Delta) = r_{\rm sm,0} + 1.73\,\Delta\,, \tag{3.22}$$

where $r_{\rm sm,0} = 2.19\,{\rm cm}$ is the intercept with the axis $\Delta = 0$ (corresponding to no fall-induced dispersal).

For very small falling heights ($z \lesssim 0.5\,{\rm m}$), there is almost no scattering in the impact point position of the drops, meaning that the drops always fall very close to the centre of the stalagmite. The stalagmite width is therefore very close to the minimum $r_{\rm sm,0}$ observed in Fig. 3.9 (a). As the falling height becomes larger, $r_{\rm sm}$ is expected to increase accordingly because of the growing impact point dispersal. In particular, the slope of Eq. (3.22) is close to 2 and, for a Gaussian distribution, the probability that a drop falls on such a surface is at least 90%. The two situations are depicted in Fig. 3.9 (b).

4.2 Initial drop spreading upon impact and minimum stalagmite width

All the drops filmed with high-speed imaging splashed at impact (Fig. 3.3) in caves, in contrast to an assumption of previous models of stalagmite growth [20]. During the impact, the drop crushes into the residual film to form a crown surrounded by a rim that grows with time, the crown corresponding to the contour wall of a circular cavity formed at the impact position of the drop. More detail regarding this phenomenon is provided in Ch. IV. The cavity made by the crushed drop in the film reaches a maximum size $r_{\rm c}$ that compares to the minimum stalagmite radius observed $r_{\rm sm,0}$. From the experimental data presented in Ch. IV obtained in a lab setting, we have $r_{\rm c} \in [3.8; 6.2]\,R_{\rm d}$ or $[1.0; 1.6]{\rm cm}$ in the present case (measurements corresponding to $z = 0.5\,{\rm m}$ and $z = 4\,{\rm m}$). We additionally measured the maximum cavity radius reached by the drops in the high-speed movies taken in caves, and found that $r_{\rm c}^{\rm cave} \simeq 1.83 \pm 0.28\,{\rm cm}$ (average $\pm$ s.d. in all videos). This value is very close to our range coming from lab measurements, although $r_{\rm c}^{\rm cave}$ is a little higher since $r_{\rm c}$ increases with z and that falling heights are larger in caves than in the lab. Our lab experiments also reveal that the drop mixing with the film lying on top of the stalagmite during the impact leaves a spot of equivalent radius denoted $R_{\rm eq}$ in the film, close to $r_{\rm sm,0}$ as well. The spot radius $R_{\rm eq}$ spans over a wider range of $[2.5; 7.2]\,R_{\rm d}$, or $[0.6; 1.9]{\rm cm}$. Both radii are illustrated in Fig. 3.9 (a), where it should be noted that we used the full range coming from lab and cave for $r_{\rm c}$, i.e., $[1.0; 1.8]{\rm cm}$.

Curl [60] had already computed a minimum stalagmite radius close to $r_{\rm sm,0}$, by dividing the drop volume by the estimated film thickness δ as $r_{\rm Curl} \simeq \sqrt{(4/3\pi R_{\rm d}^3)/(\pi\delta)}$. For $\delta = 100\,\mu{\rm m}$, which is the typical order of magnitude of films found on stalagmites, we obtain $r_{\rm Curl} = 1.6\,{\rm cm}$. A radius $r_{\rm Curl} = r_{\rm sm,0}$ would actually correspond to $\delta \simeq 50\,\mu{\rm m}$, which is a thickness commonly found after the film has experienced some gravity-induced drainage, as explained in Ch. V. Although for typical orders of magnitude found in situ, $r_{\rm Curl}$ is close to our observations, it fails at capturing the influence of the film thickness on the minimum stalagmite width as $r_{\rm Curl}$ decreases with δ and predicts a stalagmite radius of $r_{\rm Curl} = 0.9\,{\rm cm}$ for, e.g., $\delta = 300\,\mu{\rm m}$, a film thickness value that was measured on some stalagmites from Fig. 3.9 (see Tab. 2.2).

The minimum radius $r_{\rm sm,0}$ thus seems to be set mostly by the size of the spreading drop onto the stalagmite, with both $r_{\rm c}$ and $R_{\rm eq}$ varying little with the falling height of the drop. Using the bounds of our experimental intervals for $r_{\rm c}$ and $R_{\rm eq}$, we find that $r_{\rm sm,0}/r_{\rm c} \sim 1.2 - 2.2$, and $r_{\rm sm,0}/R_{\rm eq} \sim 1.2 - 3.3$. Therefore, the minimum stalagmite radius $r_{\rm sm,0}$ is always at least a little larger than the maximum expansion of the drop impacting the stalagmite, and sometimes much larger. This may be due to the widening of the stalagmite owing to the gravity-driven drainage of the water film,

which is not taken into account here (see Ch. V). This drainage is expected to vary with the shape and overall curvature of the stalagmite, hence the wide span in the value of the ratio $r_{\mathrm{sm},0}/r_{\mathrm{c}}$ (resp. $r_{\mathrm{sm},0}/R_{\mathrm{eq}}$).

5. Conclusion

In this chapter, we modelled the free fall of drops dripping from stalactites in caves, until they fall onto the stalagmite underneath. Starting from Newton's second law that we projected onto the vertical direction and integrated over time, we obtained an equation describing the velocity of freely falling drops in Sec. 3.1. We took into account the deformabiliy of the drops into the drag force, which induced the appearance of two fitting parameters into the model. The cave and lab measurements agree well with the modelling of the velocity, which presents a limit value at large falling heights, of about $\sim 10\,\mathrm{m\,s^{-1}}$.

While they all originate from a single punctiform point, drops landing on a stalagmite present the particularity of being scattered at impact, sometimes over several centimetres. We showed that this dispersal is not correlated to an external factor and therefore has to be self-induced. We postulated that the dispersal exhibited by the drop trajectory comes from the vortices shed in the wake of the drop. We took this into account in the modelling of the drop free fall, by including a randomly-oriented lift component in the aerodynamic force acting on the drop. Integrating the equations in between the successive vortices shed in the wake of the drop, we obtained Langevin-like recurrence equations describing the position and velocity of the drop. There is currently no analytical model describing the lift acting on a spherical, deformable object in a cross flow. We therefore approximated the lift coefficient acting on the drop by gathering numerical results from the literature. Even without any fitting parameter, we noted in Sec. 3.2 that the results from the experiments and the modelling agree well with one another. The model derived in this chapter should be applicable to the free fall of drops but also of similar objects.

Finally, we connected the average stalagmite width to the aerodynamics of the drop free fall. The stalagmite width is not only governed by the saturation size of the spreading drop into the film, r_{c} (or R_{eq}), but it is also and mostly conditioned by the dispersal of the drop impact position, Δ, as our measurements revealed. Because this dispersal increases with the falling height of the drops, so does the stalagmite average radius. Large stalagmites originating from a single stalactite should thus most likely be found in cave parts with higher ceilings. While our measurements and model respectively show and explain the correlation between stalagmite width, impact point dispersal and falling height, the stalagmite width may also be significantly influenced by several other factors affecting its growth, which will be the subject of the following chapters.

Summary (Ch. III)

⬥ Drops dripping from stalactites and impacting stalagmites are captured through high-speed imaging, as described in Ch. II and in Sec. 1. The main features exhibited by drops freely falling in caves, summarised in Sec. 2, are (i) their constant radius, (ii) their impacting velocity increasing with falling height, and (iii) the dispersal in their impact point position, albeit a fixed initial dripping position at the stalactite tip.

⬥ We model the fall of the drop in Sec. 3, starting from Newton's second law in which we include the non-negligible interaction (drag and lift) of the drop with the surrounding air. A vertical projection and time integration of the drop free fall equation lead to a relation between the drop impacting velocity and falling height in Sec. 3.1. A good agreement is obtained between the experimental data and the modelling which includes two fitting parameters due to the drag dependence on the drop deformability.

⬥ We show that the dispersal exhibited by the drop impact point position must be self-induced, and further postulate that it should be caused by the vortices randomly shed in the drop wake. This is taken into account in the modelling from Sec. 3.2 by assuming a random orientation of the lift acting on the drop. In lack of a model describing the lift on a deformable object such as a drop, we approximate it by the lift on a hard sphere, obtained from numerical simulations conducted by different authors at various Reynolds numbers.

⬥ In Sec. 3.2, we use a discrete time integration of the horizontal projection of Newton's second law to derive recurrence relations for the position and velocity of the drop at each vortex emission. From there, we further obtain an equation for the dispersal in the drop impact point position distribution. Once again, data coming from cave and lab settings are in good agreement with the model, which implies no other fitting parameter than the deformability correction in the drag law.

⬥ In Sec. 4, we relate the average top radius of a collection of stalagmites described in Ch. II to the dispersal in the impact point position of the associated drops, and, from there, to the falling height of these drops.

Highlights (Ch. IV)

- In Ch. IV (see next page), the mixing and ejections produced by the impact of a drop on a thin film are studied. In Sec. 1, we review the generalities of drop impacts on thin films in a film thickness range close to the one observed in caves.

- The present chapter focuses solely on lab experiments. The methodology for producing and observing impacts from both side and top views using high-speed imaging is described in Sec. 2. The top view of the impacts, in particular, allows to decipher the mixing between the drop and the film by coloring them with two different dyes. We analyse the recordings thanks to image analysis tools and a colorimetry-based algorithm, that we describe briefly in Sec. 2.2, and in more detail in Appendix B.1.

- Section 3 addresses the phenomenological aspects of the impacts from the side and top views. We classify them in four distinct scenarios. The geometry of the crown produced when the drop impacts the film, i.e., the side view, allows us to gain a deeper insight into the mixing between the drop and the film as seen from the top.

- In Sec. 4, we present a set of indicators inferred from the high-speed recordings. In Sec. 4.1, we focus on the geometrical features of the impacts while in Sec. 4.2, we cover various aspect of the mixing and splashing at impact. In particular, we are able to measure the amount of liquid ejected away during the impact, as well as the amount of liquid originating from the drop actually entering the film. We also compare our findings with the literature.

- The results are discussed in Sec. 5, with an emphasis on how each of the four scenarios affects the mixing between the drop and the film, as well as the liquid ejected away during the impact.
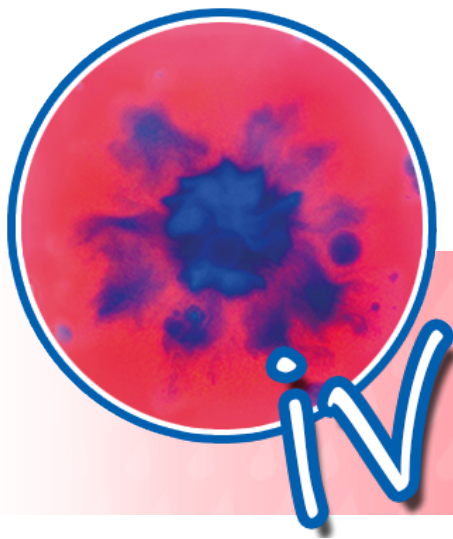
DROP IMPACT ON THIN FILM

After having only considered the constraints set by the aerodynamics of freely falling drops on the average stalagmite width, we now explore how a drop and the film covering a stalagmite interact during the impact of the drop on this film. In particular, we investigate the mixing occurring between the drop and the film, with the aim of measuring the amount of liquid originally from the drop actually entering the film. We are also interested in assessing the amount of liquid ejected away during the impact in the case where splash occurs. However, the findings from this chapter on the sole mixing and ejected volume at impact do not allow us yet to draw direct conclusions regarding the diversity of stalagmite shapes found in caves. We indeed need to take into account the interplay of all the physical processes, namely the drop free fall, the drop impact on thin film itself, the gravity-driven drainage of the film and the ion precipitation, which will be done in the subsequent chapters.

1. Overview

Despite the great shape variability exhibited by stalagmites in caves, these stalagmites all originate from the successive drops impacting the thin film covering them, thereby bringing in new ions in solution, which later precipitate and allow for the stalagmites to grow [70]. The distribution of ions following each impact results from the balance between the distribution of ions already in the film before the impact, the amount of ions brought by the drop in the film at each impact, and possibly the amount of ions leaving the film due to splashing. Owing to the sometimes very high cave ceilings (up to 25 m, see Ch. II), we observed in Sec. 3.1 from Ch. III that drops landing on stalagmites may reach impacting velocities up to $10 \, \mathrm{m \, s^{-1}}$, similarly to large raindrops [182]. However, as we also noted in Sec. 2.1 from Ch. III, by contrast with raindrops [224], the radius of the drops originating from stalactites is fairly constant and close to the capillary length, i.e., $R_\mathrm{d} \simeq 2.7 \, \mathrm{mm}$. Given these size and speed, most drop impacts on stalagmites lead to splashing. In caves, drops having a fall as short as 30 cm would actually splash when impacting the underlying film, independently of its thickness [227]. Hence, the in-between impact ion distribution depends on the mixing occurring between the drop and the film during the impact, but also almost always on the amount of ions ejected away at impact.

Drop impacts in general have been widely studied for the past decades [179, 235], partly because of their ubiquity in many industrial processes such as spray painting and cooling [37], microelectronics soldering [151], or crop spraying [221]. They also have multiple natural occurrences, e.g., the aeration of ocean surfaces [64], soil erosion [17, 18, 130], or the rain-induced foliar spreading of pathogens in crop fields [100, 144, 145]. A few studies have already characterised drop impacts

on thin liquid films for which $h/(2R_\mathrm{d}) \lesssim 10^{-1}$, as in caves. However, they focused mostly on the splash morphology [55, 127, 146, 188, 239], and more particularly on the splashing threshold [54, 185]. The influence of the fluid viscosity [7, 86, 239] was also investigated, as well as the underlying surface roughness [27, 54], or the (im)miscibility between the drop and the film [51, 136, 234]. Ersoy and Eslamian [80, 82] further characterised the various physical processes at play that induce mixing between the drop and the film during the collision. However, several features of drop impacts on thin films related to the mixing between the drop and the film have not been quantified yet, e.g., the proportion of the incoming drop volume which is ejected away in the splash droplets, or how much liquid coming from this drop would actually end up in the film after the impact. The knowledge of these quantities could also be useful in other contexts, e.g., to rationalise some of the mechanisms of rain-induced pathogen dispersal in between plant leaves [145].

In this chapter, we thus investigate the mixing and ejection processes as they would occur when drops impact stalagmites in caves. We therefore aim at studying drops with a large falling height, i.e., which are highly accelerated, impacting on thin, miscible films. To reduce the number of parameters which can possibly affect the impact, we concentrate on drop impacts on horizontal films uniformly spread out, i.e., with a constant thickness in space. To study the impacts, we perform laboratory experiments and record side and top views of high-speed movies of such impacts in a range of parameters close to actual cave values. Image analysis is used to describe the geometry of the crown from the side. Regarding the top view recordings of the impacts, we use different dyes to colour the drop and the film prior to the impact in order to identify the liquid coming from either one of them. We observe that several outcomes arise from the impacts that we conducted, depending on the initial film thickness, and have a strong influence on the final retraction phase of the crown formed during the impact, and on the amount of liquid simultaneously ejected. The retraction phase is further found to be responsible for the variability of the shape left by the drop in the film after the impact, and, therefore, for the mixing between the drop and the initial film.

We start by describing the experimental methodology in Sec. 2. Prior to the recording of the impacts, we manually measured the thickness of the film according to the technique presented in Subsec. 2.1.2. The colorimetry technique is detailed in Subsecs. 2.2.1 and 2.2.2. From the parameter range covered in the experiments, we conduct a dimensional analysis in Sec. 2.3, which allows us to classify the various impact outcomes observed in distinct scenarios in Sec. 3. These scenarios further affect the Results presented in Sec. 4. Crown geometry indicators inferred from the side view of the impacts are presented in Subsec. 4.1, while mixing parameters are shown in Subsec. 4.2. The size and spreading of the spot left by the drop in the film, in particular, are investigated. We are also able to infer the amount of liquid left by the drop in the film post-impact, the total quantity of liquid ejected away, as well as the part of liquid initially in the film which is ejected away. The results are finally discussed in Sec. 5, with an emphasis on the effect of each scenario on all the measured variables.

To extend the study of this chapter, elements of discussion regarding the effect of film thickness gradients on the crown formed at impact are provided in Subsec. 1.1 from Ch. VIII. In Subsec. 1.2 of the same chapter, we also show an example of two drops impacting the same film successively, but separated by a distance of $5R_\mathrm{d}$ and an interval of 3 min. Despite this large distance in regard of the size of the spot usually left by the drop in the film, and the long time period separating the impacts with respect to the impact time itself (see Sec. 3 in the present chapter), a non-negligible interaction can be witnessed between the spots left by the two drops. Finally, Sec. 1.3 from Ch. VIII provides insights into the mixing inside the secondary droplets ejected away at impact, which support the results obtained in Sec. 4.2 from the present chapter.

2. Producing, recording and analysing impacts

The following subsections describe our experiments of drops impacting on thin films with high velocity. More specifically, we first give an overview of the experimental methodology in Subsec. 2.1.1, along with the corresponding experimental parameters. We further describe the quantities measured in the high-speed recordings of the impacting drops. We then explain how we measure the thickness of the films with precision in Subsec. 2.1.2. A short summary of the colorimetry-based algorithm used to analyse the experiments is provided in Subsec. 2.2. The colorimetry algorithm is also thoroughly detailed in Appendix B.1. We finally carry out a dimensional analysis in which we consider all the characteristic timescales at play and variables involved in the experiment in Subsec. 2.3. All the measured variables and fluid properties are summarised in Tabs. 4.2 and 4.3.

2.1 Drop impact measurements

2.1.1 Experimental procedure

The experimental setup is schematized in Fig. 4.1 (a). Water drops were released one at a time from a given height. They fell and impacted a film of miscible liquid at rest. The film of thickness h laid on a horizontal solid surface of negligible roughness. Water has a density $\rho \simeq 1000 \, \mathrm{kg \, m^{-3}}$, a surface tension $\gamma \simeq 70 \, \mathrm{mN \, m^{-1}}$ and a kinematic viscosity $\nu \simeq 10^{-6} \, \mathrm{m^2 \, s^{-1}}$ at room temperature (20 ± 2 °C). The drops were formed at the tip of a 2 mm diameter plastic connector (Cole-Parmer, polypropylene Masterflex adapter fitting), with a flow rate of 5 μL min^{-1} imposed by a syringe pump (WPI, AL-1000). The syringe pump operated until a drop was produced, then it was stopped during the video recording and data processing. The drop fall was protected from potential parasitic air currents by a 20 cm diameter rigid tube, which was sufficiently large to neglect the aerodynamic interaction of the falling drop with the tube. The impact position could however still vary by a few millimetres for large falling heights as the drops could interact with the vortices shed in their own wake [172] (see Ch. III). High-speed movies of the impacts were recorded from the top using a Phantom Miro M110 colour camera (6200 fps), and from the side with a Photron Fastcam Mini UX monochrome camera (4000 fps). In the top view, 1 cm corresponds to 125 px and the field of view is roughly 40 × 40 mm. In the side view, 1 cm corresponds to 230 px and the field of view is 55 × 45 mm. The top camera was inclined by a very small angle with the vertical (5° − 10°). A comparison between a few matching side and top view measurements of the radius of the cavity made by the crushing drop in the film ensured that this tilt angle did not significantly affect the top view lengths, hence no correction was applied.

The liquid film was dispensed onto a hydrophilic tape (Adhesive Research, ARflow 93210) fixed to an underlying stiff plate thanks to a sandwiched layer of double-sided, white tape. The hydrophilic tape has a thickness of 102 μm, a negligible roughness, and advancing and receding contact angles of 20° and $\lesssim$ 1°, respectively. The surface of the film corresponded roughly to a 40 mm side square. The film was carefully deposited with a syringe and spread out evenly by gently tilting the plate until the entire tape surface was wet. The average film thickness was varied between 65 μm and 500 μm by dispensing the corresponding liquid volume on the tape, and measured pointwise manually prior to the impact (see section 2.1.2).

The side movies were analysed using image processing tools, which allowed to measure geometrical parameters related to the impacting drop and subsequent crown development, all listed hereafter and shown in Fig. 4.1 (b) i (see also Appendix Table 4.2). The drop radius and velocity were measured in all the side movies. The drops all had the same radius $R_{\mathrm{d}} = 2.3 \pm 0.1$ mm. The falling height was varied between 50 cm and 4 m, leading impact velocities u_{d} to be comprised be-
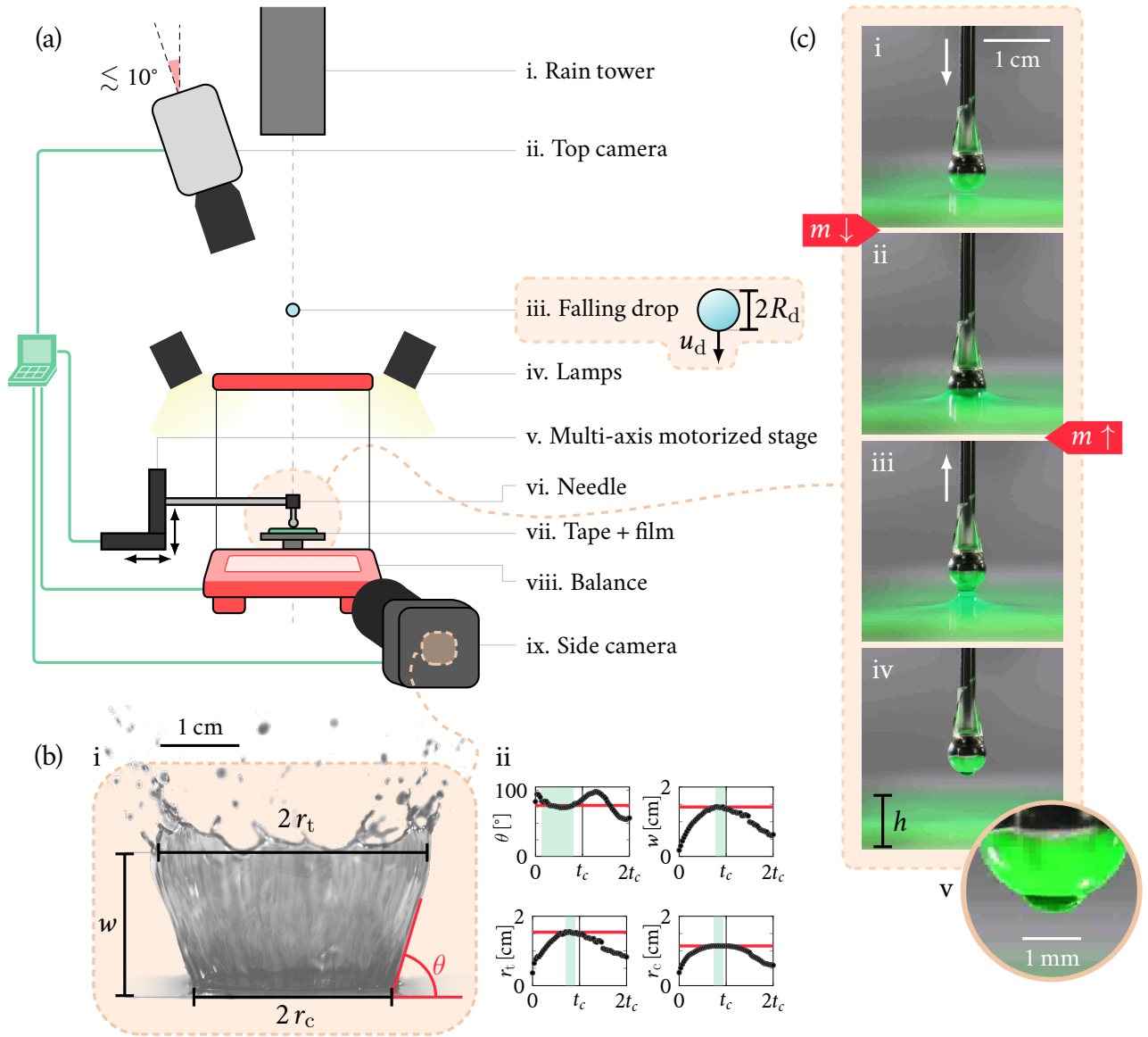
Figure 4.1: Experimental methodology. (a) Experimental setup used to release droplets from a given height onto a thin underlying film, and record the impacts from both top and side views. i. Plastic tube in which the drops fall. ii. High-speed colour camera used to record impacts from the top. iii. Falling droplet of radius R_d and impact velocity u_d, both measured from the side view (see (b)). iv. Four lamps placed in the corners of the balance. v. Stages used to displace the needle above the film, horizontally and vertically; the vertical stage is motorized and automated. vi-viii. Needle and balance used to take pointwise manual thickness measurements (see (c)) of the liquid film spread on a horizontal hydrophilic tape. ix. High-speed monochrome camera used to record impacts from the side. (b) i. Side-view geometrical measurements of the crown: crown height w, top radius r_t, cavity radius in the film r_c and inclination θ. The drop schematic of (a) iii has a size corresponding to the actual drop that produced the crown shown in this case. ii. Four examples of raw data graphs of $\theta(t)$, $w(t)$, $r_t(t)$ and $r_c(t)$, respectively, during a period of twice the capillary time t_c defined in Sec. 2.3 (15 ms), for $h = 150\,\mu\text{m}$ and $z = 1\,\text{m}$. In each graph, the green area shows the portion on which measurements are averaged as described in the text, and the average is represented by the red line. (c) Needle with glued aluminium sphere used for measuring the local film thickness, entering (i-ii) and leaving (iii-iv) a green film of thickness $h = 170\,\mu\text{m}$. i. The needle and sphere right before the sphere touches water. ii. The meniscus formed when the sphere touches the film. This event produces a decrease in the mass read by the balance since a part of the film weight is supported by the needle. The needle is moved further downward and the mass increases once the sphere touches the bottom surface of the film. The needle is then moved upward. iii. The shape of the meniscus right before it separates from the sphere. iv. The droplet left on the sphere 4 s afterwards. v. A zoom on this droplet hanging on the bottom half of the aluminium sphere. Both appear green because of light reflections from the green film.

tween 2.9 m s^{-1} and 6.6 m s^{-1}. The measurements of u_d have a mean relative error of 3 % (i.e., the average of the errors made in each movie analysis). The crown inclination θ, namely the angle made by the crown with the horizontal, varies between 50° and 105° during crown growth, with a relative error of 3 % on average for all the movies. The measurements correspond to the mean inclination from 2 ms to about 10 ms after the beginning of the impact for thicker films ($h \gtrsim 100 \text{ μm}$). They were only taken up to 6 ms for thinner films to avoid taking measurements during the crown fragmentation (see Section 3.1). The measured ranges of crown maximum height w, top and bottom radii r_t and r_c are $w/R_\text{d} \in [3 \; ; \; 10]$, $r_\text{t}/R_\text{d} \in [5 \; ; \; 9]$ and $r_\text{c}/R_\text{d} \in [4 \; ; \; 8]$. These variables are independent: they cannot be related by a simple geometrical relation as the curvature of the crown wall changes in response to the film thickness, i.e., for a given r_t/r_c ratio there might be different values of θ and w. The measurements of w, r_t and r_c all correspond to the average of the 5 largest values measured during the crown growth. The average relative errors are respectively of 12 % (w), 11 % (r_t) and 8 % (r_c). The error made when measuring the first two variables is due to the unstable rim, which altered the detection of the crown/air interface in the video. Examples of raw data obtained for $\theta(t)$, $w(t)$, $r_\text{t}(t)$ and $r_\text{c}(t)$ are shown in Fig. 4.1 (b) ii during the beginning of the impact, i.e., during the crown growth ($t \lesssim t_\text{c}$) and beginning of the retraction ($t > t_\text{c}$), with t_c the capillary time defined in Section 3. For falling heights smaller than 1 m, the maximum length j reached by the Worthington jet emitted at the end of the retraction is such that $j/R_\text{d} \in [3 \; ; \; 10]$, with a relative error of 15 %. This length was taken in the last frame before the first secondary droplet pinches off. The large error in j comes from the possible inclination of the jet (see, e.g., Fig. 4.6 (c) iii) which might occur in a plane orthogonal to the field of view.

2.1.2 Manual film thickness measurements

To estimate the film thickness, we used the average value of mechanical pointwise measurements taken in 3 to 5 spots separated by 1-2 cm, close to the centre of the film. As depicted in Fig. 4.1 (a), measurements were performed using a Ohaus Pioneer X balance (precision of 0.1 mg) and a needle attached to a high-precision motorized translation stage (smallest displacement of 0.1 μm). The balance was protected from parasitic air currents by vertical glass windows. Two other translation stages permitted to move the needle horizontally. A Thorlabs Kinesis stepper actuator controlled via an automated routine allowed to displace the needle vertically by discrete steps. At each step the needle was moved with a velocity of 250 μm s^{-1}, then it remained still until the next instruction (acceleration/deceleration of 1 mm s^{-2}). Although the displacement of the stage was almost instantaneous, the needle position and the mass on the balance were recorded only about every second, owing to the acquisition frequency of the balance. A small aluminium sphere was glued to the tip of the hollow needle in order to avoid capillary rise (Fig. 4.1 (c)). Once this sphere reached the water free surface, a small meniscus appeared, which translated into a small decrease in the mass read by the balance (Fig. 4.1 (c) i-ii). As the needle was moved further down, the sphere ended up touching the solid surface (tape) beneath the water film, increasing this time the mass read by the balance (Fig. 4.1 (c) ii-iii). Both these events allowed to obtain the difference in position of the needle and therefore the height of the water film at a given horizontal location. During this procedure, steps of 1 μm were used before the sphere could touch the water free surface. Then the step size was increased to 15 μm such that the measurement time did not exceed 1-2 min. As soon as the sphere touched the solid surface beneath the film, the needle was moved upward once then downward again, this time by steps of 1 μm. On average, the standard deviation of the manual film thickness measurements is 3 μm. The relative error ranges from 3 % for thinner films ($\lesssim 100 \text{ μm}$), to 1 % for larger ones ($\gtrsim 250 \text{ μm}$). Some liquid (volume corresponding to a sphere of radius $300 \pm 20 \text{ μm}$) remained on the tip once the sphere had come out of the water because of this meniscus, as seen in Fig. 4.1 (c) iv-v, which had usually evaporated between two successive measurements.

2.2 Mixing measurements by colorimetry

2.2.1 Film thickness and concentration profiles

To observe the mixing between the drop and the film after impact as well as the potential variations in film thickness, we have developed a colorimetry-based algorithm to analyse top view images of the experiments approximately 1 s post impact. For this purpose, we combined two food dyes to colour the drop and the film differently: red (Azorubine, E122) and green (corresponding to 3/4 of yellow, Tartrazine, E102, and 1/4 of FCF blue, E133). When bought, these commercial dyes were already in solution, with a fixed but unknown concentration. We subsequently diluted them in deionised water, with proportion (volume fraction) p_r and p_g for the red and green dyes, respectively. The colorimetry measurement is described in detail in Appendix B.1. It relies on the assumption (checked in Appendix B.2) that in a given optical and lighting set, there is a bijective relation between the (R, G, B) on-screen colour triplets and particular values of the thickness and concentrations of dyes in the film. This bijection can be formalized by considering the Beer-Lambert absorption of the light beam in the different media crossed from the light source to the camera, as well as the Fresnel reflection/refraction at the interfaces between these media. In this manner each colour channel may be independently related to the film thickness and dye concentrations. The equations obtained are further approximated by quadratic relations. To estimate at best the coefficients therein, we first used calibration pictures for which we imposed h, p_r and p_g and recorded the corresponding RGB pictures. A total of 175 water films were used, with thickness ranging in the same interval as in our experiments (and thus as in caves). Both the red and green proportions were varied between 0 and 0.075. These values were empirically chosen in order to yield distinguishable on-screen variations in the given thickness range. Calculations were not performed for each pixel but rather in 0.8 mm ($\approx$ 10 px) side square cells, where the median value of each colour channel was computed. A 4 mm
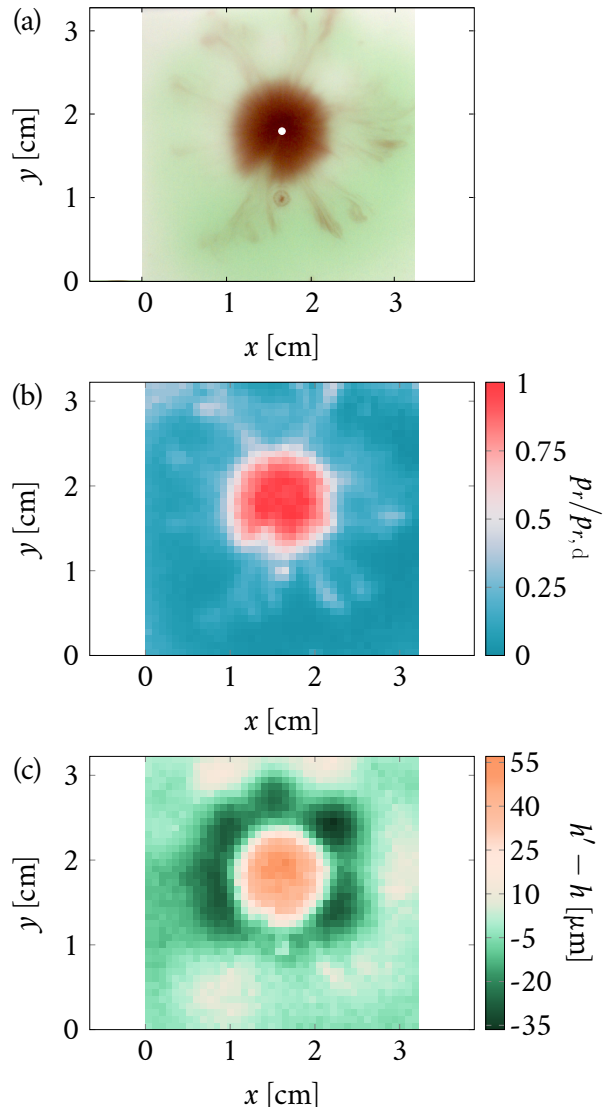
Figure 4.2: Example of an impact experiment (a) and measurements obtained with the colorimetry-based algorithm (b-c): (a) Top view picture of the spot left by the drop in the film about 1 s after the impact. The initial film thickness was $h = 103\,\mu$m and the drop had a fall of 2 m. The white dot in the centre of the photograph corresponds to the impact point. (b) Red dye proportion left in the film after the impact, normalized by the proportion in the drop, $p_r/p_{r,d}$. (c) Film thickness difference between after and before the drop impact on the film, $h' - h$ (in μm).

(≈ 50 px) wide stripe was also cut around the pictures to avoid seeing the physical edge of the tape, leaving a field of view of 32 mm × 32 mm (40 × 40 cells) to analyse.

Once the calibration was performed, from every given (R, G, B) triplet, we could infer the film thickness and red and green dye composition in a thin film of arbitrary local composition. An example of the shape observed about 1 s after the impact is shown in Fig. 4.2 (a), in the case of a drop falling from 2 m on a film of initial thickness $103 \pm 1\ \mu$m. In the actual experiments, we were interested in computing the post-impact film thickness h' and the proportion of liquid coming from the drop, which were a priori unknown. In order to obtain them, red and green dyes were mixed in equal proportion $p_{r,\mathrm{d}} = p_g = 0.05$ in the initial drop, while only green dye in the same concentration ($p_g = 0.05$) was present in the initial film. Therefore, the green dye concentration remained constant in time and space, independently of the mixing of the drop and the film, while the red dye concentration revealed the parcels of fluid that originated from the initial drop. Hence, we are left with two independent variables h and p_r to be determined. We change variables and define the partial film thicknesses in red and green respectively as $h_r = p_r h$ and $h_g = p_g h$. Since there are only two independent variables, the relation between the (R, G, B) channels and the partial thicknesses (h_r, h_g) gives an overdetermined system that is solved in the least square sense. Although neglecting the blue channel would yield a system that is not overdetermined, the procedure appeared more robust when the blue channel was considered. From the measurement of h_g given by the analysis of the (R, G, B) values in every cell, we deduced the film thickness as $h = h_g/p_g$. We further inferred the red dye proportion as $p_r = h_r/h$. Examples of measurements obtained with this algorithm are shown in Fig. 4.2 (b) and (c). The diagram of Fig. 4.2 (b) shows the red dye proportion left in the film after the impact from the picture of Fig. 4.2 (a), compared to the initial red proportion in the drop $p_{r,\mathrm{d}}$. The film thickness variation $h' - h$ between after (h') and before (h) the impact is shown in Fig. 4.2 (c).

Figure 4.3: Colorimetry calculation ($\cdot_c$) of the thickness and red dye proportion of a calibration film: (a) Initial photograph taken with the Phantom Miro M110 high-speed camera. (b) Red proportion $p_{r,\mathrm{c}}$ computed at each point in the frame of (a), divided by the actual proportion $p_{r,\mathrm{m}} = 2.5\,\%$. (c) Thickness h_c computed at each point of (a). Green dye proportion was set in every point to $p_g = 5\,\%$.

2.2.2 Comparison between manual and colorimetry measurements of the film thickness

Pointwise manual film thickness measurements were performed for the calibration process. They were also made before the impacts to ensure the film thickness uniformity. Special care was needed to level the balance, since a slight tilt angle of only 0.1° from the horizontal would would yield a 50 μm difference between two points located 30 mm apart in the film The leveling was achieved by manually adjusting the balance legs in response to any film thickness variation larger than 5 μm that was potentially observed between two points in the film. Pointwise thickness measurements further allowed getting a rough estimation of the average thickness of the deposited film. This estimation is useful for the colorimetry measurement which is based on Newton-Raphson iterative method and therefore requires an initial guess. Knowing the mean thickness of the film also allowed verifying the results provided by this algorithm. In Figs 4.3 (b) and (c) the results computed by the algorithm are represented for a given calibration film of proportions $p_{r,\mathrm{m}} = 2.5\,\%$ and $p_{g,\mathrm{m}} = 5\,\%$, shown in Fig. 4.3 (a). The manually measured thickness h_{m} for this film was $135.8 \pm 2.1\,\mu\mathrm{m}$ (average $\pm$ standard deviation over several successive measurements on the same film, taken at different locations).

Additionally, in Fig. 4.4 the film thickness computed using the colorimetry measurement and spatially averaged, $\bar{h}_{\mathrm{c}}$, is plotted against the average manual film thickness measurement, $\bar{h}_{\mathrm{m}}$, for all the experiments using the pictures taken ante impact. The coefficient of determination obtained by linear regression is 0.91. Markers in the graph go from green to red as they get further away from the bisector line. The upper left inset of the graph shows a histogram detailing the number of experiments as a function of the relative error between the average manual and colorimetry measurements, $|\bar{h}_{\mathrm{m}} - \bar{h}_{\mathrm{c}}|/\bar{h}_{\mathrm{m}}$. About 65 % of the total number of experiments have a relative error smaller than 10 %, and 92 % of the experiments have a relative error smaller than 20 %. The lower right inset of Fig. 4.4 (a) shows the coefficient of variation (c.v.) of h_{c} in space (i.e., for different cells of the same film), as a function of the corresponding average film thickness $\bar{h}_{\mathrm{m}}$. Because it is computed in every point of the picture, the c.v. is a measure of the spatial heterogeneity of the film thickness. The median (2.1 %) and interquartile interval ([1.1 ; 3.6] %) of the c.v. distribution for all the experiments are represented respectively by a green horizontal line and a shaded area in the back of the inset. The c.v. of h_{c} thus seems equivalent to the error made when measuring the film thickness manually before the impact (ranging between 1 and 3 %). Similarly to the colorimetry measurement, the error on h_{m} should thus mostly come from the heterogeneity of the film rather than from the measuring technique itself.

Because in reality the film is simply a very flat puddle, it is not surprising to find the same order of magnitude in the errors induced by the spatial heterogeneity obtained with the two methods. The c.v. is typically higher at smaller h as it is more difficult to spread a large puddle of very low thickness, even on a hydrophilic substrate. The edges of the film therefore appear whiter on screen since there is less liquid, yielding an increased inhomogeneity of the film in the zone observed during the impact. In some cases this error can be large, as illustrated in Fig. 4.4 (b). In each of them, a square indicates the margin that was removed for the calculation so as not to see any edge of the tape below the film. Nevertheless, the thickness gradient seems visible in picture i, which translates into an average colorimetry thickness $\bar{h}_{\mathrm{c}} = 66.3\,\mu\mathrm{m}$ smaller than $\bar{h}_{\mathrm{m}} = 88\,\mu\mathrm{m}$. Therefore, when taking the whole picture into account in the calculation of $\bar{h}_{\mathrm{c}}$, a large difference between $\bar{h}_{\mathrm{m}}$ and $\bar{h}_{\mathrm{c}}$ appears but this error does not come from the evaluation of the thickness by the algorithm. In Fig. 4.4 (b) ii the thickness is correctly estimated as there is only an error of 2 % on the average value. Moreover, we cannot see the edge of the tape in the computation zone in the photograph. Overall, the errors mostly come from the puddle physical edge which might still appear in the pictures ($\bar{h}_{\mathrm{c}} \lesssim \bar{h}_{\mathrm{m}}$ in 70 % of the cases), but measurements may also be sensitive to tiny differences in the lighting setup or to the positioning of the camera, i.e., elements that had to be put back in
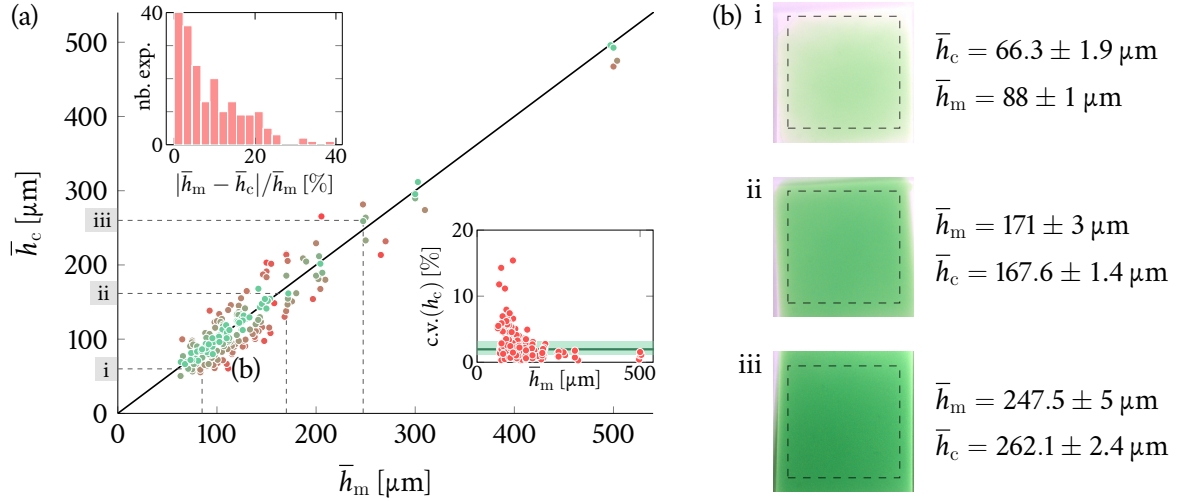
Figure 4.4: (a) Parity plot between spatially-averaged film thickness $\bar{h}_c$ computed from colorimetry measurements and corresponding film thickness manually measured and averaged, $\bar{h}_m$, prior to the impact. Symbol colour is greener (redder) for markers located closer to (further away from) the axes bisector. The left inset of the graph in (a) shows a histogram representing the number of experiments per range of relative error between manual and numerical measurements, $|\bar{h}_m - \bar{h}_c|/\bar{h}_m$. The bins are 2 % wide. The second inset in (a) shows the coefficient of variation (c.v.) of h_c, i.e., over different cells of the same film, as a function of $\bar{h}_m$. The c.v. can be seen as a measure of the spatial heterogeneity of the film, and therefore as a characteristic error bar on $\bar{h}_m$. The shaded area in this inset shows the interquartile range and the green horizontal line the median of the c.v. of h_c. (b) Examples of colorimetry and manual measurements, sometimes leading to larger errors in the average film thickness estimation because of, e.g., the visibility of the puddle edge (see i), with correspondence in the graph from (a).

place each day the experiment was carried out. In Fig. 4.4 (b) iii we observe an error of 6 % between the two spatially averaged thickness values, but this time $\bar{h}_c$ is larger than $\bar{h}_m$ due to such effects. The measurements from subsection 4.2.1 are based on integration over a smaller region, hence such spatially dependent effects on the edges should not affect the results.

2.3 Dimensional analysis

The times and nondimensional numbers involved in the following dimensional analysis are all gathered in Tab. 4.2. Most of them were already mentioned in Ch. I, and can also be found in Tab. 1.2 from the auxiliary sheet. In the considered configuration, the impacting drop first crushes on the film for a time scaling as the impact time, defined as

$$t_i = \frac{2R_d}{u_d}.$$ (4.1)

This time is $\lesssim$ 1 ms in the range of velocities covered by the experiments. The radially spreading crown formed upon impact [235] has a lifetime of the order of the capillary time, defined as

$$t_c = \sqrt{\frac{4\rho R_d^3}{3\gamma}} \simeq 15\,\text{ms}.$$ (4.2)

This timescale is also characteristic of the lifetime of liquid sheets expelled into the air from droplets impacting on poles or close to solid edges [145, 223]. A viscous boundary layer is formed along the bottom wall as the film is pushed by the impacting drop. It diffuses through the entire film thickness

in a timescale of the order of

$$t_\nu = \frac{h^2}{\nu}. \tag{4.3}$$

For the film thicknesses considered here (i.e., from 65 μm to 500 μm), this time ranges from 5 ms to 280 ms. By contrast, the time of viscous diffusion over a distance equivalent to the drop radius is about $t_{\nu,\mathrm{d}} = R_\mathrm{d}^2/\nu \simeq 6\,\mathrm{s}$. Finally, molecular diffusion also has a role after the impact, although it occurs at a much larger timescale than the other phenomena at play. When considering sub-nanometer particles and ions with a diffusion coefficient $D \sim 10^{-9}\,\mathrm{m}^2\,\mathrm{s}^{-1}$, the vertical diffusion in a 100 μm thick film would take a time

$$t_\downarrow = \frac{h^2}{D}, \tag{4.4}$$

of about 10 s to homogenize the concentration over the entire film height. To diffuse such particles horizontally over a few millimetres, the corresponding characteristic timescale $t_\rightarrow = R_\mathrm{d}^2/D$ would be of the order of 90 min.

The impacts involve seven quantities (R_d, u_d, ρ, ν, γ, D and h) that may all be expressed in terms of mass, length and time units. Hence, four nondimensional numbers govern the impacts and may be defined by comparing the characteristic timescales. First, the ratio $(t_\mathrm{c}/t_\mathrm{i})^2$ gives the Weber number defined as

$$\mathrm{We} = \frac{2\rho R_\mathrm{d} u_\mathrm{d}^2}{\gamma}. \tag{4.5}$$

It compares the inertia of the drop to its surface tension and ranges in $[525\,;\,2750]$ in our experiments, as seen in the phase diagram of Fig. 4.5. The measurement errors made when evaluating R_d and u_d give a mean relative error of 9 % when calculating We. Second, the ratio $t_\mathrm{c}/t_{\nu,\mathrm{d}}$ leads to the Ohnesorge number, which indicates how much viscosity modifies the balance of inertia and surface tension at drop scale,

$$\mathrm{Oh} = \nu \sqrt{\frac{\rho}{2\gamma R_\mathrm{d}}}. \tag{4.6}$$

It takes a constant value of 1.7×10^{-3} with a relative error of 2 %. A third ratio $\sqrt{t_\nu/t_\mathrm{c}}$ yields the dimensionless number

$$h^\star = \frac{h}{\sqrt{\nu t_\mathrm{c}}}, \tag{4.7}$$

which is a normalization of the film thickness by the thickness reached by the boundary layer in the film over the capillary timescale. A unit value for $h^\star$ corresponds to $h = 115.3\,\mu\mathrm{m}$. As also shown in Fig. 4.5, $h^\star \in [0.6\,;\,4.3]$ with a relative error of 6 %. Additionally, the Péclet number Pe may be defined to compare the molecular diffusion and convection timescales. The convection timescale is here chosen as the timescale over which the impact-induced convection is damped, i.e. the viscous diffusion time, so

$$\mathrm{Pe} = \frac{t_\downarrow}{t_\nu} = \frac{\nu}{D} \sim 10^3 \tag{4.8}$$

and molecular diffusion can be neglected during the first seconds after impact, which are fully dominated by convection (a different definition of the Péclet number is provided in Ch. VI, which corresponds to the definition of the auxiliary sheet).

As We $\gg$ 1 and $t_\nu/t_\mathrm{i} \gg 1$ for all our impacts, the capillary and diffusive timescales are much larger than the impact time. Hence, while inertia dominates the first stages of the impact, capillary and viscous forces should only compete in the later crown development. Even higher We values could be observed in situ as cave ceilings are sometimes located up to several tens of meters above the ground [70]. Droplets in caves having falling heights going from 5 cm to 50 m would yield

We $\in$ [70 ; 7000] and Oh of about 2×10^{-3} at a temperature of 12 °C [117], which are close to the experimental conditions of our impacts. The film thickness ranging from 50 μm to 500 μm would lead $h^\star$ values to be comprised between 0.4 and 4, i.e., a very similar range to ours. The particles found in the residual water film covering stalagmites, e.g., calcium ions and carbon dioxide, have diffusion coefficients of the same order as the dye molecules in our experiment, such that Pe $\gg$ 1 in caves as well. During the impact, convective transport is therefore much more effective than molecular diffusion. For impacts of actual stalagmites, molecular diffusion would play a significant role at a timescale comparable to those of ion precipitation and gravity-driven drainage, which are out of the scope of this chapter.

3.   At the juncture between two domains

Drop impact on a thin film bridges the gap between two microcosms: impacts on a dry wall and on a deep liquid reservoir. For impacts on dry wall, the liquid left by the drop recoils at the end of the movement. It forms an almost circular liquid puddle surrounded by short tails reminiscent of the fingering occurring during the impact [145]. Drop collision with a dry wall has been extensively studied, most authors focusing on the splashing threshold [168] or the maximum spreading radius reached by the impacting drop [53, 103, 139]. These quantities change for instance in response to substrate roughness [184], surface wettability and properties [9, 137], inclination [93] or curvature [155], parameters that vary much in nature. In the other limit, the drop impinges on a deep pool, i.e., of a depth h that is at least of the order of the drop radius R_d. This regime can be observed for some stalagmites with a concave summit that forms a small pool filled with water [172]. The impact produces an upward-moving cylindrical liquid sheet, the crown, due to the kinematic discontinuity between the crushing drop and the formerly resting liquid pool [179, 235]. Instabilities in the rim of this crown formed at impact are responsible for the appearance of small ligaments which subsequently destabilise into secondary droplets [54, 146, 239]. For more viscous fluids the droplets ejected from the crown typically appear in the later stages of the impact or may not be observed at all [185, 239]. As the crown grows radially and encounters new fluid from the pool, it thickens progressively and its height increases [55]. The diameter of the ligaments and subsequent ejected droplets grows accordingly [145, 239]. The crown also surrounds a hemispherical cavity growing in the liquid pool, which eventually recedes as the crown breaks up. Its typical maximum size is of the order of a few centimetres for our drop size [30, 157]. A Worthington jet may protrude from the centre of this crater and pinch off into several droplets [146, 177, 233]. Because of the strong surface and bulk perturbations caused by this dynamics, the mixing between the drop and the liquid pool is pretty effective. Once the fluid is back to rest, mixing is usually completed through molecular diffusion in all directions [80]. Furthermore, most secondary droplets fall back into the pool as they typically do not have enough horizontal momentum to travel more than a few centimetres away from the impact point (i.e., if such deep pool conditions were observed in caves, the ejected droplets would likely impact on the stalagmite again) [177].

Most stalagmites are covered by a film of water that is very thin in comparison with the impacting drop size [172]. In a similar manner to drop impact on a deep pool [77, 131, 157, 179], this type of impact leads to the formation of an ascending crown, yet presenting a smaller inclination. The crown wall surrounds a cavity of thickness smaller than that of the initial film. Even in the early expansion stages, the rim on the perimeter of the crown also turns into tiny ligaments that subsequently break into secondary droplets due to the high kinetic energy of the impacting drop [227]. Cossali et al. [55] provided a detailed description of the crown radius, height and rim thickness evolution with time as well as the number of ligaments and droplets ejected from the rim,

Scenario A. Crown fragmentation (Sec. 3.1)

(a) ii

(a) i

(b) i

(b) ii

Scenario B. Crown retraction (Sec. 3.2)

$$\frac{\text{We}}{\text{Oh}^{2/5}} = 2100 + 29\,(h^\star)^{1.44}$$

splash

splash

We

$h^\star$

Scenario C. Jetting (Sec. 3.3)

(c)

(d)

Scenario D. Crown folding (Sec. 3.4)

66
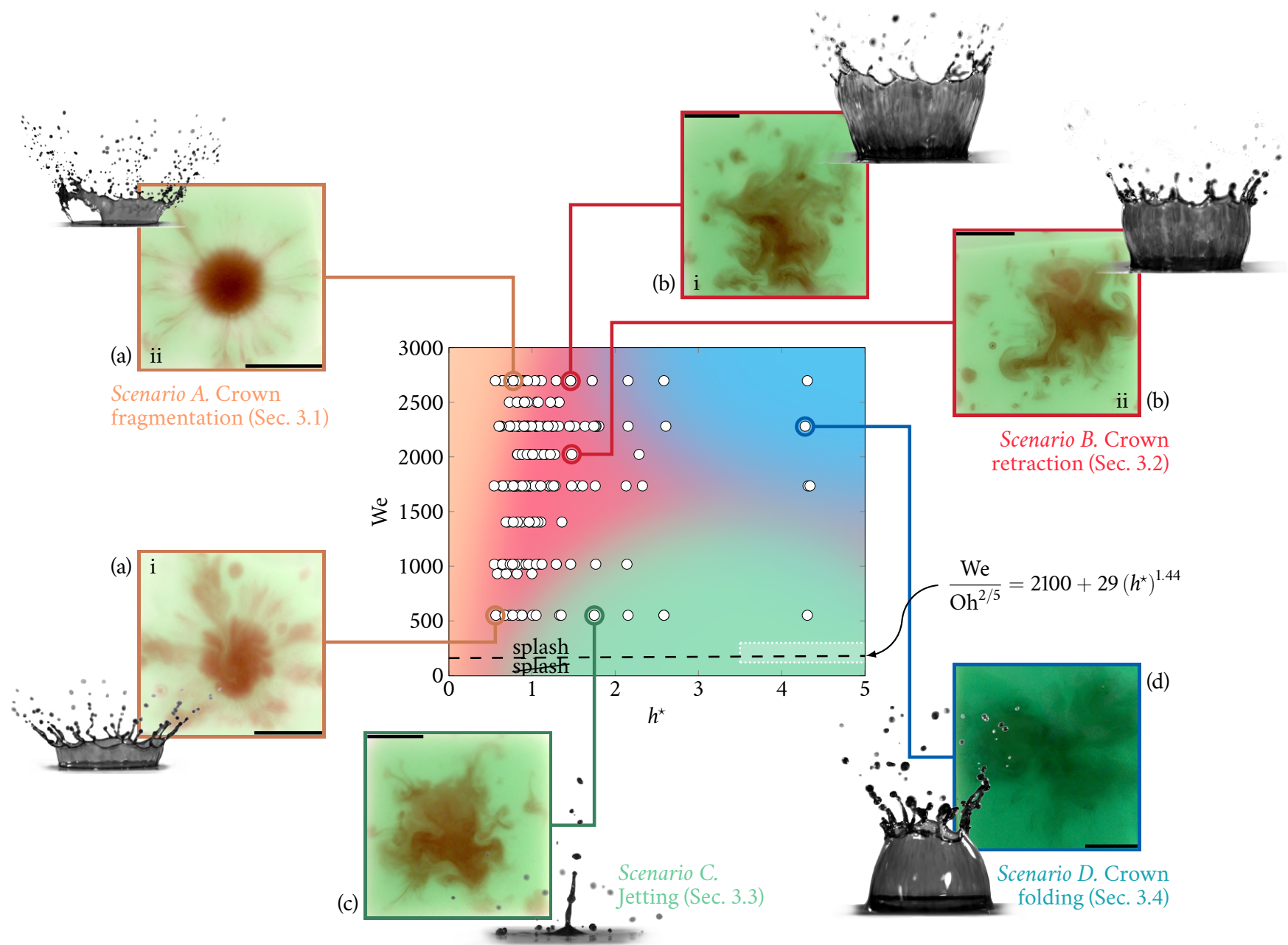
Figure 4.5: *Previous page.* Phase diagram $(h^\star, \mathrm{We})$ of the reported experiments and correspondence with the various scenarios discussed in Sec. 3. For each, the monochrome side view shows the typical shape of the crown during impact, while the colour top view shows the post-impact mixing pattern. (a) Very thin film ($h^\star < 1$), crown fragmentation and circular red spot: i. Low We ($h^\star = 0.57$, We $= 525$), ii. High We ($h^\star = 0.61$, We $= 2740$). (b) Intermediate regime ($h^\star \gtrsim 1$), crown retraction and random-like mixing pattern: i. High We ($h^\star = 1.31$, We $= 2740$), ii. Intermediate We ($h^\star = 1.31$, We $= 1675$). (c) Thick film ($h^\star \gtrsim 1.75$), low We: post-impact central jet protrusion ($h^\star = 1.81$, We $= 525$). (d) Thick film ($h^\star \gtrsim 1.75$), high We: crown folding ($h^\star = 4.37$, We $= 2250$). Background colour grading of the central graph indicates that scenario transitions are continuous. The area delimited by the white dotted line in the bottom right of the central plot represents the range of values covered in Ersoy and Eslamian [80]. The dashed black line shows the splashing criterion developed by Cossali et al. [54]: $\mathrm{We}/\mathrm{Oh}^{2/5} = 2100 + 29\,(h^\star)^{1.44}$. The scale bars are 1 cm.

in a range corresponding to $(h^\star, \mathrm{We}) \in [11\,;43] \times [300\,;840]$, with Oh $= 1.9 \cdot 10^{-3}$. Fedorchenko and Wang [86] derived a model describing the velocity of cavity submergence, central jet formation and crown ejection in impacts on film sufficiently thick to produce a Worthington jet. Wang and Chen [227] also explored the influence of viscosity on the impact outcome by varying the Ohnesorge number between 0.02 and 0.1 for $(h^\star, \mathrm{We}) \in [1.6\,;16.8] \times [380\,;3000]$. However, the range corresponding to thin films like those found on stalagmites has not been explored yet.

Our experiments reveal four main impact scenarios in different regions of the $(h^\star, \mathrm{We})$ diagram of Fig. 4.5, which are denoted scenarios A to D and described in the following sections[1]. They fall within the splashing limit derived by Cossali et at. [54] as a function of We, Oh and $h^\star$: $\mathrm{We}/\mathrm{Oh}^{2/5} = 2100 + 29\,(h^\star)^{1.44}$. In scenario A (orange), for all We and very thin films ($h^\star < 1$), the crown tears apart before the end of its expansion. In contrast, in scenario B (red) for which $h^\star \gtrsim 1$ for all We, the crown reaches a maximum height and retracts without breaking up. Scenarios C (green) and D (blue) correspond to large film thicknesses, for which $h^\star \gtrsim 2$. Scenario C is mostly characterised by the appearance of a central jet after the impact at low We. In scenario D, at high We, the crown retracts by folding upon itself. These scenarios thus differ in terms of the shape of the crown and related geometrical parameters, such as the inclination [86], and the later breaking and retraction of the crown [187]. Accordingly, the observed stains left by the drops in the film present various shapes and patterns. The total volume of liquid ejected during impact is consequently also directly affected by We and $h^\star$. The transitions between the various scenarios are not of first order though but rather continuous. This is illustrated by a colour gradient in the phase diagram at the centre of Fig. 4.5, while examples of typical impact sequences for various $h^\star$ and We are shown in Fig. 4.6 (a-d). Each subfigure in Fig. 4.6 shows frames (i-iii) taken from matching high-speed visualizations of the impacts from both side (in monochrome) and top views (in color). Each combination (a-d) of top and side views of one particular impact shows similar features (e.g., the crown growth), but due to the difference in impact dynamics, from one subfigure (a-d) to the other the corresponding instants shown are not the same. The last top view picture (iv) corresponds to the convection-induced mixing pattern. It is obtained at about 1 s (or equivalently $65\,t_c$) after impact, i.e., when convection flows have vanished while molecular diffusion has not had the time to smooth horizontal concentration gradients yet. Noteworthy features of these impact scenarios are visible in Fig. 4.5 (a-d) as well.

3.1 Crown fragmentation (scenario A)

Crown fragmentation is observed for very thin films, i.e., such that $h^\star < 1$, and mostly for strong impacts, at We $\gtrsim 1000$. This phenomenon was also observed by Wang and Chen [227], who reported crown wall fragmentation for $h^\star = 1.63$, We $= 2010$ and Oh $= 0.04$ in water-glycerol

---

[1]In Figs. 4.5 and 4.6, scenarios A to D correspond to their lowercase counterparts (a) to (d).
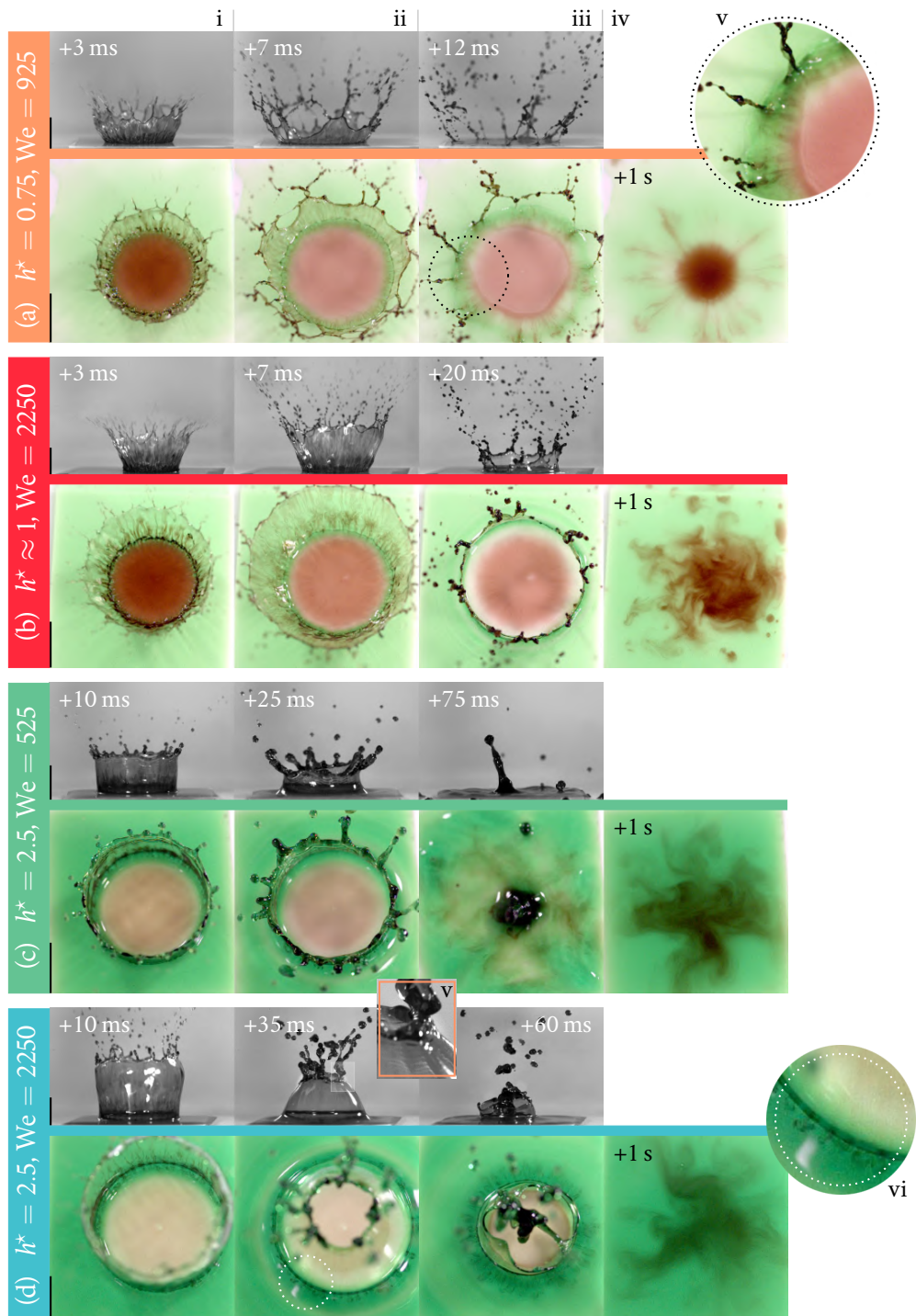
Figure 4.6: Side (monochrome, upper pictures, *s*) and top (color, bottom pictures, *t*) views of the impact sequences described in Sec. 3. For (a-d), i. shows the crown growth (*st*) and iv. the convection-induced mixing pattern (*t*). (a) Very thin film ($h^\star < 1$), intermediate We: ii. Crown break-up into ligaments (*st*), iii. Ligament fragmentation (*st*), v. Fingering-like pattern in the film (*t*). (b) Transitional regime ($h^\star \approx 1$), high We: ii. Crown maximum extension (*st*), iii. Retraction (*st*). (c) Thick film ($h^\star > 1$), low We: ii. Crown decline (*st*), iii. Post-impact central jet formation (*st*). (d) Thick film ($h^\star > 1$), high We: ii-iii. Crown folding (*st*), v. Crown capillary waves (*s*), vi. Fingering in the film (*t*). The scale bars are 1 cm. Videos corresponding to the pictures shown are available in the Supplemental Material of Parmentier 2023 [171].

solutions. The impact time, viscous diffusion time and capillary time are arranged as follows: $t_i < t_\nu < t_c$. In other words, the beginning of the impact is dominated by inertia as it is typically the case at high We [157, 223]. The crown expansion is decelerated primarily by viscous dissipation in the film, which considerably slows down the outward motion of the crown basis while the crown top keeps expanding thanks to its inertia. This translates into a very thin and inclined crown wall formed at impact (Fig. 4.6 (a) i), which becomes unstable and breaks into several thin sheets before it even starts to retract toward the centre in response to capillary forces (Fig. 4.6 (a) ii) [86, 227]. The maximum extension reached by the rim at the top is larger than the radius of the cavity formed in the film, i.e., $r_t/r_c > 1$. The liquid sheet almost immediately ($\lesssim 5$ ms) turns into ligaments that subsequently break to form more secondary droplets (Fig. 4.6 (a) iii), in a very similar manner to when an impacting drop spreads beyond the edge of a solid substrate, and subsequently fragments. [145, 223]. Compared to the other regimes, the ligaments and droplets ejected both during the growth and fragmentation phases are small and fast [187] (radii and velocities of the order of $[0.07 \ ; \ 0.25]R_d$ and $[0.3 \ ; \ 0.8]u_d$, respectively). At the same time, we observe red filaments propagating throughout the crown (Fig. 4.6 (a) i-ii). Although it is obvious that these filaments come mostly from the drop because of their color, no quantitative measurement of the mixing level between the drop and the film during crown growth could be inferred from such visualizations.

Radial convective retraction followed by expansion strokes is usually observed after an impact in a deep pool or on a dry wall [128, 179, 235]. However, in this case the liquid left from the crushing drop in the film only seems to retract without expanding much afterwards, except for late molecular diffusion-driven expansion. The viscous forces should indeed rapidly dissipate any remaining kinetic energy left following the impact, once the crown has torn apart. Hence, the mixing pattern right after impact in this case simply corresponds to a circular, very red spot. This spot is surrounded by a whiter zone that seems to indicate some depletion in the film directly around the impacted area, possibly because of the absence of rapid expansion and retraction strokes (Figs 4.5 (a) ii and 4.6 (a) iv). Outside of this region, the film appears to be left unaffected by the passage of the crown, except for a few thin radial tails. These tails come from the coalescence of the last ligaments breaking at the end of the crown fragmentation with the underlying film. Even though the coloration of the spot left by the drop seems rather uniform, its border is surrounded by a blurry zone where we distinguish some fingering pattern, similar to that observed for an impact on a dry wall (Fig. 4.6 (a) v) [80]. For impacts on very thin films at low Weber number (We < 1000), the crown does not really fragment, per se, but still breaks into ligaments before retraction actually starts. An example is shown in Fig. 4.5 (a) i. The spot left by the drop post impact is much blurrier and presents larger, more visible tails due to the coalescence of these ligaments with the film.

3.2 Crown retraction and decline (scenario B)

Scenario B is observed for high-We impacts on moderately thin films (roughly for $1 \lesssim h^\star \lesssim 2$ at We $\gtrsim 2000$) and for thinner films in the case of intermediate We impacts (e.g., for $0.75 \lesssim h^\star \lesssim 1.5$ at We $\lesssim 1000$). In the ranges considered the ratio between the viscous and capillary timescales t_ν/t_c approaches 1, while the impact time t_i is very small compared to both t_ν and t_c. The crown formed during the impact is more inclined than in scenario A, but it is not vertical yet (Fig. 4.6 (b) i) [157]. The diameter of the crown rim is also larger than the diameter of the cavity formed by the crushing drop. As $h^\star$ increases and the crown has a longer lifetime, some additional features appear that are shared by scenarios B, C and D. The crown becomes thicker over time and so do the ligaments and ejected droplets [55, 62]. It reaches its maximum height then starts retracting toward its centre without tearing apart (Fig 4.6 (b) ii) as capillary restoring forces overcome inertia. As the transition

between the various regimes is not sharp but rather continuous, some incomplete fragmentation might still occur before the end of the retraction phase; otherwise the crown tends to shrink and collapse (Fig 4.6 (b) iii) [148]. At the very end of this retraction phase only a few thick ligaments reminiscent of the rim collapse in an unpredictable manner, creating random post-impact mixing patterns. While these patterns present a great shape variability, they have a few common features: the spreading distance does not significantly vary and they typically present a more reddish region near the impact point, surrounded by volutes of less concentrated red areas (Figs 4.5 (b) i and ii, Fig. 4.6 (b) iv). The red filaments propagating through the crown wall tend to mix more with the fluid coming from the film as they have a longer lifetime (Figs 4.6 (b) i-ii). Finally, a few capillary ripples can be observed in the film directly surrounding the impact zone (Fig. 4.6 (b) iii t) [80, 235]. They start from the basis of the crown toward the unperturbed free surface of the film and become wider and last longer as the film gets thicker (Fig. 4.6 (b) ii-iii). This feature is also exhibited in the following scenarios (Fig. 4.6 (c) ii-iii and (d) ii-iii). After the crown retraction, these capillary waves dissipate rapidly the remaining kinetic energy from the impact.

3.3 Jetting (scenario C)

For even thicker films ($h^\star \gtrsim 1.5$), the ratio $t_\nu/t_c \gg 1$, indicating that capillary forces become significant players before the viscous diffusion layer reaches the free surface of the film. The three timescales are ordered as $t_i < t_c < t_\nu$. Although the crown behaviour and ensuing mixing pattern depend strongly on the film thickness, for larger $h^\star$ the influence of We becomes critical too. At low We ($1 \ll$ We $\lesssim 1000$), because the crown has little kinetic energy, it reaches a relatively small height with an almost vertical inclination (Fig 4.6 (c) i). It is also much thicker and produces larger and slower secondary droplets (Fig 4.6 (c) ii) [55, 62]. The peculiarity of these impacts is the uprising central Worthington jet [229, 233] produced at the very end of the retraction phase (Fig 4.6 (c) iii), similarly to what is observed for deep liquid reservoirs ($h^\star > 4$ [86, 131, 187]). It is due to the capillary restoring forces which induce a strong recoil of the crown, pushing all the liquid at once in the centre of the cavity.

Ersoy and Eslamian [80] already identified several mechanisms of mixing at play in a range close to ours, as indicated by the white dotted frame in the central diagram of Fig. 4.5. They covered impacts for We $\in$ [120 ; 300] and $h^\star \in$ [3.5 ; 13.8], i.e., with smaller kinetic energies and for thicker films. Nevertheless, similarities exist between such impacts and our measurements in the particular range relative to this section. They observed that expansion-retraction strokes induce mixing directly in the central cavity during the impact, while surface capillary waves propagating outside of this cavity lead to mixing around the impinged area. Ersoy and Eslamian [80] further noted that the motion of the crown wall itself, along with the ejection of secondary droplets, causes an outward flow over the film free surface outside of the crown, further enhancing the mixing. Additionally, we notice in the side view some capillary waves in the crown, just below the rim. They converge back at the impact point where they propagate through the Worthington jet [233], which may enhance its destabilisation and pinch off into one or several droplets. The observed mixing patterns present similarities with scenario B: owing to this central jet breaking into droplets that fall back in the film, the central concentrated red area is typically surrounded by more diluted twirls (Figs 4.5 (c)).

As the transitions between the various observed regimes are not sharp, for thinner films, onsets of jets more reminiscent of a mere wave might be visible. Nevertheless, only the waves sufficiently high to produce at least one droplet were considered as actual jets. Calculations performed by Yarin and Weiss [229] predicted no jet emergence between $h^\star = 0.04$ and 1, which was later corroborated

by Fedorchenko and Wang [86] and corresponds to our observations as well. Premises of jets only appear above $h^\star \simeq 1$, and the jet length increases drastically with $h^\star$.

3.4 Crown folding (scenario D)

Again in the thick film region ($h^\star \gtrsim 2$), very strong impacts (We $\gtrsim 1000$) lead to the formation of higher crowns also oriented almost vertically (Fig 4.6 (d) i) [62, 227]. In this case the characteristic timescales are still arranged as $t_i < t_c < t_\nu$, although the impact time is much smaller than the capillary time: $t_c/t_i \gtrsim 20$ in contrast to $t_c/t_i \lesssim 10$ in the former regime. In all the other regimes the crown curvature is mostly oriented outward, but in this case the crown starts bending inward at the end of the growth phase due to capillary forces (Fig 4.6 (d) ii) [229]. The diameter of the top rim is thus smaller than that of the cavity formed in the film: $r_t/r_c < 1$. While in the other cases the retraction starts at the bottom of the crown and propagates to the top, here the crown summit folds and collapses before the crown basis starts retracting. Additional capillary waves may also be observed directly in the crown, right beneath the collapsing rim (Fig. 4.6 (d) v). In some cases air entrapment at this stage may even cause the appearance of a large bubble [179] having a lifetime of a few seconds (Appendix B.4). While the rim is already collapsing, the basis of the crown still grows and feeds the rim, which consequently thickens excessively and produces massive blobs whose size is comparable to that of the impacting drop (Fig 4.6 (d) iii). The interaction between these large portions of fluid seems unpredictable and produces wider mixing patterns, where the red dye seems globally more uniformly concentrated. Although the patterns obtained look irregular, they all consist of a very few twirls whose red borders fade away more gradually in the initial green film than in the other regimes (Figs 4.5 (d) and 4.6 (d) iv). Red filaments in the crown are more scarcely distributed than in the former scenarios. The fingering pattern in the cavity formed by the crushed drop is still visible but this time it crosses the interface between the crown and the film (Fig. 4.6 (d) vi). Some red volutes evenly spread out around the collapsing crown may be observed in the film. Once the collapse comes to an end the convective motion set in the film slightly pushes and mixes up these volutes of red fluid. As depicted in the central diagram of Fig. 4.5, the transition between scenarios B and C (low We) occurs for smaller $h^\star$ than between B and D (high We).

3.5 Second-order phenomena

Drop impact on thin film at high Weber number displays drop impact-related phenomena generally observed in other contexts, including the aforementioned crown formation and fragmentation, Rayleigh-Taylor and Rayleigh-Plateau instabilities causing the rim break-up into ligaments and subsequent ejected droplets, bubble entrapment or jetting at the end of the retraction phase [179, 187, 229, 235]. A very similar phenomenon to the fingering characteristic of drop impacts on dry wall may also be observed in Figs 4.6 (a) v and (d) vi [128]. Some additional mixing might be induced away from the central red spot left by the impacting drop due to the ejected droplets which fall back into the film. These droplets may be seen bouncing and coalescing partially or completely before reentering the film [101, 122]. Depending on their concentration, number and distance of ejection, they might induce some additional calcium ion deposition and subsequent growth away from the impact point on actual stalagmites. In the present videos, except for the droplets which fell back very close to the impact point, all these droplets were viewed as an average ejected volume without further consideration.

4. Results

This section presents the measurements obtained from the side and top views of the impacts, as described in Sec. 2. Raw data are available in the Supplemental Material. The first part focuses on the crown geometry observed from side-view high-speed movies. The second part of the section aims at describing the mixing between the drop and the film using the top view of the impacts. All subsequent graphs are represented as a function of the nondimensional film thickness $h^\star$ and for various bins of We. One symbol in the graph shows the mean $\pm$ s.d. over an ensemble of 4 to 5 points, on average, obtained for close $h^\star$ and We values and considered as belonging to the same bin. Some points in the graph exhibit a very small standard deviation or may not have one in the uncommon cases (5 % of all the measurements) where there is only one measurement in the corresponding $(h^\star, \text{We})$ bin. The range of h is divided into 10 µm ($hh^\star = 0.086$) wide bins between 60 µm ($h^\star = 0.5$) and 170 µm ($h^\star = 1.5$). Then the width of the bins is progressively increased up to $h = 500$ µm ($h^\star = 4.3$). In terms of Weber number, the smallest bin, for We $\in]500 ; 1000]$, corresponds to the impacts after which jetting is observed for thicker films, i.e., when $h^\star \gtrsim 1.5$ (Fig. 4.6 (c)) while the highest one, for We $\in [2000 ; 3000[$, shows the impacts for which the crown folds upon itself before retracting when $h^\star \gtrsim 2$ (Fig. 4.6 (d)). The third bin represents the intermediate values, namely the transitional regime (Fig. 4.6 (b)). For very thin films ($h^\star < 1$), no matter the Weber number the scenario is always the same and corresponds to the crown fragmentation (Fig. 4.6 (a)).

4.1 Crown geometry

Measurements obtained from the side view of the impacts are described in Fig. 4.1 (b) and reported in Fig. 4.7. Figure 4.7 (a) shows the average inclination angle θ of the crown during the growth phase, i.e., between 2 ms and 10 ms after the beginning of the impact (or 6 ms in Scenario A). This inclination increases with $h^\star$ and exceeds 90° for $h^\star \gtrsim 2$. In Fig. 4.7 (b) we report the ratio between the maximum radial extension of the top and bottom of the crown, r_t/r_c (the maximum being computed as the average of the 5 largest measurements). It decreases with increasing $h^\star$ and becomes lower than 1 for $h^\star \gtrsim 2$, in accordance with the evolution of θ. Figure 4.7 (c) represents the maximum height w reached by the crown. Since for a small film thickness ($h^\star \lesssim 2$), the ratio r_t/r_c is more or less constant while θ increases, the maximum height w reached by the crown increases as well. The maximum height w then seems to reach a limit value at large film thickness ($h^\star \gtrsim 2$). While θ and r_t/r_c are almost independent of We, the maximum height reached by the crown is greatly affected by We as it goes from $3.6\,R_d$ to $10.3\,R_d$ when $h^\star \gtrsim 2$ (averages obtained with respectively the 5 largest and smallest measurements). Figure 4.7 (d) shows the evolution of the maximum length j of the jet protruding from the film in scenario C, before it pinches off. Although the maximum height reached by the crown in scenario C is small, the maximum length of the jet compares to the height of the crown from scenario D. Very short jets are already observed for some experiments when $h^\star \lesssim 1.5$, but not systematically. Their length seems to increase sharply with $h^\star$ when $h^\star \simeq 1$, then more slowly once $h^\star \gtrsim 1.5$. The graphs from Fig. 4.7 are completed using data obtained by Fedorchenko and Wang [86] (θ, j), and by Cossali et al. [55] $(r_t/r_c, w)$ in a similar range to ours. Except for one value of θ taken at $h^\star = 0.4$, these data usually correspond to the upper limit of our range, with $h^\star \gtrsim 4$. They are in good agreement with our observations. The jet was also reported and measured by Fedorchenko and Wang [86] for a very large film thickness ($h^\star = 46.3$) at We > 1000, which is typically observed in the deep pool limit of impacts on wetted walls [146, 177, 233].
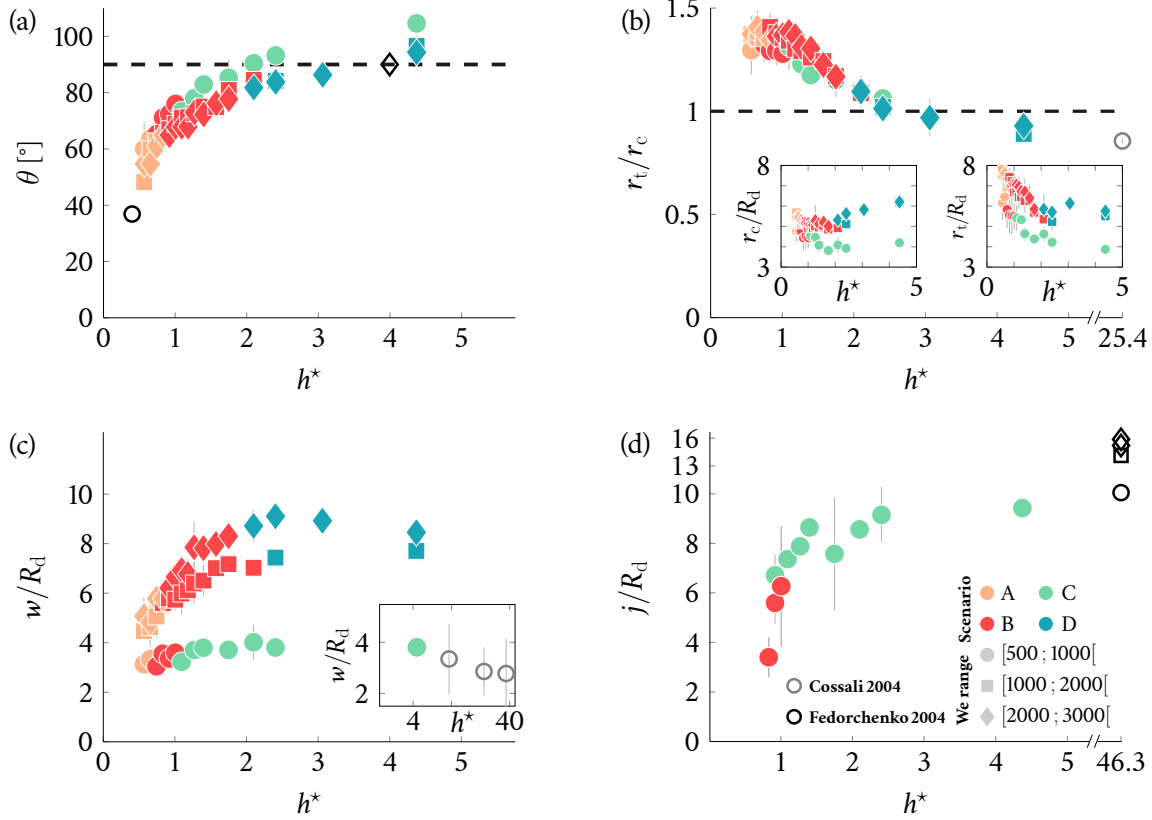
Figure 4.7: Crown geometry parameters, as described in Sec. 2 and in Fig. 4.1 (b). (a) Average inclination θ of the crown during the growth phase (solid symbols). The dotted line corresponds to $\theta = 90°$. A comparison is made with data from Fedorchenko and Wang [86] for $h^\star = 0.4$ and $h^\star = 4$ (hollow symbols). (b) Ratio between the radii of the top rim and the cavity expanding in the film, r_t/r_c (solid symbols). The hollow symbol shows the value obtained by Cossali et al. [55] for $h^\star = 25.4$ with $r_t = 5.3R_d$ and $r_c = 6.2R_d$. The dotted line shows the case where $r_t = r_c$. The insets respectively represent r_t and r_c normalized by the drop radius R_d. (c) Maximum height w reached by the top rim of the crown at various We, normalized by the drop radius R_d (solid symbols). The inset shows the measurement relative to $h^\star = 4.4$ from Scenario C, compared to data from Cossali et al. [55] (hollow symbols)), obtained for $h^\star \in \{11.1, 25.4, 43\}$. (d) Maximum length j of the jet emitted following the crown retraction at low We, normalized by the drop radius R_d. A comparison is made with data from Fedorchenko and Wang [86] for $h^\star = 46.3$ at various We. All measurements are shown as a function of the nondimensional film thickness $h^\star$. The legend from (d) is the same for all four graphs. Symbols correspond to various intervals of We: circles for We < 1000, squares for $1000 < $ We < 2000, and diamonds for We > 2000. The colour of the symbols refers to the scenarios described in Section 3.

From these geometrical measurements we may define a crown shape factor as

$$\psi = \frac{w \cot \theta}{|r_t - r_c|} . \tag{4.9}$$

The evolution of ψ with $h^\star$ is shown in Fig. 4.8 (b). For $h^\star < 1$, the crown shape is more or less the same for all We. But then as the film thickness increases beyond $h^\star = 1.5$, the shape factor decreases with increasing $h^\star$, and it does more sharply for lower We. When the ratio ψ is close to 1, the crown profile almost looks like a straight line (Fig. 4.8 ii). When the shape factor is larger than 1, the inclination θ made by the crown interface is smaller than $\mathrm{arccot}\,(|r_t - r_c|/h)$, i.e., the corresponding crown has a convex profile. By contrast, a value of ψ smaller than 1 represents the opposite case, i.e., a concave crown shape. These two cases are illustrated in Fig. 4.8 (a) i and iii, respectively. The change of sign in ψ corresponds to the case where $\theta > 90°$ (Figs 4.8 iii and iv). In the thin film region ($h \lesssim 1$), the crown thus typically takes a convex shape, while in the thick

film region ($h \gtrsim 2$) there is a change of curvature or even a crown whose bottom spreads out more than the top rim.
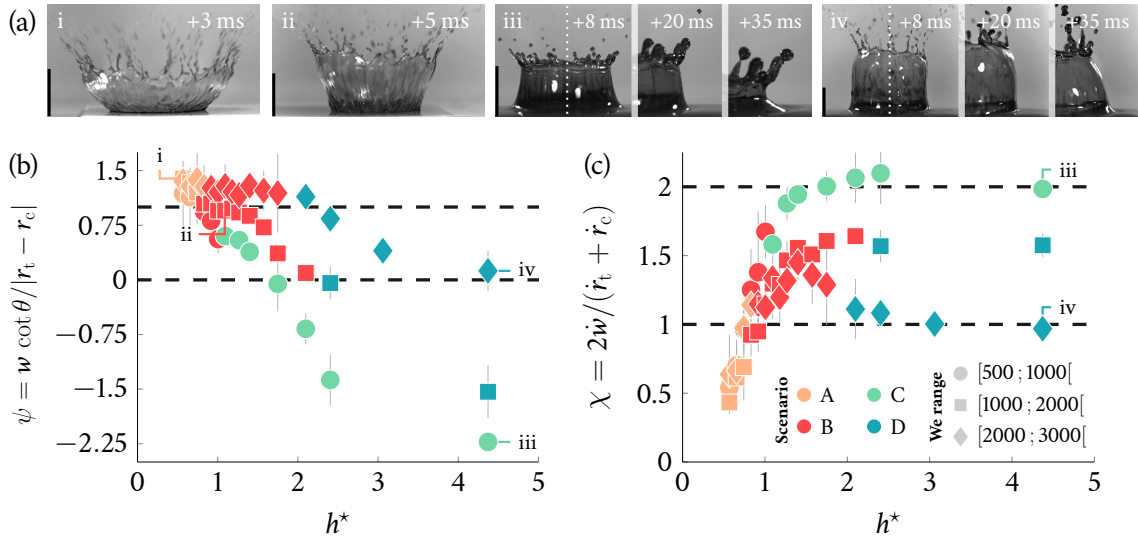
Figure 4.8: Crown shape factor and retraction velocity components. (a) Examples of crown shapes shown in the graph of (b): i. $h^\star = 0.56$, We = 1675, shape factor of 1.39, ii. $h^\star = 1.1$, We = 1675, shape factor of 1.09, iii. $h^\star = 4.3$, We = 525, shape factor of -2.24 and average velocity ratio of 1.98, and iv. $h^\star = 4.3$, We = 2740, shape factor of 0.37 and average velocity ratio of 0.95. Two frames showing the main retraction direction of the crown are added in iii and iv, with a correspondence in the graph from (c). The scale bars are 1 cm. (b) Crown shape factor ψ, and (c) ratio of crown retraction velocity components χ, both computed as a function of the nondimensional film thickness $h^\star$. The dashed line from (b) at $\psi = 0$ corresponds to a change of sign when $\theta = 90°$. The other dashed line at $\psi = 1$ corresponds to the change from a crown convex profile to a straight profile. In (c) the two dashed lines are drawn at $\chi = 1$ and $\chi = 2$. The symbol colours correspond to the scenarios identified in Section 3. The legend is the same in both graphs.

One might also compare the vertical (from top to bottom) and radial (inward) retraction velocities of the crown. The vertical retraction velocity $\dot{w}$ is estimated right after the maximum height is reached in each experiment. The radial component corresponds to the average of $\dot{r}_t$ and $\dot{r}_c$, again measured right after both radii reach their maximum. Estimations of the ratio $\chi = 2\dot{h}/(\dot{r}_t + \dot{r}_c)$ are taken for each experiment by using the derivatives of quadratic fits made in the $w(t)$, $r_t(t)$ and $r_c(t)$ curves, obtained between t_c and $t_c + 5$ ms. On average for all the experiments in a given scenario, the maximum in the $w(t)$, $r_t(t)$ and $r_c(t)$ curves is observed at about the same time. This time has a value of 16.4 ± 2.7 ms on average for all the impacts in the central jet case (scenario C, We $\lesssim 1500$) and 14 ± 1.4 ms in the crown folding case (scenario D, We $\gtrsim 1500$), so both are very close to t_c. The ratio χ is equal to 2.06 ± 0.21 in the jetting case and to 1.13 ± 0.28 in the crown folding case (averages $\pm$ s.d. of all the experiments corresponding to scenarios C and D, respectively). In other words, in scenario C the crown height decrease occurs much faster than the radial retraction, which then continues in the film after the crown has disappeared and allows for the jet to protrude. On the contrary, in scenario D both components of the retraction velocity are similar, hence the folding observed. These measurements correspond to the observations from Figs 4.6 (c-d) i and ii. The evolution of the ratio χ with the film thickness is shown in Fig. 4.8 (c). At low and intermediate We, this ratio increases with the film thickness for $h^\star \lesssim 1.5$. Then for $h^\star \gtrsim 1.5$ it reaches a limit value which is larger at lower We. For the highest We, a maximum is observed around $h^\star \simeq 1.5$ then a limit value close to 1 is reached in the thick film region. Two short sequences from scenarios C and D are shown in Figs 4.8 (a) iii and iv, respectively, where the difference in the retraction motion of the two crowns is visible.

4.2 Mixing and thickness variations

Mixing level indicators may be inferred from the film thickness variation and red proportion maps taken after each impact (Figs 4.2 (b) and (c)). We first consider the physical extension and scattering of the spot left by the drop in the film post-impact. We then deduce the quantity of water ejected during the impact, as well as the average proportion coming from the initial drop into the ejections.
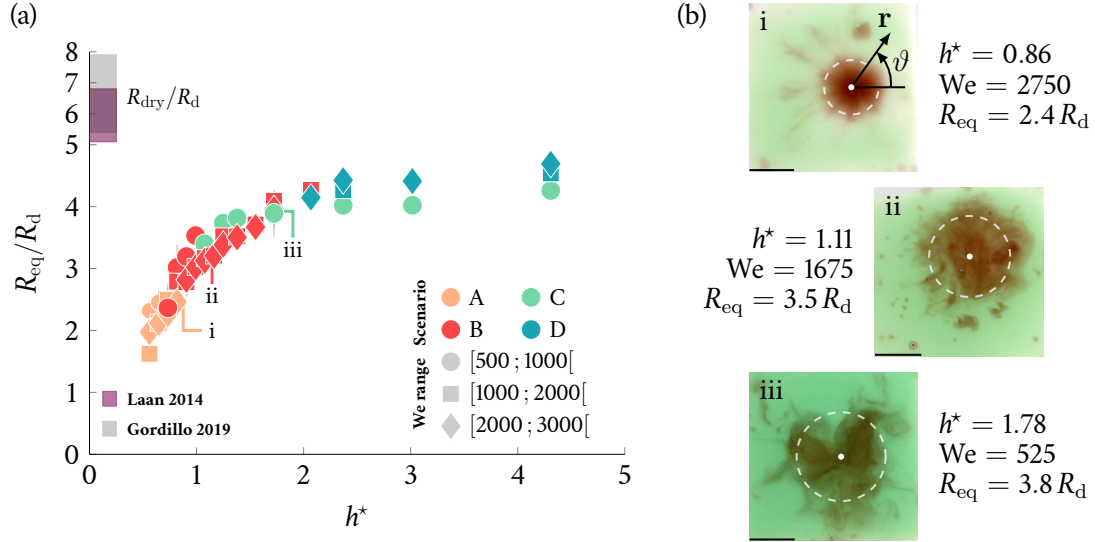
Figure 4.9: Nondimensional equivalent radius R_{eq} of the red stain left by the drop in the film, defined in Eq. (4.11): (a) Measurements of R_{eq} as a function of the nondimensional initial film thickness $h^\star$, divided in three bins of We. The grey and dotted bands represent the maximum spatial extension R_{dry}/R_d reached by a drop on a dry wall between We $= 500$ and We $= 3000$. These boundaries are estimated using the results from Laan et al. [139] (dots) and Gordillo et al. [103] (plain), respectively. The symbol colours correspond to the scenarios observed in Section 3. The roman lowercase letters show the location of the examples from (b) in the graph. (b) Examples of radii computed according to Eq. (4.11) and superimposed with the corresponding initial photographs, for the following ranges of parameters: i. very thin film, high We, ii. thin film, intermediate We and iii. thick film, low We. Picture i also shows the (r, ϑ) coordinates used to compute the integral from Eq. (4.11). The equivalent radius and drop impacting point are represented in each photograph by a white dashed circle and a white dot, respectively. The scale bars are 1 cm.

4.2.1 Equivalent moments of the red dye proportion distribution

The red spot left in the film by the crushed drop varies greatly in shape and size (see Fig. 4.5). To estimate the size variations of this spot, we first define the kth-order moment of the red dye proportion in the film as follows:

$$M_k = \int_0^{2\pi} \int_0^\infty p_r(r, \vartheta)\, r^{k+1} \mathrm{d}r\, \mathrm{d}\vartheta, \tag{4.10}$$

where r and ϑ denote the cylindrical coordinates in a frame centered at the impact point (Fig. 4.9 (b) i). The impact point position is measured in the high-speed colour videos, at the closest frame right after the drop starts crushing. The red dye concentration p_r is measured at about 1 s after the impact, as shown in the example of Fig. 4.2 (b). The normalized first-order moment represents an equivalent red spot radius R_{eq}, defined as

$$R_{eq} = \frac{M_1}{M_0}. \tag{4.11}$$

Using the normalized second-order moment, it is likewise possible to define the variance of the distribution as

$$\sigma_{\text{eq}}^2 = \frac{M_2}{M_0} - R_{\text{eq}}^2 . \tag{4.12}$$

If the red proportion distribution is a Dirac function centered in $r = R^\star$, then $R_{\text{eq}} = R^\star$ and $\sigma_{\text{eq}} = 0$. If the distribution is uniform for $r \leq R^\star$ and null for $r > R^\star$, then $R_{\text{eq}} = 2/3\,R^\star$ and $\sigma_{\text{eq}} = R^\star/(3\sqrt{2})$. The evolution of the equivalent red spot radius R_{eq} with $h^\star$ is shown in Fig. 4.9 (a), for the same three bins of We as in the previous section. Figure 4.9 (b) shows examples of the radii obtained in several cases, which are drawn directly in the corresponding pictures. For the sake of comparison, the maximum radius that would be reached by a drop colliding with a dry wall, R_{dry}, is also represented in Fig. 4.9 (a). The dry radius R_{dry} increases with We, hence it is represented as a band corresponding to the bin We $\in [500; 3000]$ with estimations from Laan et al. [139] and Gordillo et al. [103], respectively. In the same manner, Fig. 4.10 (a) shows the evolution of σ_{eq} with $h^\star$, with illustrations in Fig. 4.10 (b).
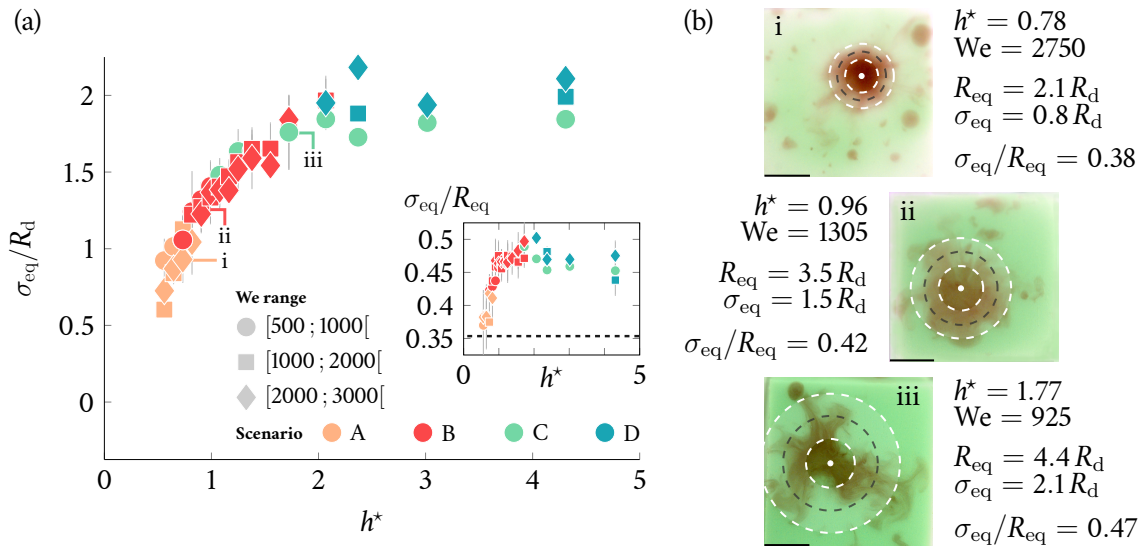
Figure 4.10: Nondimensional second order moment σ_{eq} of the red proportion in the film post impact, defined in Eq. (4.12): (a) Measurements of σ_{eq} as a function of the nondimensional initial film thickness $h^\star$, for three bins of We. The colours represent the various scenarios described in Section 3. The roman lowercase letters show the locations of the examples from (b) in the graph. The inset represents the second-order moment divided by the equivalent radius, $\sigma_{\text{eq}}/R_{\text{eq}}$. The dashed line in the inset corresponds to the theoretical uniform distribution value of $1/(2\sqrt{2})$. (b) Examples of radii R_{eq} (dashed, black) and $R_{\text{eq}} \pm \sigma_{\text{eq}}$ (dashed, white) superimposed with the corresponding initial photographs, for the following ranges of parameters: i very thin film, high We, ii. thin film, intermediate We and iii. thick film, low We. The white dots show the impact points. The scale bars are 1 cm.

We observe in Fig. 4.9 (a) that R_{eq} increases monotonously with the initial film thickness $h^\star$ and reaches a limit value at $h^\star \gtrsim 2$. The radii measured at $h^\star < 1$ are small compared to the dry radius R_{dry}. Additionally, the variation of the radius with We is less pronounced when there is a film than when there is none [128, 168]. The dry radius R_{dry} indeed goes from $5.3R_{\text{d}}$ at We $= 500$ to $7.5R_{\text{d}}$ at We $= 3000$ (averages obtained with [103, 139]). On the other hand, the largest difference observed between R_{eq} values at a given thickness range for We $= 500$ and We $= 3000$ is of about $0.4R_{\text{d}}$. We get rid of the $h^\star$ dependence by defining $R_{\text{eq}}(\text{We}) = R_{\text{eq}}(h^\star, \text{We})/\overline{R_{\text{eq}}}(h^\star)$, i.e., each radius measurement corresponding to one experiment is normalized by the average made in all the measurements corresponding to its bin of $h^\star$, disregarding We. An anova test performed for $R_{\text{eq}}(\text{We})$ (i.e., for all We from Section 3 rather than for the three bins of Fig. 4.9) yields a p-value of 2×10^{-5}. The influence of We on R_{eq} is thus statistically significant although it is lesser than

the influence of $h^\star$. The correlation coefficient between the normalized $R_{eq}(We)$ and all the We from Section 3 is -0.33, i.e., the equivalent radius slightly decreases when We increases. This is visible in Fig. 4.9 (a) up to $h^\star \lesssim 2$, the corresponding bins representing most experiments (14 bins out of 17 bins of $h^\star$). The standard deviation σ_{eq} also increases with $h^\star$, as seen in Fig. 4.10 (a). In the same manner as R_{eq}, the value of σ_{eq} is very small for $h^\star \lesssim 1$, while it reaches a more or less stationary value when $h^\star \gtrsim 2$. An anova test performed on $\sigma_{eq}(We)$ in the same manner as for $R_{eq}(We)$ gives a p-value of 8×10^{-3}, i.e., the influence of We on σ_{eq} seems significant. The correlation coefficient of $\sigma_{eq}(We)$ is -0.20, so σ_{eq} also decreases slightly with We. The inset of Fig. 4.10 shows the second-order moment σ_{eq} over the equivalent radius R_{eq}. They were computed for each experiment, then divided into bins and averaged. By averaging the measurements corresponding to the four scenarios identified in the previous section, we obtain the following values for σ_{eq}/R_{eq}: A) $37.6 \pm 2.7\,\%$, B) $44.1 \pm 1.8\,\%$, C) $43.7 \pm 0.8\,\%$, and D) $45.6 \pm 2.1\,\%$ (average $\pm$ s.d. on all measurements corresponding to a given scenario, see Fig. 4.5). The variation of the area covered by the red stain in the film is thus less pronounced in scenario A than in the others, and is also closer to the theoretical uniform distribution case for which $\sigma_{eq}/R_{eq} = 1/(2\sqrt{2}) \simeq 35\,\%$. In scenarios B, C and D, the order of magnitude of σ_{eq}/R_{eq} is the same, although a small difference may be observed between scenarios C and D.
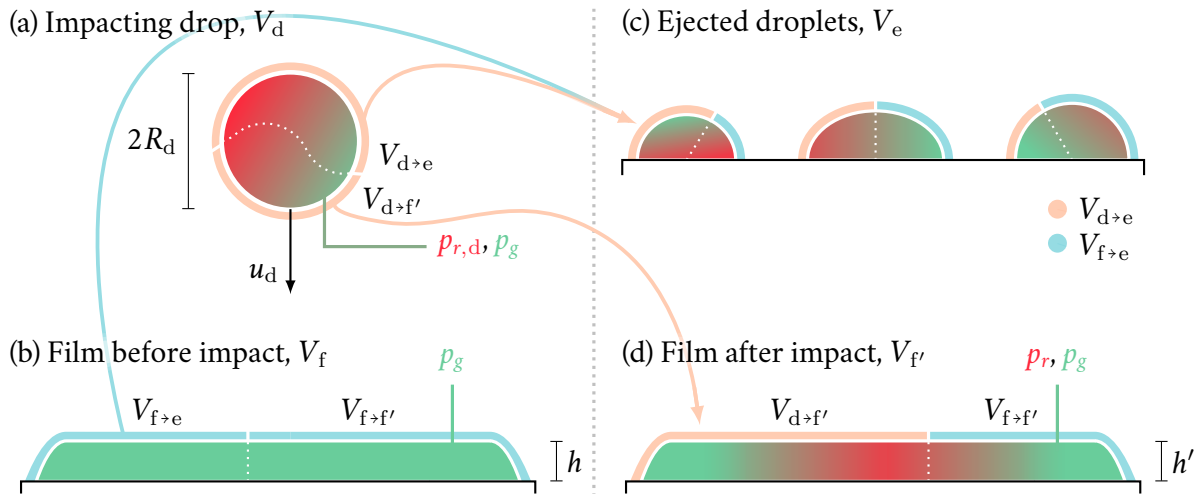
Figure 4.11: Drop, film, dye proportions and volume distribution nomenclature. (a) Impacting drop containing both red and green dyes in respective proportions $p_{r,d}$ and p_g. The drop has a radius R_d, a final velocity u_d and a volume V_d split into two contributions: $V_{d\to e}$ which goes into the ejections, and $V_{d\to f'}$ which remains in the film after the impact. (b) Initial film containing only green dye in proportion p_g, of supposedly uniform thickness h and of volume V_f divided into $V_{f\to e}$, the ejected part, and $V_{f\to f'}$, the remaining part. (c) Post-impact ejected droplets of unknown red volume fraction and of total added volume V_e coming from the sum of $V_{d\to e}$, the ejected volume initially in the drop, and $V_{f\to e}$, the ejected volume initially contained in the film. (d) Post-impact film of both unknown thickness δ' and red proportion p_r, and of known green proportion p_g. Its volume $V_{f'}$ corresponds to the addition of $V_{d\to f'}$, the volume going from the impacting drop into the film, and $V_{f\to f'}$, the part already in the film before the impact and which has not been ejected.

4.2.2 Ejected volume

We infer both the total ejected volume during the impact and the drop proportion left in the film from the raw measurements of film thickness and red dye proportion (see Fig. 4.2). As described in Fig. 4.11, we denote the impacting drop volume V_d, the initial film volume V_f and the final film volume $V_{f'}$. This film has a supposedly uniform thickness h before the impact and unknown thickness h' after the impact, where the latter may vary in space. The total volume of all the ejected

droplets is V_e. The drop volume V_d may be split into two contributions: one going into the impacted film, $V_{d \to f'}$, an the other going into the ejections, $V_{d \to e}$. The same holds for the initial film volume V_f that we may split into the part $V_{f \to f'}$ remaining in the film and the part $V_{f \to e}$ that joins the ejected droplets. The total ejected volume V_e therefore corresponds to $V_{d \to e} + V_{f \to e}$, whereas the film volume after impact $V_{f'}$ is equal to $V_{f \to f'} + V_{d \to f'}$. We call φ_e the ejected ratio, namely the ratio of the total ejected volume V_e over the impacting drop volume V_d, and write

$$
\begin{aligned}
\varphi_e &= \frac{V_{d \to e} + V_{f \to e}}{V_d} = 1 - \frac{(V_{d \to f'} + V_{f \to f'}) - (V_{f \to e} + V_{f \to f'})}{V_d} \\
&= 1 - \frac{V_{f'} - V_f}{V_d} = 1 - \frac{1}{V_d} \int_S (h' - h)\, \mathrm{d}S\,.
\end{aligned}
\tag{4.13}
$$

The integration domain S corresponds to the 40×40 cells on which h and p_r are obtained by colorimetry (see Fig. 4.2 (c)). In practice it is equivalent to a 35-40 mm side square, which is sufficiently large to take into account the thickness variations and yield an almost null difference $(h' - \delta)$ away from the impacted area (see Fig. 4.2 (c)). By averaging $|h' - \delta|$ over all the cells outside a disk of radius $2R_{eq}$ centered on the impact point, we obtain values going from 0.05 µm to 5 µm (averages of 30 best and worst cases), with a mean for all the experiments of 3 µm. Most of the worst cases correspond to the thinner films ($h^\star \lesssim 1$), for which the lighting may induce some errors on the edges of the pictures (see Section 2.2). The integration domain is also sufficiently small so that the ejected droplets that could fall into the film are neither seen in the pictures nor taken into account [55]. The only exceptions are the very slow and large droplets which induce mixing directly in the impacted zone at the end of the crown retraction or jet pinch-off. For very large film thicknesses ($h^\star \gtrsim 4$), as shown by, e.g., Figs 4.5 (d) and 4.10 (b) iii, the surroundings of the impacted area might sometimes be truncated when this area has a size close to S, although cases with a very visible truncation were left apart (see Appendix B.4). Around $h^\star \simeq 4$, the colorimetry hypotheses become less valid (see Appendix B.3) and there are fewer experiments. Although the exact results relative to these cases should thus be taken with precaution, they should not affect the conclusions relative to the following graphs.
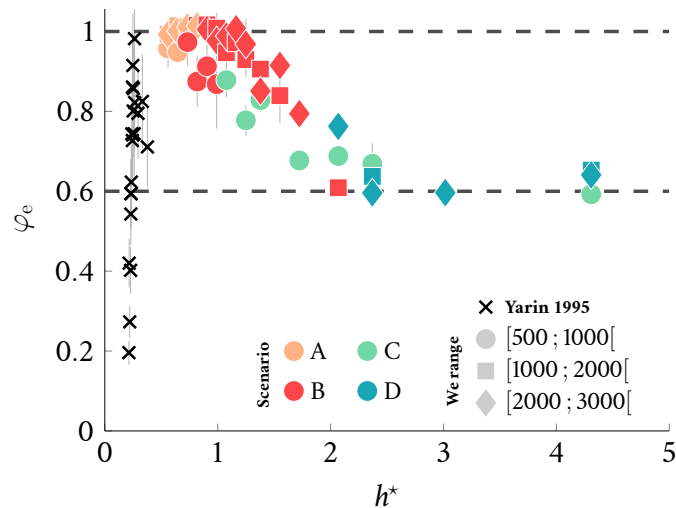
Figure 4.12: Ejected ratio φ_e from Eq. (4.13), corresponding to the total ejected volume V_e over the impacting drop volume V_d, as a function of $h^\star$ and for various bins of We. The dashed lines represent limit values exhibited by this ratio, i.e., $\varphi_e = 0.6$ and $\varphi_e = 1$. The colours correspond to the different scenarios observed and described in Section 3. The black crosses represent data from Yarin and Weiss [236], adapted to our experimental range by using $Oh = 1.7 \times 10^{-3}$ and $We = 1500$.

Figure 4.12 shows the ejected proportion φ_e as a function of $h^\star$. Our values are shown for $h^\star \geq 0.56$ (solid symbols) and compared to data from Yarin and Weiss [236] taken above the splashing threshold. These authors computed φ_e by summing the volume of all the secondary droplets that they measured in their experimental photographs, V_e, and by dividing this sum by the impacting drop volume V_d. They did not represent their experimental values as a simple function of the Weber number or nondimensional film thickness, but rather as a function of the combination $u = \text{We}^{1/2} (h^\star)^{3/4} \text{Oh}^{-1/8}$. Their range of parameters is such that $\text{Oh}_{\text{Yarin}} = 1.8 \times 10^{-2}$, $\text{We}_{\text{Yarin}} \in [250; 1500]$ and $h^\star_{\text{Yarin}} \in [0.8; 2]$, with the ejected proportion measured between $u = 18.4$ and $u = 32.4$. To adapt this to our range of parameters, we used $\text{Oh} = 1.7 \times 10^{-3}$ and $\text{We} = 1500$, and inferred from u that $h^\star \in [0.21; 0.38]$. We also represented their error bars which were estimated at 14 % of φ_e. As seen in Fig. 4.12, the ejected proportion first increases sharply with $h^\star$, going from about 0.2 to 1 (black crosses). Then, for $h^\star \gtrsim 1$, the proportion φ_e decreases with increasing $h^\star$ and reaches a limit value of about 0.6 at large film thickness, i.e., such that $h^\star \gtrsim 2$. This behaviour seems approximately independent of We. In other words, the film volume post-impact $V_{f'}$ is larger ($\varphi_e < 1$) than the initial volume V_f, though only slightly ($\varphi_e \simeq 1$) around $h^\star \simeq 1$. In this case, as much liquid is ejected as brought by the incoming drop. The average film thickness therefore remains constant although it is no longer uniform in space 1 s after the impact (see Fig. 4.2 (c)). At lower film thickness in our data (solid symbols), it is difficult to distinguish the results obtained for the two highest bins of We (We > 1000), but the measurements corresponding to scenario C overall seem to exhibit a lower ejected proportion (i.e., a larger volume going into the film at small We). Additionally, our data are in the continuity of data from Yarin and Weiss [236]. The maximum value reached by φ_e for thin films in our range is 1.03 with a relative error of 2 % (average on 5 largest measurements). The average relative error in our measurements is 5 %.
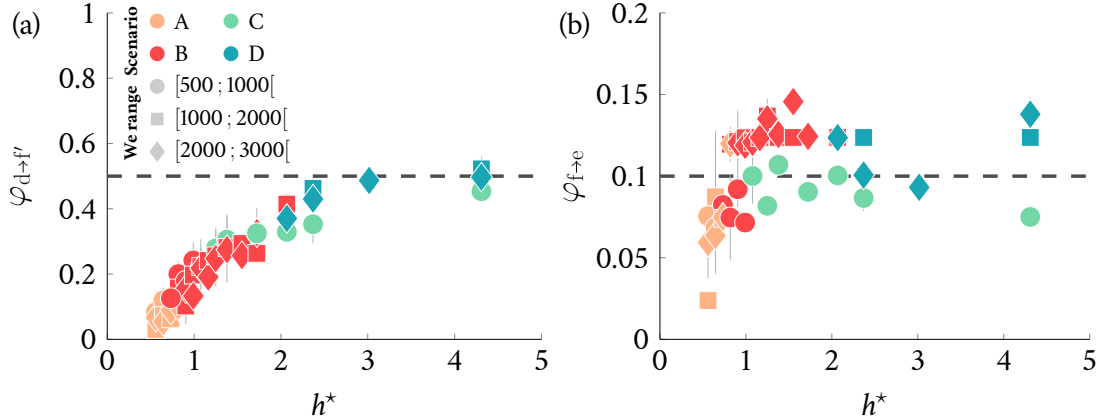
Figure 4.13: (a) Proportion of the volume coming from the drop left in the film after the impact, $\varphi_{d \to f'}$, as defined in Eq. (4.14). The dashed line shows the limit case for which $\varphi_{d \to f'} = 0.5$. (b) Ratio of the film volume lost in the ejections over the initial drop volume, $\varphi_{f \to e}$, as defined in Eq. (4.15). The dashed line shows the case for which $\varphi_{f \to e} = 0.1$. Measurements are shown as a function of the film thickness $h^\star$ and for three bins of We. The colours correspond to the different scenarios observed and described in Section 3. The legend is the same in both graphs.

4.2.3 Drop proportion left in the film post-impact

The proportion of the impacting drop that remains in the film after impact is defined as the ratio of the volume coming from the drop and remaining in the film following the impact, $V_{d \to f'}$, over

the impacting drop volume V_d:

$$\varphi_{\mathrm{d} \rightarrow \mathrm{f}'} = \frac{V_{\mathrm{d} \rightarrow \mathrm{f}'}}{V_\mathrm{d}} = \frac{1}{V_\mathrm{d}} \int_S \frac{p_r h'}{p_{r,\mathrm{d}}} \, \mathrm{d}S \, . \tag{4.14}$$

Although the integration domain S is arbitrary, it is much larger than the impinged area. As it may be seen in Fig. 4.2 (b), the red proportion in the film p_r is zero far from this zone, i.e., when $r > R_\mathrm{eq} + \sigma_\mathrm{eq}$. Contributions to the integral are thus negligible away from the impact region and the choice of S does not affect the computed integral, except in the already discussed case of very thick films for which $h^\star \gtrsim 4$. The evolution of $\varphi_{\mathrm{d} \rightarrow \mathrm{f}'}$ with $h^\star$ is shown in Fig. 4.13 (a). We observe that $\varphi_{\mathrm{d} \rightarrow \mathrm{f}'}$ overall increases with the film thickness. The Weber number does not seem to significantly influence this evolution. At $h^\star < 1$, the proportion of the drop left in the film post impact is quite small, about 0.1. Hence, a large amount of the initial drop volume ends up in the ejections. Then $\varphi_{\mathrm{d} \rightarrow \mathrm{f}'}$ increases with $h^\star$, such that the proportion of the impacting drop going into the ejections decreases. For $h^\star \gtrsim 2$, the ratio $\varphi_{\mathrm{d} \rightarrow \mathrm{f}'}$ also appears to reach a stationary value of about 0.5.

The sum of the two latter quantities can be related to another proportion:

$$\varphi_{\mathrm{f} \rightarrow \mathrm{e}} = \frac{V_{\mathrm{f} \rightarrow \mathrm{e}}}{V_\mathrm{d}} = (\varphi_\mathrm{e} + \varphi_{\mathrm{d} \rightarrow \mathrm{f}'}) - 1 \, . \tag{4.15}$$

The proportion $\varphi_{\mathrm{f} \rightarrow \mathrm{e}}$ compares the volume of fluid initially in the film and ejected away at impact, to the fixed drop volume. It is shown as a function of $h^\star$ in Fig. 4.13 (b). The variations in the graph should mostly come from additive numerical errors, given that this ratio is calculated from other numerical values rather than raw measurements. We observe that $\varphi_{\mathrm{f} \rightarrow \mathrm{e}}$ remains close to 0.1. Little fluid originating from the film therefore goes into the ejections. In other words, most of the initial film fluid remains in the film.

5. Discussion

The differences between scenarios observed qualitatively are also visible in the measurements described in the previous section. The main difference between the scenarios is the ordering of the capillary and viscous diffusion timescales t_c and t_ν. In scenario A ($h^\star < 1$) the high kinetic energy of the drop is mostly transferred to the top part of the expanding crown. At the same time viscous forces quickly slow down the motion of the crown near the film. Since nothing prevents the further extension of the top part of the crown ($t_\nu < t_\mathrm{c}$), fragmentation occurs due to the large velocity gradients appearing between the top and the bottom of the crown. Then, as the thickness is increased ($h^\star \gtrsim 1$), retraction of the crown is observed in scenario B. The expanding crown is again slowed down at its basis due to the viscous forces propagating from the solid surface to the free liquid surface of the film. But at the same time, given that $t_\nu \sim t_\mathrm{c}$, capillary forces tend to shrink the crown. Increasing further the film thickness ($h^\star \gtrsim 2$), the crowns obtained in scenarios C and D are oriented perpendicularly to the film free surface, or even start bending inward before completing their expansion phase. The capillary forces act sooner than the viscous forces in the film ($t_\mathrm{c} < t_\nu$), thereby preventing a large extension of the crown top part as in the first two scenarios, while dissipation in the film only slows down the crown basis later.

Following these observations, it is not surprising to see that all the crown geometry parameters and mixing level indicators depend strongly on $h^\star$, and that most mixing level indicators are correlated to the crown geometry (see Table 4.1). In scenario A, the viscous dissipation slowing down the crown basis translates into a very inclined and convex-looking crown, which is corroborated

Mixing and thickness variation	Crown geometry			Thickness
	θ	r_t/r_c	w	$h^\star$
R_{eq}	0.96	-0.86	0.50	0.88
σ_{eq}	0.93	-0.84	0.56	0.87
φ_{e}	-0.86	0.95	-0.28	-0.90
$\varphi_{\mathrm{d \rightarrow f'}}$	0.91	-0.88	0.44	0.90
$\varphi_{\mathrm{f \rightarrow e}}$	0.42	-0.18	0.63	0.36

Table 4.1: Correlation coefficients between the mixing level indicators (equivalent moments R_{eq} and σ_{eq}, ejected proportion φ_{e}, proportion of the drop volume going into the film $\varphi_{\mathrm{d \rightarrow f'}}$, and proportion of the film going into the ejections $\varphi_{\mathrm{f \rightarrow e}}$) and the crown geometry parameters (inclination θ, ratio of top and bottom radii r_t/r_c and height w), compared with the correlation coefficients obtained between the mixing level indicators and $h^\star$.

by the measurements of θ, r_t/r_c, w and of the crown shape factor $\psi > 1$ (Figs 4.7 and 4.8). Regarding the post-impact mixing in scenario A, the red dye is distributed on a very small radius R_{eq}, in an almost uniform manner given that $\sigma_{\mathrm{eq}}/R_{\mathrm{eq}}$ is close to the theoretical uniform distribution in this case. Such a distribution is consistent with the fragmentation of the crown observed and the viscous dissipation occurring rapidly, thereby preventing any further convective motion in the film that would lead to more mixing. In scenario B, measurements relative to the crown geometry correspond to the balance between the viscous dissipation and capillary forces, which yields a shape factor ψ close to 1. Because of the crown retraction at the end of the impact, mixing is increased and larger values are obtained for both R_{eq} and σ_{eq}. The ejected volume proportion φ_{e} is close to 1 in scenario A, i.e., there is as much liquid ejected away during the impact as in the incoming drop. The ejections also mostly contain liquid from the drop as the proportion of drop liquid in the ejections corresponds to $1 - \varphi_{\mathrm{d \rightarrow f'}} \gtrsim 0.9$. Then, as $h^\star$ increases and fragmentation is no longer observed (scenario B), φ_{e} decreases while $\varphi_{\mathrm{d \rightarrow f'}}$ increases, i.e., there is a larger proportion of the drop going into the film and a smaller one into ejections, which also represent a lower total volume.

In scenario C and D, because the capillary forces act much sooner than viscous dissipation in the film, $\theta \gtrsim 90°$ and $\psi < 1$, in a consistent manner with the observed inward orientation of the crown. Both the jet protrusion and crown folding induce additional mixing compared to the sole retraction of the crown of scenario B. The liquid falling back into the film after the end of the initial impact indeed seems to expand the mixed area as R_{eq} becomes larger. Consistently with the red volutes surrounding the post-impact red spot in the film, the standard deviation σ_{eq} also increases with $h^\star$ in scenarios C and D but at a slower rate, and the resulting concentration profile is almost uniformly distributed since $\sigma_{\mathrm{eq}}/\mathrm{Re}$ remains close to 0.45. In both scenario C and D, once $h^\star \gtrsim 2$, the ejected proportion φ_{e} approaches the same stationary value of about 0.6, i.e., some liquid from the drop is added in the film locally. The proportion of the drop left in the film post-impact, $\varphi_{\mathrm{d \rightarrow f'}}$, also seems to reach a limit value of about 0.5 when $h^\star \gtrsim 2$. This bound could possibly result from the truncation of the images at very large film thickness. Nevertheless, although $\varphi_{\mathrm{d \rightarrow f'}}$ might further increase with $h^\star$ in reality, it does not seem to get close to 1 for very large film thicknesses. The ejections produced by a drop impacting a liquid film thus seem to always contain liquid initially from the drop in a significant proportion. On the other hand, the ratio of the volume originating from the film and ejected away at impact, over the initial drop volume, $\varphi_{\mathrm{f \rightarrow e}}$, remains close to 0.1 once $h^\star \gtrsim 1$. Hence, in a consistent manner with the other observations, very little liquid coming from the film is ejected away.

The Weber number also affects crown geometry parameters, mostly in the case of scenarios C and D. In particular, a higher We results in a much higher crown, as shown in Fig. 4.7 (c). Correspondingly, large differences are observed between scenarios C and D in the crown shape factor ψ and the ratio of the retraction velocity components χ (Figs 4.8 (b) and (c)). The ratio of velocity components is notably representative of the different mechanisms involved during the retraction phase of these two scenarios. Unlike the crown geometry parameters, the mixing level indicators (R_{eq}, σ_{eq}, φ_{e}, $\varphi_{\mathrm{d \to f'}}$ and $\varphi_{\mathrm{f \to e}}$) do not significantly vary with We. Specifically, the ejected volume should mostly depend on the first stages of the impact, i.e., the crushing of the drop in the film and the crown growth. Since the crowns observed in scenarios C and D present different geometries, it is therefore surprising to observe similar values of φ_{e} in both cases once $h^{\star} \gtrsim 2$.

The relatively minor influence of We is in contrast with the dynamics of drop impact on a dry wall, in which case the splashing threshold or maximum extension of the radius formed at impact depend strongly on We [53, 103]. This radius is also much larger than the equivalent red spot radius obtained in scenario A ($h^{\star} < 1$) [53, 103, 139]. Nevertheless, retraction and expansion strokes are also observed for impacts on a dry wall [53, 179, 235], and the final size of the spot left by the drop on the wall is usually smaller than R_{dry}, i.e., this final size and the value for R_{eq} as $h^{\star} \to 0$ might be expected to become very close. The major difference in our experiments is the presence of the initial liquid film which decreases the viscous forces acting to slow the motion of the growing crown during the impact. All our experiments also lie within regimes where $t_{\mathrm{i}} < t_{\nu}$. The case where $t_{\mathrm{i}} \approx t_{\nu}$ corresponds to a film thickness $h^{\star} = 0.15$ (18 µm) at We $=$ 500 and $h^{\star} = 0.23$ (26 µm) at We $=$ 3000, i.e., a range that we could not explore, but that was partly described by Yarin and Weiss [236] (Fig. 4.12).

In Table 4.1, we report the various correlation coefficients computed between the mixing level indicators (R_{eq}, σ_{eq}, φ_{e}, $\varphi_{\mathrm{d \to f'}}$ and $\varphi_{\mathrm{f \to e}}$) and the crown geometry parameters (θ, $r_{\mathrm{t}}/r_{\mathrm{c}}$ and w). As a comparison, the correlation coefficients with $h^{\star}$ are added in the last column. We observe that the red spot radius and second-order moment, R_{eq} and σ_{eq}, along with the proportion of the drop left in the film post-impact, $\varphi_{\mathrm{d \to f'}}$, overall increase with increasing crown inclination θ and decreasing ratio of the top and bottom crown radii $r_{\mathrm{t}}/r_{\mathrm{c}}$, still in accordance with the previous discussion. Indeed, a very inclined crown wall typically leads to early fragmentation and a small red spot containing very little water coming from the drop, while for $\theta > 90°$ and $r_{\mathrm{t}}/r_{\mathrm{c}} < 1$, the longer lifetime of the crown allows the mixing between the drop and the film to last longer and to occur on a larger area. It is thus also not surprising to see that these mixing level indicators are not strongly correlated to the height of the crown. Conversely, the ejected proportion φ_{e} decreases as θ increases, and increases with $r_{\mathrm{t}}/r_{\mathrm{c}}$. A very inclined crown indeed allows the ejections to actually leave the impacted zone and not to fall back into the film after the impact. The proportion of volume initially in the film and ejected away at impact, $\varphi_{\mathrm{f \to e}}$, was found to remain almost constant (see Fig. 4.13 (b)), and is also observed to vary only little with the crown geometry parameters.

Besides the rapid expansion and retraction of the crown, the impact is also responsible for the emergence of waves at the free surface of the film, or even directly in the crown in scenarios C and D. According to Ersoy and Eslamian [80], capillary waves should participate in the mixing between the drop and the film. Measurements based on our movies yield wavelengths of 1.62 ± 0.05 mm (average $\pm$ s.d. on 49 experiments for which $h^{\star} \gtrsim 1.3$, see the raw data table from the Supplemental Material), similarly to their findings. Capillary waves should be emitted as soon as the drop has crushed and the crown starts growing [80, 235], although they were not visible in Fig. 4.5 (a). The local Capillary number in the film during the first stages of the impact is Ca $= \nu \rho \dot{r}_{\mathrm{c}}/\gamma$, with $\dot{r}_{\mathrm{c}}$ the edge velocity of the radially expanding cavity in the film, in this case measured for $t < t_{\mathrm{c}}$. In scenario A for very thin films at high We, $\dot{r}_{\mathrm{c}} \sim$ 1-2 m s^{-1}. From Jalaal et al. [120], based on a linear analysis of the lubrication theory we may estimate the wavelength

of capillary waves in a thin viscous film of thickness $h^\star = 0.75$ as $\lambda \simeq 5.03 h/\mathrm{Ca}^{1/3} = 1.6$ mm [63, 80]. According to the lubrication equation, the exponentially decaying ripples in the film have a damping time of about $t_\mathrm{d} = 3\mu\lambda^4/(16\pi^4 h^3\gamma) = 0.2$ ms, i.e., much smaller than the total crown formation and break-up timescale of a few milliseconds, and of the same order as our frame period of 0.16 ms. In scenario B, e.g., for $h^\star \gtrsim 1$, at We $= 2750$, the crown wall expands at a velocity of about $\dot{r}_\mathrm{c} \simeq 0.5$ m s^{-1}. The damping characteristic time of the capillary ripples t_d is in this case of the order of 2 ms. The capillary ripples thus also fade away before the other phenomena at play may even interact with them, and may help dissipate the remaining kinetic energy of the crown after it starts to retract toward the center. However, in the case of scenarios C and D, e.g., for $h^\star = 2$, the crown wall moves at a smaller velocity $\dot{r}_\mathrm{c} \simeq 0.05 - 0.1$ m s^{-1}, yielding a damping time of the capillary ripples $t_\mathrm{d} \in [25\ ;\ 100]$ms, which is comprised between t_c and t_ν. During the last stages of the impact in particular, these capillary ripples could help dissipate the kinetic energy of any secondary droplet or blob of liquid that falls back into the film following the retraction phase of the crown. These waves could thus be more likely to prevent any further expansion of the spot left by the drop in the film following the impact, rather than to enlarge the size of the spot. This would be consistent with the observation that $\sigma_\mathrm{eq}/R_\mathrm{eq}$ does not vary significantly between scenarios B, C and D.

6. Conclusion

The progressive filling of a thin film by successive drops of miscible liquid is a phenomenon appearing in the particular applicative context of stalagmite growth in karstic caves, but is also commonly encountered in other applications [235]. However, few studies are concerned with the hydrodynamics at play when drops impact thin films [86, 227], especially regarding the mixing that may occur both between the drop and the film, and into the ejections typically produced by these impacts [80]. Gaining a deeper insight into the variations of ion distribution at the timescale of single drop impacts would nevertheless allow us to better comprehend the growth of stalagmites and the potential differences that they exhibit in terms of, e.g., shape and size. We thus investigated in this chapter the impact of a drop on a very thin film in a laboratory setting with the aim of determining how the drop content is distributed into the film upon impact. We varied the Weber number We and nondimensional film thickness $h^\star$ in a range close to what is observed in actual caves. We identified several impact scenarios depending on these parameters, going from a very inclined and rapidly growing crown that fragments early to a short, slow and thick crown that produces an uprising central jet lately. The distribution of these scenarios sheds light on the influence of We and $h^\star$ on the final outcome of the impacts. All the measured quantities are strongly correlated to the initial film thickness $h^\star$. Part of them (crown geometry parameters and ejected proportion) were further corroborated or completed by data from the literature in ranges close to ours. On the other hand, only some crown geometry parameters such as the maximum height, shape and retraction velocity depend on We. Additionally, most of the mixing level indicators, such as the red spot radius and ejected proportion, are strongly correlated to the crown inclination and spatial extent.

In particular, the mixing level indicators between the drop and the film that we introduced depend mostly on $h^\star$ and not significantly on We. Both the equivalent radius of the spot left by the drop R_eq and the corresponding second-order moment σ_eq increase with $h^\star$ in the first two scenarios due to the transition from a crown fragmenting and disappearing in scenario A to a crown retracting and collapsing in a random manner for B. For scenarios C and D, R_eq and σ_eq seem to reach stationary values as the crown retraction dynamics (jet appearance or folding) enhances the spreading of the crushed drop in the film even more. The lack of influence of We on the equivalent radius is opposed to what is observed for impacts on dry walls. The ejected proportion φ_e first

takes a more or less constant value of about 1 in scenario A, i.e., as much volume as brought by the drop is ejected away during the impact, no matter whether it came from the drop or the initial film. Then this proportion decreases for scenario B, meaning that a certain part of the drop volume is added to the film following the impact, increasing the thickness locally. The ejected proportion finally reaches a stationary value at large film thickness in scenarios C and D, despite the differences exhibited in the shape and retraction velocity ratio of the crown in these two cases. The proportion of the initial drop remaining in the film following the impact $\varphi_{d \to f'}$ overall increases with the film thickness in a consistent manner with the observations of the various scenarios.

All these measurements indicate that the film thickness directly influences the distribution of red in the film following the impact, as well as the volume and concentration of the droplets that are ejected away. Translated to caves, this would mean that the ion distribution in the residual water film covering stalagmites varies from one impact to the other depending on the film thickness, and so would the precipitation and accumulation of these ions and subsequent stalagmite growth. Accordingly, the film thickness seems to be locally affected by each impact. Although this thickness was thought to remain constant and uniform on actual stalagmites, such measurements added to the dispersal in the impact point position of the drops show that it should not be the case. The film thickness could still display more uniformity in between impacts separated by long periods of time ($\gtrsim$ 15 min) because of the other processes at play, such as the gravity-driven drainage of this film (see Ch. V). Therefore, concluding regarding the direct influence of one drop impact on subsequent stalagmite growth is not possible without considering drainage and precipitation. This chapter has nevertheless shown that considering a constant film thickness over time and space in attempting to model stalagmite growth is not always an hypothesis that should be made. Conversely, we only considered drop impacts on almost horizontal films to simplify the study made in this chapter. The successive drop impacts on stalagmites may nonetheless present different features when less ideal conditions are encountered, as it was shown in Sec. 2 from Ch. III (see Fig. 3.3). The interaction between drop impacts localised close to each other in a short period of time ($\sim$ 1-100 s), or the presence of film thickness gradient, may both affect the spots left by the drops in the film in a non negligible manner. Preliminary experiments cover these possibilities in Ch. VIII.

Appendix

This Appendix is divided as follows: Sec. A contains tables summarising the nomenclature appearing throughout the chapter, then the colorimetry algorithm is detailed in Sec. B.

A. Nomenclature

Tables 4.2 and 4.3 gather the water physical properties, characteristic scales, nondimensional numbers and variables presented in this chapter. Both tables originally come from Parmentier et al. [171]. They therefore contain some overlapping data with Tabs. 1.1 and 1.2 from the auxiliary sheet.

SYMBOL	VALUE/RANGE	UNITS	DESCRIPTION
		Water physical properties	
ρ	1000	$\mathrm{kg\,m^{-3}}$	Density
ν	10^{-6}	$\mathrm{m^2\,s^{-1}}$	Kinematic viscosity
γ	70	$\mathrm{mN\,m^{-1}}$	Surface tension
D	$\sim 10^{-9}$	$\mathrm{m^2\,s^{-1}}$	Dye diffusion coefficient
		Characteristic scales	
		Timescales	
t_i	$[0.7\,;\,1.5]$	ms	Drop crushing time
t_c	15	ms	Capillary time
t_ν	$[5\,;\,280]$	ms	Viscous diffusion timescale over h
$t_{\nu,\mathrm{d}}$	6	s	Viscous diffusion timescale over R_d
$t_{\downarrow/\rightarrow}$	10/90	s/min	Concentration homogenization timescale by vertical/horizontal diffusion
t_d	$[0.2\,;\,200]$	ms	Capillary ripples damping time
		Length scales	
$\delta(h^\star = 1)$	115	µm	-
R_dry	$[12\,;\,18]$	mm	Maximum radius of drop impacting on dry wall
λ	1.6	mm	Capillary ripples wavelength
λ_c	2.7	mm	Capillary length
		Other	
$\dot{r}_\mathrm{c}$	$[0.05\,;\,1]$	$\mathrm{m\,s^{-1}}$	Cavity expansion velocity
V_f	$[10^{-7}\,;\,10^{-6}]$	$\mathrm{m^3}$	Film volume
		Nondimensional numbers	
Oh	$1.7 \cdot 10^{-3}$	-	Ohnesorge
We	$[525\,;\,2750]$	-	Weber
Pe	1000	-	Péclet
$h^\star$	$[0.4\,;\,4.3]$	-	Film thickness
t_ν/t_i	$[3\,;\,400]$	-	Ratio of viscous diffusion and drop crushing timescales (Reynolds)

Table 4.2: List of physical properties and characteristic scales and corresponding symbols, with their definition and typical values (see Sec. 2.3 for variable definitions).

Symbol	Value/range	Units	Description
Side view measurements			
Impacting drop			
R_d	2.3	mm	Radius
u_d	[2.9 ; 6.6]	m s^{-1}	Velocity
Film			
h	[65 ; 500]	µm	Thickness
Crown geometry			
θ	[50 ; 105]	°	Inclination
r_t	[10 ; 20]	mm	Top radius
r_c	[8 ; 18]	mm	Cavity radius
w	[6 ; 22]	mm	Height
ψ	[−2.2 ; 1.8]	mm	Shape factor
Crown retraction			
j	[8 ; 22]	mm	Jet length
χ	[0.3 ; 2.3]	mm	Retraction velocity ratio
Top view measurements			
Colorimetry measurements			
p_r	[0 ; 0.05]	-	Red dye proportion
p_g	0.05	-	Green dye proportion
h_r	[0 ; 25]	µm	Red partial film thickness
h_g	[0 ; 25]	µm	Green partial film thickness
Equivalent moments			
R_eq	[6 ; 16]	mm	Equivalent red stain radius
σ_eq	[2 ; 5]	mm	Second-order moment
Proportions			
φ_e	[0.6 ; 1]	-	Ejected volume proportion
$\varphi_\mathrm{d\rightarrow f'}$	[0 ; 0.5]	-	Drop volume proportion left in the film
$\varphi_\mathrm{f\rightarrow e}$	[0 ; 0.1]	-	Ejected film volume over initial drop volume ratio

Table 4.3: List of measured quantities and corresponding symbols, with their definition and typical values (see Sec. 2.1 for side view variable definitions and Secs. 2.2 and 4.2 for top view variable definitions).

It should be noted, though, that in Tab. 1.2 from the auxiliary sheet, the exact definition or range of parameters presented may slightly differ from the ones in the above tables, because the parameters in Tab. 1.2 correspond to the entire document while Tabs. 4.2 and 4.3 refer only to the present chapter. This is the case for, e.g., the Péclet number that we evaluated differently in Ch. VI. Because the role of this nondimensional number in Ch. VI is more relevant to the entire manuscript, we presented the version of Ch. VI in Tab. 1.2.

B. Colorimetry measurements

In the following sections, we go over the detailed calculations of the colorimetry measurement. We first apply Beer-Lambert law to our experimental setup and approximate the resulting equation in Subsec. B.1. We also review the method used to fit the coefficients appearing therein. Finally, we show how we can retrieve the thickness and red dye proportion of a given picture based on a calibration performed beforehand in Subsec. B.2.

B.1 Colorimetry measurement

In the following, the subscripts r and g respectively stand for the red and green dyes. The R, G and B subscripts represent the red, green and blue colour channels of the camera sensor, each having values that range from 0 to 1. We consider the reflectance of light over a thin film of thickness h containing several dyes i ($i \in \{r, g\}$) at concentrations c_i (in M). The incident light is non-polarized and normal to the water surface, with an intensity spectrum $I_0(\lambda)$. According to Fresnel equations, a fraction $\alpha I_0(\lambda)$ is reflected at the water/air interface, while the remainder $(1 - \alpha) I_0(\lambda)$ is transmitted into the water. The coefficient α depends on the refraction index of water, which is relatively independent of wavelength in the visible range, so $\alpha \simeq 0.02$. The transmitted light is then partly absorbed by the dyes according to Beer-Lambert's law, so the intensity of the light impacting the bottom surface of the water film is

$$I_1(\lambda) = (1 - \alpha) I_0(\lambda) \exp\left[-h \sum_i c_i \varepsilon_i(\lambda)\right], \tag{4.16}$$

where the optical path length simply equals the film thickness h, and ε_i represents the molar extinction coefficient of each dye in solution (in $M^{-1} m^{-1}$).

Again, only a fraction $\beta I_1(\lambda)$ of this light is reflected at the bottom of the water film. This light is once more absorbed by the film, so the intensity of the beam returning to the water/air interface is

$$I_2(\lambda) = \beta I_1(\lambda) \exp\left[-h \sum_i c_i \varepsilon_i(\lambda)\right]. \tag{4.17}$$

Finally, a fraction $(1-\alpha)I_2(\lambda)$ crosses the water/air interface and reaches the camera. Since $\alpha \ll 1$, subsequent reflections are neglected. The light spectrum arriving onto the camera sensor is therefore

$$\left[\alpha + \beta(1 - \alpha)^2 \exp\left(-2h \sum_i c_i \varepsilon_i(\lambda)\right)\right] I_0(\lambda). \tag{4.18}$$

Each sensor j of the camera ($j \in \{R, G, B\}$) will receive a signal X_j integrated over the wavelength spectrum:

$$X_j = \int_0^\infty \left[\alpha + \beta(1 - \alpha)^2 \exp\left(-2h \sum_i c_i \varepsilon_i(\lambda)\right)\right] I_0(\lambda) S_j(\lambda) \, d\lambda, \tag{4.19}$$

where $S_j(\lambda)$ is the camera spectrum, namely the sensitivity of sensor j to a given wavelength λ. From this equation, it is not possible to determine h and c_i without knowing the spectra of incident light $I_0(\lambda)$, absorption $\varepsilon_i(\lambda)$ and camera $S_j(\lambda)$. However, in the limit where $hc_i\varepsilon_i \ll 1$, a Taylor

series approximation of the exponential can be considered, which yields:

$$
\begin{aligned}
X_j \simeq & \int_0^\infty \left[\alpha + \beta \left(1 - \alpha\right)^2 \right] I_0(\lambda) S_j(\lambda) \, \mathrm{d}\lambda \\
& - \sum_i h c_i \int_0^\infty 2\beta \left(1 - \alpha\right)^2 \varepsilon_i(\lambda) I_0(\lambda) S_j(\lambda) \, \mathrm{d}\lambda \\
& + \sum_{i,k} h^2 c_i c_k \int_0^\infty 2\beta \left(1 - \alpha\right)^2 \varepsilon_i(\lambda) \varepsilon_k(\lambda) I_0(\lambda) S_j(\lambda) \, \mathrm{d}\lambda \\
& + \mathcal{O}\left[(h c \varepsilon)^3 I_0 S \lambda \right] \\
\simeq & \; A_j - h \sum_i B_{ij} c_i + h^2 \sum_{i,k} C_{ikj} c_i c_k
\end{aligned}
\tag{4.20}
$$

with $C_{ikj} = C_{kij}$. In the limit where there is no film on the white substrate, i.e. $h = 0$, all R, G and B values observed on screen should be close to 1. In other words, the coefficients A_j can all be set to 1. Additionally, the dyes are only diluted in water and their concentrations c_i solely depend on the proportions of dye in water, defined as p_r and p_g for the red and green dyes in the film, respectively, and $p_{r,\mathrm{d}}$ the proportion of red dye in the incoming drop. The products $B_{ij} c_i$ and $C_{ikj} c_i c_k$ can thus be replaced by their nondimensional counterparts $B'_{ij} p_i$ and $C'_{ikj} p_i p_k$, respectively.

Previous calculations hold in each point of the picture captured by the sensor only if the lighting is perfectly uniform throughout the entire film. In reality, it is not the case. There were several lamps, each of them placed in a corner of the setup and oriented as perpendicularly as possible to the underlying film, since right above this film were placed the releasing drop device as well as the camera. To take that effect into account, the (R, G, B) values can be viewed as the product of two independent contributions: the absorbance of the light by the various dyes, and the spatial non-uniformity of lighting. The film thickness and the dye proportions should also vary with the position. The three parameters $(h, p_r$ and $p_g)$ are also not independent. In the case of the calibration pictures, the film thickness is measured beforehand and considered as uniform and therefore known in every position. On the other hand, in the experiments, as we used the same green proportion in both the drop and the film, whether it is prior to or after the impact, $p_g = 0.05$ everywhere (see Section 2.2). In any case only the products $p_i h$ are unknown. We therefore consider the partial thicknesses in red and green, defined as $h_r = p_r h$ and $h_g = p_g h$. The former equation thus reduces to

$$
X_j(\boldsymbol{x}) = \left[1 - \sum_i B'_{ij} h_i(\boldsymbol{x}) + \sum_{i,k} C'_{ikj} h_i(\boldsymbol{x}) h_k(\boldsymbol{x}) \right] \ell_j(\boldsymbol{x}),
\tag{4.21}
$$

where $\ell_j(\boldsymbol{x})$ is the factor accounting for the lighting non-uniformity relative to channel color j at position $\boldsymbol{x}$. The notation from the last relation does not imply a summation on index j.

a) Coefficient fit

The fitting parameters relative to all colour channels R, G and B can be found independently from each other. As an example, we focus on the red component that we denote by a matrix $\mathbf{R} \in \mathbb{R}^{M \times N}$, whose elements are R_{mn}. To find these coefficients, $M = 175$ dyed water films of known thickness and fixed red and green proportions were photographed with the same colour high-speed camera and lighting conditions. A 50-px wide stripe (which corresponds roughly to one and a half times the capillary length) is first removed on each side of the 512×512 px pictures in order not to see the physical edges of the tape nor the diminution of the film thickness towards zero. The picture then obtained is divided into 40×40 10-px side square cells, sorted from 1 to $N = 1600$ using
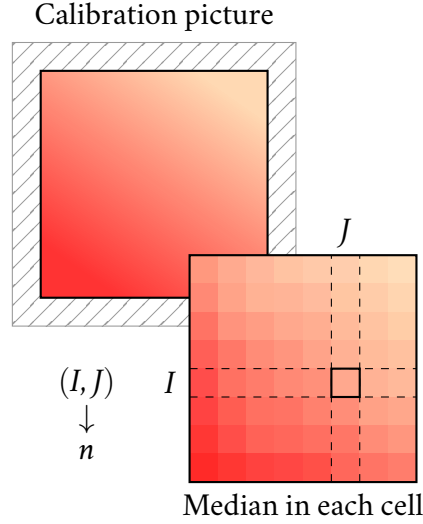
Figure 4.14: Cutting of pictures in square cells and numbering.

the index n. The spatial median of the intensity of each colour channel is taken in every cell, such that R_{mn} is the median of the red component in the nth cell of the mth experiment, as shown in Fig. 4.14. For each calibration experiment, there are actually two pictures divided in cells in which the median is computed, then the average of these medians is used in the matrix $\mathbf{R}$. The first picture is taken right after measuring the thickness of the film. Both pictures are taken when the substrate is horizontal, but the second one is taken after gently tilting the plate back and forth to avoid seeing any thickness variation that might have been caused by the needle tip entering and leaving the film.

Based on Eq. (4.21), a design matrix $\mathbf{D} \in \mathbb{R}^{M \times P}$ contains partial film thicknesses for all the calibration experiments, with P the number of dye absorption coefficients stored in an unknown vector $\boldsymbol{c} \in \mathbb{R}^{P \times 1}$. Each experiment corresponds in the design matrix to the row $\begin{bmatrix} 1 & h_r & h_g & h_r^2 & h_r h_g & h_g^2 \end{bmatrix}$. In addition to that, we also look for a vector $\boldsymbol{\ell} \in \mathbb{R}^{N \times 1}$ that accounts for the spatial lighting non-uniformity. In the case of the red channel, the fitting vectors are written as

$$
\boldsymbol{c} = \begin{bmatrix} 1 \\ -B_{rR} \\ -B_{gR} \\ C_{rrR} \\ 2\,C_{rgR} \\ C_{ggR} \end{bmatrix} \quad \text{and} \quad \boldsymbol{\ell} = \begin{bmatrix} \ell_{1,R} \\ \vdots \\ \ell_{N,R} \end{bmatrix} .
$$

We aim at finding the $(P + N)$ unknown coefficients that minimise the objective function

$$
\mathbf{E} = \mathbf{R} - \mathbf{D}\,\boldsymbol{c}\,\boldsymbol{\ell}^T \approx \mathbf{0} \tag{4.22}
$$

in the least square sense. This may be achieved by minimising the sum of the residuals $\mathcal{R}$ which corresponds to the Froebenius matrix norm of the former expression, or its square for the sake of simplicity:

$$
\boldsymbol{c}, \boldsymbol{\ell} : \ \min_{\boldsymbol{c}, \boldsymbol{\ell}} \mathcal{R}^2 = \min_{\boldsymbol{c}, \boldsymbol{\ell}} \operatorname{tr}\left(\mathbf{E}^T \mathbf{E}\right) . \tag{4.23}
$$
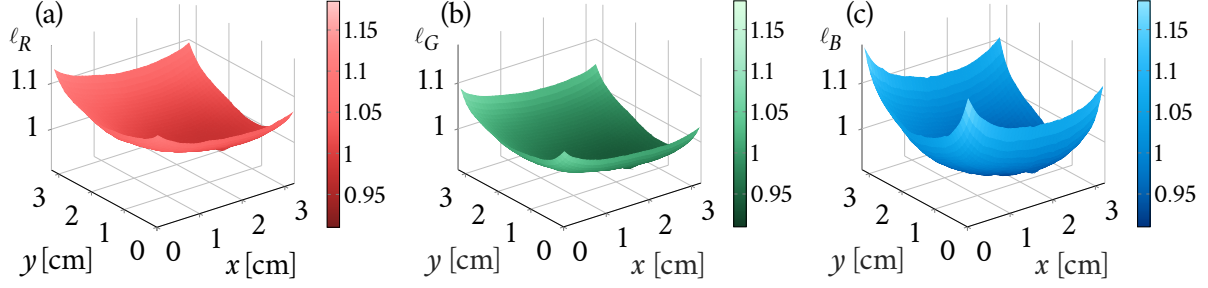
Figure 4.15: Lighting coefficients $\ell_j(\boldsymbol{x})$ relative to Eq. (4.21), for (a) $j = R$, (b) $j = G$ and (c) $j = B$. Coefficients were obtained by solving Eq. (4.22) in the least-square sense with a Newton-Raphson technique.

Cancelling the derivatives of $\mathcal{R}^2$ with respect to $\boldsymbol{c}$ and $\boldsymbol{\ell}$ each gives a set of P and N equations:

$$\partial_{\boldsymbol{c}} \mathcal{R}^2 = \mathbf{D}^T \mathbf{R} \boldsymbol{\ell} - \boldsymbol{\ell}^T \boldsymbol{\ell} \, \mathbf{D}^T \mathbf{D} \boldsymbol{c} = \mathbf{0}, \qquad (4.24)$$

$$\partial_{\boldsymbol{\ell}} \mathcal{R}^2 = \mathbf{R}^T \mathbf{D} \boldsymbol{c} - \boldsymbol{c}^T \mathbf{D}^T \mathbf{D} \boldsymbol{c} \boldsymbol{\ell} = \mathbf{0}. \qquad (4.25)$$

To solve these equations for $\boldsymbol{c}$, $\boldsymbol{\ell}$, Newton-Raphson method is applied, in which case we denote by $\boldsymbol{x}^k$ the root vector at iteration k and $\boldsymbol{f}$ the set of functions:

$$\boldsymbol{x}^k = \begin{bmatrix} \boldsymbol{c} \\ \boldsymbol{\ell} \end{bmatrix}^k, \quad \boldsymbol{f} = \begin{bmatrix} \partial_{\boldsymbol{c}} \mathcal{R}^2 \\ \partial_{\boldsymbol{\ell}} \mathcal{R}^2 \end{bmatrix}. \qquad (4.26)$$

The corresponding Jacobian matrix is given by

$$\mathbf{J} = \left[\begin{array}{c|c} -\boldsymbol{\ell}^T \boldsymbol{\ell} \, \mathbf{D}^T \mathbf{D} & \mathbf{D}^T \mathbf{R} - 2\,\mathbf{D}^T \mathbf{D} \, \boldsymbol{c} \, \boldsymbol{\ell}^T \\ \hline \mathbf{R}^T \mathbf{D} - 2\,\boldsymbol{\ell} \, \boldsymbol{c}^T \mathbf{D}^T \mathbf{D} & -\boldsymbol{c}^T \mathbf{D}^T \mathbf{D} \, \boldsymbol{c} \, \mathbb{I} \end{array} \right]. \qquad (4.27)$$

At the $(k+1)^{\text{th}}$ iteration, we have $\boldsymbol{x}^{k+1} = \boldsymbol{x}^k - \mathbf{J}^{-1}(\boldsymbol{x}^k) \boldsymbol{f}(\boldsymbol{x}^k)$, with all elements of $\boldsymbol{x}^0$ initialized to 1. The unknowns are indeed for the most part lighting variation coefficients that should be close to 1. Convergence is attained once the norm of the error between two iterates, $\left\| \boldsymbol{x}^{k+1} - \boldsymbol{x}^k \right\|$, goes below an arbitrary threshold of 10^{-3}.

b) Coefficient values

The coefficients representing the dye absorption and found with the calibration technique described here above are shown in Table 4.4, for the three colour channels. Despite the difference between their orders of magnitude, the series from Eq. (4.21) converges. As an example, we may consider the on-screen colour variations in a point of a 100 µm-thick film containing red and green dyes both in proportions of 0.05. The variations due to, e.g., B_{gR} and B_{gG}, would be respectively $B_{gR} \, p_r \, h^\star = 7 \times 0.05 \times 0.86 = 0.30$ and $B_{gG} \, p_g \, h^\star = 0.06$. Since they appear in Eq. (4.21) as decrements from 1, adding green in the film expectedly induces a larger variation to the red component than to the green one, yet they are both in the same range of values. For, e.g., a very thin film ($h^\star \ll 1$) containing only green dye, the green component would be almost 1. Additionally, the lighting spatial variations represented by the $\boldsymbol{\ell}$ vector from Eq. (4.21) are shown in Figs 4.15 (a-c), for all three colour channels. It can be seen that for a given j value, the light exposure is greater in the corners, whilst it decreases towards the centre of the picture. This is due to the four lamps

j	B_{rj}	B_{gj}	C_{rrj}	C_{rgj}	C_{ggj}
R	0.1	7.0	-6.2	-3.1	20.7
G	12.9	1.4	61.5	13.6	3.0
B	11.8	7.7	67.9	19.2	49.1

Table 4.4: Absorption coefficients from c relative to Eq. (4.21), for all three colour channels. Coefficients were obtained by solving Eq. (4.22) in the least-square sense with a Newton-Raphson technique.

placed in the corners of the experimental setup. The camera sensor has a less intense, broader spectral response to the blue colour than to the red and green, which translates into Fig. 4.15 (c) by sharper variations around the edges.

B.2 Retrieving the thickness and concentration in an arbitrary picture

Using the colour and lighting coefficients found with the calibration pictures, two out of the three parameters (film thickness, proportions of red and green dyes) can be retrieved based on an arbitrary picture. As aforementioned, before the impact the film had a uniform thickness and green proportion always fixed to $p_g = 0.05$. The impacting drop contained both red and green dyes of known proportions $p_{r,\mathrm{d}}$ and p_g, the latter having the same value as in the film. After the impact the green dye proportion is therefore known everywhere in the film. Computing the post-impact film thickness and red proportion in each point allows to assess how the drop and the film are mixing directly after impact.

To do so, we proceed in the same manner as for the calibration and first divide the post-impact picture of the film in 40×40 10-px side square cells, in which the median of red, green and blue components are computed. Focusing once again on the red component, we therefore get a vector $r \in \mathbb{R}^{N \times 1}$ containing all the red values of the N cells into which the picture was divided. The unknown is this time the matrix $\mathbf{D} \in \mathbb{R}^{N \times P}$ where each row $\begin{bmatrix} 1 & h_r & h_g & h_r^2 & h_r h_g & h_g^2 \end{bmatrix}$ corresponds no longer to the average values taken by the partial thicknesses in a given experiment, but to the partial thicknesses in a given point of the film. We aim at solving the following equation:

$$r = \mathbf{L}\mathbf{D}c, \tag{4.28}$$

with $\mathbf{L} \in \mathbb{R}^{N \times N}$ the diagonal matrix containing all the values from vector ℓ. As the system is non-linear with respect to the partial film thicknesses, it cannot be solved directly, nor for the entire picture at once, and computations should be made independently for all cells. To find the values of h_r, h_g in each case n of the discretized picture, we proceed by applying once again the Newton-Raphson technique. In this case we look in each cell n of the picture for the unknown vector $x_n = \begin{bmatrix} h_{r,n} & h_{g,n} \end{bmatrix}^T$ with $h_{i,n}$ the partial film thickness in the nth cell. We also rewrite and cancel Eq. (4.21) such that it becomes the set of functions $f_{j,n}$ to solve:

$$f_{j,n} = \left(1 - \frac{X_{j_n}}{\ell_{j_n}}\right) - \sum_i B_{ij} h_{i,n} + \sum_{i,k} C_{ikj} h_{i,n} h_{k,n} = 0. \tag{4.29}$$

The derivatives of $f_{j,n}$ with unknowns $h_{i,n}$, which correspond to the Jacobian matrix element $J_{ji,n}$, are given by

$$J_{ji,n} = -B_{ij} + 2\sum_k C_{ikj} h_{k,n}. \tag{4.30}$$

Since there are three colour channels and two unknowns, the Jacobian $\mathbf{J}_n$ in each cell is a (3×2) matrix that we use to compute the vector $\boldsymbol{x}_n^{k+1}$ at the $(k+1)^{th}$ iteration as follows: $\boldsymbol{x}_n^{k+1} = \boldsymbol{x}_n^k - \mathbf{J}_n^+(\boldsymbol{x}^k)\boldsymbol{f}_n(\boldsymbol{x}^k)$, with $\mathbf{J}_n^+ = \left(\mathbf{J}_n^T \mathbf{J}_n\right)^{-1} \mathbf{J}_n^T$.

The error is computed as the absolute difference between two consecutive iterates of the vector containing all $\boldsymbol{x}_n$, defined as $\boldsymbol{X}^k = \begin{bmatrix} \boldsymbol{x}_1^k \\ \vdots \\ \boldsymbol{x}_N^k \end{bmatrix} \in \mathbb{R}^{(2N \times 1)}$, namely $\left| \boldsymbol{X}^{(k+1)} - \boldsymbol{X}^k \right|$. Convergence is reached out when this error goes below an arbitrary threshold of 10^{-3}, which typically occurs after about 5 iterations.

B.3 Checking the hypotheses underlying the colorimetry measurement

a) Thickness variation of a thin film on a planar substrate

Mechanical thickness measurements were mostly taken close to the centre of the film because of the strong curvature exhibited by the film interface toward the edges of the substrate. Due to this curvature, spatial variations also appear to be greater in the colorimetry measurements. We may verify over which spatial extent a thin film keeps a thickness close to its maximum thickness $h_0 = 100\,\mu$m. We assume that the film lies on a horizontal substrate of side $W = 40$ mm and has a symmetric shape. In two dimensions, the liquid/air interface of the film can be modelled using the Young-Laplace equation [63]:

$$\rho g h(x) - \gamma \frac{\mathrm{d}^2 h}{\mathrm{d}x^2} = K, \tag{4.31}$$

where K is a constant pressure jump. The boundary conditions are $h(0) = h_0$ and $h(W/2) = h(-W/2) = 0\,\mu$m. Introducing the capillary length $\lambda_c = \sqrt{\gamma/(\rho g)} = 2.73$ mm $\ll W$, we find that the solution to the former equation reduces to

$$h(x) = h_0 \left(1 - \frac{\cosh\left(x/\lambda_c\right)}{\sinh\left(W/(2\lambda_c)\right)} \right). \tag{4.32}$$

The distance from the centre over which the film thickness is decreased by 3 % is 1.04 cm. On the other hand, after a distance of 1.5 cm, the film thickness only reaches 84 % of h_0. It is therefore not surprising for the colorimetry measurement technique to produce the spatial variations shown in, e.g., Fig. 4.3 (c), nor to get differences between average manual and colorimetry measurements, as shown in the graph of Fig. 4.4 (a).

b) Verification of the hypothesis made on $hc_i\varepsilon_i$

In approximating the exponential from Beer-Lambert's law by a Taylor series (see Eq. (4.20)), we assumed that $hc_i\varepsilon_i \ll 1$ was true for all the dyes used (red, yellow and blue). We verify this hypothesis in the present section. The following calculations are made using $h = 100\,\mu$m $\forall i, i \in \{r, y, b\}$. In the impact experiments, proportions of red and green $p_{r,d} = p_g = 0.05$ were used. These correspond to actual concentrations $c_r = 1038 \times 10^{-6}$ M, $c_y = 524\,\mu$M and $c_b = 106 \times 10^{-6}$ M in the drop and the film as measured by a spectrometer. The molar extinction coefficients of the dyes at their respective absorption peak wavelengths are $\varepsilon_r(516\,\text{nm}) = 20\,097\,\text{M}^{-1}\,\text{cm}^{-1}$, $\varepsilon_y(428\,\text{nm}) = 22\,974\,\text{M}^{-1}\,\text{cm}^{-1}$ and $\varepsilon_b(630\,\text{nm}) = 100\,661\,\text{M}^{-1}\,\text{cm}^{-1}$ [49, 104, 212]. We thus obtain that $hc_r\varepsilon_r = 0.21$, $hc_y\varepsilon_y = 0.12$ and $hc_b\varepsilon_b = 0.11$, i.e., these values are all $\ll 1$. For films with thicknesses larger than 500 μm we would no longer be able to apply the algorithm as we would get $hc_r\varepsilon_r \to 1$, hence the upper limit of the range considered here.

B.4 Substrate area and dismissed experiments

The tape on which the liquid film was spread out has an average side of about 40 mm. A cavity formed in the film reaching a maximum radius r_c of about 10-15 mm should therefore not interact with the edges of this substrate. For larger film thicknesses ($h^\star \gtrsim 2$), the maximum radius r_c may be closer to 20 mm. Hence, larger tapes of sides close to 55-60 mm were used in this case but the field of view remained the same as it did not prevent to see the crown expansion dynamics. However, the limited area of the film could still possibly affect the impact in two cases: (i) if the drop were to land too close to an edge, (ii) if capillary waves reflecting on the film outer borders were interacting with the developing cavity or during the retraction phase. In the first case, it would not be surprising that the crown behaviour changes in response to an impact that would occur at less than one times the maximum r_c value from the edge. This may be seen in Fig. 4.16 (a) for $h^\star = 1.3$ and We $= 2750$ where the impact point is located at 8 mm from the closest border (Fig. 4.16 (a) i), while the maximum value of r_c in this range is typically 13 mm. The crown partially breaks up when it meets the edge (Fig. 4.16 (a) ii). The remaining part of the crown is expelled in the opposite direction in an asymmetric manner, creating an elongated post-impact mixing pattern in the film (Fig. 4.16 (a) iii). As the trajectory of the drop free fall is protected from parasitic air currents, such kinds of impacts only arise when the falling height becomes sufficient for the drop to be self-deviated [172], in this case above 3 m of fall, or for We $\gtrsim 2000$. Whenever this issue was encountered, corresponding data were therefore not taken into account.

The reflection of capillary waves should not affect the impact dynamics either. As aforementioned the tape size is chosen to ensure that there is at least a 10 mm space around the crown at its maximum extension. The velocities $\dot{r}_c$ take values comprised between roughly 1 m s^{-1} and 0.1 m s^{-1} (see Section 5). A capillary wave front propagating at the same celerity [120] would need respectively 20 ms and 200 ms to cover a distance of 10 mm back and forth. These two bounds correspond to scenarios A and D, for which capillary ripples have respective damping times of the order of 0.3 ms and 30 ms (for, e.g., $h^\star = 0.5$ and $h^\star = 2.5$). These ripples would therefore fade away before having the chance to interact with the crown. Another cause, although rarely observed, for dismissing experiments from scenario D is the possible entrapment of an air bubble due to the crown folding upon itself. An example is shown in Fig. 4.16 (b) in the case of a vary large bubble, having a 13 mm radius. The bubble having a lifetime of several seconds prevents the underneath final mixing pattern to be analysed as it cannot be seen in the final frame of the movie, whose duration is only about 1 s.
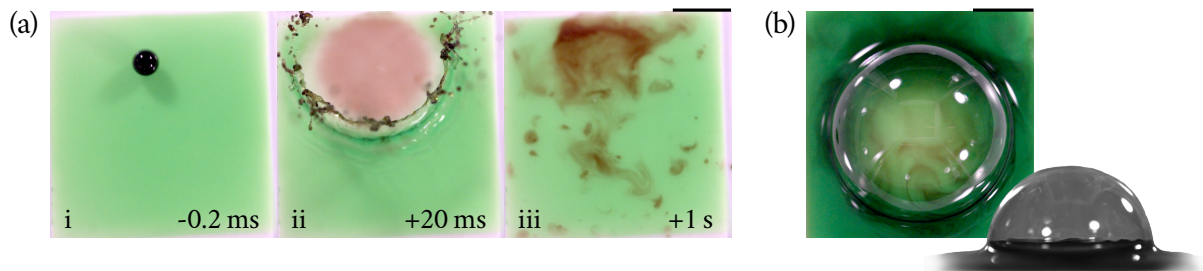
Figure 4.16: Possible rejected experiments: (a) Impact occurring too close to an edge, in this case at a distance of 8 mm of the upper border of the film in the field of view. The parameters are $h^\star = 1.3$ and We $= 2750$. The maximum radius r_c of the cavity in the film is 13 mm. (b) Air entrapment in the case of an impact for which $h^\star = 4.3$ and We $= 1675$. The scale bars are 1 cm.

Summary (Ch. IV)

⬥ In Sec. 2, we detail the experimental methodology used to produce and record side and top views of drop impacts on thin films, using high-speed imaging. We present the colorimetry-based algorithm used to analyse the top view movies of the impacts in Sec. 2.2 (and Appendix B.1). We compare the colorimetry-based and manual measurements in Sec. 2.2.2.

⬥ In Sec. 3, we review the geometrical features of the impacts and classify the impacts in four distinct scenarios. The differences arise from competing physical processes: (i) the inertia from the impact, (ii) the capillary effects in the crown and (iii) the viscous friction within the film. Based on a dimensional analysis, we define three nondimensional numbers: the Ohnesorge number, which is constant, the Weber number, We, and the nondimensional film thickness, $h^\star$. The distribution of the scenarios depends on both We and $h^\star$.

⬥ In Sec. 4, we present both geometrical indicators of the crown formed upon impact and mixing-related quantities. The crown geometry, presented in Sec. 4.1, is mostly function of the film thickness $h^\star$, except for the crown height and retraction velocity ratio which vary with We. The measurements obtained are further compared with measurements from the literature.

⬥ In Sec. 4.2, we define and measure equivalent moments characterising the dye distribution coming from the drop into the film. The equivalent spot radius, R_{eq}, and second-order moment σ_{eq}, are observed to increase with the film thickness $h^\star$ because of the improved mixing at impact.

⬥ We also infer the proportion of volume ejected at impact with respect to the initial drop volume, φ_{e}, from the colorimetry algorithm measurements. The proportion φ_{e} increases with the film thickness $h^\star$ for $h^\star \to 1^-$, then reaches ~ 1 around $h^\star \approx 1$. Then φ_{e} decreases for increasing $h^\star > 1$, until it reaches ~ 0.6 beyond $h^\star = 2$. A proportion $\varphi_{\mathrm{e}} = 1$ indicates that as much liquid is ejected away at impact as brought into the film, but does not indicate the origin of the liquid (from the drop or the initial film).

⬥ We also report measurements for $\varphi_{\mathrm{d} \to \mathrm{f}'}$, the proportion of liquid originally from the drop entering the film at impact with respect to the drop volume, and for $\varphi_{\mathrm{f} \to \mathrm{e}}$, the proportion of liquid initially in the film ending in the ejections at impact. Both increase with $h^\star$. All the results are finally discussed in Sec. 5.

Highlights (Ch. V)

- In Ch. V (see next page), we study the drainage process of a thin residual film lying over stalagmites through experimental and numerical measurements of film thicknesses varying in time and space.

- In Sec. 2, we present the experimental methods used to record thickness measurements during the filling, stationary phase and sole drainage phase of thin films over stalagmites in caves and in lab. The curves obtained are illustrated in Sec. 3. The drop inflow and stalagmite shape affect the most the thickness of the film.

- The drainage is modelled using Reynolds equation expressed in a curvilinear coordinate system in Sec. 4.2. From the equations, it can be deduced that the drainage is either dominated by the thickness gradients in the film over flat stalagmites, or by the stalagmite wall inclination for convex stalagmites.

- Numerically solving the drainage equations allows us to systematically vary the parameters influencing the film drainage in Sec. 5. The model presents a good agreement with the experimental measurements. The numerical simulations, and cave and lab experiments converge to the same results already obtained by simple theoretical scalings in Sec. 4.3.

DRAINAGE OF A THIN FILM

Following our discussions on drop impact point dispersal and mixing at impact, we now try to establish the effect of the gravity-induced drainage on subsequent stalagmite growth. The amount of ions precipitating in a particular location on the stalagmite is directly proportional to the local thickness of the film and could be affected by any velocity gradient disrupting the apparent immobility of this film. We thus aim in this chapter at assessing how the film thickness over the entire stalagmite varies in response to the inflow of drops brought into the film, the curvature of the stalagmite underneath, and environmental parameters such as the local temperature and relative humidity in the cave. To achieve this, we collected film thickness measurements on stalagmites in caves, completed by lab experiments that were also conducted on a real stalagmite. Starting from Reynolds lubrication theory expressed in a curvilinear coordinate system, we then model the drainage process as a function of the stalagmite shape and size. Finally, we relate the results of our model to the observations made in situ. Part of the discussion in this chapter is also concerned with exploring the filling dynamics of the film when an inflow of drops is actuated on an initially dry stalagmite surface.

1. Gravity currents in various contexts

Because of the hydrophilic character of calcite, stalagmites are naturally covered by very thin films. Some exceptions include stalagmites that exhibit unique shapes such as concave stalagmites, for which the dimple at their top, having an outer wall up to $\sim$ 1 cm tall, can be filled by a thick pool of water. Wet stalagmites in caves are nevertheless not the only occurrence where thin films can be found. Thin film flows arise in endless natural and industrial situations, including free soap film drainage [23], synovial fluid flow in joints [159], Bretherton bubbles forming in narrow tubes [38], ice sheet deformation [43], oil and gas transport in pipes [153], or bearing lubrication [156]. Thin film flows inherently exist because of the coexistence of multiple phases, which can stem from fluid/liquid or liquid/solid interaction [138]. The motion of a thin liquid film around a solid is very dependent on the solid geometry [85], as it is the case with optical fiber coating [74] and wall corrugation in industrial chemical processes [132], or on the deformability of the substrate, as in, e.g., hydraulic fracturing [203] or elastic Hele-shaw cells [150]. We can also mention the propagation of thin films in channels and other confined configurations, which appear in pollutant leakage from porous reservoirs in geological CO_2 storage [241], or radioactive waste disposal [154]. Among all thin film flows, we are interested in thin liquid layers propagating on solid substrates, such as stalagmites, in response to competing viscous and gravity effects, usually advancing primarily horizontally and following a liquid front, the so-called gravity currents [29].

A gravity current can either be induced by a given liquid volume spreading onto a substrate, or it can result from a constant flow feeding it [116, 198]. In both cases, the resulting behaviour of the thin film formed by the gravity current varies with the boundary conditions considered or with the other competing physical processes at play. Permeable media, for instance, induce partial fluid loss during the film drainage [153, 154], while phase change occurs in lava flows [107]. Inertia effects can become of importance too and induce high-Reynolds number phenomena, as with, e.g., dam break [166]. In many configurations concerned with thin film drainage, self-similar solutions can be derived [106, 116]. Usually, both the film thickness and the position of the front of the film can be expressed as power laws of time [154]. In the particular case of the drainage of a film over the edge of a solid substrate, it is found that the film thickness decays as $t^{-1/3}$ [106]. If capillary effects are taken into account in the case of porous media, the thickness decreases as t^{-1} when the film flows over the edge of the porous substrate, and as $t^{-1/5}$ when the fluid only flows above the substrate and into the pores of the medium but does not go beyond the edge of the substrate [153]. If inertial effects arise when drainage from the edge of a liquid reservoir is considered, this law becomes t^{-2} [166].

Based on what is known of thin film drainage, we can thus only but expect the film thickness evolution on a stalagmite to be conditioned by the geometric configuration, i.e., by the shape of the stalagmite. Although the literature concerned with thin film drainage and gravity current is abundant, there is no dedicated general model describing the film as a function of the shape of the substrate underneath, but rather a collection of cases particularised to the geometry of their respective problems [154]. In this chapter, we focus on how the underneath stalagmite shape affects the film evolution in time and space in order to better understand how this film may, in turn, affect subsequent stalagmite growth. Our primary goal is to describe the drainage of a thin film only subjected to gravity and viscosity, flowing over the edge of a substrate of general shape. We achieve this by using Reynolds lubrication theory expressed in an axisymmetric curvilinear coordinate system. Another peculiar and important aspect of thin film drainage on stalagmites is the succession of drops feeding the film. Periodically interrupted inflows feeding the film are usually not taken into account in modelling thin film drainage [154, 198], although they could be of interest for geophysical or industrial chemical applications, such as trickle-bed reactors [108]. From this general description of the filling and drainage dynamics of the film, we aim at particularising the thickness evolution for a set of actual stalagmites. We therefore took film thickness measurements on various stalagmites from caves and in a controlled lab setting, using complementary experimental techniques. Comparing these measurements to both our numerical results and theoretical arguments will finally allow us to draw conclusions regarding the potential influence of the film thickness evolution on subsequent stalagmite growth.

We start by describing the methodology followed to collect film thickness measurements in both cave and lab settings in Sec. 2. Next, in Sec. 3, we present a selection of experimental curves obtained in caves for various stalagmite shapes. In the same section, we also examine the peculiarities exhibited by the film thickness measured in the lab in response to parameters that we could not arbitrarily vary in caves, such as the dripping period of the drops. In Sec. 4, we model the film thickness evolution in time and space for a given stalagmite shape. Stalagmite shape formalism has been detailed in Ch. II. A numerical resolution of the equations obtained allows us to vary the same parameters as in the caves and in the lab in Sec. 5. Conclusions are finally presented in Sec. 6.

2. Experimental measurement techniques

We describe in this section the experimental techniques used in both cave and lab settings to measure the time evolution of the film thickness on various stalagmites. Even in the lab, we had ac-

cess to an actual stalagmite on which we conducted experiments, rather than using an artificial substrate. Added to the lab stalagmite, a total of 14 stalagmites from actual caves were used (see Tab. 2.2 from Ch. II). All the stalagmites are described in Ch. II, with a detailed explanation of the modelling of their shapes. We first explain how the measurements were taken in caves using a distance-based technique (Sec. 2.1.1) and a mass-based one (Subsec. 2.1.2), before showing how we completed our dataset by lab measurements, obtained with the help of a precise optical sensor (Sec. 2.2).
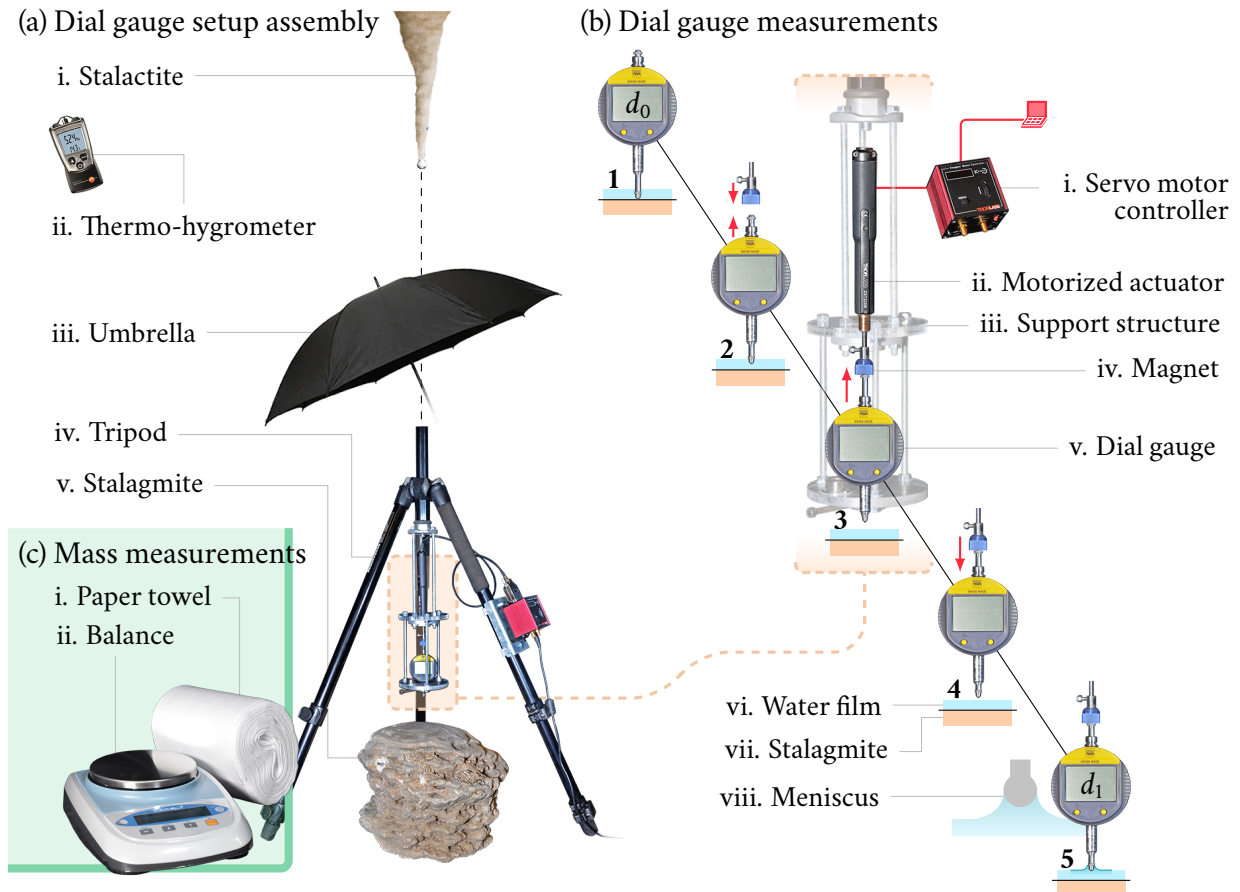
Figure 5.1: Experimental setups used to record film thickness measurements in caves with a distance-based (a-b) and a mass-based (c) technique. (a) Assembly used to perform measurements based on the positioning of a dial gauge. (i) Stalactite whose outflow of drops is stopped by the umbrella below. (ii) Portable thermo-hygrometer used to record the relative humidity and temperature in the vicinity of the stalagmite. (iii) Umbrella blocking the flow of drops. (iv) Tripod holding the support structure of the dial gauge. The beige frame emphasizes the part of the setup detailed in (b). (v) Stalagmite. (b) Operation of the dial gauge measurements. (i) Servo motor controller through which the actuator is operated, either manually or via a computer. (ii) Motorized actuator used to displace the magnet, connected or not to the needle of the gauge. (iii) Support structure holding the actuator and dial gauge in two separate parts, mounted on metallic discs and threaded shafts. The bottom disc of the structure includes a spirit level ensuring perpendicularity between the probe needle and the stalagmite surface. (iv) Magnet. (v) Dial gauge with mobile needle. (vi) Water film lying on top of the stalagmite surface. (vii) Stalagmite. (viii) Close-up of the meniscus formed when the needle end reaches the water film. The operation of the measurements is the following, with the red arrows indicating the direction of the magnet and/or the needle of the dial gauge: (b1) The tripod and support structure are positioned in such a way that the needle of the gauge enters in contact with the stalagmite surface. The distance read is d_0. (b2) The magnet is brought close to the needle, which moves upward until it attaches to the magnet. (b3) The actuator displaces the needle further upward since it is now attached to the magnet, until the needle gets out of the water. (b4) The actuator displaces the needle downward in a continuous manner, until it gets close to the water film interface. (b5) The actuator is then operated step by step to move the needle further downward, until a meniscus is formed when the needle end touches the water. The distance read is d_1. (c) Measurements based on the weighing of a small piece of paper towel only require: (i) paper towel, and (ii) a balance able to take accurate measurements around $\sim 100\,\text{mg}$.

2.1 In situ

Two measuring techniques described hereafter were used in caves: (i) pointwise high-precision comparative measurements of the water/air and water/solid interface positions (Figs. 5.1 (a-b)), and (ii) comparative mass measurements between dry and wet pieces of paper towel of known surface (Fig. 5.1 (c)).

2.1.1 Distance-based measurements

The distance-based measurements of the film thickness were obtained thanks to a homemade apparatus built around a Tesa Digico 305M mechanical dial gauge (resolution of 1 μm, precision of 2 μm, Fig. 5.1 (b) v). As shown in Figs. 5.1 (a) iv and (b) iii, the whole system was mounted thanks to an ensemble of metallic discs and threaded shafts on a Manfrotto 290 tripod. The gauge was either connected or not to a magnet fixed at the tip of a high-precision motorised translation actuator (precision of 0.1 μm, Figs. 5.1 (b) ii and iv). The actuator was displaced vertically via a Thorlabs Kinesis servo motor controller (Fig. 5.1 (b) i). To take the measurements, the needle of the dial gauge was first positioned on top of the stalagmite in order to touch the solid surface of the stalagmite, beneath the residual water film, without being connected to the magnet (Fig. 5.1 (b1)). The first value read by the gauge corresponds to distance d_0. By approaching the magnet to the gauge needle through the translation actuator, the gauge needle was taken out of the water (Figs. 5.1 (b2) and (b3)). The needle was the only moving part. The gauge itself remained in a fixed position during the entire procedure. Afterward, the actuator allowed to displace the needle downward first by hand, then by discrete automated steps of 1 μm every second once it became close to the water-air interface of the film (Fig. 5.1 (b4)), until it touched this latter by forming a meniscus visible to the naked eye. When this happened, the actuator was stopped manually (Fig. 5.1 (b5)). The distance then read by the probe corresponds to d_1, yielding $h(t) = |d_0 - d_1(t)|$, the local film thickness at time t. The metallic needle of the gauge had a 2 mm-diameter spherical tip, such that the meniscus formed was axisymmetric. Additionally, the air temperature T and relative humidity RH were measured with a Testo 610 infrared thermo-hygrometer in a close vicinity of the stalagmite, before and after recording the film thickness (Fig. 5.1 (a) ii). The relative humidity RH gives the ratio of the partial pressure of water vapor in the air at temperature T, relative to the saturation pressure of water vapor at the same temperature, i.e., RH $= p_{\mathrm{H_2O}}(T)/p_{\mathrm{H_2O,\,sat}}(T)$.

This first technique allowed to take several successive pointwise measurements in one location. To avoid the inflow of drops falling from the stalactite in the film during the measurements, an umbrella was placed above the stalagmite before positioning the dial gauge (Fig. 5.1 (a) iii). The time at which the last drop fell into the film was carefully recorded, as well as the time at which each measurement was taken afterward. Since the setup was not displaced in between measurements for a given stalagmite and location, the distance d_0, corresponding to the stalagmite solid surface, was read with the gauge only before and after all the water/air interface measurements $d_1(t)$ were taken. Doing so allowed both to avoid wasting precious time in between measurements and to ensure that the setup had not move during the entire procedure. One measurement of the water/air interface position could indeed take up to several minutes, especially when the film had already thinned as it became more and more complicated to make sure that a meniscus had formed between the film and the needle tip. The entire procedure could take about 5 to 15 min depending on the stalagmite shape and film initial thickness. We have already used a similar technique to take film thickness measurements of the order of 100 μm in a more controlled lab setting [171] (see Sec. 2.1.2 from Ch. IV). An average error of 3 μm was observed, which we can round up to ∼ 5 μm given the precision of the dial gauge. Measurements falling below 50 μm should thus be interpreted with caution.

The major technical challenges of this measuring technique were (i) the difficult positioning of the tripod around the stalagmite that ensured no bank angle of the setup, (ii) the short time frame permitted to position the setup since the drainage process started as soon as the inflow of water was stopped, (iii) the maximum relative humidity that the dial gauge was allowed to undergo for proper operation (about 80 %), and (iv) the difficult identification of the meniscus in a poorly lit environment. To ensure the horizontality of the whole device, a spirit level was added on the actuator mounting support (Fig. 5.1 (b) iii). As it was not possible to incline the device with precision, measurements were taken on the very top of the stalagmite summit for convex stalagmites in order to ensure as much perpendicularity as possible with the underlying liquid film. For concave stalagmites, measurements were taken in the middle of their cavity or on a sideways horizontal part whenever possible (see Sec. 3 from Ch. II for stalagmite description). To avoid any problem due to the high humidity environment, an insulating casing was added around the actuator. The dial gauge, however, was simply held in place by a screw and could easily be put on and taken off the setup in order to be dried out properly between measurements made on different stalagmites. The gauge was able to operate when the relative humidity was higher than 80 % but could not work for a whole day in this environment.

2.1.2 Mass-based measurements

The second film thickness measurement technique used in caves was based on weighing. A 100 µm-thick film spread on a 5 cm-radius flat stalagmite surface weighs about ~ 800 mg. Using a VWR SE1202 balance (resolution of 1 mg, precision of 10 mg, Fig. 5.1 (c) ii), we first recorded as the mass m_0 of a dry, roughly 3 cm $\times$ 3 cm piece of ZVG 1-ply white paper towel made from cellulose (Fig. 5.1 (c) i, fiber diameter of 15 ± 6 µm). Knowing the surface density of the paper towel $\rho_S = 84.7 \pm 4.1$ g m^{-2}, the exact area of the piece of paper, S, could be inferred from m_0. The square of paper towel was then carefully deposited onto the stalagmite and patted out gently in order to absorb the water of the film underneath, only over the paper towel surface. Doing so usually took about 5 s to 10 s but can be considered as instantaneous in regard of the drainage timescale. Because of the orientation of the cellulose fibers which are parallel to the stalagmite surface and of the relatively small size of the piece of paper towel compared to the entire wet stalagmite area, water was also absorbed from the sides of the piece of paper towel. Details on how to correct the measurements accordingly and regarding the error estimation are provided in Appendix A. The mass of the wet paper towel piece was then recorded as m_1, such that $\Delta m(t) = (m_1(t) - m_0)$ was the total mass of water collected from the residual film on the stalagmite at time t. These measurements allowed to obtain the spatially averaged thickness $\overline{h}_S(t)$ of the water film over the surface S covered by the piece of paper towel as follows: $\overline{h}_S(t) = \Delta m(t) / (\rho_w S)$, with $\rho_w \simeq 1000$ kg m^{-3} the water density. In comparison with a stalagmite typical size, it could be assumed that S was small and that the thickness of the film did not vary much over the area covered by the paper towel, although this assumption would become less valid if measurements were taken on a very curved surface. It could also be assumed that, although the paper towel thickness was not perfectly uniform, it was sufficiently thick to host all the water from the film underneath, hence this should not have affected the thickness measurements. Empirical testing yields a limit thickness comprised between 500 µm and 600 µm. Beyond this, the film can no longer absorb all the water at the measurement location. Finally, the pieces of paper towel were stored in a hermetically sealed environment to ensure that they did not absorb or lose any water before taking the measurements.

Although this technique was invasive and only allowed to get spatially averaged thickness measurements, it was rapid (~ 10 s vs. ~ 10 min for gauge measurements) and required no other instrument than the balance. It was used in two situations: either when the dial gauge-based apparatus could not be set in place around the stalagmite for drainage measurement, or to obtain filling

measurements. In the first case, the time at which the last drop fell into the film before taking the measurements was carefully recorded, and the umbrella was placed above the stalagmite to prevent any further filling of the film when taking the mass measurement. After taking the measurement, we removed the umbrella and waited for a sufficient amount of drops to fall onto the stalagmite in order to ensure that the filling-depletion dynamics of the film had reached a stationary state, i.e., a few hundreds of drops when the dripping period t_0 was of the order of the second and a few tens of drops when it was closer to a minute (which should be enough based on empirical observations, see Sec. 5.1.1). The weighing procedure was then repeated by increasing the amount of time spent between the positioning of the umbrella and the measurement, and the piece of paper towel was placed in the same location for each measurement.

Regarding the filling measurements, we started by completely drying out the whole surface of the stalagmite. We waited for a number of drops n to fall onto the stalagmite and cover it by a thin film of water. We then blocked the inflow of drops with the umbrella and carefully collected the water that had spread out on the stalagmite following the impacts, using the paper towel, as close as possible to the centre of the stalagmite. We then repeated the whole procedure for various n, with typical values for a given stalagmite comprised between $n = 1$ and $n = 100$[1].

2.2 In the lab

Additional film thickness measurements were made in the lab on the top part of an artificially wetted stalagmite, using an optical sensor. The controller of the sensor cannot endure condensation nor a relative humidity $> 85\%$, thus it would have been risky to bring it into caves. This technique allowed to continuously record the thickness of the film in one precise location. Both the stationary thickness reached when successive drop impacts feed the film and the drainage-induced depletion of the film could be assessed for the following variable parameters: temperature T, relative humidity RH, dripping period between two successive drops t_0, drop impact point position $\mathbf{r}_0$, and distance between the drop impact point and sensor positions, $\Delta d = |\mathbf{r} - \mathbf{r}_0|$. The ranges of parameters covered in the experiments are detailed in Sec. 3.1.

Film thickness measurements were obtained with a coaxial laser displacement sensor from Keyence, comprising a CL-P030N sensor head and a CL-3000 controller unit (Figs. 5.2 iii and ix). The unit was connected to an Aim & Thurlby Thandar Instruments EL301R power supply (24 V, 0.3 A, Fig. 5.2 ii). The sensor head had a 38 µm spot diameter, i.e., it allowed to take pointwise measurements on the stalagmite over which the sensor was installed. The sensor horizontal position could be varied but the sensor head was always placed at about its focal distance of 3 cm above the stalagmite surface to be operated properly, and as perpendicularly as possible to the surface although a small inclination ($\lesssim 2°$) should not yield significant errors. The stalagmite was stuck into the central aperture of a Thorlabs MB4560A/M aluminum breadboard (Fig. 5.2 vii). This allowed to ensure a tight positioning of the stalagmite through additional shafts screwed to the table, and to collect the water flowing on the sides of the stalagmite right under the table when the stalagmite was wet. The stalagmite had been stored for a long time in the lab and had entered in contact with contaminants such as, e.g., dust or sebum, hence some parts of the surface might no longer have

---

[1] In the case of wide stalagmites for which the falling height of the drops is very large, a large dispersal is observed in the drop impact point position (see Ch. III). Hence, when $n \lesssim 10$, we did not impose the value of n but rather waited for a succession of drop impacts located not too far from the stalagmite centre to occur, i.e., below half the stalagmite radius and not at opposite positions on the edge of the stalagmite. When $n \gtrsim 10$, we relaxed this condition but we took the measurement right after a drop impact close to the center. The measurements for small values of n were repeated so as not to introduce any bias due to the impact point position of the last drop in the measurements. The number of possible repetitions was nevertheless dependent on the dripping time t_0 which could sometimes be of several minutes.

been as hydrophilic as they would have in an actual cave. To cover the entire surface by a thin film of water, we thus first gently poured a volume of about 10 cL of water by hand over the stalagmite. Once the stalagmite was wet, there was no issue in maintaining the film during a long time by impacting it with a succession of drops. The drops were dispensed thanks to a Watson Marlow Sci-Q 205U peristaltic pump (Fig. 5.2 i, the peristaltic pump inner tube had a diameter of about 1 mm) connected to a PVC Schlauch transparent 3-mm inner diameter plastic tube whose tip was left raw but carefully cut (Fig. 5.2 viii, 5-mm outer diameter). The drops had an average radius of 2.3 ± 0.1 mm (average $\pm$ s.d. in 60 measurements made by image analysis of side view movies of drops detaching from the tube). In order to avoid splashing at impact and, hence, liquid ejections, the end of the tube was placed about 2 cm to 3 cm above the stalagmite surface [235]. The volume added in the film by each drop was therefore 53.6 ± 5.7 µL (average $\pm$ s.d. in all the measurements). The error committed in the drop radius measurements yields an accuracy of 4.5 % on the computation of their volume. The peristaltic pump allowed to vary the flow rate between 22 mL min^{-1} and 0.006 mL min^{-1}, which corresponds to an average dripping period between successive drops t_0 going from $\lesssim 1$ s to 120 s, respectively. The dripping period t_0 was always measured directly from the experimental curves given the eventuality that a simple bending or bulge in the drop dispensing tube could cause t_0 to vary in between experiments. The tube was nevertheless not moved during the recordings, so it can be safely assumed that t_0 remained constant for a given experimental curve.
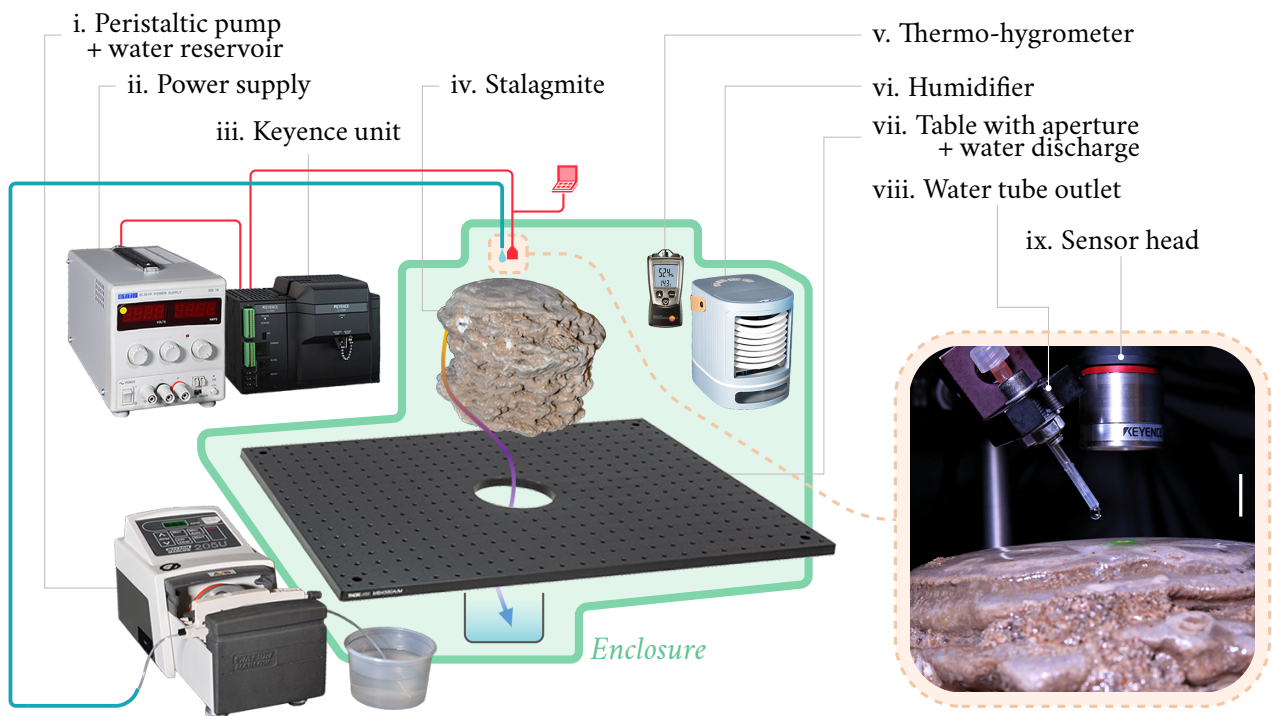
Figure 5.2: Experimental setup used to record film thickness measurements in a lab setting. The green area refers to the part of the setup that is placed in a plastic enclosure and covered by black curtains, i.e., elements iv-ix. (i) Peristaltic pump providing a constant inflow of water drops to wet the stalagmite. Water is pumped from a reservoir through a plastic tube. (ii) Power supply of the sensor controller unit. (iii) Controller unit of the sensor, which collects measurements from the sensor head and communicates them to a computer (photograph: courtesy of Keyence Corporation). (iv) Top piece of a stalagmite from Aven d'Orgnac used to take the measurements. The stalagmite is stucked in the central aperture of a breadboard table, with additional shafts to maintain it in place. The side arrow shows the path taken by water flowing along the stalagmite into the discharge, below the breadboard. (v) Portable thermo-hygrometer used to record the relative humidity and temperature in the enclosure. (vi) Commercial humidifier that allows increasing the relative humidity up to 97 % in the cage. (vii) Table with central aperture used to hold the stalagmite in place (photograph: courtesy of Thorlabs, Inc.). (viii) Close-up view of the outlet of the tube, where drops are formed. (ix) Head of the sensor, connected to the controller unit. The scale bar in the photograph relative to viii and ix is 1 cm.

To mimic as best as possible the cave environment, the whole setup was placed in a transparent plastic enclosure surrounded by black curtains, such that it was insulated from external lighting and humidity (Fig. 5.2). A humidifier with a small fan (Nor-tec air cooler, Schou Company A/S) was added in the enclosure in order to modify the relative humidity and temperature inside the enclosure (Fig. 5.2 vi), possibly with an ice bath. The air conditioning system of the room where measurements were taken indeed underwent failure during a few nights[2]. A Testo 610 thermo-hygrometer allowed to record these two parameters for each experiment (Fig. 5.2 v). The sensor head was in conformity with the IP67 standard, which ensures its liability even in very humid environments, or environments prone to liquid ejections. Relative humidity and temperature measurements were taken at least at the beginning and the end of the experiments, then averaged.

Using the optical sensor, we first recorded the distance d_0 between the sensor head and the stalagmite surface when it was dry. We then spread the aforementioned 10 cL of water by hand on the stalagmite and started the dispensing of drops in order to create and maintain a thin water film on the stalagmite. We then live recorded the distance $d_1(t)$ between the sensor head and the liquid/air interface. The film thickness therefore corresponded to $h_{\mathbf{r}}(t) = |d_0 - d_1(t)|$ at time t, in position $\mathbf{r}$. The acquisition frequency of the sensor was set to 1 kHz, which is supposedly sufficiently high to observe any thickness variation due to drainage or evaporation. It however does not allow to clearly observe the thickness variations that would be due to the crushing of the drop in the film as this phenomenon occurs during a time close to 1 ms, i.e., the time of acquisition. Moreover, the early stages of the drop impact in the film would have provoked strong variations in the curvature of the liquid interface, and therefore of the angle between the interface and the sensor head. When the drop dispenser tip was close to the sensor head position, high peaks could thus be observed in the signal corresponding to the liquid interface height.

3. Observations and phenomenology

This section first describes with the actual environmental conditions that we encountered in caves, as well as the parameters that we varied in a more controlled lab framework. We then present typical curves of film thickness vs. time obtained in both cases and focus on the parameters that influence the most the filling and drainage processes at play.

3.1 Parameter range

The environmental data relative to the stalagmites shown in Tab. 2.2, i.e., the associated falling height of the drops z, the dripping period t_0 of the drops, the temperature T and relative humidity RH of the air in the vicinity of the stalagmite, are summarised in Fig. 5.3 (a). Additionally, the graph shows how these parameters were varied during the lab experiments. The dripping period t_0 observed in caves ranges from 1 s to about 12 min. For 7 stalagmites, the drop dripping period is $\lesssim$ 10 s and for 6 others, it is comprised between 30 s and 3 min. In the lab, we varied the dripping period, t_0, from less than 1 s to about 2 min by varying the rotation speed of the peristaltic pump. Hence, we could cover the same range as in caves, except for the longest cave dripping period of 12 min. Regarding the temperature range, we have $T \in [16; 24]$ °C, which is a little higher than the range observed in caves, $T \in [11; 17]$ °C, but still close to it and partially overlapping it. The relative humidity reached in the lab enclosure spans over a wider range than in caves, with RH $\in [62; 96]$ % in the lab and RH $\in [79; 96]$ % in caves.

---

[2]This affects some of the measurements presented in the following section.
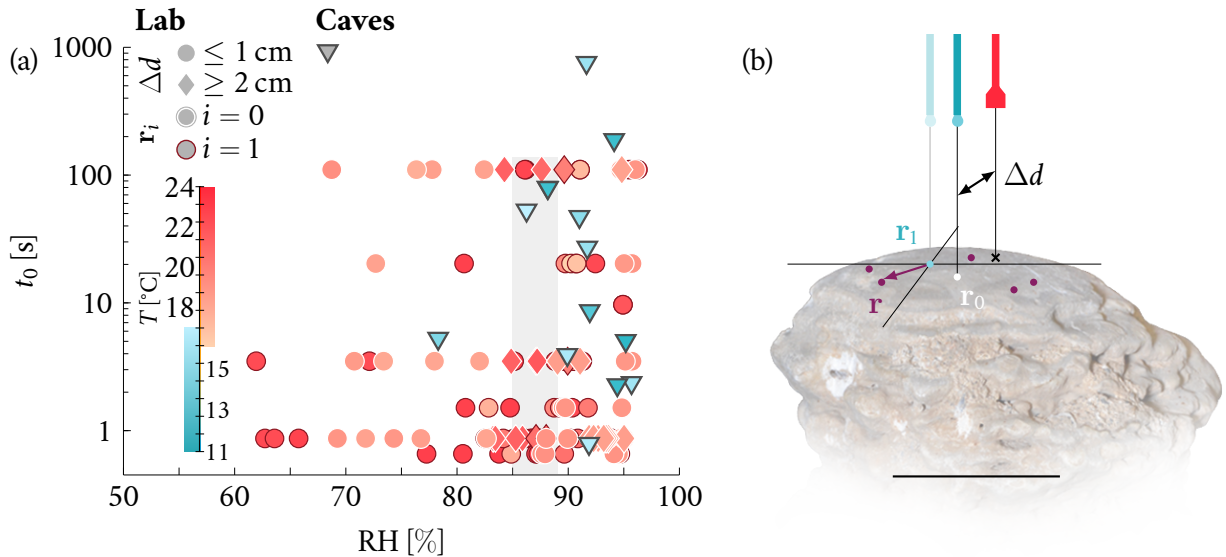
Figure 5.3: Ranges of parameters covered in the lab experiments and in the two caves. (a) Dripping period t_0 as a function of the relative humidity RH, for variable temperature T. The range of temperature reached in the lab (red colour bar) is higher than in the caves (blue colour bar), although there is an overlap between the two, hence there are two temperature colour bars. Dots and diamonds refer to lab experiments, and triangles to caves. The data relative to the lab measurements are also sorted according to the distance Δd between the sensor and the impact point position of the drops: the sensor was either placed very close to the impact point ($\Delta d \leq 1\,\mathrm{cm}$) or away from it ($\Delta d \geq 2\,\mathrm{cm}$). Finally, the markers relative to the lab measurements surrounded by a white (resp. dark) contour represent measurements made in position $\mathbf{r}_0$ (resp. $\mathbf{r}_1$). Both positions are shown in (b). The grey rectangle shows the dripping period and environmental data corresponding to the filling and variable impact point experiments. (b) Example of the positioning of the drop dispensing tube and sensor head above the stalagmite, separated by a distance Δd. The dispensing tube is positioned in $\mathbf{r} = \mathbf{r}_0$ or $\mathbf{r} = \mathbf{r}_1$, which correspond to the centre of the entire stalagmite or the centre of the summit part only, respectively, given that the layers of the stalagmite are not perfectly aligned. The purple dots show that the impact point position can be varied in a random manner in some additional experiments. The scale bar in (b) relates to the stalagmite picture and is 10 cm.

To avoid any splashing at impact (see Fig. 5.34), we positioned the water tube outlet at only 2 cm to 3 cm above the stalagmite surface in the lab [227]. Hence, the impact position of the drops was fixed and we knew precisely the volume of water entering the film at each impact. As illustrated in Fig. 5.3, the stalagmite is quite large and we positioned the tube outlet in two positions, denoted $\mathbf{r}_0$ and $\mathbf{r}_1$: because the stalagmite top layer is slightly shifted compared to the underneath layers (see Figs. 5.2 and 5.3 (b)), $\mathbf{r}_0$ is positioned in such a way that it would correspond to the overall axis of symmetry of the entire stalagmite body, while $\mathbf{r}_1$ should be very close to the centre of the summit part. From the drop impact point position, we placed the sensor head at a distance Δd which can be either $\lesssim 1$ cm, i.e., as close as possible to the drop impact point, or $\gtrsim 2$ cm. In the second case, the goal is to capture film thickness variations at a finite distance from the incoming liquid source in the film.

In Fig. 5.3, the markers relative to caves correspond to the environmental conditions in which both drainage and filling measurements were taken, as described in Secs. 2.1 and 2.1.2. On the other hand, the lab experiments shown in Fig. 5.3 mostly correspond to drainage experiments, i.e., we started to record the film thickness once the film fed by successive drops had reached a stationary state, then we interrupted the inflow of drops and kept recording the film thickness no longer fed by any drop. We tried to replicate each lab experiment shown in Fig. 5.3 in very similar conditions, for identical dripping rates and close values of T ($\pm 1\,°\mathrm{C}$) and RH ($\pm 5\,\%$). We additionally performed 5 experiments for which we manually varied the impact point position of the drops $\mathbf{r}$ while keeping the sensor at a constant position, i.e., we carefully moved the tube outlet by hand while keeping it at a vertical distance of 2 cm to 3 cm from the stalagmite surface and for

a constant dripping period $t_0 = 1$ s (see Fig. 5.3 (b)). We also performed 7 experiments for which the impact point position remains fixed in $\mathbf{r}_0$ but for t_0 varying over time. These experiments allow to observe the filling of the film as in caves. The 12 experiments with either variable impact point position $\mathbf{r}$ or variable dripping period t_0 were recorded for $T = 18.7 \pm 1.6\,°\text{C}$ and RH $= 87 \pm 2\,\%$.

3.2 Raw data examples

We introduce in this section a few examples of filling and drainage curves coming from both the caves and the lab. The relative influence of each of the parameters that we varied can be easily inferred from the curves shown.

3.2.1 In situ

We performed two types of measurements on the stalagmites in caves (see Tab. 2.2): (i) starting from an initially dried out stalagmite, we measured the film thickness h after a succession of N_d drops have impacted the stalagmite, and (ii) we also measured the film thickness evolution with time t after interrupting the inflow of drops falling into the film in a stationary state (we will come back to the possible stationary states observed in caves at the end of the discussion, see Subsec. 6).
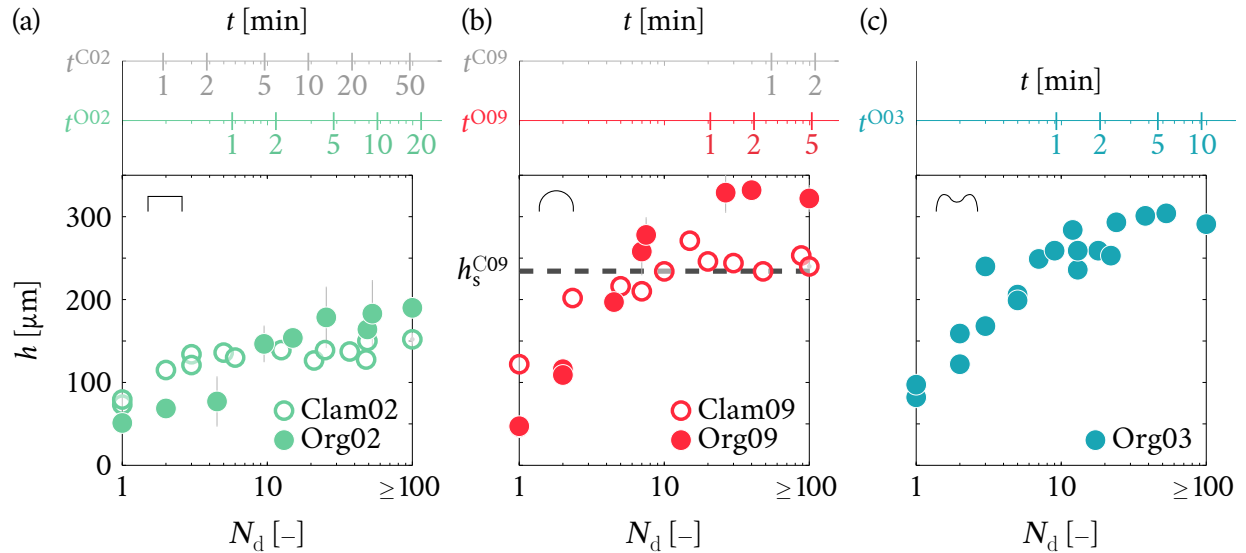
Figure 5.4: Examples of filling curves obtained in situ, showing the measured film thickness h as a function of the number of drops N_d that fell on Clam02, Clam09, Org02, Org03 and Org09, starting from an initially dry stalagmite. Graphs are sorted according to the shape of the stalagmites (see Tab. 2.2), for (a) two flat stalagmites, Clam02 ($\Psi = 1.2$, $S = 0.04$) and Org02 ($\Psi = 0.5$, $S = 2 \times 10^{-3}$), (b) two convex stalagmites, Clam09 ($\Psi = -192$, $S = 2 \times 10^{-4}$) and Org09 ($\Psi = -88$, $S = 0.02$), and (c) a concave stalagmite, Org03 ($\Psi = 21.5$, $S = 0.8$). Measurements for flat and convex stalagmites were made at the centre/highest point of the summit, and in the centre of the dimple for the concave stalagmite. In every graph, the maximum number of drops $N_d \geq 100$ simply corresponds to the first measurement made on the stalagmite, when it was certain that the film had been in stationary state for a long time. All the long-term film thickness measurements $h(N_d \geq 100)$ correspond to an average made in several measurements but error bars are often too small to be seen in the graphs ($\lesssim 10\,\mu\text{m}$). The same holds for part of Org02 and Org09 data points, which may correspond to the average of 2–3 measurements obtained for close n values given the large falling height and, consequently, the dispersal in the impact point position of the drops falling on these stalagmites. Otherwise, each marker corresponds to a single measurement. All measurements were taken using the weighing technique. The dashed line in (b) shows as an example the stationary film thickness h_s^{C09} reached by the film on Clam09 (see Sec. 4.4.2). The y–axis is the same for all three graphs. The duration t of the experiments is additionally represented in the upper x-axes (colored lines represent Org02 (a), Org09 (b) and Org03 (c), grey lines correspond to Clam02 (a) and Clam09 (b)). The dripping period t_0 corresponding to each stalagmite can be found in Tab. 2.2.
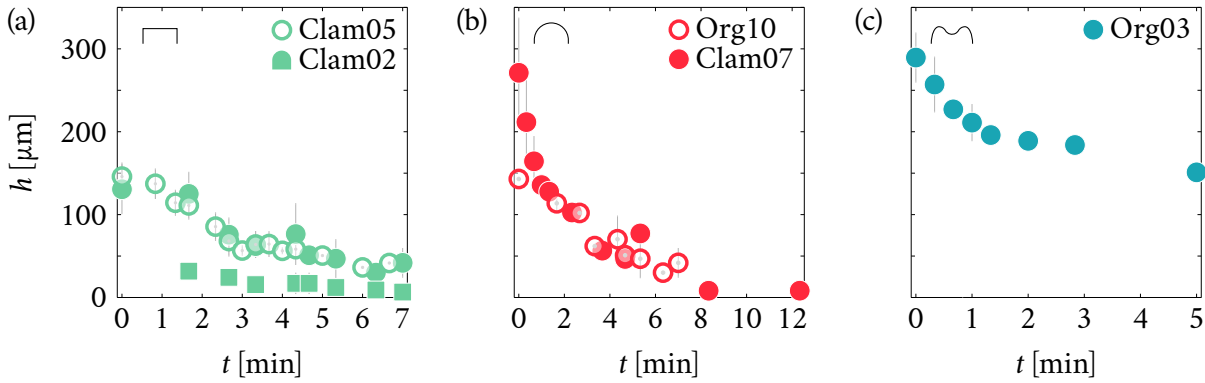
Figure 5.5: Examples of drainage curves obtained in situ, showing the measured film thickness h as a function of time t for Clam02, Clam05, Clam07, Org03 and Org10, starting from when the periodic inflow of drops falling in the film is interrupted at a time $t = 0$. Graphs are sorted according to the shape of the stalagmites (see Tab. 2.2), for (a) two flat stalagmites, Clam02 ($\Psi = 1.2$, $S = 0.04$) and Clam05 ($\Psi = 2$, $S = 0.5$), (b) two convex stalagmites, Clam07 ($\Psi = -375$, $S = 10^{-4}$) and Org10 ($\Psi = -9.7$, $S = 6 \times 10^{-5}$), and (c) a concave stalagmite, Org03 ($\Psi = 21.5$, $S = 0.8$). Measurements were taken at the center/highest point of the stalagmite summit for Clam02 (dot markers), Clam05, Clam07 and Org10. The square markers relative to Clam02 correspond to measurements made at about 1 cm from the centre of the summit. The measurements relative to Org03 were also taken on the edge of the stalagmite dimple, toward the inside of the dimple. Most points correspond to the average made in 2–3 measurements. Measurements were all made using the dial gauge, except for Org03 for which we used the weighing technique, and for Clam07 where both techniques were used (then the average of the measurements from both techniques was taken for Clam07). The y–axis is the same for all three graphs.

We present here examples of the measurements obtained using either the weighing or distance-based technique (indicated in Tab. 2.2). The filling of the film is illustrated by Fig. 5.4 for flat (a), convex (b) and concave stalagmites (c), as a function of the number of drops N_d since all stalag-mites are associated with different dripping periods t_0. The corresponding times are added above each graph. The film thickness was measured at the centre of the stalagmite summit for the flat and convex cases, and at the centre of the dimple for the concave stalagmite. We observe in each graph that the film thickness h increases monotonously with the number of drops brought into the film, at first sharply. Then h seems to reach a stationary state for large N_d, which is not the same for all stalagmites though. An example of the stationary film thickness reached by the film on Clam09 is drawn in Fig. 5.4 (b). In the particular cases of Org02 (a) and Org09 (b), the falling height of the drops is quite large ($z \gtrsim 20$ m). Hence, their impact point position is normally distributed with a standard deviation of ~ 2 cm, as explained in Ch. III. Most measurements shown in Fig. 5.4 relative to these two stalagmites therefore correspond to the average made for several close N_d values according to the procedure described in Sec. 2.1.2. Despite the fact that all the stalagmites have different shapes, sizes and associated dripping periods, the stationary film thickness h_s remains of the order of 100 µm to 300 µm. Counterintuitively, the largest value of h_s is observed for Org9, which is a convex stalagmite (Fig. 5.4 (b)) with very inclined walls that could enhance the drainage process. Understanding the possible influence of the shape factor Ψ, the scale factor S and the dripping period t_0 on h_s is thus not straightforward.

Figure 5.5 shows other examples of graphs representing the film thickness h as a function of time t, in the case of the drainage following the interruption of the drop inflow. Once again, the measurements are shown for flat (a), convex (b) and concave stalagmites (c). The film thickness was measured at the centre of the stalagmite summit for flat and convex cases, except for one curve (square markers) relative to Clam02 in Fig. 5.5 (a) which shows the film thickness at about 1 cm from the center, but still on the summit. It should be noted that the radius of Clam02 is 2.7 cm and

that there is almost no dispersal in the drop impact point position for this stalagmite ($z = 1.2$ m, dispersal $\lesssim 1$ mm). Hence, the measurements relative to this curve were made halfway between the source of liquid entering the film and the surrounding inclined wall of the stalagmite. We observe in Figs. 5.5 (a) and (b) that the film thickness h at the centre of the stalagmite decreases with time t, at a slower rate as t increases. The film thickness away from the centre also decreases but starting from a smaller initial value and at what seems to be more or less the same rate as in the centre (Fig. 5.5 (a)). Coincidentally, although the stalagmites for which measurements are shown in Fig. 5.5 (a) exhibit different sizes and have different associated dripping periods t_0, it is difficult to distinguish the two curves taken at the centre of the stalagmites from the graph. The same holds for the curves of Fig. 5.5 (b). Except during the first minute when the film thickness h is clearly larger on Clam07 than on Org10, both curves seem very similar. Measurements relative to the concave stalagmite in Fig. 5.5 (c) were taken in one location on the rim surrounding the central dimple of Org03, close to the dimple rather than close of the outer stalagmite wall. Hence, we note without surprise that the film thickness h remains far from zero after 5 min, by contrast with the curves from (a) and (b).

3.2.2 In the lab

We now focus on the raw data obtained in lab controlled conditions, but similar to the curves from the previous section. We present lab experiments for which we varied one of the parameters from Sec. 3.1 at a time. All the responses of the film thickness to these environmental parameters could be verified for different subsets of experiments than the ones shown in the following, and the observations should thus not depend on the selected curves. We also review in Appendix B.4 the details of a drop impacting a thin film at very low velocity, by contrast with the impacts leading to splashing that we covered in Ch. IV. The repeatability of the measurements is illustrated in Appendix B.1.

a) Film thickness variations caused by the drop dripping period

Several examples obtained in a lab setting of the film thickness evolution with time, $h(t)$, are shown in Fig. 5.6. These measurements were made on Lab01, with the inflow of drops feeding the film and the head of the sensor positioned at the apex of the stalagmite, such that the dripping point was in $\mathbf{r}_0$ and the distance between this position and the laser beam was $\Delta d \leq 0.5$ cm. Each time a drop was brought into the film, the thickness recorded by the sensor therefore increased instantaneously (~ 10 ms) in regard of the timescale of the experiment (~ 10 min). The curves correspond to measurements taken during two phases: (i) when the film has already reached a stationary state, so that the successive drops brought into the film cause its thickness to oscillate between two values, h^{min} and h^{max}, and (ii) when the inflow of drops is stopped, so that the main process at play is the gravity-induced drainage. Although we do not see the transient part before the film reaches its stationary state, a sufficient time (~ 5 min) has passed before the beginning of the curves displayed in Fig. 5.6 (as well as all the following graphs). Hence, these curves should not depend on conditions such as the presence of an initial film. The 6 recordings shown in Fig. 5.6 were obtained in similar environmental conditions ($T = 18.8 \pm 0.7$ °C, RH $= 90.2 \pm 0.8$ %, average $\pm$ s.d. in the average measurements made for each experiment) for various dripping periods of the drops, with t_0 ranging between 0.9 s and 14.4 s.
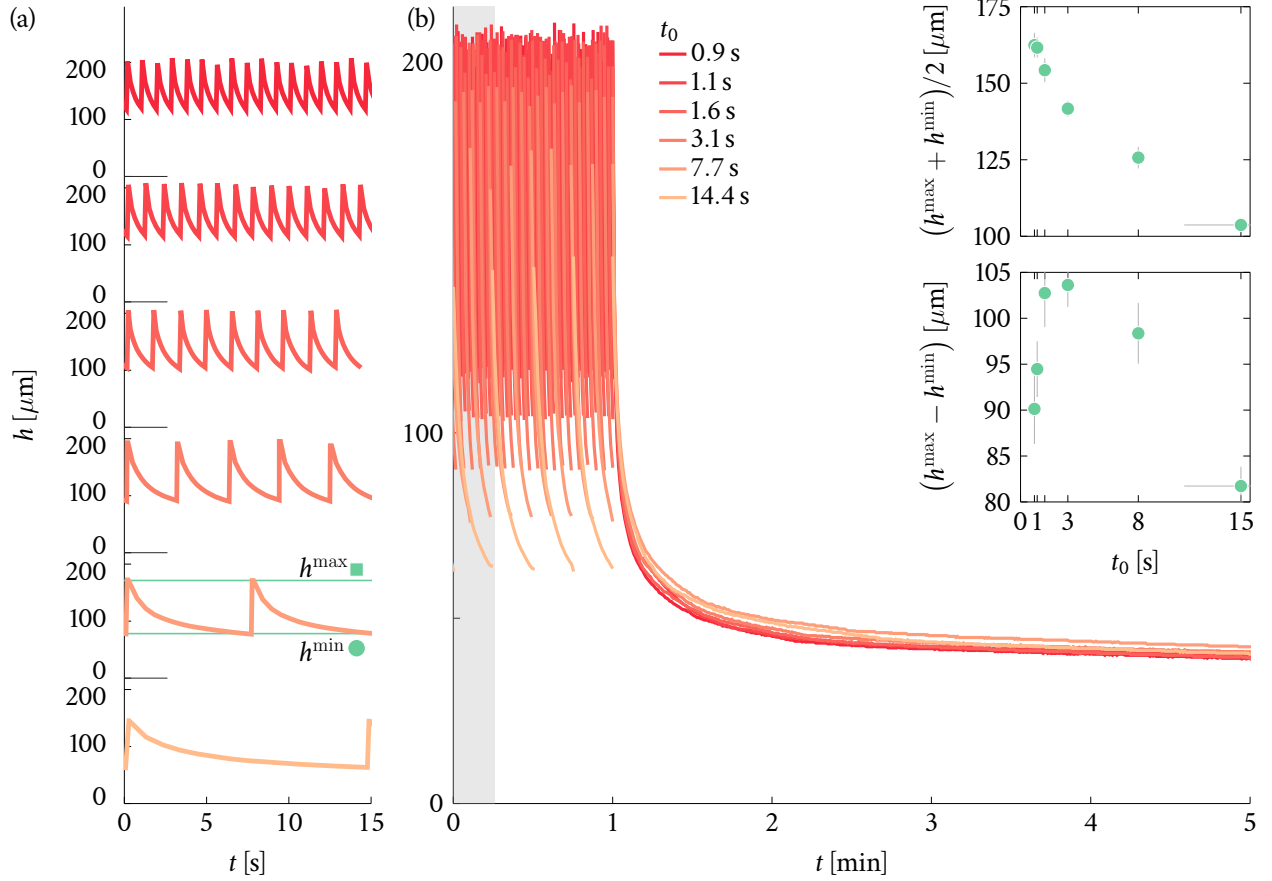
Figure 5.6: Example of film thickness recordings as a function of time in a lab setting, with variable dripping period t_0, and environmental conditions $T = 18.8 \pm 0.7\,°C$ and RH $= 90.2 \pm 0.8\,\%$ (average $\pm$ s.d. in all the curves). The dripping point was positioned in $\mathbf{r}_0$ with $\Delta d \leq 0.5$ cm. The dripping period was varied from $t_0 = 0.9$ s (red curves) to $t_0 = 14.4$ s (orange curves). (a) First 15 s of the stationary film thickness evolution with time $h(t)$, while the film was fed by successive drops at a dripping period t_0. (b) Film thickness evolution with time $h(t)$. For the first 1 min, the film in stationary state was fed by successive drops at a dripping period t_0, as in (a). The gray filled area shows the 15 s drawn in (a). The inflow of drops was interrupted at $t = 1$ min. For $t > 1$ min, no more drops were brought into the film. The upper right inset shows the average film thickness $\left(h^{\mathrm{max}} + h^{\mathrm{min}}\right)/2$ during the stationary phase ($t \leq 1$ min) as a function of the dripping period t_0, with h^{max} and h^{min} illustrated in the penultimate curve from (a). The lower right inset shows the difference $\left(h^{\mathrm{max}} - h^{\mathrm{min}}\right)$ as a function of the dripping period t_0.

In Fig. 5.6 (a), we only see the first 15 s of the recorded stationary phase during which the film is periodically fed by drops. The film thickness thus periodically increases sharply from h^{min} to h^{max}, which corresponds to the addition of a drop in the film. Then, the film thickness decreases at a slower rate from h^{max} to h^{min} in between impacts. Figure 5.6 (b) shows the stationary phase during 1 min before the inflow of drops is interrupted, then the sole drainage for 4 min. We observe once again the film thickness oscillating between h^{max} and h^{min}, then for $t \geq 1$ min, the film thickness decreases, at first quickly. For $t \gtrsim 2$ min, the decrease of the film thickness becomes slower, similarly to our former cave measurements. Additionally, the upper inset in Fig. 5.6 (b) represents the average of the minimum and maximum values reached by the film thickness during the first phase, $\left(h^{\mathrm{max}} + h^{\mathrm{min}}\right)/2$, for each experiment ($h^{\mathrm{max}}$ and h^{min} computed as the averages of all the peak values). The lower inset shows the difference between these two values, $\left(h^{\mathrm{max}} - h^{\mathrm{min}}\right)$.

In Fig. 5.7, we further represent two sequences of successive impacts on Lab01 with variable dripping period t_0 over time. The temperature and relative humidity were kept constant in each case ($T = 18.9\,°C$, RH $= 86\,\%$ in (a) and $T = 17.5\,°C$, RH $= 92\,\%$ in (b)) and the dripping point was positioned in $\mathbf{r}_0$ with $\Delta d \leq 0.5$ cm. The film was also already in a stationary state at the beginning of each curve. In Fig. 5.7 (a), the dripping period t_0 remained at a constant value of 1 s for $t \leq 1$ min
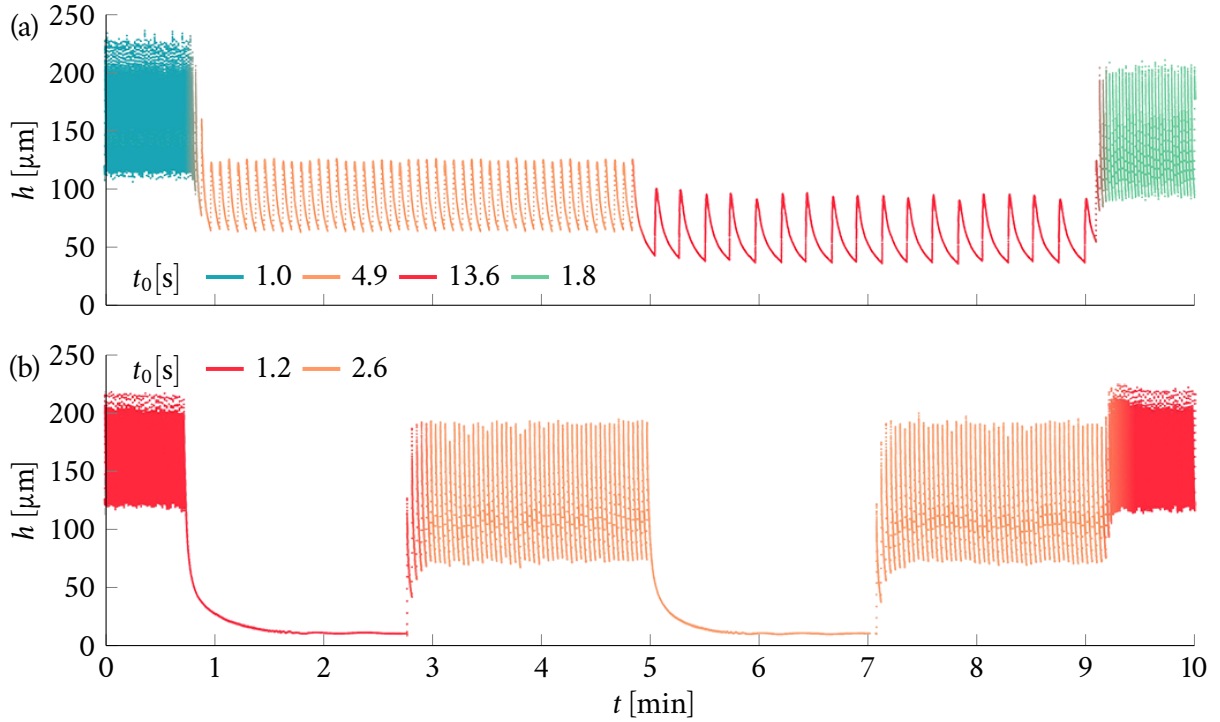
Figure 5.7: Thickness time evolution $h(t)$ of a film fed by a drop inflow with variable dripping period t_0, in a lab setting. (a) For $t \leq 1$ min, the dripping period $t_0 = 1.0$ s (blue part), for 1 min $< t \leq 5$ min, $t_0 = 4.9$ s (orange part), for 5 min $< t \leq 9$ min, $t_0 = 13.6$ s (red part) and for $t > 9$ min, $t_0 = 1.8$ s (green part). Parameters are $T = 18.9\,°C$ and RH $= 86\,\%$, with dripping point position in $\mathbf{r}_0$ and sensor-dripping point distance $\Delta d \leq 0.5$ cm. (b) For $t \leq 1$ min and $t \geq 9$ min, the dripping period $t_0 = 1.2$ s (red part), and for 3 min $\leq t \leq 5$ min and 7 min $\leq t \leq 9$ min, the dripping period $t_0 = 2.6$ s (orange part). For 1 min $\leq t \leq 3$ min (red) and 5 min $\leq t \leq 7$ min (orange), the drop inflow was stopped. Parameters are $T = 17.5\,°C$ and RH $= 92\,\%$, with dripping point position in $\mathbf{r}_0$ and sensor-dripping point distance $\Delta d \leq 0.5$ cm. Times mentioned in the caption are roughly estimated, especially in the case of (b).

before it was changed to $t_0 = 4.9$ s for 1 min $< t \leq 5$ min, then changed again to $t_0 = 13.6$ s for 5 min $< t \leq 9$ min and, finally, to $t_0 = 1.8$ s for $t > 9$ min. In Fig. 5.7 (b), the dripping period t_0 is fixed at 1.2 s for $t \leq 1$ min and $t \geq 9$ min, and changed to 2.6 s for 3 min $\leq t \leq 5$ min and 7 min $\leq t \leq 9$ min. For 1 min $\leq t \leq 3$ min and 5 min $\leq t \leq 7$ min, the inflow of drops was stopped so the only visible process is the drainage. We observe in Fig. 5.7 (a) that the film thickness adapts its value in only a few drop impacts, irrespective of whether the dripping period is increased or reduced. This is also true in the presence of a very thin film of water, as it can be seen in Fig. 5.7 (b). Although the film does not increase its thickness from an initially null value, we can still relate the number of drops to the change in average thickness from such graphs, similarly to our cave measurements.

As it can be seen in Figs. 5.6 and 5.7, $h^{\min}$ and $h^{\max}$ depend on the dripping period t_0 of the drop, and so do the average and difference of these two values. The drops brought into the film should have more or less the same volume, and almost no variation is observed from one drop to another, as it can be seen in both figures. However, the average $\pm$ s.d. over the 6 values shown in $\left(h^{\max} - h^{\min}\right)$, in the lower inset of Fig. 5.6 (b), is 95.2 $\pm$ 8.3 μm, i.e., there is a relative variation of 9 % that cannot be attributed to an error of the sensor alone. It can likewise be seen in Fig. 5.7 (a) that the difference $\left(h^{\max} - h^{\min}\right)$ is larger for shorter dripping periods t_0. We also note in Fig. 5.7 (b) that the thickness reached by the film is not dependent on the film history since the averages $\pm$ s.d. in the four portions of the curve are: (i) for $t_0 = 1.2$ s (red parts), 156.2 $\pm$ 25.0 μm ($t \leq 1$ min) and 155.3 $\pm$ 25.5 μm ($t \geq 9$ min), and (ii) for $t_0 = 2.6$ s (orange parts), 113.1 $\pm$ 30.9 μm

(3 min $\leq t \leq$ 5 min) and 111.4 $\pm$ 30.0 μm (7 min $\leq t \leq$ 9 min). In other words, the dripping period t_0 seems to dictate the value of both h^{max} and h^{min} for otherwise identical conditions (see also Appendix B.1 with examples of repeatability of the experiments).

These observations can be rationalised as follows: the average film thickness $\left(h^{\mathrm{max}} + h^{\mathrm{min}}\right)/2$ decreases with increasing dripping period t_0 as the average film thickness should mostly depend on the total flow rate feeding the film. This flow rate is inversely proportional to t_0 and, hence, diminishes with increasing t_0 (see Sec. 4.4.2). For larger dripping periods, $t_0 > 1$ s, drainage should have already set in place and it is thus not surprising to observe smaller h^{min} values. But we also note that the added thickness at each impact, $\left(h^{\mathrm{max}} - h^{\mathrm{min}}\right)$, decreases with increasing dripping period t_0 when $t_0 \gtrsim 3$ s, and therefore with decreasing local film thickness before impact h^{min}. As we showed in Ch. IV, the maximum radius r_c reached by a drop impacting a thin film decreases with increasing film thickness [80, 86, 171]. However, in the experiments presented here, there is no splashing at impact nor any crown formation but rather a puddle that is deposited onto the film and subsequently mixes within this film (see Appendix B.4). Our conclusions regarding the maximum spreading radius of the drop in the film should nevertheless still apply here. A drop impacting a thicker film is expected to reach a slightly smaller maximum spreading radius [50, 82, 171]. The added thickness at each impact, $\left(h^{\mathrm{max}} - h^{\mathrm{min}}\right)$, should thus be smaller, as it can be seen in both Fig. 5.7 and the inset displaying the thickness difference in Fig. 5.6 (b). This effect can only be observed because we do not measure the thickness directly at the centre of the impact but at a distance Δd; otherwise the added thickness value at constant drop volume, $\left(h^{\mathrm{max}} - h^{\mathrm{min}}\right)$, should be the same for all dripping periods. Below $t_0 \lesssim 1$ s, once again because of the positioning of the sensor which is not exactly at the centre of the impact, we may not capture the entire spreading of the drop in between impacts separated by a short dripping period $t_0 \lesssim 1$ s. We rather capture the competing capillary and viscous effects during the impact. Hence, in this regime, the thickness variations observed in the stationary phase of Fig. 5.6 only result from the drop crushing in the film while drainage should be the main effect dictating both h^{min} and h^{max} in between successive impacts for $t_0 > 1$ s.

b) Displacement of the sensor

In Fig. 5.8, we report examples of the film thickness measured away from the drop impact point position. First, in Fig. 5.8 (a), we compare the film thickness variations measured by positioning the sensor at various distances from the fixed drop impact point position, set in $\mathbf{r} = \mathbf{r}_1$ (see Fig. 5.3). The dripping period was kept constant at $t_0 = 1.2$ s while the distance between the sensor and the impact point, Δd, was set to about 0.5 cm, 5 cm on a slightly curved part of the stalagmite, and 7 cm near a more or less flat edge of the top part of the stalagmite, as shown in Fig. 5.8 (d). An example for $\Delta d = 2$ cm is also shown in Appendix B.2. In the first part of Fig. 5.8 (a), the film thickness is represented when an inflow of drops feeds the film for $t \leq 1$ min, with an emphasis made on a few impacts in the inset of the graph, and in the case of the sole drainage for $t > 1$ min. We observe that the film thickness at a distance of 5 cm exhibits the same periodicity as close to the impact point position of the drops for $t \leq 1$ min. However, the increase in $h(5\,\mathrm{cm})$ following the addition of a drop in the film is slightly delayed and not as sharp as in the case of $h(0.5\,\mathrm{cm})$. Moreover, the average film thickness is smaller for $\Delta d = 5$ cm. The variation between h^{max} and h^{min} is not as large for $\Delta d = 5$ cm as for $\Delta d = 0.5$ cm either. These observations are not surprising considering that the drop impact should mostly be felt on a radius of about 1 cm, as discussed in page 179. The curve obtained for $\Delta d = 7$ cm looks different as there is no evident periodicity. The average film thickness is also smaller than in the two other cases and remains almost constant, except for small variations of the order of $\lesssim 10$ μm (maximum difference between two points from the curve shown in Fig. 5.8 (a) is 7.6 μm). Hence, although the film may be in stationary state, horizontal thickness

gradients can appear in between different horizontal positions because of the drop impacts in the film and drainage at play. During the second part of Fig. 5.8 (a), for $t > 1$ min, only the drainage is experienced by the film in the three positions. Similarly to what we observed in the former section, the curves for $\Delta d = 0.5$ cm and $\Delta d = 7$ cm look alike and do not seem affected by the position of the sensor, the only difference being the film thickness from which the drainage starts. The curve relative to $\Delta d = 5$ cm seems less smooth than the two other ones and has a slightly different slope (which was also observed in other curves obtained at this position). This might be caused by the local curvature of the stalagmite at the position where the sensor was placed, which is less flat than in the two other positions, or possibly by the dewetting detailed hereafter.

In Fig. 5.8 (b), we positioned the sensor as indicated by the blue dot in Fig. 5.8 (d) and manually varied the impact point position of the drops in a random manner for 5 min, before interrupting the drop inflow for another 3 min. The dripping period cannot be inferred directly from the curve here but should be $t_0 \simeq 1$ s, i.e., there should be around 300 drop impacts in the left part of the graph. The film thickness locally increases and decreases rapidly in response to the impacts occurring close to the sensor position. Small variations are also felt when the impact is located at a few centimetres of the sensor, as in Fig. 5.8 (a), which allows the film to keep an average value over time of $89 \pm 34\,\mu$m. Even with impacts occurring away from the sensor position and drainage taking place in the mean time, the dripping period is sufficiently small to maintain a film significantly thicker than the $25\,\mu$m reached after 3 min of sole drainage. Another experiment made with the same parameters, except for the dripping period $t_0 \simeq 3.5$ s, leads to an average film thickness of $72 \pm 30\,\mu$m. For a stalagmite as large as Lab01, the dispersal in the impact point position should have a standard deviation Δ close to 3 cm (see Ch. III). Hence, if the dripping period is not sufficiently short (i.e., if the drainage timescales is shorter than t_0), on average there will not be enough impacts around the entire stalagmite to maintain a film as thick as presented in Fig. 5.8 (b), and the thickness averaged over time will be closer to the values observed during the sole drainage process ($\sim 30\,\mu$m). Although this example does not suffice to draw conclusions regarding the balance between the drop impact point dispersal and film drainage, we note the possible importance that the impact point dispersal can have on local film thickness variations and, possibly, on the ion distribution in the film following an impact.

Finally, we present in Fig. 5.8 (c) examples of the final part of the drainage curves at two positions, i.e., before reaching an almost null film thickness. The dripping point was placed in $\mathbf{r} = \mathbf{r}_1$. The red curve relates to $\Delta d = 0.5$ cm, whereas the purple curve corresponds to $\Delta d = 5$ cm, as indicated in Fig. 5.8 (d). Because of its poor surface state, Lab01 is no longer as hydrophilic as stalagmites found in situ. The film thus experiences dewetting once it becomes sufficiently thin [178]. First, in the case of the curve obtained at $\Delta d = 0.5$ cm, we observe that the film thickness diminishes smoothly until about $10\,\mu$m. From there, small oscillations can be perceived in the curve. As the film originally covering the entire stalagmite dewets, it forms individual puddles [63] which keep evaporating and draining, thus varying the local film thickness and area of the puddles in a non straightforward manner [94, 232]. This process could be responsible for the oscillations seen in the red curve. Similar oscillations are observed in the purple curve corresponding to $\Delta d = 5$ cm, for $t \gtrsim 1$ min. We also note that, before these oscillations appear, the drainage occurs at a completely different rate than for $\Delta d = 0.5$ cm owing to the local change of curvature of the stalagmite. Additionally, the film thickness starts increasing again after $t \gtrsim 2$ min. Because the sensor was positioned away from the impact point on a slightly curved edge, water keeps draining from whatever remains in the centre of the total stalagmite top surface. However, what we observe here is the puddle inflating because of this extra amount of liquid. Once the film has split into multiple puddles, it does not recover its original shape [232] and can no longer cover the entire stalagmite unless we reiterate the experiment. Although drainage is a slow process and it would be ideal to
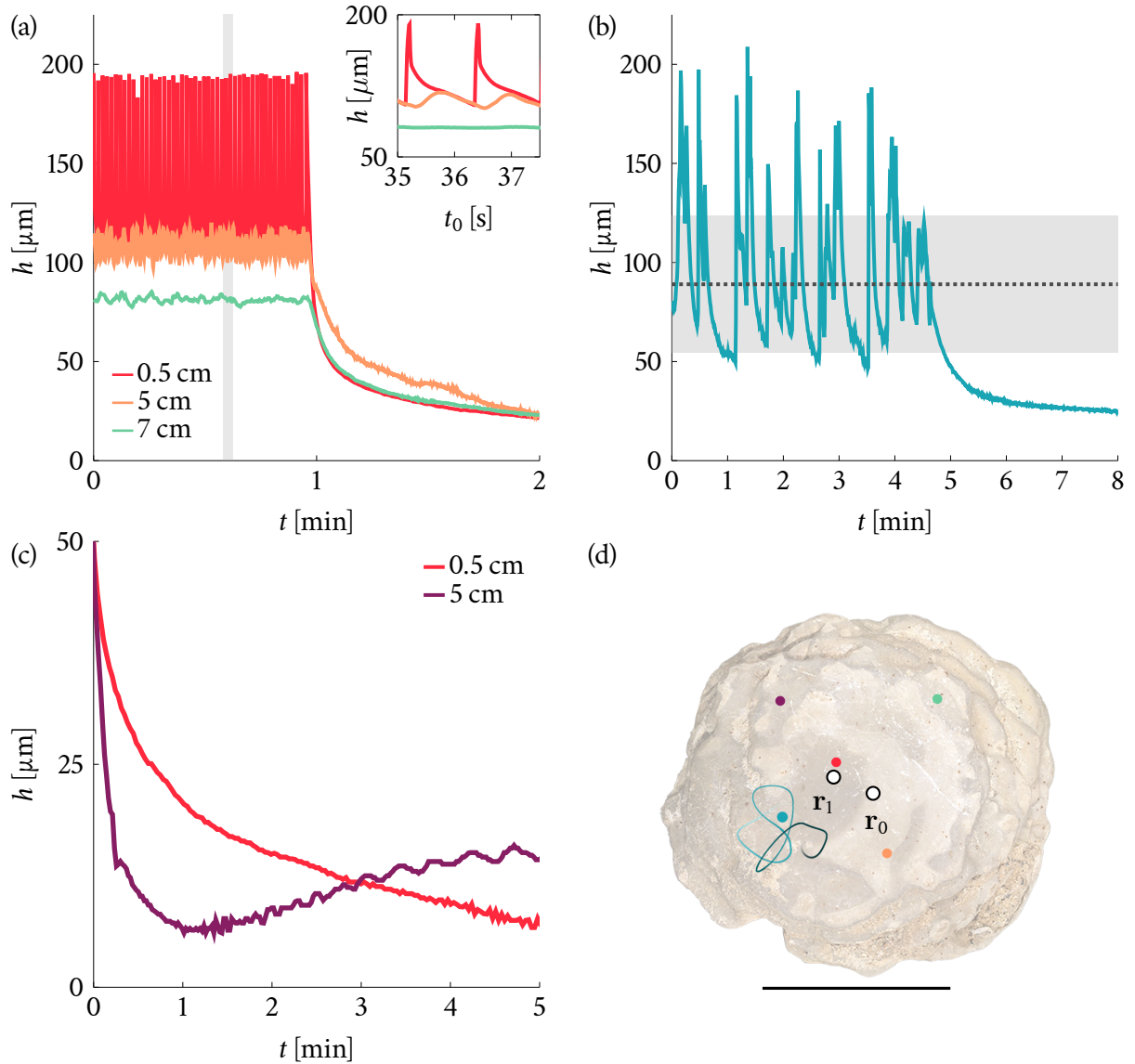
Figure 5.8: Examples of film thickness measurements in a lab setting, with variable sensor/dripping point distance Δd. (a) Time evolution of the film thickness $h(t)$ for dripping period $t_0 = 1.2$ s, dripping point positioned in $\mathbf{r}_1$, $T = 18.8\,°C$ and RH $= 86\,\%$. The inflow of drops is interrupted at $t = 1$ min. The distance between the sensor and the dripping point was set to $\Delta d \leq 0.5$ cm (red curve), $\Delta d = 5$ cm (orange curve) and $\Delta d = 7$ cm (green curve). The corresponding positions of the sensor are indicated in (d) by dots of the same colour as the curves. The gray filled area corresponds to the section of the graph shown in the inset. (b) Film thickness $h(t)$ measured by positioning the sensor as indicated by the blue dot in (d), and by manually varying the impact point position of the drops in a random manner while keeping the falling height of the drops at $\lesssim 5$ cm, with $T = 18.3\,°C$ and RH $= 88\,\%$. The dashed line and gray filled area represent the average and standard deviation of the film thickness during the first 5 min, equal to 89 ± 34 µm. For $t \geq 5$ min, no more drops impact the film. (c) Film thickness time evolution $h(t)$ during the late part of the sole drainage, following an interruption in the drop inflow with $t_0 = 1.2$ s, dripping point in $\mathbf{r}_1$, $T = 18.8\,°C$ and RH $= 86\,\%$. The distance between the sensor and the dripping point was set to $\Delta d \leq 0.5$ cm (red curve) and $\Delta d = 5$ cm (purple curve), with correspondence in (d). (d) Top view of Lab01. The white dots show the two possible positions of the dripping point $\mathbf{r}_0$ and $\mathbf{r}_1$ (see Sec. 3.1). The colour dots correspond to the positions at which the sensor was placed in the graphs from (a-c). The scale bar is 10 cm.

perform measurements (such as the slope of the curve) over a time as long as possible to minimise errors, these measurements should be made with precaution. Undesirable effects could otherwise arise and yield an incorrect interpretation of the drainage process at play. We illustrate the dewetting on Lab01 in Fig. 5.9 hereafter.

Figure 5.9: Example of dewetting on Lab01. *Left.* On the entire stalagmite. *Right.* Close-up view. For scaling, see Fig. 5.8 (d).

c) Influence of the relative humidity and temperature

We show in Fig. 5.10 (a) film thickness measurements relative to two experiments carried in the same conditions, except for the relative humidity RH in the enclosure containing the setup. The dripping tube of the drops was positioned in $\mathbf{r}_0$ while the sensor was placed at a distance $\Delta d \leq 1\,\text{cm}$ from it, the dripping period was set to $t_0 = 1.1\,\text{s}$ and the temperature was $T = 18.7\,°\text{C}$. The relative humidity in the enclosure was maintained at RH $\gtrsim 90\,\%$ and RH $\lesssim 70\,\%$ in the experiments relative to the orange and green curves, respectively. The first part of Fig. 5.10 (a) shows the stationary behaviour of the film fed by successive drops. After $t = 1\,\text{min}$, the inflow of drops was stopped and only the drainage process takes place. The inset shows the time evolution of the thickness of a thin film deposited on a $3 \times 3\,\text{cm}^2$ piece of hydrophilic tape rather than on the stalagmite, measured during 30 min. The film was placed on a balance and the recording was obtained by weighing the mass of the film, thus the thickness shown in the graph corresponds to the spatially averaged thickness of the film, $\bar{h}$. The balance is equipped with vertical windows forming a cage. The relative humidity inside the enclosure thus formed was maintained at RH $\approx 95\,\%$.

We observe in Fig. 5.10 (a) a constant vertical shift between the two curves during both the filling and drainage phases. The difference $(h(\text{RH} = 90\,\%) - h(\text{RH} = 70\,\%))$ between the average $h^{\max}$ (resp. $h^{\min}$) values of both curves is about $19\,\mu\text{m}$ (resp. $26.1\,\mu\text{m}$), while the average of the difference between the thickness $h(t \geq 1\,\text{min})$ of both curves is $25.5\,\mu\text{m}$. The only varying parameter between the curves is the relative humidity in the vicinity of the stalagmite, which directly affects the evaporation rate that is proportional to $p_{\text{H}_2\text{O, sat}}(1 - \text{RH})$ [114, 214]. The evaporation rate is thus less important at larger RH given that, at constant temperature, the saturation vapor pressure $p_{\text{H}_2\text{O, sat}}$ remains constant. This is consistent with the shift of the entire curve observed. A larger evaporation rate at lower RH should also explain the origin of the larger difference observed between the $h^{\min}$ values from the two curves during the filling phase. The evaporation thus sets in quickly, even while the drop is still completing its spreading into the film. We could think of evaporation as a constant outward flux of water that can be subtracted to the dripping flux. Therefore, an increase of relative humidity should have the same effect as a decrease of dripping period, which is suggested by the similarity between the first parts of Fig. 5.6 and Fig. 5.10 (a). The inset of Fig. 5.10 (a) additionally shows that a thin water film subjected to a high relative humidity can feature very little thickness variations over a long period of time, which is what we observed in caves. The average $\pm$ s.d. over the entire time period of the graph is indeed $491 \pm 2\,\mu\text{m}$. The liquid is close to the equilibrium between evaporation and condensation [13, 114]. Consequently, we note that for large RH values ($\geq 80\,\%$), the film thickness in the drainage experiments can remain of the order of $30\,\mu\text{m}$ to $40\,\mu\text{m}$ for several minutes (see Fig. 5.6) while it is clear that the green curve
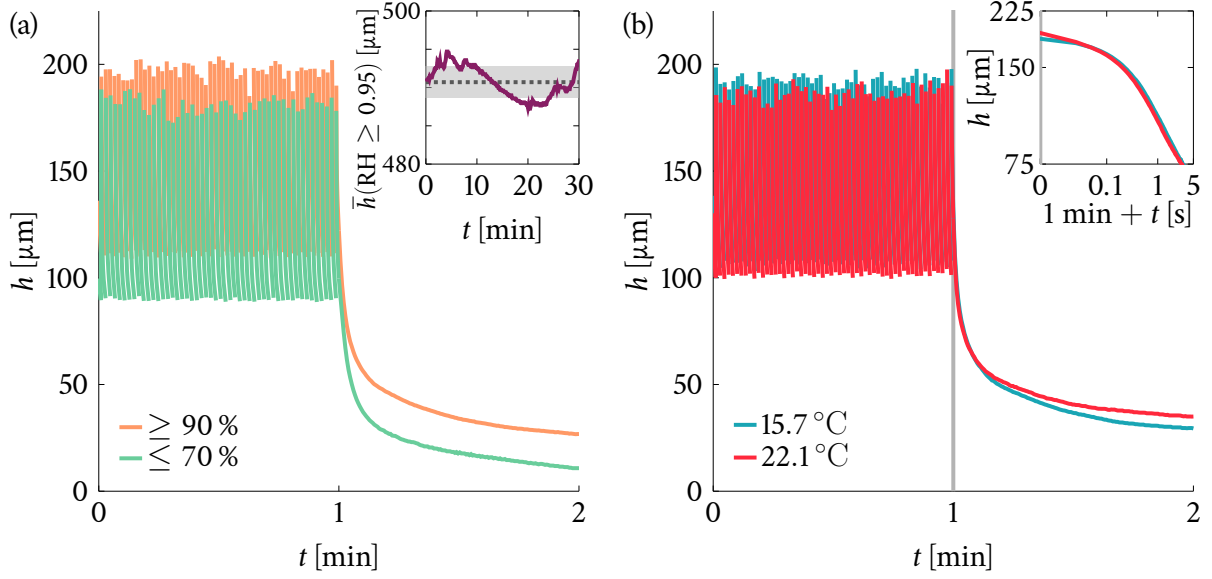
Figure 5.10: Example of the film thickness evolution with time $h(t)$ in a lab setting, with dripping point position $\mathbf{r}_0$ and sensor distance to the dripping point $\Delta d \leq 0.5$ cm. In both cases, for $t < 1$ min, the film is in stationary state and fed by successive drops at constant dripping period $t_0 = 1.1$ s, then the inflow of drops is stopped at $t = 1$ min. (a) Time evolution of the film thickness for constant temperature $T = 18.7\,°C$ and variable relative humidity. The orange curve, resp. green curve, corresponds to RH $\lesssim 70\,\%$, resp. RH $\gtrsim 90\,\%$. Variability in the RH(t) measurements over the entire experiments is $\lesssim 2\,\%$. The inset shows an example of spatially averaged film thickness evolution with time $\bar{h}(t)$ during 30 min, for RH $\gtrsim 95\,\%$. In this specific case, the curve was obtained by depositing a thin water film on a 3×3 cm^2 piece of hydrophilic tape and by weighing the mass of water on the tape. The relative humidity was maintained at a large value by adjoining the humidifier from Sec. 2.2 to the balance and by closing the remaining windows of the balance enclosure. (b) Time evolution of the film thickness for constant relative humidity RH $= 88\,\%$ and variable temperature. The blue curve, resp. red curve, corresponds to $T = 15.7\,°C$, resp. $T = 22.1\,°C$. Variability in $T(t)$ measurements over the entire experiments is $\lesssim 0.2\,°C$. The inset shows the sole drainage process in a log-log scale beyond the gray line from the main graph, for $t = 1$ min to $t = 1$ min $+ 5$ s.

from Fig. 5.10 (a) obtained at RH $= 70\,\%$ tends to 0 more quickly. In Appendix B.3, we further note that it would take only 5 min for the film thickness to decrease by 10 µm over its entire surface by evaporation in the case when RH $\leq 70\,\%$ (assuming that the evaporation rate is constant over the surface and does not depend on the film thickness), while it should take more than 15 min if RH $\geq 90\,\%$.

Figure 5.10 (b) represents two other similar curves, for which we varied the temperature while keeping a constant relative humidity RH $\approx 88\,\%$. The temperatures relative to the red and blue curves were $T = 22.1\,°C$ and $T = 15.7\,°C$, respectively, i.e., there is a difference of 6.4 °C between both cases. The main graph of Fig. 5.10 (b) also represents the successive drop impacts feeding the film for 1 min, which are then interrupted for $t \geq 1$ min. The inset shows both curves in a log-log scale during the first seconds following the interruption of drop inflow, for $t \geq 1$ min. By contrast with Fig. 5.10 (a), we note that the two curves do not exhibit strong differences during the filling phase or the very beginning of the drainage process ($t \lesssim 5$ s). The average stationary film thickness $\left(h^{\max} + h^{\min}\right)/2$ does not vary significantly and is equal to 149.5 µm for $T = 15.7\,°C$, and to 150.0 µm for $T = 22.1\,°C$. But the average film thickness difference $\left(h^{\max} - h^{\min}\right)$ (average in all the differences between successive peaks) is 4 µm smaller at larger temperature ($T = 22.1\,°C$). Such discrepancy could not be entirely inherited from the small volume variations of the drops entering the film. The Ohnesorge number of the drops (see Ch. IV), Oh $= \nu \sqrt{\rho/\left(2\gamma r_d\right)}$, indeed goes from 1.9×10^{-3} at 15.7 °C to 1.6×10^{-3} at 22.1 °C and exhibits a non-negligible 15 % difference. This difference stems from the fact that the viscosity of water decreases with increasing tempera-

ture, going from $\nu = 1.138 \times 10^{-6}\,\mathrm{m^2\,s^{-1}}$ at $T = 15\,°\mathrm{C}$ to $\nu = 9.554 \times 10^{-7}\,\mathrm{m^2\,s^{-1}}$ at $T = 22\,°\mathrm{C}$. A lower viscosity decreases the thickness of the lamella formed by a drop impacting a dry surface and increases its spreading velocity [7, 206], thus it can be expected that the same holds for the puddle spreading onto the film during the impact on a thin film here (see p. 179). The thickness difference $\left(h^{\mathrm{max}} - h^{\mathrm{min}}\right)$ at each impact is indeed slightly smaller at the higher temperature, i.e., smaller viscosity. As a comparison, we recall the time of viscous drag in the film necessary to stop the spreading drop, which can be approximated as $t_\nu = R_{\mathrm{d}}^2/\nu$. The value taken by t_ν is 4.6 s at 15.7 °C and 5.5 s at 22.1 °C. Hence, we note a difference of 20 % between the two cases.

The two curves then depart from each other during the drainage phase, beyond the initial 5 s during which they overlap. After 1 min past the drop inflow interruption, the thickness difference between the two curves is about 5 µm, a discrepancy that cannot be attributed only to the sensor nor comes from the viscosity change (which should lead to an opposite thickness variation, i.e., a faster drainage in response to a larger temperature). We observed in the previous section that dewetting of the film could be promoted because of the deteriorated surface state of the stalagmite [178]. We noted during the experiments that dewetting occurred more easily at a higher temperature. We show in Fig. 5.9 a photograph of the film after dewetting has occurred. Changes in water surface properties all indicate that the film should spread out more easily and experiences less dewetting at higher temperature as both water viscosity and contact angle decrease with increasing temperature [201]. The most likely explanation is that evaporation becomes sufficient at higher temperature for the film to become much thinner on the sides of the stalagmite, thereby preventing it from covering the entire stalagmite when it is no longer fed by drops (see Appendix B.3). The curves from Fig. 5.10 indeed indicate that the film can quickly become locally very thin when evaporation becomes important. In this case the relative humidity was kept constant but the vapor saturation pressure increases with temperature, which promotes the evaporation process [117]. From there, dewetting should occur more easily on the outer edge of the stalagmite since the film thickness has become too low for the film to maintain its shape, as it could be seen in Fig. 5.8. Hence, we cannot directly assess the effect of the temperature on the drainage process directly from our lab measurements on the long term. Regarding only the early part of drainage ($t \lesssim 5\,\mathrm{s}$), the temperature does not seem to affect drainage significantly.

It should be noted that none of the above effects could be primarily attributed to the possible temperature difference between the film and the surroundings. Although the water drops leaving the dripping tube are not at the same temperature as the air in the enclosure since they come from a large tap water reservoir outside of the enclosure at about $T_0 = 15\,°\mathrm{C}$, the water in the film should have more or less the same temperature as the air. In particular, we can consider a thin water film spread on Lab01 with uniform thickness $\overline{h} \simeq 100\,\mathrm{µm}$, and surrounding air temperature $T_\infty = 22\,°\mathrm{C}$. The time t needed for this film to reach $T = T_\infty$ is given by $T(t) = T_\infty - (T_\infty - T_0)\exp\left(-t/k\right)$, $k = \lambda/(\rho\,c_p\,\overline{h}^2)$, where $\lambda = 0.6\,\mathrm{W\,K^{-1}\,m^{-1}}$ is the water thermal conductivity and $c_p = 4187\,\mathrm{J\,K^{-1}\,kg^{-1}}$ is the water specific heat capacity [117]. The film actually needs less than 1 s to reach the same temperature as the surrounding air in these conditions. Hence, it can be safely assumed that the film almost instantaneously reaches the same temperature as the surrounding air when varying the experimental conditions.

3.3 Summary

From our observations made in situ and in a lab setting, we reckon that several physical processes may affect the thickness evolution of the residual film lying on a stalagmite. Starting from either an initially dry stalagmite or a stalagmite already covered by a very thin film of water ($h \lesssim 30\,\mathrm{µm}$), adding drops in the film will result in an increase of the film thickness h in the vicinity of the drop

impact point. For a periodic dripping period, the film thickness keeps increasing until it reaches a stationary state, during which it oscillates between a maximum value h^{max} when a drop is added, and a minimum value h^{min} once the drop has spread out and that drainage has occurred for a time t_0. The first transient part when the film thickness increases progressively is what we call the filling phase. The filling time needed for the film to reach a stationary state depends mostly on the area and curvature of the surface that must be covered by water underneath the film, i.e., the shape of the stalagmite, and on the dripping period t_0 of the drops. The film thickness difference during the filling phase, $\left(h^{\mathrm{max}} - h^{\mathrm{min}}\right)$, is mostly set by the drop volume added to the film. Nevertheless, small variations appear in $\left(h^{\mathrm{max}} - h^{\mathrm{min}}\right)$ because of the exact position of the sensor with respect to the spreading of the drop at impact, leading to local $\left(h^{\mathrm{max}} - h^{\mathrm{min}}\right)$ variations of the order of $\sim 20\,\mu\mathrm{m}$.

Beyond this initial filling phase, the thickness of the film quickly responds to variations in the dripping period of the drops. The minimum and maximum film thicknesses reached during the stationary phase, h^{min} and h^{max}, both seem to increase with shorter dripping periods. The local film thickness also depends on the distance to the impact point position. The response of the film thickness to the inflow of drops is the strongest close to the impact point position of these drops ($\sim 1\,\mathrm{cm}$), but these variations can be felt away from the impact point too. An aperiodic sequence of drops or dispersal in the impact point position results in film thickness variations in both time and space, but the spatially averaged film thickness still remains of the same order of magnitude as observed for a periodic dripping period with no impact point dispersal. Additionally, we could note throughout all the presented curves that the position in $\mathbf{r}_0$ or $\mathbf{r}_1$ of the dripping point did not affect our measurements significantly, as both these positions are located on the very flattened out central portion of the stalagmite. Hence, we can consider all the measurements without sorting them according to this parameter.

When the inflow of drops is interrupted, the major remaining process occurring is the gravity-induced drainage of the film. A transient phase during which the film thickness decreases quickly is observed at first, followed by a decrease at a slower rate. For very large times, in the absence of other physical processes, the thickness seems to decrease infinitely slowly, indicating it should follow a negative power law with time. Nevertheless, evaporation and dewetting appear in the experimental curves taken in a lab setting. We observe that the evaporation rate depends mostly on the relative humidity in the stalagmite enclosure, or, more simply, on the partial water pressure. This dependence may vertically shift the entire film thickness curve by a non-negligible offset, e.g., of about $20\,\mu\mathrm{m}$ if RH is varied from $70\,\%$ to $90\,\%$. By contrast, the temperature does not affect much the stationary film thickness, and does not seem to have much influence on the early part of the drainage either. Because dewetting occurs during the experiments, our ability to provide detailed insights regarding the later part of the drainage is limited. Dewetting of the film can be observed after a few minutes, inducing small perturbations in the local film thickness, though still large enough to be measured by the sensor. Because we cannot assess the exact evaporation rate acting on the film as a function of T and RH, we will limit our study to the influence of the dripping period and stalagmite shape on the film thickness evolution.

Other parameters that may influence the filling and drainage processes include the roughness [194] and porosity [153] of the stalagmite surface, but we will assume that their effects can be neglected in regard of the dripping period and stalagmite shape. The volume of the drops should also have a crucial role but it does not vary much in the range that we observed in caves and could be kept constant during the lab experiments. For dripping periods $t_0 < 0.8\,\mathrm{s}$, satellite droplets are more likely to form in caves and decrease the average volume of the drops falling from stalactites [98], thereby affecting the film thickness. However, we did not observe it in our cave measurements as they all correspond to $t_0 \gtrsim 1\,\mathrm{s}$. Finally, a major difference between cave and lab measurements is the splashing usually observed at impact in caves. As we are not yet concerned

with the amount of ions that can enter the film in this chapter, we will consider for now on that the entire drop volume is added to the film at each impact.

4. Modelling

This section focuses on the mathematical modelling of the film thickness as a function of time and space. The proposed model, derived in Sec. 4.2, relies on Reynolds equation [66, 116, 180]. From there, we infer scaling laws in Sec. 4.3 by comparing the order of magnitude of the different terms involved in the non-linear equations obtained. We then particularise our initial problem to a perfectly horizontal plane and to a cone of constant opening angle in Sec. 4.4. This allows us to derive the boundary conditions aiming at best representing actual stalagmites. The numerical resolution of the equations describing the drainage is presented in Sec. 4.5.

4.1 Mass balance

Among the possible inflows and outflows (in $m^3\,s^{-1}$) that can add or remove liquid from the film lying on a stalagmite in a very humid environment, we can list: (i) Q_{drip}, the inflow brought by the successive drop impacts and Q_{spl}, the ejected liquid resulting from the splash at impact, (ii) Q_{evap}, the evaporation (and condensation) flux, and (iii) Q_{drain}, the drainage flux. We consider that the ions in solution are dilute enough and do not add any mass. As we already did in the lab experiments, for the sake of simplicity we will not consider the splash at impact here since it differs according to the drop velocity and film thickness. We can also safely assume that, at least in caves and when RH $\gtrsim$ 80 % in the lab, Q_{evap} can be neglected in regard of the other fluxes. If the film is in a stationary state, we are thus left with a balance between the successive, discrete drop additions in the film, Q_{drip}, and the drainage flux Q_{drain} as

$$Q_{\mathrm{drip}} = Q_{\mathrm{drain}}\,. \tag{5.1}$$

Otherwise, if the film is not in stationary state and if we consider as an approximation that it has a uniform thickness over the stalagmite top surface[3], we have

$$\pi r_{\mathrm{sm}}^2 \partial_t h = Q_{\mathrm{drip}} - Q_{\mathrm{drain}}\,, \tag{5.2}$$

which yields an increase in the film thickness h when $Q_{\mathrm{drip}} > Q_{\mathrm{drain}}$, and a decrease in h in the opposite case. The drop inflow can be modelled as

$$Q_{\mathrm{drip}} = \frac{V_{\mathrm{d}}}{t_0}\,, \tag{5.3}$$

where the drop volume $V_{\mathrm{d}} = 4/3\pi R_{\mathrm{d}}^3 \simeq 8 \times 10^{-8}\,\mathrm{m}^3$ for $R_{\mathrm{d}} = 2.7\,\mathrm{mm}$. A 40 µm-thick film uniformly spread on a 2.5 cm-radius stalagmite has an equivalent volume. Because of the constant drop volume in caves, we infer from the above relations the same conclusion as from our literature and phenomenological reviews: the film drainage depends mostly on (i) the inflow, i.e., the drop dripping period in our case, and (ii) the stalagmite size and shape, this latter conditioning the distribution of the film over the stalagmite. The next section introduces the modelling of the flux Q_{drain}.

---

[3]We have considered a flat stalagmite in Eq. (5.2), but it appears quite clear that considering a more general stalagmite shape in the same equation would involve parameters such as Ψ and S. The only goal of Eq. (5.2) is to provide a simple description of the balance between the drop inflow and the drainage outflow.

4.2 Reynolds equation in curvilinear coordinates

Although we consider axisymmetric stalagmites, the cross-sectional profile of the stalagmite can be either flat, curved, possibly with a change of curvature, and present macroscopic irregularities. The stalagmite top surface can also become almost perpendicular to its outer wall. At the same time, the film thickness lying on top of the stalagmite is of the order of 30 µm to 300 µm, which is much smaller than the order of magnitude of all the stalagmite shape variations ranging from ~ 1 mm to 10 cm. We thus choose to represent these variations using a curvilinear system (ξ, ζ) which follows the profile of the stalagmite in every point and allows us to avoid dealing with gradients of different orders of magnitude inside the film, as illustrated in Fig. 5.11. We nevertheless do not aim at modelling the drainage of a film over a perfectly vertical surface, but simply on curved surfaces, including concave stalagmites.

We consider a water film lying on top of an axisymmetric stalagmite. As represented in Fig. 5.11, the system of coordinates (r, z) designates the radial and vertical directions and is positioned along the stalagmite axis of symmetry. On the other hand, the curvilinear system (ξ, ζ) refers to the parallel and perpendicular directions to the stalagmite surfaces, respectively. The stalagmite solid surface has an elevation $\eta(r)$ above a horizontal plane, as in Fig. 5.11. We only limit our domain of interest to the part of the stalagmite located between the axis of symmetry $r = 0$ and a maximum radius that we denote R (see Ch. II). The film thickness measured normally to the solid/liquid interface is h. The inclination is defined as the angle with the horizontal plane, counted as positive downward. If the local inclinations of the stalagmite and the film, denoted φ and φ', respectively, satisfy the condition: $\tan|\varphi - \varphi'| \rightarrow 0$, then we can consider that the vertical height of the film is $\approx h/\cos\varphi \ \forall r$. In other words, although the film may not be exactly parallel to the solid surface everywhere, the approximation remains valid as long as the film remains thin, i.e., $h \ll R$, a condition verified for most stalagmites.
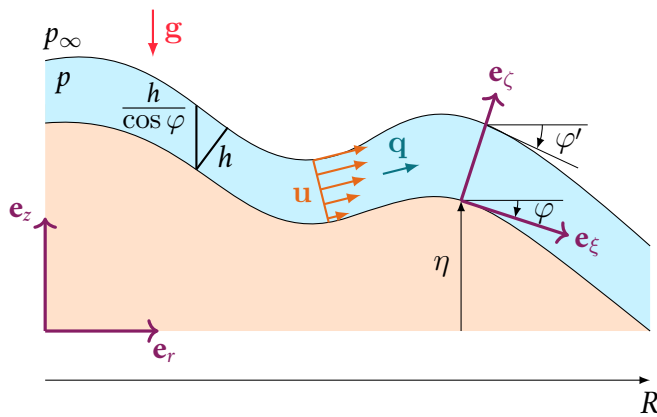
Figure 5.11: Cross-sectional sketch of an axisymmetric stalagmite (in beige) with curved upper surface and inclined wall. In position (r, z), we denote the local stalagmite elevation η, the local angle made by the stalagmite, resp. the film/air interface, with the horizontal φ, resp. φ', (both counted as positive clockwise) and we introduce the local curvilinear coordinate system (ξ, ζ). The stalagmite is covered by a thin film of water (in blue) of local thickness h. The pressure inside the film is p and the atmospheric pressure p_∞. The velocity in the film is denoted $\mathbf{u}$, while $\mathbf{q}$ represents the integrated velocity flux over the entire film height.

We denote the typical timescale over which particle velocity in the film may undergo substantial changes as T, whereas U, resp. W, represents the order of magnitude of the velocity parallel, resp. normal, to the stalagmite surface. Becaus $1/R^2 \ll 1/h^2$, the second-order derivatives parallel to the stalagmite surface can be neglected ($\partial_{\xi\xi} \approx 0$). Additionally, the velocity component normal to the solid surface is assumed negligible with respect to the component parallel to the surface: $W \ll U$. We also find by comparing the orders of magnitude of $\rho U/T$ and $\mu U/h^2$ that the inertial term of the Navier-Stokes momentum equation can be neglected. Namely, if the timescale T at which a particle changes its velocity satisfies $T \gg \rho h^2/\mu \sim 10^{-2}$ s, the corresponding Reynolds number is smaller than unity, there are no recirculation zones, and the velocity field can be assumed parallel to the stalagmite surface.

Under these approximations and in the absence of drops feeding the film, the Navier-Stokes momentum vector equation in the film reduces to

$$\nabla p = \mu \nabla^2 \mathbf{u} + \rho \, \mathbf{g} \,, \tag{5.4}$$

where $\mathbf{u} = u \, \mathbf{e}_\xi$ and $\mathbf{g} = g \, \mathbf{e}_z$ are the velocity and gravitational acceleration fields, respectively, and p is the pressure inside the film. Projecting this onto the curvilinear vectors $\mathbf{e}_\xi$ and $\mathbf{e}_\zeta$, we find

$$\partial_\xi p = \mu \partial_{\zeta\zeta} u + \rho g \sin \varphi \,, \tag{5.5}$$
$$\partial_\zeta p = -\rho g \cos \varphi \,. \tag{5.6}$$

At the solid/liquid interface between the stalagmite and the film, we consider that a no-slip condition applies: $u(\zeta = 0) = 0$. The absence of normal stress at the liquid/air interface further yields $\partial_\zeta u = 0$ and $p = p_\infty$ in $\zeta = h$, with p_∞ the atmospheric pressure in the vicinity of the stalagmite. We also consider that the stalagmite surface should be smooth and, as aforementioned, that its radius of curvature should be large enough to neglect the variations of the stalagmite elevation with the curvilinear abscissa, which translates here into $h \ll 1/\left|\partial_\xi \varphi\right|$. We therefore find that

$$p = p_\infty + \rho g \left(h - \zeta\right) \cos \varphi \,, \tag{5.7}$$
$$u = \frac{-g}{2\nu} \zeta \left(2h - \zeta\right) \left[\left(\partial_\xi h\right) \cos \varphi - \sin \varphi\right] \,. \tag{5.8}$$

We note from Eq. (5.7) that the pressure at height ζ in the film depends on the atmospheric pressure and local film thickness, in correspondence with the hydrostatic pressure in a liquid volume lying on a flat surface, but also on the inclination of the stalagmite surface underneath. This comes with no surprise as gravity is expected to have a stronger influence on a stalagmite with very inclined walls, by contrast with a flat plane. The pressure acting at the bottom of the film over a flat plane will consequently be larger than if the stalagmite and film are very inclined. We have also not taken the Laplace pressure into account in our former calculations. If we approximate a film about $100\,\mu$m thick spread on a $10\,$cm-radius stalagmite by a spherical cap, we find that the corresponding sphere radius $\mathcal{R}$ is $\sim\ 50\,$m, leading to $\gamma/(2\mathcal{R}) \simeq 3\,$mPa, with $\gamma \simeq 70\,$mN m^{-1} the water surface tension. The maximum hydrostatic pressure $\rho g h$ in the same film is of the order of $1\,$Pa. Hence, neglecting Laplace pressure is a valid assumption, as long as the surface is considered perfectly smooth. Should we find corrugations of the order of a few mm radii over the stalagmite surface, both the hydrostatic and Laplace pressure would locally become of the order of $\sim 10\,$Pa. Usually these corrugations found on the stalagmites in our dataset are located on the sides of the stalagmites and we can consider that their top surface is sufficiently smooth. We have also neglected the disjoining pressure, an assumption discussed in Appendix B.5.

In Eq. (5.8), we recognise the half-parabolic profile of the velocity field in a Poiseuille flow, though mitigated by the inclination of the stalagmite surface, exhibiting a maximum velocity at the liquid/air interface. We can further define the flux parallel to the stalagmite surface in all points, $\mathbf{q} = q \, \mathbf{e}_\xi$, with

$$q = \int_0^h u \, \mathrm{d}\zeta = \frac{-gh^3}{3\nu} \left[\left(\partial_\xi h\right) \cos \varphi - \sin \varphi\right] \,. \tag{5.9}$$

From the continuity equation integrated over the film thickness normal to the solid/liquid interface, we finally obtain

$$\partial_t h = -\frac{1}{r} \partial_\xi \left(qr\right) \tag{5.10}$$

in conservative form. It should be noted that q is here expressed in $\text{m}^2\,\text{s}^{-1}$ and does not correspond to the actual drainage flux all around the stalagmite but rather to the two-dimensional flux in the cross-section shown in Fig. 5.11. We indeed have $Q_{\text{drain}} = 2\pi r(\xi)\,q$, the actual drainage flux. From Eq. (5.9), we observe once again that the drainage is enhanced by either (i) a thicker film, (ii) a film with larger thickness variations over a certain distance, or (iii) by a stronger inclination of the stalagmite wall below the film. However, we note that these last two effects are not additive: on an almost vertical wall ($\varphi \to \pi/2$), the film thickness variations will have very little effect in regard of the last term of Eq. (5.9). On the other hand, on an almost horizontal stalagmite surface, the drainage will be mostly driven by gradients of film thickness.

4.2.1 Nature of the system of equations

Alternatively, Eqs. (5.9) and (5.10) can be written under a matrix form as

$$
\underbrace{\begin{bmatrix} 1 & 0 \\ 0 & 0 \end{bmatrix}}_{A^{(t)}} \partial_t \mathbf{U} \; + \; \underbrace{\begin{bmatrix} 0 & 1 \\ (gh^3)/(3\nu)\cos\varphi & 0 \end{bmatrix}}_{A^{(\xi)}} \partial_\xi \mathbf{U}
$$
$$
= \begin{bmatrix} 0 & -\cos\varphi/r \\ (gh)/(3\nu)\sin\varphi & -1 \end{bmatrix} \mathbf{U}, \quad \mathbf{U} = \begin{bmatrix} h \\ q \end{bmatrix}. \tag{5.11}
$$

By assuming a wave-like solution form, $\mathbf{U} = \hat{\mathbf{U}}\exp\left(i\left(n_\xi \xi + n_t t\right)\right)$, and by introducing it into the homogeneous part of the above system of equations, we find that non-trivial solutions such that $\hat{\mathbf{U}} \neq \mathbf{0}$ are ensured if $n_\xi^2 h^3 = 0$ (we exclude the case $\cos\varphi = 0$ which would refer to a vertical wall) [112]. When $h = 0$, the system becomes locally hyperbolic. A hyperbolic set of equations is in essence associated with the propagation of a wave at finite speed along a specific direction [112]. This corresponds to our liquid front advancing onto the stalagmite surface. On the other hand, the nature of the equations changes when $h \neq 0$ and the system becomes parabolic because the matrix $A = n_t A^{(t)} + n_\xi A^{(\xi)}$ is in this case not of full rank [112]. In particular, because the rank of A is equal to 1, the system admits one characteristic. Huppert [116] derived a similarity solution to Eqs. (5.9) and (5.10) in radial coordinates (see Sec. 4.4.2) in two particular cases: (i) a known liquid volume spreading under the form of a puddle over an initially dried horizontal surface, and (ii) a known flow rate continuously feeding this puddle. If the volume of the puddle is equal to, e.g., the volume of a drop V_{d} in the first case, and if the flow rate feeding the puddle is Q_{drip} in the second one (which could be approximated as V_{d}/t_0), the puddle advances over the surface by covering a disk of radius $r_0(t)$ given by

$$
r_0(t) \simeq \begin{cases} 0.9\left(\dfrac{gV_{\text{d}}^3}{3\nu}\right)^{1/8} t^{1/8}, & \text{(constant volume)}, \\[3mm] 0.7\left(\dfrac{gQ_{\text{drip}}^3}{3\nu}\right)^{1/8} t^{1/2}, & \text{(constant flow rate)}. \end{cases} \tag{5.12}
$$

The parabolic nature of the equations also indicates that they should be solved using a numerical time-marching method, while updating the film thickness spatially all at once at each time step. Solving the system therefore requires an initial condition and two boundary conditions. However, looking at Eqs. (5.9) and (5.10), we note that it is not possible to impose two conditions of null flux at once, nor a condition that would imply cancelling the film thickness at, e.g., the outer boundary of the domain. We will rather approximate the outer stalagmite wall by an inclined cone portion

of constant opening angle described in Sec. 4.4.1 hereafter, which is a valid assumption in regard of most stalagmite shapes (see Ch. II).

4.2.2 Drainage timescale

We present in Fig. 5.34 from Appendix B.4, with the frame from Fig. 5.34 (f) duplicated in Fig. 5.12 on the right, an example of a drop impact on a thin film at low velocity. From the observations made, we reckon that the drainage equations that we derived in Sec. 4.2, Eqs. (5.9) and (5.10), can be made nondimensional by using a timescale t_d, and two different length scales: one horizontal, r_d, and one vertical, h_d. This is standard practice when dealing with Reynolds lubrication equation [152, 154]. These length scales are chosen as the height and spreading radius of the puddle formed by the drop impacting the film in a non-splashing case, as illustrated in Fig. 5.34 from Appendix B.4 and in Figs. 5.12 (a) (puddle height h_d) and (b) (puddle radius r_d). We use $r_d = 1$ cm and $h_d = 100\,\mu$m, which lead to slightly smaller drop volumes than in our lab experiments

(a)

(b)

Figure 5.12: Puddle left by a drop of radius $R_d = 2.31$ mm impacting a $117\,\mu$m-thick film, about 32 ms after the beginning of the impact, from a side (a, schematic) and a top view (b, duplicate of Fig. 5.34 (f)). The height $h_d = 100\,\mu$m and radius $r_d = 1$ cm of the puddle are illustrated by arrows in (a) and (b), respectively. The scale bar in (b) is 1 cm.

and in caves ($V_d = 3.2 \times 10^{-8}\,\text{m}^3$ in the present case, against $V_d = 5.1 \times 10^{-8}\,\text{m}^3$ in the lab and $V_d = 8.2 \times 10^{-8}\,\text{m}^3$ in caves). The quantities appearing in Eqs. (5.9) and (5.10) thus write as

$$t = t' t_d, \quad r = r' r_d, \quad \xi = \xi' r_d, \quad h = h' h_d,$$

where the prime variables x' refer to the non-dimensional quantities. Inserting these notations into Eqs. (5.9) and (5.10), we find that

$$\partial_{t'} h' = \frac{g h_d^3 t_d}{\nu r_d^2} \frac{1}{r'} \frac{\partial}{\partial \xi'} \left[\frac{(h')^3}{3} \left((\partial_{\xi'} h') \cos\varphi - \left(\frac{r_d}{h_d} \right) \sin\varphi \right) r' \right]. \tag{5.13}$$

The group of variables at the front of the right-hand side corresponds to what we call the drainage timescale t_d, i.e.,

$$t_d = \frac{\nu r_d^2}{g h_d^3}, \tag{5.14}$$

which is about 12 s for our values of r_d and h_d. We note that t_d decreases sharply with increasing thickness scale h_d. If we take for instance $h_d = 200\,\mu$m by keeping the other parameters identical, we obtain $t_d \simeq 2$ s. In the lab raw data curves from Sec. B.4, we indeed witnessed that it only took a few seconds for a film thickness larger than $200\,\mu$m to fall below $50\,\mu$m. On the other hand, with $h_d = 20\,\mu$m, the drainage time t_d becomes of the order of 35 min. This is particularly corroborated by our raw data curves taken in caves, in which case we could still measure film thicknesses of the order of $20\,\mu$m after sometimes 15 min.

4.3 Relative orders of magnitude

After having derived the partial differential equations describing the drainage of a thin film over a curved solid surface, we may now infer a few scalings by comparing the relative orders of magnitude of the variables involved in the dimensional form of Eqs. (5.9) and (5.10). We proceed to do so hereafter, by first only considering a stationary case for which $Q_{\text{drip}} = Q_{\text{drain}}$ in Sec. 4.3.1, then the sole drainage in Sec. 4.3.2, to finally consider the limit between the horizontal and inclined configurations in Sec. 4.3.3. Results are summarised in Sec. 4.3.4.

4.3.1 Stationary film thickness

We focus in this section on the stationary state of the film, such that we are in the situation described by Eq. (5.1). We designate by h_s this stationary film thickness. Both h^{max} and h^{min}, or a combination of them, could be used as approximations for h_s. The difference between h^{min} and h^{max} nevertheless emanates from the successive drops impacting the film, and it would make more physical sense to use h^{min} as the stationary film thickness, i.e., the thickness after some drainage has been established:

$$h_s = h^{\text{min}}.$$

We thus avoid taking into account the transient thickness decreases related to the successive drops introduced in the film. In caves, we were not able to distinguish whether we measured h^{min} or h^{max}. However, in regard of the rapid evolution of h following a drop addition in the lab experiments, we probably captured measurements closer to h^{min} than to h^{max}. By comparing the terms of Eq. (5.9) in terms of order of magnitude, we are able to estimate the evolution of h_s as a function of the drop inflow in two cases.

First, if we assume that the stalagmite surface is not very inclined, i.e., it is more or less horizontal with $\varphi \to 0$, we may assume that $\sin \varphi \approx 0$ and that $\cos \varphi \approx 1$. The drainage flux is given by $Q_{\text{drain}} = 2\pi \xi q$. We assume that $\partial_\xi h_s \simeq -h_s/\xi$. In practice, we would most likely have $\partial_\xi h_s \simeq -k h_s/\xi$, $k < 1$, but we do not have any physical clue allowing to asses k at this stage. Using the fact that the flow of incoming drops Q_{drip} given by Eq. (5.3) should be equal to the actual drainage flux Q_{drain}, we find that

$$h_s \sim \left(\frac{3\nu V_d}{2\pi g t_0} \right)^{1/4} \tag{5.15}$$

over almost horizontal surfaces. The stationary film thickness h_s is thus observed to decrease with decreasing inflow, i.e., with increasing dripping period t_0 or decreasing drop volume V_d. More viscous drops are also expected to spread less easily [7], yielding larger values of h_s at constant volume. We also note that if we had taken, e.g., $k \sim 1/3$ in $r \to r_{\text{sm}}$ as deduced from lab experiments (see Fig. 5.8 (a)), the above estimate of h_s would only be multiplied by 1.3. Our approximation of $\partial_\xi h_s$ further yields a stationary film thickness that does no longer vary with the position on the stalagmite and corresponds more or less to the spatially averaged stationary film thickness over an almost horizontal surface of radius ξ, but this behaviour was particularised to a specific case. We should, in fact, obtain that h_s varies with the thickness gradient. If we approximate our stationary film profile in space by, e.g., $h\,(1 - \xi/r_{\text{sm}})^{1/2}$, the resulting law would follow $h_s \sim (r_{\text{sm}}/\xi)^{1/4}$ at first order, i.e., it would increase with increasing stalagmite radius. This is not surprising considering that, if the stalagmite surface is almost flat, a larger stalagmite radius implies that a larger film volume is needed to cover the entire stalagmite surface. At constant drainage outflow Q_{drain}, the film thickness must indeed increase to compensate for the fact that r increases in the term $\partial_r h_s$. This variation is not linear considering that $q \sim h_s^4/r$ from Eq. (5.9) in the present approximation.

By contrast, for large stalagmite wall inclinations, we can write $(\partial_\xi h_s) \cos\varphi \ll \sin\varphi$. When referring to a large inclination, we always assume that the stalagmite wall is inclined downward, i.e., that the stalagmite is convex. With $Q_{\text{drain}} = 2\pi r(\xi) q$, we have

$$h_s \sim \left(\frac{3\nu V_d}{\pi g t_0 \xi \sin(2\varphi)} \right)^{1/3}, \quad \xi \gg \arctan(\partial_\xi h_s).$$
$$(5.16)$$

In a similar manner as in the above case, h_s increases with increasing inflow, but does not follow the same law regarding the dripping period. We indeed obtained $h_s \sim t_0^{-1/4}$ over almost horizontal surfaces, whereas we have $h_s \sim t_0^{-1/3}$ if the stalagmite inclination becomes predominant. Additionally, we note that h_s varies non-monotonously with $\xi \sin(2\varphi)$. Without particularising the stalagmite profile, we do not know the evolution of φ with ξ. If we had, for instance, a stalagmite profile η varying as $-kr$, we would obtain that φ is constant and that $\xi \sin(2\varphi)$ evolves as $-kr/\sqrt{(1+k^2)}$ (see Eq. (5.48) further in the text), such that the stationary film thickness h_s would be $\sim r^{-1/3}$. For stalagmite profiles involving higher powers of r, e.g., describing h_s analytically becomes tedious. Hence, we cannot easily draw conclusions regarding the effect of $\xi \sin(2\varphi)$ on h_s in a general case. We also noted that, in the above case for which the film thickness gradient predominates, the stationary film thickness should depend on the size of the stalagmite, r_{sm}, because a larger horizontal stalagmite surface requires a larger liquid volume to be entirely covered while maintaining a constant drainage outflow at the outer wall. On the other hand, in this case the film thickness in Eq. (5.16) seems to only depend on the stalagmite shape. Finally, if $\xi \sin(2\varphi)$ varies non linearly, it is possible for h_s to be larger away from the centre of the stalagmite surface than close to this latter, whereas in the horizontal case the film thickness should always be the largest at the centre, i.e., at the dripping point.

4.3.2 Sole drainage

We estimate once again the relative order of magnitude of the terms involved in both Eqs. (5.9) and (5.10), this time in a non-stationary regime, which thus corresponds to Eq. (5.2) with $Q_{\text{drip}} = 0$. We consider that $\partial_t h \sim h/t$, which implies only considering larger drainage times (over a few seconds) rather than the transient phase following directly a drop impact. First, regarding the almost perfectly horizontal plane, if we have the same hypotheses as above, such that $\partial_\xi h \sim h/r$ and $\partial_t h \sim q/r$ from Eq. (5.10), we find that

$$t \sim \frac{3\nu r^2}{2g h^3},$$
$$(5.17)$$

or, in other words, that $h \sim t^{-1/3}$ in this case. By combining this relation with Eq. (5.15) for $h = h_s$ and $t = t_0$, we are able to relate the radius of the liquid front advancing in response to a drop addition in the film as

$$r_{sr} \sim \left(\frac{2 V_d^3 g t_0}{3 \pi^3 \nu} \right)^{1/8}.$$
$$(5.18)$$

By contrast, when the inclination becomes predominant in Eq. (5.10), we have $\partial_t h \sim q/\xi$, which leads to

$$t \sim \frac{3\nu \xi}{g \sin\varphi \, h^2},$$
$$(5.19)$$

or $h \sim t^{-1/2}$ for convex stalagmites. By proceeding in the same manner as above and combining this relation with Eq. (5.16) for $t = t_0$, we find that the position of the liquid front is given by

$$\xi_{\mathrm{sr}} = \left(\frac{g \sin \varphi \, V_{\mathrm{d}}^2 t_0}{12 \nu \pi^2 \cos^2 \varphi} \right)^{1/5}. \tag{5.20}$$

The radius r_{sr} of Eq. (5.18) and the above curvilinear coordinate ξ_{sr} of Eq. (5.20) can both be seen as the frontier between the region where the effect of the successive, individual drops are felt in the film, and the region located sufficiently far away from the drop impact point for the effect of the drops not to be felt anymore. Hence, this radius is denoted r_{sr}, resp. ξ_{sr}, the steady/unsteady region limit radius, resp. curvilinear coordinate. Equation (5.18) also corresponds to both Huppert's solutions from Eq. (5.12) when replacing t by t_0 and Q_{drip} by V_{d}/t_0. Hence, the radius r_{sr} defined above lies at the crossover between the constant volume and constant flow rate solutions. This comes from our approximation of Q_{drip} by a discrete collection of drops.

4.3.3 Competing stalagmite inclination and film thickness gradient-related effects

We have defined two stalagmite profiles of interest in the above calculations: the (almost) perfectly horizontal case and the inclined (or convex) one, where each of the two terms of the right-hand side of Eq. (5.9) predominates over the other. We can compute a criterion for $\xi \varphi$ to discriminate these two cases, i.e., find beyond which value of $\xi \varphi$ the inclination of the stalagmite surface has a larger effect on q than the gradient of film thickness. We recall that, in stationary state, if $|\partial_\xi h| \ll \tan \varphi$, we find that h_{s} evolves as described by Eq. (5.16). We have previously considered that $|\partial_\xi \varphi|$ was negligible in regard of $1/h$, which may not be true in this case. If we take this into account in the calculation of $\partial_\xi h_{\mathrm{s}}$, we find that, in a general manner, the comparison $|\partial_\xi h_{\mathrm{s}}| \ll \tan \varphi$ turns into

$$\frac{1}{3} \frac{h_{\mathrm{s}}}{\xi} \left(1 + 2\xi \cot \left(2\varphi \right) \left(\partial_\xi \varphi \right) \right) \ll \tan \varphi. \tag{5.21}$$

For a stalagmite with a rather smooth convex profile $\eta(r) = -kr^2$, the change in the inclination φ with respect to ξ takes the non-trivial expression $\partial_\xi \varphi = -2k \cos \varphi / \left(1 + 4k^2 \xi^2 \cos^2 \varphi \right)$. Hence, no easily derivable analytical solution can be obtained by inserting another profile than a constant inclination into Eq. (5.21). To understand better the above relation, we can assume that, at first order for relatively moderate inclinations, we have a profile close to the constant inclination case with $\partial_\xi \varphi \sim \varphi/\xi$ and that we can also use the limit for which $\sin \varphi \simeq \varphi$ and $\cos \varphi \simeq 1$. For small values of φ close to the centre of the stalagmite surface, we may indeed consider the order of magnitude of $h_{\mathrm{s}}/\xi \lesssim h_{\mathrm{d}}/r_{\mathrm{d}} = 10^{-2}$. Hence, the stalagmite elevation φ should verify $\varphi \gg 0.2°$, such that a stalagmite inclined by a few degrees at about 1 cm from its axis of symmetry can already be considered as close to the case where the inclination of the stalagmite has a non-negligible effect on q. Approximating $\sin \left(\pi/6 \right)$ by $\pi/6$, e.g., further only yields a 5 %-error, whereas this inclination can be viewed as large close to the centre of the stalagmite top surface. We therefore find that the condition for which the overall stalagmite inclination dominates, described by Eq. (5.21), becomes[4]

$$\xi \varphi \gg \left(\frac{4 \nu V_{\mathrm{d}}}{9 \pi g t_0} \right)^{1/4}. \tag{5.22}$$

If we insert the numerical values $V_{\mathrm{d}} = 8 \times 10^{-8} \ \mathrm{m}^3$ and $t_0 = 1 \ \mathrm{s}$ in the above formula, we find that $\xi \varphi$ should verify $\xi \varphi \gg 2 \times 10^{-4} \ \mathrm{m}$ for the stalagmite surface inclination to have a greater effect

---

[4]Note that φ is expressed in radians.

on drainage than the film thickness gradient. If the stalagmite overall inclination is about 0.5°, the condition for the effect of the inclination to dominate over the film thickness gradient in the expression of the flux q from Eq. (5.9) becomes $\xi \gg 2.3\,\text{cm}$, i.e., the inclination is only felt far away from the spreading radius of the drops, r_d. On the other hand, if we take $\varphi = 10°$, the inclination becomes predominant as soon as $\xi \gg 1\,\text{mm}$, so that it should already be the case when $\xi \simeq r_\text{d}$. Although it does not yield an exact angle φ separating the perfectly horizontal and inclined cases, what we infer from Eq. (5.22) is that there exists a limiting curvilinear coordinate value ξ beyond which the effect of the inclination on the film thickness becomes non negligible for a given inclination φ. For a very small inclination φ of the order of the degree and with a large inflow ($t_0 = 10\,\text{s}$ here), the inclination would only be felt at several centimetres from the centre of the stalagmite. If the inflow was decreased with, e.g., $t_0 = 100\,\text{s}$, for $\varphi = 0.5°$, we find that the condition from Eq. (5.22) would become $\xi \gg 7\,\text{mm}$.

4.3.4 Summary

A few key elements emerge from the above scaling analysis that we conducted. We can consider two limit cases displaying distinct features: (i) the almost perfectly horizontal plane, corresponding to the case for which $\varphi \to 0$ in all points of the stalagmite domain, (ii) the very inclined/convex stalagmite, which we can already consider if the overall wall inclination is of the order of 10° to 20° close to the centre. In the perfectly horizontal case, we note that the film thickness gradient $\partial_\xi h$ has the greatest effect on drainage, while the inclination of the stalagmite surface under the film predominates when the condition from Eq. (5.21) is met, which reduces to Eq. (5.22) if the stalagmite profile remains smooth and moderately inclined ($\lesssim 30°$ close to the centre). We recall the scalings obtained in both these cases in Tab. 5.1 below. In the perfectly horizontal case, the stationary film thickness should depend at first order on the size of the stalagmite r_sm, while such kind of dependence disappears in the very inclined case. We also find two different evolutions of the stationary film thickness with the drop inflow, materialised by the drop dripping period t_0. Similarly, during the drainage phase (although not shortly after the drop inflow interruption), we obtain two different scalings with time t for the perfectly horizontal and very inclined cases. From there, we find that there exists either a radius (horizontal) or a curvilinear coordinate (inclined) delimiting the frontier between the unsteady and steady regions of the film in space. These latter may be viewed as regions where the successive drop impacts are felt in the film, causing its thickness to oscillate, or, respectively, where they have no substantial effect such that the film thickness remains constant in time at a given position.

	Perfectly horizontal	Very inclined
Regime	$\partial_\xi h \gg \tan\varphi$	$\partial_\xi h \ll \tan\varphi$
Stationary film thickness	$h_\text{s} \sim r_\text{sm}^{1/4}\, t_0^{-1/4}$	$h_\text{s} \sim t_0^{-1/3}$
Sole drainage	$h \sim t^{-1/3}$	$h \sim t^{-1/2}$
Steady/unsteady frontier	$r_\text{sr} \sim t_0^{1/8}$	$\xi_\text{sr} \sim \varphi^{1/5}\, t_0^{1/5}$

Table 5.1: Summary of scalings derived from Eqs. (5.9) and (5.10). Condition indicating whether we consider the very small or very large inclination approximation, as discussed in Eqs. (5.21) and (5.22). Stationary film thickness scalings, coming from Eqs. (5.15) and (5.16). Sole drainage behaviour of the film thickness with time, from Eqs. (5.17) and (5.19). Steady/unsteady frontier region radius and curvilinear coordinate described by Eqs. (5.18) and and (5.20), respectively.

4.4 Closed-form solutions

The partial differential equations derived in Sec. 4.2 are non-linear and require to be solved numerically. We may nevertheless deduce from these equations a few elements regarding the spatial evolution of the film thickness in a stationary state. In particular, we review the simple case of a cone of constant opening angle in Sec. 4.4.1, which allows us to further develop an adequate boundary condition to our problem. We also consider the film spatial evolution over a perfectly horizontal plane in Sec. 4.4.2. This section is completed by a small perturbation analysis of the film in stationary state over a perfectly horizontal plane in Sec. 4.4.3.

4.4.1 Evolution of the film thickness over a cone of constant opening
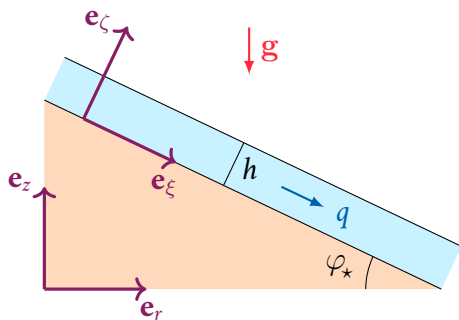
Figure 5.13: Stalagmite surface corresponding to a cone of constant opening angle $\varphi_\star$, covered by a film of thickness h, with axisymmetric coordinate system (r, z) and flux q.

We first consider the situation of Fig. 5.13, where a film of supposedly constant flux q flows over a cone with a constant opening angle $\varphi_\star$. By contrast with a plane in a Cartesian coordinate system, a film of uniform thickness on a conical substrate is not a solution to the steady drainage equations, such that, in stationary state, $h(\xi)$ should decrease with ξ. The differential equation that provides this steady shape[5] has no existing closed-form solution. Nevertheless, as long as the film remains thin and the surface sufficiently inclined, i.e., as long as $|\partial_\xi h| \ll \tan \varphi$ (see Sec. 4.3.3), the first term of the right-hand side in Eq. (5.9) is negligible by comparison with the second term. If we particularise Eq. (5.9) to the case of an inclined cone of constant opening angle, we therefore find that

$$q = \frac{g}{3\nu} h_s^3 \sin \varphi_\star,$$
(5.23)

is a valid approximation of the steady-state solution. We have already outlined the region where the flux q can be viewed as in steady-state in Sec. 4.3.2, which we will also obtain in the upcoming Sec. 4.4.3 through a linear stability analysis. We had also already determined how Eqs. (5.9) and (5.10) changed if we considered the limiting case of an inclined stalagmite, which lead under certain approximations to the scaling of Eq. (5.16). Consequently, an estimation of the stationary film thickness spatial evolution over a cone of constant opening angle $\varphi_\star$ is given by

$$h_s \simeq \left(\frac{3\nu V_d}{\pi g t_0 r \sin \varphi_\star} \right)^{1/3},$$
(5.24)

where we have used the fact that, for a constant opening angle $\varphi_\star$, $r = \xi \cos \varphi_\star$. If $\varphi_\star \to \pi/2$, the radial flux q reaches its maximum while the film thickness is minimum at a given radial position r. Because stalagmites considered as perfectly horizontal lead to an indeterminate definition, as we will review in the following section, we will make use of the condition developed for the cone in this section to approximate the drainage flux at the outer edge of perfectly horizontal stalagmites.

---

[5]A Chini equation [1].

4.4.2 Constant pointwise inflow and stationary film thickness

If we consider that the stalagmite surface is a perfectly horizontal plane, as depicted in Fig. 5.14, the curvilinear coordinates (ξ, ζ) simply coincide with the axisymmetric coordinates (r, z), and the velocity field reduces to $\mathbf{u} = u\mathbf{e}_r$. The flux $\mathbf{q} = q\mathbf{e}_r$ still corresponds to the integral of u along the entire film thickness and is also parallel to the stalagmite surface. In a stationary state for which $\partial_t h_s = 0$, we could consider that, instead of being progressively filled by a succession of drop impacts, the film is rather

Figure 5.14: Case of an inflow of flux q_0 and radius r_0, continuously feeding a stationary film of thickness h_s over a stalagmite of radius r_{sm}.

fed by an equivalent laminar jet of constant flux q_0, spread on a radius r_0. This situation is illustrated in Fig. 5.14. At the same time, the film should still be depleted through drainage at the edge of the stalagmite. When the two processes balance each other out, we find that

$$q = \frac{q_0 r_0}{r}. \tag{5.25}$$

and we obtain the corresponding stationary film thickness h_s evolution with r:

$$h_s(r) = \left[K - \frac{12\nu q_0 r_0}{g} \ln\left(\frac{r}{r_0}\right) \right]^{1/4}, \quad r > r_0, \tag{5.26}$$

where $K \in \mathbb{R}$ is a constant to determine. We could use as another boundary condition $h_s = 0$ in $r = r_{sm}$, but it would only be true when a film spreading on a dry stalagmite would be about to reach the edge of the stalagmite. The drainage occurring beyond the edge of the stalagmite would thus not be taken into account. A more general condition is the one developed in the former section, in which case we assume that the stalagmite edge is extended by a cone of constant opening $\varphi_\star$ for $r > r_{sm}$. Using Eq. (5.23) and assuming that q over the cone is uniform, with $q(r_{sm}) = q_0 r_0 / r_{sm}$, we get the following evolution for the stationary film thickness over the stalagmite:

$$h_s(r) = \left[\frac{12\nu q_0 r_0}{g} \ln\left(\frac{r_{sm}}{r}\right) + \left(\frac{3\nu q_0 r_0}{g r_{sm} \sin\varphi_\star}\right)^{4/3} \right]^{1/4}, \quad r_0 < r \leq r_{sm}, \, 0 < \varphi_\star \leq \frac{\pi}{2}. \tag{5.27}$$

We note here that the condition $h_s(r_{sm}) = 0$ would yield as a solution the first term appearing in the right-hand side main parenthesis, i.e., the case where the liquid front has spread until $r = r_{sm}$ but has not drained over the edge yet. The case of a perfectly flat plane for $\varphi_\star = 0$ is undefined because it would correspond to the final state of the aforementioned situation described by Huppert [116], where the front of the film keeps spreading over a boundless substrate, i.e., a time dependent solution. If we compare the terms from Eqs. (5.9) and (5.27), we note that there should exist a link between both equations. Going from one form to the other is not straightforward though as, in the present case, we particularised our physical domain to a flat stalagmite. Nevertheless, it is interesting to note that, in Eq. (5.9), the flux q was found to be a sum of terms proportional to h^4 and h^3, while in Eq. (5.27) above, the film thickness is a combination of terms of order $q^{1/4}$ and $q^{1/3}$.

The incoming flux q_0 is expressed as an area per unit of time. In terms of volume per unit of time, the volumetric flux, $q_0 r_0$, is equal to the drop inflow from Eq. (5.3), i.e.,

$$q_0 r_0 = \frac{V_d}{2\pi t_0}. \tag{5.28}$$
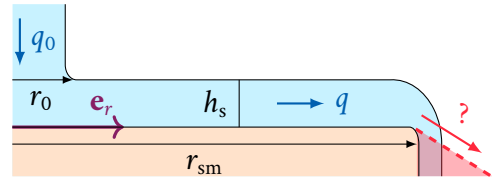
This approximation allows us to consider a constant inflow brought into the film. If we take, e.g., $t_0 = 10\,\text{s}$ and $V_{\text{d}} = 8 \times 10^{-8}\,\text{m}^3$, and introduce these values in Eq. (5.27) from a radius $r_0 = 1\,\text{cm}$ to $r_{\text{sm}} = 5\,\text{cm}$, we obtain the stationary film thickness evolution $h_s(r)$ shown in Fig. 5.15. Three cases are shown: $\varphi_\star = 90°$, $\varphi_\star = 10°$ and $\varphi_\star = 0.5°$. Additionally, the case corresponding to $h_s(r_{\text{sm}}) = 0$ is represented, i.e., the case where the liquid front has just spread until the edge of the stalagmite, for $r_{\text{sm}} = 5\,\text{cm}$, but also for $r_{\text{sm}} = 8\,\text{cm}$. We first note that the film thickness is larger at every point for a larger stalagmite radius, in accordance with our discussion on the scaling from Eq. (5.68). We also notice that, although $\varphi_\star = 10°$ should lead to a cone opening close to the horizontal, the corresponding film thickness curve is very close to the almost right-angle case ($\varphi_\star = 90°$). We indeed find that, in $r = r_0$, the difference in film thickness between the $\varphi_\star = 10°$ and $\varphi_\star = 0.5°$ cases with the curve at $\varphi_\star = 90°$ are of $0.1\,\mu\text{m}$ and $6.2\,\mu\text{m}$, respectively. Hence, it can be considered that the outer wall angle of the stalagmite has little effect on the film thickness close to the centre of the stalagmite. The solution only departs from the right-angle corner for very small $\varphi_\star$ values, as illustrated by the case of $\varphi_\star = 0.5°$. The film thickness beyond r_{sm} in this case would be of the order of the film lying on the stalagmite itself, with $h_s(r \geq r_{\text{sm}}) = 192\,\mu\text{m}$ while for $\varphi_\star = 10°$, resp. $\varphi_\star = 90°$, we only have $h_s(r \geq r_{\text{sm}}) = 70\,\mu\text{m}$, resp. $h_s(r \geq r_{\text{sm}}) = 40\,\mu\text{m}$. Finally, we note that the stationary film thickness described by Eq. (5.27) presents an inflection point in $r = r_{\text{infl}}$, which is illustrated by the coloured dashed lines in Fig. 5.15. The inflection point is located at

$$r_{\text{infl}} = r_{\text{sm}} \exp\left[\frac{g}{12\nu q_0 r_0}\left(\frac{3\nu q_0 r_0}{g r_{\text{sm}} \sin\varphi_\star}\right)^{4/3} - \frac{3}{4}\right], \tag{5.29}$$

which is about 2.36 cm for both $\varphi_\star = 90°$ and $\varphi_\star = 10°$ (the difference between the values taken by r_{infl} with a larger precision is 0.2 %). On the other hand, we observe once again that the case for which $\varphi_\star = 0.5°$ differs strongly from the two other ones since it corresponds to $r_{\text{infl}} = 2.64\,\text{cm}$.
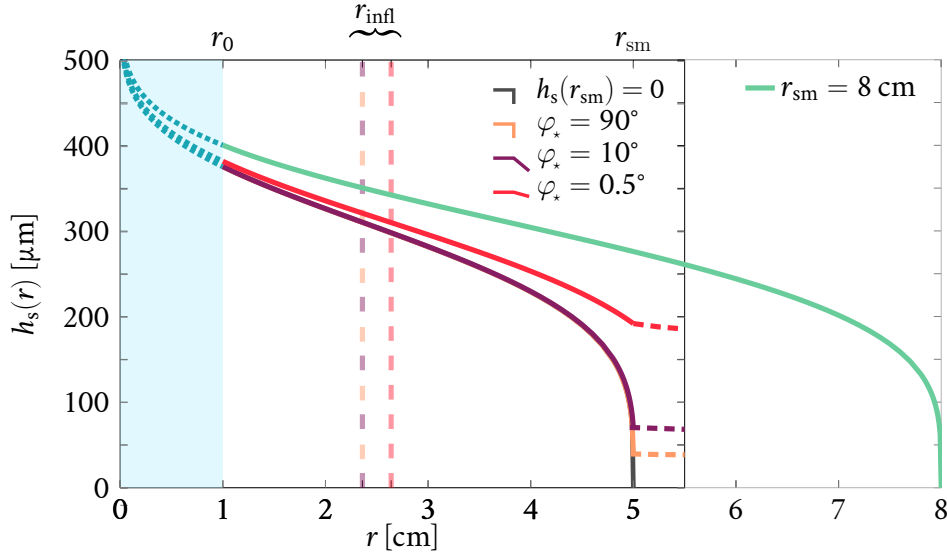
Figure 5.15: Examples of $h_s(r)$ profiles obtained by Eq. (5.27) for $t_0 = 10\,\text{s}$, $r_{\text{d}} = 2.7\,\text{mm}$, $r_0 = 1\,\text{cm}$ and $r_{\text{sm}} = 5\,\text{cm}$ in the main graph (i.e., surrounded by black axes). The secondary part of the graph (i.e., surrounded by light gray axes), for $r \geq 5.5\,\text{cm}$, shows another example of profile with the same parameters, except for the stalagmite radius set to $r_{\text{sm}} = 8\,\text{cm}$. In the main axes, the dark gray line shows the case $h_s(r_{\text{sm}}) = 0$ for $r_{\text{sm}} = 5\,\text{cm}$. In the secondary axes, the green line shows the case $h_s(r_{\text{sm}}) = 0$ as well for $r_{\text{sm}} = 8\,\text{cm}$. In the main axes, the orange, purple and red lines represent cases for which we impose a uniform flux q on a cone with constant opening angle extending the stalagmite surface, with $\varphi_\star = 90°$, $\varphi_\star = 10°$ and $\varphi_\star = 0.5°$, respectively. The dashed lines of the same colours, in the continuity of the solid lines, show the corresponding film thickness $h_s \sim r^{-1/3}$ for $r > r_{\text{sm}}$ in each case (see Eq. (5.23)). The transparent dashed vertical lines show the inflection point radius for both $\varphi_\star = 90°$ and $\varphi_\star = 10°$ (orange and purple line, $r_{\text{infl}} = 2.36\,\text{cm}$), and for $\varphi_\star = 0.5°$ (red line, $r_{\text{infl}} = 2.64\,\text{cm}$). The blue dotted lines represent the virtual extensions of the film thickness profiles for $r < r_0$ for all the curves represented in the main and secondary set of axes.

In order to understand the differences exhibited by the three curves, we can estimate the influence of the cone opening angle beyond r_{sm} on the stationary film thickness over the stalagmite. To achieve this, we approximate the thickness at a given radial position by a Taylor expansion around this position, $h_s(r)$, knowing the value of $h_s(r_\star)$ in $r = r_\star$. If we are only interested in the variations of h_s with the cone opening angle at the outer edge, $\varphi_\star$, we have, at first order, $h_s(r) \approx h_s(r_\star) + \left(\partial_{\varphi_\star} h_s(r_\star)\right) \Delta\varphi_\star$. The variations of the stationary film thickness with $\varphi_\star$ can be considered negligible if $\left|\left(\partial_{\varphi_\star} h_s(r_\star)\right) \Delta\varphi_\star\right| \ll h_s(r_\star)$. By assuming that $\Delta\varphi_\star \sim \varphi_\star$ given that, $\varphi_\star = 0 \; \forall r < r_{sm}$, we find that the condition[4]

$$\varphi_\star \gg \left[\frac{\nu V_d}{9 g t_0 r_{sm}^4 \left(\ln\left(\frac{r_{sm}}{r_\star}\right)\right)^3}\right]^{1/4} \tag{5.30}$$

must be ensured in order to neglect the variations of h_s with $\varphi_\star$. Using the same parameters as above ($t_0 = 10\,$s and $V_d = 8 \times 10^{-8}\,$m^3), for $r \to 0$, the above condition reads $\varphi_\star \gg 0.04°$ and the first term of Eq. (5.27) will always be predominant, which we have already observed from Fig. 5.15. If we now take, e.g., $r_\star = r_{sm}/2$ close to the inflection point radius r_{infl} for all three curves, we find that $h_s(r_\star)$ does not get affected by the cone opening angle $\varphi_\star$ when $\varphi_\star \gg 0.2°$. Looking at Fig. 5.15, we note that, in $r = r_{sm}/2$, the film thickness indeed departs from the right-angle corner solution ($\varphi_\star = 90°$) for $\varphi_\star = 0.5°$, which is of the same order of magnitude as our conditions gives, but not for $\varphi_\star = 10° \gg 0.2°$. A similar condition[6] as Eq. (5.30) can be particularised to $r = r_{infl}$. By taking $r_\star = 0.99 r_{sm}$, i.e., a radius very close to the edge (the case $r = r_{sm}$ yields an undetermination in Eq. (5.30)), we find that $\varphi_\star \gg 3.7°$ should be satisfied in order for the film thickness variations with $\varphi_\star$ to be negligible. In Fig. 5.15, we indeed witness that, for $\varphi_\star = 10°$, which is not extremely far from 3.7°, the film thickness is different from the right-angle corner case ($\varphi_\star = 90°$) in $r \approx r_{sm}$. Additionally, if we take the same drop volume but $t_0 = 0.1\,$s and $r_{sm} = 1.5\,$cm, i.e., a large inflow and small stalagmite radius, we find that the outer boundary condition becomes significant when $\varphi_\star < 2°$, which is still very low.

Although it is fairly simple, the above model captures the observations made both in the lab and in caves. We first note that the film is thicker at the center, close to the constant pointwise inflow position, and thinner on the outer edge of the stalagmite. Additionally, increasing the flux by reducing the dripping period t_0 between two drops increases the film thickness given that h_s is proportional to $q_0 r_0$ (or V_d/t_0) in Eq. (5.27). If we only focus on the leading term of Eq. (5.27) and take into account Eq. (5.28), we deduce that $h_s \sim t_0^{-1/4}$, as we had already found in Eq. (5.15). By keeping the remaining parameters constant, the dripping periods $t_0 = 1\,$s, 10 s and 100 s, e.g., correspond to film thicknesses $h_s(r = r_0)$ of 667 µm, 375 µm and 211 µm, respectively, which are in accordance with the former power law. However, due to its stationary nature, the model does

---

[6]Comparing the terms of Eq. (5.27) in $r = r_{infl}$, where the departure from the right-angle corner curve seems to become significant for small $\varphi_\star$, leads to the following criterion: if the condition

$$\varphi_\star \gg \arcsin\left[\frac{1}{r_{sm}}\left(\frac{8}{9}\frac{\nu V_d}{g t_0}\right)^{1/4}\right] \tag{5.31}$$

is met, then the outer boundary condition should have negligible effect on the appearance of the curve $h_s(r)$. This condition is similar to the one obtained in Eq. (5.30) because it yields $\varphi_\star \gg 0.2°$ in $r = r_{infl}$, exactly as in $r = r_{sm}/2$ with the more general condition from Eq. (5.30). The halfway radius $r_{sm}/2$ is indeed very close to the three inflection point radii. Although the above relation is specific to r_{infl}, we did not need to make use of any approximation to derive it.

obviously not capture the effect of the successive drop impacts on the film thickness, which has demonstrated to be quite important in Sec. 3. It also fails at grasping the potential importance of the stalagmite shape underneath the film, which was shown to differ for various stalagmites from caves. We may nevertheless point out that the criterion developed in Eq. (5.30) to delimit upon which value of $\varphi_\star$ the outer cone boundary condition affects the film thickness at a given radial position $r_\star$, yields similar results as our scaling analysis from the previous section (see Eq. (5.22)). Close to the edge of the stalagmite, an angle $\varphi_\star \sim 10°$ already gives a solution quite close to the right-angle corner ($\varphi_\star = 90°$). Assessing the effects on subsequent film thickness variations of (i) the inclusion of the drops in the film and (ii) of the detailed stalagmite shape, i.e., not only of the overall inclination of the stalagmite wall, will thus be our main focus in the forthcoming numerical approach from Sec. 4.5.

4.4.3 Linear stability analysis of the film interface

Before using numerical tools to solve Eqs. (5.9) and (5.10), we complete our theoretical study by performing a linear stability analysis of the film thickness spatial solution. We have indeed derived scalings enabling to retrieve the frontier between steady and unsteady regions of the film during the late part of drainage (i.e., above a few seconds, see Sec. (4.3.2)), but not in the transient case following the direct introduction of a drop into the film. We thus aim in this section at finding when the effect of the drop in the film is temporally damped, and compare the timescale obtained to our range of dripping period, t_0. If the drop takes less than 100 ms to crush into the film in the absence of splash (see Ch. IV and Appendix B.4), it might not be the case for the associated capillary waves propagating around the impacted area. The following linear stability analysis should also allow us to verify whether or not we can approximate the flux q as constant over a certain distance from the stalagmite centre, and use as the approximation made over a cone of constant opening angle as an outer boundary condition for perfectly horizontal stalagmites.

If a film lying on a flat substrate is at steady-state, the film thickness, $h_s(r)$, verifies $\partial_t h_s = 0$. We introduce small perturbations around this stationary film thickness as $h = h_s + \varepsilon(r, t)$. We assume that all powers involving ε and its spatial derivatives $\partial_r \varepsilon$ and $\partial_{rr} \varepsilon$ are of second order and can therefore be neglected, i.e., we do not consider the terms involving $\varepsilon^2, \varepsilon^3, (\partial_r \varepsilon)^2, \varepsilon(\partial_r \varepsilon)$ nor $\varepsilon(\partial_{rr}\varepsilon)$. We find that the perturbation ε follows

$$\partial_t \varepsilon \approx A(r)\partial_{rr}\varepsilon + B(r)\partial_r\varepsilon + C(r)\varepsilon, \tag{5.32}$$

where the coefficients appearing in the equation correspond to the functions

$$A(r) = \frac{gh_s^3}{3\nu}, \tag{5.33}$$

$$B(r) = \frac{g}{3\nu}\left(3h_s^2(\partial_r h_s) + \frac{h_s^3}{r}\right), \tag{5.34}$$

$$C(r) = -\frac{gh_s}{\nu}(\partial_r h_s)^2. \tag{5.35}$$

In the absence of drops feeding the film periodically, the only possibility for the film to be in stationary state is to remain uniform over the entire stalagmite surface, i.e., $h_s(r) = h_s \, \forall r$. The former

functions thus reduce to

$$A = \frac{gh_s^3}{3\nu}, \tag{5.36}$$

$$B(r) = \frac{A}{r}, \tag{5.37}$$

$$C = 0, \tag{5.38}$$

and Eq. (5.32) becomes

$$\partial_t \varepsilon = A \partial_{rr} \varepsilon + \frac{A}{r} \partial_r \varepsilon, \tag{5.39}$$

which can be solved by separation of variables. Introducing $\varepsilon(r,t) = R(r)T(t)$, we find, on the one hand, that

$$T(t) = T_0 \, e^{-t/\tau}, \tag{5.40}$$

where we impose $\tau \in \mathbb{R}$ to ensure that the perturbations are damped. As aforementioned, we are only interested in comparing the perturbation damping time associated with, e.g., the introduction of the drops in the film, to the dripping period of these drops. This leads to the following equation for $R(r)$:

$$A R'' + \frac{A}{r} R' + \frac{1}{\tau} R = 0. \tag{5.41}$$

The former relation can also be written as

$$r^2 R'' + rR' + \left(\frac{r^2}{A\tau} + n^2 \right) R = 0, \tag{5.42}$$

where we recognise the Bessel equation of order $n = 0$. The general solution to this equation is given by [1]

$$R(r) = K_1 \, \mathcal{J}_0 \left(r\sqrt{\frac{1}{A\tau}} \right) + K_2 \, \mathcal{Y}_0 \left(r\sqrt{\frac{1}{A\tau}} \right), \tag{5.43}$$

where $\mathcal{J}_0$ and $\mathcal{Y}_0$ are the Bessel functions of first and second kinds, respectively. Because the functions $\mathcal{Y}_n$ are singular at the origin, we must impose $K_2 = 0$. Gathering results from Eqs (5.40) and (5.43), we end up with the following solution for the film thickness perturbation $\varepsilon(r,t)$:

$$\varepsilon(r,t) = \sum_k E_k \, \mathcal{J}_0 \left(r\sqrt{\frac{\nu}{gh_S^3 \tau_k}} \right) e^{-t/\tau_k}, \tag{5.44}$$

where the E_k are the amplitudes corresponding to the different modes k of the perturbations. The associated damping times of the perturbations are the τ_k.

We can replace r by specific values in Eq. (5.44) in order to find the corresponding damping times of the first few modes of oscillations k, τ_k, leading to the first zeros of $\mathcal{J}_0$, and compare this to our dripping period t_0. Film thickness perturbations associated with $r = R_d$, the drop radius (2.7 mm), and relative to the first mode $k = 1$, are damped within 160 ms and in less than 30 ms for the subsequent modes, which is less than the impact time itself. In Ch. IV, we had also found that capillary ripples provoked in the film by the drop slowing down during impact are usually damped after $\lesssim$ 200 ms depending on the impact velocity. It is not surprising to obtain similar orders of magnitude considering that results from Ch. IV come from a linear analysis of the lubrication theory [38, 120], although this analysis did not include gravity as it is the case above (Jalaal et al. [120] actually focus their study on the deposition of a drop on a thin film, similarly to our

lab experiments). The damping time of the first mode of perturbation associated with $r = r_\mathrm{d}$, the puddle spreading radius at impact (1 cm, see Fig. 5.12), is about 2 s, which can be compared to the time around which the transition between the early and late parts of the drainage phase arises (see, e.g., Fig. 5.6). Past the first few seconds during which the decrease in thickness corresponds to the last drop impact in the film, the drainage was indeed observed to occur at a much slower pace in all the curves from Sec. 3. This transition usually occurs a little later than 2 s and should correspond to the aforementioned viscous time $t_\nu \simeq h^2/\nu$ (see Sec. 2.3 from Ch. IV and auxiliary sheet), equal to about 5 s. The perturbations relative to $r = r_\mathrm{d}$ that could be present at the film surface should simply be damped before the drop spreading in the film stops due to viscous drag. Finally, perturbations associated with the typical stalagmite size should thus be damped after an even longer time. We find for, e.g., $r = 7.5$ cm in the case of Lab01, that τ_k is of the order of 2 min.
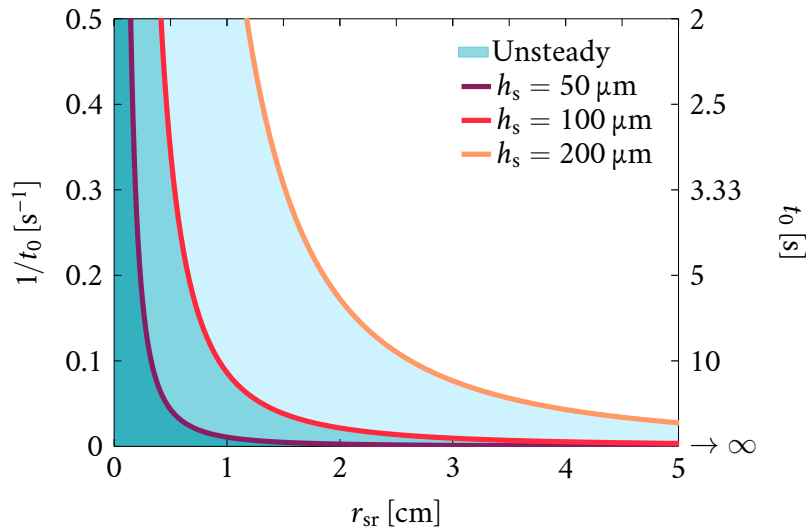
Figure 5.16: Stationary radius r_sr defined by Eq. (5.45) as a function of the dripping frequency $1/t_0$ (the right ordinate axis shows the corresponding dripping period t_0), for $k = 1$. Three examples are shown: for $h_\mathrm{s} = 50\,\mu$m (purple curve), $h_\mathrm{s} = 100\,\mu$m (red curve) and $h_\mathrm{s} = 200\,\mu$m (orange curve). The blue regions indicate the unsteady parts where considering a domain size $r < r_\mathrm{sr}$ is not a valid assumption as perturbations related to the corresponding t_0 value can still be felt in the film. The film thickness should remain unperturbed by the successive drop impacts outside of these regions, for $r > r_\mathrm{sr}$.

We also reckon that the perturbations should be damped when the exponential in the expression of Eq. (5.44) becomes negligible, i.e., when its argument $-t/\tau_k \to -\infty$. Perturbations associated with the dripping period between drops are such that $\tau_k = t_0$. The drainage timescale of the film having a stationary thickness h_s, and considered at a certain measuring distance r_sr from the drop dripping point, is given by $t_\mathrm{d} = \nu r_\mathrm{sr}^2/(gh_\mathrm{s}^3)$ (see Eq. (5.14)). To ensure that perturbations associated with the dripping period are damped at a distance r_sr from the dripping point of the drops, we therefore need $t_\mathrm{d}/t_0 \gg 1$. In other words, we can define

$$r_\mathrm{sr} = k \left(\frac{gh_\mathrm{s}^3 t_0}{\nu} \right)^{1/2} \tag{5.45}$$

as the boundary beneath which the perturbations associated with the dripping period t_0 and film thickness h_s should still be felt. The factor k is a coefficient that should depend on the stalagmite shape, as the two scalings from Eqs. (5.18) and (5.20) indicated. Far beyond the above value of r_sr, i.e., $r \gg r_\mathrm{sr}$, we can consider that we are sufficiently away from the dripping point for the film to no longer be perturbed by the successive drop impacts. Hence, the stationary thickness boundary

condition derived from the cone (Eq. (5.23)) applies for $r \gg r_{sr}$. The relation from Eq. (5.45) should be considered with care as we have defined it assuming that the film had a uniform thickness in space. It has indeed been shown in Fig. 5.15 that this is not the case. Nevertheless, we see in Eq. (5.45) that r_{sr} decreases with decreasing film thickness h_s. The film can further be expected to become thinner around the outer edge of the stalagmite in most cases (see Fig. 5.15), thus applying the condition from Eq. (5.45) should be safe enough in practice. We should still remain careful if the thickness on the outer edge of the stalagmite becomes larger than at the centre (see Eq. (5.16)). We report in Fig. 5.16 examples of the curve from Eq. (5.45) for $k = 1$ and $h_s = 50\,\mu$m, $h_s = 100\,\mu$m and $h_s = 200\,\mu$m. We note that, for $t_0 = 10$ s and $h_s = 100\,\mu$m, e.g., the stationary radius is $r_{sr} \approx 1$ cm, which is the order of the drop spreading radius r_d. In Fig. 5.8 (a), for $t_0 \simeq 1$ s on Lab01 (which is convex but with a top surface quite flattened out, see Fig. 5.9), we had also noted that film thickness variations were already quite damped at a distance $\Delta d = 5$ cm and almost non existent at $\Delta d = 7$ cm. Our measurements taken at $\Delta d \leq 1$ cm, on the other hand, clearly fell within the unsteady region. Hence, the stationary radius r_{sr} associated with Lab01 should lie somewhere between these values, and should be smaller than the average top radius r_{sm} of Lab01. Because h_s is related to t_0 (see Eqs. (5.15) and (5.16) and Fig. 5.24 (b) further in the text), there should exist a unique value of r_{sr} associated with a given stalagmite, which should be contained within the value of the coefficient k appearing in Eq. (5.45). Finally, we note that the condition from Eq. (5.45) is also the same as the one developed in Eq. (5.18) by using as a drop volume approximation $V_d \simeq \pi r_{sr}^2 h_s$. This yields $r_{sr} = (2h_s^3 g t_0 / 3\nu)^{1/2}$, with $\sqrt{(2/3)} = 0.82$.

4.5 Numerical approach

In the former sections, we have reduced the system of partial differential equations describing the drainage of the thin film lying over a stalagmite of general surface, i.e., Eqs. (5.9) and (5.10), to a set of scalings in Sec. 4.3. We also considered the particular case of a perfectly horizontal plane for which a closed-form solution exists in Sec. 4.4. However, as there is no known analytical solution to the system constituted of Eqs. (5.9) and (5.10) in an unsteady case, we solve it numerically by implementing a scheme based on finite volume formalism. If we consider the stalagmite to be axisymmetric, the problem is one-dimensional in space. Using the nondimensionalization presented in Sec. 4.2.2 (which also involved $q = q' g h_d^4 / (\nu r_d)$), we recall the nondimensional version of Eqs. (5.9) and (5.10):

$$\partial_t h' = -\frac{1}{r'}\partial_{\xi'}\left(q'r'\right) , \tag{5.46}$$

$$q' = -\frac{(h')^3}{3}\left(\partial_{\xi'}h'\cos\varphi - \left(\frac{r_d}{h_d}\right)\sin\varphi\right) . \tag{5.47}$$

According to our observations from Appendix B.4 and the scaling defined in Sec. 4.2.2, we also nondimensionalise the stalagmite elevation coordinate as $\eta = \eta' h_d$. For the sake of simplicity, the variables presented in the remaining of this section will be written without the prime notation (x and not x') but correspond to nondimensional variables as per defined above. We compute the flux q through Eq. (5.9) $\forall\xi$, which requires the knowledge not only of the current film thickness h, but also of the curvilinear coordinate ξ and local curvature φ. We then update the film thickness h at the next time step using Eq. (5.10), except at the times of drop impacts where we also consider a source term, as detailed in the following subsection. We therefore need to discretise the values of h, q, r, ξ, and φ, the two latter depending directly on $\eta(r)$. From Fig. 5.11, the local inclination

of the stalagmite φ is indeed found to be $\varphi = \arctan\left(\partial_r \eta\right)$ while ξ is the arc length of the curve $\eta(r)$, i.e.,

$$\xi(r^\star) = \int_0^{r^\star} \left(1 + (\partial_r \eta)^2\right)^{1/2} \, \mathrm{d}r. \tag{5.48}$$

As shown in Fig. 5.17, we start by defining the stalagmite profile $\eta(r)$ with a large precision (10^4 sample points). The maximum height of the stalagmite is H and the coordinate r goes from 0 to R, the horizontal truncation of our domain, as illustrated in Fig. 5.11. We consider the three shapes already described in Ch. II, i.e., flat, convex and concave stalagmites. These shapes were commonly described by Eq. (2.1), which we recall hereafter:

$$\eta(r\,;S,\Psi) = S r^2 \left(\Psi - r^2\right), \, r \leq R, \tag{5.49}$$

with Ψ the shape factor and S the scaling of the stalagmite profile. The values of S and Ψ measured on the stalagmites from our dataset are presented in Tab. 2.2 from Ch. II. The physical truncation of the domain chosen when measuring Ψ and S was 5 cm, which thus corresponds to $R = 5$ in nondimensional form. We obtained closed-form solutions of the drainage equation in the case of a perfectly horizontal stalagmite of given radius in Sec. 4.4.2. In the following numerical simulations we will approximate flat stalagmites by the degenerate case $\eta = 0$, $r \leq R$, with R becoming the non-dimensional stalagmite radius. The numerical simulations conducted for perfectly horizontal stalagmites will thus include an additional boundary condition that we described in Sec. 4.4.1 and that we will discretise in Sec. 4.5.1. However, we will keep our measurements for Ψ and S for the stalagmites from our dataset classified as flat because actual stalagmites are not as perfectly horizontal as considered in Sec. 4.4.2.
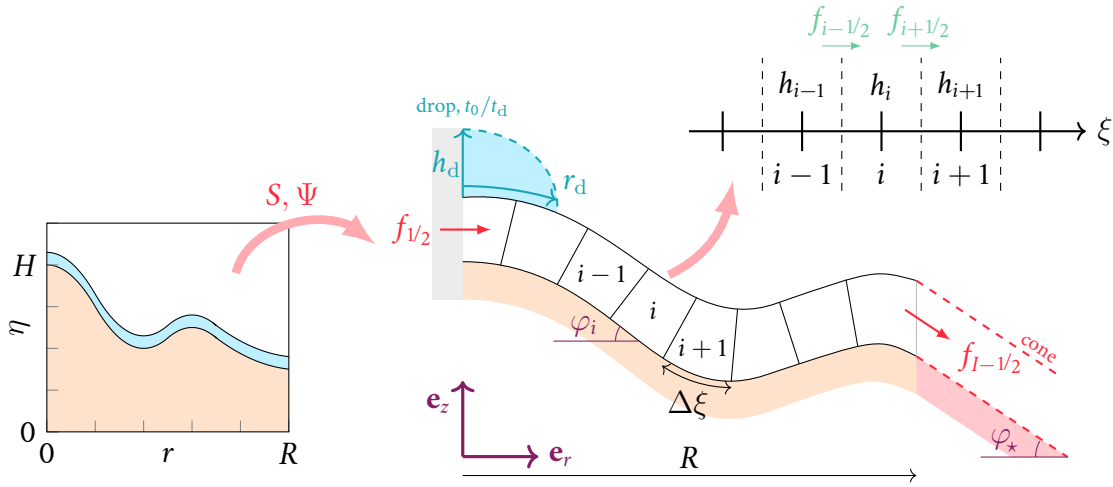
Figure 5.17: Illustration of the numerical discretisation: from a defined stalagmite shape $\eta(r)$ with associated scale and shape parameters S and Ψ, we discretise the domain from $r = 0$ to $r = R$ into $(I+1)$ cells of size $\Delta\xi$. Cell-centered values of, e.g., the local angle φ_i are computed in the middle of the cells while fluxes f_i are computed at the cell faces, i.e., between two adjacent cells. The boundary condition applied in $r = 0$ is a null flux in the upwind direction, while we use the solution of the cone of constant opening angle $\varphi_\star$ at the outer boundary. Drops are added into the film at the numerical dripping period corresponding to t_0/t_{d}.

We then define a grid containing I cells of width $\Delta\xi$ along the curvilinear coordinate ξ, surrounded by $(I+1)$ faces, as depicted in Fig. 5.17. The grid point ξ_i corresponds to the centre of the cell i. We sample the radial coordinate r into another grid of I points by interpolating the positions of the corresponding values of ξ_i in the originally large vector ξ. For flat stalagmite profiles, the discretisation of the radial coordinate r will result in a r_i vector such that $r_i = i\Delta r$. However, for

curved profiles, the discrete vector r_i will have variable step sizes $\Delta r_i = r_{i+1} - r_i$, $i = 0, \ldots, I - 1$. Nevertheless, given the order of magnitude difference between h_d and r_d, the Δr_i are in practice very close to each other. The discretisation could be done using an opposite approach where the r_i would always be equally distant from each other while the ξ_i would be unequally spaced, but the derivatives appearing in Eqs (5.9) and (5.10) depend on ξ and not on r. We therefore expect the discrete derivatives with ξ to be numerically more stable if $\Delta \xi$ is kept constant. In the same manner, we interpolate the value of φ_i at the corresponding ξ_i positions.

We also denote the non-dimensional film thickness h_i^n at the centre of cell i, $i = 0, \ldots, I$, and at a discrete time $n \geq 0$. As illustrated in the stencil from Fig. 5.17, the discrete flux $q_{i+1/2}^n$ at time step n corresponds to the flux between two adjacent cells i and $i + 1$ and is therefore evaluated as

$$q_{i+1/2}^n = \frac{1}{3} \left(h_{i+1/2}^n \right)^3 \left[\left. (\partial_\xi h) \right|_{i+1/2} \cos \varphi_{i+1/2} - \left(\frac{r_\mathrm{d}}{h_\mathrm{d}} \right) \sin \varphi_{i+1/2} \right] , \tag{5.50}$$

where the $i \pm 1/2$ indices correspond to the faces surrounding cell i. We proceed by evaluating q at the faces and not at the centre of the cell because of the h^3 term which multiplies the entire right-hand side of Eq. (5.50). If we tried to estimate both q and h at the centre of cell i, we would only get odd or even indices in our numerical approximation of the equation. Hence, a null thickness would automatically cancel the flux in cell i as well. The use of the $i \pm 1/2$ indices is a solution to the odd–even decoupling problem [112] and implies the definition of h and q at different grid points. However, in Eq. (5.50) above, the value of $h_{i+1/2}$ at the face is unknown. Nevertheless, in a thin film approximation, h is not expected to vary strongly in between two adjacent cells. We may thus approximate the film thickness at the face as the average between the two known thicknesses at the centre of cells i and $i + 1$, which yields

$$h_{i+1/2} = \frac{1}{2} \left(h_i + h_{i+1} \right) , \quad i = 0, \ldots, I, \tag{5.51}$$

where the same operation can be applied to the cell-centered local inclination of the stalagmite φ to obtain $\varphi_{i+1/2}$. The above face value corresponds to the value evaluated at $\xi_i + \Delta \xi/2$. We additionally need the value of the radial coordinate r at this face, which is calculated as $r_i + \Delta r_i/2$ given that the r_i are not equidistant[7]. Evaluating the flux q through Eq. (5.50) also requires to compute the derivative of h with respect to the curvilinear coordinate ξ at the face between two adjacent cells, which we achieve using a central scheme as

$$\left. (\partial_\xi h) \right|_{i+1/2} \approx \frac{h_{i+1} - h_i}{\Delta \xi} . \tag{5.52}$$

Updating h over time using Eq. (5.46) requires to compute the divergence of the product of the flux and the radial coordinate. We thus also define f at the face between adjacent cells i and $(i + 1)$, at time step n, as the following quantity: $f_{i+1/2}^n = q_{i+1/2}^n \, r_{i+1/2}$. The divergence of qr over cell i can therefore be estimated as

$$\left. \partial_\xi (qr) \right|_i \approx \frac{f_{i+1/2} - f_{i-1/2}}{\Delta \xi} . \tag{5.53}$$

From Eq. (5.10), we also define F in the centre of cell i as

$$F(h_i) = \frac{1}{r_i} \left(\frac{f_{i+1/2} - f_{i-1/2}}{\Delta \xi} \right) . \tag{5.54}$$

---

[7]As a remark, r_i is not exactly equal to $r(\xi_i)$ because of the non-linearity of the equations, but it should yield a sufficiently close approximation. The r_i could also be sampled at the mid-points.

Finally, the time derivative of h is evaluated at time step n using a fourth-order Runge-Kutta method, which yields

$$h^{n+1} \approx h^n + \frac{\Delta t}{8} \left[k_1 + 3 k_2 + 3 k_3 + k_4 \right], \tag{5.55}$$

where Δt is the fixed numerical time step and

$$k_1 = F\left(h_i^n\right), \quad k_2 = F\left(h_i^n + \Delta t \frac{k_1}{3}\right),$$
$$k_3 = F\left(h_i^n + \Delta t \left(\frac{-k_1}{3} + k_2\right)\right), \quad k_4 = F\left(h_i^n + \Delta t \left(k_1 - k_2 + k_3\right)\right). \tag{5.56}$$

4.5.1 Boundary conditions

Because Eq. (5.9) is parabolic (see Sec. 4.4), we need one initial condition and two boundary conditions, one at each end of our spatial domain. In the following, the film will always be initialised at zero everywhere until drops start to be added over the stalagmite surface, i.e., we start from a dry stalagmite. In this case, the system formed by Eqs. (5.9) and (5.10) becomes locally hyperbolic because it describes a front advancing over a solid surface, as we discussed in Sec. 4.2.1, hence there is no need for a second boundary condition. Given the axisymmetric configuration of the system, we will assume that at the centre of the stalagmite, corresponding to the first cell of the spatial domain, the drainage can only occur in the upwind direction, as illustrated in Fig. 5.17. This first cell, in particular, is always considered as perfectly horizontal no matter the shape of the stalagmite. We have $h_{1/2}^n = \left(h_0^n + h_1^n\right)/2$ and $f_{1/2}^n = q_{1/2}^n \Delta\xi/2$, where the flux at the outer face of the first cell writes as

$$q_{1/2}^n = -\frac{1}{3} \left(h_{1/2}^n\right)^3 \left(\frac{h_1^n - h_0^n}{\Delta\xi}\right). \tag{5.57}$$

Using finite difference to approximate the time derivative with $F(h_0^n) = 2/\Delta\xi \left(2 f_{1/2}^n / \left(\Delta\xi/2\right)\right)$, the boundary condition in $i = 0$ reads as

$$h_0^{n+1} = h_0^n - \frac{4\Delta t\, q_{1/2}^n}{\Delta\xi}. \tag{5.58}$$

Regarding the outer edge of the stalagmite, we use the approximate condition derived in Sec. 4.4 relative to a cone with constant opening $\varphi_\star$, which is also depicted in Fig. 5.17. The opening angle can be considered as equal to $\varphi_{I-1/2}$ for convex and concave profiles, while we need to impose a value for $\varphi_\star$ in the perfectly horizontal case. Only very small $\varphi_\star$ were shown to affect the drainage at the centre of the stalagmite in Eq. (5.30) ($\varphi_\star \lesssim 1°$ to $2°$). The flux at the inner face of the last cell is given by[8]

$$q_{I-1/2}^n = \frac{\left(h_{I-1/2}^n\right)^3}{3} \left(\frac{r_\mathrm{d}}{h_\mathrm{d}}\right) \sin \varphi_{I-1/2}, \tag{5.59}$$

with the film thickness at the inner face approximated by $h_{I-1/2}^n = \left(h_I^n - h_{I-1}^n\right)/2$. We further obtain $f_{I-1/2}^n = q_{I-1/2}^n \left(R - (1/2)\Delta\xi \cos \varphi_{I-1/2}\right)$ and $F(h_I^n) = (1/R)\left(2 f_{I-1/2}^n / \left(\Delta\xi/2\right)\right)$, which leads

---

[8]Or, alternatively, $q_{I-1/2}^n = \dfrac{\left(h_{I-1/2}^n\right)^3}{3} \left(\dfrac{r_\mathrm{d}}{h_\mathrm{d}}\right) \sin \varphi_\star$ in the perfectly horizontal case.

to

$$h_I^{n+1} = h_I^n - \frac{2\,\Delta t \left(2R - \Delta\xi \cos\varphi_{I-1/2}\right) q_{I-1/2}^n}{R\Delta\xi} \,.$$ (5.60)

4.5.2 Drop addition and convergence

In Sec. 4.2, we obtained the conservative form of the film thickness evolution with time. Since we start our resolution from an initially dry stalagmite, an inflow of successive drop impacts must be added over the stalagmite to create and maintain the liquid film over the stalagmite. We will therefore be able to proceed in the same manner as during the cave and lab experiments and compare both the experimental and numerical filling and drainage dynamics of the film. To take the succession of drops into account, Eq. (5.10) can be reformulated by including punctual source terms as follows (in nondimensional form, hence t has no dimension):

$$\partial_t h + \frac{1}{r}\partial_\xi (qr) = \sum_k \mathcal{H}_d(\xi)\,\delta\!\left(t - k\left(\frac{t_0}{t_d}\right)\right), \, k \in \mathbb{N}\,,$$ (5.61)

where δ is the Dirac distribution and $\mathcal{H}_d$ is the thickness added locally on a radius $r = 1$ (i.e., r_d in dimensional form) and height $h = 1$ (i.e., h_d) in the film. Numerically, the drop dripping period t_0 is materialised by n_0, the number of time steps between two drop additions in the film, such that the dripping period corresponds to $n_0\Delta t$ (see Fig. 5.17). For $n_0\Delta t = 1$, the time between two drop additions corresponds to $t_0 = t_d$, the drainage timescale defined by Eq. (5.14). In an axisymmetric or curvilinear coordinate system, we consider that there is no dispersal in the impact point distribution of the drops. The effect of impact point dispersal will be covered in the following chapter. Inserting a shift in the position of the drop impact point by keeping an axisymmetric formulation would indeed correspond to the addition of a ring of liquid into the film rather than an actual drop. We compare in Appendix C.1 different drop shapes that could possibly be used.

In the results presented hereafter, we will only use the drop shape defined by

$$\mathcal{H}_d(\xi) = \begin{cases} 1 - \left[\xi \cos\left(\varphi(r)\right)\right]^2 \,, & r \leq 1, \\ 0\,, & r > 1\,. \end{cases}$$ (5.62)

We also discuss the convergence of our numerical scheme in Appendix C.2 for various combinations of $(\Delta t, \Delta\xi)$. At fixed Δt, the main issue with our numerical calculations arises from the film thickness becoming infinite for a grid step size $\Delta\xi$ too small because we of the unstable explicit Runge-Kutta time integration used. For limiting $\Delta\xi$ values, without actually diverging, the film thickness around the centre of the domain ($r = 0$) can also present spurious oscillations. Besides that, even for large time and grid step sizes Δt and $\Delta\xi$, the accuracy of the solution remains reasonable. For instance, $\Delta t = 10^{-4}$ and $\Delta\xi = 0.1$ only lead to errors $\lesssim 3\,\%$ in the film thickness compared to the solution obtained at very precise values of $\Delta t = 10^{-6}$ and $\Delta\xi = 10^{-2}$.

The former equations do not allow to fully model the very early stage of film thickness variations following the addition of a drop in the film, corresponding to the crushing and spreading of this drop. We indeed did not take inertial and capillary effects into account when deriving Eqs. (5.9) and (5.10). Although we saw in Secs. 3 and 4.4 that the drop may perturb the film for a few seconds following the impact, we only add the drop at one particular time iteration. By contrast with the experiments, this addition could be viewed as instantaneous in regard of the subsequent drainage of the film. Nevertheless, a few iterations are needed for the thickness variations to be damped into the film, just as in the case of actual drop impacts. It is thus not possible to grasp the exact dynamics of drop impact and reproduce numerically, e.g., the variations in $\left(h^{\mathrm{max}} - h^{\mathrm{min}}\right)$ associated with

the dripping period variations, observed in the inset of Fig. 5.6 (at least not from a physical point of view, although we could artificially vary the value of h_d added at impact). However, the modelled inclusion of the drop in the film should still lead to timescales similar to the ones observed during the lab measurements.

5. Results

We are now able to simulate the evolution of the film thickness numerically for different values of the previously identified parameters, i.e., the dripping period t_0 and stalagmite shape Ψ and scale S. The temperature and relative humidity were also observed to affect the film thickness evolution, but to a much lesser extent than the dripping period and stalagmite shape. We thus do not consider them in this numerical study. To take them into account, the evaporation should be modelled as a negative source term in Eq. (5.61). The viscosity is also dependent on the temperature, but it does no longer appear in the nondimensional form of the equations and a variable viscosity should simply correspond to a scaling of the drainage timescale. In Sec. 5.1, we start by presenting a simulation example on a perfectly horizontal stalagmite and deduce from it filling and drainage empirical laws. We then analyse the response of the film to a variable dripping period in Sec. 5.2, and to a variable stalagmite shape (convex, flat or concave) in Sec. 5.3. Finally, we systematically vary these parameters altogether and compare the results obtained to our cave and lab experimental measurements in Sec. 5.4. Note that variables are expressed in their dimensional form from now on (otherwise their nondimensional equivalent is specified by a prime notation x').

5.1 Example of the film thickness evolution on a perfectly horizontal stalagmite and empirical drainage law

We start by looking at the simple case of a perfectly horizontal stalagmite whose radius is three times the drop spreading radius, $R' = 3$ (or $R = 3\,r_d$). We have $S = \Psi = 0$ and we must impose an outer edge angle, here set to $\varphi_\star = 45°$. For these radius and angle values, the outer boundary condition should not affect the filling and drainage at the centre of the stalagmite, as described in Eqs. (5.18) and (5.20) (or Eq. (5.45)). The dripping period relative to the simulation is constant and chosen equal to the drainage timescale, $t_0 = t_d$[9]. We define a dimensionless time N_d corresponding to the number of drops that would have dripped within a duration t, i.e., $N_d = t/t_0$. The stalagmite is initially dry. We cover it by successive drop impacts for a time equal to $75\,t_0$, or 75 drops, before stopping this inflow. We then record the film thickness response to the absence of inflow during a time equal to $100\,t_0$, or the equivalent of 100 drops. Numerically, the number of drops during the filling and in the absence of drops are denoted $N_\text{fill} = 75$ and $N_\text{fill} = 100$, respectively. The results obtained are shown in Figs. 5.18 (a-d) below. In Figs. 5.18 (a) i–iii, we show the film thickness $h(r,t)$ as a function of the position along the coordinate r for selected times (or numbers of drops), while in Fig. 5.18 (b) we trace the film thickness $h(r,t)$ as a function of the number of drops N_d at two specific locations indicated in (a) i. In Figs. 5.18 (c) and (d) , we represent two close-up views from (b): one during the filling after the film has reached a stationary state (c), and a log-log scaled view of the part with no droplet addition in the film, i.e., for $N_d \geq N_\text{fill}$ (d).

---

[9]Reminder from Eq. (5.14): $t_d \simeq 12\,\text{s}$ for horizontal and vertical length scales equal to $h_d = 100\,\mu\text{m}$ and $r_d = 1\,\text{cm}$, respectively.
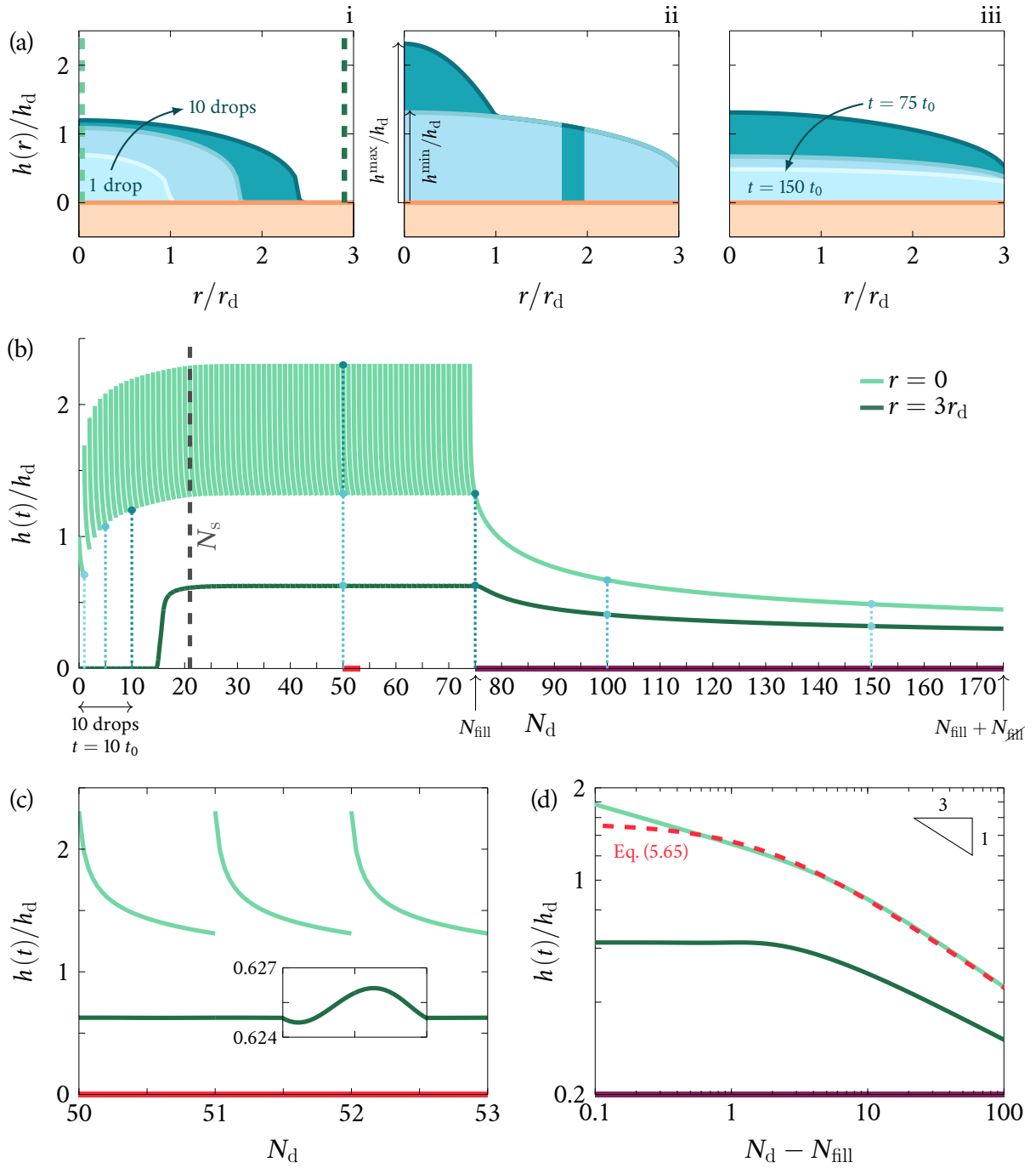
Figure 5.18: Numerical film thickness variations in space (a) and time (b-d) for a flat stalagmite, with parameters $t_0 = t_d$, $R = 3r_d$, $\varphi_\star = 45°$, $N_{\text{fill}} = 75$, $N_{\text{fill}} = 100$. (a) Film thickness profile h (blue) as a function of the radial coordinate r over the stalagmite (orange): i. After $N_d = 1$, 5 and 10. ii. After $N_d = 49^+$ (right at the drop addition time step, dark blue) and $N_d = 50$ (light blue). The dark blue band in the middle reveals the $N_d = 49^+$ profile under the profile for $N_d = 50$. iii. After $N_d = 75$, 100 and 150. (b) Film thickness h as a function of the number of drops added in the film. The light green curve corresponds to the thickness at the centre, in $r = 0$. The dark green curve shows the film thickness in $r = 3r_d$ (calculations were not made in the grid cell where we impose the boundary condition, though). Both positions are illustrated by vertical dashed lines in (a) i. The gray vertical dashed line shows the number of drops after which the film is in stationary state, $N_s = 21$. The blue vertical dotted lines and dots represent the moments shown in graphs (a) i–iii. The red and purple areas represent the portions of the graph displayed in the close-up views from (c) and (d). (c) Close-up view of the periodic filling of the film for 3 drops, between $N_d = 50$ and 53. The inset shows a vertical zoom on $h(r = R)$ between $N_d = 51.5$ and 52.5. (d) Close-up view of the film drainage for $N_d \geq N_{\text{fill}}$, in a log-log scale. The red dashed line corresponds to Eq. (5.65), with $a = 1.82$, $b = 1.75$ and $m = 3.28$. The legend from (b) is the same for (c) and (d).

Figure 5.18 (a) i shows the film thickness profile after 1, 5 and 10 times the dripping period has passed since the latest drop addition, at the exact time step before a new drop gets added into the film in each case. In other words, Fig. 5.18 (a) i shows the state of the film after 1, 5 and 10 drops have spread out, respectively. We observe that the film does not cover the entire stalagmite yet, even after 10 drops. Similarly, in Fig. 5.18 (a) ii, we see the film thickness after an equivalent time of 50 drop impacts has passed, right before the 51st drop is added into the film. The shape of the film at the exact time when the 50th drop is added is also represented, i.e., it corresponds to the end of the 49th drop topped with the drop shape. We observe that, except over the drop radius, the film profile remains identical between the end of the 49th and the end of the 50th drops. The film has therefore reached a stationary state and thereby oscillates between two limit profiles, having a central thickness going from h^{max} (maximum value) to h^{min} (minimum value) over the course of one dripping period. The film also covers the entire stalagmite at this point. In Fig. 5.18 (a) iii, we show the film after N_{fill} drops have been added to the film, i.e., right at the beginning of the drainage process, then after the equivalent of $N_{fill} + 25$ and $2N_{fill}$ drops (without any actual drop addition). The film profile flattens out with time at first sharply, then at a slower pace. In Fig. 5.18 (b), the film thickness $h(r = 0)$ measured at the centre of the stalagmite is represented as a function of the number of drops N_d, and so is the film thickness in $r = R$ (we compute this thickness at the penultimate grid point before the outer edge of the stalagmite, so that it does not directly represent the arbitrary boundary condition). The same behaviour is observed: the film thickness first increases at the centre while it remains null for a certain amount of drops at the outer edge of the stalagmite. Then, the film ends up covering the entire stalagmite and remains in stationary state as long as drops are feeding it, with a significant difference between $h(r = 0)$ and $h(r = R)$. Finally, we observe the sole drainage process for $N_d \geq N_{fill}$. During the drainage phase, the difference between $h(r = 0)$ and $h(r = R)$ progressively diminishes but does not seem to become null in the time window shown in the graph. Hence, spatial gradients in the film thickness remain. Without these, there would not be any drainage since the profile of the stalagmite underneath is completely horizontal (see Eq. (5.9)).
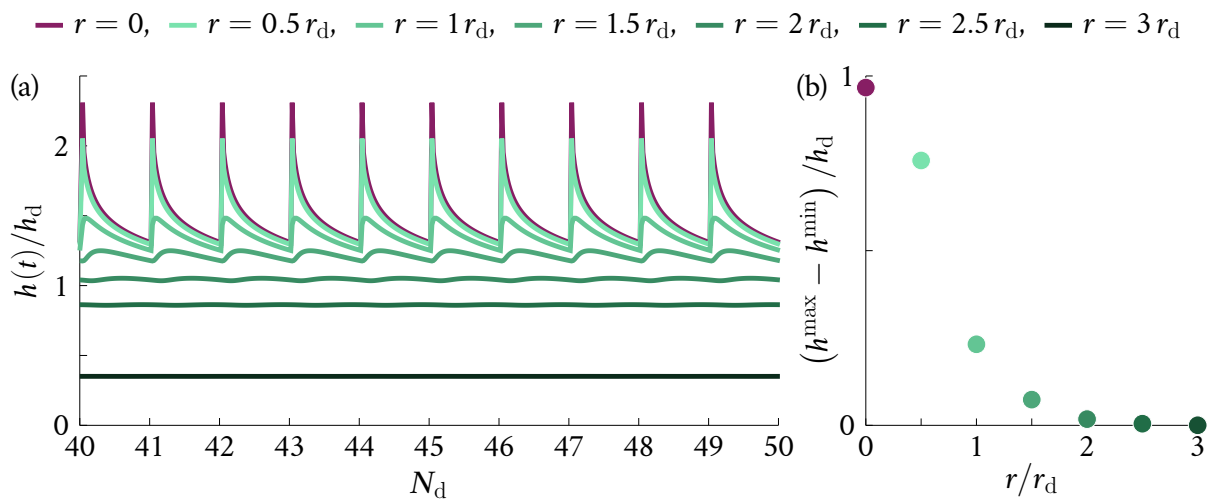
Figure 5.19: Amplitude of oscillations of the film thickness relative to the numerical simulation from Fig. 5.18, run with parameters $t_0 = t_d$, $R = 3r_d$ and $\varphi_\star = 45°$. (a) Film thickness as a function of the number of drops during the stationary phase at different radial positions, between $N_d = 40$ and $N_d = 50$ (in correspondence with the film thickness variations from Fig. 5.18 (b)). (b) Amplitude difference, $h^{max} - h^{min}$, of the film thickness variations shown in (a). The legend above the graphs refers to both graphs (information from the legend are already contained in (b)).

Figure 5.18 (c) provides a more accurate view of the film periodic variations when drops are added into it, once again for $h(r = 0)$ and $h(r = R)$, between $N_\mathrm{d} = 50$ and $N_\mathrm{d} = 53$. The strong thickness variations at the centre of the stalagmite seem not to be present in the main view of Fig. 5.18 (c) at the edge of the stalagmite, in $h(r = R)$. However, we note in the vertical close-up of Fig. 5.18 (c) that these oscillations are actually present, but with an amplitude of $7.5 \times 10^{-4} h_\mathrm{d}$. In fact, solving a parabolic equation as Eq. (5.10) numerically by periodically modifying the shape of the film should always yield small oscillations of the film profile everywhere. Nonetheless, compared to the time average film thickness $h(r = R)$ of about $0.625 h_\mathrm{d}$ during the stationary phase, these oscillations can be considered as negligible. We further represent the film thickness variations at different positions along the stalagmite in Fig. 5.19 (a). In Fig. 5.19 (b), the amplitudes of the oscillations from Fig. 5.19 (a), i.e., $h^\mathrm{max} - h^\mathrm{min}$ from each curve, are shown as a function of their radial position. We note that the oscillations are progressively damped as the distance from the centre increases. Within a radius of about $\sim r_\mathrm{d}$, the amplitude of the oscillations remains non negligible. This is not surprising considering that the drops are added over a radius r_d. Past $r = 2 r_\mathrm{d}$, the oscillations seem to become negligible with respect to the oscillations at lower r. These observations are in accordance with the criteria defined in Eqs. (5.18) and (5.20) (or Eq. (5.45)) and the lab experiments from Fig. 5.8. In the particular simulation presented in Fig. 5.18, the approximation of the outer boundary condition by a cone of constant opening with a constant flux q was thus valid.

5.1.1 Filling and stationary phase

As aforementioned, the film thickness at the centre of the stalagmite ($r = 0$) first increases before oscillating between minimum and maximum stationary values, h^min and h^max. We call N_s the number of drops after which the film thickness reaches a stationary state at the centre of the stalagmite. In the case presented in Fig. 5.18, we find $N_\mathrm{s} = 21$ according to the following empirical rule:

$$N_\mathrm{s} = N_\mathrm{d} \in \mathbb{Z} : \left| h^{N_\mathrm{d}}(r = 0) - h^{N_\mathrm{d}+1}(r = 0) \right| \leq \epsilon, \quad \epsilon = 10^{-2}, \tag{5.63}$$

where $h^{N_\mathrm{d}}(r = 0)$ designates the film thickness right after the addition of the N_d^th drop (i.e., h^max). We also pointed out in Fig. 5.18 (b) that the film does not immediately reach the outer edge of the stalagmite ($r = R$) at the beginning of the filling phase, hence its thickness at this position remains null for a certain time. We note from Fig. 5.18 (b) that the film reaches its stationary state at the centre after it has spread out until the outer edge of the domain, while at this outer edge position the film seems also instantaneously in stationary state.

The predefined criterion was set in accordance with the experiments, because these latter do not present the same accuracy as the numerical simulations. We can also estimate the number of drops needed for the film to reach a stationary state in the experimental curves from Sec. 3 based on the same criterion. We assume that no matter whether it was taken in caves or in a lab setting, the filling curve obeys the following exponential law:

$$h(N_\mathrm{d}) \approx h_\mathrm{s} \left[1 - \exp\left(-\frac{N_\mathrm{d} \log 100}{N_\mathrm{s}^{0.99}} \right) \right], \tag{5.64}$$

where $N_\mathrm{s}^{0.99}$ is a parameter to adjust for each curve, which corresponds to the number of drops after which the film thickness reaches 99 % of the stationary film thickness h_s. The value of h_s was inferred from our first measurement of the film thickness made on a given stalagmite and for measurements taken after over 100 drop impacts, when it could be safely assumed that the film was in stationary state. The curve fitted on experimental data points and the number of drops $N_\mathrm{s}^{0.99} = 7$

obtained in the case of Clam06 are also shown in Fig. 5.20 (a)[10]. Regarding the lab measurements, we estimated the number $N_s^{0.99}$ in the same manner for several dripping periods and, therefore, for several stationary film thicknesses h_s which are reported in the inset of Fig. 5.25 (a) further in the text. Our criterion was defined purely arbitrarily, but it should be noted that the number N_s is only there to provide an estimated number of drops needed to fill the film rather than a precise value.
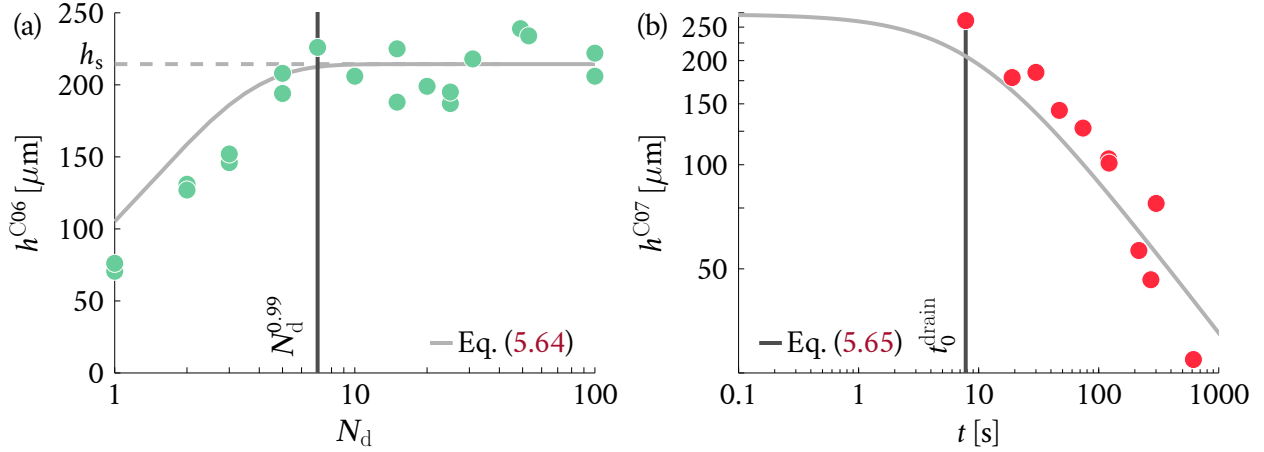
Figure 5.20: Fit on the experimental curves. (a) Example of filling curve with cave measurements made on Clam06 (green markers). The gray solid curve shows the fit from Eq. (5.64) fitted based on the experimental data for $h_s = 214\,\mu m$, with h_s represented by the dashed grey line. The square root of the residuals between the fitted curve and the measurements is $34\,\mu m$. The number of drops $N_s^{0.99}$ obtained using Eq. (5.64) is 7 (with $N_s^{th} = 6$ for Clam06). (b) Example of drainage curve with cave measurements made on Clam07 (red markers). The gray solid curve shows the fit from Eq. (5.65) fitted on the experimental data, with $t_0^{drain} = 7.8\,s$ (see Tab. 2.2), $a = 735.39\,\mu m\,s^{1/m}$, $b = 9.07\,s$ and $m = 2.22$

5.1.2 Fit of the drainage curve

In Fig. 5.18 (b), we noted that the film thickness decreases monotonously, at first rapidly then at a slower pace after the equivalent of ~ 5 drops (i.e., $5t_d$) following the interruption of the drop inflow. This translates into a cusp in the log-log scaled curves from Fig. 5.18 (d). Both curves seem to follow a power law for large times, i.e., once the rapid transient part has passed. In this particular case, we find that the corresponding power is close to $-1/3$ [106, 154] for the film thickness at the centre of the stalagmite, $h(r = 0)$. Given the cusp presented by the curve, we empirically pose that, in a given spatial position, the film thickness should vary as follows:

$$h(r,t) = \frac{a(r)}{(t + b(r))^{1/m(r)}}, \tag{5.65}$$

with $a > 0$, $b \geq 0$ and $m > 0$ to adjust. The parameters relative to $h(r = 0)$ in Fig. 5.18 (d) are $a = 1.82$, $b = 1.75$ and $m = 3.28$. We see in Fig. 5.18 (d) that these three parameters vary with r as we indeed find that, in $r = R$, $a = 0.86$, $b = 1.18$ and $m = 4.4$. In the following, we will only focus on finding these parameters in the case of $h(r = 0)$ and we will not consider their potential variations with the distance from the centre for a particular stalagmite.

If there was no time shift b in the former expression, the film thickness would become infinite at a null time. The time shift b thus indicates at which level of the master curve $a t^{-1/m}$ the drainage

---

[10]Using a looser criterion such as $t_{0.9}$, resp. $t_{0.95}$, would yield, in the case of Clam06, a stationary number of drops $N_s = 3$, resp. 5, which do not seem to capture the stationary state yet in regard of the curve from Fig. 5.20 (a). The value of $t_{0.999}$ would lead to $N_s = 11$, which seems a bit strict given that $N_s = 7$ already appears located where the experimental measurements do no longer sustain significant variations with respect to h_s.

starts, in accordance with our lab observations that, for a given stalagmite profile, temperature and relative humidity, the sole drainage process remains identical (see Sec. 3, Fig. 5.6). The time shift b is thus expected to vary with the stationary film thickness and, therefrom, with the dripping period and stalagmite shape and size. The literature [106, 116, 153, 154, 166] also indicates that the exponent m should vary depending on the overall inclination and size of the stalagmite. Finally, we note that all three parameters are not independent from each other. The factor a can be expressed as a function of the stationary film thickness h_s, i.e., the thickness reached by the film right before the drainage process starts:

$$a = h_\mathrm{s} b^{1/m}, \quad t = 0. \tag{5.66}$$

The factor a can be considered as a dimensional parameter allowing to retrieve the film thickness based on the time shift b and exponent m of the law obtained for $h(t)$.

To estimate the values of these parameters, we first assume that b remains finite and that, for large t values, we have $b \ll t$. In practice, the raw data curves from Sec. 3 seem to indicate that considering $t \gtrsim 30\,\mathrm{s}$ as the large time values (i.e., beyond the cusp) is sufficient for the experimental measurements. In the case of Fig. 5.18, large times can be considered when $N_\mathrm{d} \gtrsim 5$. We can then find the values of a and m by simple use of the normal equations, with

$$\log h \approx \log a - \frac{1}{m} \log t, \quad t \to \infty. \tag{5.67}$$

In caves, the film thickness measurements could be taken up to $+15\,\mathrm{min}$ after stopping the drop inflow. While we tried our best to record the exact times at which we interrupted this inflow and took the measurements in caves, there is still an uncertainty associated with the first measurement, especially considering that it usually corresponds to a mass-based measurement. Hence, we leave this time of first measurement, denoted t_0^drain, as a parameter to adjust for each curve, that we reported in Tab. 2.2. These measurements are of the order of about $30\,\mathrm{s}$, in accordance with the predefined large time threshold. For the lab measurements, the fit was performed on the measurements comprised between $t = +30\,\mathrm{s}$, i.e., for large times as well, and $t \approx +240\,\mathrm{s}$ following the interruption of the drop inflow. By restricting our range below $t = +240\,\mathrm{s}$, we avoid considering the dewetting of the film, which was not observed in caves (see Sec. 3), although in an ideal case we would have considered the exact same range as in the caves. Regarding the numerical simulations, we fit the parameters on the film thickness values comprised between $t = 5t_\mathrm{d}$ (or $N_\mathrm{d} = 5$) and $t \sim 100t_\mathrm{d}$ (or $N_\mathrm{d} = N_\mathrm{fill} \sim 100$), respectively. We further verify that the residue of the drainage fit from the numerical simulations falls below an empirical nondimensional threshold of 10^{-3} to ensure that the numerical simulations can be compared with one another (see, e.g., the aspect of the drainage curves after the same time in Fig. 5.21). This yields N_fill to be comprised between about 80 and 150. With the typical value of $t_\mathrm{d} = 12\,\mathrm{s}$, these numerical times correspond to the bounds considered in caves.

Once a and m have been estimated, Eq. (5.66) can be used to approximate b in the cave measurements. As discussed in Sec. 4.4.2, the stationary film thickness h_s is taken as h^min. In caves, we cannot estimate exactly the value of h^min, though. The value of h_s was thus simply obtained by averaging measurements for $N_\mathrm{d} \geq 100$. It potentially corresponds to a combination of h^max and h^min because of the precision of our measurements. For the lab data and numerical simulations, we proceed to estimate b by minimising the sum of residuals during the first dripping periods after the last drop addition into the film, i.e., over $\sim 5t_0/t_\mathrm{d}$ (or up to $t \approx +30\,\mathrm{s}$ in the lab measurements for long dripping periods). In this manner, we ensure that Eq. (5.65) fits at best the curves obtained.

5.1.3 Equivalent drainage coefficients over the filled dimple of concave stalagmites

We should finally note that, in the case of numerical simulations performed for concave stalagmites, i.e., for $\Psi > 1$, the film only subjected to drainage may never tend back to a null thickness at the centre of the stalagmite without additional effects such as evaporation or splash. We thus expect the value of m to become increasingly large for large protuberance heights H (see Sec. 3.2 from Ch. II), i.e., for larger Ψ or S. We can either apply the fit from Eq. (5.65) on $h(r = 0)$, or on $h(r = 0) - H$, with H the height of the protuberance surrounding the dimpled centre of the stalagmite, to characterise the drainage process on concave stalagmite shapes. In the second case, we could retrieve a null value for $h(r = 0) - H$ after some time has passed, and compare these results to their $\Psi < -1$ counterpart. We designate by $\widetilde{a}, \widetilde{b}$ and $\widetilde{m}$ the parameters obtained by fitting Eq. (5.65) on $h(r = 0) - H$ in the same manner as described above. These measurements will be visible in Figs. 5.26 and 5.28 from Sec. 5.4.
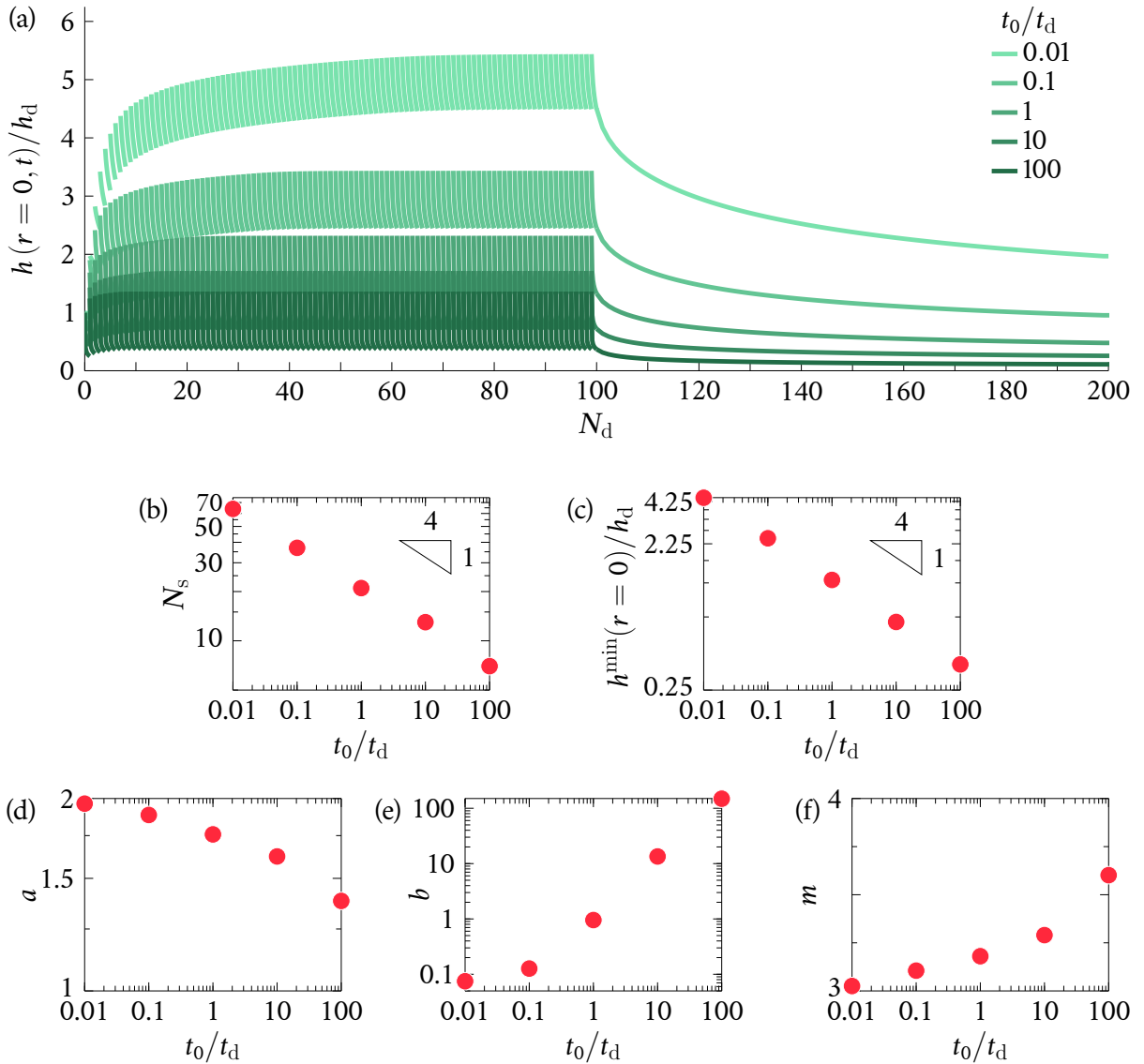
Figure 5.21: Numerical film thickness evolution with time, for variable dripping period. The simulations were conducted for $N_{\text{fill}} = N_{\widetilde{\text{fill}}} = 100$, with $R = 3r_d$ and $\varphi_\star = 45°$. (a) Film thickness as a function of the number of drops N_d, for t_0/t_d going from 0.01 (light green curve) to 100 (dark green curve). All the graphs from (b) to (g) are shown as a function of the dripping period t_0/t_d, in a log-log scale. (b) Stationary number of drops N_s obtained with Eq. (5.63). (c) Stationary film thickness h_s, corresponding to h^{min}. (d-f) parameters a, b and m obtained by means of Eq. (5.65).

145

5.2 Effect of the dripping period on a perfectly horizontal stalagmite

For a given stalagmite profile, increasing or decreasing the inflow of drops in the film was experimentally observed to modify the film thickness both locally and away from the impact point, although it was clear that the influence of the dripping period is the greatest at the impact point position. We vary in this section the numerical dripping period of the drops t_0/t_d while keeping the same stalagmite profile as in the previous section, a perfectly horizontal stalagmite of radius $R' = 3$ and outer edge angle $\varphi_\star = 45°$. In Fig. 5.21 (a), we represent the film thickness during the filling and drainage phases for $t_0/t_d \in [10^{-2} \, ; 10^2]$ at the centre ($r = 0$) of the stalagmite. If $t_0/t_d = 0.1$, 10 drops are added to the film over one characteristic drainage timescale t_d. Since all the curves from Fig. 5.21 (a) are represented as a function of N_d and show the same number of drop additions $N_{\text{fill}} = 100$, followed by sole drainage for an equivalent number of time steps $N_{\text{fill}} = N_{\text{fill}}$, the darkest curve should last 10^4 times longer than the lightest curve in dimensional values. The data from Figs. 5.21 (b-f) show the number of drops N_s defined in Eq. (5.63), after which the film reaches its stationary state (b), the stationary film thickness defined as $h_s(r = 0) = h^{\min}(r = 0)$ during the filling phase (c), as well as the three parameters from the sole drainage fit defined in Eq. (5.65): the factor a (d), the time shift b (e) and the exponent m (f), all inferred from the curves in (a) and presented as a function of the dripping period t_0/t_d. We observe in Fig. 5.21 (a) and (b) that the film takes a larger number of drops to reach a stationary state when the drop inflow is more important, i.e., when the dripping period t_0/t_d is smaller (which corresponds to a larger drop frequency). In Fig. 5.21 (c), in correspondence with this observation we note that the stationary film thickness is larger for a smaller dripping period t_0 during the filling phase. We obtain a scaling $h^{\min}(r = 0) = h_s \sim t_0^{-1/4}$, in accordance with the law derived in Eq. (5.15). We retrieve this law for N_s. The number of drops needed to fill the film until it reaches a stationary state over a perfectly horizontal stalagmite is therefore proportional to h_s.

The film thickness remains larger for smaller dripping period t_0/t_d during the drainage phase of Fig. 5.21 (a) as well. Following that, the sole drainage seems faster for smaller dripping period t_0, but not sufficiently to allow the curves to cross each other after some finite time. We observe in Fig. 5.21 (d) that the factor a decreases with increasing dripping period t_0/t_d, and, hence, with decreasing average film thickness. This is not surprising considering that a should be proportional to h_s, by virtue of Eq. (5.66). At the same time, both the time shift b and the exponent m from Figs. 5.21 (e) and (f) increase with increasing dripping period t_0/t_d. If all the curves had the same exponent m, a larger time shift b would simply indicate that the drainage starts from a smaller initial height, which is in accordance with the observations made for a and b and the interdependence of all the three fitting parameters of Eq. (5.65). In other words, the rapid decrease from a theoretically infinite initial film thickness that would occur for very short times is cut short by a larger time shift b, at a level corresponding to a. Added to that, a film initially thicker when the sole drainage starts induces a smaller exponent m, which indeed corresponds to a faster drainage process. If $t > 1$, for $n < m$, we have[11] $t^{-1/n} < t^{-1/m}$. Hence, if $n < m$, it takes a shorter time to reach a certain film thickness h_1 starting from $h_0 > h_1$. In other words, after a certain time $t_\star$, the thickness reached is smaller in the case of $t_\star^{-1/n}$ than for $t_\star^{-1/m}$. The drainage thus occurs at a faster rate for n than for m if $n < m$. As we saw in Eq. (5.9), the flux q is proportional to h^3. The time evolution of the film thickness is described by Eq. (5.10) and is due to the divergence of the flux. It is thus not surprising that the drainage occurs faster for a thicker film and, hence, for a smaller dripping period t_0/t_d. This variation should also be nonlinear, as the graphs from Figs. 5.21 (d-f) seem to

---

[11] If $t > 1$, for $n < m$, we have $t^n < t^m$, $t^{1/n} > t^{1/m}$, $t^{-n} > t^{-m}$ and $t^{-1/n} < t^{-1/m}$.
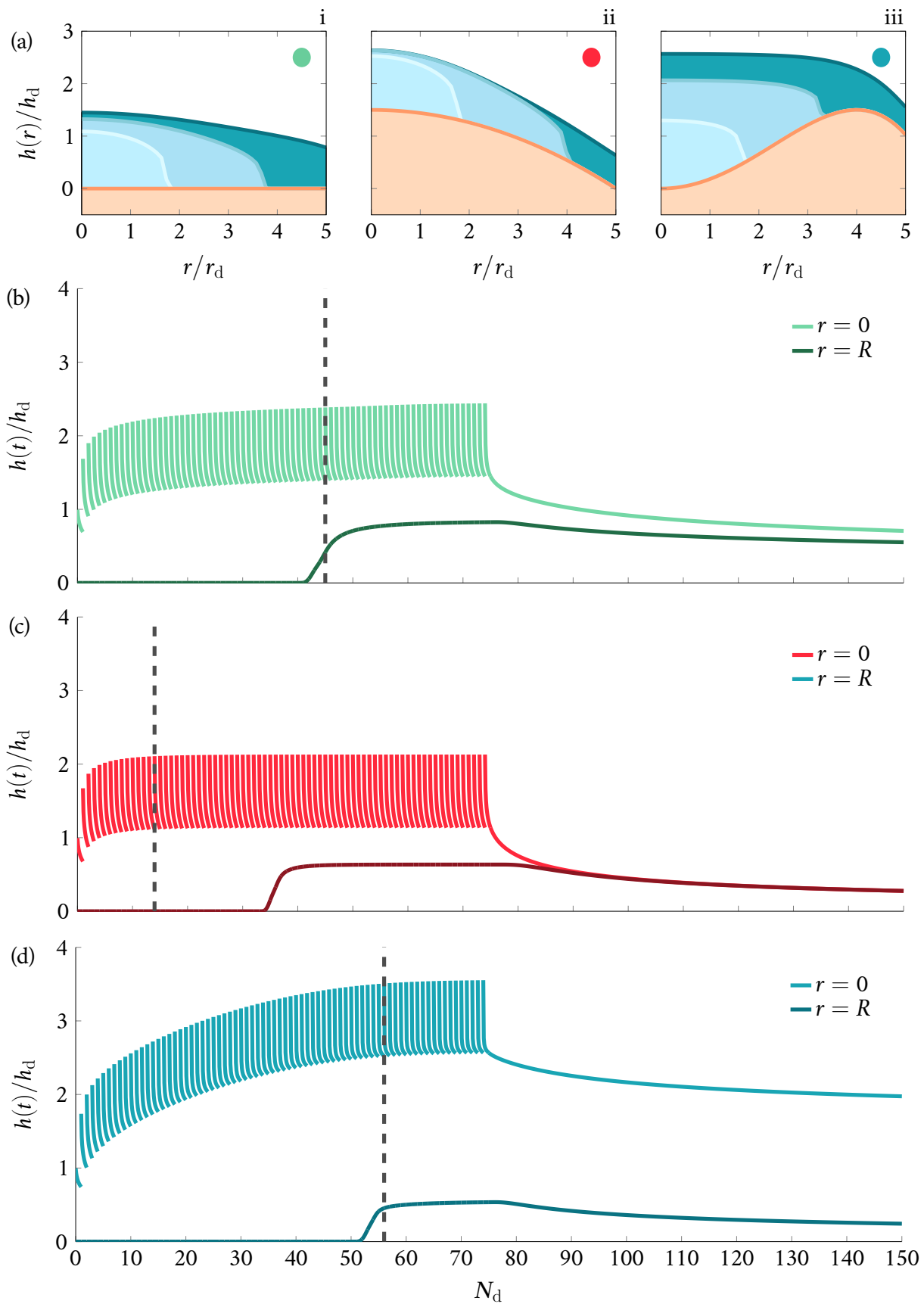
Figure 5.22: *Previous page.* Numerical film thickness evolution with time and space, for various stalagmite shapes. The simulations were conducted for $N_{\text{fill}} = N_{\cancel{\text{fill}}} = 75$, with $R = 5r_{\text{d}}$. (a) The three stalagmite profiles to which the curves presented in (b), (c) and (d) correspond: i. Perfectly horizontal stalagmite with $\Psi = S = 0$ and $\varphi_\star = 45°$. ii. Convex stalagmite with $\Psi = -215$ and $S = 2.5 \times 10^{-4}$. iii. Concave stalagmite with $\Psi = 31.5$ and $S = 6 \times 10^{-3}$. In all three graphs, the orange filled area corresponds to the stalagmite shape and the blue filled areas to the film profile $h^n(r)$ at the same 3 instants: for $N_{\text{d}} = 5$ (i.e., after the 5th drop has spread out, light blue), $N_{\text{d}} = 25$ (blue) and $N_{\text{d}} = 75$ (dark blue). (b-d) Film thickness evolution with time $h_i(t)$ at two positions: at the centre in $r = 0$ (lighter color) and close to the outer edge in $r = R$ (darker color). The case presented in green in (b), resp. in red in (c) and in blue in (d), corresponds to the perfectly horizontal stalagmite from (a) i, resp. the convex stalagmite from ii and the concave stalagmite from iii. The gray vertical dashed line shows the value of N_{s} in each graph ((a) $N_{\text{s}} = 44$, (b) $N_{\text{s}} = 14$ and (c) $N_{\text{s}} = 57$).

indicate. Although m increases with t_0/t_{d}, we note that these variations are nonetheless minor and that m remains close to 3, in accordance with the scaling from Eq. (5.17) that we had obtained when the thickness gradient dominates in Eq. (5.9).

5.3 Effect of the sole stalagmite shape at constant inflow

The film thickness h should also depend on the geometrical aspects of the stalagmite beneath the film. As aforementioned, we only focus on the global curvature, shape and size of the stalagmite through the predefined parameters Ψ and S, without considering local aspects of the film evolution that could be induced by the surface state, porosity or roughness [154]. In Fig. 5.22, we present the evolution of the film over three different stalagmites: a perfectly horizontal stalagmite of radius $R' = 5$ with $\varphi_\star = 45°$, a convex stalagmite for which $\Psi = -215$ and $S = 2.5 \times 10^{-4}$, and a concave stalagmite with $\Psi = 31.5$ and $S = 6 \times 10^{-3}$. The shapes over a domain of size $R' = 5$ are shown in Figs. 5.22 (a) i–iii, where we note that the values of Ψ and S were chosen to produce a protuberance of comparable height $H = 1.5h_{\text{d}}$ in the convex and concave cases. In each of these subfigures, we additionally represent the film after 5, 25 and 75 drops have spread into it. The three remaining graphs of Figs. 5.22 (b), (c) and (d) display the corresponding evolution with the number of drops of the film thickness at the centre and outer edge of the stalagmite (in $r = 0$ and $r = R$), similarly to Fig. 5.18, for the perfectly horizontal, convex and concave cases from (a), respectively. We have commonly set $N_{\text{fill}} = N_{\cancel{\text{fill}}} = 75$. In each graph from Figs. 5.22 (b-d), we further represent the number of drops after which the film has reached a stationary state, N_{s}, according to Eq. (5.63).

We observe that, after only 5 drops, none of the films presented is in stationary state. The films on the flat and concave stalagmites reach a stationary state after 44 and 57 drops, respectively, which are quite close values. In the same manner, this stationary state is reached shortly after the film thickness at the outer edge, $h(r = R)$, has started to increase. However, because of the presence of the protuberance, the film thickness at the centre is larger in the concave case than in the perfectly horizontal one, and so is the difference $(h(r = 0) - h(r = R))$. The thickness reached during the stationary state at the centre of the concave stalagmite even overcomes the height of the protuberance by about the height of one drop, h_{d}, since $h_0^{\min} \gtrsim 2.5$ in Fig. 5.22 (c). Regarding the convex stalagmite, we observe that the stationary state of the film is reached after only 22 drops, at a moment when the film does not even cover the entire stalagmite yet. The thickness at the centre in the convex and perfectly horizontal cases are comparable and oscillate between roughly h_{d} and $2h_{\text{d}}$.

Once the sole drainage phase starts, we note that the thickness decrease is the fastest for the convex stalagmite. The thickness at the centre, $h(r = 0)$, even reaches the same value as $h(r = R)$ after the equivalent of a few drops. By contrast with the horizontal case for which the drainage cannot appear without the existence of thickness gradients in between two positions of the film, in this case the inclined shape of the stalagmite suffices to induce drainage (see Eq. (5.9)). Regarding the concave stalagmite, the film thickness at the outer edge, $h(r = R)$, shows a similar behaviour as

in the flat and convex cases. On the other hand, the thickness at the centre of the dimple, $h(r = 0)$, remains close to 2 even after $N_{\text{fill}} = 75$ has passed. The drainage exponents obtained are $m = 3.6$ for the horizontal stalagmite, $m = 2.2$ for the convex stalagmite, and $m = 5.6$ and $\widetilde{m} = 2.9$ for the concave stalagmite (see Sec. 5.1.3). For $t > 1$, we know that the drainage occurs at a slower rate for n than for m if $n > m$. It is not surprising to obtain the smallest, resp. largest, value of m for the convex case (c), resp. concave case (d), since the drainage seems the fastest on the convex stalagmite, resp. the slowest on the concave stalagmite. Additionally, we note that the value found for $\widetilde{m}$ in the concave case is of the same order as the exponents m found in the horizontal and convex case. Hence, the drainage process allows the film at the centre of the concave stalagmite to retrieve a value close to the height of the protuberance at the same rate as it decreases the film thickness on other stalagmite shapes. Although from a numerical point of view, the exponent $m = 5.6$ found for the concave stalagmite should eventually yield a null thickness $h(r = 0)$ (i.e., an extremely small thickness), it should not be the case in reality. In caves, the film would simply remain in the dimple or evaporate, or escape slowly through variations in the stalagmite outer wall (see, e.g., Fig. 2.1).

All these observations are in accordance with the shape variations presented. The convex stalagmite has an overall downward slope, which tends to ease the flow of the film toward the edge and sides of the stalagmite. We also note that the film thickness at the centre of the convex stalagmite does not depend on whether or not the film completely covers the stalagmite, i.e., it is only governed by the inclination close to the impact point position. On the other hand, the protuberance of the concave stalagmite prevents the film from flowing over it as long as the film thickness around the centre does not become larger than the height of this protuberance. If the protuberance of a concave stalagmite becomes very large, it appears clear that the drainage at the centre will become increasingly slower, thereby allowing m to increase up to infinite values. The value of $\widetilde{m}$, on the other hand, seems comparable to the horizontal and convex cases. Hence, the drainage at the centre of a concave stalagmite depends on the outer wall.

5.4 Comparison between numerical and experimental cave and lab measurements

The following analysis presents both numerical results and experimental measurements obtained for the stationary film at the centre of the stalagmite, $h_{\text{s}}(r = 0)$, the filling of this film prior to the stationary state (N_{s}), and drainage fitting parameters (see Figs. 5.21 (b-c) and (d-f), a, b and m), for variable dripping period (t_0) and variable stalagmite shapes and scales (Ψ and S, respectively). The numerical stalagmite profile is defined until a dimensional radial coordinate R (see Fig. 5.17), which should not affect the results according to Eq. (5.45). We have already discussed that perfectly horizontal stalagmites lead to an indeterminate definition. In this case, the truncation radial coordinate R of the numerical domain becomes the stalagmite radius.

Whenever possible, we assumed that the outputs of the experiments and numerical simulations depended on the entry parameters (t_0, Ψ, S and R) as power laws. The fitting parameters coming from these power laws are reported in Tab. 5.3 for the power laws relative to the numerical simulations and Tab. 5.2 for the experimental measurements. To perform these fits, we use the nondimensional dripping period $t_0' = t_0/t_{\text{d}} = t_0 g h_{\text{d}}^3/(\nu r_{\text{d}}^2)$, the nondimensional stalagmite radius $R' = R/r_{\text{d}}$ and the drop volume $V_{\text{d}} = \pi r_{\text{d}}^2 h_{\text{d}}$. The variables Ψ and S are kept as such since they are not related to dimensional physical variables, like the drop height or the stalagmite radius. We also note that, when we perform calculations related to the actual cave or lab measurements, the radius used will be $R = r_{\text{sm}}$, the average top radius measured in Ch. II and reported in Tab. 2.2. Finally, to simplify the upcoming sections, we divide them when possible into discussions relative to either the numerical simulations or experimental measurements.

5.4.1 Stationary phase

a) Numerical simulations

We first show in Fig. 5.23 (a) the evolution of the numerically computed stationary film thickness h_s, i.e., the minimum film thickness $h^{\min}$, as a function of Ψ for a fixed value of $S = 1$, while in Fig. 5.23 (b) we show h_s for variable S, with limited Ψ values comprised between -5 and 5. The inset of Fig. 5.23 (a) displays the number of drops N_s needed to reach the stationary phase as a function of Ψ for $S = 1$, also obtained numerically. In Fig. 5.23 (c), we represent h_s for perfectly horizontal stalagmites of variable size R, and in Fig. 5.23 (d) we show the corresponding stationary number of drops N_s. In Figs. 5.23 (a), (c) and (d), the dripping period t_0/t_d is also varied, from 10^{-1} to 10^1 in Fig. 5.23 (a), and from 10^{-2} to 10^2 in Figs. 5.23 (c) and (d). In Fig. 5.23 (b), the dripping period is set to $t_0/t_d = 1$.

We observe in Fig. 5.23 that h_s strongly varies with the shape factor Ψ for curved stalagmite profiles (convex and concave), and, to a lesser extent, with the radius of the stalagmite R for perfectly horizontal stalagmite. In the perfectly horizontal case, we once again retrieve the prediction of Sec. 4.4.2 from the results presented in Fig. 5.23 (c): the exponents of the power law for the dripping period t'_0 and radius R', inferred from this data, are summarised in Tab. 5.3. The dashed lines shown in Fig. 5.23 (c) correspond to the following law in dimensional form:

$$h_s^{\bullet}(r = 0) = \left(\frac{\nu V_d}{\pi g t_0} \frac{R}{r_d} \right)^{1/4} . \tag{5.68}$$

From this relation, we note that, all parameters otherwise kept constant, h_s increases with increasing inflow ($V_d \uparrow$, $t_0 \downarrow$) or a more viscous fluid ($\nu \uparrow$), as expected. The stationary film thickness at the stalagmite centre further increases with increasing stalagmite radius over the drop radius ratio R/r_d. If both the volume of the added drops and their frequency are kept constant, a wider stalagmite ($R \uparrow$) requires a larger total volume to be completely covered by the successive identical drops of radius r_d. The above law indeed describes a process related to the balance between the drop inflow, Q_{drip} and drainage outflow, $Q_{\mathrm{drain}} \sim h_s^4/R$ for perfectly horizontal stalagmites (see Eq. (5.9)). Consequently, as already conveyed by the discussion relative to Eq. (5.15), at constant outflow, a larger stalagmite radius yields a larger film thickness. Because of the profile taken by the film on perfectly horizontal stalagmites (see Sec. 4.4.2), the thickness at the centre should likewise increase. We retrieve the same scaling as we had obtained in Eq. (5.15) by using $Q_{\mathrm{drain}} = 2\pi r_d q$ and $\partial_r h_s \sim h_s/R$ in our calculations, and by acknowledging that $(3/2)^{1/4} = 1.11 \approx 1$. This scaling is also similar to Eq. (5.27) from the constant pointwise inflow calculations (Sec. 4.4.2), except for the factor related to the stalagmite radius which was found to be $(12 \ln (R/r_d))^{1/4}$. In the constant pointwise inflow calculations, however, we had computed the stationary film thickness over the entire stalagmite starting from a given radius r_0. In the present case and in Eq. (5.27), we only computed the film thickness at $r = 0$. Finally, we comment on the approximation of h_s as following a power law in R. In Sec. 4.4.2, we had derived that h_s evolves primarily as $(\ln (R/r_d))^{1/4}$. Hence, the numerical evolution of h_s could follow a similar law. We obtain a good agreement for $R \gtrsim 2r_d$ using this parameter (which is not represented here), which could explain the small discrepancies observed at larger R in Fig. 5.23. However, this fit fails at capturing the behaviour of h_s for $R \lesssim 2$, which could be explained by the fact that R lies inside the region of instability in this case. Hence, the power law based on R yields a better fit in this case, although it might actually correspond to a first-order approximation of $(\ln (R/r_d))^{1/4}$ which somehow encompasses the behaviour of h_s at $R \lesssim 2r_d$ because the drops are added over a radius r_d.
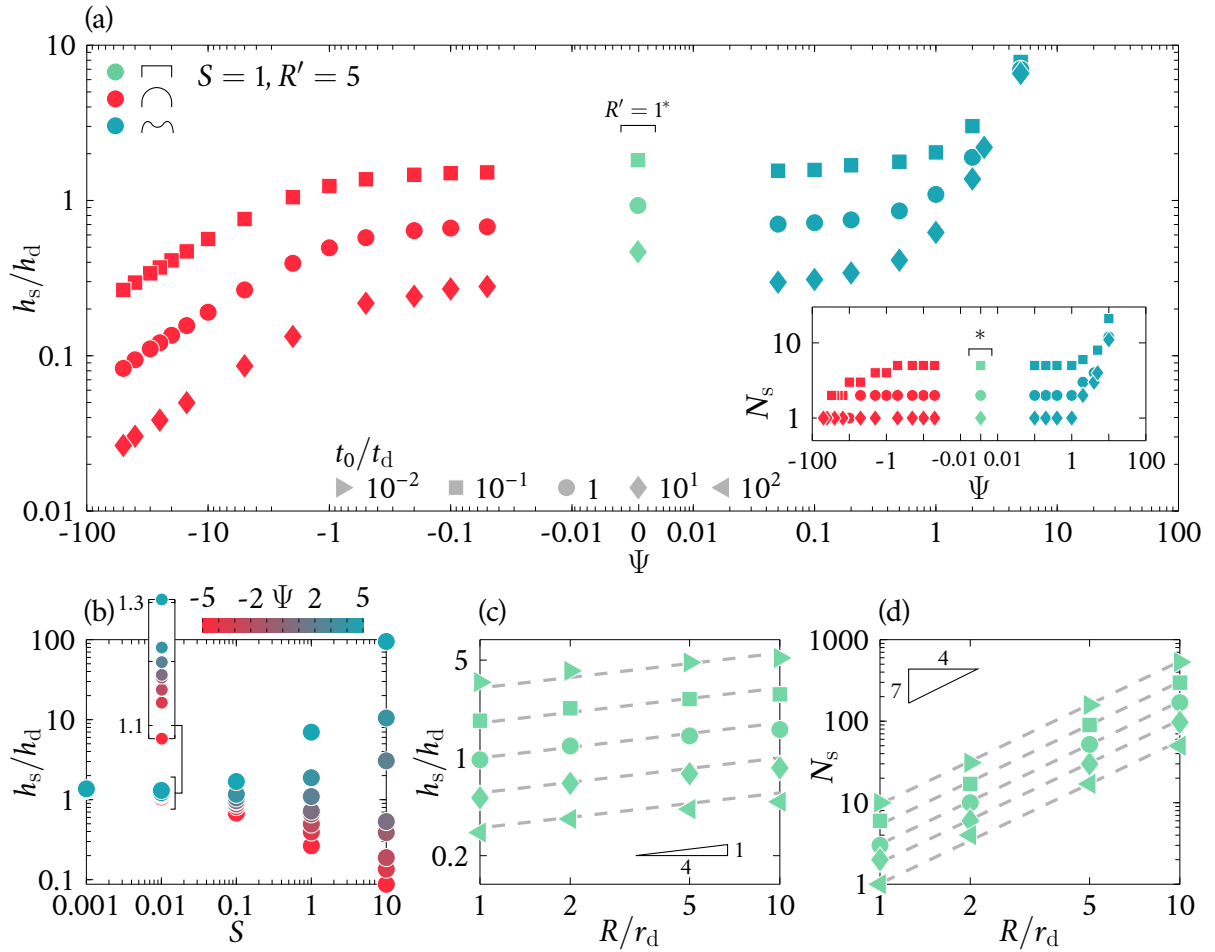
Figure 5.23: Stationary film thickness h_s computed numerically, for variable shape parameter Ψ, scale parameter S, perfectly horizontal stalagmite radius R' and dripping period t'_0. All results were obtained for $R' = 5$ (a-b), or for $\varphi_\star = 45°$ in the perfectly horizontal case (c-d). The legends in (a) are the same for all subfigures, except for the symbol colour from (b) which is precised by the colour bar in (b). The symbol represents the dripping period used: $t'_0 = 0.01$ (▶), $t'_0 = 0.1$ (■), $t'_0 = 1$ (●), $t'_0 = 10$ (◆) and $t'_0 = 100$ (◀). The colour corresponds to the stalagmite general shape: convex (●), perfectly horizontal (●) and concave (●). (a) Thickness h_s on a curved stalagmite as a function of the shape Ψ, at fixed scale $S = 1$, for a domain size $R' = 5$ and for variable dripping period t'_0. The values computed for $\Psi = 0$ (perfectly horizontal case) correspond to a radius $R' = 1$. The inset shows the number of drops needed for the film to reach a stationary state, N_s, as a function of Ψ and presented in correspondence with the main graph. Note that the $*$ symbol indicates the number N_s corresponding to the perfectly horizontal case obtained at $R' = 1$. (b) Thickness h_s as a function of the scale S, for Ψ varying between -5 and 5, as indicated by the colour bar, at $t_0/t_d = 1$. The upper left inset shows a close-up view of h_s for $S = 0.01$. (c) Thickness h_s on a perfectly horizontal stalagmite as a function of R, for variable dripping period t'_0. (d) Number of drops needed for the film to reach a stationary state on a perfectly horizontal stalagmite, N_s, as a function of R' and for variable dripping period t'_0. The dashed lines in (c) and (d) correspond to the curves $(R')^{1/4}$ and $(R')^{7/4}$, respectively, with coefficients from Tab. 5.3.

The values obtained for the stationary film thickness at $R' = 1$ in a perfectly horizontal case ($\Psi = S = 0$) and $t_0/t_d = 10^{-1}$, 1 and 10 have been added in Fig. 5.23 (a) as a comparison, because this radius corresponds roughly to the flattened out portion close to the centre of the stalagmite for variable Ψ (see graphs from Fig. 2.4). Small discrepancies may be observed between the values at $R' = 1$ and the closest values of Ψ shown in Fig. 5.23 (a). These discrepancies may be due to the fact that, even with $|\Psi| < 1$, small film thickness gradients should still appear before reaching $r = r_d$ (the radial coordinate, $r' = 1$) in the stalagmite profiles from Ch. II. The value of $R' = 1$ also lies within the unsteady region of Fig. 5.16, thus the values shown in this case in

Fig. 5.23 (a) should be taken with precaution. Nevertheless, there is a good agreement between the values at $R' = 1$ and the closest values of Ψ shown in Fig. 5.23 (a). The stationary film thickness h_s tends to decrease below this central value corresponding to $R' = 1$, i.e., for $\Psi < 0$. For $\Psi > 0$, the film thickness h_s increases with Ψ. These observations are consistent with our preliminary notes relative to Sec. 5.3. However, the slope $\partial h_s / \partial \Psi$ is much larger for $\Psi > 1$ than for $\Psi < -1$. In Tab. 5.3, which summarises the coefficients relative to the scaling laws derived from the graphs in Fig. 5.23, we note that the stationary film thickness h_s on a convex stalagmite evolves as

$$h_s^{\bullet}(r = 0) = 0.58 \left(\frac{-1}{\Psi S} \frac{\nu V_d}{\pi g t_0 h_d^2} \right)^{1/2}, \quad \Psi < -1, \tag{5.69}$$

i.e., it decreases with increasingly negative values of Ψ, or stalagmites having an outer wall with a larger downward inclination, as expected. Drainage should indeed be promoted by negative (oriented downward) stalagmite profile gradients (see Eq. (5.9)). Surprisingly, in Eq. (5.69) we also note that we do not retrieve the same law as the one developed for the inclined case in Eq. (5.16). Although we find that h_s increases with increasing inflow ($V_d \uparrow$, $t_0 \downarrow$), we note here that the scalings relative to both these variables are not the same as previously found since we had $h_s \sim (V_d / t_0)^{1/3}$ in Eq. (5.16), against $h_s \sim (V_d / t_0)^{1/2}$ here. This difference might stem from the fact the, in Eq. (5.69), the film thickness is evaluated at the centre of the stalagmite, which was not the case for Eq. (5.16). We actually had to assume $\xi \gg \arctan(\partial_\xi h_s)$, and found that Eq. (5.16) is only valid at a certain distance from the stalagmite centre, where the inclination becomes sufficient to overcome the film thickness gradients. Hence, the two equations do not exactly describe the same film thickness evolution. The above scaling from Eq. (5.69) thus corresponds to a case where the inclination of the stalagmite has a significant effect on the stationary film thickness, but in a region where the inclination remains small. We indeed always impose the first cell of the numerical domain to remain horizontal (see Sec. 4.5.1). To sum up, the main difference between the perfectly horizontal and convex cases is that the stationary film thickness in $r = 0$ decreases as $\sim t_0^{-1/2}$ in the convex case rather than as $\sim t_0^{-1/4}$ in the perfectly horizontal case above.

Additionally, we note in Fig. 5.23 (a) that the film thickness values related to concave stalagmites do not vary significantly anymore with t_0 at large $\Psi > 1$, by contrast with the horizontal and convex cases. In this case, we find that h_s evolves as

$$h_s^{\bullet}(r = 0) = 0.57 \, h_d \, \Psi^2 S, \quad \Psi > 1. \tag{5.70}$$

We have already noticed that h_s should be of the order of the protuberance height for the film to reach a stationary thickness with concave stalagmites in Sec. 5.3. Given our definition of the stalagmite profile from Eq. (5.49), we know that the maximum height of the protuberance is located at $r = \sqrt{\Psi/2}$, with a height growing as $\psi^2 S / 4$. It is therefore not surprising to obtain the same scaling for h_s above $\Psi = 1$. By increasing the shape factor Ψ in the above equation, we shift the position of the protuberance toward the outer wall of the stalagmite and increase the protuberance height, thereby increasing h_s. The stationary film thickness also increases with taller added drops ($h_d \uparrow$). Since h_s corresponds to the thickness above which the film drains over the protuberance of the stalagmite, adding taller drops should allow the film to further exceed the protuberance height. The filling for the concave case should be seen as twofold: first, we need to fill the central dimple of the stalagmite, then the liquid further added simply corresponds to the volume added on top of the full dimple as if it were seen as an actual solid. Following this, we note that the film thickness above the protuberance should also depend on the dripping period t_0, but we did not have a sufficient amount of data to conclude regarding this effect. The simulations conducted

for $\Psi > 10$ at $S = 1$ indeed become increasingly long ($\sim$ days instead of $\lesssim 1$ min for convex and flat cases), thus assessing this effect would require the use of other numerical tools.
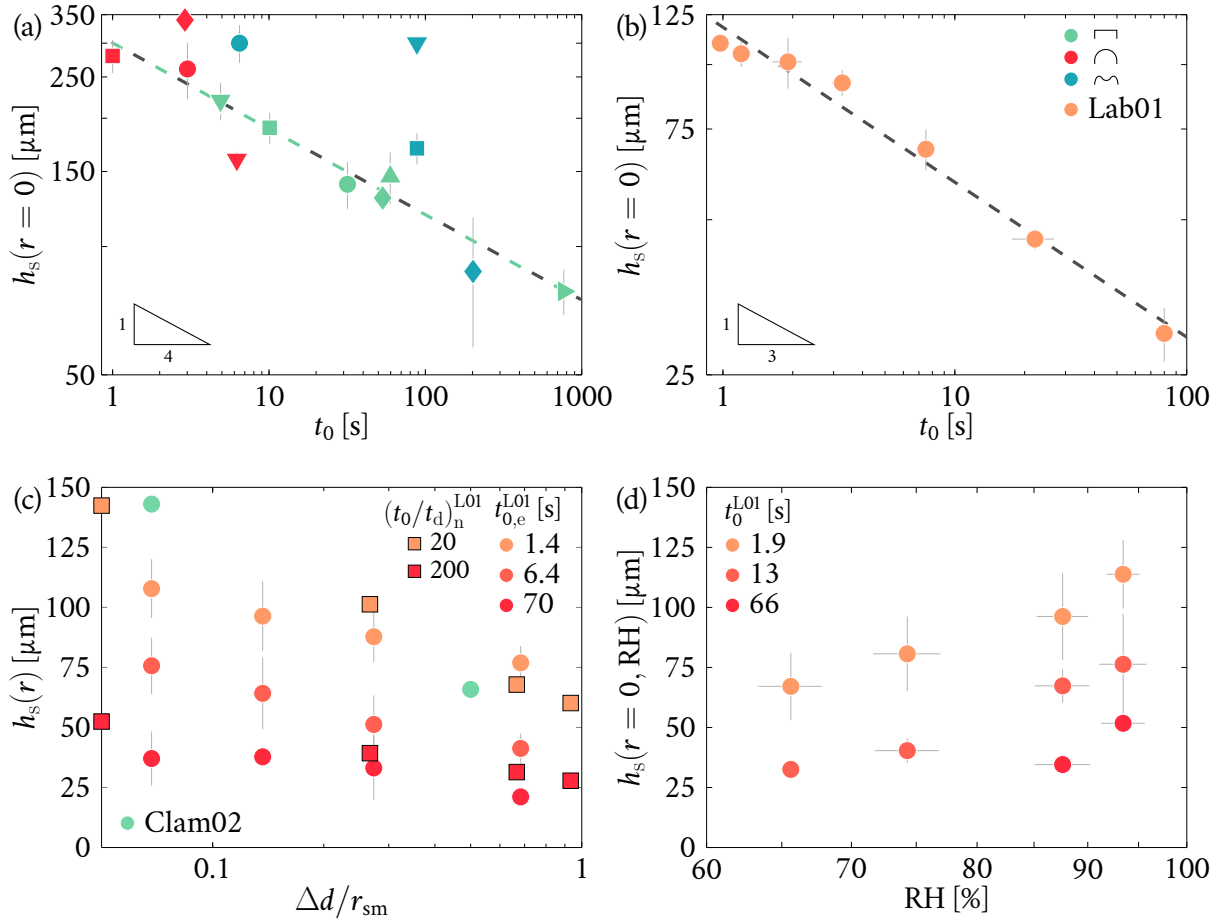
Figure 5.24: Experimental cave and lab stationary film thickness measurements. (a) Cave film thickness h_s as a function of the dripping period t_0. Symbol correspondence is indicated in Tab. 2.2. The dashed line shows the power law fit made on the stalagmites classified as flat (green markers). (b) Lab film thickness h_s as a function of the dripping period t_0. Only the measurements for which $\Delta d \leq 1$ cm, $T \leq 21°$ and RH $\geq 80\%$ are taken into account. The dashed line shows the fit made on the measurements. (c) Lab film thickness h_s as a function of the distance from the drop dripping point to the sensor, Δd, compared to the stalagmite average radius r_{sm}. Only the measurements for which $T \leq 21°$ and RH $\geq 80\%$ are taken into account. The symbol colour indicates the average dripping period t_0 taken on the measurements presented (3 peristaltic pump modes were used). The stationary film thickness obtained through numerical simulations corresponding to the parameters Ψ and S from Tab. 2.2 is also illustrated, with $t_0/t_d = 20$ and 200 according to the measurements from Fig. 5.30 (a) (the values chosen for t_0/t_d match the corresponding values from the lab experiments with the dripping periods that we imposed). As measurements could be obtained in two positions on Clam02, the corresponding stationary film thickness values are represented by the green markers (see Fig. 5.20 (a)). (d) Lab film thickness h_s as a function of the relative humidity RH. Only the measurements for which $\Delta d \leq 1$ cm and $T \leq 21°$ are taken into account. The symbol colour indicates the average dripping period t_0 taken on the measurements shown in the graph (all peristaltic pump modes are represented). One data point corresponds to ~ 5 measurements.

Regarding the effect of the scale S on h_s, we observe in Fig. 5.23 (b) that, below $S = 0.1$, the values of h_s remain very close to each other no matter the value of Ψ. We indeed have a ratio between the two Ψ extrema of $h_s(\Psi = 5)/h_s(\Psi = -5) = 1.2$ at $S = 10^{-2}$, while at $S = 1$ we have $h_s(\Psi = 5)/h_s(\Psi = -5) \simeq 200$. The profile gradients caused by values of $|\Psi| > 1$ are therefore sufficiently scaled down below $S = 0.1$ to become negligible with respect to the added drop. Depending on the sign of Ψ, the stalagmite profile will respond differently to a given scaling S,

thus we could not find a common law for the evolution of h_s with S. The scaling S is rather involved in each of the above described laws in a different manner. This is clearly illustrated by Fig. 5.23 (b) where we observe that, for the largest $\Psi = 5$, e.g., the film thickness is multiplied by 10 for S going from 1 to 10, while we need to go over two decades ($S = 0.1$ to $S = 10$) to divide the value of h_s relative to $\Psi = -5$ by 10. We thus infer from this that, in the concave case ($\Psi > 1$), the film thickness should be proportional to S, as is the height of the protuberance of the stalagmite profile, while in the convex case ($\Psi < -1$), the scaling factor becomes $S^{-1/2}$. These factors have been taken into account in Eqs. (5.69) and (5.70).

b) Experimental measurements

We now concentrate on the measurements coming from the experiments that we described early in the text, in Secs. 2 and 3. In Fig. 5.24, we show the stationary film thickness h_s obtained from cave measurements in (a) and lab measurements in (b-d). As aforementioned, we could not discern whether our cave measurements of h_s corresponded to $h^{\max}$ or $h^{\min}$, but the lab measurements show the value of $h^{\min}$, as in the numerical version. Figure 5.24 (a) gathers the measurements made for all the flat, convex and concave cave stalagmites as a function of their associated drop dripping period t_0. In Figs. 5.24 (b), (c) and (d), we report the lab measurements obtained on stalagmite Lab01 as a function of the imposed dripping period t_0, the distance between the dripping point and the sensor Δd, and the relative humidity RH in the enclosure during the measurements RH, respectively. To avoid taking into account the variability of several parameters at once, we only considered in Fig. 5.24 (b) the experiments conducted for $\Delta d \leq 1$ cm and RH $\geq 80\%$ as both these parameters were shown to modify the stationary film thickness behaviour. Albeit the little influence of the enclosure temperature on the stationary film thickness, we also removed measurements obtained for $T \geq 21\,°C$ to be consistent with the graphs presented in the following section. In Fig. 5.24 (c), we considered variable dripping point-sensor distances Δd for RH $\geq 80\%$ and $T \leq 21\,°C$, that we present as a function of the ratio between Δd and the stalagmite radius r_{sm} (see Tab. 2.2). We separated the dripping period in three ranges for each Δd as we conducted the experiments by only focusing on three peristaltic pump rates when varying the distance Δd. Additionally, Fig. 5.24 (c) shows the stationary film thickness measured on Clam02 in two positions (the value at $\Delta d / r_{sm} = 0.6$ was estimated from Fig. 5.5 (a)). In Fig. 5.24 (d), we present the results obtained for variable humidity RH for $\Delta d \leq 1$ cm and $T \leq 21\,°C$. In this case the average dripping periods correspond to the averages obtained by dividing our data into three: $t_0 \to 1$ s (on average for all the experiments within this range, $t_0 = 1.9$ s), $t_0 \to 1$ min ($t_0 = 66$ s on average), with the last range corresponding to the intermediate values ($t_0 = 13$ s on average).

Using the experimental measurements presented in Figs. 5.24 (a) and (b), we also estimated the evolution of the film thickness in cave and lab with the dimensional dripping period t_0, which is reported in Tab. 5.2. The fit on the cave data was only performed with the flat stalagmites (see Tab. 2.2) as there is too much disparity between the Ψ and S values related to the few convex stalagmites for which we collected measurements. We observe a good agreement with our theoretical and numerically obtained laws (for flat stalagmites, $h_s \sim t_0^{-1/4}$, for convex ones, $h_s \sim t_0^{-1/2}$ at the centre and $h_s \sim t_0^{-1/3}$ away from the centre) as we get an exponent for t_0 of -0.21. On the other hand, the lab measurements, which have a much better precision, give an exponent of -0.30. This value is in between the two laws obtained above from the numerical simulations for horizontal and convex stalagmites, and it is close to the value obtained initially in Eq. (5.16). Although Lab01 was classified as convex, its top is quite flattened out, as indicated by its scaling $S = 0.1$. The fact that we retrieve a law close to the horizontal case rather than to Eq. (5.69) may be caused by this. Another explanation could be the fact that, even though we tried to position the sensor as close as possible

Meas. var.	Indep. var.	Exponent	Factor
	Cave		
$h_\mathrm{s} / \max h_\mathrm{s}$	$t_0 / \min t_0$	-0.21	1.02
	Lab		
$h_\mathrm{s} / \max h_\mathrm{s}$	$t_0 / \min t_0$	-0.30	1.08
$a / \max a$	$t_0 / \min t_0$	-0.29	0.94
$b / \min a$	$t_0 / \min t_0$	1.05	1.43
m	$t_0 / \min t_0$	0.12	2.48

Table 5.2: Cave and lab fit coefficients from raw data curves expressed as a function of the dripping period t_0. The measured dependent variables include the stationary film thickness h_s in cave and in lab, and the parameters a, b and m from the drainage fit of Eq. (5.65). Columns 3 and 4 show the exponent and multiplying factor relative to each measured variable. The second line, e.g., should be read as $h_\mathrm{s} / \max h_\mathrm{s} \sim 1.08 \, (t_0 / \min t_0)^{-0.3}$.

to the dripping point of the drops, there was still a non-negligible distance between them (of the order of 0.5 cm to 1 cm). The fit obtained for Lab01 might thus correspond to the case prescribed by Eq. (5.69), valid only at a certain distance from the impact point position.

The measurements made on Lab01 also provide information on additional parameters that we could not systematically vary in the numerical simulations in order to keep a limited amount of parameters in our study, namely the distance Δd between the drop dripping point and the sensor, and the relative humidity RH (although varying the distance Δd numerically is easily done, as illustrated by Fig. 5.19, but would increase further the number of graphs presented in this chapter). We have indeed witnessed in Figs. 5.18 and 5.22 that the film thickness stationary state and drainage were affected by the distance with the dripping point. Regarding the influence of Δd on h_s, we observe in Fig. 5.24 (c) that h_s decreases with the distance from the impact point, as we had already noted in Fig. 5.8. This decrease is nevertheless not very pronounced as, for $\Delta d \to r_\mathrm{sm}$, the film thickness barely reaches $2/3$ of the film thickness measured at the centre, in $r = 0$. On the other hand, in Fig. 5.24 (c) we additionally represented the stationary film thickness in the two positions from which we could measure it on Clam02 (see Fig. 5.4 (a)). We note a much larger difference between the two film thickness values in this case. Clam02 was considered as flat and indeed has a shape factor $\Psi = 1.2$. Our experimental measurements are thus once again consistent with our former observations that on flat stalagmites, there exist large gradients in the film thickness allowing to promote the drainage while on convex stalagmites, the film has a more uniform thickness because it cannot increase much at the centre and that drainage is promoted by the stalagmite shape. In accordance with our above discussion on the fact that Lab01 is not the stalagmite with the most inclined outer wall, we note that the variation of h_s with Δd remains significant as we get p-values of 2×10^{-3}, 2×10^{-3} and 2×10^{-2} by conducting distinct anova tests for the three dripping periods presented in Fig. 5.24 (c) (anova tests were conducted on the 23, 22 and 11 experiments relative to the three dripping periods, which have then been sorted and averaged in Fig. 5.24 (c)). Additionally, we have performed numerical simulations using the parameters Ψ and S relative to Lab01 (see Tab. 2.2 in Ch. II and in the auxiliary sheet), and computed the thickness of the film in stationary state at locations corresponding to the locations of the lab measurement (not in $\Delta d / r_\mathrm{sm} \simeq 0.15$ though, as this is too close to our numerical drop radius r_d). We used $t_0 / t_\mathrm{d} = 20$ and $t_0 / t_\mathrm{d} = 200$ as these values correspond to the longest and shortest experimental dripping period that we imposed on Lab01, respectively (we will discuss this further in the text, see Sec. 6.2). There is a good agreement between the values and overall trend observed in the numerical and experimental data from Fig. 5.24 (c). In Fig. 5.24 (d), as we had already spotted in Fig. 5.10, we observe that h_s increases slightly with the relative humidity in the vicinity of the stalagmite. This effect is significant too as

we get p-values of 1×10^{-3} and 7e−5 by performing anova tests for the two shortest dripping periods of Fig. 5.24 (d) (same as in Fig. 5.24 (c) but we had 26 and 18 experiments, respectively). Finally, we note that the numerical results should correspond to an environment with a 100 % relative humidity, while the measurements from Fig. 5.24 (c) correspond to a lower relative humidity. From Fig. 5.24 (d), we know that h_s decreases with decreasing RH, such that the numerical simulations might overestimate the film thickness in comparison with the lab experiments. Nevertheless, this effect does not seem significant in Fig. 5.24 (c).

5.4.2 Filling

The stationary film thickness h_s could be related to the independent parameters Ψ, S, R and t_0 by assuming power laws that fitted the measurements obtained. We have previously noted (see Sec. 5.2) that N_s was proportional to h_s. We now review the effect of Ψ, S, R and t_0 on N_s, the non-dimensional number of drops until the stationary state is reached. We have observed in Sec. 5.2 and Fig. 5.23 (a) that the stationary film thickness h_s is smaller for convex stalagmite ($\Psi < -1$). Correspondingly, in the inset of Fig. 5.23 (a), for very negative $\Psi < -1$ values, the stationary number of drops N_s remains almost equal to 1. Additionally, we note without surprise from Fig. 5.23 (a) and its inset, and from Figs. 5.23 (c) and (d), that N_s is correlated to the stationary film thickness h_s, such that it increases with Ψ from this minimum value of $N_s = 1$. For a fixed drop volume and stalagmite surface, a larger film thickness will indeed be attained by means of a larger number of drops. Small values of N_s are also more easily reached when the dripping period is longer than the drainage timescale (e.g., for $t_0/t_d = 10$) since it was shown that, in this regime, the stationary film thickness is smaller. Because of the correlation between h_s and N_s, the same conclusions as drawn above regarding the effect of the scaling S apply, hence we did not represent the evolution of N_s with S graphically. Proceeding in the same manner as with h_s, we assume that power laws potentially relate N_s to Ψ, S, R and t_0. We report the fitting parameters obtained from these power laws in Tab. 5.3. The fits obtained for the numerically computed values of the stationary number of drops, N_s, translate into the three following laws, first for perfectly horizontal stalagmites[12]:

$$N_s^{\bullet}(r = 0) = 3.2 \left(\frac{\nu V_d}{\pi g t_0 h_d^4} \frac{R^7}{r_d^7} \right)^{1/4}, \tag{5.71}$$

for convex stalagmites:

$$N_s^{\bullet}(r = 0) = 2.3 \left(\frac{-1}{\Psi S} \frac{\nu V_d}{\pi g t_0 h_d^4} \right)^{1/4}, \; \Psi < -1, \tag{5.72}$$

and for concave stalagmites:

$$N_s^{\bullet}(r = 0) = 1.5 \Psi^2 S, \; \Psi > 1. \tag{5.73}$$

We notice that both Eqs. (5.71) and (5.72) have a common feature in accordance with the results obtained for h_s: the stationary number of drops N_s increases for a larger drop inflow ($V_d \uparrow$, $t_0 \downarrow$). In the perfectly horizontal case, N_s is also found to increase with the ratio R/r_d as more drops are necessary to cover the stalagmite surface and reach the stationary film thickness in this case, although the scaling is not identical to h_s (see Eq. (5.68)). The law described by Eq. (5.72) for the convex case does not take into account this progressive filling of the stalagmite surface that could be compared to a growing pile of sand. By contrast, the stationary number of drops N_s on a con-

---

[12]We verified these scalings with other values for ϵ in Eq. (5.63) which only affects the upfront factor in the equations, hence the arbitrarity of the criterion is not important.

cave stalagmite is unsurprisingly proportional to the protuberance height, just like h_s. If we compare Eqs. (5.71), (5.72) and (5.73) to Eqs. (5.68), (5.69) and (5.70), we actually find that N_s evolves as $\sim h_s/h_d (R/r_d)^{3/2}$ in the perfectly horizontal case, as $\sim (h_s/h_d)^{1/2}$ in the convex case, and as $\sim h_s/h_d$ in the concave case, respectively.

Because N_s is not supposed to provide a precise number of drops needed for the film to reach its stationary state but rather an order of magnitude, we may rationalise our findings for N_s with a common law for all three stalagmite types. We assume that a succession of drops of volume $V_d = 4/3\pi R_d^3$ is needed to cover an initially dry stalagmite of radius r_{sm}, which we can alternatively write as $V_d = \pi r_d^2 h_d$. We consider that, once the stalagmite surface gets fully covered, the film has reached a stationary state and is uniform, i.e., equal to h_s everywhere. This is an approximation since we have shown multiple times that this is not the case, as, e.g., through Eq. (5.27) and Fig. 5.15 when the film is fed by an equivalent microjet. The volume of such a film over a flat stalagmite surface is $\pi r_{sm}^2 h_s$. We can estimate the theoretical number N_s^{th} of drops needed to fill the film as the ratio of the stationary film volume over the drop volume, i.e.,

$$N_s^{th} = \frac{3\, r_{sm}^2 h_s}{4\, R_d^3} = \left(\frac{r_{sm}}{r_d}\right)^2 \left(\frac{h_s}{h_d}\right). \tag{5.74}$$

In the case of actual stalagmites, we do not know exactly the corresponding values of h_d and r_d, but we know the drop radius $R_d = 2.7$ mm, which we will use for the cave measurements (and $R_d = 2.3$ mm for the lab measurements). We report the values obtained for both N_s^{th} and $N_s^{0.99}$, measured as explained in Sec. 5.1.1, in the parity plot of Fig. 5.25 (a), for each stalagmite for which we were able to take filling measurements (see Tab. 2.2). Additionally, values of N_s^{th} and $N_s^{0.99}$ obtained for Lab01 for various dripping periods t_0 are also shown in the graph, with the dripping periods visible in the inset of Fig. 5.20 (a). Regarding the radius r_{sm} used in the particular case of Eq. (5.74), we considered the average top radius of stalagmites as described in Sec. 3.2 and used in Ch. III. This radius could indeed be related to the region over which most drops fall. Although in the case of a flat or concave stalagmite, considering the stalagmite surface covered by the film as πr_{sm}^2 is not a strong assumption, it is not necessarily true for convex stalagmites. For example, we may compare the areas corresponding to either a paraboloid cap of a certain height and cross radius r_{sm}, $A_{parab.\,cap}$ or to a disk of radius r_{sm}, A_{disk}, in the case of, e.g., Clam07 and Org10. We illustrate our measurements in Fig. 5.25 (b). Clam07 is convex-looking but more flattened out than Org10. The average top radius of Clam07 is taken at about 1 cm from its apex centre. On the other hand, the average top radius r_{sm} measured for Org10 corresponds to the cross radius of the stalagmite profile at about 3 cm below its apex centre. We find that $A_{disk}/A_{parab.\,cap}$ is equal to 97 % for Clam07, and 82 % for Org10. A larger error is thus committed in the case of Org10 but it should not significantly affect the number of drops found using Eq. (5.74).

Due to our approximations, the estimated liquid volume from Eq. (5.74) should be larger than in reality, and the theoretical number of drops N_s^{th} could thereby be slightly smaller than the number $N_s^{0.99}$ inferred from the raw data curves, at constant film thickness. By contrast during the time of measurement, the drainage might also have started, i.e., some of the liquid from the impacted drops should have already drained, leading to a slightly larger number of drops than the measurement obtained for $N_s^{0.99}$. Some evaporation might also have appeared, although it should not be significant in caves. These effects might partially compensate. Most markers in Fig. 5.25 (a) are indeed found below the axes bisector. Nevertheless, we observe in Fig. 5.25 (a) a good agreement between the two estimated numbers of drops N_s^{th} and $N_s^{0.99}$, with a coefficient of determination $\mathcal{R}^2 = 0.96$. We can compare the actual volume of the constant drop inflow case $V_{cst.\,infl.}$ over a perfectly
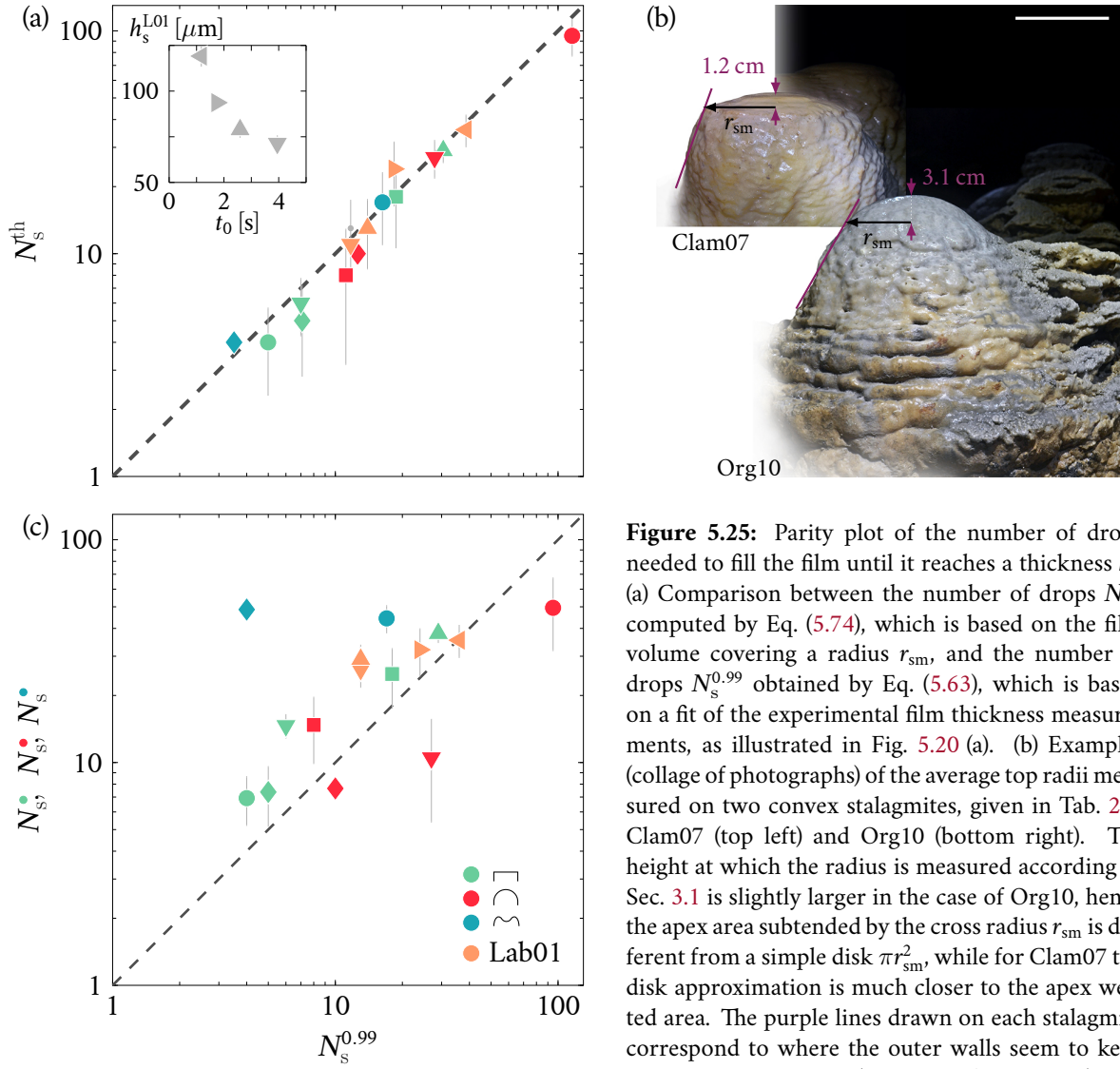
Figure 5.25: Parity plot of the number of drops needed to fill the film until it reaches a thickness h_s. (a) Comparison between the number of drops N_s^{th} computed by Eq. (5.74), which is based on the film volume covering a radius r_{sm}, and the number of drops $N_s^{0.99}$ obtained by Eq. (5.63), which is based on a fit of the experimental film thickness measurements, as illustrated in Fig. 5.20 (a). (b) Examples (collage of photographs) of the average top radii measured on two convex stalagmites, given in Tab. 2.2: Clam07 (top left) and Org10 (bottom right). The height at which the radius is measured according to Sec. 3.1 is slightly larger in the case of Org10, hence the apex area subtended by the cross radius r_{sm} is different from a simple disk πr_{sm}^2, while for Clam07 the disk approximation is much closer to the apex wetted area. The purple lines drawn on each stalagmite correspond to where the outer walls seem to keep a constant inclination (see Sec. 3 from Ch. II). The scale bar is 10 cm and refers to both stalagmites. (c) Comparison between the stationary number of drops N_s obtained from the scalings relative to the three stalagmite shapes, Eqs. (5.71) (perfectly horizontal/flat), (5.72) (convex) and (5.73) (concave), and the measured stationary number $N_s^{0.99}$ (see Fig. 5.20 (a)). In (a) and (c), the green, red and blue markers correspond to flat ($\bullet$), convex ($\bullet$) and concave ($\bullet$) cave stalagmites, respectively. The inset in (a) shows the stationary film thickness h_s reached by the film at the centre of the stalagmite as a function of the dripping period t_0 set for the measurements made on Lab01 (orange markers). The legend from (c) and inset from (a) refers to both (a) and (c). Vertical error bars come from the errors made on r_{sm}, R_d, t_0 and h_s measurements.

horizontal stalagmite, corresponding to the volume for $r \geq 1$ cm in Fig. 5.14, to the equivalent approximated film volume $V_{approx} = \pi r_{sm}^2 h_s$, with h_s the average of the film thickness in the constant pointwise inflow for $r \geq 1$ cm. We obtain $V_{approx}/V_{cst.\,infl.} \approx 1.14$ for $r_{sm} = 5$ cm. With our selected criterion (see Eq. (5.63)), we also have an average relative error of 18 % for the stalagmites approximated as flat (green symbols) (average in the individual errors), against an average relative error of 10 % for all the measurements shown in Fig. 5.25 (a). For Lab01, in accordance with our previous results, we also note in Fig. 5.25 (a) that both estimated numbers of drops increase with decreasing dripping period t_0, and hence with increasing film thickness h_s. An anova test performed on $N_s^{0.99}$ with respect to the stalagmite radius r_{sm} yields a p−value of 4×10^{-3}, i.e., r_{sm} has a significant influence on $N_s^{0.99}$. Although $N_s^{0.99}$ was not computed by using the stalagmite radius (see Eq. (5.64)), it is not surprising to find that this latter has a clear influence on the number of drops needed for the film to reach a stationary state since it was shown that h_s depends on $r_{sm}^{1/4}$. Finally, we

note in Fig. 5.25 (a) that the shape of the stalagmite (flat, convex or concave) has no strong visible effect on the number of drops needed to fill the film either. This is not surprising in the flat and concave cases, but it is for convex stalagmites. However, as we justified above, the area actually wetted by the drops is not significantly different from the approximate disk of radius $r_{\rm sm}$, especially because $S \ll 1$ for our convex stalagmites (see Tab. 2.2). Although we have only used $\pi r_{\rm sm}^2$ as a proxy of the stalagmite actual surface area wetted by drops to compute $N_{\rm s}^{\rm th}$ and we could use parameters describing better the stalagmite shape variations, such as Ψ and S, it is clear that the precision in the experimental measurements does not justify going to such lengths here (we could not repeat the measurements several times for all $N_{\rm d}$ going from 1 to 100, thus the value of $N_{\rm s}^{0.99}$ is also approximate).

The relation from Eq. (5.74) was in theory derived for a perfectly horizontal case, and indeed almost corresponds to our above numerical law from Eq. (5.71) obtained from the numerical simulations for the perfectly horizontal case. Specifically, if we use the scaling obtained by various means for $h_{\rm s}$ over a perfectly horizontal stalagmite (see, e.g., Eq. (5.68)) and insert it into Eq. (5.74) with $R = r_{\rm sm}$, we obtain

$$N_{\rm s} = \left(\frac{\nu V_{\rm d}}{\pi g t_0 h_{\rm d}^4} \frac{r_{\rm sm}^9}{r_{\rm d}^9} \right)^{1/4} , \tag{5.75}$$

such that there is a missing factor $(r_{\rm sm}/r_{\rm d})^{1/2}$ which appears when we compare the above relation to Eq. (5.71). This difference might come once again from the fact that the effect of the successive drops are considered in the numerical simulations, while in Eq. (5.74) we simply divided the approximate volume of the film by the volume of the drops, without acknowledging the in-between impact spreading of each drop. We nevertheless retrieve in both cases the correct scaling of the stationary number of drops with the drop inflow, $N_{\rm s} \sim (V_{\rm d}/t_0)^{-1/4}$, as well as the fact that $N_{\rm s}$ decreases with increasing added thickness at impact ($h_{\rm d} \uparrow$).

We have computed, as a comparison, the stationary number of drops $N_{\rm s}$ derived from the scalings of Eqs. (5.71) to (5.73), using the stalagmite measured radius $r_{\rm sm}$ for flat stalagmites (approximated as perfectly horizontal), and the shape factor Ψ and scale S for convex and concave stalagmites, all gathered from Tab. 2.2. To avoid confusion we will refer to the values of $N_{\rm s}$ derived from the scalings as $N_{\rm s}^{\rm num}$ in this section. The graph showing the three types of numbers $N_{\rm s}^{\rm num}$ as a function of $N_{\rm s}^{0.99}$ is presented in Fig. 5.25 (c). There is a relatively good agreement between $N_{\rm s}^{\rm num}$ and $N_{\rm s}^{0.99}$ when $N_{\rm s}^{\rm num}$ is obtained from Eqs. (5.71) or (5.72), i.e., for flat and convex stalagmites. However, the number $N_{\rm s}^{\rm num}$ relative to concave stalagmites obtained from Eq. (5.73) overestimates the stationary number of drops needed to fill the film, $N_{\rm s}^{0.99}$. In total, we obtain a coefficient of determination $\mathcal{R}^2 = 0.53$ from Fig. 5.25 (c). The fact that $N_{\rm s}^{\rm num}$ is larger for concave stalagmites comes from our definition of the stationary number of drops, i.e., the number of drops needed to fill the dimple in the case of concave stalagmites. With, e.g., Org07 (blue diamond), the stationary film thickness was estimated at 87.4 µm while the protuberance height is close to 1 cm. Hence, the dimple is never entirely filled with liquid, which cannot escape through drainage. The value that we obtain for $N_{\rm s}$ does thus not correspond to a balance between the dripping drop inflow and the drainage outflow, but the film still maintains a stationary state which cannot be attributed to the effect of evaporation (see Tab. 2.2 and Appendix B.3). The splash at impact, which leads to an ejected ratio $\varphi_{\rm e} \approx 1$ at the film thickness and falling height relative to Org07, seems to be at the origin of this stationary state: all the liquid entering the film following a new impact replaces the liquid leaving the former film because of the splash. Hence, it is also possible for the film to remain in stationary state in the case where $Q_{\rm drain} \approx Q_{\rm spl}$ (see Eq. 5.3), without any intervention of the

	h_s	N_s	a	b	m
Measured parameter					
Perfectly horizontal					
Exponent R'	1/4	7/4	1/2	–	-1/8
Exponent t_0'	-1/4	-1/4	-1/30	1	1/30
Factor	1	3.2	0.87	1	4.3
Convex					
Exponent S	-1/2	-1/2	-1/2	–	–
Exponent $-\Psi$ ($\Psi < -1$)	-1/2	-1/4	-1/2	1/2	–
Exponent t_0'	-1/2	-1/4	–	1	–
Factor	0.58	2.3	0.62	0.74	2
Concave					
Exponent S	1	1	1	–	1
Exponent Ψ ($\Psi > 1$)	2	2	2	–	–
Exponent t_0'	–	–	–	1	–
Factor	0.57	1.5	0.47	2.7	–

Table 5.3: Fitting parameters and exponents from the scalings appearing in Figs. 5.23, 5.26 and 5.28, obtained by assuming that h_s, N_s, a, b and m evolve as power laws with Ψ, S, R and t_0. The first row shows the variable output parameter for which the fit is obtained. This parameter evolves with either R' in the case of perfectly horizontal stalagmites or Ψ and S for convex and concave stalagmites, as well as with the dripping period t_0'. For each case (perfectly horizontal, convex, concave), we show the exponents from the power laws, then the multiplying factor relative to each measured variable. The second column of the table in the convex case, e.g., can be read as follows: $h_\mathrm{s} = 0.58\,(-\Psi)^{-1/2}\,(t_0')^{-1/2}\,S^{-1/2}$.

drainage. The relation obtained in Eq. (5.74) therefore describes the stationary state of the film in a more general sense, while the scalings derived in Eqs. (5.71) to (5.73) correspond to the stationary state as defined in Eq. (5.1), i.e., a perfect balance between the drop inflow and the drainage outflow.

5.4.3 Sole drainage

a) Numerical simulations

In the former section, we focused on the filling and stationary state of the film fed by a drop inflow. In the following graphs, we present the parameters a, b and m from the drainage fit of Eq. (5.65), that we recall here:

$$h(0,t) = \frac{a(0)}{(t + b(0))^{1/m(0)}},$$

along with the values of $\widetilde{a}$, $\widetilde{b}$ and $\widetilde{m}$ in the concave cases (see Sec. 5.1.3). We note that all these parameters are once again only evaluated in $r = 0$. In Figs. 5.26 (a), (c) and (e), we represent the evolution of a as a function of Ψ, S, R' and t'_0 respectively. We do the same in Figs. 5.26 (b), (d) and (f) for b. We also add in Figs. 5.26 (a) and (b) the values of a and b obtained for a perfectly horizontal stalagmite for which $R' = 1$. In Figs. 5.28 (a), (b) and (c), we show how m varies in response to Ψ, S, R' and t'_0 as well. Once again we assume that a, b and m evolve as power laws of the entry parameters. The coefficients and exponents corresponding to these power laws, when they exist, are reported in Tab. 5.3. In the inset of Figs. 5.28 (a) and (c), we further show how $\widetilde{m}$ evolves with Ψ, S and t'_0. The corresponding $\widetilde{a}$ and $\widetilde{b}$ are represented in Figs. 5.28 (d) and (e) and in their respective insets.

We observe in Figs. 5.26 (a) and (c) that a increases with Ψ or R in a similar manner as the stationary film thickness h_s. This is not surprising considering that a can be interpreted as being proportional to h_s, as we showed in Eq. (5.66). However, the dependence of a on the dripping period t'_0 seems rather weak. By comparison, the time shift b depends almost solely on the dripping period and not on the stalagmite shape, as show Figs. 5.26 (b) and (d). There is nonetheless a factor 10 between $\Psi = -100$ and $\Psi = 0.1$. We also note that the perfectly horizontal case values of a and b shown for $R' = 1$ in Figs. 5.26 (a) and (b) are in good agreement with the values found for $|\Psi| \lesssim 1$. Hence, the parameter a seems to continuously increase with increasing Ψ. However, we find different scalings for the various stalagmite shapes considered, just as it was the case for h_s. For perfectly horizontal stalagmite profiles, we have reported in Tab. 5.3 that a evolves as

$$a^{\bullet}(r = 0) \simeq 0.87\, h_{\mathrm{d}} \left(\frac{R}{r_{\mathrm{d}}}\right)^{1/2}, \tag{5.76}$$

in which case we did not take into account the very small variability of a in response to the dripping period, which was found to be $\sim t_0^{-1/30}$. The time shift b for perfectly horizontal stalagmites, on the other hand, was assumed not to vary with R and is given by

$$b^{\bullet}(r = 0) = t_0. \tag{5.77}$$

For concave stalagmites, as we have reported in the power law summary from Tab. 5.3, we obtain once again an almost identical law for a as the one we had found for h_s, i.e.,

$$a^{\bullet}(r = 0) = 0.47 h_{\mathrm{d}}\, \Psi^2 S, \ \Psi > 1. \tag{5.78}$$
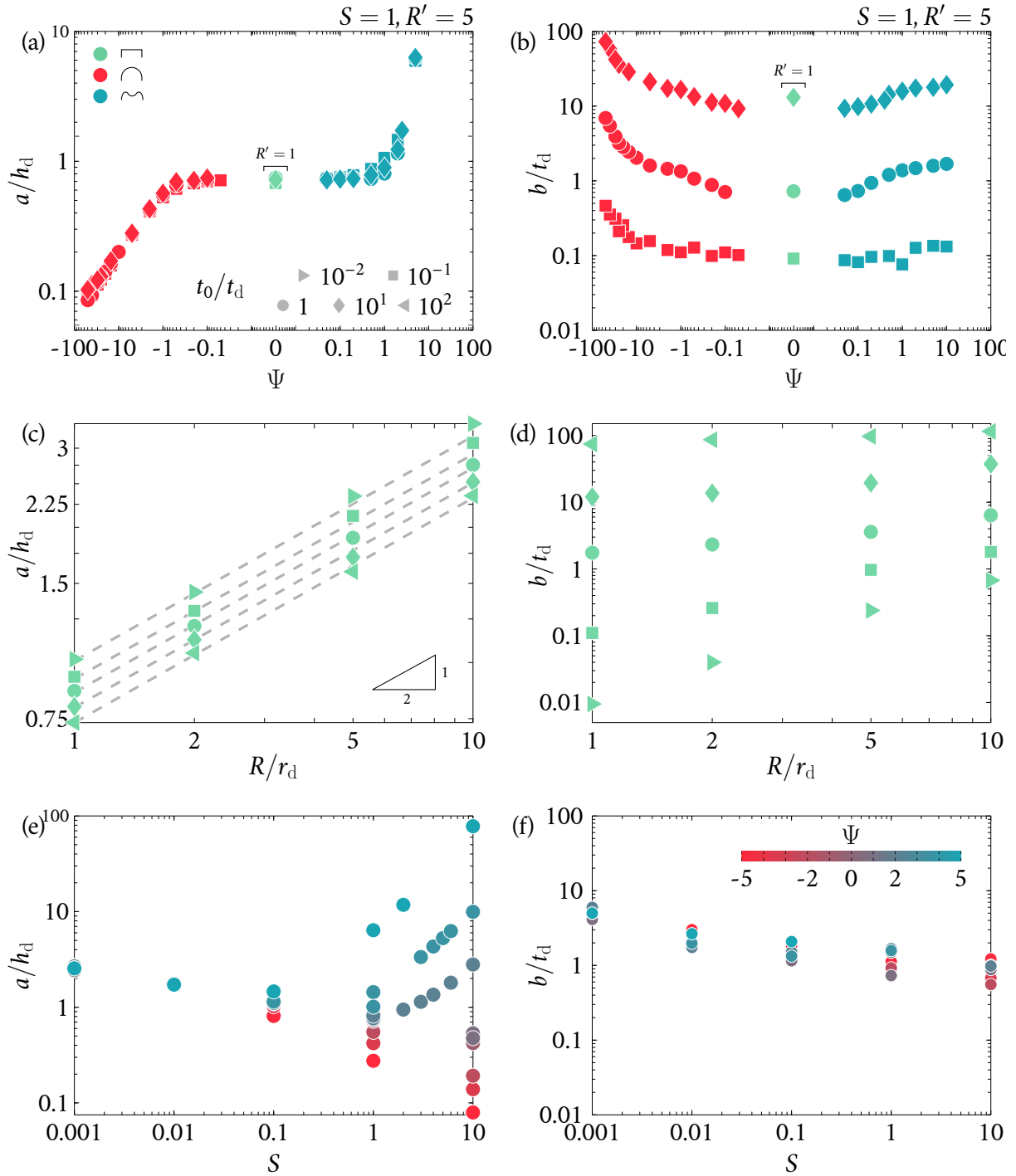
Figure 5.26: Fitting parameters of the drainage curve, a and b, obtained numerically for variable shape parameter Ψ, scale S, perfectly horizontal stalagmite radius R' and dripping period t'_0. All results were obtained for $R' = 5$ (a-b, e-f), or for $\varphi_\star = 45°$ in the perfectly horizontal case (c-d). The legends in (a) are the same for all subfigures, except for the symbol colour from (e) and (f) which is precised by the colour bar in (f). The symbol represents the dripping period used: $t'_0 = 0.01$ ($\triangleright$), $t'_0 = 0.1$ ($\blacksquare$), $t'_0 = 1$ ($\bullet$), $t'_0 = 10$ ($\blacklozenge$) and $t'_0 = 100$ ($\triangleleft$). The colour corresponds to the stalagmite general shape: convex ($\bullet$), flat ($\bullet$) or concave ($\bullet$). (a-b) Factor a and time shift b as a function of the shape Ψ, at fixed scale $S = 1$, for variable dripping period t'_0. The values computed for $\Psi = 0$ (perfectly horizontal case) correspond to a radius $R' = 1$. (c-d) Factor a and time shift b as a function of the perfectly horizontal stalagmite radius R', for variable dripping period t'_0. The dashed lines in (c) show the curves $(R')^{1/2}$, with coefficients from Tab. 5.3. (e-f) Factor a and time shift b as a function of the scale S, for Ψ varying between -5 and 5, as indicated by the colour bar.

162

The time shift b also solely depends on the dripping period as

$$b^{\bullet}(r = 0) = 2.7 t_0 \, , \ \Psi > 1 \, . \tag{5.79}$$

Because concave and flat stalagmites have a particular filling dynamics which cannot be matched by the drainage before the stalagmite becomes completely covered by the film (or before the dimple gets filled), it is perfectly normal to find that the parameter a behaves very similarly to h_s in terms of the response to the shape and size of the stalagmite (see Eqs. (5.68) and (5.70)). The only difference is in the effect of R on a for perfectly horizontal stalagmite, as it can be seen in Eq. (5.76). In Eq. (5.68), we had found that $h_s \sim (R/r_d)^{1/4}$, but we had noted that this approximation might not be the optimal one.

In Fig. 5.28 (b), for the perfectly horizontal case, we observe that the drainage curve exponent m decreases slightly with R' for perfectly horizontal stalagmites. A smaller value of m is associated with a faster drainage process. We know from Eq. (5.9) that the drainage flux q is proportional to h^3. Since the film thickness increases with the stalagmite radius R' (see, e.g., Eq. (5.68)), it is not surprising to find that larger stalagmite radii lead to faster drainage (smaller m) at a fixed dripping period. However, these variations are not substantial, and from our analysis we can only conclude that

$$m^{\bullet}(r = 0) \simeq 4 \, . \tag{5.80}$$

The dripping period t_0' also has a negligible effect on m. The above value found for m implies that h decreases as $\sim t^{-1/4}$. We further observe in Fig. 5.28 (a) that m remains more or less constant for $|\Psi| \lesssim 1$, but is close to $m = 3$ in this case. There is thus a small discrepancy in the exponent m relative to the perfectly horizontal case found for $R' = 1$ and the actual values for $|\Psi| \lesssim 1$ in Fig. 5.28 (a). The scaling found in Eq. (5.17) indicated that $h \sim t^{-1/3}$ during sole drainage when the term in $(\partial_\xi h) \cos\varphi$ dominates in the expression of the flux q (see Eq. (5.9)), which actually corresponds to the value of $m = 3$ found for flat stalagmites for which $|\Psi| \lesssim 1$, and not to the perfectly horizontal case. Although the perfectly horizontal case matches quite well the scalings obtained during the stationary phase of the film, it fails at capturing the exact drainage over slightly inclined stalagmites, that would correspond to $|\Psi| \lesssim 1$. The value found for $m \simeq 4$ in the perfectly horizontal case actually corresponds to Eq. (5.15), which describes a balance between both the filling and the drainage of the film in a stationary state.

If we now take a look at the concave case presented in Fig. 5.28 (a), we observe that the increase in m becomes quite sharp once $\Psi > 1$, such that we have

$$\lim_{\Psi \to +\infty} m^{\bullet}(r = 0) = +\infty \, . \tag{5.81}$$

A larger m corresponds to a slower drainage process. As we already mentioned in the previous section, increasing Ψ for a concave stalagmite implies that the height of the protuberance increases as well. The film thickness height inside the dimple is therefore much larger, and can less easily be drained out over the sides of the protuberance, leading to a larger m. For an infinitely tall protuberance, the value of m should thus indeed become infinite as the dimple would stay filled forever without the intervention of another process allowing to empty the dimple. A taller protuberance is also accompanied by a much more inclined outer wall at a given scaling S. Hence, the drainage will occur much faster beyond that wall, and in the centre of the stalagmite we therefore find values of $\widetilde{m}$ (the exponent computed by considering the case where h reaches the height of the protuberance H rather than a null value, see Sec. 5.1.3) decreasing sharply with increasing $\Psi > 1$ in the inset of Fig. 5.28 (a). We also note in Fig. 5.28 (d) that $\widetilde{a}$ increases very slightly with increasing $\Psi > 1$.
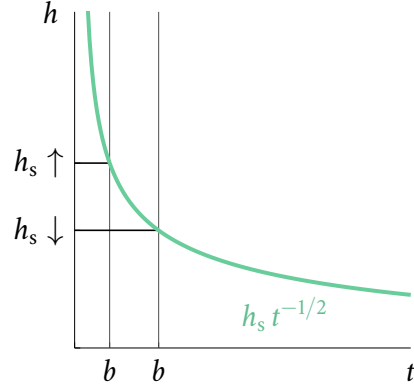
Figure 5.27: *(Right).* Illustration of the parameter a and b variations during the sole drainage in the convex case, for which $m = 2$.

In this case, $\widetilde{a}$ corresponds more or less to the supplemental thickness above the height of the protuberance, $(h - H)$. Since increasing Ψ increases H but also shifts the position of the protuberance further away from the centre, we note that, to ensure that the film can flow beyond the outer wall of the stalagmite, the thickness at the centre should reach a slightly larger value. If we consider that the film keeps the same profile above the protuberance in stationary state, just as in the case of the stationary constant pointwise inflow over a flat stalagmite that we described analytically in Sec. 4.4.2, the height at the centre of the dimple should indeed increase with the radius of the dimple, i.e., with Ψ. The inset of Fig. 5.28 (d) reveals without surprise that $\widetilde{b}$ is only conditioned by the dripping period.

For convex stalagmites, or more generally for stalagmites inclined downward, we know that the drainage is promoted by the inclination of the stalagmite profile beyond a certain curvilinear coordinate, as described by Eq. (5.16). We find the following law for a for convex stalagmites:

$$a^\bullet(r = 0) = 0.62 h_\mathrm{d} \left(\frac{-1}{\Psi S} \right)^{1/2} , \, \Psi < -1, \tag{5.82}$$

which is exactly the same as the law obtained for h_s in Eq. (5.69). On the other hand, the evolution of b is described by

$$b^\bullet(r = 0) = 0.74 \left(-\Psi \right)^{1/2} t_0 , \, \Psi < -1 . \tag{5.83}$$

As aforementioned, decreasing the parameter $\Psi < -1$ yields a more inclined stalagmite outer wall, accompanied with an increased surface area to be covered by the film. The drainage process thus starts from a smaller height, which is confirmed by the fact that a decreases with decreasing $\Psi < -1$. For a given curve $h \sim t^{-1/m}$, starting the drainage from a smaller thickness corresponds to a positive shift in the beginning of the drainage process, in accordance with the fact that b increases with decreasing $\Psi < -1$. To understand better this, we can take a look at Fig. 5.28 (a), where we observe that m reaches a minimum constant limit value of about 2 below $\Psi < -1$. This was also reported in Tab. 5.3:

$$m^\bullet(r = 0) = 2 , \, \Psi < -1 . \tag{5.84}$$

The drainage process in general starts as if we had removed the first part of the curve $t^{-1/m}$ after the time shift set by b, at the height corresponding to $ab^{-1/m}$. If drainage starts from a smaller stationary film thickness h_s, the time at which the cut in the curve $t^{-1/m}$ occurs should therefore increase, as we illustrate in Fig. 5.27. A constant exponent m thus induces a response to the stalagmite shape Ψ of both a and b. The value $m \simeq 2$ that we obtain for convex stalagmites confirms our scaling obtained in Eq. (5.19), in which we had already found that h decreases as $t^{-1/2}$ during the sole drainage phase on convex stalagmites.

Regarding the scaling S, in all the graphs from Figs. 5.26 (e-f) and Figs. 5.28 (c) and (e) we see that for $S < 1$, there is no effect of S on any of our measured parameters, as expected. We also observe in

Fig. 5.26 (e) and Tab. 5.3 that a behaves once again as h_{s}. The value of a increases with increasing S for concave stalagmites ($\Psi > 1$) and decreases as $S^{-1/2}$ for convex stalagmites ($\Psi < -1$). On the other hand, we note in Fig. 5.26 (e) that b remains almost constant with S. There is also an effect of the scaling on m in the concave case ($\Psi > 1$), as illustrated by Fig. 5.28 (c). However, as discussed above, m remains constant for convex stalagmites ($\Psi < -1$), hence we find without surprise that this is the case in Fig. 5.28 (c) as well. The effect of the scaling S on m in the concave case ($\Psi > 1$) can be explained by the same reason as already discussed with Ψ: the protuberance height and centre film thickness are proportional to S, yielding a slower drainage since the film cannot escape the interior of the dimple. A protuberance scaled by S is likewise accompanied by a more inclined outer wall, leading to a faster drainage beyond the wall. In the centre of the stalagmite we therefore find values of $\widetilde{m}$ decreasing with S, as represented in the inset of Fig. 5.28 (c). The effects of the shape Ψ and scaling S on m and $\widetilde{m}$ are thus very similar. We also once again note in Fig. 5.28 (e) and its inset that $\widetilde{a}$ is proportional to S, just as a, and that $\widetilde{b}$ remains almost constant, even for large S.

b) Experimental measurements

We present in Figs. 5.29 (a), (c) and (e) the values of a, b and m obtained for the lab measurements as a function of the imposed dripping period t_0. We only show the measurements corresponding to $\Delta d \leq 1\,\mathrm{cm}$, $T \leq 21\,^\circ\mathrm{C}$ and RH $\geq 80\,\%$ to focus only on the effect of the dripping period and avoid taking into account any dewetting that may occur at $T > 21\,^\circ\mathrm{C}$ (see Sec. 3). In Figs. 5.29 (b), (d) and (f), the values of a, b and m obtained numerically are represented as a function of their experimental counterpart, inferred from the cave dataset. For the numerical a and b, we used the scalings derived from Fig. 5.26 and described further in the text. For the flat stalagmites from our dataset, we note that we used the scalings derived from the numerically computed perfectly horizontal case, as it is the only approximation for which we have found a scaling. This scaling is based on r_{sm}, that we reported in Tab. 2.2. We indeed do not have any law relating a and b to Ψ and S for $|\Psi| < 1$. The exponents m from Figs. 5.29 come from simulations performed by using the Ψ and S values from Tab. 2.2 (in this case, we had the opportunity to use Ψ and S even for the flat stalagmites from our dataset), as well as the ratio t_0/t_{d} visible in Fig. 5.29 (a) that we will discuss in the next section. We only represent in Figs. 5.29 (b), (d) and (f) the stalagmites for which we could conduct drainage measurements (see Tab. 2.2).

Figure 5.28: *Next page.* Drainage curve exponent m computed numerically, for variable shape parameter Ψ, scale parameter S, flat stalagmite radius R' and dripping period t_0'. All results were obtained for $R' = 5$ (a, c-e), or with $\varphi_\star = 45°$ in the perfectly horizontal case (b). The legends in (a) are the same for all subfigures, except for the symbol colour from (c), resp. (e), which is precised by the colour bar in (c), resp. (e). The symbol represents the dripping period used: $t_0' = 0.01$ (▶), $t_0' = 0.1 t_{\mathrm{d}}$ (■), $t_0' = 1$ (●), $t_0' = 10$ (◆) and $t_0' = 100$ (◀). The colour corresponds to the stalagmite general shape: convex (●), flat (●) or concave (●). (a) Drainage exponent m as a function of the shape Ψ, at fixed scale $S = 1$ and for variable dripping period t_0'. The values computed for $\Psi = 0$ (perfectly horizontal case) correspond to a radius $R' = 1$. The two thin grey horizontal lines simply emphasise the values of $m = 2$ and $m = 3$ for readability. The inset shows the analogous exponent $\widetilde{m}$ as a function of Ψ, obtained in the concave case when only considering the drainage process allowing the film thickness to reach the height of the dimple rather than a null value. (b) Drainage exponent m as a function of the perfectly horizontal stalagmite radius R', for variable dripping period t_0'. (c) Drainage exponent m as a function of the scale S, for Ψ varying between -5 and 5, as indicated by the colour bar. The inset shows the corresponding values of $\widetilde{m}$ as a function of S. (d) Factor $\widetilde{a}$ obtained for concave shapes, when only considering that the film thickness reaches the height of the dimple rather than a null value, as a function of Ψ and for variable t_0'. The inset shows the corresponding time shift $\widetilde{b}$. (e) Same but with $\widetilde{a}$ as a function of the scale S, with the inset showing the corresponding time shift $\widetilde{b}$. The colour bar is the same as in (c), with a reduced version in (e).
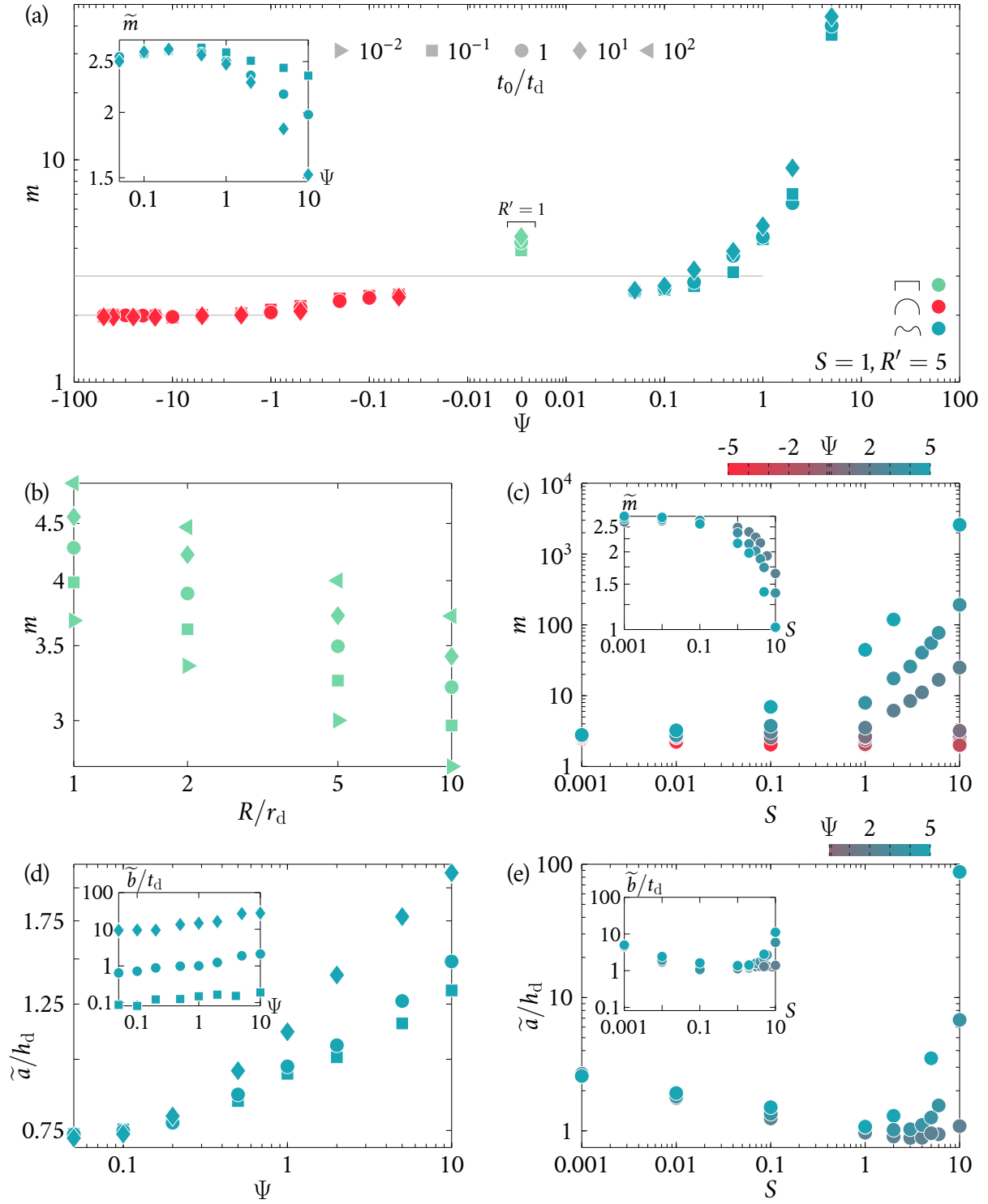
In Figs. 5.29 (a) and (c), we note that the measurements obtained in the lab for a and b both vary with the imposed dripping period t_0. In Fig. 5.29 (a), we retrieve without surprise for a the scaling that we had already found for h_s, with an exponent of -0.29 for t_0, as shown in Tab. 5.2. The evolution of b also agrees with our former findings, since we obtain from Fig. 5.29 (b) (see also Tab. 5.2) that b evolves with t_0 to the power 1.05 from the lab measurements. The evolution of m with t_0 in the lab remains quite moderate, but an anova test leads to a p-value of 2×10^{-3}. The dripping period should therefore have a significant effect on m. The effect of t_0 could potentially be attributed to our early observation from the lab raw data (see Fig. 5.6) that the difference between the maximum and minimum film thickness, $\left(h^{\max} - h^{\min}\right)$, decreased with increasing dripping period at the location at which we took our measurements. We could not reproduce such an effect numerically, but this could lead to slight variations in the transient phase preceding the drainage process in the lab curves. Although we have just discussed the effect of t_0 on m, we note in Fig. 5.29 (e) that $m = 3.08 \pm 0.64$ (average $\pm$ s.d. in all the measurements), which is in accordance with the scaling found for h_s and a in the lab and from the numerical simulations. Nevertheless, the dynamic of drop impact into a thin film is a complicated phenomenon and we cannot conclude without further investigation regarding the cause of this variation of m with t_0 in the lab. The temperature could also still play a role, although we ensured that all problematic experiments were not considered in the data presented in Fig. 5.29.

At last, after having found scaling laws for the parameters a and b in Eqs. (5.76-5.84), we may now compare them to the experimental raw data from the caves. In Figs. 5.29 (b) and (d), we compare with the a and b values from the cave measurements the values that we found from these scaling laws, in which we used the measurements for Ψ, S and t_0 from Tab. 2.2. In Fig. 5.29 (b), we observe a good agreement between the values obtained for a by the two approaches, with a coefficient of determination $\mathcal{R}^2 = 0.88$. On the other hand, some disparities are visible for b in Fig. 5.29 (d), and we only find a coefficient of determination $\mathcal{R}^2 = 0.52$. If we compute this coefficient of determination without considering the concave stalagmites which exhibit a different behaviour, we obtain $\mathcal{R}^2 = 0.64$ for b. This appears slightly better but we may not have enough data to draw a definite conclusion. Although in the case of the stationary film thickness, and hence of a, we could obtain satisfactory measurements that were also repeatable, the poor coefficient of determination found for b could also be attributed to the precision of our late drainage measurements. The time needed to position the dial gauge could indeed be sometimes of several minutes, preventing us from correctly capturing the beginning of the drainage curve associated with some stalagmites. We also assumed that b was independent of, e.g., R, although this might not be entirely accurate. On the other hand, since in caves the film is not subjected to evaporation or dewetting as in the lab, we had enough data to clearly identify the exponent m associated with each drainage curve. Figure 5.29 (f) illustrates this by displaying the values of m^{num} obtained from the numerical simulations using the parameters from Tab. 2.2 and Fig. 5.30 (a), as a function of our cave measurements. As aforementioned, the value used for m^{num} comes from numerical simulations, rather than scaling laws as for a and b, performed by using the values of Ψ and S even for flat stalagmites, i.e., instead of r_{sm}. The reasons for this are: (i) we found that the perfectly horizontal case approximates quite well the film stationary state and thereby the values of a and b, such that we had scalings for all stalagmite types (flat approximated by the perfectly horizontal case, convex and concave) regarding these two variables, but (ii) the perfectly horizontal case does not approximate correctly the exponent m obtained for flat stalagmites for which $|\Psi| \lesssim 1$, and (iii) we could not retrieve a common scaling for m in the concave case. The coefficient of determination from Fig. 5.29 (f) is $\mathcal{R}^2 = 0.86$. We also note in Fig. 5.29 (f) that the numerical exponent m^{num} relative to Lab01 reproduces well the value obtained at a dripping period of 1 s.
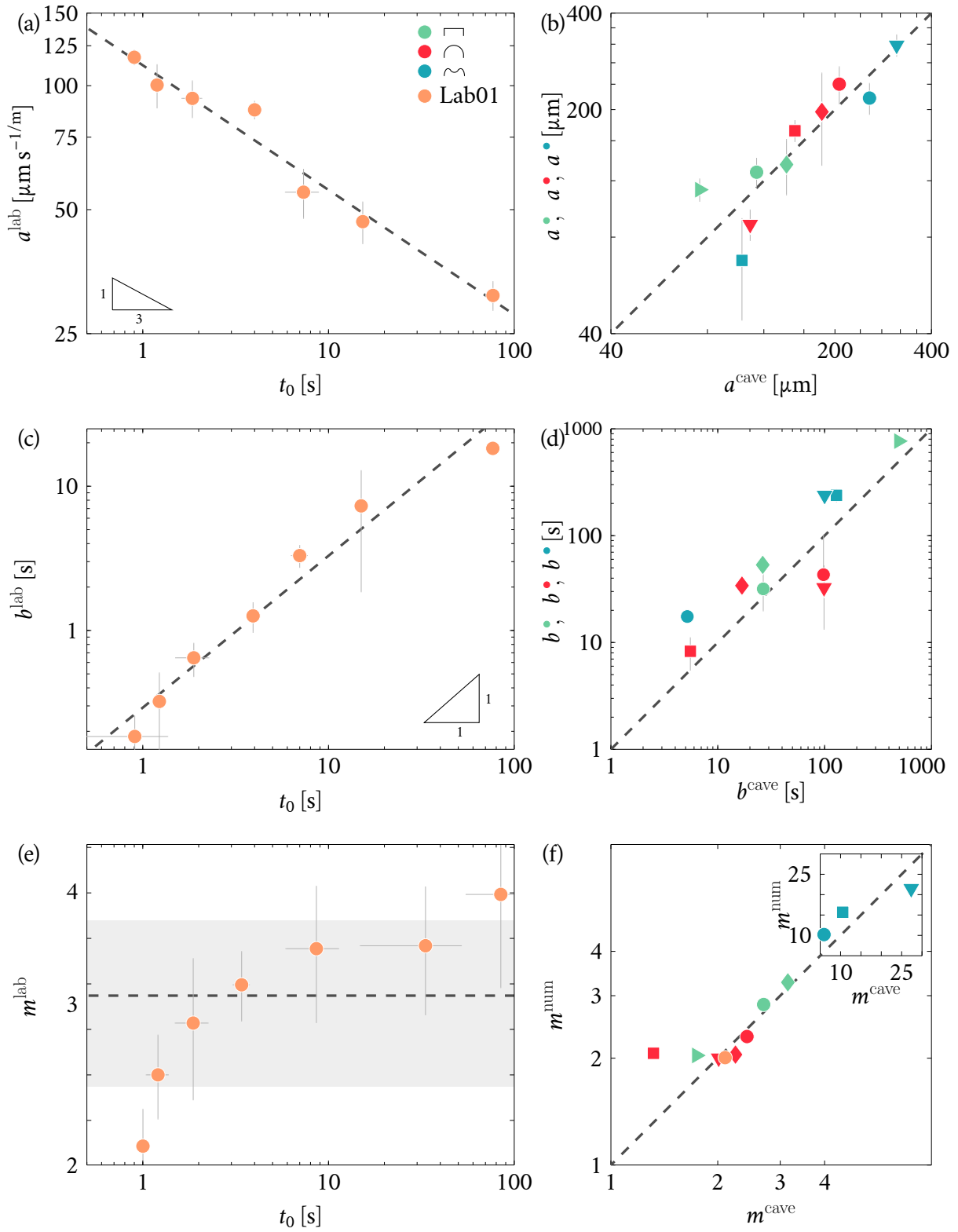
Figure 5.29: Drainage parameters a, b and m found in lab and caves. *Left panels.* Measurements of a (a), b (c) and m (e) as a function of the dripping period t_0 in the lab, for $\Delta d \leq 1$ cm, $T \leq 21$ °C and RH ≥ 80 %. The dashed line in (a) and (c) represents the scaling relative to either a or b from Tab. 5.2. The dashed line and grey area in (e) correspond to the average $\pm$ s.d. of m. *Right panels.* Comparisons between the computed values of a (b) and b (d) using Eqs. (5.76-5.84) and the parameters from Tab. 2.2, and the experimental values obtained from the fit of the drainage curve according to the procedure from Sec. 5.4.3. (c) Comparison between the exponents obtained from numerical simulations conducted by using the parameters from Tab. 2.2 and the drainage timescales derived in Fig. 5.25 (b), and the exponents measured directly from the cave raw data (f). The larger values of m, corresponding to the concave stalagmites, are shown in the inset to alleviate the ranges from the main graph and allow for a better visibility. The value found for Lab01 at a dripping period of 1 s is also displayed in the graph from (f). The green, red and blue markers correspond to convex (●), flat (●) or concave (●) cave stalagmites, respectively. The orange markers correspond to Lab01 (●). The legend from (a) is the same for all the graphs.

Finally, we note that we could also proceed in an opposite manner as what we did here: instead of attempting to measure the values of Ψ and S from photographs of the stalagmites, we could rather take our raw data measurements and find the correspondence from the laws of Eqs. (5.76-5.84). By keeping the same scaling $S = 10^{-4}$ for Clam07, e.g., we find that the corresponding Ψ that would match our measurement of a is -277, instead of the value of -375 that we had originally found. In the same manner, for Org08 we had $\Psi = 26$ for a scaling $S = 0.6$. By using the correspondence with Eq. (5.70), we find that Ψ should rather be 37.5.

6. Discussion and conclusions

In this chapter, we were interested in assessing the evolution over time and space of a thin film over a stalagmite, in order to better comprehend the gravity-induced drainage and its potential implications for stalagmite growth modelling, to which we will come back in Ch. VI. In Sec. 3, we started by reviewing measurements of film thickness on stalagmites that we conducted both in caves and in a lab setting. The measurements from caves provide us with a great variability of stalagmite shapes as we included flat, convex and concave stalagmites into our dataset (see Ch. II), but do not allow to asses the separate effects of all the parameters that may affect the evolution of the film thickness over time and space. On the other hand, in the lab, we could conduct measurements on a given stalagmite shape by systematically varying, for instance, the dripping period of the drops, t_0, or the distance between the dripping point of the drops and the sensor position where the film thickness was measured, Δd, and by measuring the temperature, T, and relative humidity, RH, in the vicinity of the stalagmite. The experimental measurements can be divided in three phases: (i) starting from an initially dry stalagmite, the film is progressively fed by a succession of drop impacts, (ii) after a certain number of drop impacts, the film has reached a stationary state during which it evolves between a maximum and minimum values, (iii) once the inflow of drops is interrupted, the sole drainage decreases the thickness of the film, at first rapidly, then at a slower pace after a few seconds. We observed from these experiments that the parameters affecting the most the film thickness are (i) the inflow of drops, i.e., the dripping period t_0, (ii) the shape of the stalagmite underneath the film, described by the shape factor Ψ and scale S (see Ch. II).

We completed the experimental measurements by modelling the drainage of the film using Reynolds equation expressed in a curvilinear coordinate system in Sec. 4. From the equations that we obtained, i.e., Eqs. (5.9) and (5.10), we inferred different theoretical scalings in Sec. 4.3. We concluded that there are two main regimes of drainage depending on the stalagmite shape underneath the film: (i) for flat stalagmites, the drainage is induced by the thickness gradients within the film, and (ii) for convex stalagmites, the drainage is caused by the inclination of the stalagmite wall. Both flat and convex stalagmites can be found in caves, and were also part of our dataset. The drainage equations are non-linear and require to be solved numerically. Nevertheless, we obtained an analytical solution for the stationary film thickness evolution over a perfectly horizontal stalagmite in Sec. 4.4.2. An approximate solution of the film thickness evolution over a cone of constant opening angle could also be derived in Sec. 4.4.1. This latter was used as a boundary condition for the numerical resolution of the equations over perfectly horizontal stalagmites, that we described in Sec. 4.5. The boundary condition obtained in this manner actually corresponds to a quasi-steady film thickness. Hence, we also derived in Sec. 4.4.3 a radius of steady/unsteady region limit in order to verify whether the boundary condition can be applied in the numerical simulations or not.

By solving the drainage equations in Sec. 5 numerically, we simulated the evolution of the film thickness in time and space for variable stalagmite shapes and dripping periods in a more systematic manner than what we could obtain from the experimental measurements. We began by looking at a simple numerical simulation conducted on a perfectly horizontal stalagmite, from

which we could observe that the numerical film thickness behaves similarly as in the cave and lab experiments, i.e., it increases for a certain number of drops before reaching a stationary state. At steady-state, the numerical film thickness also oscillates between a maximum and minimum value. During the sole drainage phase following the interruption of the drop inflow into the film, we noted in the numerical simulation, as well as in the cave and lab experiments, that the film thickness follows a law defined by Eq. (5.65), i.e., $h = a (t + b)^{-1/m}$. The three parameters a, b and m were found to vary with t_0, Ψ and S for curved stalagmite profiles, and R for flat stalagmites. We first focused in Sec. 5.2 on the effect of the drop inflow on the film at steady-state and during drainage on a perfectly horizontal stalagmite. At constant stalagmite radius, a larger inflow yields a thicker film which drains at a faster rate, in correspondence with the scalings found in the previous section, i.e., Eqs. (5.15) and (5.17). We then took a look at the effect of the stalagmite shape (convex, concave or flat) on the film thickness evolution over time and space, at constant inflow. We observed that the film was the thinnest on the convex stalagmite, while the drainage on the convex stalagmite also seemed the fastest. We then systematically varied both the dripping period t_0 and the stalagmite shape Ψ and scale S for curved stalagmites, and R for flat ones, in Sec. 5.4. We inferred measurements for the stationary film thickness h_s, the number of drops needed to reach this stationary film thickness, N_s, as well as the parameters relative to the drainage curve fit, i.e., a, b and m, all evaluated at the stalagmite centre ($r = 0$). We could further relate all these parameters to the dripping period t_0 and stalagmite profile (either Ψ and S for convex or concave stalagmites, and R for flat stalagmites) through a set of power laws fitted on the measurements and summarised in Tab. 5.3. Similarly, power laws were also estimated for the experimental measurements, and were reported in Tab. 5.2.

In the light of the above results derived from the cave and lab experiments and numerical simulations, we now have a better understanding of the influence of the dripping period, t_0, and stalagmite shape (Ψ, S for curved stalagmites and R for flat stalagmites) on subsequent film thickness variability. For flat and convex stalagmites, the stationary film thickness h increases with increasing drop inflow, by virtue of the scalings derived in Sec. 4.3. For flat stalagmites, we know from these scalings, but also from the stationary constant pointwise inflow solution derived analytically in Sec. 4.4.2, that the stationary film thickness at the stalagmite apex ($r = 0$) evolves as $h_s \sim t_0^{-1/4}$, which we could verify in the cave experiments and numerical simulations. The stationary film thickness at the apex of convex stalagmites, though, is numerically found to be $h_s \sim t_0^{-1/2}$. Our original scaling for the stationary film thickness over an inclined stalagmite predicted that $h_s \sim t_0^{-1/3}$, which was however not evaluated at the same position as in the numerical simulations. The scaling $h_s \sim t_0^{-1/2}$ is only valid at the centre of the stalagmite, while the scaling $h_s \sim t_0^{-1/3}$ from Eq. (5.16) implies that the stalagmite inclination dominates the film thickness gradients, which does not occur exactly at the centre but a little away from it. This difference might explain why we found a $t^{-0.3}$ scaling for the stalagmite Lab01 in the lab, which we had initially classified as convex. The measurements could indeed not be taken directly at the inflow source into the film but at a distance $\lesssim r_d$ from it.

The stationary film thickness is also influenced by the stalagmite shape. For perfectly horizontal stalagmites, we obtained that $h_s \sim R^{-1/4}$. This fit may only be approximate as we had found that $h_s \sim (\ln R)^{-1/4}$ in the pointwise inflow solution from Sec. 4.4.2. The film thickness nevertheless increases with the stalagmite radius for perfectly horizontal stalagmites, a result that we had already obtained from the scalings presented in Sec. 4.3. The film being at steady-state implies that, in the absence of splash or evaporation as we hypothesised, the inflow of drops, Q_{drip}, should be equal to the outflow of the film through drainage, Q_{drain}. In the case of a perfectly horizontal stalagmite, we also inferred from the drainage flux equation, i.e., Eq. (5.9), that the thickness gradients in the film dominate over the inclination of the stalagmite surface, with $\partial_\xi h_s \gg \tan \varphi$. Hence, the

flux q evolves as $\sim h_s^4/R$ in this case. A larger stalagmite radius R thus implies that, at constant inflow, the film thickness should likewise increase. This effect is visible in Fig. 5.15. Conversely, the film thickness decreases with more negative values of Ψ in the case of convex stalagmites. At fixed truncation radius R and inflow Q_{drip}, the constant volume of liquid spread onto a stalagmite of larger area should indeed yield a thinner film at the apex of the stalagmite (see Ch. II). This can also be interpreted as the fact that h_s increases with less negative values of Ψ, i.e., with a stalagmite profile becoming flatter. For concave stalagmites, we found that the film thickness increases with the protuberance height, since the film cannot reach a stationary state without filling the dimple of the stalagmite first, at least if we leave out the splash of the drops.

Additionally, the number of drops necessary for the film to reach steady-state during the filling, N_s, increases linearly with the film thickness. We have also estimated in Sec. 5.4.1 the number of drops needed for the film to reach a stationary state using the scalings obtained from either the numerical study or a theoretical argument stating that this number of drops is simply proportional to the total volume of the film lying on the stalagmite (see Eq. (5.74)). This second argument took into account the actual stationary state of the film that we observed in caves. In the numerical simulations, for flat and concave stalagmites, stationary state is only reached after the surface is entirely covered, resp. the dimple is entirely filled. We thus found a better approximation for the stationary number of drops using the simple model from Sec. 5.4.1 since the film can reach another steady state than the one corresponding to the balance between the drop inflow and the drainage outflow. A balance between the drop inflow and the evaporation could exist, or between the drop inflow and the splash of the drop at impact. This latter case could be observed for, e.g., Org07, a concave stalagmite with a partially filled dimple. In this case, the successive drop impacts should thus be taken into account for modelling the evolution of the film over the stalagmite.

The fitted parameters relative to the drainage curve, a, b and m, are also affected by the dripping period and stalagmite shape parameters. We found that, for flat and concave stalagmites, the factor a evolves exactly as the stationary film thickness, while b is almost exclusively correlated to the dripping period t_0. Additionally, for convex stalagmites, while the factor a solely depends on the shape and size of the stalagmite, the time shift b is conditioned by both the stalagmite shape Ψ and associated dripping period t_0. For the flat and concave cases, b only depends on the dripping period t_0. This may come from the fact that, in the convex case, the drainage occurs much faster because of the large stalagmite inclination, with the aforementioned constant exponent $m = 2$ (see Eq. (5.19)) for all stalagmites with $\Psi < -1$. The perfectly horizontal stalagmite also usually yields a good approximation of most scalings, except for the exponent m in the case of pure drainage over flat stalagmites. By contrast, we could retrieve our initial scaling (see Eq. (5.17)) and value of $m \simeq 3$ in the numerical simulations conducted for flat stalagmites with $|\Psi| \lesssim 1$ (i.e., which were not perfectly horizontal). The exponent m also varies, although rather slightly, with R or Ψ. A larger stalagmite or a stalagmite with a larger Ψ, i.e., with a taller protuberance, was shown to lead to a larger stationary film thickness h_s. A larger film thickness should yield, in turn, a faster drainage (i.e., a larger decrease in $\partial_t h$) because, as shown in Eq. (5.9), the drainage flux is proportional to h^3. In the concave case, in particular, the drainage process allowing the film to return to a thickness equal to the height of the protuberance (associated with $\widetilde{m}$) is therefore very fast. However, the drainage process allowing the film thickness at the centre of the stalagmite dimple to return to a null value on concave stalagmites becomes increasingly slow as we increase the value of $\Psi \gg 1$. Once the film thickness at the centre of the dimple has become close to the height of the protuberance, it becomes difficult for the film to flow beyond the protuberance. In the absence of other processes such as the evaporation, the film thus remains at the centre of the dimple. Finally, using our former results derived from the numerical resolution of our model, and the shape Ψ and size S measured for each stalagmite, we were also able to compare the values found in caves and in

lab for the drainage parameters a, b and m. We found a good agreement between our experimental data and the laws derived from the simulations. Although our results gave quite a good match with our experimental measurements, we note that in the lab experiments, other effects arise, such as, e.g., the relative humidity RH. Nevertheless, this did not prevent us from finding the same laws as from the numerical simulations, at least in the case of h_s, a and b.

6.1 Conclusions

In this chapter, pursuing our goal of understanding the influence of the stalagmite shape and size on the film drainage, we performed experimental measurements of the film thickness on stalagmites from actual caves. We completed these experiments by measurements on an actual stalagmite in a lab setting, where we could control the variations of several parameters such as the dripping period, the relative humidity in the enclosure surrounding the stalagmite or the distance from the impact point to the sensor. The measurements included three phases: the filling, stationary state and sole drainage of the film. We modeled the drainage process by using Reynolds lubrication equation, that we expressed in a curvilinear coordinate system to account for the stalagmite shape variations. In the particular case of a flat stalagmite of given radius, we were able to derive an analytical solution to our problem. There is however no simple analytical steady solution for the film thickness as a function of our parameterisation of the stalagmites, described by a shape factor Ψ and a scale S. Nonetheless, the governing equations provided several scalings for limiting cases, including the flat stalagmites for which the drainage is mostly due to the film thickness gradients existing in the film, while for convex stalagmites the inclination of the stalagmite predominates over the film thickness gradients. In the absence of analytical solutions, we solved the equations describing the drainage numerically, which allowed us to systematically vary the parameters influencing the drainage, including the drop dripping period, t_0, the shape factor, Ψ and the scale, S, for convex stalagmites, and the radius R for flat stalagmites. We obtained different scalings for several measured variables, such as the stationary film thickness of the film at the centre of the stalagmite, with respect to the shape and scale considered, i.e., Ψ, R and S. These scalings allowed us to replicate the experimental conditions numerically. We have obtained a good agreement between our data taken from the lab and cave and our modelling of the drainage.

We also noted that, as described in the literature [154], the shape underneath the film has a strong effect on the drainage process. We also retrieved a range of exponents m quite close to simple scalings that we could directly derive from Reynolds equation already, and also to existing studies [106, 153, 166]. However, instead of focusing on a particular geometry as it is often the case in the literature, we described the drainage as a function of variable shapes. Finally, to complete our current model, numerous other effects affecting the film thickness could be taken into account: the dispersal in the impact point distribution of the drops, the drop impact dynamic and potential splash, the temperature and relative humidity, the evaporation, the dewetting, the porosity of the stalagmite surface, or event the rugosity of the surface. We also focused our study on the film thickness at the centre of the stalagmite for the sake of simplicity. Nevertheless, we observed that this thickness varies with the distance to the drop dripping point. To go further into the description of the drainage of the film on stalagmites, we could also take a deeper look into the space variations of our drainage parameters a, b and m.

6.2 Outlook: stalagmite classification

In view of the very different shapes exhibited by the stalagmites from our dataset, the question arises as to whether these shapes can be, for instance, related to a specific drainage timescale or

characteristic length. Similarly to Eq. (5.14), a characteristic drainage timescale associated with each stalagmite from Tab. 2.2 may be defined as

$$t_{\mathrm{d,sm}} = \frac{\nu r_{\mathrm{sm}}^2}{g h_{\mathrm{s}}^3} \, . \tag{5.85}$$

We first point out that we used the timescale computed by Eq. (5.85) to obtain the value of t_0/t_{d} that we should use in numerical simulations in order to reproduce our stalagmite dataset, along with the measurements already obtained for Ψ and S in Ch. II. The time defined above is represented against the measured drop dripping period associated with each stalagmite, t_0, in Fig. 5.30 (a). The uncertainty in the drainage time $t_{\mathrm{d,sm}}$ was obtained from the uncertainty in the radius and stationary film thickness measurements. We observe that stalagmites classified as either flat or concave (green and blue markers) all fall within the region for which $t_{\mathrm{d,sm}} \lesssim t_0$, except for Org02 (green square). It should nonetheless be noted that Org02 is the only flat stalagmite located below a high cave ceiling ($z = 19.4\,\mathrm{m}$), such that its radius may have been extended by other effects such as drop impact point dispersal [172]. We indeed have a standard deviation in the impact point position distribution of $\Delta = 4.6\,\mathrm{cm}$ for Org02 (see Fig. 3.7 from Ch. III). Even with several arbitrary dripping periods, we also find all the points corresponding to Lab01 (orange markers) are far from the axis bisector, hence it can be safely assumed that with the actual dripping period associated with this stalagmite, this would also be the case. From Eq. (5.85), we note that a larger radius r_{sm} would lead to a larger characteristic drainage time t_{d}, and so would a smaller film thickness h_{s}, in accordance with our former discussion.

In the same manner, we defined in Eq. (5.45) the radius outlining the steady/unsteady region. This radius r_{sr} defines the limit beyond which film thickness variations from the drop impacting the centre of the stalagmite is not felt any longer, and can also be adapted to our stalagmite raw dataset as

$$r_{\mathrm{s,sm}} = k \left(\frac{g h_{\mathrm{s}}^3 t_0}{\nu} \right)^{1/2} , \tag{5.86}$$

where k should depend on the stalagmite shape. In Fig. 5.30 (b), we report the radius $r_{\mathrm{s,sm}}$ obtained for the stalagmites described in Tab. 2.2 as a function of their average top radius r_{sm} (see Sec. 3.1). We observe in Fig. 5.30 (b) that the markers relative to most flat and concave stalagmites (green and blue markers) are located on the axes bisector or above it, meaning that $r_{\mathrm{sm}} < r_{\mathrm{s,sm}}$. A few measurements are located under the bisector, especially the radius of Org02, for which we can once again argue that $r_{\mathrm{sm}}^{\mathrm{O02}}$ can be increased by the large dispersal in the impact point position of the drops falling on this stalagmite. By contrast, for all the convex cases, we have $r_{\mathrm{s,sm}} < r_{\mathrm{sm}}$. The definition of Eq. (5.86) would correspond to Eq. (5.85) if we had $t_0 = t_{\mathrm{d}}$ and $r_{\mathrm{sm}} = r_{\mathrm{sr}}$, which we do not in regard of Figs. 5.30 (a) and (b).

The film lying on a stalagmite in caves should a priori be at steady-state, i.e., such that $Q_{\mathrm{drip}} = Q_{\mathrm{drain}}$, with $Q_{\mathrm{drip}} \sim V_{\mathrm{d}}/t_0$ and $Q_{\mathrm{drain}} \sim V_{\mathrm{drain}}/t_{\mathrm{d}}$, with V_{drain} the volume leaving the stalagmite through drainage. Hence, without taking the potential splash of drops at impact into account, as we did until now, the ratio between these volumes should be proportional to $k = V_{\mathrm{d}}/V_{\mathrm{drain}} = t_0/t_{\mathrm{d}}$, where k varies with the stalagmite shape. The factor k could be retrieved empirically from the data shown in Fig. 5.30, but we do not have any theoretical argument allowing us to rationalise this parameter. A possibility would be to express the film thickness at the edge of the stalagmite, i.e., in r_{sm}, with the eventuality that this radius lies within the unsteady region. Comparing $h_{\mathrm{s}}(r = 0)/h_{\mathrm{s}}(r = R)$ should yield an approximation for k, and, hence the potential to classify the stalagmites based on their sole shape. For instance, we note from the two graphs below that, for

convex stalagmites, resp. concave stalagmites, k should be of the order of 1/100 to 1/10, resp. of the order of 10 to 100.
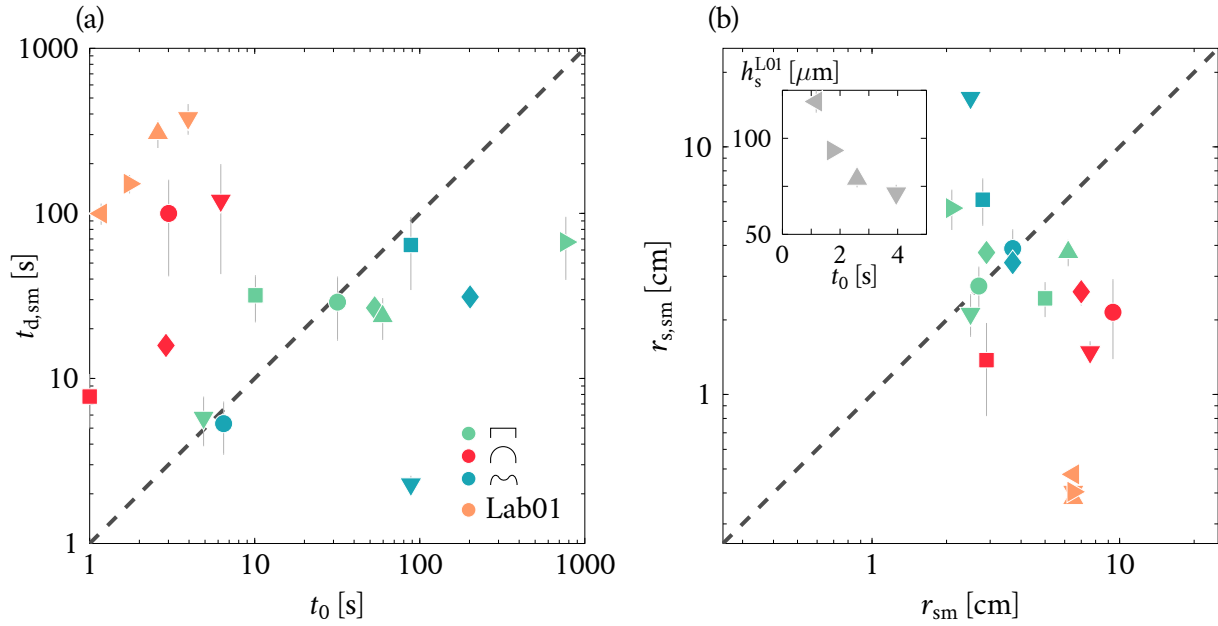
Figure 5.30: Stalagmite classification. (a) Comparison between the drop dripping period t_0 relative to the stalagmites from Tab. 2.2 and the drainage timescale t_d associated with each stalagmite, computed according to Eq. (5.85). (b) Comparison between the stalagmite average top radius r_{sm} from Tab. 2.2 (see Sec. 3.1) and the steady radius $r_{s,sm}$ associated with each stalagmite, computed according to Eq. (5.86). The legend of (a) and inset of (b) relate to both graphs. The green, red and blue markers correspond to flat (●), convex (●) and concave (●) cave stalagmites, respectively. The inset of (b) shows the stationary film thickness h_s reached by the film at the centre of the stalagmite as a function of the dripping period t_0 set for the measurements made on Lab01 (orange markers). The symbol corresponding to each stalagmite is indicated in Tab. 2.2. Vertical error bars in both (a) and (b) come from the errors made on r_{sm}, R_d and h_s measurements.

Appendix

Complementary information to some sections of the main text is provided hereafter. We start by going over the error made with the mass-based film thickness measurement technique. We then review a few elements that supplement our lab observations, and conclude by presenting numerical convergence tests relative to the drainage model.

A. Error made with the mass-based measurements

We first discuss and try to estimate the errors possibly impacting the film thickness measurements using each of the two techniques from caves and presented in Sec. 2.1. Regarding the error made by using the dial gauge technique, as it is a similar technique as the one used in Ch. IV for measuring the film thickness, we consider that the error is of the same order. The major differences between the two technique are (i) the size of the meniscus formed when touching the film with the needle and (ii) the threshold leading to the recording of the film/air interface position. We provide hereafter an estimation of the error made in the case of the mass-based measurements.
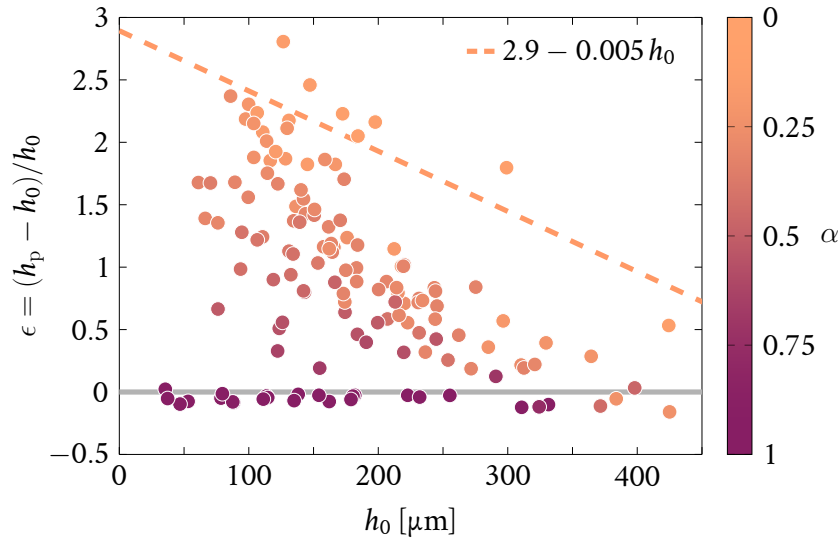
Figure 5.31: Estimation of the relative error made by measuring the spatially averaged film thickness with the paper towel and mass-based technique used in caves. Measurements were conducted in a lab setting. The thickness h_0 corresponds to the reference film thickness measured by direct weighing of the film on the balance, while the thickness h_p is the film thickness measurement inferred from the weighing of the paper towel, according to the technique described in Sec. 2.1.2. The colour mapping of the markers represents the ratio between the paper towel piece area A_p and the area of the hydrophilic tape over which the film has been spread out, A_0 (going from 1 in mauve ●, to → 0 in orange ●). The gray line corresponds to the ideal case where there would be no error. The dashed orange line was obtained by a linear fit on the data corresponding to $A_\mathrm{p}/A_0 \leq 0.05$.

In Fig. 5.31, we report measurements of the error made by the the mass-based technique used in caves (see Sec. 2.1.2). This technique consisted in weighing the mass difference of a $3 \times 3\,\mathrm{cm}^2$ piece of paper towel before and after depositing it on the stalagmite. From there, we inferred the spatially averaged film thickness over the area covered by the piece of paper towel. We reproduced the experiment in a lab setting. We started by spreading out a film of known thickness on a piece of hydrophilic tape of area A_0 (Adhesive Research, ARflow 93210), attached to a rigid plate by double-sided tape. The spatially averaged film thickness used as a reference and denoted h_0 was evaluated by simple weighing of the film. We then used a piece of paper towel of area A_p to collect water from this film and measured the difference between the wet and dry paper towel masses to estimate the

average film thickness h_p over A_p. It should be noted that A_p may differ from A_0, which allows us to replicate at best the cave conditions where we encountered stalagmites of very different sizes.

In Fig. 5.31, it can be seen that the ratio between the areas of the paper and hydrophilic tape, called $\alpha = A_\mathrm{p}/A_0$, significantly affects the relative error made by measuring the mass of the film with the paper towel, that we define as

$$\epsilon = \frac{h_\mathrm{p} - h_0}{h_0} \,. \tag{5.87}$$

We note that for $\alpha = 1$, i.e., when the substrate and paper towel piece have the same area, the error committed is about $-5.1 \pm 3.3\,\%$ (average $\pm$ s.d. in 22 measurements for which $\alpha = 1$). Hence, in this situation the thickness is a little undervalued, which can be attributed to the imperfect absorption of the paper towel, as well as the possible evaporation occurring between the measurements of h_0 and h_p and when the paper towel has absorbed the water from the film. Once $\alpha < 1$, i.e., when the paper towel area becomes smaller than the hydrophilic tape area, there is a non negligible measurement error because of the water absorption from the sides of the paper towel. Given the radii of the stalagmites for which measurements were taken (see Tab. 2.2), cave mass-based measurements fall within the range $\alpha \in [0.1\,;0.5]$. We thus had to rescale our mass-based measurements according to the law derived from Fig. 5.31 at the α corresponding to the particular stalagmite. There also exists a thickness above which the piece of paper towel becomes saturated, such that liquid flows both into the pores of the paper towel but also above it. With the paper towel used, we empirically find that this thickness is between $500\,\mu\mathrm{m}$ and $600\,\mu\mathrm{m}$, this latter value also corresponding to the interset of the dashed line drawn in Fig. 5.31 with the abscissa axis. By chance, we did not encounter thicknesses larger than $350\,\mu\mathrm{m}$ in caves, hence it can be safely assumed that we could always absorb and locally dry the film without considering this issue where we took the measurements.

B. Additional lab observations

We provide hereafter a few elements allowing a better understanding of the phenomenology described in Sec. 3. We first assess the repeatability of the lab measurements. We also present an example of a lab curve obtained at a different distance Δd between the sensor and the dripping point position than the distances shown in Fig. 5.8. The rate of evaporation during the lab measurements is then estimated. We finally review in details the impact of a drop on a thin film from a very low height, as already briefly illustrated in Fig. 5.12, before estimating the film disjoining pressure that has been neglected in Sec. 4.2.

B.1 Repeatability of the lab experiments

In Fig. 5.32, we represent two raw data curves (blue and red) taken in the lab in identical conditions, without having to move the sensor positioned at $\Delta d = 0.5\,\mathrm{cm}$ in between the measurements. The two curves were recorded the same day over the span of about an hour, hence we could maintain the following parameters with minimal error: $t_0 = 3.1\,\mathrm{s}$, $T = 18.4\,^\circ\mathrm{C}$, $\mathrm{RH} = 91\,\%$ and $\mathbf{r} = \mathbf{r}_0$. We show in Fig. 5.32 (a) the last minute during which the film is fed by successive drops, followed by the first minute of sole drainage. Figure 5.32 (b) shows a close-up view of 3 drop impacts during the stationary phase of the film, while in Fig. 5.32 (c) a log-log scaled view of the drainage process can be seen, as indicated by the grey arrows. We note a very good correspondence between both curves, which are actually difficult to distinguish.
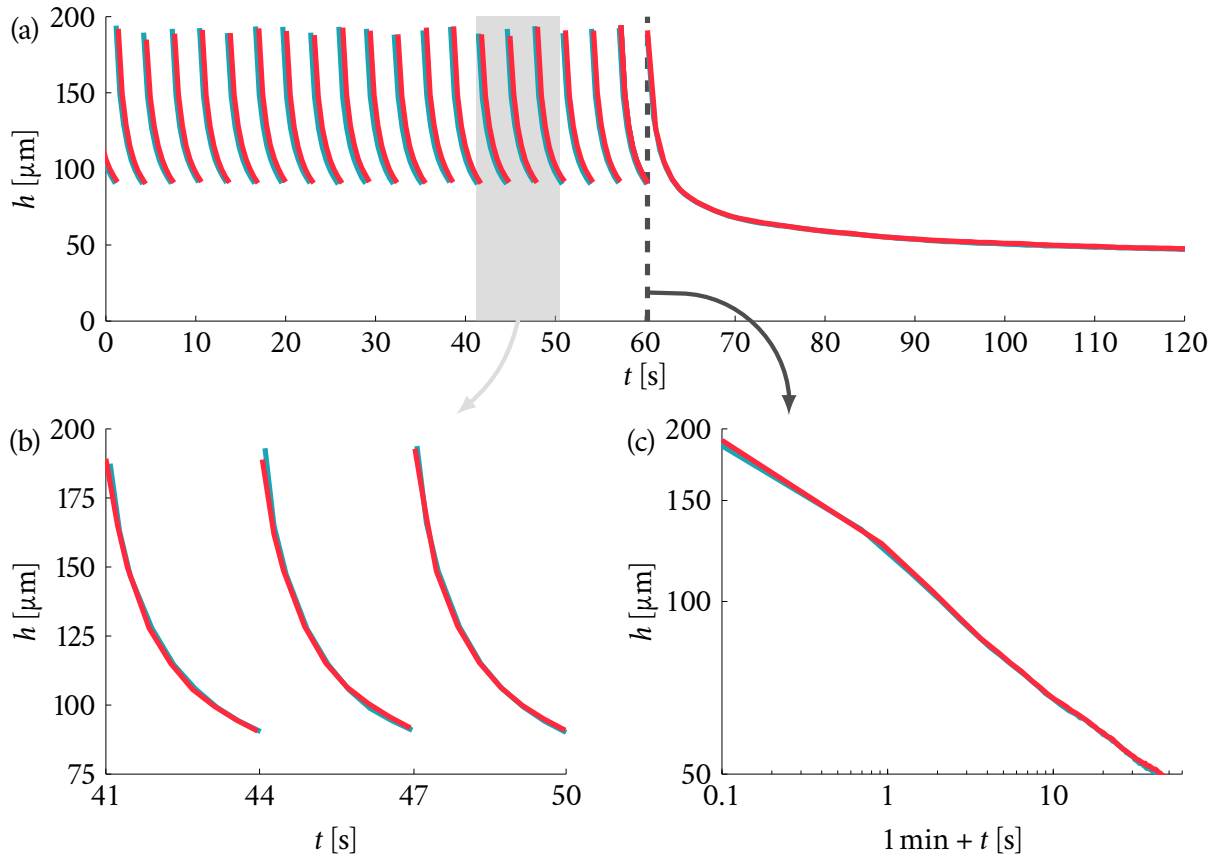
Figure 5.32: Comparison between two film thickness recordings (red and blue curves) taken in the lab in the following identical conditions: $T = 18.4\,°C$, RH $= 91\,\%$, $\mathbf{r} = \mathbf{r}_0$, $\Delta d \leq 0.5$ cm and $t_0 = 3.1$ s. (a) Thickness of the two films for the last minute during which they were fed by successive drops in stationary state, then after the interruption of the drop inflow for 1 min. Both curve positions were fitted so that the last local maximum film thickness h^{max} occurs at $t = 1$ min (indicated by the dashed line). (b) Close-up view of the stationary state of both films for $41\,\mathrm{s} \leq t \leq 50\,\mathrm{s}$, which corresponds to 3 drop impacts. The grey area and grey arrow in (a) indicate the part of the curves shown in (b). (c) Log-log scaled graph of the sole drainage of the two films, i.e., the part of (a) corresponding to $t \geq 1$ min. The dashed line and dark grey arrow in (a) correspond to the beginning of (c).

B.2 Examples of a lab curve at 2 cm from the impact point

We present in Fig. 5.33 another example of the film thickness measured at a distance $\Delta d = 2$ cm from the dripping point position. This example relates to Fig. 5.8 (a) and allows to see more clearly
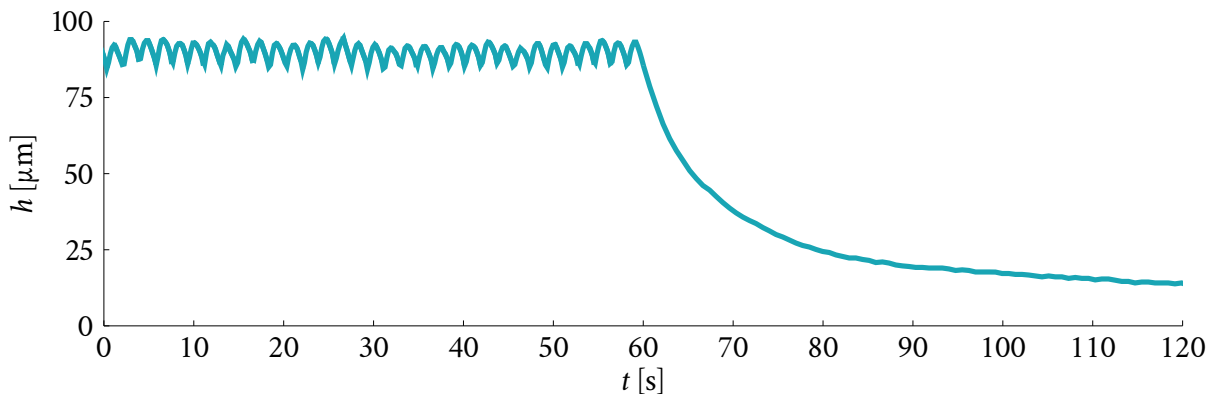
Figure 5.33: Additional example of a lab raw data curve obtained at a sensor/dripping point distance $\Delta d = 2$ cm, with the dripping point positioned in $\mathbf{r} = \mathbf{r}_1$. The temperature is $T = 20.5\,°C$ and the relative humidity RH $= 88\,\%$. The drop inflow is maintained at $t_0 = 1.8$ s until it is stopped after 1 min, before the sole drainage appears. For main figure, see Fig. 5.8 (a) (note that the dripping period presented here is slightly longer than in Fig. 5.8 (a)).

how the film thickness variations recorded by the sensor are affected by Δd during the stationary phase of the film. The parameters correspond more or less to the parameters of Fig. 5.8 (a), except for the dripping period which is slightly longer here ($t_0 = 1.8$ s instead of 1.2 s), which therefore yields a similar stationary film thickness to Fig. 5.8 (a) for $\Delta d = 5$ cm.

B.3 Evaporation rate

We consider a thin film lying on top on Lab01, as in the case of the raw data curves shown in Sec. 3 (see p. 114). For the sake of simplicity, we assume that the stalagmite has a perfectly horizontal top surface with a radius $r_{\mathrm{sm}} \simeq 10$ cm, which is entirely covered by a thin film of spatially averaged thickness $\bar{h} = 100\,\mu$m. We try to estimate in this section the time needed for the film to be depleted by the evaporation process only, with a thickness decrease of about 10 μm that supposedly occurs uniformly. We thus also consider that no other process such as drainage, e.g., depletes the film parallel to evaporation, as we only care about comparing the typical timescales of the various processes involved. In the data presented in Sec. 3, we illustrated the influence of the relative humidity and temperature on the film thickness variability using experiments performed at either a constant temperature with variable relative humidity, or vice-versa. In this section, we will use values close to our experiments and first compare the evaporation process at the constant temperature $T = 20\,°$C with $\mathrm{RH}_0 = 70\,\%$ and $\mathrm{RH}_1 = 90\,\%$. In the second case, for $\mathrm{RH} = 90\,\%$, we will use $T_0 = 15\,°$C and $T_1 = 25\,°$C.

The rate of evaporation can be approximated by [114, 214]

$$\dot{m} = M_0\, p_{\mathrm{H_2O,\,sat}}(T)\,(1 - \mathrm{RH})\,, \tag{5.88}$$

where $\dot{m}$ is the decrease in the total mass of the film over time per unit area, and the quantity $M_0 = 4.3 \times 10^{-8}\ \mathrm{kg\,Pa^{-1}\,m^{-2}\,s^{-1}}$ a constant. At a temperature of $20\,°$C, the saturation vapor pressure of water is $p_{\mathrm{H_2O,\,sat}} = 2340$ Pa. By keeping the other parameters constant, the former law indicates that going from RH_0 to RH_1 simply divides the mass rate of evaporation by 3, and therefore multiplies the time of evaporation by 3. We find that $\dot{m}(\mathrm{RH}_0) = 3.0 \times 10^{-5}\ \mathrm{kg\,m^{-2}\,s^{-1}}$ and $\dot{m}(\mathrm{RH}_1) = 1.0 \times 10^{-5}\ \mathrm{kg\,m^{-2}\,s^{-1}}$. The corresponding film thickness reductions, $\dot{h} = \dot{m}/\rho$, occur at $\dot{h}_0 = 3.0 \times 10^{-8}\ \mathrm{m\,s^{-1}}$ and $\dot{h}_1 = 1.0 \times 10^{-8}\ \mathrm{m\,s^{-1}}$, respectively. While it only takes about 5 min to deplete the entire film by 10 μm when the relative humidity is RH_0, for RH_1 this film thickness decrease should take more than 16 min. Considering that neither the film thickness nor the evaporation rate should be uniform over the stalagmite surface, it is thus not surprising that, in the vicinity of the measurements, the change in relative humidity has the strong effect illustrated by Fig. 5.10 (a). Additionally, we can compute the evaporation rate by keeping the relative humidity at $\mathrm{RH} = 90\,\%$ for a variable temperature. At $15\,°$C (resp. $25\,°$C), the saturation vapor pressure of water is $p_{\mathrm{H_2O,\,sat}} = 1705$ Pa (resp. 3171 Pa). The corresponding evaporation mass rates per unit area are $\dot{m}(T_0) = 7.3 \times 10^{-6}\ \mathrm{kg\,m^{-2}\,s^{-1}}$ and $\dot{m}(T_1) = 1.4 \times 10^{-5}\ \mathrm{kg\,m^{-2}\,s^{-1}}$. The time needed in each case to deplete the film by 10 μm over its entire surface is approximately equal to 12 min and 22 min, respectively. Hence, in contrast to Fig. 5.10 (a), evaporation has little effect in the curves shown in Fig. 5.10 (b).

B.4 Releasing a drop on a thin film from a very low height

We show in Fig. 5.34 an example of a drop impacting a thin film at low velocity. The drop has a radius $R_{\mathrm{d}} = 2.31$ mm and the film a spatially averaged thickness $\bar{h} = 117\,\mu$m (or $h^\star \approx 1$, see Ch. IV). The drop is released from the same tube as the one used in the drainage experiments (see Sec. 2.2), at a height of 4 cm above the film interface. The drop thus reaches a velocity close to $\sim 1\,\mathrm{m\,s^{-1}}$

at impact and has a corresponding Weber number of 50 (see Chs. III and IV). As it can be seen in Figs. 5.34 (a) and (b), the drop crushes in the film by forming a circular puddle, whose radius increases with time. After about 12 ms, the rim surrounding the puddle has started to destabilise (Fig. 5.34 (c)). The spot left by the drop in the film appears darker as the water drop contains dye whereas the film does not. We observe that the radius of the spot left by the drop in the film keeps increasing with time in Figs. 5.34 (d) and (f), but at a slower pace. The spot reaches an average radius of the order of 1 cm after about 20 ms.

From the moment the puddle starts to merge with the film, we also observe some capillary waves emitted around the puddle (Figs. 5.34 (c-g)). Additionally, it can be observed that the remainder of the drop left in the film is slowed down due to the capillary force and viscous drag counteracting the drop initial inertia, as in the case of high-speed impacts from Ch. IV. The spot visible in Figs. 5.34 (f-h) is indeed shrinking, and reaches a minimum after about 64 ms (Fig. 5.34 (g)). Then, this spot remains of more or less the same size for about 1 s before it grows again (Figs. 5.34 (i-j)). Nevertheless, this effect is minor as after 7 s (Fig. 5.34 (j)), the spot radius has only increased up to $\sim$ 1.2 cm, which is barely larger than the size of the spot shown in Fig. 5.34 (e). From these observations, we infer that the typical radius of the puddle formed by the drop entering in a thin film at low velocity is $\sim$ 1 cm. We can approximate the volume of a puddle of radius r_d and height h_d as $\pi r_d^2 h_d$, which is equal to the incoming drop volume $V_d \simeq 5.2 \times 10^{-8} \, \text{m}^3$. If we choose $r_d = 1.2$ cm and assume that the puddle has a uniform thickness, we find that the corresponding value of h_d is 114 µm.
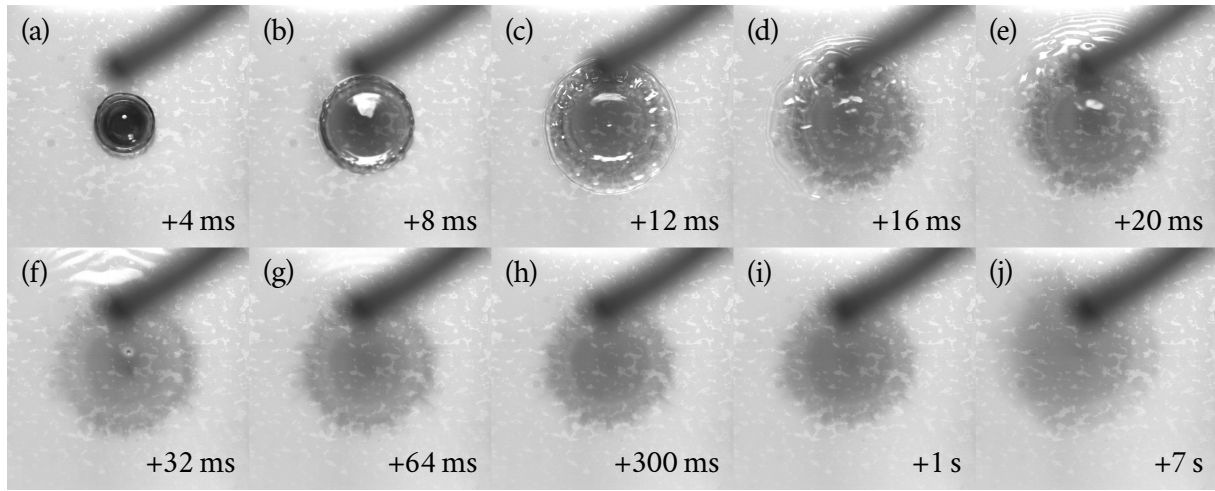
Figure 5.34: Example of an impact of a 2.31 mm radius dyed water drop on a transparent water film of spatial average thickness equal to 117 µm. The falling height of the drop is 4 cm, hence the visible tube outlet in the top part of the picture is out of focus. The successive pictures show the drop spreading from 4 ms (a) to 7 s (j) after it has started to impact the film. The spot left by the drop in the film reaches an average radius of $\sim$ 1 cm between (d) and (e). The pattern in the background is due to the adhesive coating holding the hydrophilic tape in place (Adhesive Research, ARflow 93210). The video was recorded using a Photron Fastcam Mini UX monochrome camera. The scale bar is 1 cm.

B.5 Disjoining pressure

When deriving the governing equations of the flow (see Eqs. (5.5) and (5.6)), we assumed that the disjoining pressure in the water film lying on the stalagmite was negligible in comparison to the hydrostatic pressure. We discuss this hypothesis here. The disjoining pressure stems from bringing different material interfaces together. It can be viewed as the added free energy (per unit volume)

of the entire system made of the two materials, with respect to the sum of the distinct free energies of the two systems standing at an infinite distance from one another. In another context, it can also be interpreted as the pressure needed to separate two plates joined by an intervening liquid film from each other. The disjoining pressure can either be positive or negative, and originate from repulsive or attractive forces between the two interfaces, respectively. In total, the pressure p in the film should be written as

$$p = \rho g h + \frac{\sigma}{2R} + \Pi_D(h),\tag{5.89}$$

where $\Pi_D(h)$ is the disjoining pressure, which depends on the film thickness h. We have already shown that the Laplace pressure term $\sigma/(2R)$ is negligible with respect to the hydrostatic pressure.

The disjoining pressure between water and the main constituent of the stalagmite surface, i.e., calcite, mostly comes from two contributions which both act at a short range: (i) the Van der Waals forces caused by the variability in the polarization of nearby molecules at the interface between the materials, (ii) the electronic double layer formed at the interface, due the difference in ionic charges between the materials. The first of these contributions to the disjoining pressure is modeled as follows [31]:

$$\Pi_D^{\text{VdW}}(h) = -\frac{A_H}{12\pi h^3},\tag{5.90}$$

where $A_H \simeq 2 \times 10^{-20}\,\text{J}$ is the Hamaker constant of the calcite-water system [31]. Because it leads to a negative pressure, the above relation describes an attraction between calcite and water. Because calcite and water molecules should be neutral, the contribution from the electronic double layer is minor compared to the Van der Waals forces. At the typical scale of the film, for $h = 100\,\mu\text{m}$, we obtain $\Pi_D^{\text{VdW}} = -6 \times 10^{-10}\,\text{Pa}$, which is completely negligible with respect to the hydrostatic pressure of about 1 Pa. The disjoining pressure only becomes of the same order of magnitude as the hydrostatic pressure for $h \simeq 500\,\text{nm}$. As seen in our lab experimental curves from Sec. 3, dewetting occurs before the film thickness can reach such a low value. As it results from molecular interaction and only becomes predominant at very small scales ($\Pi_D^{\text{VdW}}(h = 10\,\text{nm}) = -500\,\text{Pa}$), we conclude as expected that the disjoining pressure could indeed be neglected in our calculations.

Another type of interaction that may contribute to the disjoining pressure is the hydration force appearing when two polar solid surfaces are separated by a thin liquid film of water ($< 3\,\text{nm}$) [192]. This force is attributed to water adsorption and decays with the spacing between the surfaces. As a side note, studies have showed that hydration forces at the scale of newly formed calcite grains can become repulsive and lead to porosity in the upper layers of the stalagmite. These forces arise between two calcite surfaces in highly concentrated aqueous solution. Due to this repulsion, extended periods of water exposure may weaken calcite formations and sometimes lead to the apparition of cracks or fractures. On the other hand, calcite surfaces separated by an air layer experience attractive forces at the molecular level [192].

C. Model approximations

This last section focuses on assessing the impact of several simplifications made in the numerical model developed in Sec. 4.5 (drop addition in the film, boundary conditions). We also look into the convergence and accuracy of the solution depending on the values chosen for Δt and $\Delta \xi$.

C.1 Drop shape

Since we do not take into account the strong liquid interface disturbances occurring when a drop impacts a thin film in our resolution, the successive drop impacts are modeled as simple thickness protuberances added locally to the film. We start by varying the shape of these protuberances, i.e.,

the function $\mathcal{H}_d(r; h_d, r_d)$ defined in Sec. 4.5.2, and try to choose the one approximating at best the physics at play. We review three options here: (i) a cylinder, (ii) a portion of cone, and (iii) a truncated paraboloid, which are respectively described by

$$\mathcal{H}_d^{\sqcap} = \begin{cases} h_d, & r \leq \sqrt{2}r_d/2, \\ 0, & r > \sqrt{2}r_d/2, \end{cases} \tag{5.91}$$

$$\mathcal{H}_d^{\wedge} = \begin{cases} h_d\left(1 - \left(\dfrac{\sqrt{2}}{2}\dfrac{r}{r_d}\right)\right), & r \leq \sqrt{2}r_d, \\ 0, & r > \sqrt{2}r_d, \end{cases} \tag{5.92}$$

$$\mathcal{H}_d^{\cap} = \begin{cases} h_d\left(1 - \left(\dfrac{r}{r_d}\right)^2\right), & r \leq r_d, \\ 0, & r > r_d. \end{cases} \tag{5.93}$$

The coefficients appearing in the cylinder and conic drop formulations allow us to ensure that all three kinds of drops have the same volume and that our comparison is physically sound. We compare simulations performed with each of these drop types in Fig. 5.35 for a flat stalagmite of radius $R = 2$ with an outer boundary angle of $\varphi_\star = 45°$. The time step, numerical dripping period and space grid size are $\Delta t = 10^{-4}$, $n_0 = 10^4$ and $\Delta\xi = 0.04$, respectively. In Fig. 5.35, a succession of 25 drops can be seen, followed by sole drainage for an equivalent time, i.e., $t_{\text{fill}} = t_{\text{fill}} = 25\Delta t n_0 t_d$. We present the numerical curves in dimensional values to compare them to a curve obtained in a lab setting ($T = 18.9°C$, RH $= 89\%$, $\mathbf{r} = \mathbf{r}_0$, $\Delta d \leq 0.5$ cm, $t_0 = 1$ s). We multiplied our numerical film thickness by $h_d = 93\,\mu m$ to match at best the height reached by the lab data at each drop addition, and used $t_d = t_0$ so that the dripping period between the numerical drops corresponds to the dripping period from the lab. To ease the reading, the complete lab curve was not drawn in the main graph. We indeed observe that all three numerical curves collapse well on each other. We also represent in the inset of Fig. 5.35 a close-up view of the drop addition after $t = 20$ s in the numerical simulations, such that the film has reached a stationary state. The average made for 10 drop additions from the lab curve is shown in the inset of the graph as well (it does not correspond to $t = 20$ s, but the drop additions all occurred during the stationary phase).
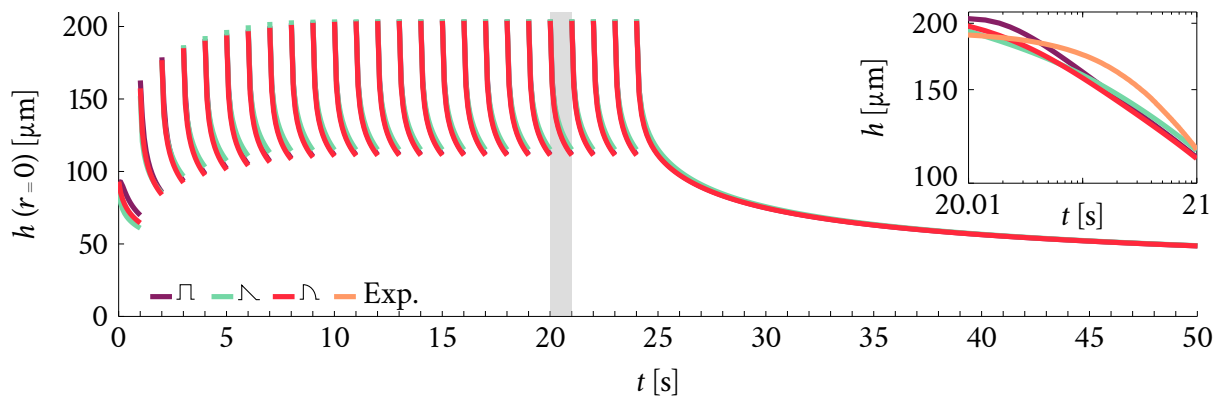
Figure 5.35: Comparison between different drop shapes added to the film. The purple, green and red curves correspond to numerical simulations solved for the three shapes defined by Eqs. (5.91)-(5.93), with parameters $\Delta t = 10^{-4}$, $n_0 = 10^4$, $\Delta\xi = 0.04$, $R = 2$, $\varphi_\star = 45°$. The curves showing the film thickness as a function of time are presented in their dimensional form using $h_d = 93\,\mu m$ and $t_d = 1$ s. The inset shows a close-up view of the three curves for $20.01\,\text{s} \leq t \leq 21\,\text{s}$, as indicated by the gray area in the main graph. The additional orange curve from the inset corresponds to the average in 10 drop additions from a lab curve with following parameters: $T = 18.9°C$, RH $= 89\%$, $\mathbf{r} = \mathbf{r}_0$, $\Delta d \leq 0.5$ cm and $t_0 = 1$ s.

Although we observe in the inset of Fig. 5.35 that the curve corresponding to the cylindrical drop is larger at the very beginning of the numerical drop insertion into the film, all three curves approximate well the actual behaviour of the drop spreading into the film in the lab experiment. The root mean square errors (RMSE) between the lab measurements and the three numerical drop additions relative to the data of the inset are 13.3 µm (cylinder), 9.8 µm (cone) and 11.8 µm (paraboloid), respectively. The RMSE computed for $t \geq 25$ s, i.e., during the sole drainage, are 4.3 µm (cylinder), 4.1 µm (cone) and 4.4 µm (paraboloid), respectively. Additionally, on average for 30 realisations of the simulation with the aforementioned parameters and each drop type, the times taken by the simulations are 45.8 s (cylinder), 40.3 s (cone) and 42.1 s (paraboloid). While keeping $\Delta t = 10^{-4}$ as well as all the other numerical parameters constant, we further obtain divergence (see following section) as soon as $\Delta \xi \leq 0.0244$ (cylinder), $\Delta \xi \leq 0.0235$ (cone), and $\Delta \xi \leq 0.0238$ (paraboloid). From our observations, we note that the differences between the three studied shapes are not significant, although conic and paraboloid drops yield a smaller error with respect to the lab measurement, as well as a slightly better convergence. Since we consider the first cell of the domain to be perfectly horizontal, adding conic drops would make less physical sense that paraboloid drops, which actually present a null derivative in $r = 0$. Hence, we model the drop addition into the film according to Eq. (5.93).

C.2 Mesh and time step convergence

Because the scheme we used in Sec. 4.5 is explicit, numerical simulations can be subjected to divergence after a few iterations, or possibly to spurious oscillations which appear during the filling phase if the time step is too large. We ensured that these problems did not occur in the results presented. Since we encountered different geometrical configurations, i.e., convex, flat and concave stalagmites, there is no unique criterion allowing to define a region of stability based on $(\Delta t, \Delta \xi)$ values. Nevertheless, we can estimate the characteristic velocity of the flow in the flat and mild convex/concave cases (i.e., $|\Psi| \lesssim 1, |S| \lesssim 1$) to get an approximate CFL condition [57]. This velocity is the largest when the first few drops spread on the initially dry stalagmite since the film thickness added by the drops is $\geq h_\mathrm{d}$ on a distance $\leq r_\mathrm{d}$, hence the gradient $\partial_\xi h$ is around its maximum. For concave cases involving large protuberance with, e.g., $H \gtrsim 10$, the velocity gradients would become larger due to the large upward inclinations involved. Hence, we usually needed to use a smaller Δt in these concave cases. For the largest Ψ presented in Sec. 5.4, we had to use $\Delta t = 10^{-7}$ or even $\Delta t = 10^{-8}$. It might be more beneficial to consider a better time integration, such as an implicit one, for these limit cases. In dimensional form, the time step Δt corresponds $\Delta t\, t_\mathrm{d}$, with the drainage timescale $t_\mathrm{d} \simeq 12$ s, and the grid step size corresponds $\Delta \xi\, r_\mathrm{d}$, with the characteristic drop radius $r_\mathrm{d} = 1$ cm. From Huppert's solution [116] of the gravity current spreading radius at constant volume shown in Eq. (5.12), we can derive the velocity taken by a drop to spread out over one time step $\Delta t\, t_\mathrm{d}$ as

$$u(\Delta t\, t_\mathrm{d}) = 0.11 \left(\frac{g V_\mathrm{d}}{3 \nu} \right)^{1/8} (\Delta t\, t_\mathrm{d})^{-7/8} . \tag{5.94}$$

For a non-dimensional time step $\Delta t = 10^{-3}$ and $V_\mathrm{d} = \pi r_\mathrm{d}^2 h_\mathrm{d}$, we get $u \approx 3.8 \ \mathrm{m\,s^{-1}}$. In these conditions, if we aim at respecting the CFL condition given by

$$C = \frac{u(\Delta t\, t_\mathrm{d})\, \Delta t\, t_\mathrm{d}}{\Delta \xi\, r_\mathrm{d}} \leq 1, \tag{5.95}$$

then we should restrict the non-dimensional grid step size to be $\Delta \xi \gtrsim 5000\, \Delta t$.

To complete our former study, we also take a look at the potential error made in the numerical calculations when using large time steps Δt or large grid step sizes $\Delta \xi$. We use a test case for which $\Psi = 0.5$ and $S = 1$ and present the error made for h^{max}, h^{min}, a, b and m in Fig. 5.36. In Fig. 5.36 (a), we impose $\Delta \xi = 0.05$ and vary the non-dimensional time step $\Delta t \in \{10^{-5}, 10^{-4}, 10^{-3}\}$. The results obtained at a time step $\Delta t = 10^{-6}$ are considered as a reference. In the same manner, in Fig. 5.36 (b), we impose $\Delta t = 10^{-4}$ and vary the non-dimensional grid step size $\Delta \xi \in \{0.02, 0.05, 0.1, 0.2\}$ while considering that $\Delta \xi = 0.01$ as a reference. In both Figs. 5.36 (a) and (b), we note that the error decreases with either decreasing time step Δt or grid step size $\Delta \xi$. Moreover, the relative error for $\Delta t = 10^{-3}$ and $\Delta \xi = 0.1$ is already $\lesssim 3\%$ for all measurements, respectively. These parameter values were used in the results presented above and may thus be considered as yielding acceptable errors.
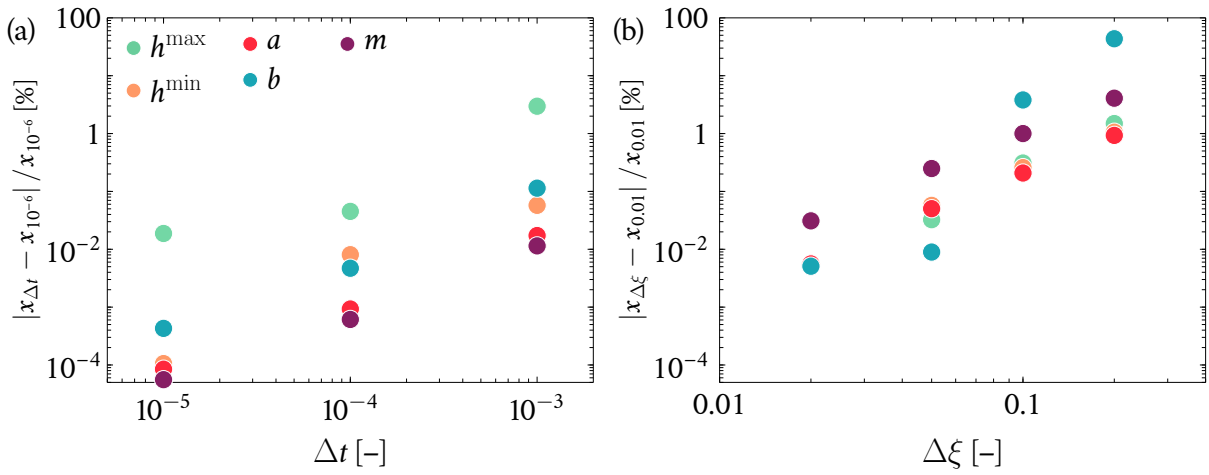
Figure 5.36: Error in the measurements of h^{max}, h^{min}, a, b and m as a function of the chosen time step Δt (a) and grid step size $\Delta \xi$ (b). The error in (a) is computed with respect to the case $\Delta t = 10^{-6}$ taken as a reference, with $\Delta \xi = 0.05$. The error in (b) is computed with respect to the case $\Delta \xi = 0.01$ taken as a reference, with $\Delta t = 10^{-5}$. The legend is the same in both graphs. In all cases, we used $N_{\mathrm{fill}} = 25$, $N_{\mathrm{fill}} = 100$, $n_0 = 1/\Delta t$ and $R = 5$.

Summary (Ch. V)

⬥ The film thickness was measured in caves and in a lab setting on various stalagmites. The experimental techniques used are described in Sec. 2. In Sec. 3, examples of film thickness evolution curves are presented. The measurements include three phases: the filling of the film as a response to the drop inflow, the stationary state of the film and the sole drainage following the interruption of the drop inflow. We observe that the main parameters influencing the film thickness evolution are the drop inflow rate and stalagmite shape.

⬥ We model the drainage of a thin film over a surface of general shape in Sec. 4, starting from Reynolds lubrication equation expressed in a curvilinear coordinate system. The equations indicate that the drainage is either dominated by the film thickness gradients appearing in the film over a flat stalagmite, or depends on the stalagmite inclination underneath the film. A characteristic drainage timescale is defined in Eq. (5.14).

⬥ The equations of drainage are solved numerically as described in Sec. 4.5. The numerical simulations consist in the addition of drops over an initially dry stalagmite followed by the interruption of this drop inflow after a steady state has been reached, allowing us to produce similar results to the lab and cave measurements. The outer boundary condition used relies on the assumption that a quasi-steady-state has been reached at the outer limit of the domain. This conditions is derived in the case of the drainage of a film over a cone of constant opening in Sec. 4.4.1.

⬥ From the observations made from the numerical resolution of a simple example in Sec. 5.1, we infer that the sole drainage curve may be approximated by a power law of time including three fitting parameters: a factor proportional to the stationary film thickness, a time shift and an exponent for the power law.

⬥ We numerically vary the response of the film to the drop inflow and stalagmite shape in a set of simulations presented in Secs. 5.2, 5.3 and 5.4. We deduce that the stationary film thickness increases with the drop inflow as in the experiments, and, for a flat stalagmite, with the stalagmite radius. Over a convex stalagmite, the film thickness decreases if the shape presents more inclined walls. These results are in agreement with scalings that we derived from the drainage equations in Sec. 4.3, except for the convex case. At the apex of a convex stalagmite, the scaling is not the same as away from the stalagmite centre. The scalings obtained can further be retrieved from the cave and lab measurements. The model also allows verifying the measurements from the caves at the end of Sec. 5.4.3.

⬥ Additionally, in Sec. 5.4.2, we present a simple model based on the balance between the volume reached by the film at steady-state in caves and the inflow of drops to estimate the number of drops needed to fill the film until it reaches a stationary state. We conclude that the splashing at impact must be taken into account in some cases, particularly for concave stalagmites.

Highlights (Ch. VI)

◆ In Ch. VI (see next page) and specifically in Sec. 1, we implement a complete model of stalagmite growth by adding to the drainage model from Ch. V an equation describing the ion evolution in the film, based on an advection-reaction equation, and an equation describing how the stalagmite profile is updated between drop impacts.

◆ The dimensionless equations indicate that the stalagmite growth is mostly conditioned by the added concentration at impact, by the ratio of the dripping period and drainage timescale, t_0/t_{d}, and by the ratio of the drainage and precipitation timescales, $t_{\mathrm{d}}/t_{\mathrm{p}}$.

◆ In Sec. 2, we obtain different stalagmite profiles by varying these parameters. The simulations conducted allow inferring the shape and scale factors relative to the stalagmite profile, Ψ and S, defined in Ch. II, as well as the growth rate of the stalagmite. This growth rate can be compared with the growth rate from Dreybrodt's model, defined in Eq. (1.7) from Ch. I.

◆ In Sec. 2.3, we present a set of preliminary simulations in which additional effects may be included, such as an initial convex stalagmite profile, or the inclusion of the dispersal exhibited by the drop impact point position into the model.
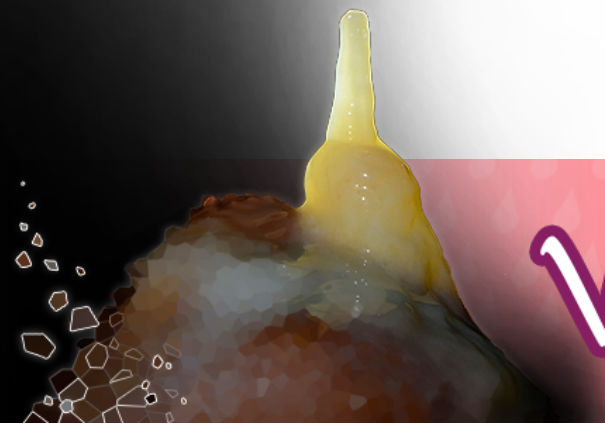
Now that we separately studied the dispersal in the impact point position of the drops, the mixing between the ions from the drop and those already present in the film lying on the stalagmite, as well as the sole drainage of this film, we can combine all these processes and take into account the ion precipitation in the film. In this chapter, we first describe the spatio-temporal ion distribution evolution within the film. We then couple the equation obtained to the film drainage and to the local stalagmite growth. Finally, we solve our system of equations to reproduce a few typical stalagmite shapes, with a focus on the particular regimes already described in Ch. I. It is recommended to read Chs. I, IV and V before the present chapter.

Credits: header photograph by P. Crochet [58].

1. Coupling between drainage and precipitation

The drainage of the residual film lying on the stalagmite could be modelled on its own in the previous chapter. However, the ion concentration distribution and gradients inside the film are in essence dependent on the film thickness in every point. Hence, we need to know the film thickness and velocity in every point of the film in order to compute the evolution in time and space of the ion concentration, and thereby of the subsequent stalagmite growth. The ions in solution are indeed at the origin of the local stalagmite growth. As we recalled in Sec. 1.2 from Ch. I, the chemical reaction allowing for stalagmites to grow is the precipitation of calcium ions Ca^{2+} into calcite $CaCO_3$, which is conditioned by the partial pressure of dissolved CO_2 in the film. We detail the modelling of the flux of calcium ions in the film through an advection-reaction equation in Secs. 1.1 and 1.2, and the modelling of the stalagmite growth using a linear approximation of Fick's law of diffusion in Sec. 1.3. The equations obtained are non-linear and require to be solved using a numerical approach detailed in Sec. 1.4. A few examples of the time evolution of stalagmite profiles in limiting cases are then shown in Sec. 2, along with parameters related to the stalagmite growth.

1.1 Ion distribution equation

To asses the quantity of calcite precipitating at one location, and therefore evaluate the change of stalagmite shape over time, we need to compute the precipitation rate which depends on the calcium ion concentration at this location. The calcium ions present in the film over the stalagmite have a concentration $\left[Ca^{2+}\right]$ (in $[mol\,cm^{-3}]$), which will now be denoted c. The other species involved in the reaction do not need to be modelled as bicarbonate and calcium ions precipitate in a $1:1$ ratio, and the other species in solution do not have any effect on the amount of calcite that

precipitates [173], except for the carbon dioxide. We assume for the sake of simplicity that there is always enough carbon dioxide to maintain a constant rate of precipitation in the film. We also assume that this carbon dioxide gets distributed uniformly throughout the film and that, outside of the film, the partial pressure p_{CO_2} in the vicinity of the stalagmite remains constant as well. Hence, the precipitation is only affected by the concentration in calcium ions. To conjugate the effects of both the gravity-driven drainage of the film and the change in the ion distribution inside the film, we not only need to solve (i) the equation of the film thickness evolution with the stalagmite shape and successive drop impacts from the previous chapter, but also (ii) the equation describing the evolution of the calcium ions over time and space. Simultaneously, the precipitation of the ions at a specific location changes the shape of the stalagmite underneath, which in turns affects the drainage and ion distribution. We therefore also need (iii) an equation describing the response of the stalagmite shape to the freshly precipitated calcite, and we need to update the shape gradients appearing in the two other equations accordingly. The drainage was modelled in the former chapter and does not require any other substantial modification than the update of the stalagmite profile over time in the numerical resolution.

To model the evolution of the calcium ion distribution with time and space, we keep the former curvilinear formalism for axisymmetric stalagmites, as illustrated in Fig. 6.1, and express once again the variables as a function of the coordinates (ξ, ζ). Because we integrated the Navier-Stokes equation over the entire film thickness and did no longer consider the velocity gradients appearing inside the film in the former chapter, we keep proceeding in the same manner here as the thin film hypothesis remains valid. We therefore neglect the diffusion of ions perpendicularly to the stalagmite surface and consider it as instantaneous. This hypothesis may not always be valid

Figure 6.1: Mass balance from Eq. (6.2) on a ring of film liquid V_{ring} located between the curvilinear coordinates ξ_1 and ξ_2.

as the diffusion timescale of species having a diffusion coefficient of $D \sim 10^{-9}$ m^2 s^{-1} (see Tab. 1.0 from Ch. I and Tab. 1.1 from auxiliary sheet) is about $t_\downarrow \sim h_d^2/D = 10$ s. We should therefore take with precaution any result possibly related to dripping periods much shorter than this timescale. We note that in Ch. V, though, we had observed that the film thickness quickly decreased during the first instants following the impact of the drop in the film. If we considered as a characteristic length scale h_d/k, $k \in \mathbb{R}$, the diffusion timescale would be divided by k^2. Hence, diffusion and drainage should only compare during the very first instants following the impact of the drop in the film, during a time where the effects related to the drop impact also play a role. We also hypothesise that, even though the ions cannot precipitate unless the solution is supersaturated, i.e., $c > c_{sat}$, with c_{sat} the saturation concentration, there is no effect of the flow of ions on the film drainage [70].

We first define the total quantity of calcium ions C in a liquid ring of volume V_{ring} as

$$C = \int_{V_{ring}} c \, dV, \tag{6.1}$$

where the liquid ring has a width $\Delta\xi = (\xi_2 - \xi_1)$ and is centered at $\xi_1 + \Delta\xi/2$, as illustrated in Fig. 6.1. The stalagmite surface is inclined by an angle φ at this position. The volume of the ring is given by $V_{ring} = 2\pi r \Delta\xi h$ (we have already considered that $\partial_\xi \varphi$ is negligible with respect to $1/h$ in Ch. V). We can write a mass balance for C in the liquid ring, i.e., between position ξ_1 and ξ_2, as

$$\partial_t C = -\dot{C}_{dif} + \dot{C}_{in} - \dot{C}_{out} - \dot{C}_{pre}, \quad \xi_1 \leq \xi < \xi_2, \tag{6.2}$$
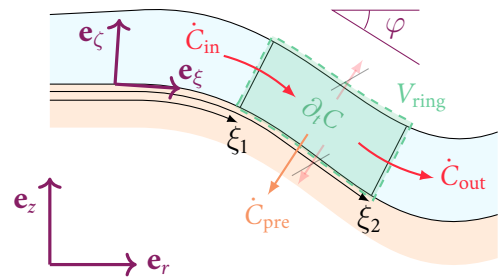
where $\dot{C}_{\mathrm{dif}}$ is the diffusive flux (corresponding to the sum of the diffusive fluxes through the faces of the liquid ring), $\dot{C}_{\mathrm{in}} - \dot{C}_{\mathrm{out}}$ is the net flux of ions flowing into and out of the ring of liquid located between ξ_1 and ξ_2, and $\dot{C}_{\mathrm{pre}}$ is the flux of ions precipitating over this liquid ring. To compare the order of magnitude of the diffusion and advection terms, we may define the Péclet number relative to the flow as $\mathrm{Pe} = UL/D$, with U a characteristic velocity, L a characteristic length and D the molecular diffusion coefficient. The characteristic velocity can be computed as the ratio of the characteristic length L over the drainage timescale defined by Eq. (5.14) from Ch. V, i.e., $U \sim L/t_{\mathrm{d}}$. The drainage described in the former chapter is indeed responsible for the advection fluxes of ions in the film. If we consider the diffusion parallel to the stalagmite surface, the length L can be chosen as $r_{\mathrm{d}} = 1$ cm, the drop radius. We thus find that the Péclet number relative to the direction parallel to the stalagmite surface is given by

$$\mathrm{Pe}_{\rightarrow} = \frac{g h_{\mathrm{d}}^3}{\nu D} \simeq 8600 \,. \tag{6.3}$$

The molecular diffusion parallel to the surface has therefore a negligible effect on the ion redistribution in the film, with respect to advection. We will therefore leave it out of our calculations. In the case where the inclination dominated the drainage regime in Ch. V, we had observed that the corresponding inclination term in the equations relative to the drainage was multiplied by a factor $r_{\mathrm{d}}/h_{\mathrm{d}}$. Including this into the above Péclet number would yield $\mathrm{Pe}_{\searrow} \simeq 9 \times 10^5$. Hence, the drainage over an inclined plane seems more efficient in comparison with the diffusion of ions in the film. By choosing as a characteristic length $L = h_{\mathrm{d}} = 100\ \mu$m, we can also compute the Péclet number relative to the diffusion in the direction perpendicular to the stalagmite surface. We obtain $\mathrm{Pe}_{\downarrow} = (g h_{\mathrm{d}}^5)/(\nu D r_{\mathrm{d}}^2) \simeq 0.9$, in accordance with the diffusion timescale $t_{\downarrow} \simeq 10$ s computed above.

As depicted in Fig. 6.1, the flux of ions $\dot{C}_{\mathrm{in}} - \dot{C}_{\mathrm{out}}$ corresponds to the sum of the upstream and downstream fluxes (flowing through the left and right faces of V_{ring} in Fig. 6.1). By virtue of the thin film hypothesis, we consider that the variables are averaged along ζ, such that there is no flux aligned with ζ (flowing through the upper and lower faces of V_{ring} in Fig. 6.1) in $\dot{C}_{\mathrm{in}} - \dot{C}_{\mathrm{out}}$. There should indeed be no flux through the upper face because the ions do not cross the liquid-air interface. The flux through the lower face, on the other hand, corresponds to the precipitation of ions and is not taken into account in the advection flux. The above mass balance can thus be written in integral form as

$$\partial_t \int_{V_{\mathrm{ring}}} c\, \mathrm{d}V = - \int_{\sum_i A_i} c\, \overline{\mathbf{u}} \cdot \mathbf{n}_{\mathrm{ext}}\, \mathrm{d}A - \int_{V_{\mathrm{ring}}} \frac{P}{h}\, \mathrm{d}V , \tag{6.4}$$

where $\overline{\mathbf{u}} = \overline{u}\, \mathbf{e}_{\xi}$ is the average velocity parallel to the stalagmite surface, A_i are the areas of the vertical faces surrounding V_{ring} and the vector $\mathbf{n}_{\mathrm{ext}}$ designates the outer normal unit vector to a face. Because the faces reduce to the left and right ones from Fig. 6.1, the outer normal vector relative to the left face, resp. right face, is[1] $\|\,(-\overline{\mathbf{u}})$, resp. $\|\,\overline{\mathbf{u}}$. In the above equation, we have also defined P as the precipitation rate per unit of surface area (in $[\mathrm{mol\ m^{-2}\ s^{-1}}]$). The ions can indeed be considered as precipitating only over A_{ring}, the annulus of stalagmite surface covered by V_{ring}, equal to $2\pi r \Delta \xi$. As aforementioned, we neglect the ion diffusion perpendicular to the stalagmite surface toward and from the surface A_{ring}, and assume that it can be averaged along the ζ-coordinate. Using

---

[1] $\|$ sign means parallel.

the divergence theorem, we rewrite Eq. (6.4) as

$$\partial_t \int_{V_{\text{ring}}} c \, \mathrm{d}V = - \int_{V_{\text{ring}}} \nabla \cdot (c \, \overline{\mathbf{u}}) \, \mathrm{d}V - \int_{V_{\text{ring}}} \frac{P}{h} \, \mathrm{d}V, \qquad (6.5)$$

We also consider that c is uniform over the liquid ring volume V_{ring}. This volume can be considered as infinitesimal, which corresponds the limiting case for which $\xi_2 \to \xi_1$. The divergence operator in the curvilinear coordinate system from Fig. 6.1 writes as $\nabla \cdot \mathbf{q} = (-1/r) \, \partial_\xi (qr)$ (see Sec. 4 from ch. V), with $\mathbf{q} = q\mathbf{e}_\xi$. The above equation can thus be written as

$$(\partial_t c) \, h + c \, (\partial_t h) = -\frac{1}{r} \, \partial_\xi (c\overline{u}hr) - P. \qquad (6.6)$$

The divergence of the ion concentration may also be expressed as

$$-\frac{1}{r} \partial_\xi \, (c\overline{u}hr) = -\overline{u}h \, (\partial_\xi c) - \frac{1}{r}c \, \partial_\xi (\overline{u}hr) \ . \qquad (6.7)$$

Acknowledging the fact that $\partial_t h = (-1/r) \, \partial_\xi(\overline{u}hr)$ since $q = \overline{u}h$, we find that the second term of the left-hand side of Eq. (6.6) and the second term of the right-hand side of Eq. (6.7) cancel out. From Eq. (6.6), we can state that the net flux of ions primarily comes from the difference between the number of ions downstream and upstream, entrained by the film drainage as

$$\partial_t c = -\overline{u} \, (\partial_\xi c) - \frac{P}{h}, \qquad (6.8)$$

where $\overline{u}$ is obtained using Eq. (5.9) from Ch. V:

$$\overline{u} = \frac{1}{h} \int_0^h u \, \mathrm{d}\zeta = -\frac{gh^2}{3\nu} \left[(\partial_\xi h) \cos \varphi - \sin \varphi \right] \ . \qquad (6.9)$$

The decrease in C caused by the precipitation of ions can be modelled by Fick's law at the bottom of the film. As a first approximation, we consider that this corresponds to having a uniform precipitation rate per unit area in the film, P, such that the last term of the right-hand side of Eq. (6.5) becomes $\dot{C}_{\text{pre}} = P V_{\text{ring}}/h$. Buhmann and Dreybrodt [41] already studied the dissolution rate of calcium ions in a thin film in both open and closed conditions, i.e., the film can either be surrounded by air or confined in between calcite structures, as in small cave wall fractures, for instance. Starting from the kinetics of reaction of the dissolved ion species in the film, they concluded that the flux of calcite dissolution could be approximated as varying linearly with the concentration. We proceed in the same manner here and consider, as a first order approximation, that the precipitation rate increases linearly with the supersaturated concentration in calcium ions as

$$\dot{C}_{\text{pre}} = \frac{\alpha}{h} \, (c - c_{\text{sat}}) \, V_{\text{ring}}, \qquad (6.10)$$

where α and c_{sat} are the kinetic reaction constant and the saturation concentration of calcium ions in the film, respectively, at given temperature, pH and partial pressure in carbon dioxide [70]. The value of α and c_{sat} computed by Buhmann and Dreybrodt [41] for both closed and open systems are reported in Tabs. 6.1 and 6.2 from Appendix A, respectively. The above approximation is valid for films of thickness comprised between about 50 µm and 500 µm [70]. Below this range, the amount of precipitated calcium ions is equal to the amount of CO_2 converted in H_2CO_3. The CO_2 conversion dictates the precipitation rate α, which therefore varies significantly with h [70].

For $h > 500\,\mu m$, the diffusion of species in solution becomes limiting [70]. If we compute the vertical diffusion timescale for $h = 500\,\mu m$, we indeed find that $t_\downarrow = 250\,s$, which might be longer than the drainage timescale (see Sec. 4 in Ch. V). In the simulations conducted for various shapes and dripping periods in Ch. V, we could note that, for convex or more or less flat stalagmites, the stationary film thickness remained comprised between roughly $0.5h_d$ and $5h_d$ (which corresponds to the range $[50\ ;\ 500]\,\mu m$ for $h_d = 100\,\mu m$), although these values were mostly attained at the limits of the range of dripping periods covered in the experiments and simulations (see Figs. 5.4, 5.6 and 5.23 from Ch. V).

In the subsequent modelling, we will consider α and c_{sat} as arbitrarily-tuned parameters comprising the environmental variables, i.e., the temperature and the differential in carbon dioxide partial pressure between the film and the surrounding atmosphere, which dictates the precipitation rate and, thereby, the stalagmite growth rate. The value of $\dot{C}_{pre}$ is positive, resp. negative, when $c > c_{sat}$, resp. $c < c_{sat}$, i.e., when precipitation occurs, resp. dissolution. We further note that Eq. (6.10) above is an approximation of Fick's first law of diffusion [88], if we consider that the gradient $\partial_\zeta c \simeq (c - c_{sat})/h$, which is in accordance with the linear approximation made by Buhmann and Dreybrodt [41]. Correspondingly, we would also have a form of diffusion coefficient $\alpha V_{ring}/A_{ring}$. This diffusion coefficient can also be written more simply as αh. Although we left the diffusion out of the discussion, we note that the parameter α from Dreybrodt's model conveys an approximation of how fast the ions reach the stalagmite surface, i.e., diffuse throughout the film.

Gathering the above relations, we note that the evolution of the ion concentration distribution in the film can be described by a classical advection-diffusion-reaction equation [175], although in a limiting case since molecular diffusion is neglected. We thus have

$$\partial_t c = \frac{gh^2}{3\nu}\left[(\partial_\xi h)\cos\varphi - \sin\varphi\right](\partial_\xi c) + \frac{\alpha}{h}(c_{sat} - c)\ . \tag{6.11}$$

This equation can be nondimensionalised by using the same horizontal and vertical length scales as in the former chapter, i.e., $\xi = \xi' r_d$ and $h = h' h_d$, respectively. We also use the same timescale $t = t' t_d$ in order to solve both the advection-reaction and drainage equations simultaneously. For the ion concentration, we use $c = c' c_{sat}$, hence we have $c'_{sat} = 1$. Regarding the kinetic reaction constant α, it has the same dimension as a velocity. Because precipitation supposedly occurs in the normal direction to the stalagmite surface, we approximate $\alpha = h_d/t_p$, by introducing t_p, the precipitation timescale, as[2]

$$t_p = \frac{h_d}{\alpha}. \tag{6.12}$$

This timescale corresponds to the time needed for a pile of precipitated ions to stack over a height h_d, if the precipitation occurs at a constant rate α the entire time, i.e., within an infinite ion reservoir. This timescale is also in agreement with Eq. (6.10) above. We have indeed found that αh acts as a form of diffusion coefficient, such that the corresponding time related to the precipitation reaction is $t_p = h_d^2/(\alpha h_d) = h_d/\alpha$, if we use the drop height as the characteristic thickness. Inserting these relations into Eq. (6.11), we find that

$$\partial_{t'} c' = \frac{(h')^2}{3}\left[(\partial_{\xi'} h')\cos\varphi - \left(\frac{r_d}{h_d}\right)\sin\varphi\right](\partial_{\xi'} c') + \frac{1}{h'}\left(\frac{t_d}{t_p}\right)(1 - c')\ , \tag{6.13}$$

---

[2]The timescale t_p corresponds to the *decay time* T_d defined by Dreybrodt by using h instead of h_d, see Eq. (10.12) in [70].

where we note the appearance of the ratio of drainage and precipitation timescales in the reaction term of the right-hand side, $t_\mathrm{d}/t_\mathrm{p}$. Following the definitions of the important timescales at play from Sec. 2 in Ch. I, we thus expect to obtain different regimes of stalagmite growth whenever $t_\mathrm{p} \lesseqgtr t_\mathrm{d}$.

In the following, we will discuss the inclusion of the ions coming from the drops into the film in Sec. 1.2, complete the model by deriving the equation used to update the stalagmite surface because of the precipitation at play in Sec. 1.3, then present the numerical approach to solve the system of equations obtained in Sec. 1.4.

1.2 Drop addition, mixing and ejected proportion

Besides diffusion and advection, the calcium ions could be redistributed by the splash and mixing occurring during the impact of a drop on a thin film. Because the drop impact is very short ($\lesssim$ 100 ms), we have already assumed that we could neglect the drop impact dynamic and possible splash, and only considered the successive drops entering the film as simple artificial increases in the film thickness over a radius r_d and height h_d. Hence, no changes are made compared to the previous chapter regarding the numerical drop addition in the film (see Sec. 4.5.2) in terms of thickness. Nevertheless, not taking into account the complex dynamics of the splashing drop at impact does not prevent us from including our results on the mixing from Ch. IV into the modelling of the ion addition. We indeed obtained in Fig. 4.13 from Ch. IV the evolution of the proportion of liquid coming from the drop and entering the film at impact. We can thus consider several possible profiles of ion quantity added to the film at each impact depending on the local film thickness. To include the ions brought by the successive drops into the film, Eq. (6.2) should be modified accordingly, which yields

$$\partial_t C = \dot{C}_\mathrm{in} - \dot{C}_\mathrm{out} - \dot{C}_\mathrm{pre} + \sum_n C_\mathrm{d}(\xi\,;c_\mathrm{d})\,\delta\left(t - nt_0\right), \tag{6.14}$$

where δ is the Dirac distribution, and where the added ion quantity at impact, C_d, is given by

$$C_\mathrm{d} = \begin{cases} c_\mathrm{d}\,\varphi_\mathrm{d\rightarrow f'}\,V_\mathrm{d}\left(1 - \left(\dfrac{r}{R_\mathrm{eq}}\right)^2\right), & r \leq R_\mathrm{eq}, \\ 0, & r > R_\mathrm{eq}. \end{cases} \tag{6.15}$$

In the former relation, the drop concentration c_d is computed as $c_\mathrm{d} = C_\mathrm{d}/V_\mathrm{d}$ by assuming that the ions are uniformly distributed inside the impacting drop. Instead of also using the drop radius r_d from the previous chapter to describe the ion distribution brought by the drop into the film, we can use the equivalent spot radius R_eq derived from the mixing experiments in Ch. IV (see Fig. 4.9). In practice, ions would be distributed all over r_d, just as the liquid from the drop, but given the experiments conducted in Ch. IV, we noted that the ions could sometimes be mostly localized only over a radius $R_\mathrm{eq} < r_\mathrm{d}$ with a higher concentration (see Figs. 4.5 and 4.6). The value of c_d is the calcium ion concentration in the falling drop, which must be imposed and is also assumed to be uniform throughout the drop. The resulting quantity of ion is $c_\mathrm{d}V_\mathrm{d}$, with V_d the drop volume. The amount of ions actually entering the film is mitigated by $\varphi_\mathrm{d\rightarrow f'}$, the ratio of the drop volume actually left into the film over the falling drop volume (see Fig. 4.13 (a) in Ch. IV). Both R_eq and $\varphi_\mathrm{d\rightarrow f'}$ can be estimated as a function of the local film thickness when the drop is added into the film. For typical values of the film thickness, e.g., $h \in \{50\,\mu\mathrm{m}, 100\,\mu\mathrm{m}, 200\,\mu\mathrm{m}, \gtrsim 300\,\mu\mathrm{m}\}$, we have $R_\mathrm{eq}/r_\mathrm{d} \in \{0.25, 0.5, 0.7, 1\}$ and $\varphi_\mathrm{d\rightarrow f'} \in \{0.1, 0.2, 0.4, 0.5\}$, respectively. In Ch. IV, we had also estimated that part of the original content of the film ends up in the ejected droplets at impact,

which was represented by $\varphi_{f\to e}$. However, we noted in Fig. 4.13 (b) from Ch. IV that $\varphi_{f\to e}$ was of the order of 0.1. The concentration inside the film is further expected be more dilute than in the successive drops at the impact times, so that it can be safely assume that the loss of ions caused by $\varphi_{f\to e}$ is negligible with respect to the added ions at impact. We discuss in Appendix B the possible effect that the distribution chosen for c_d may have on subsequent stalagmite growth. We will only make use of Eq. (6.15) in the following.

1.3 Complete model in curvilinear coordinates

In order to model the stalagmite growth from the precipitated calcite, we need an additional equation describing the stalagmite shape variations over time. We have called $\eta(r)$ the elevation profile of the stalagmite with respect to the radial coordinate in Ch. II. The addition of stalagmite elevation due to precipitation at position r over a time period Δt can be approximated, at first order, by

$$\eta(r, t + \Delta t) \approx \eta(r, t) + \partial_t \eta(r, t)\Delta t \,. \tag{6.16}$$

We assume that this growth is perfectly axisymmetric, so that we can keep making use of the curvilinear coordinate system describing all the previous equations. The effect of a non-axisymmetric growth will be reviewed in Sec. 2.3.4. The local stalagmite growth, perpendicular to the former interface $\eta(r, t) \; \forall r$, is given by

$$\partial_t \eta \;=\; \dot{C}_{pre} \frac{m_{m,CaCO_3}}{\rho_{CaCO_3} A_{ring}} \,, \tag{6.17}$$

where $m_{m,CaCO_3} = 100.1 \,\mathrm{g\,mol^{-1}}$ is the molar mass of calcite, $\rho_{CaCO_3} = 2.71 \,\mathrm{g\,cm^{-3}}$ its density and A_{ring} the ring of stalagmite surface of width $\Delta\xi$ positioned at $\xi + \Delta\xi/2$, as defined in Sec. 1.1. We note that, while fresh calcite is usually a slightly porous material [192] of seasonally variable grain density [72, 211], we cannot take this aspect into account in the modelling presented here. We therefore assume that the calcite formed upon precipitation is a homogeneous and continuous solid. Using the definition of $\dot{C}_{pre}$ from Eq. (6.10) and the fact that the film volume of the ring positioned at $\xi + \Delta\xi/2$ is $V_{ring} \approx h A_{ring}$, we have

$$\partial_t \eta = \frac{\alpha}{h} \frac{V_{ring}}{A_{ring}} \frac{m_{m,CaCO_3}}{\rho_{CaCO_3}} (c - c_{sat}) \simeq \alpha \frac{m_{m,CaCO_3}}{\rho_{CaCO_3}} (c - c_{sat}) \,, \tag{6.18}$$

The growth is positive for precipitation ($c > c_{sat}$) and negative for dissolution ($c < c_{sat}$). Looking at the order of magnitude of the kinetic constant α in Tabs. 6.1 and 6.2 in Appendix A, we note that $\alpha \in [10^{-9} ; 10^{-5}] \;\mathrm{m\,s^{-1}}$, and that $c_{sat} \in [4 ; 40] \times 10^{-7} \,\mathrm{mol\,cm^{-3}}$. If we use the following parameters: $\alpha = 10^{-7} \,\mathrm{m\,s^{-1}}$ (for $h = 100 \,\mu\mathrm{m}$ in Tab. 6.1) and $c_{sat} = 10^{-6} \,\mathrm{mol\,cm^{-3}}$ with the concentration difference $(c - c_{sat}) \sim c_{sat}$ (i.e., we have locally added c_{sat} in the film), we find that $\partial_t \eta \simeq 3.7 \times 10^{-12} \,\mathrm{m\,s^{-1}}$. If we assume that all the ions precipitate within 10 s at a constant rate of precipitation in all points of the film, the growth per drop would be of about 37 pm over the entire stalagmite. If we further consider that drop dripping period is a little over every 10 s, such that it would be equivalent to 7500 drop impacts per day, we have a net stalagmite growth over the year of approximately 100 μm, in correspondence with the observations from the literature presented in Sec. 1.5. We note that by multiplying α by a given factor k, if the ion concentration is uniform over the entire stalagmite and if the film is at steady-state, the growth rate is simply multiplied by the same factor k. Hence, we would only need $1/k$ impacts to obtain the same stalagmite growth. In nondimensional form, using once again $\eta = \eta' h_d$, $t = t' t_d$, $c = c' c_{sat}$ and $\alpha = h_d/t_p$, the former

equation becomes

$$\partial_{t'}\eta' = \frac{c_{\text{sat}} m_{m,\text{CaCO}_3}}{\rho_{\text{CaCO}_3}} \left(\frac{t_{\text{d}}}{t_{\text{p}}}\right)(c'-1) \,. \tag{6.19}$$

With this equation, as well as Eqs. (6.13), (6.14), (6.15),and (5.46) and (5.47) from Ch. V, we have a complete system of coupled equations describing the drainage of the film, occurring simultaneously with the ion precipitation and stalagmite growth. Since we cannot solve this system of non-linear equations analytically, we proceed numerically by using the approach described in the next section. The drop addition is explained at the end of the section.

1.4 Numerical scheme

In this section only, all the variables x are used in their non-dimensional form, but for the sake of simplicity we write them as x rather than x'. We proceed to solve the system of equations derived in the former section numerically, as in Ch. V, and apply the same formalism, that we represent for the ion concentration in Fig. 6.2. By keeping the same stencil as described in Sec. 4.5 from Ch. V (see Fig. 5.17), we define the discrete values of the ion concentration c_i at the centres of the cells $i = 1, \ldots, I$ of fixed size $\Delta\xi$, positioned at ξ_i. We also use the same cell-centered values as in Ch. V for the film thickness, h_i, and the local stalagmite inclination, φ_i. We can thus rewrite Eq. (6.13) as

$$(\partial_t c)\Big|_i \approx h_i^2 \left[(\partial_\xi h)\Big|_i \cos\varphi_i - \left(\frac{r_{\text{d}}}{h_{\text{d}}}\right)\sin\varphi_i \right] (\partial_\xi c)\Big|_i + \frac{1}{h_i}\left(\frac{t_{\text{d}}}{t_{\text{p}}}\right)(1-c_i), \quad h_i > 0 \,, \tag{6.20}$$

If the film thickness locally cancels, i.e., $h_i = 0$, the concentration c_i is by default set to 0 as well since the solution of ions cannot exist without the presence of the film. This situation only arises when the stalagmite, initially dry, gets progressively covered by drop impacts at the beginning of a simulation. For this reason, we note from the former relation that there is no need for odd-even decoupling [112] as it was the case with the numerical resolution of the film drainage (see Sec. 4). We use the same central finite difference formula to evaluate the first-order spatial derivatives, except that this time the derivatives are evaluated at the cell centres. This yields the following approximation for the thickness gradient:

$$(\partial_\xi h)\Big|_i \approx \frac{h_{i+1/2} - h_{i-1/2}}{\Delta\xi} \,, \tag{6.21}$$

and for the ion concentration gradient:

$$(\partial_\xi c)\Big|_i \approx \frac{c_{i+1/2} - c_{i-1/2}}{\Delta\xi} \,. \tag{6.22}$$

The film thickness $h_{i\pm1/2}$, and ion concentration $c_{i\pm1/2}$, correspond to the film thickness and ion concentration evaluated at the faces of the cells, respectively. We can approximate these values as we did in Ch. V by their average between cells i and $i \pm 1$, as shown in Fig. 6.1. For, e.g., the ion concentration $c_{i+1/2}$, this leads to

$$c_{i+1/2} \approx \frac{1}{2}(c_i + c_{i+1}) \,, \quad i = 0, \ldots, I \,. \tag{6.23}$$

The above equations hold for all the steps $n \geq 0$ of the simulations, which are separated by the same constant time step Δt as in Ch. V. To estimate the time derivative of the ion concentration c

at position i and time step n, we use the explicit first-order Euler scheme, i.e.,

$$\left. (\partial_t c) \right|_i^n \approx \frac{c_i^{n+1} - c_i^n}{\Delta t} \,. \tag{6.24}$$

Numerically, we also update the stalagmite profile growing perpendicularly to the coordinate ξ in every point using Eq. (6.19), which now becomes

$$\eta_i^{n+1} \approx \eta_i^n + \frac{\Delta t \, c_{\text{sat}} m_{m,\text{CaCO}_3}}{\rho_{\text{CaCO}_3}} \left(\frac{t_d}{t_p} \right) (c_i^n - 1) \,, \tag{6.25}$$

where the stalagmite elevation η_i^n is also evaluated at the centre of the cells, just as c_i^n. We note that, because the precipitation only occurs if the solution is supersaturated, the condition $c_i^n > 1$ must be ensured in order to produce precipitation and a positive local stalagmite elevation, i.e., a stalagmite growing upward. The case of dissolution corresponds to $c_i^n < 1$ in the former relation, and will be covered briefly in Sec. 2.3.3. If $c_i^n = 1$, nothing happens and the stalagmite profile remains identical.

The drainage equation resolution providing the film thickness h_i^n is the same as in Ch. V, except for the stalagmite profile which is updated at each time step. This translates into the computation of new values of ξ and φ at the centres of the cells at time step n, i.e., we can define ξ_i^n and φ_i^n. To update ξ, we simply use its definition from Eq. (5.48) in Ch. V by including the change in η at time step n, which corresponds to the elevation that will be used in the calculations at time step $(n + 1)$, i.e.,

$$\xi_i^{n+1}(r_i) = \int_0^{r_i} \left(1 + \left(\left. (\partial_r \eta) \right|_{r_i}^{n+1} \right)^2 \right)^{1/2} \mathrm{d}r \approx \sum_{\Delta r_i} \left(\Delta r_i^2 + \left(\Delta \eta_i^{n+1} \right)^2 \right)^{1/2} \,, \tag{6.26}$$

where $\Delta \eta_i^{n+1} = \eta_i^{n+1} - \eta_i^n$. The local inclination at every radial coordinate (at the centre of the cell) is updated accordingly, by using

$$\varphi_i^{n+1} = \arctan \left(\left. (\partial_r \eta) \right|_{r_i}^{n+1} \right) = \arctan \left(\frac{\Delta \eta_i^{n+1}}{\Delta r_i} \right) \,. \tag{6.27}$$

The grid step, $\Delta \xi$, which is maintained constant along the stalagmite profile, can therefore slightly vary from one step to another. If it were to become too large with respect to the value set initially for $\Delta \xi$, an extra cell would be added to the grid, and the film thickness, h, the ion concentration, c, and stalagmite elevation, η, would be interpolated over the new grid. As illustrated in Fig. 6.1, because the variations of η are very small compared to the film thickness (the aforementioned growth of 37 pm per drop corresponds to $37 \times 10^{-8} h_d$, and this value is a priori computed over several time steps), in practice there is no need to update the number of grid cells, and the changes in ξ and φ are relatively small. We can also safely assume that the film thickness obtained over the stalagmite elevation $\eta^n(r)$ at time step n simply remains the same over the updated elevation $\eta^{n+1}(r)$. In other words, the film is locally shifted upward wherever needed, but the elevation changes are only taken into account in the calculations of the film thickness and ion concentration at step $n + 1$.

To account for the ions coming from the drop at impact, we cannot proceed in the same manner as in Ch. V, in which case we simply added liquid over the existing film where the drop arrived in the film. If the concentration of ions in the film over a liquid ring of volume V_{ring} can be considered as uniform within this ring, it varies with the radial position r, i.e., from one cell to another.
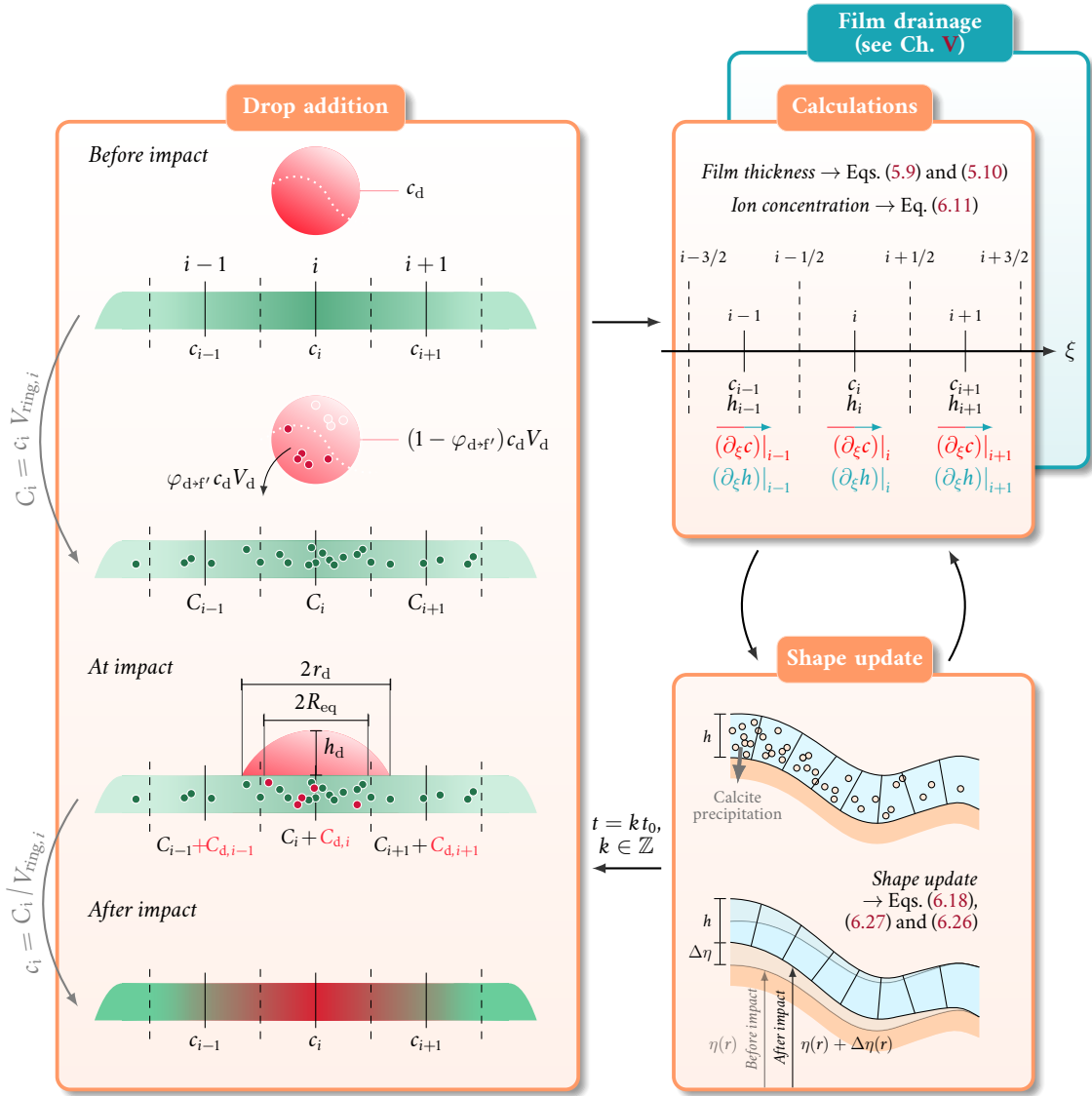
Figure 6.2: Illustration of the complete numerical model. The *Drop addition* panel shows graphically the steps from Eqs. (6.28)-(6.30), i.e., the calculation of the ion quantity in the drop and the film from the known ion concentrations (before impact), the addition of the ions from the drop and the ions from the film (at impact), and the calculation of the ion concentration from the quantity of ions in the film (after impact). The part of the drop containing ions and entering the film is $\varphi_{\mathrm{d \to f'}} c_{\mathrm{d}} V_{\mathrm{d}}$. The drop radius is r_{d} (see Ch. IV) but the ion distribution only spreads on a radius R_{eq} (see Ch. IV). The *Calculations* panel represents the stencil used to compute the ion concentration, approximated by Eqs. (6.20)-(6.24). The evolution of the film thickness because of drainage is computed using the scheme from Sec. 4.5 in Ch. V. The *Shape Update* panel shows how the stalagmite profile is increased by $\Delta \eta$ in between impacts, when new matter is added ($\Delta \eta > 0$, or removed if $\Delta \eta < 0$) in every cell.

Because of this, the new concentration following the impact of a drop, c^{n+1}, cannot be written as a linear combination of the concentration in the film before impact, c^n, and the concentration in the drop, c_{d}^n. This would only be true for a constant film thickness. However, the quantity of ions contained in the liquid ring of volume V_{ring}, C^n, remains extensive. We therefore proceed to add the ions coming from a drop in the film by first computing the quantity of ions in each cell at time step n as

$$C_i^n = c_i^n V_{\mathrm{ring}, i}^n \approx \pi r^2 (\Delta \xi^n) \, h_i^n \, c_i^n \,. \tag{6.28}$$

Next, the new quantity of ions can be calculated by summing the ions initially in the film and the new ones from the drop, i.e.,

$$C_i^{n+1} = C_i^n + C_{\mathrm{d}, i}^n \,, \tag{6.29}$$

where $C_{\mathrm{d},i}^n$ is given by Eq. (6.15). The value of $C_{\mathrm{d},i}^n$ is null for all the cells located at $r > R_{\mathrm{eq}}$. We then update the concentration in the film by reverting the operation from Eq. (6.28), yielding

$$c_i^{n+1} = \frac{C_i^{n+1}}{V_{\mathrm{ring},i}^{n+1}} \approx \frac{C_i^{n+1}}{\pi r^2 (\Delta \xi^{n+1}) \, h_i^{n+1}} \,. \tag{6.30}$$

In the above relation, we use for the new film thickness h_i^{n+1} the value obtained by adding the drop at impact, as described in Sec. (4.5.2) from Ch. V. Since this time step only consists in adding the drop in the film, the values of $\Delta \xi^{n+1}$ and φ_i^{n+1} remain unchanged between n and $(n + 1)$. This procedure is illustrated in Fig. 6.2. After the drop addition, the calculations are continued as described above.

Finally, we note that the number of impacts necessary to reach an average stalagmite growth of $1\,\mu\mathrm{m\,y^{-1}}$ to $1000\,\mu\mathrm{m\,y^{-1}}$ as in caves [17] is of the order of 10^5 to 10^6 drop impacts (using once again the estimation of $\partial_t \eta \sim 10^{-12}\,\mathrm{m\,s^{-1}}$). Getting significant stalagmite profile variations over decades of growth would require even more drop impacts, yielding a very large number of operations and resources with the numerical scheme used here. Over such long periods, the environmental parameters of the stalagmite are also expected to vary, at least seasonally [20]. Since we do not have access to experimental records of stalagmite growth to compare the simulations that we could obtain, it seems pointless to go at such lengths without even having a basic understanding of the influence of the environmental parameters defined in Sec. 1.5 hereafter. The goal of this chapter is thus not to run simulations allowing to model a century-worth growth of stalagmite, but rather to grasp the effect that the environmental parameters may each have on subsequent stalagmite growth, by keeping all the other variables constant. The growths obtained will therefore be relatively small, such that it will not significantly affect the drainage of the film and induce time-variable processes, as already discussed. If we start from an initially perfectly horizontal stalagmite surface, the entire simulation can therefore be seen as conducted over a flat plane. The same holds if we impose a convex or concave stalagmite profile of height varying over the order of $\sim h_{\mathrm{d}}$ to $\sim 1000 h_{\mathrm{d}}$. Hence, the drainage regime (either dominated by the film thickness gradients or the inclination of the stalagmite surface, see Sec. 6), remains the same during the entire simulation. We shortly review the effect of these two drainage regimes in Sec. 2.3.2.

1.5 Three input parameters

Following the above discussion, we note that the independent variables of the complete model are:
- t_0 / t_{d}, the ratio of the dripping period and drainage timescale, that was already varied in Ch. V. We recall that a lower dripping period t_0 / t_{d}, i.e., a larger inflow Q_{drip}, yields a longer filling phase of the film and larger stationary film thickness h_{s}. At steady-state for a fixed stalagmite surface, the drainage outflow Q_{drain} should indeed match the inflow Q_{drip}, which is only achieved if either h or $\partial_\xi h$ increases, i.e., for increasing h at the centre of the stalagmite (see Eq. (5.3) and Sec. 5.2 from Ch. V).
- $t_{\mathrm{d}} / t_{\mathrm{p}}$, the ratio of the drainage and precipitation timescales, which indicates how these two processes compete. For $t_{\mathrm{d}} / t_{\mathrm{p}} \gg 1$, i.e., $t_{\mathrm{p}} \ll t_{\mathrm{d}}$, we expect the ions to have precipitated long before the film has spread them through drainage. By contrast, for $t_{\mathrm{d}} / t_{\mathrm{p}} \ll 1$, the ions should have been redistributed more uniformly throughout the film because drainage will transport them before they can precipitate.
- c_{sat}, the ion saturation concentration, assumed constant everywhere in the film and over time for a given simulation. Although both c_{sat} and t_{p} (representing α) are related to the ion precipitation, the precipitation timescale indicates how the ions get distributed in the film

197

spatially, while c_{sat} dictates the average vertical growth rate to which the stalagmite is subjected at steady-state. While the ratio $t_{\text{d}}/t_{\text{p}}$ can change in response to a change in t_{d} though, the value of c_{sat} is directly dependent on the environmental conditions, i.e., the partial pressure in carbon dioxide, pH or temperature in the vicinity of the stalagmite (see Tabs. 6.1 and 6.2).

Additionally, we fix the ion concentration in the impacting drops appearing in Eq. (6.15), c_{d}, at the saturation value of the ion concentration, c_{sat}, so that $c'_{\text{d}} = 1$ in all the drops. Although the drop ion concentration could differ from c_{sat} for actual stalagmites, tuning c_{d} by multiplying it by a factor k, e.g., will result in also multiplying the stalagmite growth by this factor k. However, this has the exact same effect as multiplying the ion saturation concentration c_{sat} by k. Hence, there is no need to take into account both parameters from a numerical point of view. The parameters related to the mixing between the drop and the film, and thereby to the local film thickness at impact, are the aforementioned equivalent spot radius, R_{eq}, and proportion of the drop left in the film post impact, $\varphi_{\text{d}\to\text{f}'}$. They will yield different results for variable conditions (t_0/t_{d}, $t_{\text{d}}/t_{\text{p}}$, c_{sat}) while always maintaining a constant drop ion concentration. Finally, we know from the literature reviewed in Ch. I that the kinetics of precipitation and dissolution of calcite are very similar to one another. Because of the fine balance existing between these two processes in typical cave conditions [70], we consider that dissolution only corresponds to a change of sign in Eq. (6.15) while the absolute values of α and c_{sat} remain the same. We will not cover this process thoroughly but still give an example of simulation involving dissolution in Sec. 2.3.

2. Resulting stalagmite shape temporal evolution

By solving the system of equations that we obtained in the previous section, we are now able to simulate various stalagmite profiles in response to the three aforementioned tune parameters, t_0/t_{d}, $t_{\text{d}}/t_{\text{p}}$ and c_{sat}. We start by comparing simple test cases and review the effect of each parameter on local stalagmite growth. If the stalagmite grows under constant environmental conditions, we can measure the average growth between profiles separated by a certain number of impacts, and estimate the corresponding shape Ψ and scale S of these stalagmite profiles. We then pursue our discussion by comparing the two timescale ratios at once in Sec. 2.2. Several regimes might indeed arise from the comparison of the drop dripping period t_0, the drainage timescale t_{d} and the ion precipitation timescale t_{p}. We also compare the growth rate obtained to Dreybrodt's model. Finally, we perform a few simulations by varying, e.g., the initial shape of the stalagmite or by changing the parameters over the course of a simulation in Sec. 2.3.

2.1 Examples of stalagmite profile evolution

In this section, we show examples of the stalagmite profile evolution with time for various sets of parameters. We start by reviewing the sole effect of either c_{sat}, t_0/t_{d} or $t_{\text{d}}/t_{\text{p}}$ on the resulting stalagmite profile evolution. We will then vary t_0/t_{d} and $t_{\text{d}}/t_{\text{p}}$ simultaneously in Sec. 2.2. Only the sole precipitation is covered in the following examples. An example containing dissolution will be presented in Sec. 2.3. To keep this chapter short, the parameters inferred from the simulations are introduced in the first example for which one parameter is varied at a time from the next section, i.e., there is no dedicated section as it was the case in Chs. IV and V. Hence, it is advised to read the following sections in the assigned order.

2.1.1 Effect of the dripping period

We compare in Figs. 6.3 and 6.4 the results from two numerical simulations performed in identical conditions, except for the ratio t_0/t_d. The parameters used are $c_{sat} = 5 \times 10^{-7}$ mol cm^{-3} and $t_d/t_p = 1$, and the simulations are run for 10^4 drop impacts, i.e., for $N_d = 10^4$ (see Sec. 5.1 from Ch. V). The dripping period to drainage timescale ratio used in both cases is equal to $t_0/t_d = 0.5$ and $t_0/t_d = 2$ in Figs. 6.3 and 6.4, respectively. We can also write these comparisons as $t_0 < t_d = t_p$ and $t_d = t_p < t_0$, respectively. In each figure, panels (a) and (b) represent the film thickness, h, and ion concentration, c, respectively, at the stalagmite centre, as a function of the number of drops N_d during the first 50 drop impacts. The insets of these two panels each show the last 10 drop impacts of the simulations. It should be noted that panels (b) in each figure represent $c/c_{sat} - 1$. The ions in solution only precipitate because the solution is supersaturated, i.e., once the precipitation has occurred, the ion concentration remains at c_{sat}, such that c never vanishes in the simulations. The panel (c) in each figure illustrates the stalagmite profile calculated every 1000 drop impacts from a perfectly horizontal plane at $N_d = 0$, for up to $N_d = 10^4$. At each time step during the simulations, we are able to infer the shape and scale parameters, resp. Ψ and S, from the current stalagmite profile. To do so, we proceed in the same manner as described in Sec. 3.2 from Ch. II, except that, instead of gathering experimental data points from stalagmite profile photographs, we can infer the parameters directly from the $\eta(r)$ curves computed numerically. The shape parameter, Ψ, and scale, S, are represented in panels (d) and (e) of Figs. 6.3 and 6.4, respectively. Finally, in panel (f) of Figs. 6.3 and 6.4, we show the difference in growth rate between two consecutive impacts at the centre of the stalagmite, i.e., in $r = 0$, as a function of the number of impacts, N_d. Because all the drops impact the stalagmite at the centre, the growth rate is always maximum at $r = 0$. The maximum growth difference between consecutive impacts is defined as

$$\Delta\eta^{max}(N_d) = \eta(r = 0, N_d) - \eta(r = 0, N_d - 1). \tag{6.31}$$

With the drop typical height set to $h_d = 10^{-4}$ m, we note that, in Figs. 6.3 (c) and (f), and 6.4 (c) and (f), the actual height reached by the stalagmite is of the order of 1 µm to 10 µm, and that the maximum growth difference per impact is comprised between 0.1 nm and 1 nm.

In Figs. 6.3 (a) and (b), as well as in Figs. 6.4 (a) and (b), we observe that both h and c reach a stationary state after a few tens of impacts, then remain in this state due to the small variations of η over the number of impacts covered in regard of the film thickness. The film thickness and ion concentration in the insets of Figs. 6.3 (a) and (b), and Figs. 6.4 (a) and (b), i.e., at the end of the simulations, indeed exhibit the exact same behaviour as for $N_d \in [40 ; 50]$ in the corresponding main graphs. If the film thickness is at steady-state, without splashing at impact, the inflow brought by the successive drops in the film is compensated by the drainage outflow over the side of the stalagmite at each impact, or $Q_{drip} = Q_{drain}$ (see Eq. 5.3 from Ch. V). If the ion concentration is at steady-state, the renewal of the ions brought by the successive drops perfectly balances out the amount of ions lost through precipitation, or $\partial_t C = 0$ in Eq. (6.2). We note that, even if we were able to define a similar criterion for the number of drops after which c reaches a steady state as we did for h in the former chapter, h and c might still not be at steady-state after the same amount of drops. This can be witnessed in Figs. 6.4 (a) and (b) where c is clearly at steady-state after only 2 or 3 drops while h is still in a transient phase. Because the simulations are usually run up to at least $N_d = 1000$, we will therefore not define the number of drops after which either the film thickness or concentration reaches a stationary phase, but simply assume that the parameters Ψ and $\Delta\eta^{max}$ should be at steady-state for $N_d \gtrsim 100$. This aligns closely with the limit value found for N_s in Ch. V (see, e.g., Sec. 5.2 from Ch. V). Similarly, the equivalent spot radius, R_{eq}, and drop proportion left in the film post impact, $\varphi_{d \triangleright f'}$, both depending on h, should remain constant past the initial transient phase of h. We represented their values measured for $N_d \geq 100$ in Figs. 6.3 (c) and 6.4. (c). As we

already emphasised in Sec. 1.3, we do not model stalagmite growth for a sufficiently long time to observe variations in h and c as a result of stalagmite shape variations, although these variations should eventually appear after a sufficient amount of drops. Hence, although we consider that the film thickness and ion concentration are at steady-state, this is only a steady-state due to the very short stalagmite growth that we model.

We start by comparing the film thickness and ion concentration from Figs. 6.3 (a-b) and 6.4 (a-b). As we could expect from the former results obtained for the sole drainage, the stationary film thickness increases with increasing inflow, i.e., it is larger in Fig. 6.3 (a) than in Fig. 6.4. (a). A value of $t_0/t_d = 0.5$ indeed corresponds to the equivalent of two drop impacts for a given drainage timescale t_d, while the inflow relative to $t_0/t_d = 2$ would correspond to the equivalent of half a drop impact over t_d. The resulting inflow is 4 times smaller for $t_0/t_d = 2$ than for $t_0/t_d = 0.5$ (using $Q_{drip} = V_d/t_0$, see Sec. 4.3). We also note in both Figs. 6.3 (c) and 6.4. (c) that, in accordance with the results from Figs. 4.9 and 4.13 regarding the mixing at impact in Ch. IV, the equivalent spot radius, R_{eq}, and proportion of the drop left in the film post impact, $\varphi_{d \rightarrow f'}$, are larger for a larger film thickness, i.e., for $t_0/t_d = 0.5$ (Fig. 6.3). Hence, the amount of ions entering the film at impact should likewise increase, although slightly as the difference between $\varphi_{d \rightarrow f'}$ in both cases is not substantial (about 15 %). With a larger film thickness at the centre of the stalagmite in Fig. 6.3 (a) and by a simple mass balance, we would therefore expect c in Fig. 6.3 (b) to be smaller than in Fig. 6.4 (b) (if C remains identical, a larger film thickness h should yield a smaller concentration c over the same area). However, this is not the case. We recall that, because t_d/t_p remains constant in between both cases, the case for which $t_0/t_d = 0.5$, resp. $t_0/t_d = 2$, actually corresponds to $t_0 = 0.5t_p$, resp. $t_0 = 2t_p$. Hence, the shorter dripping period and larger inflow $t_0/t_d = 0.5$ correspond to the case where the time between two drop impacts is not sufficient for the ions in solution to precipitate, nor to be drained away from their impact point position by gravity. By contrast, when $t_0/t_d = 2$, the ions in solution have enough time not only to precipitate but also to be drained away in between two impacts. It is therefore not surprising to find that c is larger in Fig. 6.3 (b) than in Fig. 6.4 (b). Because $t_d = t_p$, the characteristic length scale over which the ions precipitate should correspond to the characteristic drainage length scale that has been set to r_d by virtue of the definition of the drainage timescale (see Eq. (5.14) in Ch. V). We thus observe in Fig. 6.3 (c), when ions precipitate at the same time as they are drained away, that the stalagmite extends over $r = 2r_d$, i.e., one additional r_d from their original impact point position. On the other hand, the spatial extension of the stalagmite in Fig. 6.4 (c) is bounded below $r = r_d$.

As aforementioned, the proportion of ions entering the film at impact, $\varphi_{d \rightarrow f'}$, is slightly larger for $t_0/t_d = 0.5$ (Fig. 6.3) than for $t_0/t_d = 2$ (Fig. 6.4) and so is the actual quantity of ions entering the film. We have also already noted that c remains larger at the centre of the stalagmite for $t_0/t_d = 0.5$. The maximum in-between impacts growth, $\Delta\eta^{max}$, is therefore larger in Fig. 6.3 (f) than in Fig. 6.4 (f). Consequently, the stalagmite from Fig. 6.3 (c) also appears taller than the one from Fig. 6.4 (c). By mass conservation, because the stalagmite from Fig. 6.3 (c) is also wider than the one from Fig. 6.4 (c), the height difference between both stalagmites turns out to be relatively small. We note that this comparison is based on the total number of drops, which is identical, but not on the total actual time of the simulations, which is different since the ratio t_0/t_d differs from Fig. 6.3 to Fig. 6.4. Obtaining the same stalagmite growth for the same time period rather than the same number of drops, but different t_0/t_d ratios, would thus imply that the actual values of both t_0 and t_d vary. Because the added mass at each impact is spatially distributed differently, we could also consider the added volume at impact rather than the added height. However, in stalagmite growth reconstruction [19], the thickness of the annually laminated layers appearing in the stalagmite cut is usually considered rather than the added volume per year. This added volume could be
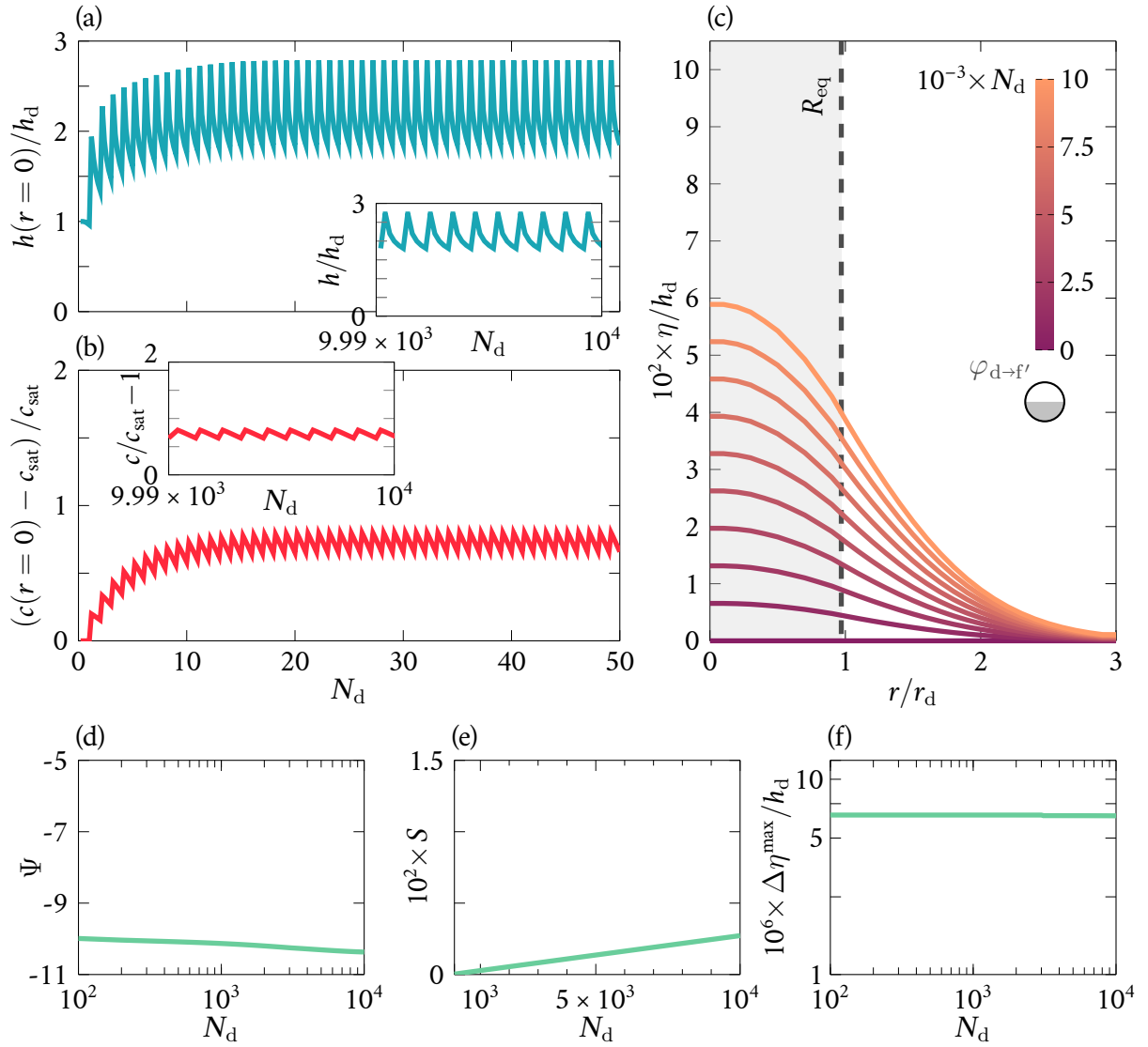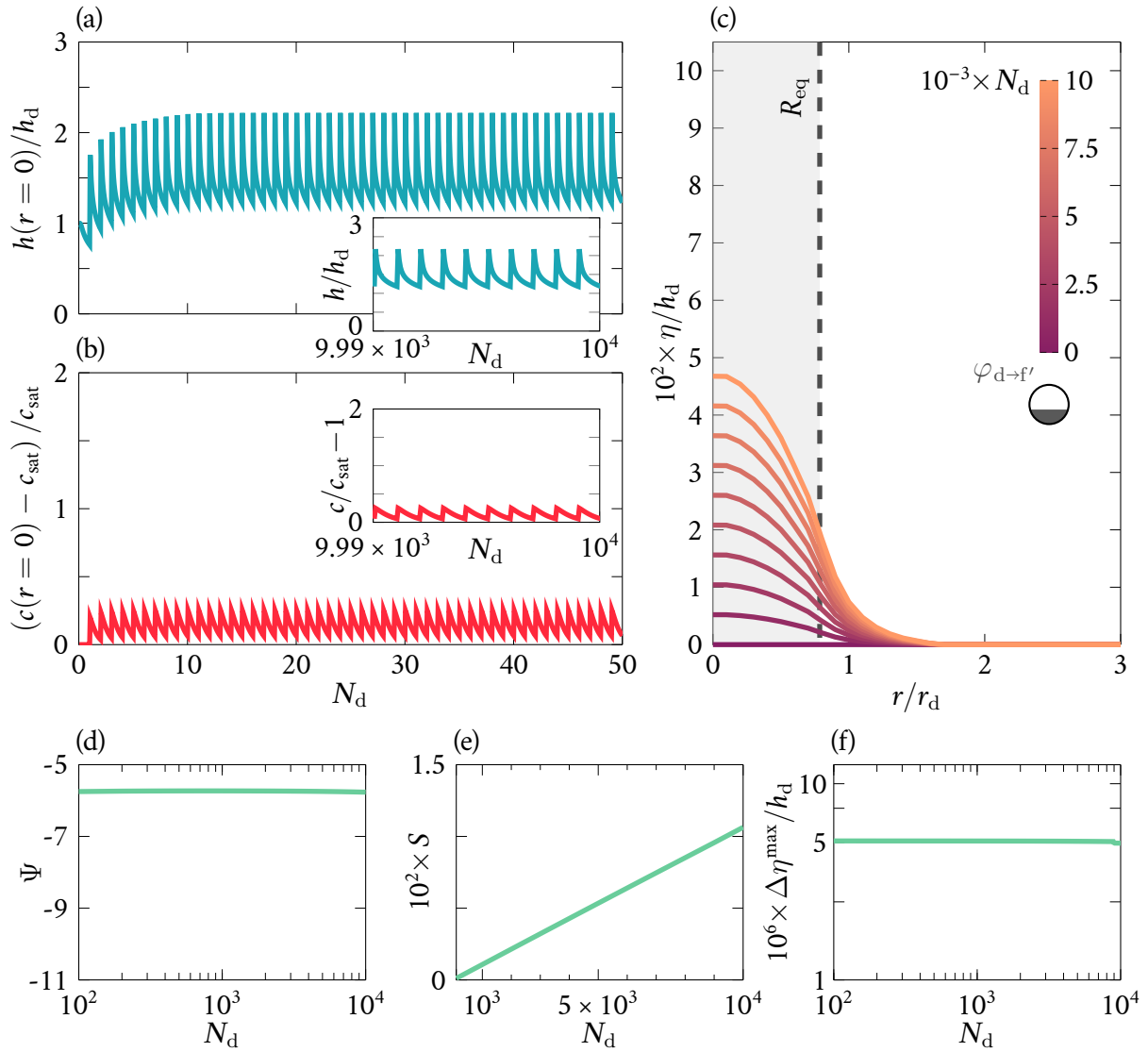
Figure 6.3: Example of stalagmite profile evolution with the number of drop impacts (time), from an initially perfectly horizontal surface. The following parameters were used: $c_{sat} = 5 \times 10^{-7}$ mol cm^{-3}, $c_d = c_{sat}$, $t_0/t_d = 0.5$ and $t_d/t_p = 1$. (a) Evolution of the film thickness, h, with the number of drop impacts, N_d, during the first 50 impacts, at the centre of the stalagmite. The inset shows the last 10 impacts. (b) Evolution of the concentration difference, $(c - c_{sat})$, with the number of drop impacts, N_d, during the first 50 impacts, at the centre of the stalagmite. The inset shows the last 10 impacts. (c) Stalagmite elevation, η, as a function of the radial coordinate, r, for up to 10^4 drop impacts. Intermediate lines show the elevation every 1000 drop impacts, as indicated by the colour bar. (d-f) Evolution with the number of drop impacts, N_d, of the stalagmite shape factor, Ψ, (d), the stalagmite scale, S, (e), and the in-between impact stalagmite growth, $\Delta\eta$, (f). All three curves (d-f) are only represented beyond the transient phase, for $N_d \geq 100$. The equivalent radius of the spot left by the drop in the film, $R_{eq} = 0.97\,r_d$, is represented by the shaded gray area and vertical dashed line in (c). The proportion of the drop left in the film post-impact, $\varphi_{d \to f'} = 0.49$, corresponds to the partially filled disk below the colour bar in (c)[3].

---

[3]In the disk relative to $\varphi_{d \to f'}$ in the subsequent figures, it can be noted that both the coloured portion as well as the gray hue correspond qualitatively to the value of $\varphi_{d \to f'}$.

Figure 6.4: Example of stalagmite profile evolution with the number of drop impacts (time), from an initially perfectly horizontal surface. The following parameters were used: $c_{sat} = 5 \times 10^{-7}$ mol cm^{-3}, $c_d = c_{sat}$, $t_0/t_d = 2$ and $t_d/t_p = 1$. (a) Evolution of the film thickness, h, with the number of drop impacts, N_d, during the first 50 impacts, at the centre of the stalagmite. The inset shows the last 10 impacts. (b) Evolution of the concentration difference, $(c - c_{sat})$, with the number of drop impacts, N_d, during the first 50 impacts, at the centre of the stalagmite. The inset shows the last 10 impacts. (c) Stalagmite elevation, η, as a function of the radial coordinate, r, for up to 10^4 drop impacts. Intermediate lines show the elevation every 1000 drop impacts, as indicated by the colour bar. (d-f) Evolution with the number of drop impacts, N_d, of the stalagmite shape factor, Ψ, (d), the stalagmite scale, S, (e), and the in-between impact stalagmite growth, $\Delta\eta$, (f). All three curves (d-f) are only represented beyond the transient phase, for $N_d \geq 100$. The equivalent radius of the spot left by the drop in the film, $R_{eq} = 0.79\,r_d$, is represented by the shaded gray area and vertical dashed line in (c). The proportion of the drop left in the film post-impact, $\varphi_{d\to f'} = 0.42$, corresponds to the partially filled disk below the colour bar in (c).

difficult to measure in actual stalagmite cuts, especially because the laminae are not always easily distinguishable everywhere in the cut (see, e.g., the hiatus in Fig. 1.11 (b)). Additionally, we observe in Figs. 6.3 (f) and 6.4 (f) that $\Delta\eta^{\mathrm{max}}$ remains constant over the 10^4 drop impacts from the simulations, such that the various profiles represented for η in Figs. 6.3 (c) and 6.4 (c) are all equidistant at $r = 0$. Surprisingly though, the stalagmite does not grow 4 times faster when the flux of calcite in the incoming drops is multiplied by 4, i.e., when t_0 is divided by 4. We indeed have a constant growth rate of $\partial_t\Delta\eta^{\mathrm{max}} = \Delta\eta^{\mathrm{max}}/t_0$, with t_0 equal to either $0.5t_{\mathrm{d}}$ or to $2t_{\mathrm{d}}$. Using the actual values found for $\Delta\eta^{\mathrm{max}}$ in both cases, we obtain $\partial_t\Delta\eta^{\mathrm{max}} = 13 \times 10^{-10}$ m s^{-1} and $\partial_t\Delta\eta^{\mathrm{max}} = 2.5 \times 10^{-10}$ m s^{-1}, respectively, i.e., a ratio of 5.2. Both the width and height of the stalagmite have an effect on the resulting shape and scale parameters, Ψ and S. We indeed observe in Figs. 6.3 (d-e) and Figs. 6.4 (d-e) that there are significant differences between the respective values of Ψ and S. Although it is not perfectly the case in Fig. 6.3 (d), we nevertheless note that Ψ remains constant in Figs. 6.3 (d) and 6.4 (d). As expected, the values of Ψ are negative since they correspond to convex stalagmite profiles. The stalagmite in a stationary state of growth therefore keeps a constant shape Ψ while only S varies. With a ratio of $1/4$ at constant t_{d} between the two dripping periods t_0 relative to Figs. 6.3 and 6.4, respectively, we note that Ψ is almost divided by 2 between Figs. 6.3 (d) and 6.4 (d), whereas S is almost multiplied by 3 between Figs. 6.3 (e) and 6.4 (e). These effects will be further investigated in Sec. 2.2.

2.1.2 Effect of the precipitation timescale

We now take interest in the effect of the ratio $t_{\mathrm{d}}/t_{\mathrm{p}}$ on the stalagmite profile, for otherwise identical conditions. We conducted two simulations for which $c_{\mathrm{sat}} = 5 \times 10^{-7}$ mol cm^{-3}, $t_0/t_{\mathrm{d}} = 1$, and $t_{\mathrm{d}}/t_{\mathrm{p}} = 0.2$ and $t_{\mathrm{d}}/t_{\mathrm{p}} = 5$, represented in Figs. 6.5 and 6.6, respectively, for 10^4 drop impacts. These timescale comparisons can also be written as $t_0 = t_{\mathrm{d}} < t_{\mathrm{p}}$ and $t_{\mathrm{p}} < t_0 = t_{\mathrm{d}}$, respectively. All panels (a-f) of both figures represent the same variables as in Figs. 6.3 and 6.4 from the previous section. We once again observe that both h and c are at steady-state after less than the 50 impacts shown in Figs. 6.5 (a-b) and 6.6 (a-b), respectively. In Figs. 6.5 (d) and (f), and Figs. 6.6 (d) and (f), we also note that Ψ and $\Delta\eta^{\mathrm{max}}$, respectively, both remain constant.

We first note in Figs. 6.5 and 6.6 that the parameters mostly related to the balance between the drop inflow and drainage outflow of the film, h, and consequently R_{eq} and $\varphi_{\mathrm{d}\to\mathrm{f}'}$, take similar values. This is not surprising considering that we imposed $t_0/t_{\mathrm{d}} = 1$. Hence, the film thickness evolutions with N_{d} presented in Figs. 6.5 (a) and 6.6 (a) look very much alike. One of the major differences between Figs. 6.5 and 6.6, though, is the behaviour exhibited by the ion concentration in the film. For a dripping period equal to the drainage timescale, the ratio $t_{\mathrm{d}}/t_{\mathrm{p}} = 0.2$, or $t_{\mathrm{d}} = 0.2t_{\mathrm{p}}$, indicates that the ions are redistributed in the film by drainage following the impact before they can all precipitate and before a new drop arrives to renew the ions in solution. On the other hand, for $t_0/t_{\mathrm{d}} = 1$ and $t_{\mathrm{d}}/t_{\mathrm{p}} = 5$, or $t_{\mathrm{d}} = 5t_{\mathrm{p}}$, the ions brought at each impact precipitate long before they can be drained away or renewed by a drop impact. Consequently, the ion concentration in Fig. 6.5 (b) always remains larger than in Fig. 6.6 (b).

Because in the case for which $t_{\mathrm{d}}/t_{\mathrm{p}} = 5$, there is almost no spatial redistribution of the ions in the film between impacts, we note that the stalagmite width remains of the order of R_{eq} in Fig. 6.6 (c). By contrast, the drainage dominating the precipitation when $t_{\mathrm{d}}/t_{\mathrm{p}} = 0.2$ yields a much wider stalagmite in Fig. 6.5 (c). Since $\varphi_{\mathrm{d}\to\mathrm{f}'}$ is almost the same in the two cases considered, the values displayed by the maximum in-between drop impacts growth, $\Delta\eta^{\mathrm{max}}$, also remain close. It is difficult to read in the graphs of Figs. 6.5 (f) and 6.6 (f), but $\Delta\eta^{\mathrm{max}}$ is about 10 % smaller for $t_{\mathrm{d}}/t_{\mathrm{p}} = 0.2$ than for $t_{\mathrm{d}}/t_{\mathrm{p}} = 5$. Because drainage is faster in the case of Fig. 6.5, ions get distributed over a larger region, which might explain the wider stalagmite obtained. The comparison of the timescale ratios, t_0/t_{d} and $t_{\mathrm{d}}/t_{\mathrm{p}}$, may also lead to different actual values of the three timescaless
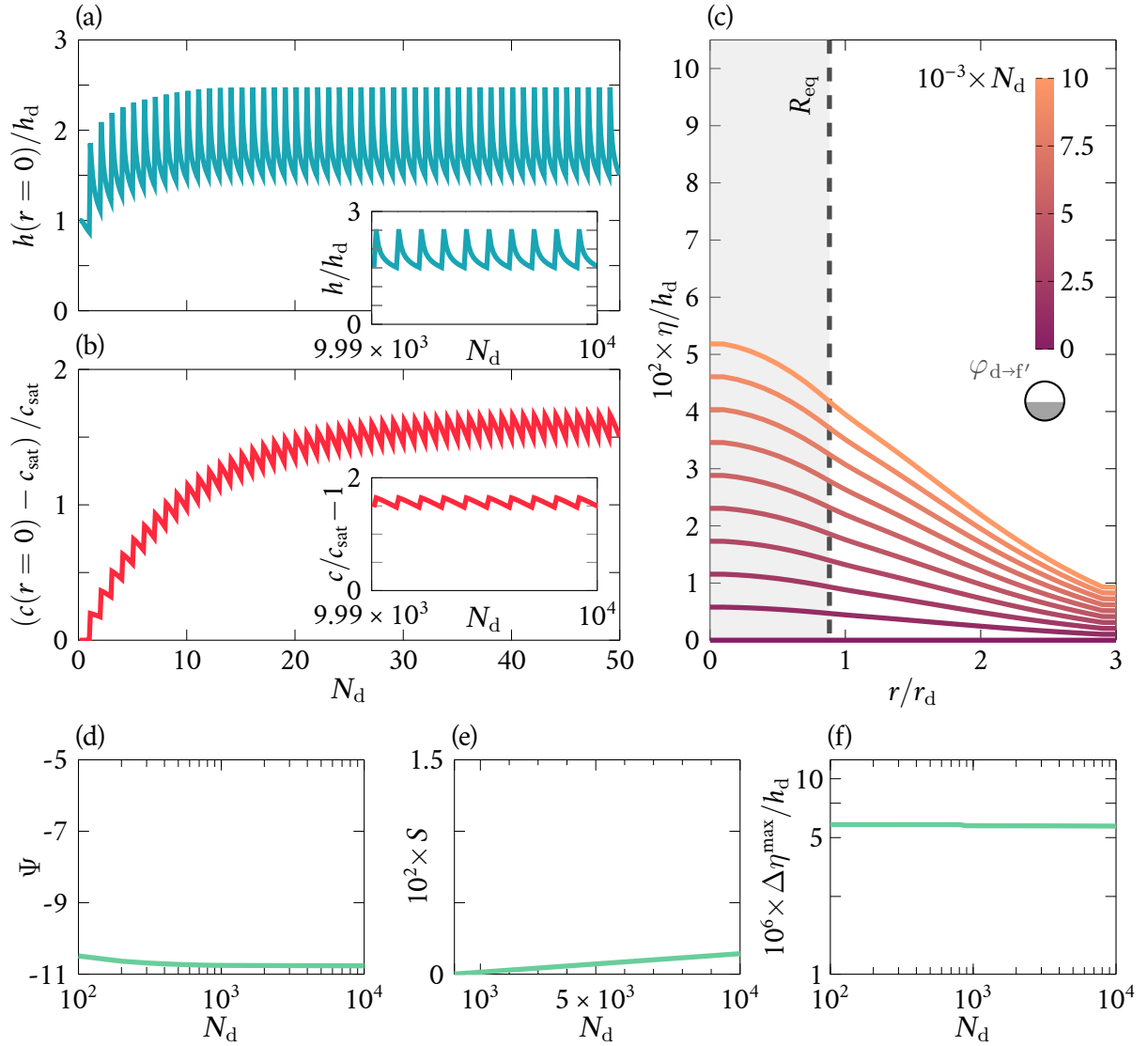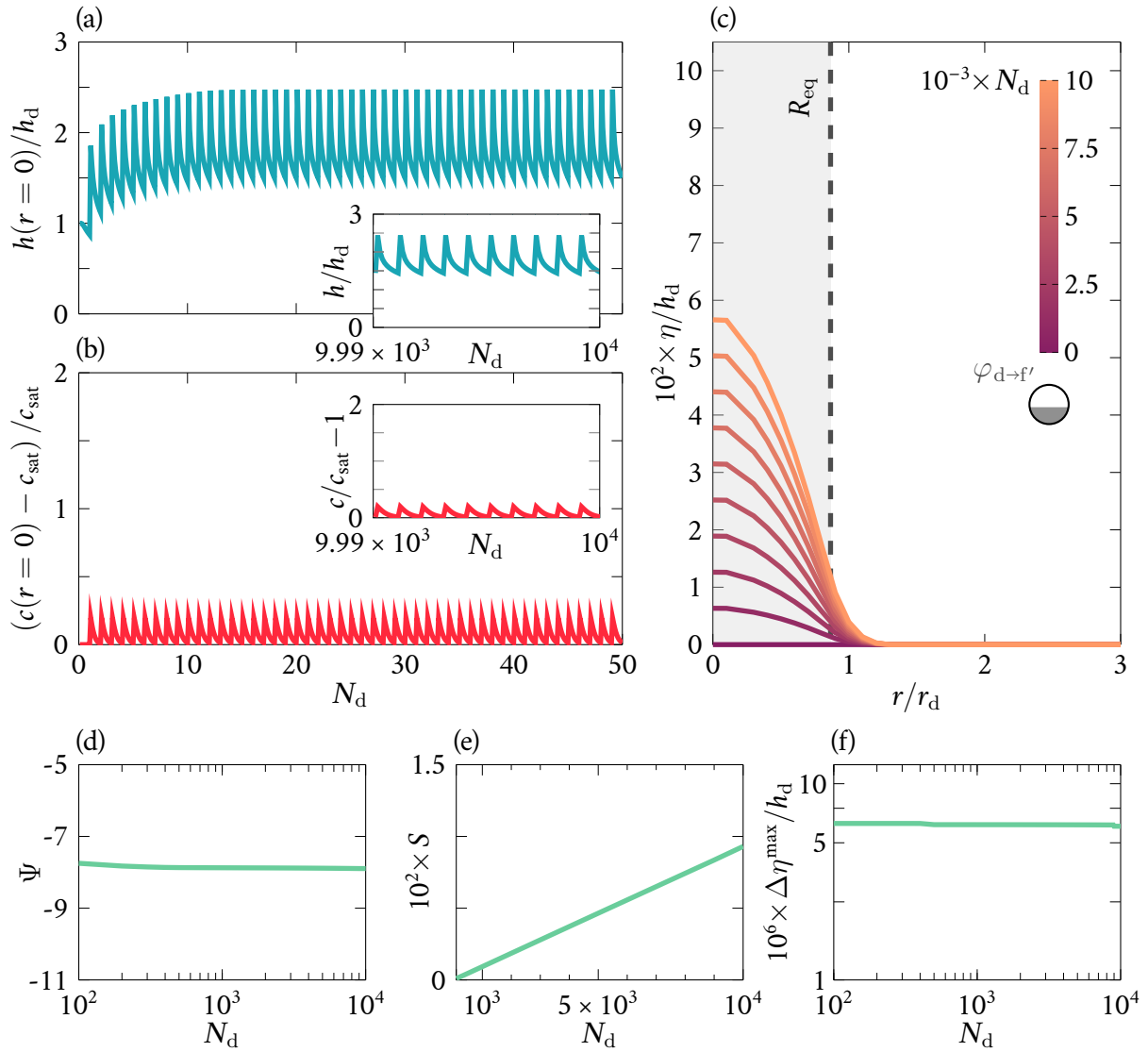
Figure 6.5: Example of stalagmite profile evolution with the number of drop impacts (time), from an initially perfectly horizontal surface. The following parameters were used: $c_{sat} = 5 \times 10^{-7}$ mol cm^{-3}, $c_d = c_{sat}$, $t_0/t_d = 1$ and $t_d/t_p = 0.2$. (a) Evolution of the film thickness, h, with the number of drop impacts, N_d, during the first 50 impacts, at the centre of the stalagmite. The inset shows the last 10 impacts. (b) Evolution of the concentration difference, $(c - c_{sat})$, with the number of drop impacts, N_d, during the first 50 impacts, at the centre of the stalagmite. The inset shows the last 10 impacts. (c) Stalagmite elevation, η, as a function of the radial coordinate, r, for up to 10^4 drop impacts. Intermediate lines show the elevation every 1000 drop impacts, as indicated by the colour bar. (d-f) Evolution with the number of drop impacts, N_d, of the stalagmite shape factor, Ψ, (d), the stalagmite scale, S, (e), and the in-between impact stalagmite growth, $\Delta\eta$, (f). All three curves (d-f) are only represented beyond the transient phase, for $N_d \geq 100$. The equivalent radius of the spot left by the drop in the film, $R_{eq} = 0.88\,r_d$, is represented by the shaded gray area and vertical dashed line in (c). The proportion of the drop left in the film post-impact, $\varphi_{d\rightarrow f'} = 0.46$, corresponds to the partially filled disk below the colour bar in (c).

Figure 6.6: Example of stalagmite profile evolution with the number of drop impacts (time), from an initially perfectly horizontal surface. The following parameters were used: $c_{sat} = 5 \times 10^{-7}$ mol cm^{-3}, $c_d = c_{sat}$, $t_0/t_d = 1$ and $t_d/t_p = 5$. (a) Evolution of the film thickness, h, with the number of drop impacts, N_d, during the first 50 impacts, at the centre of the stalagmite. The inset shows the last 10 impacts. (b) Evolution of the concentration difference, $(c - c_{sat})$, with the number of drop impacts, N_d, during the first 50 impacts, at the centre of the stalagmite. The inset shows the last 10 impacts. (c) Stalagmite elevation, η, as a function of the radial coordinate, r, for up to 10^4 drop impacts. Intermediate lines show the elevation every 1000 drop impacts, as indicated by the colour bar. (d-f) Evolution with the number of drop impacts, N_d, of the stalagmite shape factor, Ψ, (d), the stalagmite scale, S, (e), and the in-between impact stalagmite growth, $\Delta\eta$, (f). All three curves (d-f) are only represented beyond the transient phase, for $N_d \geq 100$. The equivalent radius of the spot left by the drop in the film, $R_{eq} = 0.87 r_d$, is represented by the shaded gray area and vertical dashed line in (c). The proportion of the drop left in the film post-impact, $\varphi_{d \to f'} = 0.45$, corresponds to the partially filled disk below the colour bar in (c).

hence the difference in the seemingly precipitated volume due to a certain number of drop impacts. We also observe that, as in the previous section, the differences exhibited by the stalagmites in Figs. 6.5 (c) and 6.6 (c) translate into different shape factors, Ψ, and scales, S, in Figs. 6.5 (d-e) and Figs. 6.6 (d-e), respectively. We further note that the case from Fig. 6.5, resp. Fig. 6.6, is very similar to the case presented in Fig. 6.3, resp. Fig. 6.4. Hence, there seems to exist different combinations of the ratios t_0/t_d and t_d/t_p yielding similar stalagmite shapes, scales and growth rates. However, this might come from the nondimensionalisation of the equations performed in Sec. 1.3: changing either t_0/t_d at fixed t_d/t_p or changing t_d/t_p at fixed t_0/t_d may indeed correspond to the same sole change in t_d.

2.1.3 Effect of the saturation concentration and scaling

This section emphasizes the effect of c_{sat} on subsequent stalagmite growth through the examples presented in Figs. 6.7 and 6.8. The simulations used to obtain both figures were run for 10^4 drop impacts, with $t_0/t_d = 1$ and $t_d/t_p = 1$. For Fig. 6.7, we used $c_{sat} = 10^{-7} \, \text{mol cm}^{-3}$, whereas for Fig. 6.8, we used $c_{sat} = 10^{-6} \, \text{mol cm}^{-3}$, i.e., an ion saturation concentration ten times larger. In Tabs. 6.1 and 6.2, we see that c_{sat} increases due to either a larger partial pressure in carbon dioxide in the vicinity of the stalagmite, p_{CO_2}, or a smaller temperature. If p_{CO_2} increases, the amount of ions that can be in solution in the film before the solution becomes saturated increases since the CO_2 conversion sets the kinetics of the precipitation reaction [70]. By using $c_d = c_{sat}$, we therefore add more ions in the drops impacting the film and increase the total number of ions in the solution. Hence, if c_{sat} is multiplied by a factor k, we expect the average ion concentration at steady state, and thereby the growth rate, to be multiplied by k as well. Equation (6.19) indeed indicates that the growth rate varies proportionally to c_{sat} since we used $c_d' = c_d/c_{sat}$, that we set to 1 (or $c_d = c_{sat}$). In Eq. (6.18), using $c_d = c_{sat}$ in the impacting drops yields $((1 + \varphi_{d \to f'})c_{sat} - c_{sat})$. Because both t_0/t_d and t_d/t_p are the same in the two cases and because the stalagmite profile variations are not significant in comparison with the film thickness, we note without surprise that the film thickness, h, and ion concentration, c, look identical in Figs. 6.7 (a-b) and Figs. 6.8 (a-b), respectively. Therefore, the proportion of the drop going into the film $\varphi_{d \to f'}$, is almost the same in both cases (0.46 in Fig. 6.7 and 0.45 in Fig. 6.8), and the growth rate is proportional to $\varphi_{d \to f'} c_{sat}$. Similarly, the shape factor Ψ of the two stalagmites is equal to -7.7, as indicated by Figs. 6.7 (d) and 6.8 (d). We also note in both Figs. 6.7 (c) and. 6.8 (c) that the stalagmites extend over a radius of about $2r_d$.

The main visible difference between the two cases is the growth rate of the stalagmites, since it is directly proportional to c_{sat} (see Eq. (6.18)). We therefore observe that the maximum in-between impacts growth $\Delta\eta^{max}$ is multiplied by 10 from Fig. 6.7 (f) ($c_{sat} = 10^{-7} \, \text{mol cm}^{-3}$) to Fig. 6.8 (f) ($c_{sat} = 10^{-6} \, \text{mol cm}^{-3}$). The stalagmite from Fig. 6.7 (f) is likewise 10 times shorter than the stalagmite from Fig. 6.8 (f). This translates into a scale S slope also multiplied by 10 from Fig. 6.7 (f) ($c_{sat} = 10^{-7} \, \text{mol cm}^{-3}$) to Fig. 6.8 (f) ($c_{sat} = 10^{-6} \, \text{mol cm}^{-3}$). Hence, the ion saturation concentration c_{sat} has no other effect on the stalagmite growth than to rescale a given stalagmite profile obtained at fixed t_0/t_d and t_d/t_p values. There is thus no need to systematically vary c_{sat} to observe its effect on subsequent stalagmite growth, at least in the limiting case that is considered here, where the stalagmite grows at a steady-state such that the stationary film thickness remains constant. The dynamics exhibited by Figs. 6.7 and 6.8 would likely be different if the stalagmite growth became sufficient (i.e., of the order of h_d rather than $h_d/10$ as in the cases presented here) to affect the behaviour of the film thickness over time, which would in turn change the concentration and, thereby, subsequent growth. As mentioned in the beginning of the chapter, we will not conduct such long simulations that could yield stalagmite profiles varying over time. However, we will vary t_0/t_d and t_d/t_p over the course of a simulation in the next section so as to get a preliminary observation of the features exhibited by time-variable stalagmite profiles.
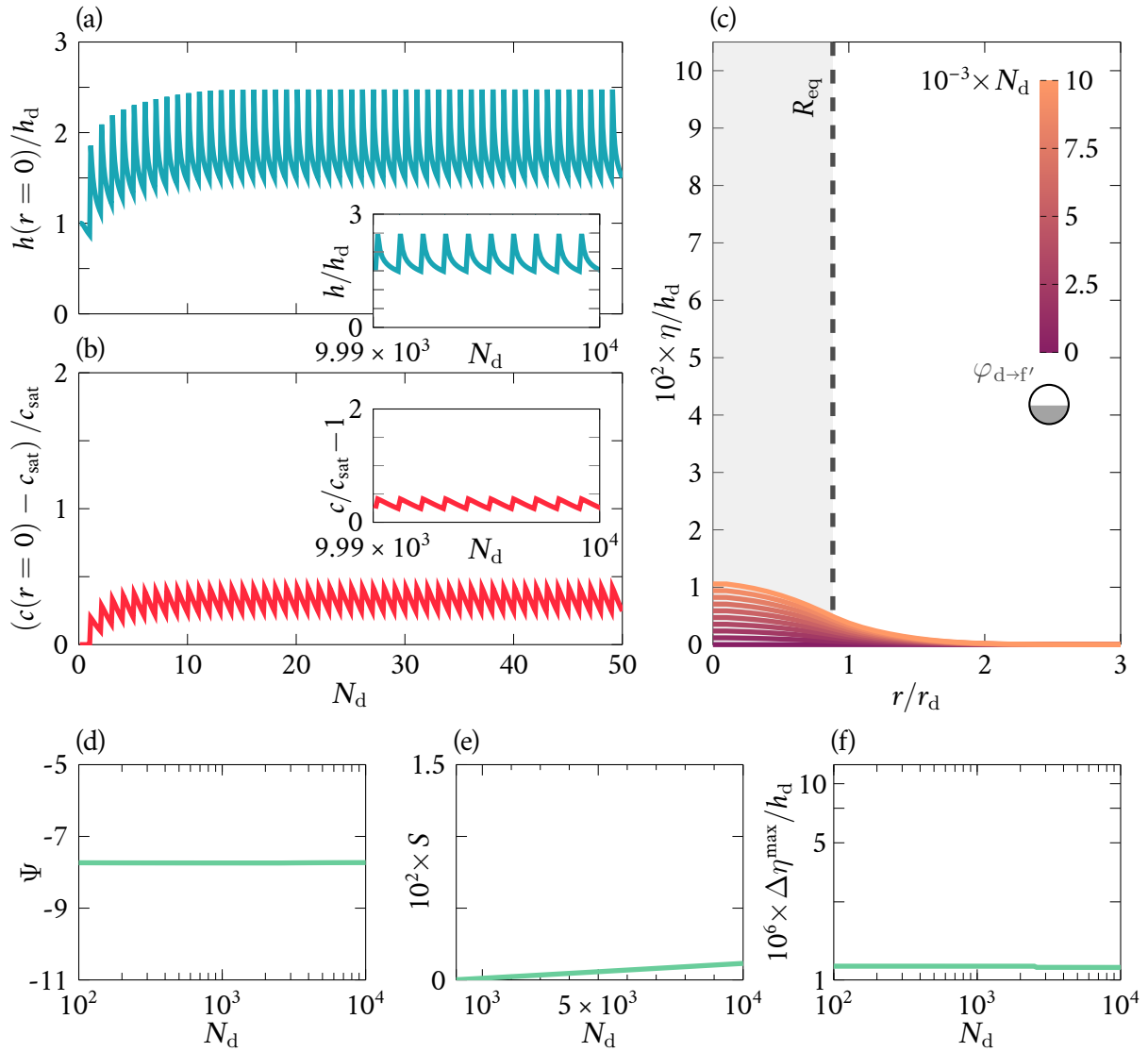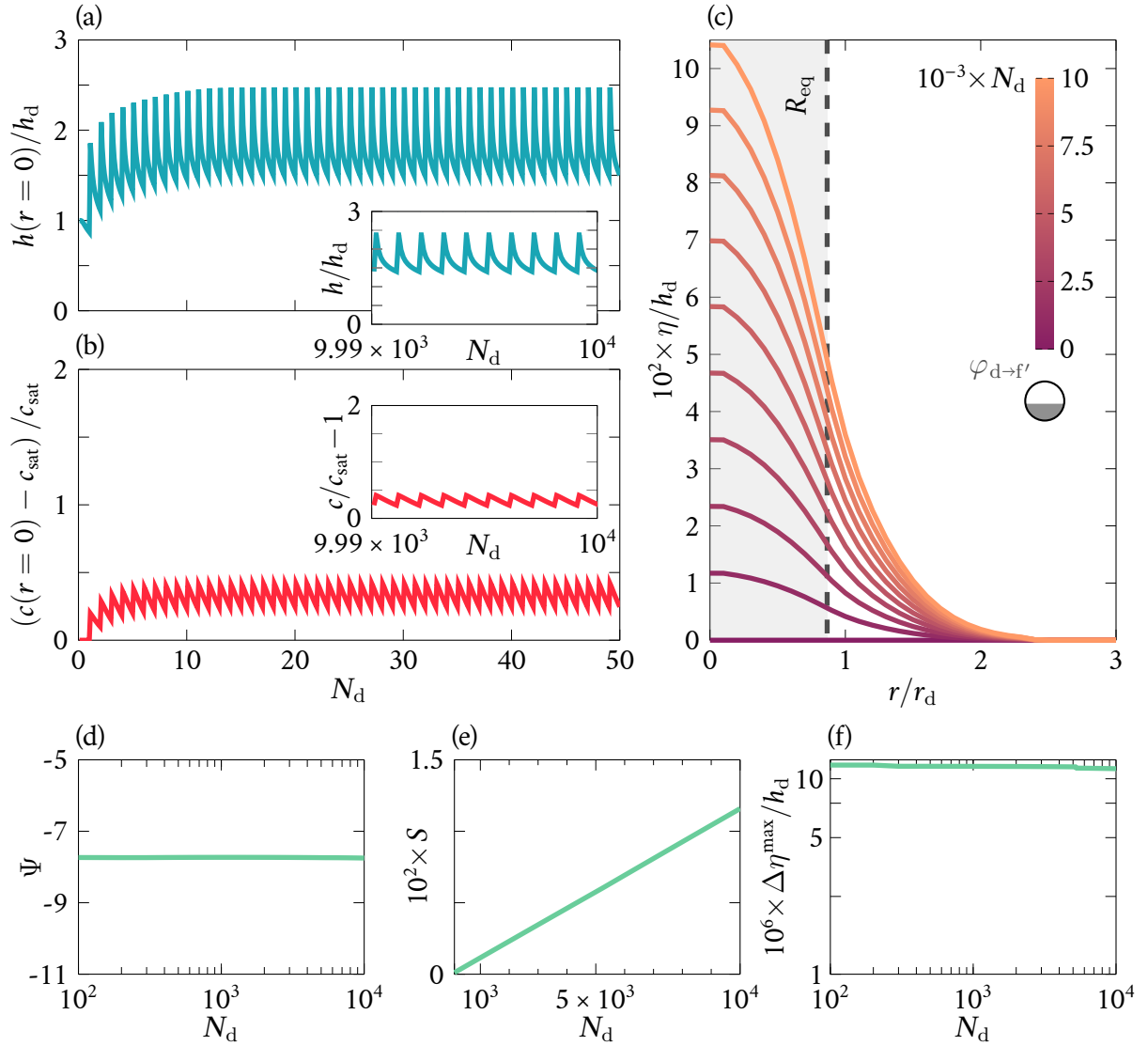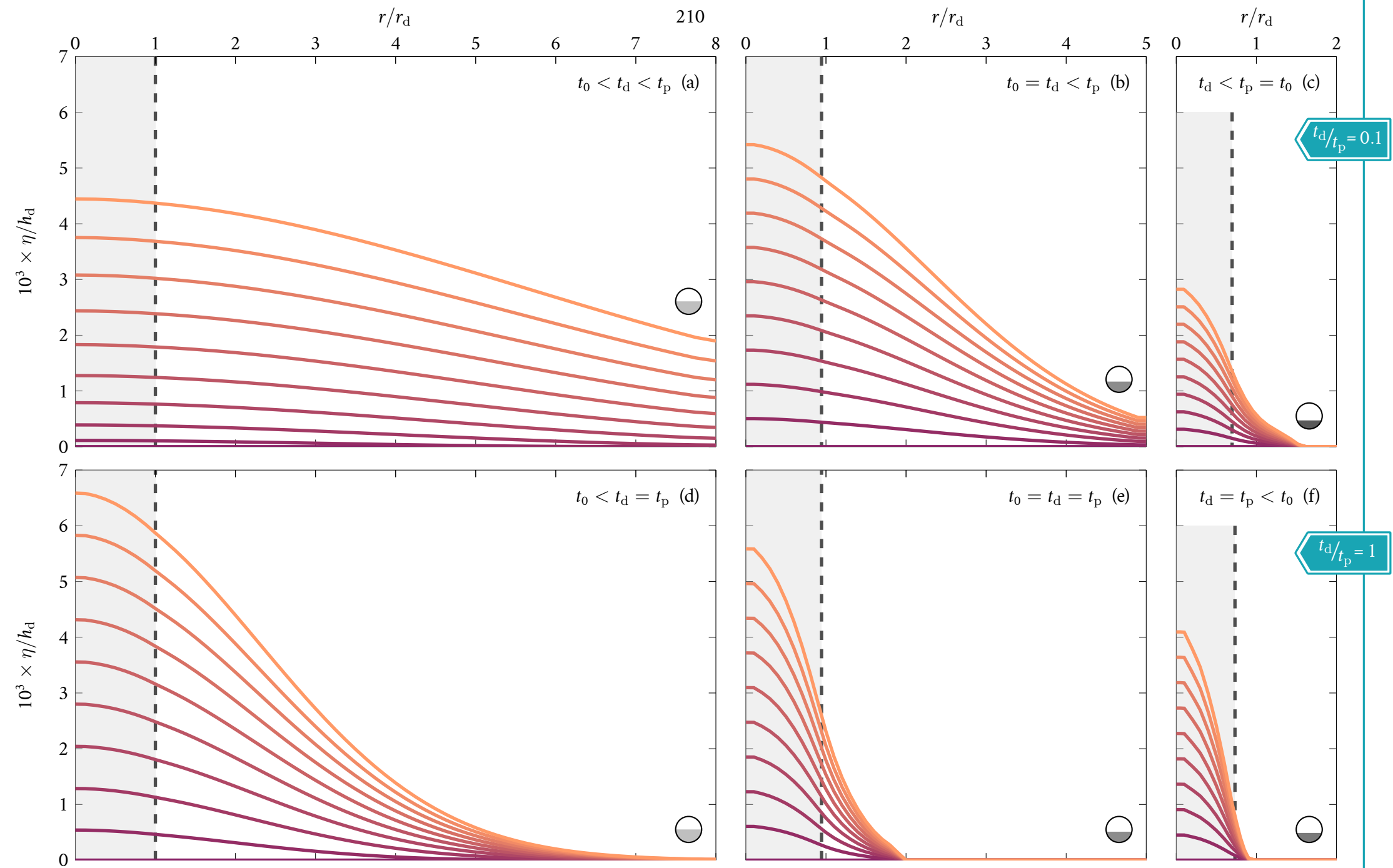
Figure 6.7: Example of stalagmite profile evolution with the number of drop impacts (time), from an initially perfectly horizontal surface. The following parameters were used: $c_{sat} = 1 \times 10^{-7}$ mol cm^{-3}, $c_d = c_{sat}$, $t_0/t_d = 1$ and $t_d/t_p = 1$. (a) Evolution of the film thickness, h, with the number of drop impacts, N_d, during the first 50 impacts, at the centre of the stalagmite. The inset shows the last 10 impacts. (b) Evolution of the concentration difference, $(c - c_{sat})$, with the number of drop impacts, N_d, during the first 50 impacts, at the centre of the stalagmite. The inset shows the last 10 impacts. (c) Stalagmite elevation, η, as a function of the radial coordinate, r, for up to 10^4 drop impacts. Intermediate lines show the elevation every 1000 drop impacts, as indicated by the colour bar. (d-f) Evolution with the number of drop impacts, N_d, of the stalagmite shape factor, Ψ, (d), the stalagmite scale, S, (e), and the in-between impact stalagmite growth, $\Delta\eta$, (f). All three curves (d-f) are only represented beyond the transient phase, for $N_d \geq 100$. The equivalent radius of the spot left by the drop in the film, $R_{eq} = 0.88 r_d$, is represented by the shaded gray area and vertical dashed line in (c). The proportion of the drop left in the film post-impact, $\varphi_{d \to f'} = 0.46$, corresponds to the partially filled disk below the colour bar in (c).

Figure 6.8: Example of stalagmite profile evolution with the number of drop impacts (time), from an initially perfectly horizontal surface. The following parameters were used: $c_{sat} = 1 \times 10^{-6}$ mol cm^{-3}, $c_d = c_{sat}$, $t_0/t_d = 1$ and $t_d/t_p = 1$. (a) Evolution of the film thickness, h, with the number of drop impacts, N_d, during the first 50 impacts, at the centre of the stalagmite. The inset shows the last 10 impacts. (b) Evolution of the concentration difference, $(c - c_{sat})$, with the number of drop impacts, N_d, during the first 50 impacts, at the centre of the stalagmite. The inset shows the last 10 impacts. (c) Stalagmite elevation, η, as a function of the radial coordinate, r, for up to 10^4 drop impacts. Intermediate lines show the elevation every 1000 drop impacts, as indicated by the colour bar. (d-f) Evolution with the number of drop impacts, N_d, of the stalagmite shape factor, Ψ, (d), the stalagmite scale, S, (e), and the in-between impact stalagmite growth, $\Delta\eta$, (f). All three curves (d-f) are only represented beyond the transient phase, for $N_d \geq 100$. The equivalent radius of the spot left by the drop in the film, $R_{eq} = 0.87 r_d$, is represented by the shaded gray area and vertical dashed line in (c). The proportion of the drop left in the film post-impact, $\varphi_{d \to f'} = 0.45$, corresponds to the partially filled disk below the colour bar in (c).

2.2 Comparison between the drop dripping period, the drainage timescale and the precipitation timescale

Following the observations made in the few introductory examples of the previous section, we know that the effect of c_{sat} on a stalagmite in a steady-state of growth is rather straightforward. As we could deduce from Eq. (6.18), using kc_{sat} instead of c_{sat} results in a stalagmite height multiplied by the factor k. Hence, we only focus on varying t_0/t_{d} and $t_{\text{d}}/t_{\text{p}}$ simultaneously in this section. We compare the stalagmite profile evolution over time, computed numerically, in the limiting regimes that were already mentioned in Sec. 2 from Ch. I. We analyse the effect of the two timescale ratios t_0/t_{d} and $t_{\text{d}}/t_{\text{p}}$ that both vary in the set $\{0.1 \, ; \, 1 \, ; \, 10\}$, for otherwise identical conditions. In Figs. 6.9 (a-i), we represent the corresponding profiles obtained for 1000 drop impacts (note that the figure spans two pages). The stalagmite elevation η is shown as a function of the radial coordinate r, with intermediate lines every 100 drop impacts, starting from an initially perfectly horizontal surface. We fixed the ion saturation concentration at $c_{\text{sat}} = 5 \times 10^{-7} \, \text{mol} \, \text{cm}^{-3}$. As it was the case in the examples from the previous section, we may consider that the stalagmite elevation rate, $\partial_t \eta$, is sufficiently slow for the stationary film thickness and average concentration at the centre of the stalagmite to remain in the same steady-state during the time span shown in Figs. 6.9 (a-i) (see Sec. 2.1.3), i.e., to vary between the same maximum and minimum values. Hence, all the impacts can be considered as occurring in identical conditions, at least past the short transient phase at the beginning of the simulations. In each case presented in Figs. 6.9 (a-i), we also represented the corresponding equivalent radius of the spot left by the drop in the film, R_{eq}, as well as the proportion of ions coming from the impacting drop actually entering the film, $\varphi_{\text{d→f′}}$ (see Sec. 1.2, Ch. IV or auxiliary sheet for values).

We observe in Fig. 6.9 that, at fixed $t_{\text{d}}/t_{\text{p}}$ (i.e., for a given row in Fig. 6.9), a smaller t_0/t_{d}, resp. larger, yields a wider stalagmite, resp. narrower, in accordance with the examples from Sec. 2.1. A smaller t_0/t_{d} indeed induces a larger drop inflow because a larger amount of drops fall on the stalagmite within a limited time period, thereby increasing the total quantity of ions actually entering the film over this time period. At fixed t_0/t_{d} (i.e., for a given column in Fig. 6.9), the ratio $t_{\text{d}}/t_{\text{p}}$ also has an effect on the shape of the stalagmite. A smaller $t_{\text{d}}/t_{\text{p}}$, resp. larger, leads to a wider and shorter stalagmite, resp. narrower and taller. If $t_{\text{p}} < t_{\text{d}}$ ($t_{\text{d}}/t_{\text{p}} > 1$), for instance, the ions in solution start to precipitate before the film can spread them out through drainage and redistribute them spatially, thereby decreasing their concentration in each point of the film. Hence, for $t_{\text{p}} < t_{\text{d}}$, the ions mostly precipitate close to the stalagmite centre while for $t_{\text{p}} > t_{\text{d}}$, the ions precipitate both close and away from the centre at lower concentration values, in accordance with the conclusions already drawn from Sec. 2.1.2. We can therefore conclude that the effects of decreasing t_0/t_{d} and $t_{\text{d}}/t_{\text{p}}$ are additive. A combination of a shorter dripping-to-drainage ratio, t_0/t_{d}, and a shorter drainage-to-precipitation ratio, $t_{\text{d}}/t_{\text{p}}$, yields, e.g., the very wide stalagmite from Fig. 6.9 (a). By contrast, when both t_0/t_{d} and $t_{\text{d}}/t_{\text{p}}$ increase, we may obtain a very narrow profile, as the one from Fig. 6.9 (i). We further note that both stalagmite profiles displayed in Figs. 6.9 (a) and (i) have similar heights, while the stalagmite from (a) is over ten times wider than the one shown in (i). This comes from the fact that, at constant number of drop impacts, the total quantity of ions brought into the film is larger for smaller t_0/t_{d}, as aforementioned, but also from the inclusion of the mixing between the drop and the film into the numerical calculations. The proportion of the drop entering the film post impact, $\varphi_{\text{d→f′}}$, is indeed smaller for thinner films caused by a larger t_0/t_{d}. Should we had left the mixing out of the modelling, the total quantity of ions precipitating and allowing for the stalagmite to grow in Fig. 6.9 (i), would have been larger. By mass conservation, the stalagmite would have been much taller. Two simple runs at arbitrarily
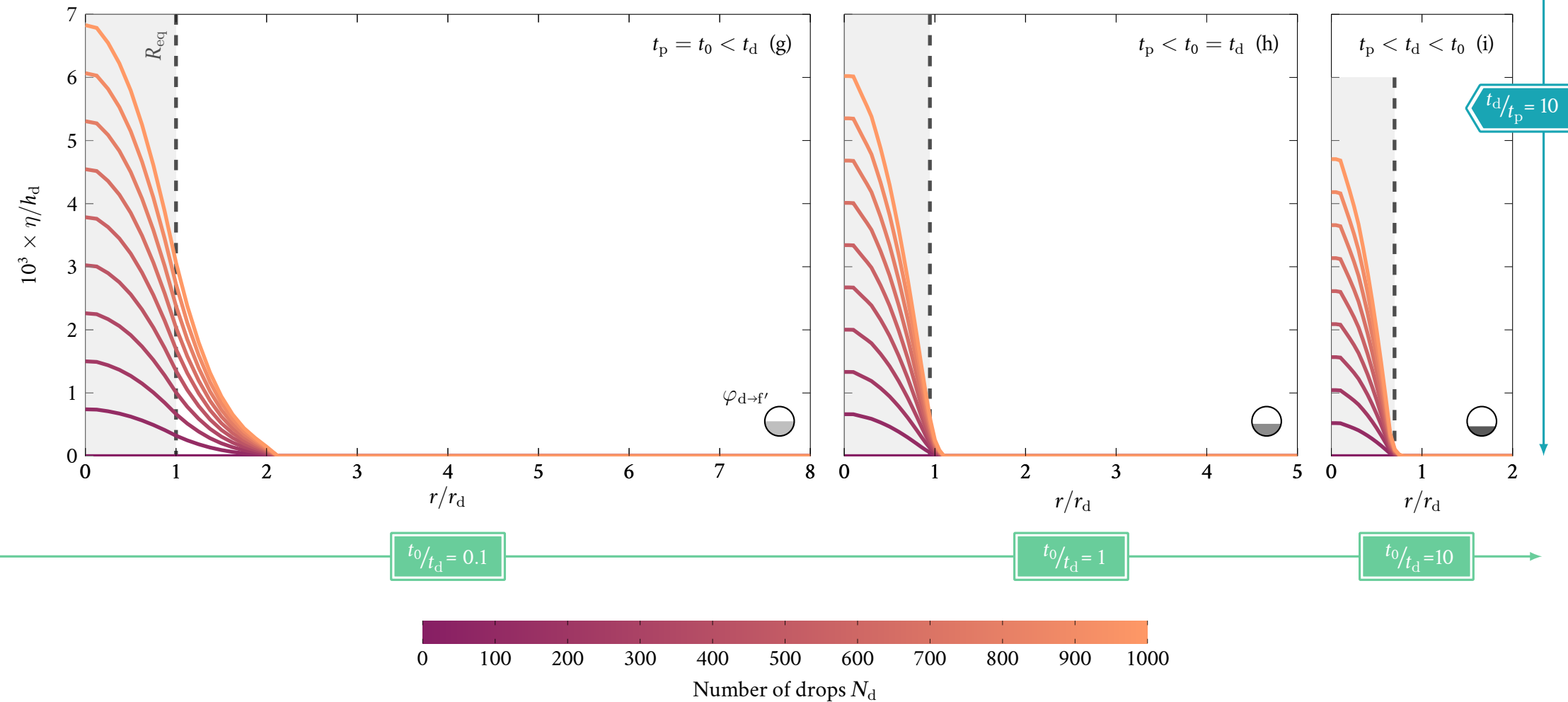
Figure 6.9: *Figure spreads across both pages.* Examples of stalagmite profile evolution with time in limiting cases. The stalagmite always grows from an initially perfectly horizontal surface. Both time ratios t_0/t_d and t_d/t_p are varied in $\{0.1\,;\,1\,;\,10\}$, according to the horizontal green (t_0/t_d) and vertical blue (t_d/t_p) axes. Each case (a-i) represents the equivalent of 1000 drop impacts. The intermediate stalagmite profiles are shown as a function of the radial coordinate r every 100 drop impacts, as indicated by the colour bar below graphs (g-i). The values of η shown in the ordinate axes are comprised between 10^{-8} m and 7×10^{-8} m. The simulations were obtained by fixing $c_{sat} = 5 \times 10^{-7}$ mol cm^{-3}, and by using $c_d = c_{sat}$ in each incoming drop. The equivalent spot radius left by the drop, R_{eq}, and ion proportion initially in the drop ending up in the film, $\varphi_{d \to f'}$, are represented in each case (a-i), as captioned in (g). The equivalent radius R_{eq} corresponds to the grayed area and the dashed line, while the drop symbol at the bottom right of each graph illustrates $\varphi_{d \to f'}$.

constant R_{eq} and $\varphi_{d \to f'}$, performed for the same timescale ratios of Figs. 6.9 (a) and (i), indeed give a height ratio of about 1.6 by comparing the maximum height at the centre of the stalagmite of (i) to the one of (a), at $N_d = 1000$.

Additionally, we note that some combinations of ratios yield almost identical stalagmite profiles, i.e., of similar width and shape, with the exception of the scale of the stalagmite, S. However, this difference in scale might come from our inclusion of the factor $\varphi_{d \to f'}$ at impact as well, which thus differs for variable t_0/t_d, no matter the value of t_d/t_p. We actually obtain almost identical values for all the proportions of drop entering the film post impact, $\varphi_{d \to f'}$, for fixed t_0/t_d values in Fig. 6.9. The combinations for which the stalagmite profiles can be paired are the conjugates of the matrix corresponding to all the subfigures from Fig. 6.9, i.e., (b) and (d) form a pair, and so do (c) and (g), as well as (f) and (h). The combinations corresponds to the following sequences of timescale ratios: $t_0 = t_d < t_p$ and $t_0 < t_d = t_p$ ((b) and (d), resp.), $t_p = t_0 < t_d$, and $t_d < t_p = t_0$ ((c), and (g), resp.), and $t_d = t_p < t_0$ and $t_p < t_0 = t_d$ ((f) and (h), resp.). These timescale orderings suggest that, when two timescales are equal to each other and differ from the third one, reproducing the stalagmite profile is achievable by rearranging the timescales while adhering to the rule: two equal timescales and one different third timescale. We further note that the profile from Fig. 6.9 (e) looks very similar to the profiles from Figs. 6.9 (c) and (g). This comes as no surprise given that the aforementioned orderings of timescales relative to Figs. 6.9 (c) and (g) are $t_p = t_0 < t_d$ and $t_d < t_p = t_0$, respectively, while the timescale ordering relative to Fig. 6.9 (e) is $t_p = t_0 = t_d$, i.e., it is a combination of both orderings at once. The pairs appearing in Fig. 6.9 thus seem to correspond to the t_0/t_p timescale ratio (dripping period over precipitation timescale) as they are all located on the inverted diagonal of Fig. 6.9.

We inferred the stalagmite shape, scale, and other parameters from all the stalagmite profile evolutions presented in Fig. 6.9, as well as from additional simulations conducted at $t_d/t_p = 0.01$ and $t_d/t_p = 100$, while keeping $t_0/t_d \in \{0.1 \,;\, 1 \,;\, 10\}$. In Fig. 6.10, we report these parameters, which include the shape factor, Ψ (a), the scale, S (b), and the maximum in-between impacts growth, $\Delta\eta^{\max}$ (c), as well as the corresponding values of the spot radius left by the drop in the film, R_{eq} (d), and the proportion of the drop going into the film post impact, $\varphi_{d \to f'}$ (e). The simulations allowing to measure all these parameters were conducted for $N_d \geq 1000$. Because only S varies continuously with the number of impacts, we have taken its value precisely at $N_d = 1000$, while the other parameters remain constant even for $N_d \geq 1000$.

In accordance with our former observations (see also Tab. 2.2 from Ch. II and the auxiliary sheet), we note in Figs. 6.10 (a) and (b) that Ψ and S both decrease with decreasing dripping-to-drainage and drainage-to-precipitation ratios, t_0/t_d and t_d/t_p, respectively. At fixed S, a more negative Ψ implies a more convex, i.e., inclined downward, stalagmite shape. At fixed Ψ, a smaller scale S, on the other hand, implies a vertically shrunk stalagmite profile, which therefore decreases the inclination close to the centre of the stalagmite. The scale S has a predominant effect on the stalagmite inclination close to the centre, i.e., for $r \to 0$, as indicated by Eq. (5.49) in Ch. II. We therefore infer from Figs. 6.10 (a) and (b) that decreasing either t_0/t_d or t_d/t_p tends to widen the stalagmite, which becomes less inclined close to its axis of symmetry, in correspondence with our observations from Figs. 6.10 (a), (b) and (d). By contrast, increasing t_0/t_d or t_d/t_p yields a smaller $|\Psi|$ and larger S, i.e., a narrower stalagmite with a larger inclination close to the centre. However, given the radius R_{eq} over which the ions are brought into the film, we have already noted in Sec. 2.1, and we can also identify it in Figs. 6.10 (f), (h) and (i), that the stalagmite width remains approximately dictated by R_{eq}. Since R_{eq} remains bounded, the values obtained for Ψ converge for $t_d/t_p = 100$ in Fig. 6.10 (a). These measurements are in accordance with the relative effects of t_0/t_d and t_d/t_p that we discussed at the beginning of the section. For small values of t_0/t_d and t_d/t_p, e.g., in the case $t_0 < t_d < t_p$, the effect of the successive drops can be averaged over time. Following an impact, neither the drainage nor the precipitation may affect the ion concentration in the film before a new drop
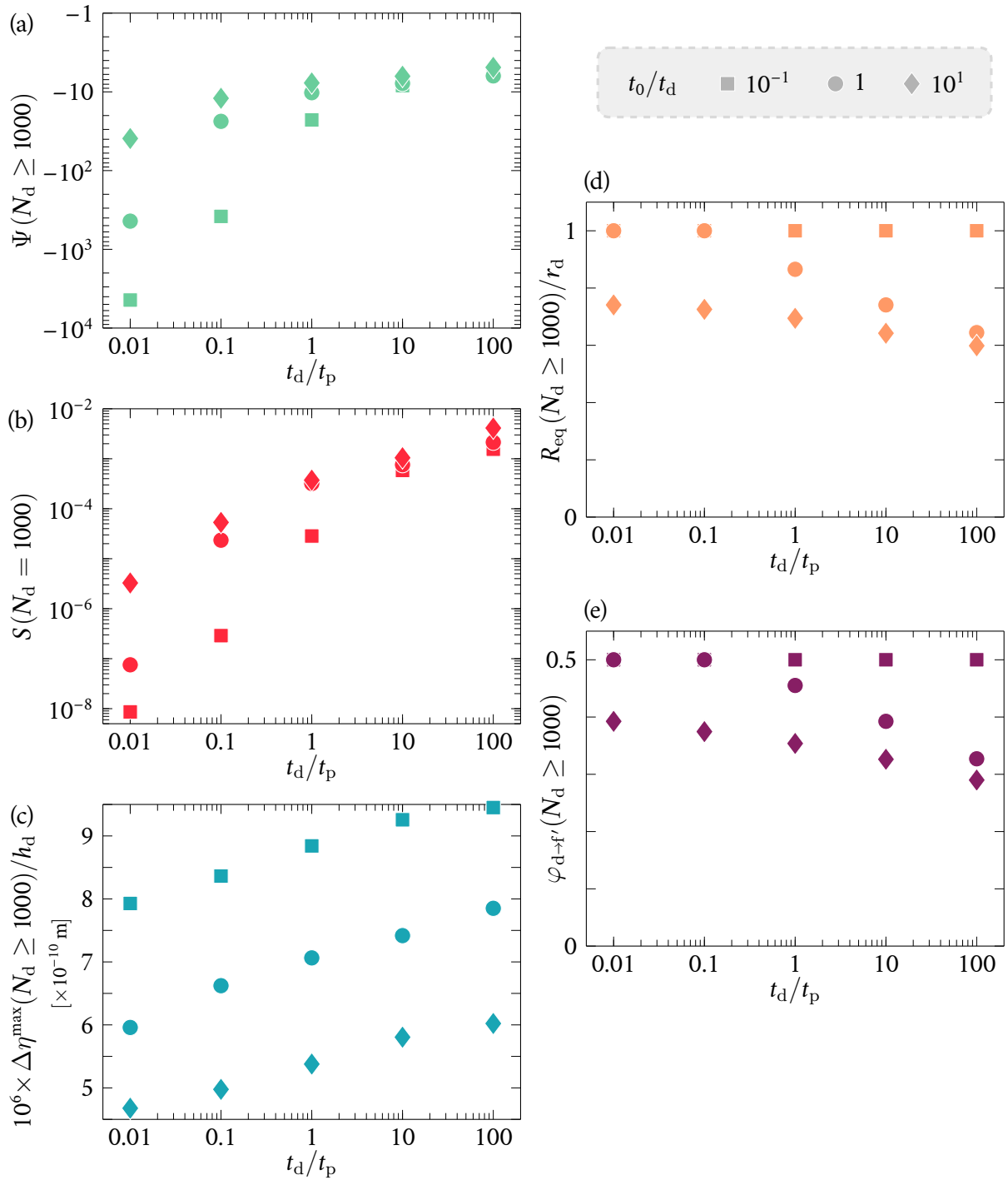
Figure 6.10: Stalagmite evolution parameters inferred from simulations conducted for $c_{sat} = 5 \times 10^{-7}$ mol cm^{-3}, $c_d = 0.1 c_{sat}$, $t_0/t_d \in \{0.1 ; 1 ; 10\}$ and $t_d/t_p \in \{0.1 ; 1 ; 10\}$. The graphs present the stalagmite shape, Ψ, (a), the stalagmite scale S, (b), the in-between impacts growth, $\Delta\eta^{max}$, (c), the equivalent radius of the spot left by the drop impact in the film, R_{eq}, (d), and the proportion of the incoming drop going into the film at impact, $\varphi_{d \rightarrow f'}$, (e). All the graphs are shown as a function of the drainage-to-precipitation timescale ratio, t_d/t_p, with the symbols corresponding to the dripping period-to-drainage timescale ratio, t_0/t_d. The legend for t_0/t_d in the upper right corner is the same for all graphs. All the simulations were conducted starting from an initially dry horizontal surface for at least 1000 drop impacts. The variables correspond to the averages taken over the 50 drop impacts following $N_d \geq 1000$, with the exception of the stalagmite scale S which shows the value obtained at $N_d = 1000$ because S continuously increases with N_d (see Sec. 2.1).

arrives. This situation corresponds to the model derived by Dreybrodt [70] and indeed yields convex stalagmites. By contrast, large values of t_0/t_d and t_d/t_p could lead to, e.g., the case $t_p < t_d < t_0$, in which all the ions would precipitate before they can be redistributed spatially through the drainage at play, or renewed by a drop impact.

The maximum growth between successive impacts, $\Delta\eta^{\mathrm{max}}$, is also dependent on both t_0/t_d and t_d/t_p. As already discussed, a larger inflow, i.e., a smaller dripping-to-drainage ratio t_0/t_d, leads to a larger ion quantity brought into the films by the more numerous drops over a given time. Consequently, the growth rate increases with decreasing t_0/t_d, as it can be witnessed in Fig. 6.10 (c). Additionally, if the drainage-to-precipitation ratio t_d/t_p increases, as aforementioned the precipitation occurs before the drainage spreads out the ions in solution spatially, decreasing their local concentration. The local stalagmite elevation at the stalagmite centre thus increases with t_d/t_p, as seen in Fig. 6.10 (c). However, this increase does not stem from an actual increase in the ion quantity brought into the film by each drop impact, as it is the case with the effect of t_0/t_d on $\Delta\eta^{\mathrm{max}}$, it is simply due to the distribution of ions in the film. There is actually a smaller ion quantity brought by the drop impacts into the film when t_d/t_p increases, as illustrated by Figs. 6.10 (d) and (e) where we observe that both R_{eq} and $\varphi_{\mathrm{d \rightarrow f'}}$ decrease slightly with t_d/t_p. To understand the graphs
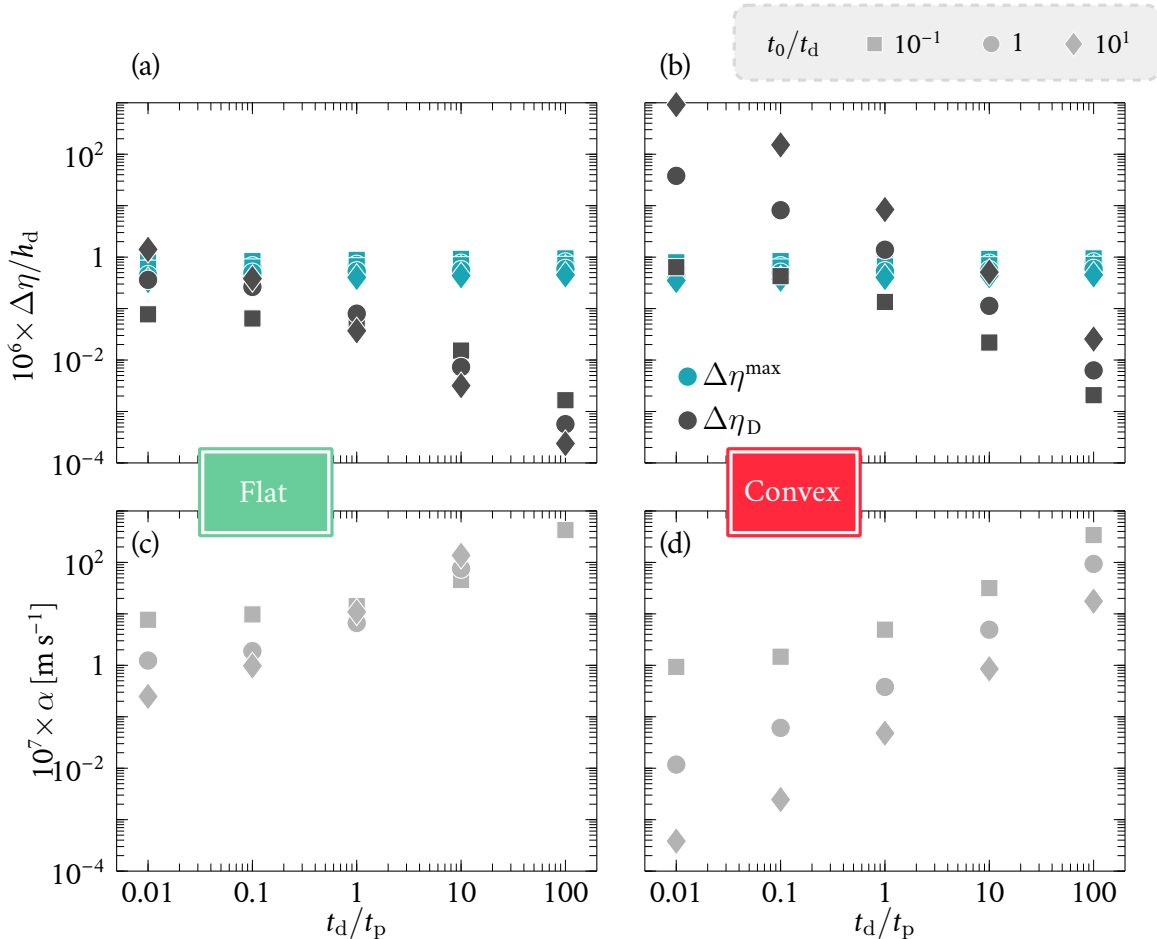
Figure 6.11: Comparison between the results obtained for the average growth rate using the model developed in Sec. 1, and the model developed by Dreybrodt et al. [41, 42, 70, 133]. (a-b) Growth rate $\Delta\eta$ as a function of the drainage-to-precipitation timescale, t_d/t_p, for various values of the dripping-to-drainage ratio, t_0/t_d, indicated by the legend above (b). The legend above (b) is the same for all four graphs (a-d). The values obtained using either our model, $\Delta\eta^{\mathrm{max}}$, or Dreybrodt's model, i.e., $\Delta\eta_D$ from Eq. (6.33), are indicated by the color from the legend inside (b) (lower left corner). In (a), the value used for $\mathcal{S}$ is approximated by Eq. (6.34), and in (b) by Eq. (6.35). (c-d) Precipitation rate α obtained by equating $\Delta\eta^{\mathrm{max}} = \Delta\eta_D$ in (a) and (b), respectively.

of Figs. 6.10 (d) and (e), we must take into account our knowledge of the stationary film thickness, mixing at impact and stalagmite shape for each combination of t_0/t_d and t_d/t_p. If t_0/t_d increases, the inflow brought by the successive drops decreases, and so does the central film thickness. The equivalent spot left by the drop at impact, R_{eq} as well as the proportion of the drop entering the film post impact, $\varphi_{d\to f'}$, were both found to decrease with the local film thickness in Ch. IV. If t_d/t_p increases, we have already observed on multiple occasions that the stalagmite becomes narrower. As discussed above regarding the graphs of Ψ and S (Figs. 6.10 (a) and (b)), a narrower stalagmite for larger t_d/t_p values becomes more inclined toward the centre, thereby promoting drainage and reducing the film thickness at the centre of the stalagmite (see, e.g., Secs. 4.4 and 5.4 in Ch. V). Hence, it is not surprising to see both R_{eq} and $\varphi_{d\to f'}$ decrease with increasing t_d/t_p. Finally, we note in Figs. 6.10 (d) and (e) that, for $t_0/t_d = 0.1$, the inflow, and therefore the film thickness, are always sufficient to maintain R_{eq} and $\varphi_{d\to f'}$ close to their maximum values.

Using the model developed by Dreybrodt et al. [41, 42, 70, 133], it is possible to derive an equation relating the average growth rate over a time period t_0, i.e., between two drop impacts, to the entry parameters of the model, corresponding to t_0, t_p, c_{sat} and α, as well as to the film thickness h_s, the concentration of ions in the drop, c_d, and the proportion of ions initially in the drop going into the film post impact, $\varphi_{d\to f'}$ (this parameter is, to the best of our understanding, equivalent to the mixing parameter defined in Eq. (10.10) in [70], p. 265). Because the authors consider the film thickness to be uniform in space and do not include the drainage of the film in their modelling, we make use of the stationary film thickness h_s as an approximation of their film thickness. We directly transcribe Eq. (10.14) from Dreybrodt et al. [70] (p. 266), but using our own nomenclature, as

$$\partial_t \langle c \rangle = \frac{h_s \, \varphi_{d\to f'} \, c_d \left[1 - \exp\left(-\frac{t_0}{t_p} \right) \right]}{t_0 \left[1 - (1 - \varphi_{d\to f'}) \exp\left(-\frac{t_0}{t_p} \right) \right]} \,, \tag{6.32}$$

By using Eq. (5.15) from Ch. V to express the stationary film thickness as a function of the dripping period t_0 and the fact that we set c_d to c_{sat}, it is possible to express the above equation as

$$\partial_t \langle c \rangle = S \left(\text{shape}, \frac{t_0}{t_d} \right) \frac{\alpha \, \varphi_{d\to f'} \, c_{sat}}{\left(\frac{t_d}{t_p} \right)} \left[\frac{1 - \exp\left(-\frac{t_0}{t_d} \right) \left(\frac{t_d}{t_p} \right)}{1 - (1 - \varphi_{d\to f'}) \exp\left(-\frac{t_0}{t_d} \right) \left(\frac{t_d}{t_p} \right)} \right] \,, \tag{6.33}$$

where the ratios t_0/t_d and t_d/t_p appear, as well as the precipitation reaction rate α, and where the function S (shape, t_0/t_d) depends on the scaling considered for h_s. We had indeed found from the numerical simulations conducted in Ch. V two scalings for perfectly horizontal and convex stalagmites, yielding

$$S^{\bullet} \left(\text{perf. horiz.}, \frac{t_0}{t_d} \right) = \left(\frac{r_{sm}}{r_d} \right)^{1/4} \left(\frac{t_0}{t_d} \right)^{-5/4} \,, \tag{6.34}$$

and

$$S^{\bullet} \left(\text{convex}, \frac{t_0}{t_d} \right) = 0.58 \left(\frac{-1}{\Psi S} \right)^{1/2} \left(\frac{t_0}{t_d} \right)^{-1/2} \,, \tag{6.35}$$

respectively (see Tab. 5.3 in Ch. V). The stalagmite profiles obtained using the model developed by Dreybrodt et al. [41, 42, 70, 133] have not been rationalized, thus we propose to use both scal-

ings because the stalagmite profiles that they obtain seem convex but rather flattened out on the top. We infer the values of $\varphi_{d \to f'}$ and either r_{sm}/r_d or ΨS in Eq. (6.33) from the data presented at variable t_0/t_d and t_d/t_p and fixed $c_{sat} = 5 \times 10^{-7} \, \text{mol cm}^{-3}$ in Figs. 6.9 and 6.10 (e). We estimated the stalagmite radius r_{sm}/r_d from the simulations such as the ones shown in Fig. 6.9 as the mid-height radius of the stalagmite, i.e., $r(\eta = \max \eta/2)$, although it should be noted that this radius corresponds to the radius of a convex stalagmite. To compare the average growth rate defined by Dreybrodt at al. [41, 42, 70, 133] in terms of ion concentration as $\partial_t \langle c \rangle$ to our maximum growth rate in between impacts at the centre of the stalagmite, $\Delta \eta^{\max}$, we use the following relation:

$$\Delta \eta_D \approx \partial_t \langle c \rangle \, \frac{m_{m,\text{CaCO}_3} \, t_0}{\rho_{\text{CaCO}_3}} \, . \tag{6.36}$$

We use for t_0 the value corresponding to the ratio t_0/t_d, multiplied by the $\sim 12 \, \text{s}$ found as being the characteristic drainage timescale corresponding to $h_d = 100 \, \mu\text{m}$ and $r_d = 1 \, \text{cm}$ in Ch. V (see Eq. (5.14)). The values obtained by our model from Fig. 6.10 (c) and the corresponding values obtained by Eqs. (6.33)-(6.36) are reported in Fig. 6.11. We refer to this latter value, i.e., obtained using the model developed by Dreybrodt et al. [41, 42, 70, 133], as $\Delta \eta_D$.

In Figs. 6.11 (a) and (b), we compare the values obtained for $\Delta \eta^{\max}$ in Fig. 6.10 (c) to the values of $\Delta \eta_D$ using Eq. (6.33) with S either approximated by Eq. (6.34) (Fig. 6.11 (a)), or by Eq. (6.35) (Fig. 6.11 (b)). In these two graphs, we have used $\alpha = 10^{-7} \, \text{m s}^{-1}$ as it is a mid-value from Tabs. 6.1 and 6.2, and because it also corresponds to the value of $h_s = h_d$ in laminar flow conditions. However, we have no other clue regarding the value of α which would best approximate $\Delta \eta_D$ to compare it to the value we found for $\Delta \eta^{\max}$ in Fig. 6.10 (c). We thus evaluate this precipitation growth rate by leaving it as a factor found by equating both $\Delta \eta_D$ and $\Delta \eta^{\max}$, i.e., $\alpha = \Delta \eta_D / \Delta \eta^{\max}$, which gives the results shown in Figs. 6.11 (c) and (d), for either the flat or convex approximation. The values from Dreybrodt's model approximate quite well the cases where $t_d/t_p \leq 1$ and $\forall t_0/t_d$, for the flat case, as illustrated by Fig. 6.11 (a). The model also gives a good agreement for the convex case for some combinations of t_0/t_d and t_d/t_p, as it can be seen in Fig. 6.11 (b). However, we observe that using the perfectly horizontal stalagmite approximation in Dreybrodt's model is not accurate as $\Delta \eta_D$ and $\Delta \eta^{\max}$ do not overlap for $\alpha = 10^{-7} \, \text{m s}^{-1}$ in Fig. 6.11 (a). The order of magnitude found for α as a fit parameter to equate both $\Delta \eta_D$ and $\Delta \eta^{\max}$ is also sometimes out of the range presented in Tabs. 6.1 and 6.2. We indeed observe in Fig. 6.11 (c) that we should impose $\alpha \geq 10^{-4} \, \text{m s}^{-1}$ to produce the stalagmites corresponding to $t_d/t_p > 1$ and $t_0/t_d > 1$. In Fig. 6.11 (b), we observe a better agreement between most $\Delta \eta_D$ and $\Delta \eta^{\max}$ for $t_d/t_p \leq 1$. However, once again for $t_d/t_p > 1$ and $\forall t_0/t_d$, the value that should be imposed for α is out of range, as it can be seen in Fig. 6.11 (d). The difference between the values found for $\Delta \eta_D$ using Eq. (6.32) and $\Delta \eta^{\max}$ using our model might stem from the approximations made in Dreybrodt's model regarding the drainage of the film. In this model, the film is indeed assumed to be uniform in space, such that including the shape of the stalagmite, which dictates the film thickness at the centre, may yield different values of film thickness than the one that should be used by approximating the film as perfectly uniform and having, thereby, the same thickness everywhere. Our modelling also includes the effect of the drainage on the stalagmite growth, which was not done by Dreybrodt et al. [41, 42, 70, 133]. As it could be concluded from the previous chapter, this effect should be taken into account because it influences directly the film thickness and, hence, the mixing between the drop and the film, which in turn dictates the quantity of ions that precipitate into the film. We note that the worst disagreement between the data from Fig. 6.11 arises for $t_d/t_p > 1$, i.e., when the precipitation occurs faster than drainage, and that the ions precipitate before they can get spread out away from the impact point position. By averaging the effect of the successive drops on the film thickness, Dreybrodt's model is not able to capture this particular regime. This comes in particular from the assumption that

the ion concentration evolution with time is always identical, whether the ions precipitate during a time t_0 shorter, equal to or longer than t_p, such that it is impossible for all the ions in the film to have precipitated before a new drop arrives (we refer to the discussion relative to Fig. 10.8 in [70]). Additionally, we can also note that in Dreybrodt's model, the growth rate is calculated as an average value, while in Fig. 6.10 (c), the maximum growth at the centre is considered, such that it might yield larger values. Finally, we can point out that, under some of the restricting approximations of Dreybrodt's model that we discussed above, the values found for α in Tabs. 6.1 and 6.2 could also not be exhaustive, such that the values obtained for α in Fig. 6.11 (c) and (d) would not be out of range.

2.3 Other peculiarities

We present in this section a few examples of other simulations that we are able to conduct using the model described in Sec. 1.3, leading to stalagmite shapes changing in time and concave shapes.

2.3.1 Time-variable environmental conditions

In Figs. 6.12 and 6.13, we present two examples of stalagmite growth simulations, started from an initially horizontal plane, for which either t_0/t_d or $t_\mathrm{d}/t_\mathrm{p}$ is varied at fixed $t_\mathrm{d}/t_\mathrm{p}$, resp. t_0/t_d, for $c_\mathrm{sat} = 5 \times 10^{-7}\,\mathrm{mol\,cm^{-3}}$. Both simulations were conducted until $N_\mathrm{d} = 5000$, each graph from Figs. 6.12 (c) and 6.13 (c) showing intermediate profiles every 500 impacts, except in the region $2500 \leq N_\mathrm{d} \leq 3000$ for which intermediate profiles are shown every 100 impacts as the transition in either t_0/t_d or $t_\mathrm{d}/t_\mathrm{p}$ is made at $N_\mathrm{d} = 2500$. In Fig. 6.12, we varied the dripping period from $t_0/t_\mathrm{d} = 0.05$ for $N_\mathrm{d} < 2500$, to $t_0/t_\mathrm{d} = 1$ for $N_\mathrm{d} \geq 2500$, while keeping $t_\mathrm{d}/t_\mathrm{p} = 1$. In Fig. 6.13, the precipitation timescale was changed from $t_\mathrm{d}/t_\mathrm{p} = 10$ for $N_\mathrm{d} < 2500$, to $t_\mathrm{d}/t_\mathrm{p} = 0.01$ for $N_\mathrm{d} \geq 2500$, with $t_0/t_\mathrm{d} = 1$. In both Figs. 6.12 and 6.13, the graphs from (a) and (b) represent the minimum and maximum values of the film thickness and concentration, h^min and h^max, and c^min and c^max, respectively, over the 5000 drop impacts. The variations between impacts were not represented as they would not be visible. The shape Ψ, scale S and maximum in-between impacts growth $\Delta\eta^\mathrm{max}$ are represented as a function of N_d in the graphs from (d), (e) and (f) for each stalagmite of Figs. 6.12 and 6.13, respectively.

We observe in Fig. 6.12 (c) that, in accordance with all the cases already discussed in the previous sections, the stalagmite profile is first very wide, with a radius $> 5r_\mathrm{d}$ .The dripping-to-drainage ratio $t_0/t_\mathrm{d} = 0.05$ indeed corresponds to a large drop inflow, and, with $t_\mathrm{d}/t_\mathrm{p} = 1$, the ions in solution cannot precipitate before a new drop arrives in the film. Once this inflow is reduced to $t_0/t_\mathrm{d} = 1$, the stalagmite profile changes and narrows down to a radius close to $2r_\mathrm{d}$ within less than 500 impacts. The top part of the stalagmite (for $N_\mathrm{d} \geq 2500$) was obtained by using the same parameters as in Fig. 6.9 (e). It can be seen that both the top part of Fig. 6.12 (c) and Fig. 6.9 (e) resemble one another, except for the fact that the stalagmite of the top part of Fig. 6.12 (c) develops over an already (slightly) inclined plane. Correspondingly, the stalagmite from Fig. 6.13 (c) shows two distinct types of profiles corresponding to $t_\mathrm{d}/t_\mathrm{p} = 10$ and $t_\mathrm{d}/t_\mathrm{p} = 0.01$. We once again observe a quick adaptation of the stalagmite profile in response to the change in $t_\mathrm{d}/t_\mathrm{p}$ around $2500 \leq N_\mathrm{d} \leq 3000$. However, by contrast with Fig. 6.12, the top part of the stalagmite from Fig. 6.13 cannot be compared to the profiles from Fig. 6.9. For $N_\mathrm{d} \geq 2500$, the ions in solution precipitate over the already existing stalagmite which displays a radius of $\sim r_\mathrm{d}$ until $N_\mathrm{d} = 2500$. Hence, a protuberance corresponding to the bottom part can be seen in the top part of the stalagmite. This comes from the fact that, for $t_\mathrm{d}/t_\mathrm{p} = 0.01$, or $t_\mathrm{p} = 100t_\mathrm{d}$, the film flows over the already existing stalagmite faster than the ions precipitate within this film. The ions get thus carried away from the centre before they precipitate, thereby extending the total radius of the stalagmite.

These observations can also be witnessed in the graphs from Figs. 6.12 (a-b) and Fig. 6.13 (b), where we note changes in both the film thickness and ion concentration shortly after $N_\mathrm{d} = 2500$. This change does not appear clearly in Fig. 6.13 (a) for the film thickness, though. In Figs. 6.12 (a) and (b), below $N_\mathrm{d} = 2500$, the large inflow brought into the film yields without surprise a large film thickness. Consequently, since the ions do not precipitate entirely before a new drop arrives in the film, the concentration also remains large. Once the inflow is decreased for $N_\mathrm{d} \geq 2500$, both the film thickness and ion concentration decrease accordingly. In Fig. 6.13 (b), the inflow is never varied since we keep $t_0/t_\mathrm{d} = 1$ for the entire simulation, which is why no change can be observed in Fig. 6.13 (a). However, because we varied $t_\mathrm{d}/t_\mathrm{p}$ from 10 to 0.01, which can also be written as $t_\mathrm{p} = 0.1t_\mathrm{d}$ and $t_\mathrm{p} = 100t_\mathrm{d}$, respectively, the ion concentration varies for $N_\mathrm{d} \geq 2500$ in Fig. 6.13 (b), although we note that its value is not multiplied by 1000 as it is the case for t_p. During the part of the simulation for which $t_\mathrm{d}/t_\mathrm{p} = 10$, the ion concentration remains close to 0 the entire time as ions precipitate in the film almost instantaneously between successive drop impacts, while for $t_\mathrm{d}/t_\mathrm{p} = 0.01$, i.e., $N_\mathrm{d} \geq 2500$, the ion concentration remains very large as ions do barely precipitate over a drop impact period. The curves of c^min and c^max in Fig. 6.13 (b) are even not really distinguishable.

Finally, variations are also observed in Figs. 6.12 (d-f) and Figs. 6.13 (d-f) for $N_\mathrm{d} \geq 2500$. The shape factor Ψ, in particular, shows a significant change in Fig. 6.12 (d), in accordance with the stalagmite profile shown in Fig. 6.12 (c). The shape factor in Fig. 6.13 (d) only exhibits a slight variation as it actually measures the shape of the protuberance at the centre of the stalagmite from Fig. 6.13 (c), which does not change much once $N_\mathrm{d} \geq 2500$. Although the scale S of both stalagmites varies in Figs. 6.12 (e) and 6.13 (e), we note that it keeps increasing for the entire simulation, but at different rates. This is corroborated by the maximum in-between impacts growth, $\Delta\eta^\mathrm{max}$, in both Figs. 6.12 (f) and 6.13 (f), respectively. In Fig. 6.12 (f), for $N_\mathrm{d} \geq 2500$, the maximum growth at the centre of the stalagmite decreases because the inflow and, therefore, total quantity of ions added to the film, decreases. The variation in Fig. 6.13 (f) looks different. For $N_\mathrm{d} = 2500$, $\Delta\eta^\mathrm{max}$ drops sharply, then increases again around $N_\mathrm{d} \simeq 3000$, after the stalagmite has adapted its new profile in Fig. 6.13 (c). For $2500 \leq N_\mathrm{d} \leq 3000$, the ion concentration indeed increases because the ions suddenly no longer precipitate as easily as they did before ($t_\mathrm{p} = 100t_\mathrm{d}$). All the changes caused by an inflow variation witnessed in Fig. 6.12 thus seem almost instantaneous, while in Fig. 6.13 we note that it takes a larger number of drop impacts for the ion concentration and related parameters, i.e., the maximum growth at the centre and the stalagmite profile, to reach a new steady-state. We also note that the inflow variation from Fig. 6.12 caused variations in the film thickness and, thereby, the ion concentration, while changing only the drainage-to-precipitation ratio $t_\mathrm{d}/t_\mathrm{p}$ in Fig. 6.13 only affects the concentration but not the film thickness. If these changes were responsible for significant stalagmite profile variations, i.e., of the order of $\sim h_\mathrm{d}$ or more, the film thickness would also respond to a variable $t_\mathrm{d}/t_\mathrm{p}$.

Despite small differences, both examples of Figs. 6.13 and 6.13 exhibit a rather quick response of less than 500 drop impacts (compared to $\sim$ 5000 to 10 000, the total number of impacts) to new environmental conditions. In Sec. 1.5 from Ch. I, we could indeed note from the examples presented in Figs. 1.11 and 1.12 that the stalagmite laminae present distinct features from one year to another. The difference in grain density can also vary within a few months since this difference is one of the markers allowing to identify the laminae in cross-sectional cuts of actual stalagmites [20]. Additionally, the environmental conditions of the stalagmite can also vary quickly. For instance, daily modifications were witnessed in experimental records of t_0 [98]. Although the examples of Fig. 6.13 would not correspond to an entire year in the lifetime of an actual stalagmite, even by adjusting the actual times of t_0, t_d and t_p, they show that the stalagmite profile can adjust quickly to a new environment. However, from Fig. 6.13 (b), we observe that it would be difficult to retrieve
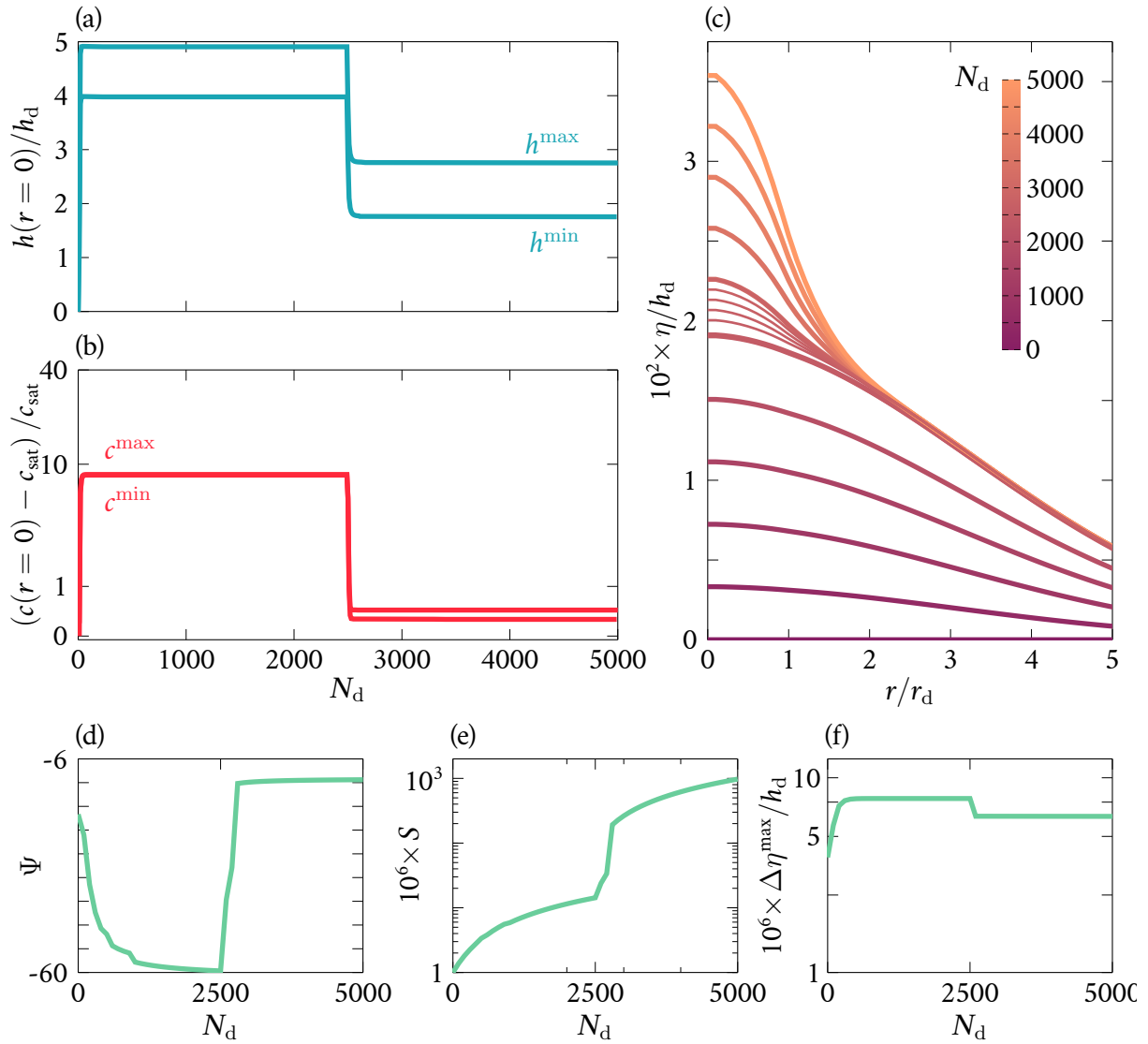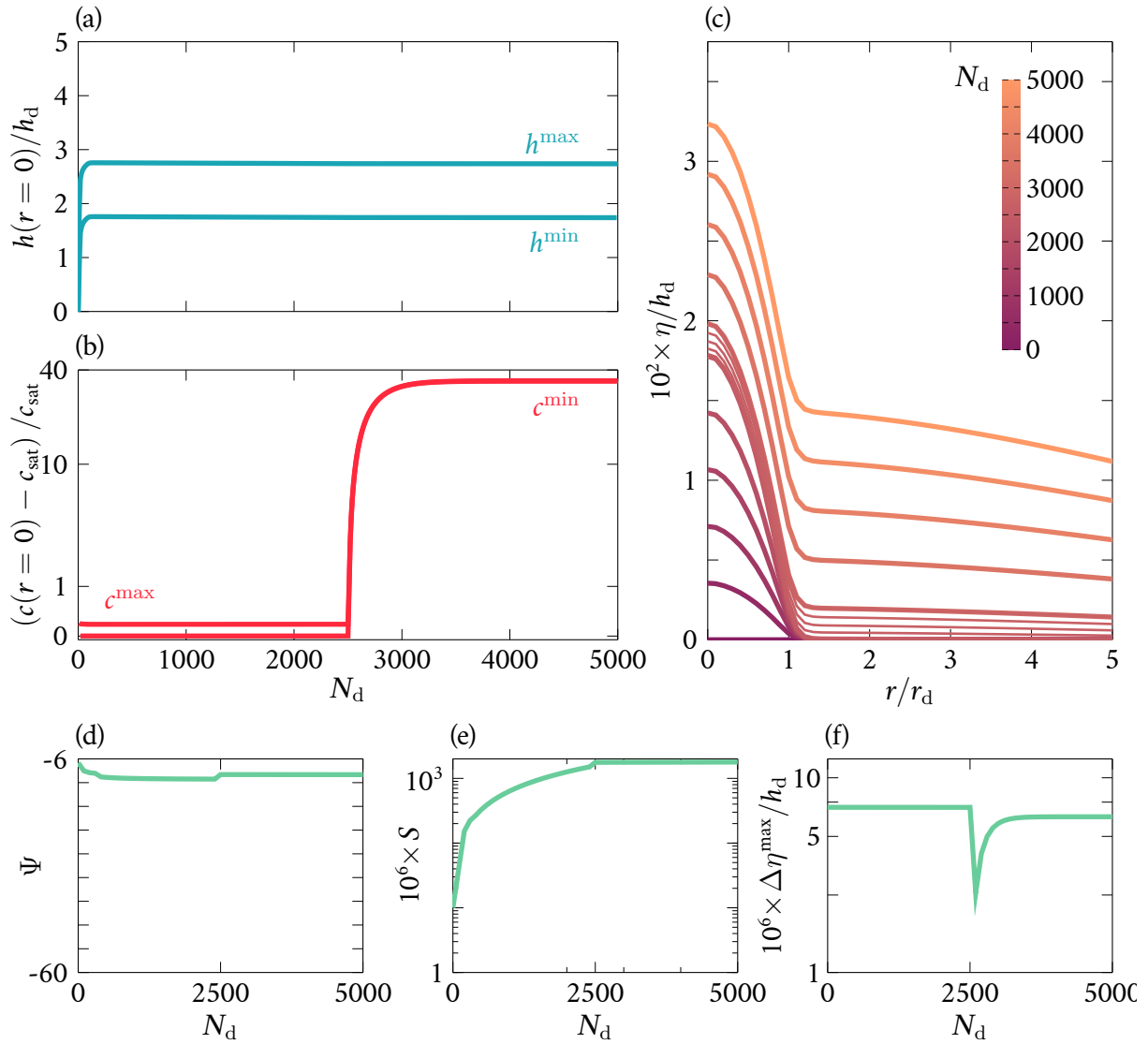
Figure 6.12: Examples of stalagmite profile evolution from an initially perfectly horizontal surface, up to 5000 drop impacts, in response to time-variable parameters with constant $c_{\text{sat}} = 5 \times 10^{-7}$ mol cm^{-3}. For $N_d < 2500$, $t_0/t_d = 0.05$ and, for $N_d \geq 2500$, $t_0/t_d = 1$, with $t_d/t_p = 1$. (a) Maximum and minimum values of the film thickness evolving as a function of N_d. (b) Maximum and minimum values of the ion concentration evolving as a function of N_d. (c) Stalagmite elevation profile, η, as a function of the radial coordinate, r. Intermediate lines show the elevation profile every 500 drop impacts, as indicated by the colour bar. The thinner lines show the elevation profile every 100 drop impacts between $N_d = 2500$ and $N_d = 3000$. (d-f) Shape factor Ψ (d), scale S (e) and maximum in-between impacts growth $\Delta\eta^{\text{max}}$ (f), all drawn as a function of N_d.

Figure 6.13: Examples of stalagmite profile evolution from an initially perfectly horizontal surface, up to 5000 drop impacts, in response to time-variable parameters with constant $c_{sat} = 5 \times 10^{-7}$ mol cm^{-3}. For $N_d < 2500$, $t_d/t_p = 10$ and, for $N_d \geq 2500$, $t_d/t_p = 0.01$, with $t_0/t_d = 1$. (a) Maximum and minimum values of the film thickness evolving as a function of N_d. (b) Maximum and minimum values of the ion concentration evolving as a function of N_d. (c) Stalagmite elevation profile, η, as a function of the radial coordinate, r. Intermediate lines show the elevation profile every 500 drop impacts, as indicated by the colour bar. The thinner lines show the elevation profile every 100 drop impacts between $N_d = 2500$ and $N_d = 3000$. (d-f) Shape factor Ψ (d), scale S (e) and maximum in-between impacts growth $\Delta\eta^{max}$ (f), all drawn as a function of N_d.

the exact set of parameters that have led to the particular shape presented once $N_\mathrm{d} \geq 2500$. By contrast, the parameters used in Fig. 6.13 (a) could easily be retrieved by measuring the shape Ψ and scale S of the top and bottom parts of the stalagmite. It should be noted, though, that the adaptation of the stalagmite to new environmental conditions was here analysed when the initial stalagmite profile is flat. Given the order of magnitude of actual growth, even for variable conditions, the profile of the stalagmite always remains flat from the point of view of the film. We explore in the following section the effect that an initially inclined stalagmite profile has on the evolution with time of this stalagmite profile.

2.3.2 Convex profiles and effect of the surface inclination on local growth

Thus far, the considered stalagmites grew from an initially perfectly horizontal plane. Given the relatively small number of drop impacts, the growth remained small in regard of the film thickness. Stalagmites thus most likely remained in a regime where drainage is dominated by film thickness gradients, as detailed in Sec. 5.4 from Ch. V. The results from Sec. 2.2, which explored the effect of the ratios t_0/t_d and $t_\mathrm{d}/t_\mathrm{p}$ on Ψ, S, $\Delta\eta^\mathrm{max}$, R_eq and $\varphi_\mathrm{d \to f'}$, might yield qualitatively different relations when the initial stalagmite profile is not horizontal. Similarly, conclusions drawn from the former section on time-variable conditions could no longer be applicable if the local inclination dominates the drainage of the film, rather than the film thickness gradients, as it was the case in the above examples. Assessing the potential effects that setting initial values to Ψ and S may have on subsequent stalagmite growth is out of the scope of this work. The present chapter indeed focuses on introductory examples of stalagmites at steady-state. Nevertheless, we propose to take a look at a few cases of interest to examine the fundamental aspects of the effect of a convex initial stalagmite profile on subsequent stalagmite growth. In Figs. 6.14 (a-c), we show examples of stalagmite profiles growing over time, starting from an initial convex profile set to $\Psi = -15$ and $S = 1$. The profile is illustrated in Fig. 6.14 (d). The graphs from Figs. 6.14 (a), (b) and (c) correspond to $t_0/t_\mathrm{d} = 0.1$ and $t_\mathrm{d}/t_\mathrm{p} = 1$, $t_0/t_\mathrm{d} = 10$ and $t_\mathrm{d}/t_\mathrm{p} = 1$, and $t_0/t_\mathrm{d} = 1$ and $t_\mathrm{d}/t_\mathrm{p} = 10$, respectively. The graphs from Figs. 6.14 (e), (f) and (g) show the same simulations but started from an initially perfectly horizontal surface, as illustrated by Fig. 6.14 (h). It should be noted that the profiles from (a-c) are shown as a function of the radial coordinate r and not the curvilinear coordinate ξ following the stalagmite surface, for comparison with the profiles from (e-g).

We observe in all the pairs of graphs shown in Figs. 6.14 (a) and (e), (b) and (f), and (c) and (g), that, although the environmental conditions are the same, the final shape obtained slightly differs according to the initial profile (convex or perfectly horizontal). This is particularly true for the profiles of Figs. 6.14 (b) and (f), and (c) and (g), in which case the dripping period, drainage timescale and precipitation timescales are equal, $t_0 = t_\mathrm{d} = t_\mathrm{p}$ ((b) and (f)), or such that the precipitation timescale is shorter than the two other ones, $t_\mathrm{p} < t_0 = t_\mathrm{d}$ ((c) and (g)). Hence, the ions in solution in the film should precipitate before or at the same time as the film spreads out over the stalagmite because of

Figure 6.14: *Next page.* Examples of stalagmite profile evolution with time over an initial convex profile (a-c), compared to an equivalent flat case (e-g). Each case (a-c), (e-g) represents a stalagmite profile obtained after 5000 drop impacts. The intermediate profiles are shown as a function of the radial coordinate r every 1000 drop impacts, as indicated by the colour bar below graph (h). Hence, the convex surface actually corresponds to $\eta(r, t) - \eta(r, t = 0)$. The simulations were obtained by fixing $c_\mathrm{sat} = 5 \times 10^{-7}$ mol cm^{-3}. The parameters used are: for (a) and (d), $t_0/t_\mathrm{d} = 0.1$ and $t_\mathrm{d}/t_\mathrm{p} = 1$, for (b) and (f), $t_0/t_\mathrm{d} = 1$ and $t_\mathrm{d}/t_\mathrm{p} = 1$, and for (c) and (g), $t_0/t_\mathrm{d} = 1$ and $t_\mathrm{d}/t_\mathrm{p} = 10$. The initial stalagmite profile relative to (a-c), resp. (e-g), is illustrated in (d), resp. (h). The profile from (d) corresponds to $\Psi = -15$ and $S = 1$. The profile from (h) represents the initial perfectly horizontal case. The equivalent spot radius left by the drop, R_eq, and ion proportion initially in the drop ending up in the film, $\varphi_\mathrm{d \to f'}$, are represented in each case (a-c) and (e-g), as captioned in (a). The equivalent radius R_eq corresponds to the grayed area and the dashed line, while the drop symbol at the bottom right of each graph illustrates $\varphi_\mathrm{d \to f'}$.
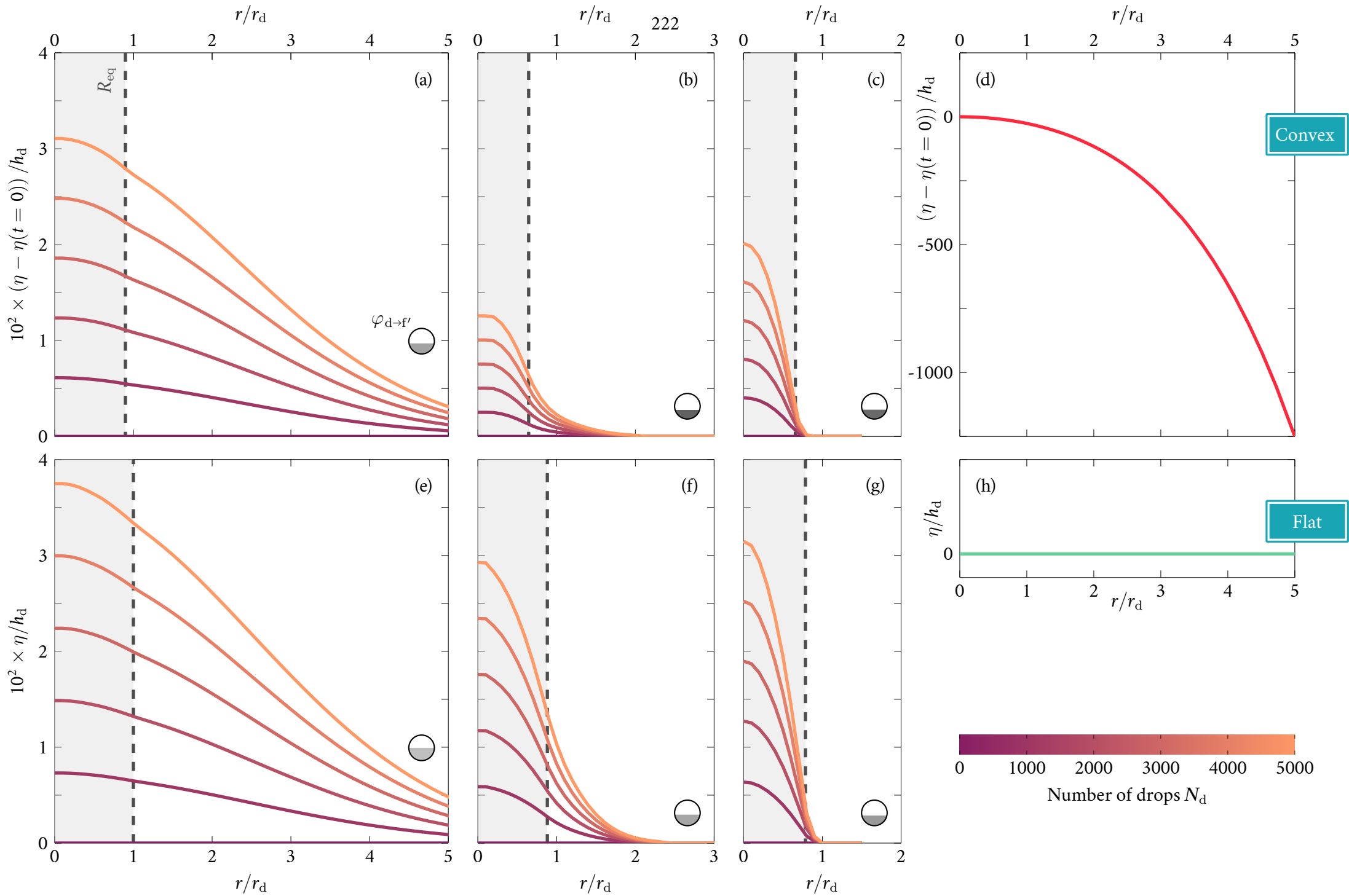
the drainage process. Additionally, we note in Figs. 6.14 (a-c) that the growth rate at the centre of the convex stalagmite is smaller than in Figs. 6.14 (e-g), respectively, because the total height reached by the stalagmite is smaller as well. This is once again due to the drainage over an inclined stalagmite surface, which leads to smaller film thicknesses than over a perfectly horizontal stalagmite. A thinner film also induces a smaller equivalent radius left by the drop in the film post impact, R_{eq}, and a smaller proportion of the drop content ending up in the film, $\varphi_{\mathrm{d \rightarrow f'}}$. The total quantity of ions entering the film thus decreases. In terms of spatial extent, we also note that stalagmites from Figs. 6.14 (a-c) seem narrower than their counterpart from Figs. 6.14 (e-g), but we cannot state whether this is caused by the lower amount of ions in the film or another effect. Nevertheless, we note that $r \approx \xi \cos \varphi$ close to the centre, such that the spatial extent of the stalagmite along ξ in the convex case from Figs. 6.14 (a-c) might actually be comparable to the spatial extent of the stalagmite along r in the flat case from Figs. 6.14 (e-g). From these simple examples, although we cannot assess the exact effect of the initial convex profile of the stalagmite, we can still conclude that the dynamics of drainage caused by an inclined surface seems to have a non-negligible effect on subsequent growth.

2.3.3 Dissolution-precipitation balance and concave profiles

We come back in this section to our former discussion on the balance that may exist between either Q_{drip} and Q_{drain}, or between Q_{drip} and Q_{spl} (see Sec. 5.4.1 from Ch. V). In Fig. 6.15, we start by presenting an example of the evolution of the stalagmite profile with added ion precipitation at each impact, starting from an initially concave stalagmite profile. However, to reproduce the equivalent of drops splashing at impact, which we had left out of the simulations until now, we artificially add ions at the same frequency as if drops were added in the film, but stop adding fluid at the impacts. We only add one drop at the beginning of the simulation to produce a film, then pursue by only adding ions and letting them precipitate. Hence, the film does not cover the entire stalagmite but only fills part of the dimple in the centre. We consider that we are in the range of values corresponding to $\varphi_{\mathrm{e}} \approx 1$, which is a valid approximation for a film thickness of $1.2 h_{\mathrm{d}}$ if $h_{\mathrm{d}} = 100\,\mu\mathrm{m}$ (see Fig. 4.12 in Ch. IV). The parameters of the simulation are $c_{\mathrm{sat}} = 5 \times 10^{-6}\,\mathrm{mol\,cm^{-3}}$, $t_0/t_{\mathrm{d}} = 1$, $t_{\mathrm{d}}/t_{\mathrm{p}} = 5$, $\Psi = 20$ and $S = 0.05$. With this stalagmite initial profile, the film thickness remains at about $1.2 h_{\mathrm{d}}$. In Fig. 6.15 (a), the entire stalagmite profile is represented up to $r = 2 r_{\mathrm{d}}$, while Fig. 6.15 (b) shows a close-up view up to $r = r_{\mathrm{d}}$. We observe that, because of the ion precipitation and renewal, the stalagmite elevation η grows upward at the centre, where the film is located, but not on the sidewalls. After a long time, the stalagmite profile should thus eventually flatten out. This is not surprising since the ions are only added at centre of the stalagmite and the film never drains away on the stalagmite sides as long as it cannot overcome the protuberance.

We now reintroduce the added thickness at impact, i.e., both the film and ions are renewed by the successive drop impacts. In Fig. 6.16, we present two parts of a simulation conducted for $t_0/t_{\mathrm{d}} = 1$, $t_{\mathrm{d}}/t_{\mathrm{p}} = 1$ nd $c_{\mathrm{sat}} = 1 \times 10^{-5}\,\mathrm{mol\,cm^{-3}}$. The beginning of the simulation, for $0 \leq N_{\mathrm{d}} < 2500$, is shown in Fig. 6.16 (a), while Fig. 6.16 (b) shows the remaining of the simulation, for $2500 \leq N_{\mathrm{d}} \leq 5000$. The simulation was started from a concave shape with $\Psi = 3$ and $S = 0.1$ to conform to the profiles set using Eq. (5.49), but starting from any initial profile would also lead to subsequent similar profiles. In Fig. 6.16 (a), using the same ion saturation concentration c_{sat} and the same drop ion concentration c_{d}, we arbitrarily changed the sign of the term $(c - 1)$ in
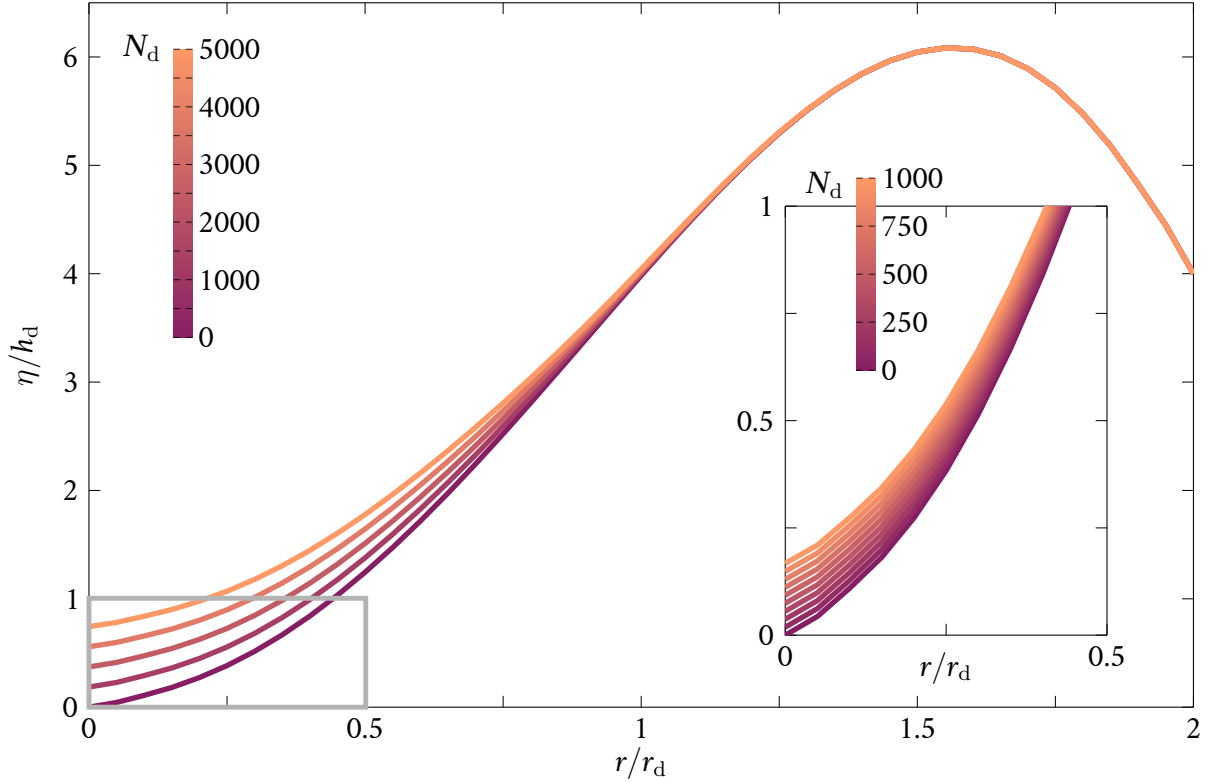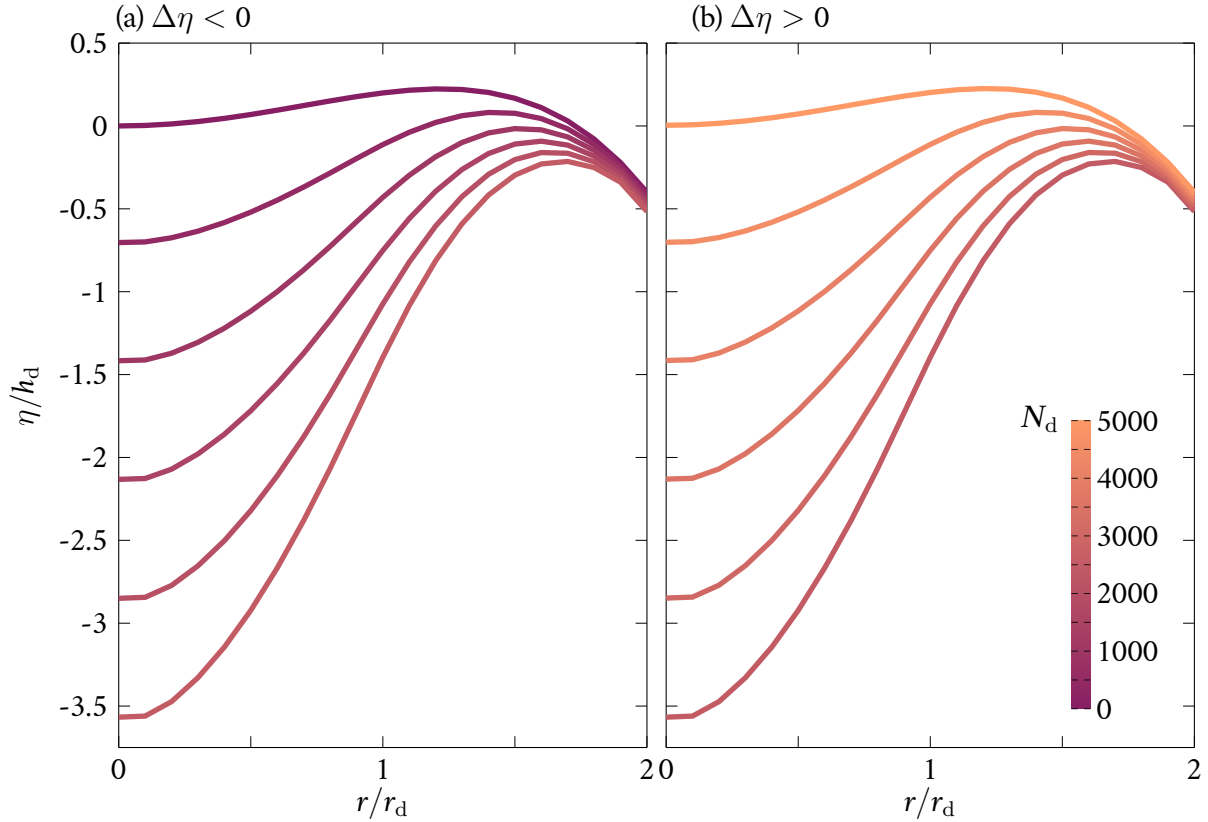
Figure 6.15: Dissolution imposed instead of precipitation: example of simulation conducted for $t_0/t_d = 1$, $t_d/t_p = 5$ and $c_{sat} = 5 \times 10^{-6}$ mol cm^{-3}, for 5000 drop impacts, starting from a stalagmite profile with shape $\Psi = 20$ and scale $S = 0.05$. In this case, only one drop is added at the beginning of the simulation to produce a film, then liquid is no longer added to this film. The ions that would be contained within a drop are still added at each successive impact but the film thickness no longer varies. The simulation is conducted as if the drops were producing splash at each impact, such that as much liquid volume is ejected away as brought into the film by the drops (case where $\varphi_e = 1$, see Ch. IV). The graphs show the stalagmite elevation, η, as a function of the radial coordinate, r. The inset represents a close-up view of the part of the stalagmite surrounded by the gray frame, showing only the first 1000 impacts. Intermediate lines are shown every 1000 impacts in the main graph, and every 100 impacts in the inset.

Eq. (6.19) to produce dissolution instead of precipitation. We refer to this as $\Delta\eta < 0$ in Fig. 6.16 (a), by opposition to $\Delta\eta > 0$ in Fig. 6.16 (b). Because drops are added during the entire simulation, the film always fills the entire dimple of the stalagmite.

We observe in Fig. 6.16 (a) that, in the dissolution case, the stalagmite gets progressively more and more scooped out in the centre, just as it could build up in the case of precipitation. We note that, because the film covers the entire stalagmite and drains above the protuberance, ions get distributed everywhere in the film and the stalagmite elevation also decreases on the protuberance, but at a slower rate. Without changing anything but the sign of $(c-1)$ in Eq. (6.19), the added $\Delta\eta$ becomes positive and leads to precipitation again in Fig. 6.16 (b). We observe that the stalagmite grows back upward and progressively flattens out, as in the case of Fig. 6.15 above. Both Figs. 6.16 (a) and (b) actually look almost identical, except for the direction of growth. We indeed used the same parameters in both cases, except for the difference in sign in Eq. (6.19). However, we note that, if the concave stalagmite profile can be maintained when dissolution occurs, or for a certain amount of drops when precipitation occurs again, the balance between the inflow caused by the dripping drops and the drainage of the film does not change the dynamics of growth, except for the direction (downward or upward). At least in the range of parameters that we varied, by considering the splash at impact or that the dimple of the stalagmite could be entirely filled, we could not find a combination of t_0/t_d and t_d/t_p that would allow to maintain the concave profile indefinitely, nor a combination of t_0/t_d and t_d/t_p that would allow to create a concave profile

without including the dissolution instead of the precipitation. Hence, this concave profile seems to be the result of either dissolution occurring during a certain time sufficiently long to create a noticeable dimple in the centre of the stalagmite, or an unstable shape that cannot sustain in time. This is in accordance with the example of, e.g., Fig. 1.11 (b) in Ch. I [20], where the concave profile observed for a few years was then successively covered by flat then convex profiles. We also rarely observed concave stalagmites in the caves that we visited, and cannot find many of them in the cross-sectional cuts presented in the literature (see Fig. 1.11 in Ch. I).

Figure 6.16: Dissolution imposed instead of precipitation: example of simulation conducted for $t_0/t_d = 1$, $t_d/t_p = 1$ and $c_{sat} = 1 \times 10^{-5}\,\text{mol\,cm}^{-3}$, for 5000 drop impacts, starting from a stalagmite profile with shape $\Psi = 3$ and scale $S = 0.1$. For $0 \leq N_d < 2500$, dissolution was imposed instead of precipitation (a), then precipitation is reestablished for $2500 \leq N_d \leq 5000$ (b), as materialised by the sign of $\Delta\eta$. The graphs show the stalagmite elevation, η, as a function of the radial coordinate, r. Intermediate lines are shown in both (a) and (b) every 500 impacts, in correspondence with the scale bar from (b), which is applicable to both graphs.

2.3.4 Impact point dispersal

In the former simulations, we included effects related to drop impacts in caves, i.e., related to the mixing at impact from Ch. IV, as well as the drainage of the film from Ch. V, but we did not include the dispersal observed in the impact point position of the drops yet. However, we noted in Ch. III that this dispersal has a non-negligible effect on stalagmite average width for large falling heights. As aforementioned, we cannot include the dispersal directly when solving the equations in an axisymmetric coordinate system because adding drops away from the stalagmite centre in this case would correspond to the addition of liquid rings of volumes instead of actual drops. Hence, we need to derive the equations in a two-dimensional Cartesian coordinate system. This procedure is reviewed in Appendix C. The Cartesian grid is nondimensionalised by r_d, as we did in the former simulations. We also vary the position of the drop impact in a random manner, by imposing that

the distribution is a Gaussian centred in $(0, 0)$ with a standard deviation Δ (see Ch. III). We show in Fig. 6.17 an example of simulation obtained for $t_0/t_d = 0.1$, $t_d/t_p = 1$, $c_{sat} = 5 \times 10^{-6}$ mol cm^{-3}, starting from an initially flat stalagmite. We thus have $t_0 < t_d = t_p$, such that drops should impact the film before the ions in solution have enough time to spread out by drainage or precipitate. We also impose dispersal in the drop impact point position, set to $\Delta = 5r_d$, which is relatively large if we take $r_d = 1$ cm. The simulation is shown during 5000 drop impacts, which should be sufficient for the stalagmite to reach a stationary state. We could observe that the stalagmite obtained with the same timescale ratios but no dispersal at impact, i.e., the stalagmite from Fig. 6.9 (d), had a radius of about $\lesssim 3r_d$. In the case of Fig. 6.17, we note that the stalagmite radius is on average larger. We also observe in Fig. 6.17 that the stalagmite surface is not smooth, as it was the case in the previous simulations, but present corrugations. The dripping period t_0 being shorter than the two other timescales indicates that the effect of the drops could be averaged over long periods of time. Nevertheless, this does not seem to be the case here because of the dispersal in the impact point position.

In Figs. 6.18 (a)-(c), we present additional examples of stalagmite growth over 5000 drop impacts coming from simulations conducted for $c_{sat} = 5 \times 10^{-6}$ mol cm^{-3} and for: (a) $t_0/t_d = 0.1$, $t_d/t_p = 1$, without dispersal in the drop impact point position, (b) $t_0/t_d = 0.1$, $t_d/t_p = 1$ with $\Delta = 5r_d$, and (c) $t_0/t_d = 0.1$, $t_d/t_p = 0.1$, with $\Delta = 5r_d$. In Fig. 6.18 (a), in the absence of dispersal we obtain a very similar stalagmite profile as in Fig. 6.9 (d), which is not surprising given that both simulations were conducted for the same timescale ratios. However, in Fig. 6.18 (b), by including the dispersal we note once again that the stalagmite radius increases and that its surface becomes corrugated. In Fig. 6.18 (c), the timescales are changed but the dispersal is maintained. While the height reached by the stalagmite decreases in response to the change in t_d/t_p, we note that the stalagmite radius remains of the same order as in Fig. 6.18 (b) because of the dispersal in the drop impact point position. Hence, we conclude as in Ch. III that the dispersal in the drop impact point position is not negligible and set constraints on the radius reached by the stalagmite. A distribution associated with $\Delta = 5$ cm, as we used in the present case, would correspond to a falling height of about 20 m (see Sec. 3.2 from Ch. III).
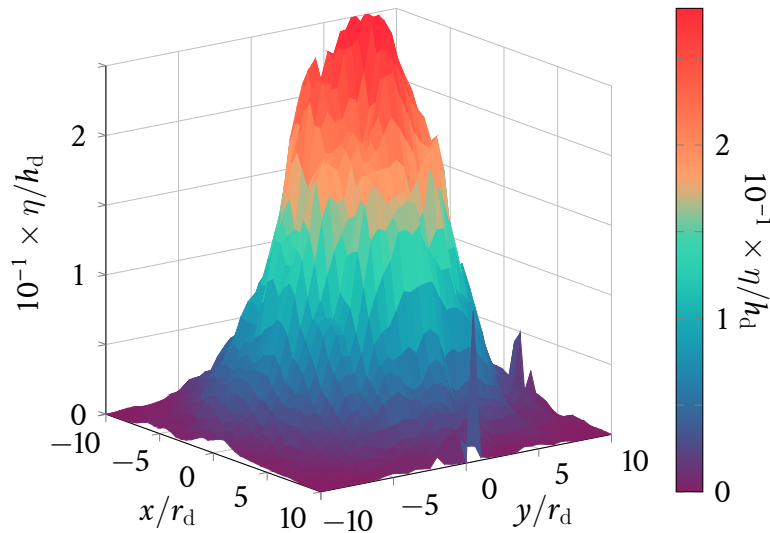
Figure 6.17: 2D-Cartesian case including impact point dispersal: example of simulation conducted for $t_0/t_d = 1$, $t_d/t_p = 1$ and $c_{sat} = 5 \times 10^{-6}$, for 5000 drop impacts, with $\Delta = 5r_d$. The simulation was obtained by using the 2D-Cartesian scheme described in Appendix C. The colour bar indicates the height of the stalagmite.
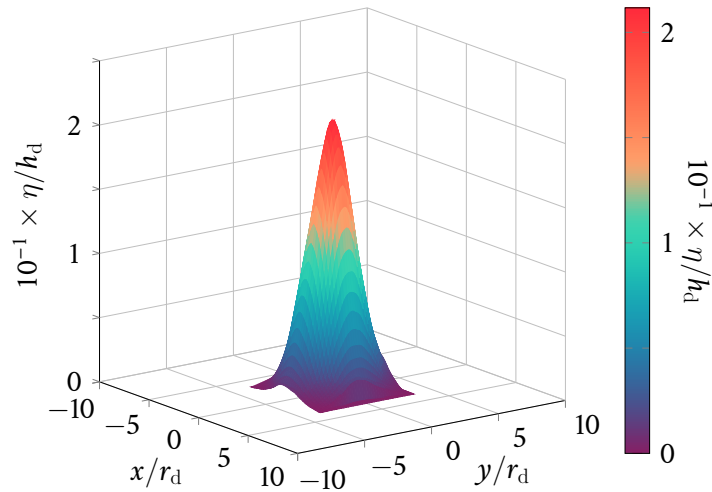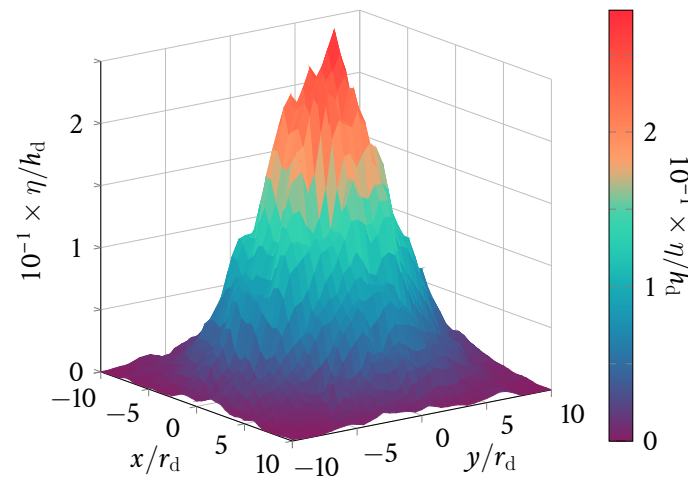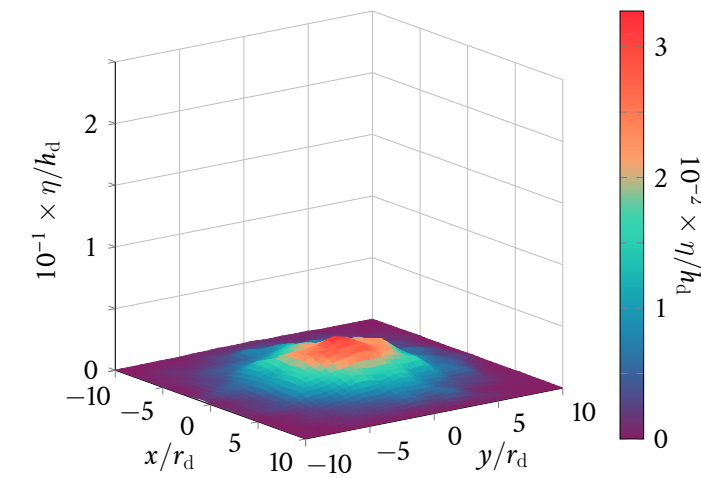
Figure 6.18: 2D-Cartesian case possibly including dispersal in the impact point position: examples of simulation conducted for variable parameters. The simulations were realised for 5000 drop impacts, with the 2D-Cartesian scheme described in Appendix C. (a) $t_0/t_d = 0.1$, $t_d/t_p = 1$ and $c_{sat} = 5 \times 10^{-6}$ mol cm^{-3}, without dispersal in the drop impact point position. (b) $t_0/t_d = 0.1$, $t_d/t_p = 1$ and $c_{sat} = 5 \times 10^{-6}$ mol cm^{-3}, with $\Delta = 5r_d$. (c) $t_0/t_d = 0.1$, $t_d/t_p = 0.1$ and $c_{sat} = 5 \times 10^{-6}$ mol cm^{-3}, with $\Delta = 5r_d$. The colour bars are positioned directly next to the graphs to which they refer. They indicate the height of their corresponding stalagmite.

3. Conclusion

In this chapter, we combined and studied briefly the possible effects caused by the drop dripping period, the drainage of the thin residual film lying on top of the stalagmite and the precipitation of the ions in solution in this film on subsequent stalagmite growth. Using the equations developed in the previous chapter for the drainage of the film and an advection-reaction equation describing the evolution of the ion concentrations in the film in time and space, we completed the model by a equation describing the ion precipitation, and, thereby, the evolution of the stalagmite profile. We also included the mixing between the drop and the film at impact when modelling the inclusion of the drop into the film numerically, at least in terms of added concentration at impact. We indeed neglected the intricate dynamics related to the splash of drops at impact as there are already several effects at play in the complete model. Hence, the drop volume is always assumed to be entirely added to the film while this may not be accurate for certain film thicknesses. From the complete model, we inferred that three parameters play a major role in shaping the stalagmite over time and space: (i) the ratio of the dripping period between the drainage timescale, t_0/t_d, (ii) the ratio between the drainage and precipitation timescales, and (iii) the saturation concentration of the ions in solution, c_sat.

We first varied either t_0/t_d, $t_\mathrm{d}/t_\mathrm{p}$ or c_sat to assess their sole effect in numerical simulations conducted for a few thousands of drop impacts, starting from an initially perfectly horizontal stalagmite. The values reached by the stalagmite profiles obtained are thus very small with respect to the growth observed in reality over a few decades, or even only one year. Nevertheless, doing so allows for both the film thickness and ion concentration in the film to remain in the same steady-state, and allows eliminating any time-related effects due to, e.g., film thickness variations on subsequent stalagmite growth. We observed that increasing the inflow of drops, or decreasing t_0/t_d, widens the stalagmite, while reducing the inflow, or increasing t_0/t_d, narrows it down. Regarding the effect of $t_\mathrm{d}/t_\mathrm{p}$, the stalagmite also becomes wider, resp. narrower, when $t_\mathrm{d}/t_\mathrm{p} > 1$, resp. $t_\mathrm{d}/t_\mathrm{p} < 1$. This is due to the ordering of the three timescales. If t_p is smaller than both t_0 and t_d, the ions should precipitate before they are spread out over the stalagmite by the film drainage, or before new ions are added to the film. Conversely, if $t_0 < t_\mathrm{d}, t_\mathrm{p}$, new ions are added to the film before they can either spread out by drainage or precipitate, such that the ion concentration always remains $\gg 1$ in this regime. The resulting stalagmite profile therefore depends on the balance between all three timescales, i.e., between the drop inflow, the film drainage and the ion precipitation. Changing c_sat, on the other hand, has no effect on the shape of the stalagmite, per se, only on the growth rate between two drop impacts, and, therefore, on the final height reached by the stalagmite.

Past the transient phases of h and c at the beginning of the simulations, all the parameters relative to the stalagmite growth, i.e., Ψ, $\Delta\eta^\mathrm{max}$, R_eq and $\varphi_\mathrm{d \rightarrow f'}$, could be observed to remain constant. The only remaining variable parameter is S, the scale of the stalagmite. Given our definitions of Ψ and S for convex stalagmites in Eq. (2.1) from Ch. II, we know that a constant Ψ for variable S implies that the stalagmite profile remains anchored at a zero value at a certain distance from the centre, while the stalagmite total height increases for increasing S. Hence, the growth of the stalagmite itself can be considered at steady-state, at least in the case that we considered where the total height reached remains negligible with respect to h_d. We could therefore infer values of Ψ, S $\Delta\eta^\mathrm{max}$, R_eq and $\varphi_\mathrm{d \rightarrow f'}$ from simulations conducted by systematically varying t_0/t_d and $t_\mathrm{d}/t_\mathrm{p}$. We observed that the shape factor Ψ and scale S increased with either increasing t_0/t_d or increasing $t_\mathrm{d}/t_\mathrm{p}$, both effects being additive. A larger Ψ or S means that the stalagmite appears wider and taller, in accordance with the aforementioned ordering of the three timescales at play once again. Without surprise, the equivalent radius of the spot left by the drop in the film post impact, R_eq, and the proportion of the drop volume entering the film at impact, $\varphi_\mathrm{d \rightarrow f'}$, both increase with increasing

inflow, and therefore with increasing initial film thickness (see Chs. IV and V). The growth rate at the centre of the stalagmite, $\Delta\eta^{\text{max}}$, mostly increases with increasing inflow as well, because of the combined effects of increasing R_{eq} and $\varphi_{\text{d}\rightarrow\text{f}}$, which cause a larger amount of ions to enter the film at each drop impact. We compared the values found for $\Delta\eta^{\text{max}}$ using our model to the values obtained from Dreybrodt's model [41, 42, 70, 133]. We obtained agreement between both cases mostly for $t_{\text{d}}/t_{\text{p}} < 1$, but we could not recover the same growth rates when $t_{\text{d}}/t_{\text{p}} > 1$, i.e., when the ion precipitation occurs before the drainage spreads out the ions radially.

Finally, we varied a few extra parameters in the simulations to illustrate their potential effect on stalagmite growth, without systematically studying their impact. Hence, the conclusions drawn from these additional simulations may be specific to the cases shown. We first changed either the dripping-to-drainage ratio, t_0/t_{d}, or the drainage-to-precipitation ratio, $t_{\text{d}}/t_{\text{p}}$, after half the simulation had passed. We obtained resulting stalagmite profiles varying accordingly, and possibly resembling the former profiles identified for corresponding values of t_0/t_{d} and $t_{\text{d}}/t_{\text{p}}$ in the steady-state simulations. However, in the case where the stalagmite width increases because of the change in, e.g., $t_{\text{d}}/t_{\text{p}}$ during the simulation, the protuberance formed initially (during the first half of the simulation) remains visible during the second half of the simulation. We also tried to conduct a few simulations on an initially convex-looking stalagmite. The conclusions drawn regarding the effect of t_0/t_{d} and $t_{\text{d}}/t_{\text{p}}$ on stalagmite growth seem to remain true in this case, but the effect of the drainage of the film caused by an inclined plane is non-negligible and most likely changes parameters such as Ψ or S. For instance, we could observe that, because the drainage is more efficient over an inclined stalagmite surface, the film thickness decreases, causing the total amount of ions entering the film, and thereby the growth rate, to diminish as well. We further noted from simple examples that dissolution, occurring instead of precipitation because of specific environmental conditions, may explain why some stalagmites appear to be concave rather than flat or convex. We could not produce a non-transient concave stalagmite shape numerically, although the question remains open. We attempted to include an approximate splash at impact, but the growth occurring only at the centre of the stalagmite dimple should eventually flatten out, just as in the case where the film fills out the dimple during the entire simulation. Finally, we rewrote the equations describing the film drainage, ion concentration evolution and stalagmite elevation evolution in a two-dimensional Cartesian coordinate system in order to include the effect of the impact point dispersal in the simulations. As already concluded from Ch. III, this effect increases considerably the stalagmite width. We also conducted a simulation for $t_0/t_{\text{d}} = t_{\text{d}}/t_{\text{p}} = 1$, which included a slight dispersal in the impact point position of the drops, for a very large number of drop impacts. From all the conclusions that we could draw in the simulations conducted either at steady-state or not, over an initially flat, convex or concave stalagmite, we expect the response of the stalagmite growth to differ as soon as the three timescales at play are no longer equal to each other.

Appendix

A. Reaction kinetic constant and saturation concentration values

This appendix contains the tables from Dreybrodt [70] used to approximate the precipitation rate α in open and closed conditions, for various partial pressures in carbon dioxide p_{CO_2}, temperatures and film thicknesses h. The open conditions correspond to a film with a liquid/air interface. The closed conditions correspond to liquid confined between solid surfaces, for instance the liquid that may be inside fractures found within karst systems. Both tables also contain the saturation concentration values corresponding to the carbon dioxide partial pressures, p_{CO_2}, and temperatures[4].

	h [μm]	$p_{CO_2} = 3 \times 10^{-4}$ atm			$p_{CO_2} = 10^{-3}$ atm			$p_{CO_2} = 5 \times 10^{-3}$ atm		
		5 °C	10 °C	20 °C	5 °C	10 °C	20 °C	5 °C	10 °C	20 °C
Laminar	10	0.041	0.0714	0.232	0.0619	0.11	0.358	0.153	0.25	0.679
	20	0.076	0.135	0.407	0.134	0.233	0.75	0.294	0.467	1.36
	50	0.197	0.341	1.04	0.33	0.583	1.69	0.647	1.11	2.74
	100	0.37	0.635	1.84	0.619	1.08	2.76	1.0	1.54	3.13
	300	0.803	1.29	2.91	0.979	1.61	3.29	0.969	1.47	2.87
	500	0.915	1.29	2.57	0.907	1.40	2.64	0.926	1.35	2.63
	1000	0.636	0.919	1.60	0.68	1.0	1.63	0.85	1.21	2.0
Turbulent	1000	3.3	5.7	13.5	5.2	8.0	14.7	7.25	8.3	11.0
	2000	5.9	9.5	20.0	8.4	11.5	17.5	7.9	8.8	12.0
	5000	11.5	16.5	26.0	12.0	14.5	18.5	8.0	9.0	12.0
	10 000	16.0	20.6	28.5	13.5	15.0	19.0	8.0	9.0	12.0
	20 000	20.0	24.0	30.0	13.5	15.0	19.0	8.0	9.0	12.0
Eq.	c_{sat} [10^{-4} mol L^{-1}]	6.75	6.3	5.6	10.0	9.3	8.3	17.0	16.2	14.3

Table 6.1: Open system conditions for the precipitation reaction growth rate α (in m s^{-1}) estimated by Dreybrodt et al. [42, 70] for various partial pressures in carbon dioxide, p_{CO_2}, temperatures (environmental parameters) and film thicknesses, h. As indicated in the left column, calculations were obtained for either laminar or turbulent flow conditions. The last row also shows the saturation concentration values, c_{sat}, corresponding to the environmental parameters. Adapted from Dreybrodt [70], Table 7.1 p. 155.

---

[4]$1 \, \mathrm{mol \, cm^{-3}} = 10^3 \, \mathrm{mol \, L^{-1}}$.

	h [μm]	$p_{CO_2} = 0.01$ atm			$p_{CO_2} = 0.03$ atm			$p_{CO_2} = 0.05$ atm			$p_{CO_2} = 0.10$ atm		
		5 °C	10 °C	20 °C	5 °C	10 °C	20 °C	5 °C	10 °C	20 °C	5 °C	10 °C	20 °C
Laminar	10	0.714	1.6	7.14	0.606	1.1	3.33	0.666	1.19	3.33	0.833	1.39	3.23
	20	1.3	2.8	13.3	1.18	2.1	6.25	1.25	2.25	5.26	1.05	1.73	3.33
	50	3.13	6.4	21.7	2.13	3.5	8.93	1.49	2.5	5.0	1.06	1.73	3.33
	100	5.26	9.6	21.7	2.04	3.5	8.7	1.49	2.47	4.76	1.06	1.73	3.23
	200	5.13	9.5	18.2	2.0	3.46	6.9	1.46	2.44	4.76	1.05	1.70	3.17
	500	4.76	8.4	16.1	2.0	3.3	6.5	1.43	2.43	4.67	1.04	1.68	3.07
	1000	4.08	7.7	12.7	1.89	3.25	5.9	1.4	2.29	4.46	1.01	1.61	2.95
Turbulent	10	1.08	3.3	9.75	0.63	1.08	4.1	0.655	1.17	3.37	0.82	1.37	3.5
	30	2.9	7.3	22.0	1.8	3.3	9.5	1.97	3.32	8.14	2.28	3.5	6.0
	50	5.08	10.2	27.5	2.9	5.1	13.0	3.13	5.09	10.4	3.3	4.7	7.8
	100	8.6	15.1	34.0	5.4	8.75	17.0	5.2	7.3	13.0	4.54	6.05	9.0
	200	13.2	20.5	45.0	8.2	11.3	19.0	6.9	8.9	13.9	5.5	7.0	10.2
Eq.	c_{sat} [10^{-7} mol cm^{-3}]	6.4	5.5	4.1	16.6	14.4	11.0	24.3	21.4	16.9	38.38	35.1	28.0

Table 6.2: Closed system conditions for the precipitation reaction growth rate α (in m s^{-1}) estimated by Dreybrodt et al. [42, 70] for various partial pressures in carbon dioxide, p_{CO_2}, temperatures (environmental parameters) and film thicknesses, h. As indicated in the left column, calculations were obtained for either laminar or turbulent flow conditions. The last row also shows the saturation concentration values, c_{sat}, corresponding to the environmental parameters. Adapted from Dreybrodt [70], Table 7.2 p. 165.

B. Effect of the concentration distribution profile on the numerical resolution

We shortly review in this appendix the effect of the distribution set for the ion quantity added at impact, C_d, on subsequent stalagmite growth. We observed in the experiments presented in Ch. IV (see Figs. 4.5 and 4.6) that the spot left by the drop in the film always seemed to present a larger dye concentration (equivalent to the presently discussed ion quantity) close to the drop impact point position, then to become more diffuse away from this position. The spot left by the drop in the film was also usually surrounded by tails or twirls of diffuse dye. Close to the impact point position, the edge of the more concentrated portion of the spot left by the drop appeared sharp and clear. Because we cannot describe exactly the distributions obtained in Ch. IV, which vary with the film thickness, we approximate them by a distribution decreasing monotonously from a maximum value toward 0 at the edge defined by R_{eq}, the equivalent radius of the red spot left by the drop in the film (see Eq. (4.11) in Ch. IV and Sec. 1.2). To compute the concentration of the ions added at impact numerically, we need to divide the added quantity by the local film thickness h. Numerically, this thickness already decreases in the few cells surrounding the centre of the stalagmite, i.e., as $r \to 0$. Imposing a uniform ion quantity is therefore not physical as it would lead to a local increase in the concentration on the edge of the local drop addition in the film, which is not observed experimentally since the results were obtained on a flat plane (see

Ch. IV). Hence, we postulate that the quantity of ions added at impact is not perfectly uniform and decreases toward 0 as $r \to R_{eq}$ to avoid dealing with a non-monotonous concentration distribution following a drop addition in the film in simulations. Nevertheless, close to the centre, i.e., for $r \to 0$, the distribution should still be approximately uniform. We propose to consider two profiles matching this description: a portion of a paraboloid, as we used for the drop thickness addition, and a bell-like distribution extending over the same radius. Other distributions, such as a hemisphere, could be considered as well. We illustrate two simulations obtained by using these two ion quantity distributions in Fig. 6.19. Because we are interested in assessing the effect of the ion distribution, t_0/t_d was kept constant and we only varied the drainage-to-precipitation timescale ratio from $t_d/t_p = 20$ in Figs. 6.19 (a) i (paraboloid distribution) and (a) ii (bell-like distribution), to $t_d/t_p = 0.05$ in Figs. 6.19 (b) i (paraboloid distribution) and (b) ii (bell-like distribution). The parameters imposed in and inferred from each simulation are presented in Tab. 6.3. We note that, for $t_d/t_p = 0.05$, when the drainage dominates the precipitation of the ions in redistributing the ions in the film, both the paraboloid and bell-like drop ion distribution yield the exact same results, as it can be seen in Figs. 6.19 (b) i and (b) ii. However, for $t_d/t_p = 20$, differences can be witnessed between Figs. 6.19 (a) i and (a) ii. These differences mostly stem from the fact that, in the paraboloid distribution the concentration abruptly vanishes at the radius R_{eq}, while with the bell-like distribution this occurs more gradually. Hence, artificial accumulation appears at the basis of the stalagmite, as illustrated by the green dashed circle in Fig. 6.19 (a) ii. This accumulation also leads to a wider stalagmite at its base. To avoid effects related to this numerical artifact, we only considered the paraboloid distribution in the main text.

	Fig. 6.19 (a)		Fig. 6.19 (b)	
	i	ii	i	ii
t_0/t_d	1	1	1	1
t_d/t_p	20	20	0.05	0.05
c_{sat} [mol cm^{-3}]	5×10^{-7}	5×10^{-7}	5×10^{-7}	5×10^{-7}
Ion distribution	paraboloid	bell-like	paraboloid	bell-like
R_{eq}/r_d	0.80	0.80	0.96	0.95
$\varphi_{d \to f'}$	0.43	0.43	0.49	0.48
Ψ	-8.3	-0.88	-51	-51
S	10^{-3}	0.02	4.4×10^{-6}	5×10^{-6}
$\Delta\eta^{max}/h_d$	6.7×10^{-6}	7.4×10^{-6}	6.2×10^{-6}	6.2×10^{-6}

Table 6.3: Influence of the drop ion distribution profile: inputs and outputs obtained from the simulations conducted in Fig. 6.19. The label of the figure is shown in the upper row. *From top to bottom. (Input parameters)* Dripping period over drainage timescale ratio, t_0/t_d; drainage timescale over precipitation timescale ratio, t_d/t_p; ion saturation concentration, c_{sat}; distribution used to describe the ion quantity added at impact, corresponding to either the paraboloid distribution or the bell-like distribution. *(Output variables)* Equivalent radius of the spot left by the drop in the film post impact, R_{eq} (see Eq. (4.10) in Ch. IV); proportion of the impacting drop going into the film, $\varphi_{d \to f'}$ (see Eq. (4.14) in Ch. IV); shape parameter Ψ of the stalagmite profile (see Eq. (5.49) from Ch. II); scale S of the stalagmite profile (see Eq. (5.49) from Ch. II); maximum growth rate at the stalagmite centre, $\Delta\eta^{max}$ (see Eq. (6.31)).
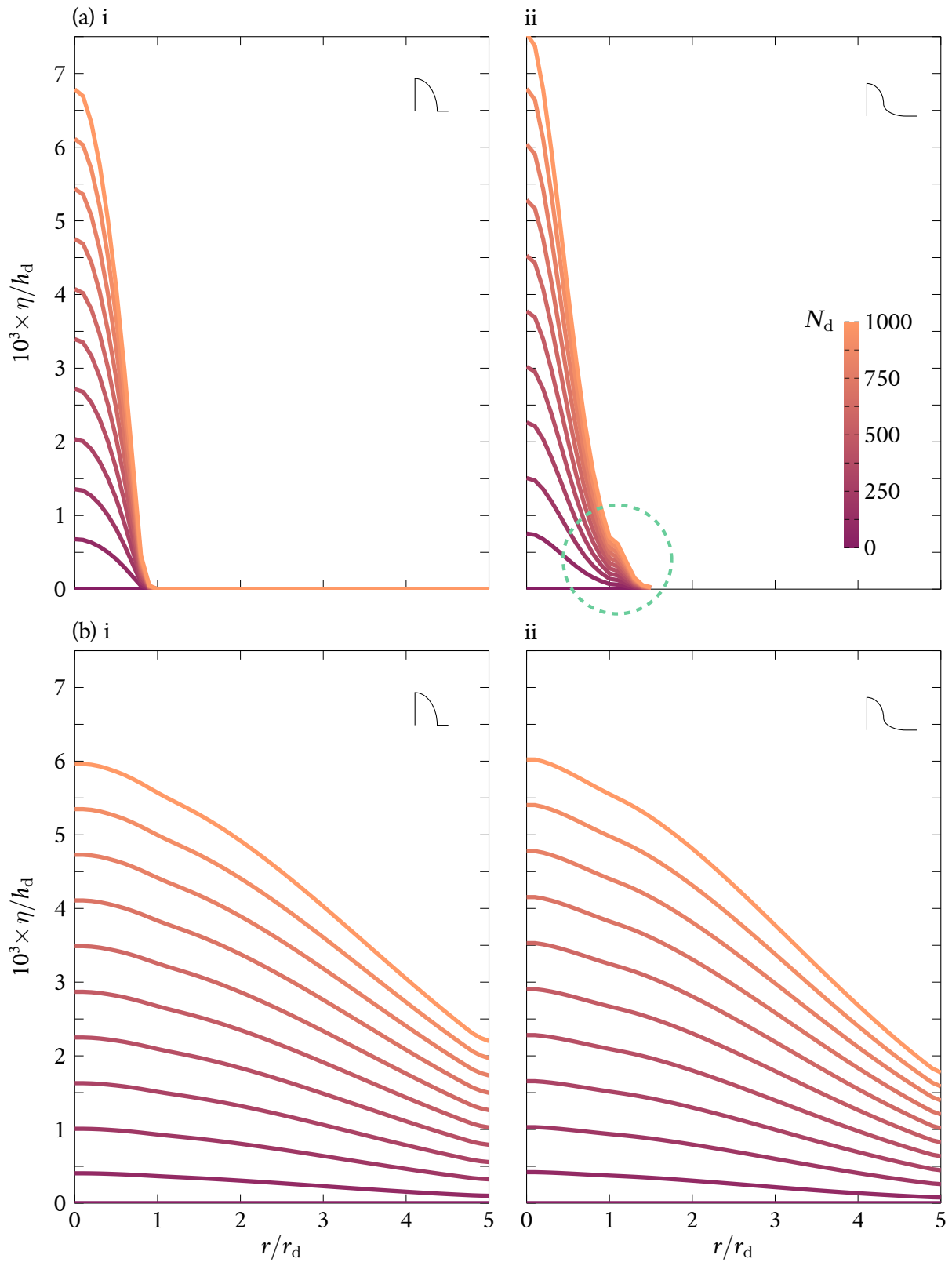
Figure 6.19: Influence of the drop ion distribution profile: examples of simulations all conducted for $t_0/t_d = 1$, variable t_d/t_p and $c_{sat} = 5 \times 10^{-7} \, \text{mol cm}^{-3}$, for 1000 drop impacts, starting from an initially perfectly horizontal stalagmite profile. In both (a) i and ii, computations were made for $t_d/t_p = 20$, while in (b) i and ii, they correspond to $t_d/t_p = 0.05$. In simulations from (a) i and (b) i, a paraboloid-like distribution was used to described the ion quantity in the drop at each impact, as depicted by the upper right symbol. In simulations from (a) ii and (b) ii, a bell-like distribution was used. The four graphs show the stalagmite elevation, η, as a function of the radial coordinate r. Intermediate lines corresponding to 100 drop impacts are shown, in accordance with the colour bar from (a) ii, which is applicable to the four graphs. The green dashed circle in (b) ii shows the local accumulation caused by the Gaussian profile as discussed in the main text.

233

C. Two-dimensional Cartesian resolution of the equations

This last appendix shortly presents the equations of the complete stalagmite growth model expressed in a two-dimensional Cartesian coordinate system, as well as the numerical scheme used to obtain the graphs from Sec. 2.3.4. The equations governing the drainage, Eqs. (5.10) and (5.9) from Ch. V, were expressed in the curvilinear coordinate system of Fig. 5.17, that we recall in Fig. 6.20 (a) (it is the same figure). The flux $\mathbf{q}$ thus reduced to its component aligned with $\mathbf{e}_\xi$. By virtue of the thin film hypothesis, the film thickness h could be averaged along the perpendicular coordinate to the stalagmite surface, ζ, and only depended on the gradients aligned in parallel with the stalagmite surface, i.e., $\parallel \mathbf{e}_\xi$. All the spatial variations of the stalagmite elevation, η, were contained within the local inclination with the horizontal, φ. To use Cartesian coordinates, we assume that the stalagmite grows on top of a perfectly horizontal plane, containing both horizontal vectors $\mathbf{e}_x$ and $\mathbf{e}_y$. The stalagmite elevation η is the elevation from the initial perfectly horizontal plane. The normal to this horizontal plane, oriented upward, i.e., in the direction of growth, is $\mathbf{e}_z$. We still consider that all the quantities can be averaged along the perpendicular coordinate to the stalagmite initial horizontal surface, z. If the stalagmite elevation increases locally, this approximation remains true as long as the variations of η are sufficiently smooth.

In Fig. 6.20, we designate by δ the film thickness as obtained by drawing a vertical to the stalagmite surface in every point, while h still corresponds to the film thickness perpendicular to the stalagmite, as it was done in Ch. V. Once again assuming that the variations of η are sufficiently
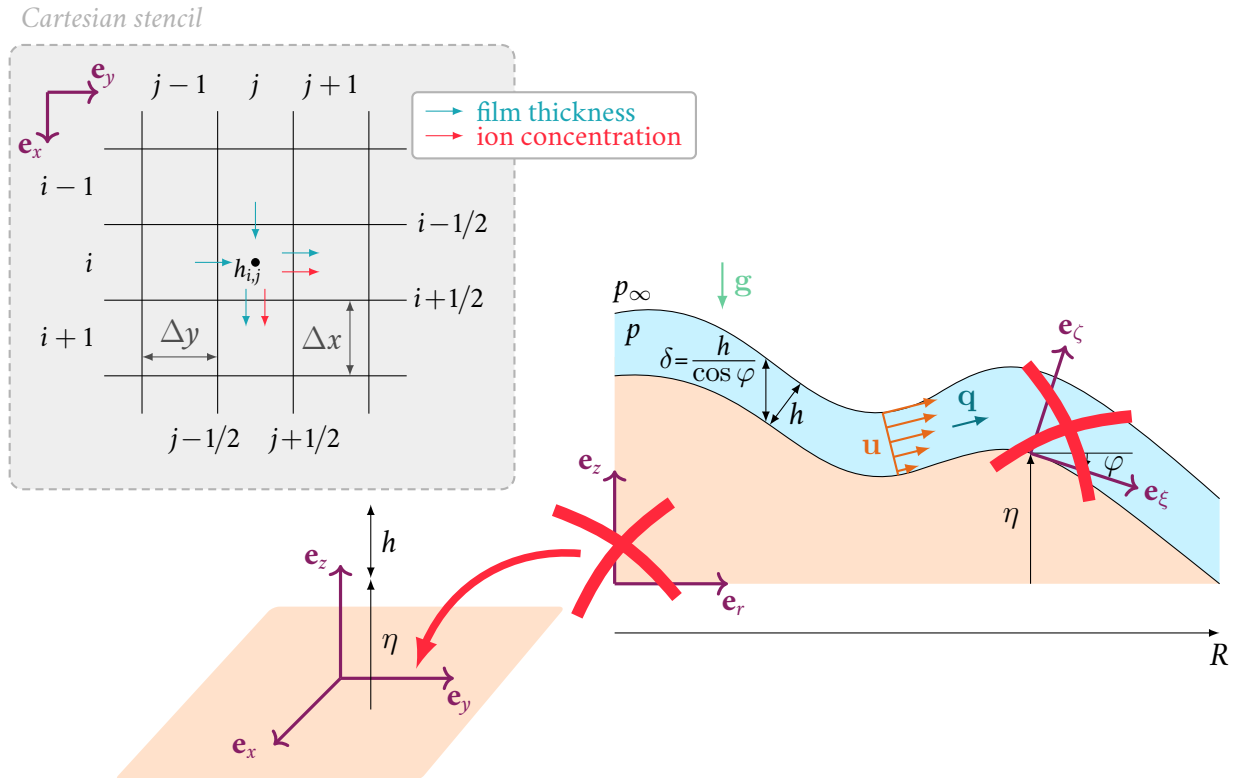
Figure 6.20: Schematic from Fig. 5.17, updated for the two-dimensional Cartesian resolution. From a defined stalagmite shape $\eta(r)$, we discretize the domain from $x = -R/2$ to $x = R/2$, and from into $y = -R/2$ to $y = R/2$, into $(I+1) \times (J+1)$ cells of size $\Delta x \times \Delta y$, with $\Delta x = \Delta y$. The cell-centered values of the local film thickness h_i are computed in the middle of the cells while the fluxes are computed at the cell faces, i.e., between two adjacent cells. The outer boundary condition uses the solution of the cone of constant opening angle $\varphi_\star$. Drops are added into the film at the numerical dripping period t_0/t_d.

smooth, we could consider that $\delta = h \cos \varphi$ in all points of the film. In the following, the film thickness h will represent the vertical film thickness (originally δ), i.e., the film thickness parallel to $\mathbf{e}_z$. This corresponds exactly to the version of h defined in Ch. V, but only when the stalagmite surface remains almost horizontal (i.e., $\varphi \simeq 0$). In a Cartesian coordinate system rather than a curvilinear one, we also obtain a vectorial flux $\mathbf{q}$ whose components are aligned with both horizontal directions, $\mathbf{e}_x$ and $\mathbf{e}_y$. As long as the stalagmite elevation variations remain small, i.e., not larger than h_d, which is the order of magnitude of the thickness of a film covering a stalagmite, this remains true. Otherwise the flux would be aligned with $\cos \varphi \mathbf{e}_x$ and $\cos \varphi \mathbf{e}_y$. Starting from Navier-Stokes equations and using the same hypotheses as in Sec. 4.2 from Ch. V, we find that, in a two-dimensional Cartesian coordinate system, the flux $\mathbf{q}$ becomes

$$\mathbf{q} = \frac{-gh^3}{3\nu} \nabla_{\boldsymbol{x}} (h + \eta) , \tag{6.37}$$

where we designate by $\nabla_{\boldsymbol{x}} = \partial_x \mathbf{e}_x + \partial_y \mathbf{e}_y$ the horizontal gradient operator. The variations of the film thickness in time and space, obtained from the continuity equation, can now be expressed as

$$\partial_t h = -\nabla_{\boldsymbol{x}} \cdot \mathbf{q}, \tag{6.38}$$

Additionally, the equation derived for the ion concentration in the film becomes

$$\partial_t c = \frac{gh^2}{3\nu} \left(\nabla_{\boldsymbol{x}} (h + \eta) \right) \cdot \left(\nabla_{\boldsymbol{x}} c \right) + \frac{\alpha}{h} \left(c_{\text{sat}} - c \right) , \tag{6.39}$$

and the one relating the ion precipitation to the stalagmite growth becomes

$$\partial_t \eta = -\frac{\alpha \, m_{m,\text{CaCO}_3}}{\rho_{\text{CaCO}_3}} \left(c_{\text{sat}} - c \right) . \tag{6.40}$$

In order to approximate the solution to the above equations numerically, we define the Cartesian grid from Fig. 6.20. The cells have a size set to $\Delta x = \Delta y$, and are labeled by indices i and j along $\mathbf{e}_x$ and $\mathbf{e}_y$, respectively. At time step n, the film thickness, $h_{i,j}$, ion concentration, $c_{i,j}$, and stalagmite profile, $\eta_{i,j}$, are evaluated at the centre of the cell (i, j). The numerical time derivatives can be approximated in the same manner as described in Ch. V and in Sec. 1.4 (see, e.g., Eq. (6.24)). The spatial derivatives, however, must be adapted to the Cartesian grid. For the sake of simplicity, we will consider in the following equations that $\eta = 0 \ \forall (x, y)$, but including η in the calculations is straightforward. To solve Eqs. (6.37) and (6.38), we keep the same upwind formalism as in Ch. V. Specifically, we use the following approximation (where η has been set to 0):

$$\nabla_{\boldsymbol{x}} \cdot \left(h^3 \nabla_{\boldsymbol{x}} h \right) \approx \quad \frac{1}{\Delta x} \left(h_{i+1/2,j}^3 \left(\nabla_{\boldsymbol{x}} h \right) \Big|_{i+1/2,j} - h_{i-1/2,j}^3 \left(\nabla_{\boldsymbol{x}} h \right) \Big|_{i-1/2,j} \right)$$
$$+ \frac{1}{\Delta y} \left(h_{i,j+1/2}^3 \left(\nabla_{\boldsymbol{x}} h \right) \Big|_{i,j+1/2} - h_{i,j-1/2}^3 \left(\nabla_{\boldsymbol{x}} h \right) \Big|_{i,j-1/2} \right) \tag{6.41}$$

The spatial gradients are evaluated as

$$\left(\nabla_{\boldsymbol{x}} h \right) \Big|_{i+1/2,j} \approx \frac{1}{\Delta x} \left(h_{i+1,j} - h_{i,j} \right) \tag{6.42}$$

and, similarly,

$$\left(\nabla_{\boldsymbol{x}} h \right) \Big|_{i,j+1/2} \approx \frac{1}{\Delta x} \left(h_{i,j+1} - h_{i,j} \right) . \tag{6.43}$$

The conjugates of these two gradients evaluated in $(i - 1/2, j)$ and $(i, j - 1/2)$, respectively, have a similar expression. The values of $h_{i\pm 1/2, j}$ and $h_{i, j\pm 1/2}$ correspond to the film thickness evaluated at the faces of the cell (i, j). We can use the same approximation as in Ch. V and Sec. 1.4 to compute them, which we recall hereafter. For $h_{i+1/2, j}$, we have

$$h_{i+1/2, j} \approx \frac{1}{2} \left(h_{i+1, j} + h_{i, j} \right) , \tag{6.44}$$

and, for $h_{i, j+1/2}$,

$$h_{i, j+1/2} \approx \frac{1}{2} \left(h_{i, j+1} + h_{i, j} \right) . \tag{6.45}$$

To estimate the first term of the right-hand side of Eq. (6.39) (still for $\eta = 0$), we use the following scheme [112], i.e.,

$$
\begin{aligned}
h^2 \left(\nabla_x h \right) \cdot \left(\nabla_x c \right) \approx \quad & h^2_{i+1/2, j} \left(\nabla_x h \right) \Big|_{i+1/2, j} \left(\nabla_x c \right) \Big|_{i+1/2, j} \\
& + h^2_{i, j+1/2} \left(\nabla_x h \right) \Big|_{i, j+1/2} \left(\nabla_x c \right) \Big|_{i, j+1/2} .
\end{aligned}
\tag{6.46}
$$

Summary (Ch. VI)

- In Sec. 1, we derive a complete model of stalagmite growth consisting of (i) the drainage equations from Ch. V, (ii) an equation describing the evolution of the ions in solution in the film, and (iii) an equation describing the evolution of the stalagmite profile.

- A dimensionless version of the equations in Sec. 1.5 indicates that the stalagmite growth depends primarily on the added concentration at impact, the ratio of the dripping period and drainage timescale, t_0/t_d, and the ratio of the drainage and precipitation timescales, t_d/t_p.

- In Sec. 2.1, we asses the separate effects of the ratios t_0/t_d, t_d/t_p and the ion saturation concentration c_{sat} on the stalagmite growth. We infer from the simulations that the stalagmite growth reaches a steady-state after only a few tens of impact in the conditions that we impose. From there, we deduce that c_{sat} only affects the height of the stalagmite while t_0/t_d and t_d/t_p change the size and shape of the stalagmite.

- In Sec. 2.2, we vary both t_0/t_d and t_d/t_p altogether. The simulations conducted allow inferring the shape factor Ψ and scale S describing the stalagmite profile, defined in Ch. II, as well as the growth rate of the stalagmite. This growth rate can be compared with the growth rate from Dreybrodt's model, which was defined in Eq. (1.7) from Ch. I, for flat and convex stalagmites. We find that the growth rate from Dreybrodt's model and our results are in agreement for $t_d/t_p \lesssim 1$, but not beyond this value.

- In Sec. 2.3, we vary additional parameters in the simulations, such as the initial profile of the stalagmite or the dripping period sequence over time. From there we note that the stalagmite response to a change in environmental conditions is only of the order of a few hundreds of drops, at least in the conditions of growth that we imposed.

- Finally, in Sec. 2.3.4, we add the dispersal in the impact point position of the drops to the simulations. We thus have to express the equations and the numerical scheme in a 2D Cartesian coordinate system, described in Appendix C. Without surprise given the results from Ch. III, it is observed that the dispersal in the drop impact point position widens the stalagmite.

CONCLUSION

Little drops of water,
Little grains of sand,
Make the mighty ocean
And the pleasant land.

Thus the little minutes,
Humble though they be,
Make the mighty ages
Of eternity.

Julia A. F. Carney

1. A complex history

Palaeoclimatology plays a preponderant role in shaping our contemporary understanding of the environment and climate. Palaeoclimatology studies mostly rely on the analysis of recordings and measurements obtained from environmental proxies such as the successive laminae presented by stalagmites in karstic caves. Combined with dating methods based on, e.g., radiation decay, the various physical features exhibited by the laminae can be related to past events such as monsoon seasons [228], wildfire occurrences [164], or even the much longer glaciation cycles [231]. Stalagmites are found on the floor of karstic caves and present a large variability of shapes and sizes. They grow through the progressive precipitation and accumulation of calcium ions into calcite [70]. The ions are found in solution within a thin residual liquid film lying on top of the stalagmite, fed by successive drops falling from the cave ceilings. These drops are loaded in ions coming from the soil above the cave, which are at the origin of calcite precipitation. The soil is infiltrated by water as a result of the combination of rainfall, evapotranspiration and runoff over the cave surface [83]. The seasonality or vegetation above the cave, for instance, should thus influence the ion content of the drops, and, therefore, affect the subsequent precipitation of ions on stalagmites [76].

A clear link should therefore exist between the climate and environment histories above he cave, and the final shape exhibited by the stalagmites. However, the existing models of stalagmite growth do not take into account some important physical processes taking place when drops impact stalagmites. For instance, the gravity-driven drainage of the film, caused by the curved shape usually presented by stalagmites, is not taken into account, while it is clear that this drainage could possibly affect the distribution of ions into the film and, thereby, the subsequent stalagmite growth. Another parameter currently not included in models of stalagmite growth is the mixing occurring between the drop and the film upon impact. Most drop impacts in caves further lead to splashing at impact [227] due to the high cave ceiling, and thus to the ejection of secondary droplets away from the stalagmite. Finally, in previous models describing stalagmite growth, it was often admitted that drops all fall at the same position located at the apex of the stalagmite [70], although this assumption is not based on any physical evidence. Additionally, the oxygen and carbon isotope fractionation within the film covering the stalagmite is responsible for the oxygen and carbon imprints finally

appearing in the stalagmite records. The isotope variations in $\delta^{18}O$ and $\delta^{13}C$ are the most commonly used signals allowing to reconstruct palaeoclimate variations. Isotope fractionation may nevertheless be sensitive to physical processes such as the evaporation of the film. Deciphering the variations in isotope resulting only from the temperature (for ^{18}O) and the soil content (for ^{13}C) remains a major challenge in most stalagmite cross-sectional cut analyses [231]. Accurately identifying the physical processes that may affect the ion distribution and film thickness variations is therefore key to help better distinguish the processes at the origin of isotope fractionation variations.

2. Chapter overview

In this work, we studied fundamental aspects of major stages of the drop trajectory, starting from the drop formation at the tip of the stalactite hanging from the cave ceiling. Except for Ch. VI, experimentation, and more particularly high-speed imaging, plays a crucial role in the investigations that we conducted. We recall that the sites visited for the cave measurement campaigns used in Chs. III and V were described in Ch. II, along with all the studied stalagmites. We started by focusing only on the drop free fall, from the moment it drips from the stalactite tip until it reaches the stalagmite top in Ch. III. We then explored the mixing occurring between the drop and the film at impact in Ch. IV. The drainage of the thin film lying on the stalagmite was the subject of Ch. V. Finally, in Ch. VI we assembled elements from the previous chapters, to which we added the description of the ion concentration variations within the film in order to obtain an original model of stalagmite growth. We review the contributions from each of these chapters in the following section. Perspectives are then discussed in Ch. VIII.

2.1 More than just a lab phenomenon

Drops freely falling into air following their formation at the tip of a tiny vessel are more commonly found in lab experiments conducted on all types of drop impacts than in nature [128, 235]. Yet, caves provide an ideal framework to study the dispersal appearing in the drop impact point position at impact. In Ch. III, from high-speed recordings of drop impacts on stalagmites obtained from several caves, we indeed observed that the scatter of the drop impact point increased with the drop falling height, and could reach several centimetres. Because it is also observed in a lab setting where no external factor is able to influence the drop trajectory, we concluded that this dispersal must be self-induced. We hypothesised that it came from the vortices shed in the wake of the drop. The vortices are randomly emitted past a certain distance of fall [33, 237], and should interact with the drop by inducing a series of short horizontal shifts to its entire trajectory. Starting from Newton's second law to which we added a randomly-oriented aerodynamic force as a result of the vortex shedding, we obtained two Langevin-like equations describing the position and velocity of the drop at each vortex emission. Integrating these equations over the entire drop trajectory provided a relation between the dispersal in the drop impact point position and the drop falling height. The results from the modelling showed a good agreement with the experimental data taken in caves as well as in a lab setting. Finally, we could relate the dispersal observed to the top radius of a set of stalagmites described in Ch. II. Stalagmites found under short cave ceiling heights presented smaller radii that can be associated with the radius reached by the impacting drop as it crushes into the film. By contrast, stalagmites located in parts of caves with ceiling heights of the order of several metres presented a larger radius increasing with the dispersal in the drop impact point position, and, hence, with the falling height of the drops.

2.2 Experimental exploration of the mixing between a drop and a thin film

The successive drops falling on stalagmites are responsible for renewing both the liquid and ion content from the film lying on the stalagmite. Hence, these drops are solely responsible for stalagmite emergence and growth. Drop impact on a film having a thickness of the same order of $\sim 100\,\mu\mathrm{m}$ as the films found in caves, leads to splashing for falling heights as short as 30 cm [227]. When the film is spread on a surface area having a radius of the same order as the stalagmite radius, i.e., typically less than 10 cm, part of the ejections produced during the impact may not land back onto the stalagmite [145]. Hence, the ions in these ejections do not contribute to subsequent stalagmite growth. Simultaneously, mixing occurs between the drop and the film both at the drop impact location and within the ejections, yielding a loss of initial film content into the ejections. Assessing which part of the original drop content actually ends up in the film, an essential parameter to modelling stalagmite growth which had not been previously estimated [70, 133], was thus the focus of Ch. IV.

We conducted a series of experiments of drops impacting thin liquid films in a lab setting, using two dyes to colour the drop and the film. Through high-speed recordings of both top and side views of the experiments, our analysis revealed four scenarios of drop impacts. The side view of the impacts shed light on the dependence on the film thickness of the geometry of the crown formed at impact, while the top view of the impacts allowed us to estimate the mixing level between the drop and the film and the amount of liquid ejected away. A colorimetry algorithm based on Beer-Lambert law was developed to estimate the volume fraction of each of the dyes used to colour the drop and the film from the top view of the impacts. For very thin films such that $h^\star < 1$ (with $h^\star$ the nondimensional film thickness, see Sec. 2.3 from Ch. IV), fragmentation of the crown formed upon impact appeared before the crown started retracting toward the impact point position. The resulting spot left by the drop in the film thus corresponded to a small circular spot of uniform colouration. For $h^\star \gtrsim 1$, the crown retraction was no longer hindered by early fragmentation and the subsequent seemingly random collapse of the crown induced more mixing between the drop and the film. The spot left by the drop in the film presented variable colouration and was surrounded by dye tails reminiscent of the crown retraction. For thicker films ($h^\star \gtrsim 2$), additional processes, such as the uprising Worthington jet following the crown retraction, induced even more mixing in the film. The resulting radius of the spot left by the drop in the film thus increased with the film thickness.

Including additional results from the literature [236], we also obtained an estimation of the proportion of the drop ejected away at impact. For very thin films ($h^\star \ll 1$), this proportion ranged from 0.2 to 1, such that the ejected volume of liquid was smaller than the drop volume, and the film following the impact became locally thicker than the initial film. For $h^\star \to 1$, the proportion became approximately equal to 1, thus there was as much liquid ejected away as brought by the drop into the film. For $h^\star \gtrsim 1.5$, the proportion decreased again to remain close to 0.6 when $h^\star > 2$. We further estimated the proportion of drop content actually entering the film at impact, as well as the amount of liquid coming from the initial film which ends up in the ejections. While there always seemed to be little loss from the initial film into the ejections, the proportion of liquid originally from the drop going into the ejections increased with the film thickness $h^\star$, from about 0.1 to 0.5 in the range covered by the experiments.

2.3 A century-old equation adapted for axisymmetric, curved surfaces

Originally intended to describe the pressure distribution in liquid film bearings and evaluate the dynamic viscosity of oil [180], Reynolds equation for lubrication theory has since long been used in countless applications involving thin liquid films [154]. In Ch. V, we particularised it to the

drainage-induced flow of a thin film over a stalagmite. Many stalagmites can be considered as axisymmetric, which reduces the dimension of the problem. In Ch. II, we had already defined the stalagmite profile along a particular radial angle as a function of curvilinear coordinates following the stalagmite surface in every point. In Ch. V, we came back to this definition to express the Reynolds equation in this set of coordinates. The evolution of the film thickness over time and space could be further obtained by taking into account the continuity equation and by integrating the velocity profile inside the film over the entire film thickness. From the equations obtained, we found that the flux is related to the film thickness, the gradient of film thickness along the stalagmite surface and the local inclination of the stalagmite surface with the horizontal (see Eqs. (5.9) and (5.10) from Ch. V). Two regimes of drainage could be established from there: the drainage can either be dominated by the film thickness gradient, or by the stalagmite inclination. The first of these two regimes is therefore responsible for the film drainage over a flat or perfectly horizontal stalagmite surrounded by an inclined wall away from the centre (i.e., at several centimetres away), while convex stalagmite profiles are associated with the inclination-based regime of drainage.

In addition to the drainage, we also took interest in the filling of the film, which is established following a succession of drop impacts onto an initially dry stalagmite surface. After a certain number of drop impacts, the film reaches a stationary state during which its thickness oscillates between maximum and minimum values following the periodic discrete inflow associated with each drop. However, past a given radius, denoted the stationary radius (see Eqs. (5.18) or (5.45) from Ch. V), the periodic variations of the film thickness is not observed any longer and the film thickness remains steady as in the case of a constant continuous inflow. At steady-state, a larger inflow of drops yields a larger drainage outflow along the outer walls of the stalagmite. Because the drainage flux increases with the film thickness, a larger inflow thus also yields a larger film thickness. The filling, stationary state and sole drainage phases of the film resulting from either an inflow of drops, or the interruption of this inflow in the case of the sole drainage, were studied both experimentally and numerically. The equations describing the evolution of the film thickness over time and space were indeed non-linear and could only be solved analytically in the particular case of a film at steady-state lying on a perfectly horizontal stalagmite.

Experimental film thickness measurements during the three aforementioned phases were conducted on stalagmites in both cave and lab settings. A mass-based technique was used to obtain the filling measurements in caves, while the sole drainage was evaluated using a home-built apparatus based on a dial gauge to obtain the film thickness from differential distance measurements at the stalagmite apex. Both these techniques only allowed for instantaneous measurements, while an optical sensor available for the lab measurements allowed to record the film thickness evolution over time with a sampling frequency of 1000 Hz, i.e., lab measurements could be considered as continuous in regard of the drainage. The lab measurements further permitted to introduce drop impacts in the film during the recordings in order to obtain oscillating film thickness measurements during the stationary phase, which was not possible in caves. The caves provided a great variability of stalagmite shapes, and even included concave stalagmites, whereas the lab measurements allowed to systematically vary parameters such as the dripping period of the drops, t_0. The measurements could be compared to the results provided by the numerical resolution of the evolution in time and space of the film thickness, using the equations that we developed (see Eqs. (5.9) and (5.10) from Ch. V). Results provided by the simulations using a set of entry parameters from the analysed stalagmites showed a good agreement with the experimental measurements. Similarly, we could also retrieve the theoretical time scalings inferred from the equations describing the drainage in both the experimental measurements and numerical simulations. At steady-state, the film thickness over a perfectly horizontal stalagmite depends on the drop dripping period as $h_{\rm s} \sim t_0^{-1/4}$, while for convex stalagmites this law becomes $h_{\rm s} \sim t_0^{-1/2}$ (with $h_{\rm s}$ the stationary film thickness,

see Sec. 4.3 from Ch. V). During the sole drainage, the transient film thickness at the centre of the stalagmite decreases as $h \sim t^{-1/3}$ on top of horizontal stalagmite surfaces and $h \sim t^{-1/2}$ on convex ones. The modelling thus both confirmed the experimental results and allowed to comprehend the differences exhibited by drainage on various types of stalagmites. Finally, we also showed that the effects of the successive drop impacts into the film could be averaged for convex stalagmites, while in the case of flat or concave stalagmites, it is not an assumption that should be made.

2.4 An updated model of stalagmite growth

In Ch. VI, we studied numerically the combined effects of the succession of drops impacting the film, the drainage of the film and the ion precipitation on subsequent stalagmite growth. In addition to the drainage of the film, we described the evolution of the ion concentration over time and space using an advection-reaction equation in the same curvilinear coordinate system as the drainage equation, in the limiting case where horizontal diffusion is neglected and vertical diffusion assumed at steady-state. We included the results from the mixing between the drop and the film from Ch. IV to estimate the amount of ions that should enter the film at each impact based on the local film thickness reached by the film. A linearised version of Fick's law describing the change in the stalagmite profile as a result of the ion precipitation, i.e., the growth rate in all points of the stalagmite surface, completed the model. We could therefore simulate the response of the stalagmite shape to the amount of ions brought by the drop and ratios between three timescales: the dripping period, the drainage timescale and the precipitation timescale. In the absence of experimental records of entry parameters conditioning the stalagmite growth at our disposal, such as, e.g., temperature or partial pressure in carbon dioxide records, we did not conduct simulations over several years of growth. We rather performed simulations of stalagmites only starting to grow during a few thousands of identical drop impacts. In this case, the film thickness and ion concentration profiles established after a few tens of impacts remain in steady-state during the entire simulation.

We showed that, under constant conditions, the stalagmite shape reached a stationary state and does no longer change except for its scale (see Ch. II). The vertical growth rate of the stalagmite depended on the amount of ions brought by the drops into the film, as already demonstrated by Dreybrodt's model [70]. However, the amount of ions in the drop had no effect on the shape reached by the stalagmite. The final shape of the stalagmite depended on how the timescale ratios $t_0/t_{\rm d}$ and $t_{\rm d}/t_{\rm p}$ compared with one another, i.e., on the ordering of t_0, $t_{\rm d}$ and $t_{\rm p}$. We observed that, at constant $t_{\rm d}/t_{\rm p}$, e.g., reducing $t_0/t_{\rm d}$, or increasing the drop inflow with respect to the drainage, tended to widen the stalagmite. Regarding the effect of $t_{\rm d}/t_{\rm p}$ at constant $t_0/t_{\rm d}$, the stalagmite also became wider with decreasing $t_{\rm d}/t_{\rm p}$. These two effects were additive and could yield very large or narrow stalagmite profiles. We also conducted simulations during which we varied one of the ratios $t_0/t_{\rm d}$ or $t_{\rm d}/t_{\rm p}$ while keeping constant the other one. The stalagmite shape response to reach another steady-state was of the order of a few hundreds of drop impacts. We also briefly investigated other effects, such as the initial profile (convex or concave) from which the stalagmite grew. The convex profile modified the drainage dynamics according to the regimes discussed in Ch. V, which in turn affected the shape taken by the stalagmite, even when the shape should have been mostly conditioned by the precipitation of the ions occurring faster than drainage and dripping (i.e., $t_{\rm p} < t_0, t_{\rm d}$). Regarding the concave initial profile, we could not find a combination of timescales that allowed to maintain this profile, which ended up returning to a flat or convex profile after a certain number of drop impacts. Hence, the concave shape did not seem to be stable but it might also have stemmed from effects that we did not include in the modelling. Finally, we could also include the dispersal presented by the impact point position distribution of the drops

from Ch. III in simulations conducted in a two-dimensional Cartesian coordinate system. This dispersal also had a significant effect on the final size of the stalagmite, as it was already concluded in Ch. III.

3.   Contributions and outlook

Throughout the chapters discussed above, we obtained results of interest both for drop physics and stalagmite modelling in the context of palaeoclimate reconstruction. In particular, some short-comings of former stalagmite growth models could be addressed (see Sec. 1.4 from Ch. I). The dispersal in the drop impact point position of the drops, for instance, was shown to set constraints on stalagmites associated with a large drop falling height, while previous models of stalagmite growth hypothesised that all drops fell at the apex of the stalagmite regardless of their falling height. The model obtained in Ch. III was in good agreement with the experimental data collected from both cave and lab environments, but could still be improved as numerous simplifying hypotheses were made. First, the lift coefficient acting on a deformable object such as a drop in a cross-flow should be better estimated. The deformability of the drop could also lead to recirculation inside the drop [238]. Other effects may induce shifts in the final impact point position of the drop, such as irregularities at the stalactite surface, the background air currents in the cave [34], the internal oscillations of the drop, the interaction between the vortices shed in the wake of two successive drops [238], or the Magnus effect set by some initial rotational speed of the drop [39]. Slight seasonal drop volume variations can also appear in caves and affect the impact point distribution of the drops over time [98].

The analysis conducted in Ch. IV provided a key missing element identified in existing models of stalagmite growth, which had not been previously estimated: the level of mixing between the drop and the film. The mixing occurring between a drop and a thin film is a process that has indeed not been extensively studied in the literature [80]. Without knowing how the drop and the film mix at impact, it is neither possible to determine the ion content actually ending up in the film, nor where the ions are distributed following one impact. To be more accurate, a thorough analysis of the ion loading through the soil above the caves should complete the study of Ch. IV. The stalagmite growth modelling presented in Ch. VI should also take into account the possible splash of drops at impact, as well as the ratio $\varphi_{\mathrm{f}\to\mathrm{e}}$ modulating the part of the initial film that is lost into the ejections. However, it should be noted that the quantities presented in Ch. IV were only measured on horizontal films of uniform thickness, by only focusing on one impact at a time. In the following chapter (Ch. VIII), we present a few experiments showing how the post-impact spot left by the drop in the film changes in response to, e.g., the presence of non-negligible thickness gradients in the initial film.

We also established that the drainage of the film, which had previously not been included in stalagmite growth modelling, significantly affects the thickness of the film and, therefore, the drop impact outcome. Depending on how the timescale ratios t_0/t_{d} and $t_{\mathrm{d}}/t_{\mathrm{p}}$ compare with each other, although it might be true in some regimes, the effect of the successive drops cannot always be averaged over time and drainage should be taken into account in stalagmite growth modelling. The study conducted in Ch. V also contributed to clarifying the respective roles played by the film thickness gradient and inclination of the surface with the horizontal on the film drainage. The filling phase of the film, which we added to our study, is usually not included in the literature investigating the drainage of a thin film in various contexts [154]. The modelling of the drainage could be further improved by considering non-axisymmetric stalagmites, or by acknowledging other effects that were assumed not to affect the drainage in Ch. V. For instance, the Laplace pressure or stalagmite rugosity and porosity could also affect the drainage [153].

Finally, although the stalagmite growth modelling discussed in Ch. VI included the effects of the drop impacts and film drainage, which had previously not been considered, simplifying hypotheses that had to be made might not be accurate. The vertical diffusion of the ions into the film, e.g., could have a non-negligible effect on ion distribution and precipitation in the film as it may have the same order of magnitude as the drainage and precipitation timescales. The precipitation of the ions at the bottom of the film, in particular, resulted from a linear approximation of Fick's law, which might no longer be valid when taking the ion diffusion into account. The evaporation of the film was not considered either, while it had been shown to have a potentially non-negligible effect on drainage in the lab experiments presented in Ch. V. To be accurate, the simulations conducted in Ch. VI should also span a larger number of drops and take into account time-variable effects such as seasonal variations in the entry parameters. Comparing such simulations with actual paleoclimate records and stalagmite cuts could nevertheless reveal difficult because of poorly characterised effects such as, e.g., the oxygen and carbon isotope fractionation [56]. Another possibility would be to grow calcite crystals from scratch in a lab setting, in conditions allowing for fast growth compared to caves.

Hence, some physical processes operating during stalagmite growth have not been taken into account yet in the model derived in Ch. VI, and simplifying assumptions might still be the subject of discussion. Nevertheless, we hope that our results will offer a fresh perspective on stalagmite growth modelling for palaeoclimate reconstruction, and contribute to improving its robustness and predictive capability.

MIXING AND MORE

Trying to explore the intricate physics related to the entire trajectory of a drop in a cave, we sometimes had to make restricting hypotheses that do not capture perfectly the reality. These simplifications were already discussed at the end of the previous chapter. The shortcomings of the drainage modelling in Ch. V, e.g., included the absence of the Laplace term in the pressure gradient, which originated from the fact that we considered perfectly smooth stalagmite surfaces and may not always be accurate. A few elements could also improve the complete stalagmite growth model presented in Ch. VI. For instance, as simplifying approximations, the splash of drops and the proportion of the initial film ending into the ejections with respect to the drop volume were not considered. Besides these modelling approximations, we concluded from Chs. V and VI that individual drop impacts may directly influence the local and short-term stalagmite growth in some regimes, while we only focused in Ch. IV on studying these impacts in very particular cases, namely on horizontal, quiescent thin films of uniform thickness. A better inclusion of the mixing between the drop and the film in more general cases would therefore be an improvement to our stalagmite growth model. This final chapter thus focuses on conducting a few preliminary experiments to improve our knowledge of drop impacts on thin films in a broader context than presented in Chapter IV.

1. Additional mixing experiments

Although we thoroughly described the mixing occurring during the impact of a drop on a film having a thickness of the same order as found in caves, we focused our study on horizontal, quiescent films. In Ch. III (see Fig. 3.3), e.g., we showed examples of impacts on a concave stalagmite containing a pisolite and on the inclined wall of a convex stalagmite, which have little in common with the impacts from Ch. IV. A better description of stalagmite growth should thus include such types of impacts. Knowing the proportion of liquid coming from the drop and going into the film or being ejected away during these types of impacts is indeed challenging. We also noted in Ch. V that the dripping period of the drops is one of the parameters affecting the most the subsequent drainage of the film. In our experiments, we did not consider the possible interaction that successive impacts may have with one another either. However, it has recently been shown that a train of drops falling with a time period shorter than the total impact time on a thin film leads to non-trivial interactions between the successive drops. For instance, the air trapped in between the successive developing crowns following the impacts tends to deform the wall of the external crowns [148]. A higher splashing threshold is also observed for the successive drops with respect to the first ones of the train [148]. The angle of ejections made by the secondary droplets formed in a drop train yields measurements comparing well [162] with the former study of the crown angle performed by Fe-

dorchenko and Wang [86], which was also similar to our crown inclination measurements in Ch. IV as we had obtained a good agreement between both datasets (see Fig. 4.7 (a)). Different empirical laws for the splashing threshold have further been derived depending on the substrate hydrophobicity [53] and rugosity [184], which could locally vary over the stalagmite surface. Nevertheless, the literature is not abundant regarding the effect of such parameters on the mixing between the drop and the film. In the following sections, we present a few preliminary experiments based on three major processes that could improve stalagmite growth modelling if explored systematically: (i) the effect of a film thickness gradient on the mixing occurring at impact, (ii) the interaction that may appear between two successive drops, and (iii) the mixing within the ejections, specifically, the partition of the ejections between the liquid coming from the impacting drop and the liquid originally found in the film.

1.1 Impact on a wetted step

Stalagmites can present irregularities smaller, larger or close to the size of the drop at their surface, and have more or less inclined walls, all these effects leading to the appearance of film thickness spatial gradients. As seen in Ch. V, drainage does not suffice to provide the film with a velocity comparable to the velocity of the growing crown [48], but that does not mean that impacts cannot be affected by these local thickness variations. Because we cannot infer the mixing occurring between the drop and the film from direct cave measurements, or replicate all the possible stalagmite surface variations in a lab setting, we propose to approximate stalagmite surface variations at first order by a rectangular wetted step of constant height. The height of the step should be comprised between the typical film thickness ($\sim 100\,\mu$m) and the drop radius (~ 2 mm)[1]. Below the film thickness order of magnitude, we could expect the step to have a similar effect on the impact outcome as the surface state or rugosity [184]. On the other hand, a step of height larger than the millimetre would lead to impacts on films that we can no longer classify as thin; for $h = 1$ mm, we would indeed already obtain $h^\star = 7.4$, which falls far within the impacts on deep reservoir region in Ch. IV (see, e.g., Fig. 4.5).

We conducted a few experiments in a similar manner to those presented in Ch. IV, the only difference being the presence of the step below the hydrophilic tape, as illustrated in Figs. 8.1 (a) and (c). The step was made of cured polydimethylsiloxane (PDMS). After mixing and degassing the pre-polymer components of the PDMS at a 10 : 1 weight ratio (Sylgard 184, Dow Corning Inc.), the PDMS was poured over feeler gauge strips of known thickness prior to curing, then carefully cut to match half the area of the experimental samples from Ch. IV (about 4 cm × 4 cm). A piece of double-sided tape of about 4 cm × 4 cm was first placed onto a rigid plastic plate, then half of this tape was covered by the PDMS step. Two rectangular pieces of hydrophilic tape of the same size (Adhesive Research, ARflow 93210) were then positioned over the step and the free remaining part of the double-sided tape. The bonding between PDMS and the hydrophilic tape was sufficient to avoid using any other adhesive between these two layers. Finally, the assembly made of the plate covered by the double-sided tape, the PDMS step and the hydrophilic tape was weighed before and after covering it by a thin film of water in order to know the spatially averaged film thickness above and next to the step. If both the step and remaining double-sided tape part have the same area A, knowing the total mass of fluid m_f indeed leads to $h_1 = m_f/(\rho A) + e/2$ and $h_0 = h_1 - e$, where we denote h_0 the average film thickness over the step, h_1 the average film thickness outside of the step and e the already known step thickness (measured with a simple dial gauge), as illustrated in Fig. 8.1 (c). Impacts were produced in the same manner as described in Sec. 2 of Ch. IV, with

248

a fixed drop falling height of 50 cm. Hence, any drop produced in these conditions has the same radius $R_d = 2.3$ mm and velocity $V_d = 3$ m s^{-1}, and same corresponding Weber number We = 525 (see Eq. (4.5) from Ch. IV). The same dyes as mentioned in Sec. 2 were also used in the drop and in the film. Due to an issue with one of the sensors of the camera, colours in the photographs presented hereafter were altered numerically to match as best as possible the experiments of Ch. IV, taken in the same conditions (no measurement has been inferred from the colours of the pictures presented here)[2]. In Fig. 8.1 (b), an example of a drop impact on a wetted step (this step in particular was formed using an adhesive tape piece of known thickness equal to 200 µm) is shown from the side. We describe this process in more detail hereafter.

In Fig. 8.2, we present an example of a drop impact on a 530 µm-high wetted step. The film has a thickness $h_0 = 75$ µm on the step (lower half of the pictures) and $h_1 = 605$ µm outside of the step (upper half). As depicted in Fig. 8.2 (a), the drop falls into the film at a distance $d = 0.9$ mm $= 0.4R_d$
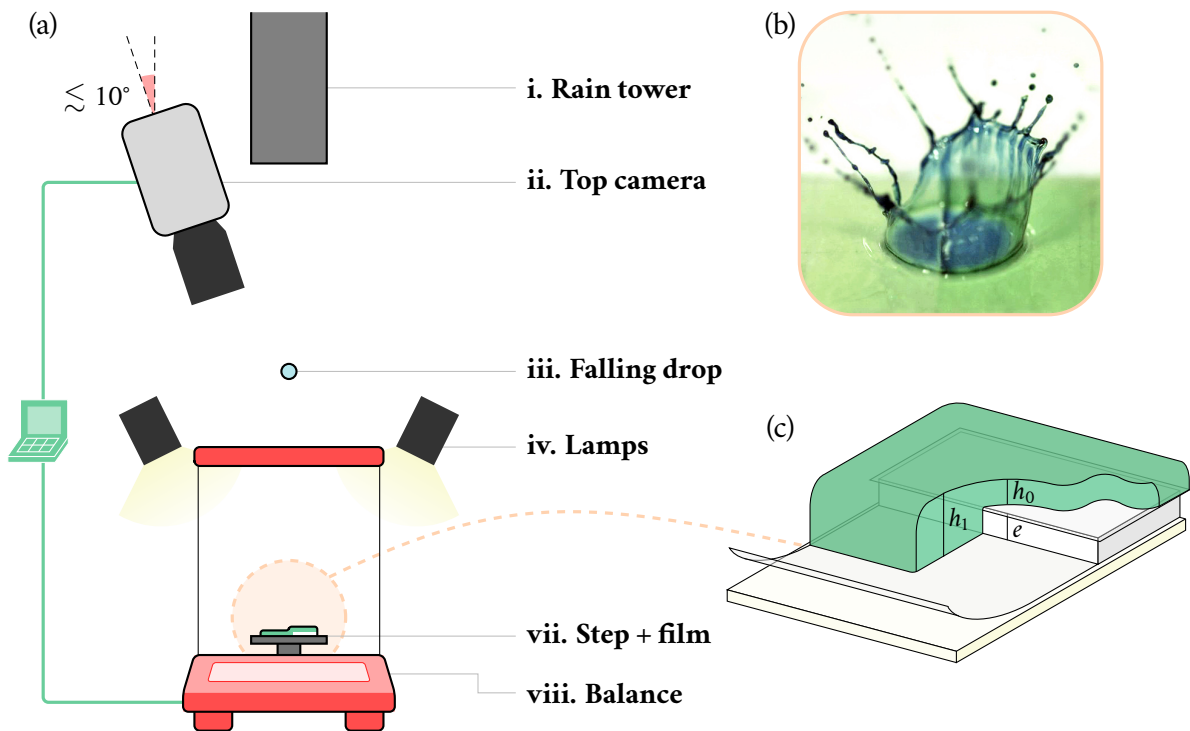
Figure 8.1: Experimental methodology for the drop impact on a wetted step. (a) Experimental setup used to release droplets from a given height onto a thin underlying film, and to record the impacts from a top view. This setup is very similar to the one described in Sec. 2 from Ch. IV. i. Plastic tube in which the drops fall. ii. High-speed color camera used to record impacts from a top view. iii. Falling drop of radius R_d and impact velocity u_d. iv. Four lamps placed in the corners of the balance to light up the impact. v. The impact substrate, consisting of a wetted step. (b) Example of impact from a side view about 30 ms after the beginning of the impact, showing two crown sections of different widths, heights, thicknesses and whose left part is already retracting. (c) Close-up schematic view of the wetted step, consisting of a double-sided tape piece covered partially by hydrophilic tape, and partially by a PDMS step of height e, covered itself by another piece of hydrophilic tape. The ensemble is covered by a thin film of minimum thickness h_0 over the step, and maximum thickness h_1 otherwise.

---

[2]We also point out that the impact of the drop should not deform the PDMS step as PDMS has a Young's modulus of over 1 MPa. A drop impact creates a force varying in amplitude with time, but which does not overcome 0.1 N for less than 1 ms in our parameter range [202]. Such a force acting on the area covered by the drop at the beginning of the impact, πR_d^2, would yield a local pressure of 6×10^4 Pa. Hence, the maximum compression deformation that could be induced if the drop was impacting the sole PDMS layer would be of the order of 1 %. Since the PDMS layer is attached to a much more rigid plate and is protected by the hydrophilic tape and film thickness, the actual possible deformation can be considered negligible and should not affect the outcome of the impact.

from the step, on the thinner part of the film (lower half of the pictures), corresponding to $h_0^\star = 0.65$ and $h_1^\star = 5.3$. In Fig. 8.2 (b), we observe, as in Ch. IV, that the drop crushes into the film to form a growing crown. However, as it appears clearly in Figs. 8.2 (c-d), the crown has a smaller radius[3] in the thicker part of the film (upper half of the pictures), and a larger one in the thinner part of the film (lower half of the pictures). Because of that, the crown also seems to grow slower in the thicker part of the film. Figure 8.2 (c) emphasizes the thinning of the crown wall appearing at the junction between the upper and lower parts. This thinning of the crown wall results from the aforementioned different radii and growing velocities of the two parts of the crown, which may induce shear stresses in the crown wall around the junction. In Fig. 8.2 (e), following the thinning of the crown at the junction between the two parts, fragmentation starts on the thinner part of the film (lower half of the pictures). In Figs. 8.2 (f) i and ii, we note that, right after fragmentation has started, the rim in the thinner part of the film is forming jets which destabilise into secondary droplets. Fragmentation of the lower part of the crown continues in Figs. 8.2 (g-i), accompanied by further ejection of secondary droplets while the upper part of the crown starts retracting toward the impact point position. In Fig. 8.2 (j), we note that, at the end of the retraction phase of the upper part of the crown, the remaining of the crown falls upon itself to form a tail. This tail takes the same appearance as the jets that could be observed at the end of the impacts occurring at We $\lesssim$ 1500 and $h^\star \gtrsim 1$ in Ch. IV, and also destabilises into droplets before falling into the film in Figs. 8.2 (k-l). Because of the particular retraction motion of the upper part of the crown, which only corresponds to half of the usual crowns that we studied in Ch. IV, the tail falls into the film far from the position of the step.

In Fig. 8.2 (m), it can be seen that both parts of the crown and all the ejected secondary droplets have either fallen into the film or outside of it. While the pattern obtained in the lower part of Fig. 8.2 (m) corresponds to what we could observe in Ch. IV (see Figs. 4.5 and 4.6), the upper part of Fig. 8.2 (m) does not look like anything that we have already encountered. By contrast, the lifetime of the lower part of the crown is estimated between 6 ms and 10 ms while the upper crown has survived for over $\sim$ 30 ms, in accordance with the crown lifetimes that we could observe in Ch. IV for films of thicknesses similar to h_0 and h_1, respectively. Hence, the same physical competing effects as

Figure 8.2: *Next page.* Example of a drop impact on a wetted step. The drop of radius $R_d = 2.34$ mm and velocity $u_d = 3 \, \text{m s}^{-1}$ impacts a 530 µm-high PDMS step. The film has a thickness of 75 µm on the step (lower part of the pictures) and 605 µm outside the step (upper part), corresponding to $h_0^\star = 0.65$ and $h_1^\star = 5.3$. (a) The drop right before the impact. The centre of the drop is located at a distance $d = 0.9$ mm $= 0.4 R_d$ from the edge of the step. (b) Crown formation in both parts of the film. (c) Close-up view on the thinning of the crown occurring at the left junction between the upper and lower parts of the crown. (d) Growing of both parts of the crown, with a clearly larger lower radius. (e) Beginning of the fragmentation in the lower part of the crown. (f) Close-up view of the rim detachment and crown fragmentation on each side: i - left and ii - right. On each side, the rim has thinned upon detachment from the crown by forming a jet, further destabilising into secondary droplets. (g) Remaining jets following the crown fragmentation in the lower part and further upper crown growth. (h) Secondary droplets resulting from the jets destabilising in the lower part and retraction of the upper crown (occurring mostly in a direction parallel to the step). (i) End of the retraction phase in the upper part. Retraction is also visible in the spot left by the drop in the lower part, with a visible darker front growing toward the spot center. (j) Jet formation in the upper part, in a direction normal to the step. (k) Destabilisation of the jet in the upper part. (l) The remaining of the jet falls into the film. (m) Mixing pattern about 120 ms after the impact, with visible tails ended by twirls right beneath the step in the lower part, and a longer tail reminiscent of the crown asymmetric retraction and break-up in the upper part. The frame rate of the original movie is 1300 fr s^{-1}. The scale bar is 1 cm but does not apply to pictures (c) and (f) i and ii. The colours in the pictures were numerically altered to match at best the experiments from Ch. IV due to a camera sensor issue.

---

[3]In this particular chapter, we can refer indifferently to the radius of the portion of the crown developing into the film, r_c, or to the radius of the crown rim at the top of the crown, r_t, as we do not have sufficient data to particularize their respective evolution yet.
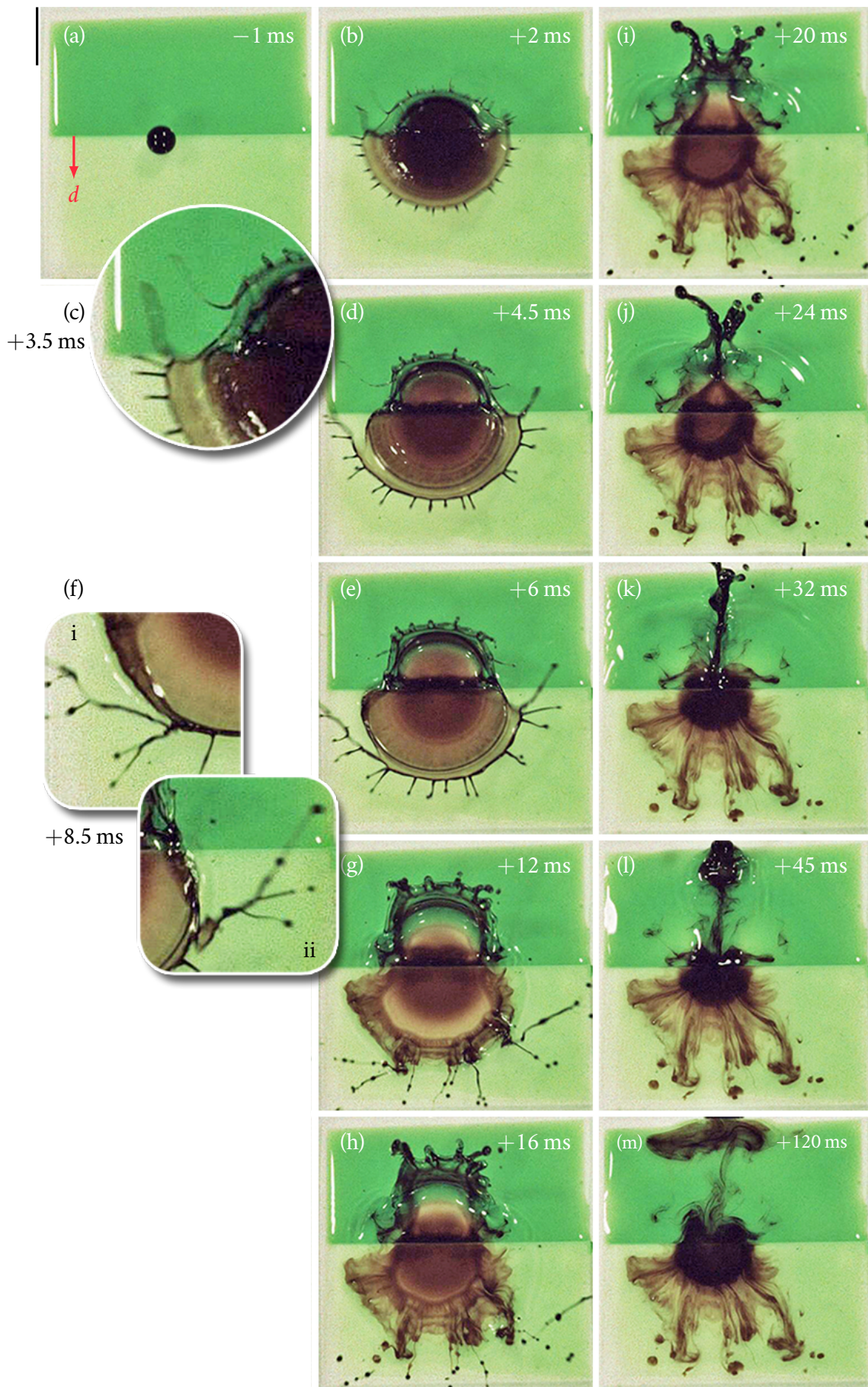
already described in Ch. IV seem responsible for the crown formation, growth, fragmentation and/or retraction, i.e., the large inertia of the drop in the beginning of the impact, quickly caught by capillary and viscous effects that tend to constrict the crown back toward the impact point position or slow it down (which leads to retraction), but may not always be sufficient (when fragmentation appears). In each part of the film, the only visible effect played by the step in the very beginning of the crown development ($\lesssim$ 5 ms) is the change in initial film thickness, to which all crown geometrical aspects are related (radius, growth velocity, see Fig. 4.7 from Ch. IV). But the appearance of the final spot left by the crown into the film is directly related to the end of the retraction phase of the crown, which differs from the experiments of Ch. IV. In the thicker part of the film, the presence of the step thus leads to the tail falling in the film in the opposite direction of the step, that we observed in place of the usual central, uprising jet.

The outcome of the impact can also be affected by the film thickness on either side of the step, h_0 and h_1, or the distance between the drop impact point position and the position of the step, d. We show in Fig. 8.3 a few examples of the various impact outcomes that we could observe in the small set of experiments that we conducted. In Fig. 8.3 (a), the film thicknesses on the two sides of the step are $h_0^\star = 1.74$ and $h_1^\star = 5.2$, respectively. These values can be considered as thick in regard of the experiments from Ch. IV. The distance between the drop impact point position and the step is $d = 3.2R_\mathrm{d}$ on the thicker part of the film. The drop thus impacts the film quite far from the step given that in this film thickness range, both the maximum radius reached by the crown r_c and spot equivalent radius R_eq are of the order of $4R_\mathrm{d}$ (see Figs. 4.7 and 4.9 from Ch. IV). In Fig. 8.3 (a) i, the crown thus looks almost identical as the crowns shown in Figs. 4.5 and 4.6 from Ch. IV, as if it did not sense the effect of the step although a small portion of the crown can be witnessed growing over the step. However, even over the step, the film is so thick that it does not seem to hinder the crown growth. As a consequence, we also observe in Fig. 8.3 (a) ii a very similar pattern of mixing as those from Ch. IV.

In Fig. 8.3 (b), the film thicknesses on both sides of the step are of similar order as in (a) ($h_0^\star = 2.3$ and $h_1^\star = 6.9$), but the drop impacts the film on the thinner part of the film, at $d = -0.7R_\mathrm{d}$. Pictures from Figs. 8.3 (b) i-ii were shown side by side with Figs. 8.3 (a) i-ii for comparison, so we start our discussion by Fig. 8.3 (b) iii, displaying the crown after only 7 ms following the beginning of the impact. The crown can be seen as it has already expanded over the thinner part of the film, i.e., over the step (lower half of the pictures), and has even reached the thicker part of the film (upper half of the pictures). We note that capillary waves are visible in the thicker part of the film around the basis of the crown. The motion of the upper portion of the crown seems to be impeded on the thicker film side, as the crown appears distorted. This is confirmed by Fig. 8.3 (b) i, where the crown has retracted toward the step in the thicker part of the film, while in the thinner part of the film, retraction is only starting, in accordance with the crown lifetimes observed in Ch. IV for film thicknesses of $h^\star \approx 2$. The opposite could be seen in Fig. 8.2, where fragmentation was observed to first start in the thinner part of the film, while retraction in the thicker part only started later, in agreement with the results from Ch. IV. The resulting spot left by the drop in the film in Fig. 8.3 (b) ii is mostly located in the thinner part of the film. We note that the retraction in the thinner part of the film though, following the early retraction in the thicker part, has also induced a tail in this very thicker part, as it was the case in Fig. 8.2.

In Fig. 8.3 (c), the film thicknesses on both sides of the step are $h_0^\star = h_1^\star = 0.65$, corresponding to $h = 75\,\mu\mathrm{m}$. This value is actually shorter than the step height in this case of $e \approx 200\,\mu\mathrm{m}$, such that the surface of the film should present a discontinuity at the step. Hence, although the exact process is certainly more complex and out of the scope of this study, we can conceive that the drop gets more or less cut in half as it impacts the film close to the step ($d = 0.4R_\mathrm{d}$). The
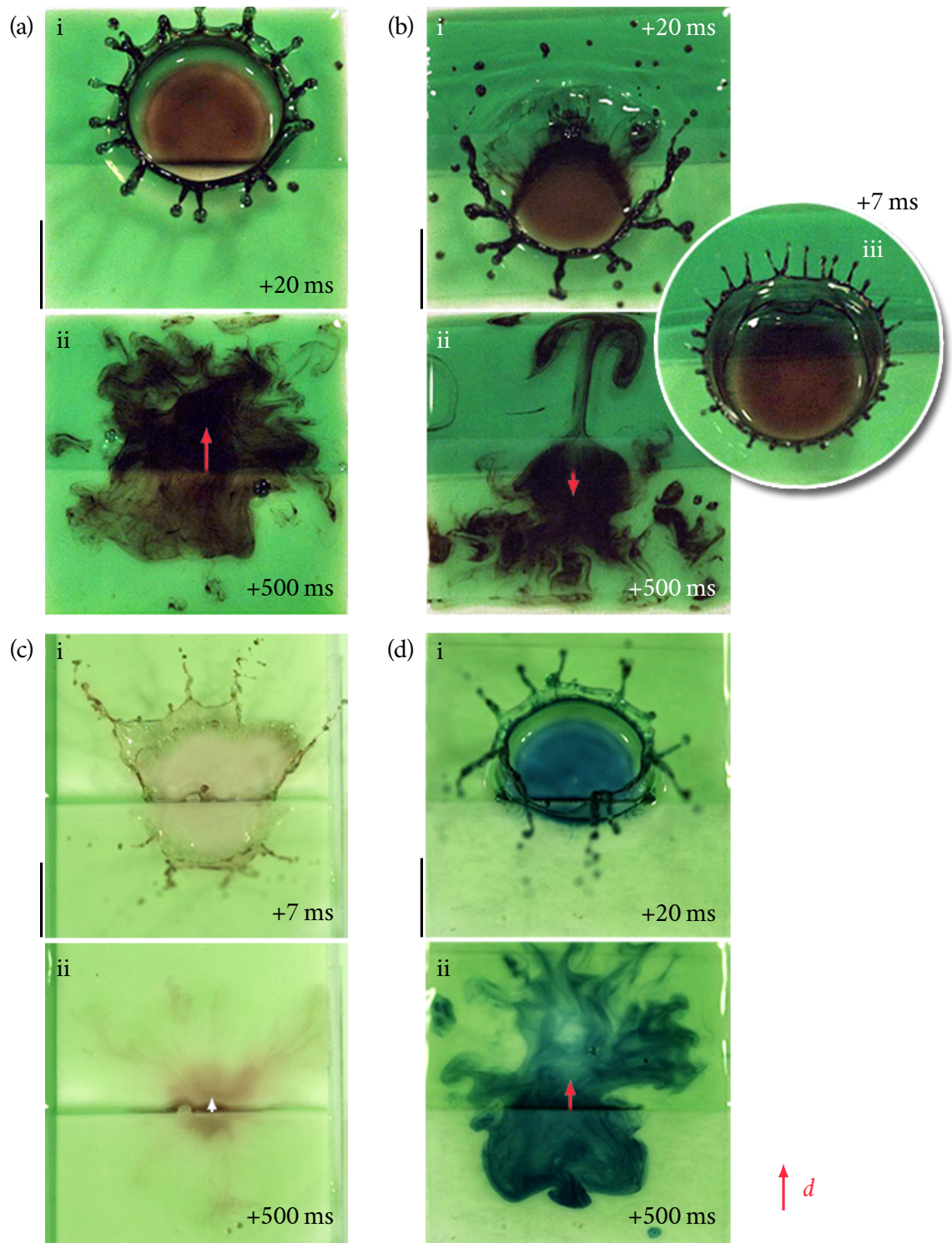
Figure 8.3: Examples of drop impacts on wetted steps with variable thicknesses, h_0 and h_1, and variable distance between the impact point position and step, d. The step is always located in the bottom section of the pictures. The distance d is indicated by a red (or white) arrow, starting from the junction between the two parts of the film, and is considered as positive upward. Parameters are (a) $h_0 = 200\,\mu m$ and $h_1 = 600\,\mu m$ ($h_0^\star = 1.74$ and $h_1^\star = 5.2$), and $d = 7.3\,mm = 3.2\,R_d$, (b) $h_0 = 265\,\mu m$ and $h_1 = 795\,\mu m$ ($h_0^\star = 2.3$ and $h_1^\star = 6.9$), and $d = -1.7\,mm = -0.7\,R_d$, (c) $h_0 = h_1 = 75\,\mu m$ ($h_0^\star = h_1^\star = 0.65$), and $d = 0.8\,mm = 0.4\,R_d$, and (d) $h_0 = 215\,\mu m$ and $h_1 = 415\,\mu m$ ($h_0^\star = 1.87$ and $h_1^\star = 3.6$), and $d = 2.9\,mm = 1.3\,R_d$. The instants at which the pictures were taken, following the moment where the drop starts crushing into the film, are indicated in the pictures. Picture (b) iii emphasises the capillary waves appearing in the upper section of the film when the crown spreads into this section. The scale bars are 1 cm and each refer to the (i-ii) (or i-iii) subfigures of a given panel. The colours in the pictures were numerically altered to match at best the experiments from Ch. IV due to a camera sensor issue.

253

two resulting crowns formed at impact almost seem to evolve independently from one another, and correspond to the crowns observed in Ch. IV in the same film thickness range. We indeed observe fragmentation of both crowns after only 7 ms following the beginning of the impact (see Sec. 3 from Ch. IV). The resulting spot left by the drop in Fig. 8.3 (c) ii also seems only slightly affected by the step as it looks similar to the spot observed for $h^\star = 0.65$ in Fig. 1.13 (in the same Weber number range).

Finally, in Fig. 8.3 (d), the film thicknesses on both sides of the step are also relatively thick since $h_0^\star = 1.87$ and $h_1^\star = 3.6$, and the distance from the drop impact point position to the step is of the order of the drop radius, i.e., $d = 1.3R_{\rm d}$. We observe in Fig. 8.3 (d) i that the part of the crown formed in the thinner part of the film has already started to retract toward the step. This asymmetrical retraction of both parts of the crown induces a similar motion as in Fig. 8.2. We indeed observe in Fig. 8.3 (d) ii an elongated pattern in the upward direction, i.e., from the thinner to the thicker part of the film. However, the case of Fig. 8.3 (d) is not as exacerbated as Fig. 8.2 because the film can be considered as thick, even in the thinner part.

From these preliminary examples, we note that a complex dynamics emerges between the drop and the film because of the step beneath the film. A large number of parameters that may affect the outcome of the impact can be identified, which include but are not limited to the falling height of the drops (or Weber number), the height of the step, the thickness of the film on both sides of the step, and the distance from the impact point position to the edge of the step. Given the few experiments conducted, it is not possible to clearly determine the influence of any of these parameters on the subsequent mixing between the drop and the film. Regardless, we can still note that if the drop impact occurs too far from the step, the crown formed at impact may not feel the presence of the step, at least if the film on both sides of the step is sufficiently thick (see Fig. 8.3 (a)). We also observed different dynamics of retraction at impact when the distance between the drop impact point position and the step was varied. For instance, the retraction of the crown does not start from the same side (thicker or thinner part of the film) depending on whether the drop impacts the film on the step (thinner part of the film) or outside of it (thicker part of the film), as illustrated by Figs. 8.2 and 8.3 (b). If the film is sufficiently thin on either side of the step, fragmentation of the crown may occur instead of retraction, which yield various patterns of mixing between the drop and the film following the impact (see Figs. 8.2 and 8.3 (d)). We also noted that the crowns in each side of the film may evolve independently in the case where the step is taller than the film thickness outside of the step, as exemplified by Fig. 8.2 and 8.3 (c). Taking into account the effect of film thickness variations on the impact outcome thus reveals intricate and complex dynamics, even in a simple case where the film thickness is only twofold and does not present a continuous gradient throughout the entire film.

1.2 Two successive, close drop impacts

Two sessile drops spread on a dry wall can coalesce as soon as they touch each other [75]. This is also true when a drop impacts a dry wall, at a position very close to another sessile drop of the same liquid [47, 210]. In this case, even if the impacting drop and the sessile drop are separated by up to $3R_{\rm d}$, because the impacting drop spreads out [103, 139], it ends up coalescing with the first sessile drop [47]. On an oblique wall (inclined with the horizontal), a drop impact close to a sessile drop further yields a displacement of the two merged drops [5]. Analogously, two drops impacting a dry wall simultaneously with different velocities can also coalesce if their respective spreading radii become sufficient for them to touch each other [176].

By contrast, limited research has been conducted on two drop impacts on a thin liquid film, except in the context of a train of identical drops falling at the exact same position [148, 162, 236].

Ersoy and Eslamian [81] performed impact experiments using two drops of identical radius, but coloured differently, impacting dry walls and thin films (quasi-)simultaneously. An example in Fig. 8.4 below depicts the quasi-simultaneous impacts of a yellow and a blue drop (time lag of ~ 1 ms, which we inferred from Fig. 7 in Ersoy and Eslamian [81]) on a film of thickness $h^\star = 3.6$ (see Ch. IV), at a distance of $4.5R_d$. In Fig. 8.4 (a), the two growing crowns formed by the impacting drops can be seen 8 ms after the beginning of the impacts. Because the radius r_c ($\approx r_t$, see Fig. 4.7 in Ch. IV) reached by the two similar crowns is about $3R_d$, they end up touching each other and merging. An upward sheet thus starts growing along the intersect line of the two crown walls which are no longer able to continue their outward motion. This sheet further destabilizes into secondary droplets falling back into the film afterward, thereby creating the pattern observed in Fig. 8.4 (b), 500 ms after the beginning of the impact. We observe in Fig. 8.4 (b) that, despite the fact that both crowns interacted with each other during the impact, the spots left by the two drops in the film are easily distinguishable from one another. The only visible evidence of mixing between the two drops is the intersect line which appears green. However, we know from Sec. 2.3 in Ch. IV that molecular diffusion has not set in yet after only 500 ms. Impacts performed at higher Weber number We, i.e., for drops with larger impacting velocities, could also lead to additional mixing processes that do not appear in the present case.

We have conducted a similar experiment in which two drops of identical radius impact the same thin film, but successively rather than simultaneously. We only recorded the impacts from the top by using the same experimental setup as described in Fig. 4.1 from Ch. IV (except for the side view recording), which is also illustrated in Fig. 8.1. We added a second tube terminated by the same 2 mm-diameter plastic connector as in Ch. IV to be able to produce two impacts with different dyes. In Figs. 8.5 (a-e), we show a red and green dyed drop (as in Ch. IV) impacting a green film of initial thickness $h^\star = 0.78$ with a Weber number We $= 1440$ (see Eq. (4.5) from Ch. IV). In Figs. 8.5 (f-j), we show the exact same time instants of the second drop, dyed in blue, impacting the film. Coincidentally (see Fig. 8.4), both drops are separated by a distance of $5R_d$. The second drop impacts the film about 2 min after the first one. The spots left by the two drops 5 min after the beginning of the first impact can be seen in Fig. 8.5 (k).

We observe in Figs. 8.5 (a-e) and (f-j) that the two drop impacts are almost identical, and, unsurprisingly, both look very similar to the impacts presented in Figs. 4.5 (a) ii and 4.6 (a) in scenario A (see Ch. IV). Given the time period of 2 min in between both impacts, the film should indeed have had the opportunity to recover a more or less horizontal, uniform thickness. Moreover, the second drop impact occurs at a position sufficiently far away from the first drop impact for the film surface to remain almost unperturbed at the second impact position during the first impact (see Fig. 4.2 in Ch. IV). In this regime, corresponding to scenario A, we have also obtained that the volume ejected away at impact is equivalent to the proportion of drop volume entering the film, with
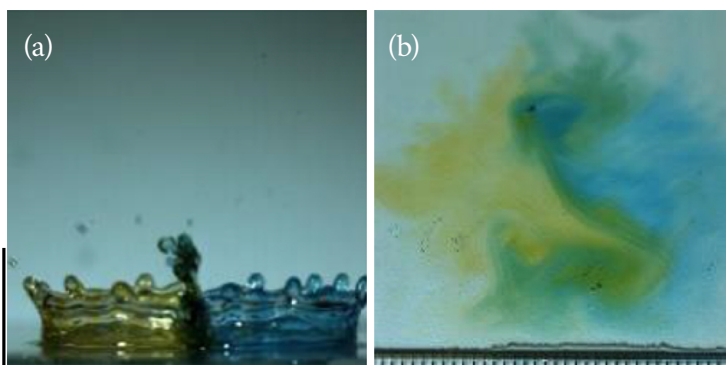
Figure 8.4: Example of two quasi-simultaneous drop impacts on the same thin film, with $R_d = 2.1$ mm, $h \approx 400\,\mu$m ($h^\star = 3.6$), and We $= 230$. The drops are separated horizontally by a distance of $4.5R_d$. (a) Side view at $+8$ ms following the impact. (b) Top view at $+500$ ms. The scale bar is 1 cm and is the same for both pictures. Adapted from Ersoy and Eslamian [81] (Figs. 7 and 19).
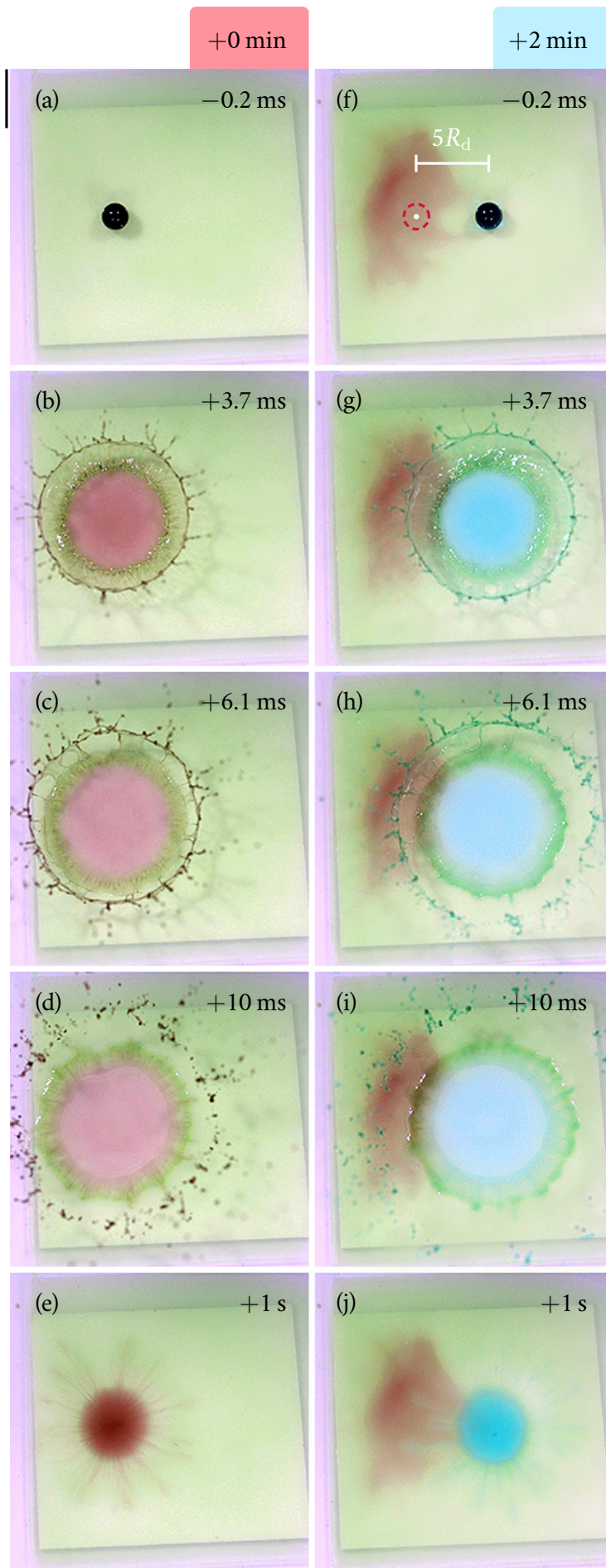
Figure 8.5: Example of two successive drop impacts on the same 90 μm-thick film (space average thickness), both drops having a velocity of 4.8 m s^{-1}. The first drop contained both red and green dyes as in the experiments presented in Ch. IV, the second drop contained blue dye. Impact parameters correspond to $h^\star = 0.78$ and We = 1440 (see Ch. IV). Panels (a-e) and (f-j) show the same time instants of the two impacts, separated by about 2 min. The impact point position of the first drop is indicated in (f) by the white dot, the dashed red circle corresponding to the first drop outline. The distance between both impact point positions is $5R_d$. Between the two impacts, as it can be noted in the right bottom corner of (f-k), some evaporation has started to set in, thereby depleting the film and reducing its local thickness (the film appears whiter). (a)/(f) The drop right before it impacts the film. (b)/(g) The drop has started crushing into the film, leading to the formation of a growing crown with secondary droplet ejections. (c)/(h) The crown has started to destabilise into thin sheet fragments. (d)/(i) The last secondary droplets are ejected away while the remaining of the drop that penetrated into the film starts to retract toward the impact point. (e)/(j) After complete retraction, the spot left by the drop looks exactly like the one shown in Fig. 4.6 (a) iv and Fig. 4.5 (a) ii. (k) The spots left by the two drops about 5 min after the beginning of the first impact, and 3 min after the second one. Both spots have enlarged and some mixing between the red and blue dyes may be observed. The scale bar in (a) refers to (a-j), the one in (k) only refers to (k). Both scale bars are 1 cm.
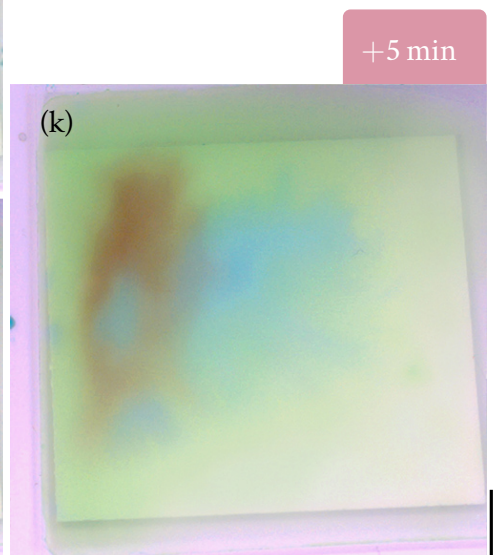
the ejected ratio $\varphi_e \simeq 1$ (see Fig. 4.12 in Ch. IV). Hence, both the first and second drop impacts should occur in identical conditions. We therefore note in Figs. 8.5 (e) and (j) that the spots left about 1 s after the beginning of each impact present the same features as discussed in Ch. IV for scenario A. The dye is concentrated almost entirely over the equivalent radius R_{eq}, defined in Eq. (4.11), this radius being roughly equal to $2R_d$ here. Correspondingly, not much dye is left around this area, except for a few tails reminiscent of the crown fragmentation that can be witnessed in Figs. 8.5 (c-d) and (h-i) for the red and blue drops, respectively (see Sec. 3.1 in Ch. IV). We also observe in Figs. 8.5 (g-j) that the second drop impact does not seem to affect the spot left by the first impact. We had indeed measured that, for the range of parameters relative to this impact, the radius of the cavity spreading into the film, r_c, is of the order of $\lesssim 5R_d$, which is the distance between the two impact point positions. The second impact itself thus does not induce any significant mixing between the second impacting drop and the spot left by the first drop.

Additionally, by contrast with the experiment from Fig. 8.4, the two crowns growing at impact cannot interact with one another since the impacts do not occur simultaneously. Nevertheless, we note that, between Figs. 8.5 (j) and (k), some mixing has occurred as the blue spot has spread out until it encountered the red spot. Over a time span of a few minutes, molecular diffusion has indeed had the time to set in. This effect could be considered as negligible in regard of all the other competing physical processes in Ch. IV (inertia, capillarity and viscous forces). In the case presented in Fig. 8.5 though, it seems to become the driving mechanism allowing to get some mixing in between two drop impacts separated by a large distance and a long time period, by comparison with the drop radius and impact time, respectively. Other phenomena[4] could also be responsible for this mixing, though, among which we can list the evaporation of the film, visible in Figs. 8.5 (j) and (k) in the lighter lower right area. This evaporation does not appear to be uniform and could induce non-negligible film thickness gradients and dewetting of the film over the substrate, thereby creating a flow directed toward the upper left corner of the substrate. We can further mention that, after the crown fragmentation, the remaining of the drop in the film retracts toward the centre until all the liquid meets in one point, forming a very circular spot in the film. When the crown does not fragment, an uprising jet can even be formed (see Figs. 4.5 (c) and 4.6 (c) in Ch. IV). However, as it is the case in drop impacts on dry walls [128, 235], this retraction could be followed by a non-negligible and slower outward spreading phase, widening the spot that was left by the drop after only 1 s.

Besides the initial film thickness, many other parameters could play a major role when considering two drop impacts on the same film: the timing between the two impacts ((quasi-)simultaneous, separated by a time of the order of the impact time ($\lesssim 1$ s), or much longer), the distance between the two impact positions, which can affect the growing crowns formed at impact if the impacts are simultaneous [81], or the relative inertia (i.e., radii or impacting velocities) of the two drops. Even in cases that may seem limiting, as we present in Fig. 8.5, mixing can occur because of physical processes, such as molecular diffusion, that could be ruled out when studying one impact at a time. We indeed show two impacts separated by a distance larger than the maximum radius of the cavity spreading into the film at impact, and by a very long time period in regard of the impact timescale, yet we are still able to discern some mixing in Fig. 8.5. On actual stalagmites, we could also add the effect of the gravity-induced drainage, which would further enhance the mixing between the two spots left by the drop. Unless they have already all precipitated, it is thus not trivial to assess exactly how ions coming from two successive drops would get redistributed between impacts.

---

[4]A slight inclination of the substrate underneath the film could also yield a non-negligible spreading of the spots left by the drops, however this spreading would be oriented along a specific direction for both impacts. As this is not the case here, the possible effect of the substrate inclination can be ruled out.

1.3 Secondary ejections

To the best of our knowledge, there is currently no dedicated study describing the content of the ejected secondary droplets during the impact of a drop on a film, whether this one can be considered as thin or not. In the case of stalagmites though, these secondary droplets could carry ions on the sides of their landing stalagmite, or onto adjacent or close stalagmites, thereby leading to local calcite addition away from their impact point. The knowledge of the secondary droplet content could be of interest in other applications, including pathogen dispersal and leaching on plant leaves [100, 145], or content dispersal from drop impact-induced soil erosion [147, 163]. Our conclusions from Ch. IV indicated that the impacting drop content actually entering the film mostly changed with the initial film thickness, thus we expect the content of the secondary droplets to be affected by this initial film thickness as well. The literature [144, 145, 236] and our own experiments further suggest that the size, velocity and trajectory of the secondary droplets vary with the film thickness, as well as with the incoming drop impacting velocity.
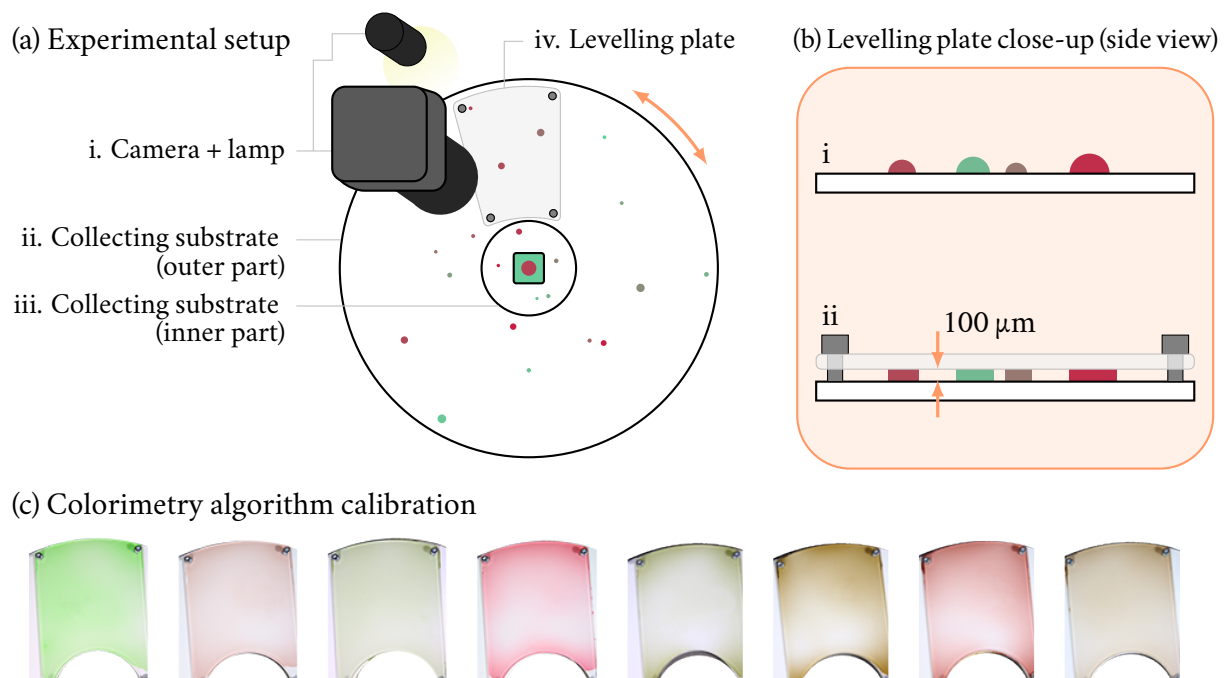
Figure 8.6: Experimental methodology. Prior to panels (a-b), impacts were conducted in the same manner as described in Fig. 4.1 (a) to produce the ejections drawn in both schematics. (a) Top view of the setup. i. Fixed camera and lamp allowing to record pictures of the droplets. ii-iii. Two-piece collecting substrate over which drops have landed. The outer part has a diameter of 35 cm, the inner one a 14 cm-diameter. The outer part can be pivoted such that all the regions of interests containing droplets can be successively positioned under the camera. The inner part can be removed to be positioned under the camera. iv. Levelling transparent plate allowing to frame the droplets. (b) Side view of the levelling plate operation. i. Following the impact, droplets of all sizes and colours are dispersed over a region of interest of the collecting substrate. The region of interest of the collecting substrate is positioned under the camera. ii. When the levelling plate is placed on top on the region of interest of the collecting substrate, droplets are framed such that they all have the same thickness of 100 μm. The plate has 4 bolts which can be tightened in order to maintain a constant spacing between the levelling plate and the underneath substrate. The screws are not attached to the collecting substrate but simply placed on top of it. A second levelling plate corresponding to the inner part of the collecting substrate (see (a) iii) was also used, which is not represented here but operates on the same principle. The main levelling plate has a width of about 13 cm following the rounded edge of the collecting substrate, a maximum length of 13 cm and a minimum length of about 11 cm in the middle. The second levelling plate has a diameter of 14 cm and a central square hole of 4 cm long sides (see Fig. 8.7 for better visualisation). (c) Examples of calibration pictures that could be used to implement the same colorimetry algorithm as described in Ch. IV, for this set of data. These pictures represent the levelling plate covering a thin film of the same thickness as imposed to the ejected droplets (see (c)), but with known red and green dye concentrations.

We propose to look at preliminary examples of collections of secondary droplets ejected during impacts similar to those presented in Ch. IV. The experimental setup used is schematised in Fig. 8.6. By using the same colorimetry technique as presented in Ch. IV, we could retrieve the concentration content of the ejected droplets from photographs of these droplets. In the case of the direct photographs of the impacts shown in Ch. IV, we had used the fact that the green dye volume fraction was the same everywhere in the film, and thereby known, to assess both the film thickness and red dye concentration in every point of the photographs. We proceeded in a similar manner here and recorded photographs of the secondary droplets from the top. We kept using the same green dye volume fraction in both the impacting drop and the film (set to $p_g = 0.05$, see Ch. IV), such that any secondary droplet containing red dye came from the liquid originally in the impacting drop. To avoid any effect related to the three-dimensional aspect of the secondary droplets, we imposed a constant, fixed height to these droplets so that they form a cylinder rather than a spherical cap or assimilated shape [63]. Knowing the constant height and green dye concentration in the secondary droplets, it is therefore possible to infer their exact content along with their radius from top photographs. We could use dyed drops impacting transparent films, but the film dye eases the detection of the droplets during the image analysis processing. To obtain the top photographs, as illustrated in Figs. 8.6 (a) ii-iii, we placed the thin film on which the drop impact was performed at the centre of a 35 cm-diameter circular plate of white, matt plastic, to which we refer as the collection substrate. This substrate was divided between a central disk and an outer annulus. The thin film, created in the same manner as described in Ch. IV by pouring a small volume of water over a 4 cm × 4 cm hydrophilic piece of tape, was positioned on the central piece of the collection substrate. The outer annulus could be freely rotated and was placed on a rigid, wooden plate. A Canon EOS 5D mark III camera was placed at a fixed position on top of the outer annulus from the collection substrate, at a distance of about 30 cm, next to a powerful LED lamp (Fig. 8.6 (a) i).

In Figs. 8.6 (a) i and (b), we illustrate how the secondary droplets could be maintained at a constant height while photographs of them were taken. We positioned on top of the outer annulus of the collection substrate a transparent, rigid plate assorted by four bolts in all the corners of the plate, that we call levelling plate. By positioning the levelling plate on top of 100 μm-thick gauge strips, we could tighten the nuts of the bolts to achieve a constant spacing everywhere between the levelling plate and the surface underneath. Hence, by placing the levelling plate on top of the ejected droplets, we ensured that these latter had a constant, known thickness. Once a photograph of an area covered by secondary droplets was obtained, we removed the levelling plate, wiped it out carefully and rotated the outer annulus of the collecting substrate in order to capture a new sub-collection of droplets. We repeated this procedure until we had covered the entire annulus. Given the dimensions of the levelling plate (about 13 cm in maximum length and width, and 11 cm in minimum length, see Figs. 8.6 (a) iv and 8.7 (a)), we usually needed 6 or 7 photographs per experiment. A second levelling plate was used to capture the secondary droplets ejected directly around the contour of the film, which had the exact same size as the central disk of the collection substrate (see Figs. 8.6 (a) iii and 8.7 (a)). To use the colorimetry algorithm presented in Ch. IV, a set of calibration pictures are needed, such as the ones shown in Fig. 8.6 (c). They represent the levelling plate relative to the outer annulus of the collection substrate, positioned over films of variable, known red and green dye volume fractions. Without thoroughly discussing the issues arising with this experiment and the solution to address them, we can note that they mostly consisted of:
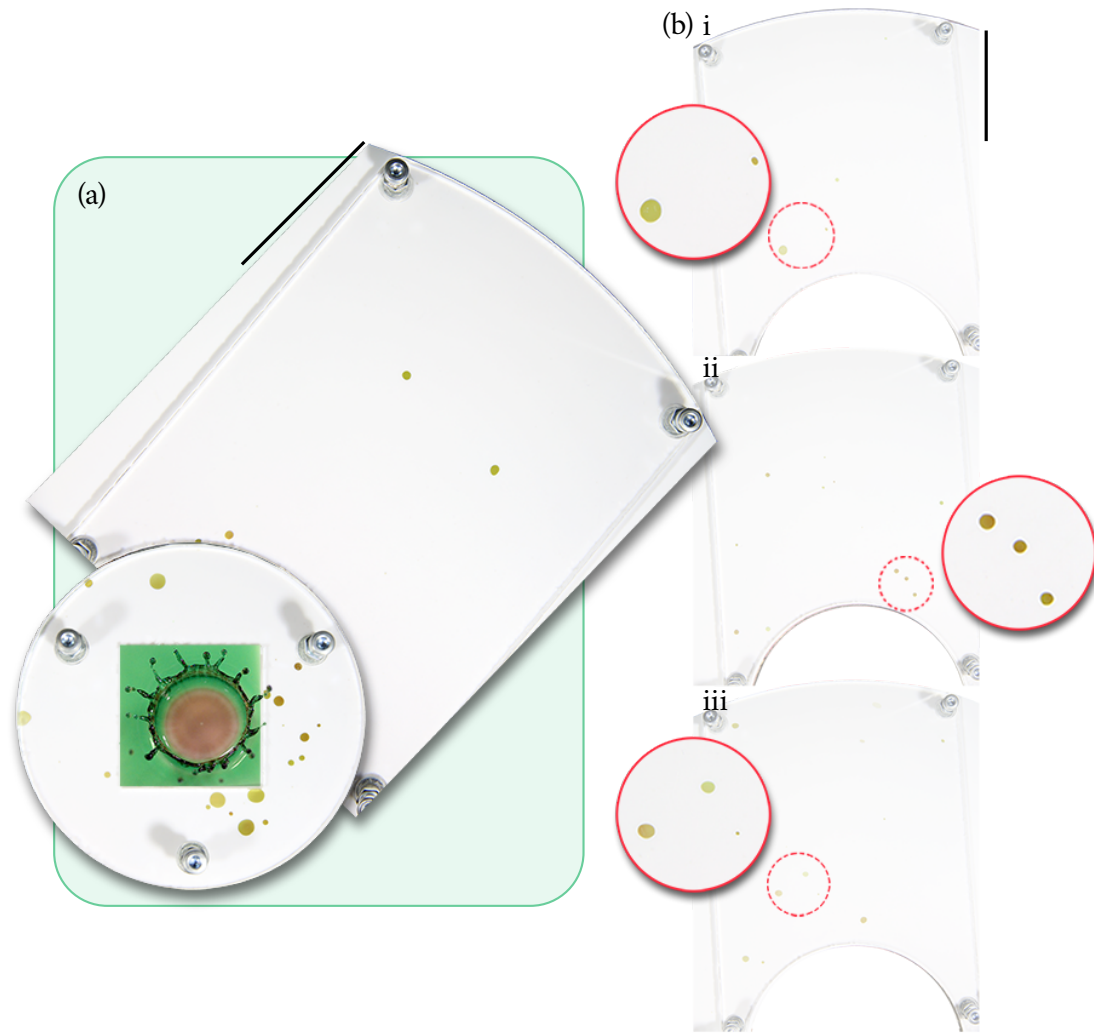
Figure 8.7: Example of collection and recording of the secondary droplets ejected away during the impact of a drop on a 300 µm-thick film, which corresponds to $h^\star = 2.61$. (a) A drop containing red and green dyes has just impacted a thin green film and produced secondary droplets which have been ejected at various distances from the impact point position. The central illustration from (a) only serves as a reminder of the kind of impacts that can be observed on 300 µm-thick films but does not correspond to this particular experiment (scaling is appropriate with respect to the radii of the ejected droplets). Around the impacted area, the levelling plates press and maintain the ejected droplets at a fixed thickness. The levelling plate right around the film is only used once while the levelling plate positioned further away from the film is used several times to capture the droplets ejected all around the film. In between two photographs, the levelling plate is wiped out carefully and the substrate underneath is subjected to a sufficient rotation to capture a new sub-collection of droplets. (b) i-iii. Three examples of photographs of the levelling plate used to capture the droplets ejected the furthest away from the film (at least in the area that we could cover). In each photograph, a close-up view of some droplets is presented, as indicated by the red dashed circles. The scale bars are 5 cm. The scale bar in (a) refers only to (a), and the scale bar in (b) i refers to (b) i-iii. The close-up views in (b) do not correspond to the scale bar (note that the close-up view areas all have the exact same size, which is the same size as in Fig. 8.8, and correspond more or less to twice the emphasized areas in the original pictures).

(i) the fact that some ejected droplets landed outside of the area covered by our collection substrate, (ii) the coffee-ring effect displayed by some tiny secondary droplets that had evaporated before the photograph was taken, (iii) the limited resolution of the camera with respect to the significant aspect ratio between the area over which the secondary droplets can possibly land (over a $\sim$ 50 cm radius) and their minimum size (about 100 µm or smaller [145]), which is around 10^8, and (iv) the difficulty in maintaining a thin film under the levelling plate during the calibration (see lighter areas in
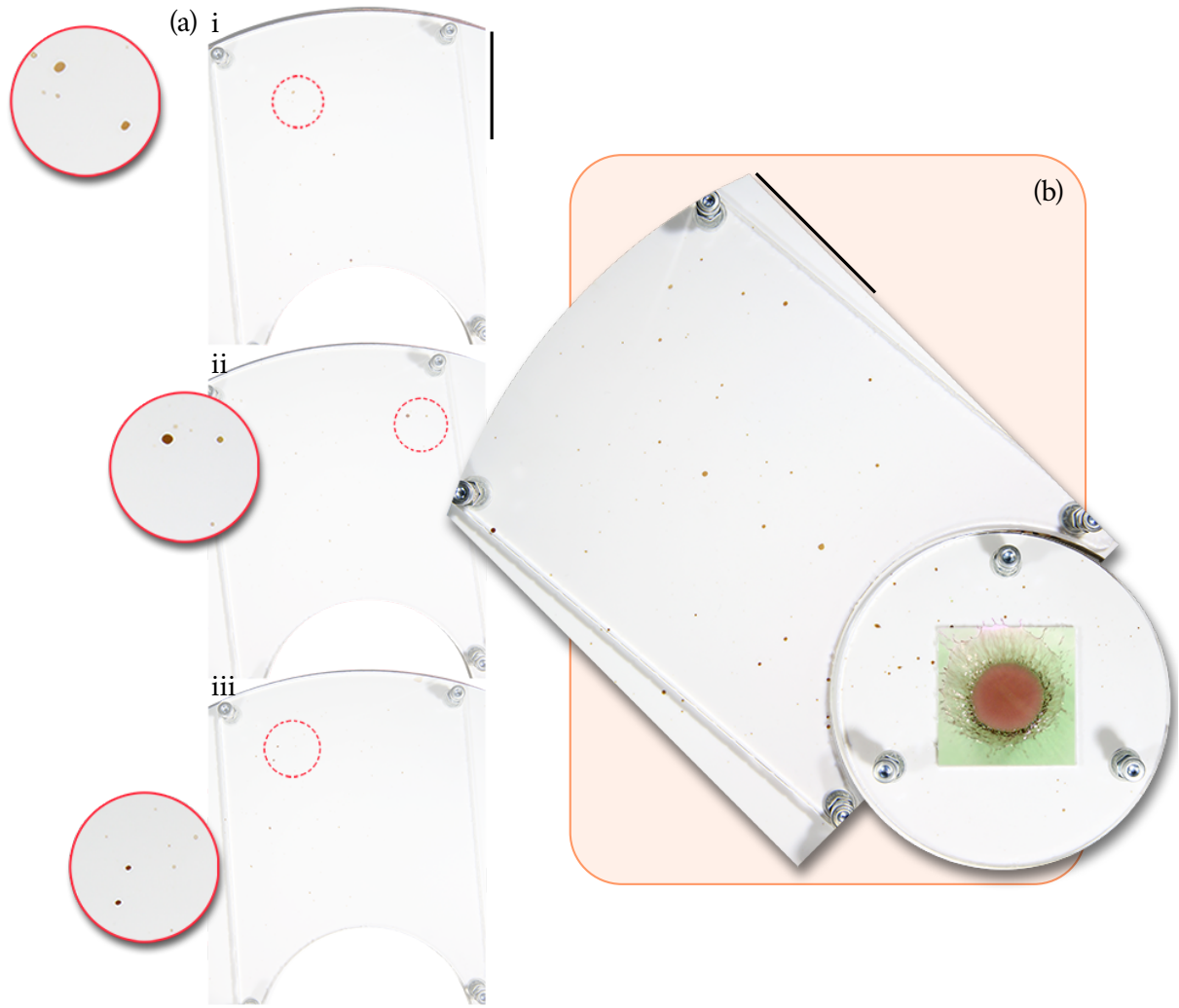
Figure 8.8: Same as Fig. 8.7, but for a 85 μm-thick film, which corresponds to $h^\star = 0.74$ (the (a) and (b) panels have been inverted purely for graphical purpose).

the pictures of Fig. 8.6 (c)).

A complete, systematic analysis over the range of initial film thicknesses and drop impacting velocities already covered in Ch. IV is likewise out of the scope of this work. In the light of the regimes established within our study of drop impacts on thin films, we can nevertheless observe the differences appearing among two distinct cases, which are illustrated in Figs. 8.7 and 8.8. First, in Fig. 8.7, we show a partial collection of secondary droplets produced by the impact of a 2.3 mm-radius drop on a 300 μm-thick film, which corresponds to $h^\star = 2.61$. In Fig. 8.7 (a), we see the two levelling plates covering droplets both very close to the film and away from it. In Figs. 8.7 (b) i-iii, a close-up view on some droplets from other examples of photographs taken of the outer annulus levelling plate are shown. The same visualisations obtained by impacting a drop on a 85 μm-thick film, for which $h^\star = 0.74$, are shown in Figs. 8.8 (a) i-iii (close-up views of the secondary droplets) and (b) (the two levelling plates). The photographs presented were selected because they exhibit general features of the secondary droplets ejected for these film thicknesses. The observations made are thus not specific to these photographs. We observe that, in Fig. 8.7 (a), few secondary droplets were ejected away from the impact point position (usually no more than 4-5 per photograph) while many secondary droplets having a smaller radius are visible in Fig. 8.8 (b). A larger number of ejected droplets presenting a large radius variability are visible close to the impact point position in Fig. 8.7 (a), while in Fig. 8.8 (b), the radii of the ejected droplets close to the impact point

are similar to the radii of the ejected droplets away from the impact point. In Ch. IV, specifically in Fig. 4.13, we had observed that the part of the drop actually entering the film during the impact, $\varphi_{d \to f'}$, was smaller than 0.2 for $h^\star < 1$, then increased with increasing film thickness while remaining $\lesssim 0.5$ in the range covered by our experiments. Parallel to that, we had inferred from our measurements that the volume of the initial film actually going into the ejections, $\varphi_{f \to e}$, remains of the order of ~ 0.1 times the impacting drop volume for the entire film thickness range covered in the experiments. These results are in accordance with the observations that can be made here. In Figs. 8.7 (a) i-iii, we indeed note that the droplets seem greener than the droplets of Fig. 8.8 (b) i-iii, which present a brown colour as a result of the mixing between the red and green. Hence, a larger amount of liquid originating from the film seems to be contained within the drops over the thicker film shown in Fig. 8.7. The droplets from Fig. 8.7 (a) i-iii also seem to present a larger colour variability, although the droplets from Fig. 8.8 (b) i-iii are not easily distinguishable and may present a similar variability that we are not able to assess. Although we cannot infer the exact values of $\varphi_{d \to f'}$ and $\varphi_{f \to e}$ from the measurements presented in this section, these preliminary experiments tend to confirm the conclusions from Ch. IV.

2. A series of complex processes

In this chapter, we proposed to conduct a few preliminary experiments on the mixing occurring during the impact of a drop on a thin film in various contexts. We had indeed only explored the impacts on horizontal films of uniform thickness in Ch. IV, while it was observed that not all impacts resemble the impacts presented in, e.g., Figs. 4.5 and 4.6 from Ch. IV. Among all the possibilities that can be found in the case of drop impacts on stalagmite, three experiments were carried out. First, we observed drop impacts on a film of variable thickness, which could occur as a result of the drainage of the film. We approximated the thickness gradients that may exist in the film at first order by a rectangular step covered by a thin film. The experiments revealed that the height of the step, the distance between the drop impact point position and the edge of the step, the position of the drop impact relative to the step (either on top of it or in the thicker part of the film), and the relative film thicknesses on each side of the step, could all possibly affect the outcome of the impact. For instance, an impact close to a step covered by a film presenting a significant thickness difference yields an asymmetric retraction of the crown formed upon impact. From there, instead of collapsing toward the impact point position, the crown may lead to the formation of an elongated tail. We also reviewed how two drop impacts may interact with one another, since the dripping period of drops in caves can become $\lesssim 1$ s. Recent studies [81] have shown that drops impacting simultaneously the same film at a distance sufficiently short for the two crowns formed during impact to touch each other lead to mixing inside the intersect line between the crowns. Our experiment also showed that, even if the drops are separated by a large distance and long time period with respect to the drop radius and impact time, respectively, mixing could still appear in the film. In this case though, the mixing would most likely be due to molecular diffusion setting in after the drop impacts, a process that could be eluded until now. The last experiment focused on the mixing occurring inside the ejected secondary droplets at impact. We showed that the impact on the thicker film produced a smaller number of droplets with larger radii, which also seem to land closer to the stalagmite. By contrast, the impact on the thinner film led to the ejection of smaller droplets further away from the impact point position. The droplets ejected by the impact on the thicker film also presented a greener colour. Hence, we could retrieve qualitatively the results presented in Ch. IV regarding the proportions $\varphi_{d \to f'}$ and $\varphi_{f \to e}$. Although these experiments are only preliminary, they show that the drop impact on a thin film involves even more complex physics than what could manifest from the experiments of Ch. IV. We hope that future contributions will

allow to decipher the dynamics at play during the impacts presented in this chapter, and help improve stalagmite growth modelling for palaeoclimate reconstruction, as well as other applications in which drop impacts on thin films play a preponderant role.

REFERENCES

1. Abramowitz, M. and Stegun, I. *Handbook of Mathematical Functions with Formulas, Graphs, and Mathematical Tables*. Dover Publications, 1964.

2. Achenbach, E. "Vortex shedding from spheres". In: *J. Fluid Mech.* 62 (1974), pp. 209–221. DOI: 10.1017/s0022112074000644.

3. Adnew, G. A. et al. "Temperature dependence of isotopic fractionation in the $CO_2 - O_2$ isotope exchange reaction". In: *Rapid Commun. Mass. Spectrom.* 36.12 (2022). DOI: 10.1002/rcm.9301.

4. Agrawal, M. et al. "Nonspherical liquid droplet falling in air". In: *Phys. Rev. E* 95 (3 2017), p. 033111. DOI: 10.1103/PhysRevE.95.033111.

5. Ahmad, S., Tang, H., and Yao, H. "Oblique impact of two successive droplets on a flat surface". In: *Int. J. H. M. Tran.* 119 (2018), pp. 433–445. DOI: 10.1016/j.ijheatmasstransfer.2017.11.129.

6. Aitken, M. J. *Thermoluminescence Dating*. New York: Academic Press, Elsevier, 1998.

7. Almohammadi, H. and Amirfazli, A. "Droplet impact: Viscosity and wettability effects on splashing". In: *Journal of Colloid and Interface Science* 553 (2019), pp. 22–30. DOI: 10.1016/j.jcis.2019.05.101.

8. Ambravaneswaran, B., Phillips, S. D., and Basaran, O. A. "Theoretical Analysis of a Dripping Faucet". In: *Phys. Rev. Lett.* 85 (2000). DOI: 10.1103/physrevlett.85.5332.

9. Antonini, C., Amirfazli, A., and Marengo, M. "Drop impact and wettability: from hydrophilic to superhydrophobic surfaces". In: *Phys. Fluids* 24 (2012). DOI: 10.1063/1.4757122.

10. Arnold, A. J. and Fristrup, K. "The Theory of evolution by natural selection: A Hierarchical expansion". In: *Paleobiology* 8.2 (1982), pp. 187–210. DOI: 10.1017/S0094837300004462.

11. Asmerom, Y. et al. "Multidecadal to multicentury scale collapses of Northern Hemisphere monsoons over the past millennium". In: *Proc. Natl. Acad. Sci. U.S.A.* 110 (2013). DOI: 10.1073/pnas.1214870110.

12. Asrat, A. et al. "Paleoclimate change in Ethiopia around the last interglacial derived from annually-resolved stalagmite evidence". In: *Quat. Sci. Rev.* (2018), pp. 1–14. DOI: 10.1016/j.quascirev.2018.06.016.

13. Assouline, S., Narkis, K., and Or, D. "Evaporation from partially covered water surfaces". In: *Water Resour. Res.* 46 (2010). DOI: 10.1029/2010WR009121.

14. Bagchi, P. and Balachandar, S. "Effect of turbulence on the drag and lift of a particle". In: *Phys. Fluids* 15.11 (2003), pp. 3496–3513. DOI: 10.1063/1.1616031.

15. Baker, A. et al. "A composite annual-resolution stalagmite record of North Atlantic climate over the last three millennia". In: *Sci. Rep.* 5.10307 (2015). DOI: 10.1038/srep10307.

16. Baker, A. et al. "Analysis of the climate signal contained within δ^{18}O and growth rate parameters in two Ethiopian stalagmites". In: *Geochim. Cosmochim. Ac.* 71 (2007), pp. 2975–2988. DOI: 10.1016/j.gca.2007.03.029.

17. Baker, A. et al. "Annually Laminated Speleothems: a Review". In: *Int. J. Speleol.* 37.3 (2008). DOI: 10.5038/1827-806x.37.3.4.

18. Baker, A. et al. "Testing theoretically predicted stalagmite growth rate with recent annually laminated samples: Implications for past stalagmite deposition". In: *Geochim. Cosmochim. Ac.* 62.3 (1998), pp. 393–404. DOI: 10.1016/s0016-7037(97)00343-8.

19. Baker, A. et al. "The properties of annually laminated stalagmites A global synthesis". In: *Rev. Geophys.* 59 (2021). DOI: 10.1029/2020RG000722.

20. Baker, A. J., Mattey, D. P., and Baldini, J. U. L. "Reconstructing modern stalagmite growth from cave monitoring, local meteorology, and experimental measurements of dripwater films". In: *Earth Planet. Sc. Lett.* 392 (2014), pp. 239–249. DOI: 10.1016/j.epsl.2014.02.036.

21. Baldini, J. U. L. "Cave atmosphere controls on stalagmite growth rate and palaeoclimate records". In: *Geological Society, London, Special Publications* 336 (2010), pp. 283–294. DOI: 10.1144/SP336.15.

22. Baldini, J. U. L. et al. "Detecting and quantifying palaeoseasonality in stalagmites using geochemical and modelling approaches". In: *Quaternary Sci. Rev.* 254 (2021), p. 106784. DOI: 10.1016/j.quascirev.2020.106784.

23. Barigou, M. and Davidson, J.F. "Soap film drainage: theory of experiment". In: *Chem. Eng. Sci.* 49.11 (1994). DOI: 10.1016/0009-2509(94)80066-9.

24. Basaran, O. A. "Nonlinear oscillations of viscous liquid drops". In: *J. Fluid Mech.* 241 (1992), pp. 169–198. DOI: 10.1017/S002211209200199X.

25. Beard, K. V. "Terminal Velocity and Shape of Cloud and Precipitation Drops Aloft". In: *J. Atmos. Sc.* 33 (1976), pp. 851–864. DOI: 10.1175/15200469(1976)033<0851:TVASOC>2.0.CO;2.

26. Becker, E., hiller, W. J., and Kowalewski, T. A. "Experimental and theoretical investigation of large amplitude oscillations of liquid droplets". In: *J. Fluid Mech.* 231 (1991), pp. 189–210. DOI: 10.1098/rspl.1879.0015.

27. Beczek, M. et al. "The differences in crown formation during the splash on the thin water layers formed on the saturated soil surface and model surface". In: *PloS One* 12.7 (2017). DOI: 10.1371/journal.pone.0181974.

28. Belkofsi, R., Adjaoud, O., and Belabbas, I. "Pressure induced phase transitions and elastic properties of CaCO3 polymorphs: a density functional theory study". In: *Model. Simul. Mater. Sc.* (2018). DOI: 10.1088/1361-651X/aacbed.

29. Benjamin, T. B. "Gravity currents and related phenomena". In: *J. Fluid Mech.* 31 (1968), pp. 209–248. DOI: 10.1017/S0022112068000133.

30. Berberović, E. et al. "Drop impact onto a liquid layer of finite thickness: Dynamics of the cavity evolution". In: *Phys. Rev. E* 79 (2009). DOI: 10.1103/PhysRevE.79.036306.

31. Bergström, L. "Hamaker constants of inorganic materials". In: *Adv. Colloid Interfac.* 70 (1997), pp. 125–169. DOI: 10.1016/S0001-8686(97)00003-1.

32. Billiau, Marc. *Photography of a bat in Remouchamps Cave, Belgium.* 2012. URL: https://www.fotocommunity.com/photo/serotine-bat-mark-billiau/29099721 (visited on 10/2023).

33. Bouchet, G, Mebarek, M, and Dusek, J. "Hydrodynamic forces acting on a rigid fixed sphere in early transitional regimes". In: *Eur. J. Mech. B-Fluid* 25 (2006), pp. 321–336. DOI: 10.1016/j.euromechflu.2005.10.001.

34. Bourges, F et al. "Microclimates of L'Aven d'Orgnac and other french limestone caves (Chauvet, Esparros, Marsoulas)". In: *Int. J. Climatol.* 26 (2006), pp. 1651–1670. DOI: 10.1002/joc.1327.

35. Bradley, R. S. *Paleoclimatology. Reconstructing Climates of the Quaternary.* Third Edition. Academic Press, Elsevier, 2015. ISBN: 978-0-12-386913-5. DOI: 10.1016/C2009-0-18310-1.

36. Brahim, Y. A. et al. "Hydroclimate variability in the Caribbean during North Atlantic Heinrich cooling events (H8 and H9)". In: *Sci. Rep.-UK* 12 (2022). DOI: 10.1038/s41598-022-24610-x.

37. Breitenbach, J., Roisman, I.V., and Tropea, C. "From drop impact physics to spray cooling models: a critical review". In: *Exp. Fluids* 59.55 (2018). DOI: 10.1007/s00348-018-2514-3.

38. Bretherton, F. P. "The motion of long bubbles in tubes". In: *J. Fluid Mech.* 10.2 (1961), pp. 166–188. DOI: 10.1017/S0022112061000160.

39. Briggs, L. J. "Effect of spin and speed on the lateral deflection (curve) of a baseball; and the Magnus effect for smooth spheres". In: *Am. J. Phys.* 27.8 (1959), pp. 589–596. DOI: 10.1119/1.1934921.

40. Brusatte, S. L. et al. "The extinction of the dinosaurs". In: *Biol. Rev.* 90 (2015), pp. 628–642. DOI: 10.1111/brv.12128.

41. Buhmann, D. and Dreybrodt, W. "The kinetics of calcite dissolution and precipitation in geologically relevant situations of karst areas: 1. Open system". In: *Chem. Geol.* 48.1 (1985), pp. 189–211. DOI: 10.1016/0009-2541(85)90046-4.

42. Buhmann, D. and Dreybrodt, W. "The kinetics of calcite dissolution and precipitation in geologically relevant situations of karst areas: 2. Closed System". In: *Chem Geol* 53 (1985), pp. 109–124. DOI: 10.1016/0009-2541(85)90024-5.

43. Bulthuis, K. et al. "Uncertainty quantification of the multi-centennial response of the Antarctic ice sheet to climate change". In: *The Cryosphere* 13.4 (2019), pp. 1349–1380. DOI: 10.5194/tc-13-1349-2019.

44. Burns, S. et al. "A 780-year annually resolved record of Indian Ocean monsoon variation in a speleothem from south Oman". In: *J. Geophys. Res.* 107 (2002). DOI: 10.1029/2001jd001281.

45. Carman, P. C. and Haul, R. A. W. "Measurement of diffusion coefficients". In: *Proc. R. Soc. A* 222 (1954), pp. 109–118. DOI: 10.1098/rspa.1954.0056.

46. Caster, R. V. and Matar, O. K. "Dynamics and stability of thin liquid films". In: *Rev. Mod. Phys.* 81 (2009), pp. 1131–1198. DOI: 10.1103/RevModPhys.81.1131.

47. Catrejón-Pita, J. R. et al. "Mixing and internal dynamics of droplets impacting and coalescing on a solid surface". In: *Phys. Rev. E* 88 (2013). DOI: 10.1103/PhysRevE.88.023023.

48. Che, Z., Deygas, A., and Matar, O. K. "Impact of droplets on inclined flowing liquid films". In: *Phys. Rev. E* 92 (2015). DOI: 10.1103/PhysRevE.92.023032.

49. Chebotarev, A. N. et al. "The Brilliant Blue FCF Ion-Molecular Forms in Solutions According to the Spectrophotometry Data". In: *Russ. J. Phys. Chem. A* 91.10 (2017), pp. 1907–1912. DOI: 10.1134/S0036024417100089.

50. Chen, B., Tian, R., and Mao, F. "Analysis of special phenomena of droplet impact on horizontal liquid film at low velocity". In: *Ann. Nucl. Energy* 136 (2020). DOI: 10.1063/1.1708605.

51. Chen, N., Chen, H., and Amirfazli, A. "Drop impact onto a thin film: Miscibility effect". In: *Phys. Fluids* 29 (2017). DOI: 10.1063/1.5001743.

52. Clanet, C. and Lasheras, J. C. "Transition from dripping to jetting". In: *J. Fluid Mech.* 383 (1999), pp. 307–326. DOI: 10.1017/s0022112098004066.

53. Clanet, C. et al. "Maximal deformation of an impacting drop". In: *J. Fluid Mech.* 517 (2004), pp. 199–208. DOI: 10.1017/s0022112004000904.

54. Cossali, G. E., Coghe, A., and Marengo, M. "The impact of a single drop on a wetted solid surface". In: *Exp. Fluids* 22 (1997), pp. 463–472. DOI: 10.1007/s003480050073.

55. Cossali, G. E. et al. "The role of time in single drop splash on thin film". In: *Exp. Fluids* 36 (2004), pp. 888–900. DOI: 10.1007/s00348-003-0772-0.

56. Couchoud, I. "Oxygen and carbon stable isotopes in speleothems as palaeoenvironmental recorders". In: *Quaternaire* 19.4 (2008), pp. 271–295. DOI: 10.4000/quaternaire.4532.

57. Courant, R., Friedrichs, K., and Lewy, H. "Über die partiellen Differenzengleichungen der mathematischen Physik". In: *Math. Ann.* 100 (1928), pp. 32–74. DOI: 10.1007/BF01448839.

58. Crochet, Philippe. *Various photographs of caves and speleothems (2017–2023).* URL: https://www.philippe-crochet.com/ (visited on 10/2023).

59. Curl, R. L. "Minimum Diameter Stalactites". In: *J. Caves Karst Stud.* 34.4 (1972), pp. 129–136.

60. Curl, R. L. "Minimum Diameter Stalagmites". In: *J. Caves Karst Stud.* 35.1 (1973), pp. 1–9.

61. Cuvier, G. *Recherches sur les ossements fossiles: où l'on rétablit les charatères de plusieurs animaux dont les révolutions du globe ont détrui les espèces.* Paris: G. Dufour et E. D'Ocagne, 1825.

62. Davidson, M. R. "Spreading of an inviscid drop impacting on a liquid film". In: *Chem. Eng. Sci.* 57 (2002), pp. 3639–3647. DOI: 10.1016/S0009-2509(02)00266-X.

63. De Gennes, P.-G., Brochard-Wyart, F., and Quéré, D. *Capillarity and wetting phenomena. Drops, bubbles, pearls, waves.* Springer, 2004. DOI: 10.1007/978-0-387-21656-0.

64. Deike, L. "Mass transfer at the ocean–atmosphere interface: The Role of wave breaking, droplets, and bubbles". In: *Annu. Rev. Fluid Mech.* 54 (2022), pp. 191–224. DOI: 10.1146/annurev-fluid-030121-014132.

65. Dennis, P. F., Rowe, P. J., and Atkinson, T. C. "The recovery and isotopic measurement of water from fluid inclusions in speleothems". In: *Geochim. Cosmochim. Ac.* 65.6 (2001), pp. 871–884. DOI: 10.1016/S0016-7037(00)00576-7.

66. Dowson, D. "A generalized Reynolds equation for fluid-film lubrication". In: *Int. J. Mech. Sci.* 4.2 (1962), pp. 159–170. DOI: 10.1016/S0020-7403(62)80038-1.

67. Dreybrodt, W. "A possible mechanism for growth of calcite speleothems without participation of biogenic carbon dioxide". In: *Earth and Planet Sc. Lett.* 58.2 (1982), pp. 293–299. DOI: 10.1016/0012-821X(82)90202-3.

68. Dreybrodt, W. "Chemical kinetics, speleothem growth and climate". In: *Boreas* 28 (1999), pp. 347–356. DOI: 10.1111/j.1502-3885.1999.tb00224.x.

69. Dreybrodt, W. "Deposition of calcite from thin films of natural calcareous solutions and the growth of speleothems". In: *Chem. Geol.* 29 (1980), pp. 89–105. DOI: 10.1016/0009-2541(80)90007-8.

70. Dreybrodt, W. *Processes in Karst Systems. Physics, Chemistry, and Geology*. Springer series in physical environment, 1988. DOI: 10.1007/978-3-642-83352-6.

71. Dreybrodt, W. "The kinetics of calcite precipitation from thin films of calcareous solutions and the growth of speleothems: Revisited". In: *Chem. Geol.* 32.1 (1981), pp. 237–245. DOI: 10.1016/0009-2541(81)90146-7.

72. Duan, W. et al. "The growth mechanism of the aragonitic stalagmite laminae from Yunnan Xianren Cave, SW China revealed by cave monitoring". In: *Boreas* 41 (2012), pp. 113–123. DOI: 10.1111/j.1502-3885.2011.00226.x.

73. Duan, Z., He, B., and Duan, Y. "Sphere Drag and Heat Transfer". In: *Sci. Rep.-UK* 5 (2015). DOI: 10.1038/srep12304.

74. Duprat, C., Ruyer-Quil, C., and Giorgiutti-Dauphiné, F. "Spatial evolution of a film flowing down a fiber". In: *Phys. Fluids* 21 (2009). DOI: 10.1063/1.3119811.

75. Eggers, J., Lister, J. R., and Stone, H. A. "Coalescence of liquid drops". In: *J. Fluid Mech.* 401 (1999), pp. 293–310. DOI: 10.1017/S002211209900662X.

76. Elias, S. A. and Mock, C. J. *Encyclopedia of Quaternary Science*. Second Edition. Elsevier, 2013. ISBN: 978-0-444-52747-9.

77. Engel, O. G. "Crater depth in fluid impacts". In: *J. Appl. Phys.* 37 (1966), pp. 1798–1808. DOI: 10.1063/1.1708605.

78. Epstein, S. et al. "Revised carbonate-water isotopic temperature scale". In: *Bull. Geol. Soc. Amer.* 64 (1953), pp. 1315–1326. DOI: 10.1130/0016-7606(1953)64[1315:RCITS]2.0.CO;2.

79. Ern, P. et al. "Wake-induced oscillatory paths of bodies freely rising or falling in fluids". In: *Annu. Rev. Fluid Mech.* 44 (2012), pp. 97–121. DOI: 10.1146/annurev-fluid-120710-101250.

80. Ersoy, N. E. and Eslamian, M. "Capillary surface waves formation and mixing of miscible liquids during drop impact onto a liquid film". In: *Phys. Fluids* 31 (2019). DOI: 10.1063/1.5064640.

81. Ersoy, N. E. and Eslamian, M. "Central uprising sheet in simultaneous and near-simultaneous impact of two high kinetic energy droplets onto dry surface and thin liquid film". In: *Phys. Fluids* (2020). DOI: 10.1063/1.5135029.

82. Ersoy, N. E. and Eslamian, M. "Phenomenological study and comparison of droplet impact dynamics on a dry surface, thin liquid film, liquid film and shallow pool". In: *Exp. Therm. Fluid Sc.* 112 (2020). DOI: 10.1016/j.expthermflusci.2019.109977.

83. Evans, J. P. and Jakeman, A. J. "Development of a simple, catchment-scale, rainfall-evapotranspiration-runoff model". In: *Environ. Modell. Softw.* 13 (1998), pp. 385–393. DOI: 10.1016/S1364-8152(98)00043-7.

84. Fairchild, I. J. and Baker, A. *Speleothem Science: From Process to Past Environments*. Wiley-Blackwell, 2012.

85. Falla, R. et al. "Mesh adaption for two-dimensional bounded and free-surface flows with the particle finite element method". In: *Comp. Part. Mech.* 10 (2023), pp. 477–518. DOI: 10.1007/s40571-022-00541-2.

86. Fedorchenko, A. I. and Wang, A.-B. "On some common features of drop impact on liquid surfaces". In: *Phys. Fluids* 16.5 (2004), pp. 1349–1365. DOI: 10.1063/1.1652061.

87. Ferron, G. A. and Soderholm, S. C. "Estimation of the times for evaporation of pure water droplets and for stabilization of salt solution particles". In: *J. Aerosol. Sci.* 21.3 (1990), pp. 412–429. DOI: 10.1098/rspa.2019.0556.

88. Fick, A. "V. On liquid diffusion". In: *London Edinburgh Dublin Philos. Mag. J. Sci.* 10.63 (1855), pp. 30–39. DOI: 10.1080/14786445508641925.

89. Ford, D. and Williams, P. *Karst hydrogeology and geomorphologys*. London: Unwin Hyman Ltd., 1989.

90. Franke, H. W. "The Theory behind stalagmite shapes". In: *Studies Speleol.* 1 (1965), pp. 89–95.

91. Fritts, H. C. *Tree rings and climate*. New York: Academic Press, Elsevier, 1976.

92. Fu, B. et al. "Evaporation heat transfer in thin-film region with bulk vapor flow effect". In: *J. Heat Transfer* 140 (2018). DOI: 10.1115/1.4037448.

93. Garcia-Geijo, P., Riboux, G., and Gordillo, J. M. "Inclined impact of drops". In: *J. Fluid Mech.* 897 (2020). DOI: 10.1017/jfm.2020.373.

94. Gelderblom, H. et al. "How water droplets evaporate on a superhydrophobic substrate". In: *Phy. Rev. E* 83 (2011). DOI: 110.1103/PhysRevE.83.026306.

95. Genty, D., Baker, A., and Barnes, W. "Comparison of annual luminescent and visible laminae in stalagmites". In: *Comptes Rendus de l'Académie des Sciences - Series IIA - Earth and Planetary Science* 325.3 (1997), pp. 193–200. DOI: 10.1016/S1251-8050(97)88288-2.

96. Genty, D., Baker, A., and Vokal, B. In: *Chem. Geol.* 176.1 (2001), pp. 191–212. DOI: 10.1016/S0009-2541(00)00399-5.

97. Genty, D., Baker, A., and Vokal, B. "Intra- and inter-annual growth rate of modern stalagmites". In: *Chem. Geol.* 176 (2001), pp. 191–212. DOI: 10.1016/s0009-2541(00)00399-5.

98. Genty, D. and Deflandre, G. "Drip flow variations under a stalactite of the Père Noël cave (Belgium). Evidence of seasonal variations and air pressure constraints". In: *J. Hydrol.* 211 (1998). DOI: 10.1016/s0022-1694(98)00235-2.

99. Genty, D. et al. "Rainfall and cave water isotopic relationships in two South-France sites". In: *Geochim. Cosmochim. Ac.* 131 (2014), pp. 323–343. DOI: 10.1016/j.gca.2014.01.043.

100. Gilet, T. and Bourouiba, L. "Fluid fragmentation shapes rain-induced foliar disease transmission". In: *J. R. Soc. Interface* 12 (2015). DOI: 10.1098/rsif.2014.1092.

101. Gilet, T. et al. "Critical parameters for the partial coalescence of a droplet". In: *Phys. Rev. E* 75 (2007). DOI: 10.1103/PhysRevE.75.036303.

102. Goldscheider, N. et al. "Global distribution of carbonate rocks and karst water resources". In: *Hydrogeol. J.* 28 (2020). DOI: 10.1007/s10040-020-02139-5.

103. Gordillo, J., Riboux, G., and Quintero, E. S. "A theory on the spreading of impacting droplets". In: *J. Fluid Mech.* 866 (2019). DOI: 10.1017/jfm.2019.117.

104. Gräb, P. and Geidel, E. "Spectroscopic studies of food colorings". In: *World J. Chem. Ed.* 7.2 (2019), pp. 136–144. DOI: 10.12691/wjce-7-2-13.

105. Gradzinaki, M. "Bacterial influence on speleothem oxygen isotope composition: An example based on cave pisoids from Perlová Cave". In: *Geol. carpath.* 54.3 (2003), pp. 199–204. DOI: 10.1016/0031-9422(81)85134-5.

106. Gratton, J. and Minotti, F. "Self-similar viscous gravity currents: phase-plane formalism". In: *Journal of Fluid Mechanics* 210 (1990), pp. 155–182. DOI: 10.1017/S0022112090001240.

107. Griffiths, R. W. "The Dynamics of Lava Flows". In: *Ann. Rev. Fluid Mech.* 32 (2000), pp. 477–518. DOI: 10.1146/annurev.fluid.32.1.477.

108. Guo, R. et al. "Flow characteristics and thickness distribution of liquid film in trickle bed reactor". In: *Powder Technol.* 407 (2022). DOI: 10.1016/j.powtec.2022.117739.

109. Hays, J. D., Imbrie, J., and Shackleton, N. J. "Variations in the Earth's orbit: Pacemaker of the Ice Ages". In: *Science* 194 (1976), pp. 1121–1132. DOI: 10.1126/science.194.4270.1121.

110. Hendy, C. H. "The isotopic geochemistry of speleothems - I. The calculation of the effects of different modes of formation on the isotopic composition of speleothems and their applicability as palaeoclimatic indicators". In: *Geochim. Cosmochim. Ac.* 35 (1971), pp. 801–824. DOI: 10.1016/0016-7037(71)90127-X.

111. Hill, C. A. and F., P. "The Classification of cave minerals and speleothems". In: *Int. J. Speleol.* 24 (1995), pp. 77–82. DOI: 10.5038/1827-806X.24.1.5.

112. Hirsch, C. *Numerical computation of internal and external flows*. Elsevier, 2007. ISBN: 978-0-7506-6594-0. DOI: 10.1016/B978-0-7506-6594-0.X5037-1.

113. Hoffmann, D. L. et al. "U-Th dating of carbonate crusts reveals Neandertal origin of Iberian cave art". In: *Science* 359 (2018), pp. 912–915. DOI: 10.1126/science.aap7778.

114. Holton, J. R. *An introduction to dynamic meteorology*. 4th ed. International Geophysics Series. Burlington, MA: Elsevier Academic Press, 2004. ISBN: 9780123540157. URL: http://books.google.com/books?id=fhW5oDv3EPsC.

115. Howison, S. D. et al. "Droplet impact on a thin fluid layer". In: *J. Fluid Mech.* 542 (2005), pp. 1–23. DOI: 10.1017/s0022112005006282.

116. Huppert, H. E. "The propagation of two-dimensional and axisymmetric viscous gravity currents over a rigid horizontal surface". In: *J. Fluid Mech.* 121 (1982), pp. 43–58. DOI: 10.1017/S0022112082001797.

117. Incropera, F. P. et al. *Incropera's Principles of heat and mass transfer*. Wiley, 2017. DOI: 10.1007/s00348-018-2514-3.

118. Innes, J. L. "Lichenometry". In: *Prog. Phys. Geog.* 9.2 (1985), pp. 187–254. DOI: 10.1177/030913338500900202.

119. IPCC. *Climate Change 2022: Impacts, Adaptation, and Vulnerability. Contribution of Working Group II to the Sixth Assessment Report of the Intergovernmental Panel on Climate Change*. Ed. by Cambridge University Press. Cambridge, UK and New York, NY, USA, 2022. DOI: 10.1017/9781009325844.

120. Jalaal, M., Seyfert, C., and Snoeijer, J. H. "Capillary ripples in thin viscous films". In: *J. Fluid Mech.* 880 (2019), pp. 430–440. DOI: 10.1017/jfm.2019.734.

121. Jaubert1, J. et al. "Early Neanderthal constructions deep in Bruniquel Cave in southwestern France". In: *Nature* 534 (2016). DOI: 10.1038/nature18291.

122. Jayaratne, O. W. and Mason, B. J. "The coalescence and bouncing of water drops at an air/water interface". In: *Proc. R. Soc. A* 280 (1383 1964), pp. 545–565. DOI: 10.1098/rspa.1964.0161.

123. Jeffery, W. R. "Adaptive evolution of eye degeneration in the mexican blind cavefish". In: *J. Hered.* 96.3 (2005), pp. 185–196. DOI: 10.1093/jhered/esi028.

124. Johnson, T. A. and Patel, V. C. "Flow past a sphere up to a Reynolds number of 300". In: *J. Fluid Mech.* 378 (1999), pp. 19–70. DOI: 10.1017/s0022112098003206.

125. Jones, D. A. and Clarke, D. B. *Simulation of Flow Past a Sphere using the Fluent Code.* Australia: Maritime Platforms Division. DSTO Defence Science and Technology Organisation, 2008.

126. Jones, P. "The reliability of global and hemispheric surface temperature records". In: *Adv. Atmos. Sci.* 33 (2016), pp. 269–282. DOI: 10.1007/s00376-015-5194-4.

127. Josserand, C., Ray, P., and Zaleski, S. "Droplet impact on a thin liquid film: anatomy of the splash". In: *J. Fluid Mech.* 802 (2016), pp. 775–805. DOI: 10.1017/jfm.2016.468.

128. Josserand, C. and Thoroddsen, S. "Drop impact on a solid surface". In: *Annu. Rev. Fluid Mech.* 48 (2016), pp. 365–391. DOI: 10.1146/annurev-fluid-122414-034401.

129. Josserand, C. and Zaleski, S. "Droplet splashing on a thin liquid film". In: *Phys. Fluids* 15 (2003), pp. 1650–1657. DOI: 10.1063/1.1572815.

130. Joung, Y. and Buie, C. "Aerosol generation by raindrop impact on soil". In: *Nat. Commun.* 6 (2015). DOI: 10.1038/ncomms7083.

131. Ju, W. et al. "Visual experimental study of droplet impinging on liquid film and analysis of droplet evolution characteristics". In: *Exp. Comput. Multiph. Flow* (2020). DOI: 10.1007/s42757-020-0081-3.

132. Kalliadasis, S. et al. *Falling liquid films.* 4th ed. London: Springer, 2012, p. 535. ISBN: 978-1-84882-366-2. URL: www.springer.com/series/34.

133. Kaufmann, G. "Stalagmite growth and palaeo-climate: the numerical perspective". In: *Earth and Planet Sc. Lett.* 214 (2003), pp. 251–266. DOI: 10.1016/s0012-821x(03)00369-8.

134. Keeling, C. D. "The Concentration and isotopic abundances of carbon dioxide in the atmosphere". In: *Tellus* 12.2 (1960), pp. 200–203. DOI: 10.3402/tellusa.v12i2.9366.

135. Kim, M., Moon, M. B.-U., and Hidrovo, C. H. "Enhancement of the thermo-mechanical properties of PDMS molds for the hot embossing of PMMA microfluidic devices". In: *J. Micromech. Microeng.* 23.9 (2013). DOI: 10.1088/0960-1317/23/9/095024.

136. Kittel, H. M., Roisman, I. V., and Tropea, C. "Splash of a drop impacting onto a solid substrate wetted by a thin film of another liquid". In: *Phys. Rev. Fluids* 3 (2018). DOI: 10.1103/PhysRevFluids.3.073601.

137. Koch, K. and Grichnik, R. "Influence of surface structure and chemistry on water droplet splashing". In: *Phil. T. R. Soc. A* 374 (2016). DOI: 10.1098/rsta.2016.0183.

138. Kumar, K., Nikolov, A. D., and Wasan, D. T. "Effect of film curvature on drainage of thin liquid films". In: *J. Colloid Interf. Sci.* 256 (2002), pp. 194–200. DOI: 10.1006/jcis.2001.8096.

139. Laan, N. et al. "Maximum diameter of impacting liquid droplets". In: *Phys. Rev. Appl.* 2 (2014). DOI: 10.1103/PhysRevApplied.2.044018.

140. Labuhn, I. et al. "A high-resolution fluid inclusion $\delta180$ record from a stalagmite in SW France: modern calibration and comparison with multiple proxies". In: *Quaternary Sci. Rev.* 110 (2015), pp. 152–165. DOI: 10.1016/j.quascirev.2014.12.021.

141. Lachiet, M. S. "Are aragonite stalagmites reliable paleoclimate proxies? Tests for oxygen isotope time-series replication and equilibrium". In: *Geol. Soc. Am. Bull.* 110 (2015), pp. 1521–1533. DOI: 10.1130/B31161.1.

142. Lamb, H. "On the oscillations of a viscous spheroid". In: *Proc. Lond. Math. Soc.* 13 (1881). DOI: 10.1112/plms/s1-13.1.51.

143. Lázár, A. et al. "Insights into the amorphous calcium carbonate (ACC) → ikaite → calcite transformations". In: *CrystEngComm* 25 (2023), pp. 738–750. DOI: 10.1039/D2CE01444K.

144. Lejeune, S. and Gilet, T. "Drop impact close to the edge of an inclined substrate: Liquid sheet formation and breakup". In: *Phys. Rev. Fluids* 4 (2019). DOI: 10.1103/PhysRevFluids.4.053601.

145. Lejeune, S., Gilet, T., and Bourouiba, L. "Edge effect: Liquid sheet and droplets formed by drop impact close to an edge". In: *Phys. Rev. Fluids* 3 (2018). DOI: 10.1103/PhysRevFluids.3.083601.

146. Levin, Z. and Hobbs, P. V. "Splashing of water drops on solid and wetted surfaces: Hydrodynamics and charge separation". In: *Philos. T. R. Soc. S.-A* 269 (1971), pp. 555–585. DOI: 10.1098/rsta.1971.0052.

147. Li, H. et al. "Response of soil aggregate disintegration to antecedent moisture during splash erosion". In: *CATENA* 234 (2024). DOI: 10.1016/j.catena.2023.107633.

148. Liang, G. et al. "Successive impact of multiple droplets on liquid film". In: *Eur. J. Mech. B - Fluids* (2018). DOI: 10.1016/j.euromechflu.2018.09.011.

149. Linge, H. et al. "Variability in luminescent lamination and initial 230Th/232Th activity ratios in a late Holocene stalagmite from northern Norway". In: *Quat. Geochronol.* 4 (2009), pp. 181–192. DOI: 10.1016/j.quageo.2009.01.009.

150. Lister, J. R., Peng, G. G., and Neufeld, J. A. "Viscous control of peeling an elastic sheet by bending and pulling". In: *Phys. Rev. Lett.* 111 (2012), pp. 194–200. DOI: 10.1103/PhysRevLett.111.154501.

151. Liu, Q. and Orme, M. "High precision solder droplet printing technology and the state-of-the-art". In: *J. Mater. Process. Tech.* 115 (2001), pp. 271–283. DOI: 10.1016/S0924-0136(01)00740-3.

152. Liu, Y., Zheng, Z., and Stone, H. A. "The influence of capillary effects on the drainage of a viscous gravity current into a deep porous medium". In: *J. Fluid Mech.* 817 (2017), pp. 514–559. DOI: 10.1017/jfm.2017.125514.

153. Liu, Y., Zheng, Z., and Stone, H. A. "The influence of capillary effects on the drainage of a viscous gravity current into a deep porous medium". In: *J. Fluid Mech.* 817 (2017), pp. 514–559. DOI: 10.1017/jfm.2017.125514.

154. Liu, Y., Zheng, Z., and Stone, H. A. "The influence of capillary effects on the drainage of a viscous gravity current into a deep porous medium". In: *J. Fluid Mech.* 817 (2017), pp. 514–559. DOI: 10.1017/jfm.2017.125514.

155. Liu, Y. et al. "Symmetry breaking in drop bouncing on curved surfaces". In: *Nat. Commun.* (2015). DOI: 10.1038/ncomms10034.

156. Lugt, P. M. "A Review on grease lubrication in rolling bearings". In: *Proc. R. Soc. Lond. A* (2008), pp. 470–480. DOI: 10.1080/10402000802687940.

157. Macklin, W. C. and Metaxas, G. J. "Splashing of drops on liquid layers". In: *J. Appl. Phys.* 47 (1976). DOI: 10.1063/1.323218.

158. Manning, S. W. et al. "Severe multi-year drought coincident with Hittite collapse around 1198–1196 BC". In: *Nature* 614.2 (2023), pp. 719–724. DOI: 10.1038/s41586-022-05693-y.

159. Maqbool, K. et al. "Study of non-Newtonian synovial fluid flow by a recursive approach". In: *Phys. Fluids* 34 (2022). DOI: 10.1063/5.0121918.

160. Marengo, M. et al. "Drop collisions with simple and complex surfaces". In: *Current Opinion in Colloid & Interface Science* 16.4 (2011), pp. 292–302. DOI: 10.1016/j.cocis.2011.06.009.

161. Mariethoz, G. et al. "Chaos and irregularity in karst percolation". In: *Geophys. Res. Lett.* 39 (2012). DOI: 10.1029/2012gl054270.

162. Markt, D. et al. "Computational characterization of the secondary droplets formed during the impingement of a train of ethanol drops". In: *Int. J. Engine Res.* (2019). DOI: 10.1177/1468087419879623.

163. Mazur, R. et al. "Soil deformation after one water-drop impact - The effect of texture and soil moisture content". In: *Geoderma* 417 (2022). DOI: 10.1016/j.geoderma.2022.115838.

164. McDonough, L. K. et al. "Past fires and post-fire impacts reconstructed from a southwest Australian stalagmite". In: *Geochim. Cosmochim. Ac.* 325 (2022), pp. 258–277. DOI: 10.1016/j.gca.2022.03.020.

165. Meyers, S. R. and Malinverno, A. "Proterozoic Milankovitch cycles and the history of the solar systems". In: *Proc. Natl. Acad. Sci. U.S.A.* 115.25 (2018), pp. 6363–6368. DOI: 10.1073/pnas.1717689115.

166. Momen, M. et al. "Inertial gravity currents produced by fluid drainage from an edge". In: *J. Fluid Mech.* 827 (2017), pp. 640–663. DOI: 10.1017/jfm.2017.480.

167. Moodie, T.B. "Gravity currents". In: *J. Comput. Appl. Math.* 144 (2002), pp. 49–83. DOI: 10.1016/S0377-0427(01)00551-9.

168. Moreira, A. L. N., Moita, A. S., and Panão, M. R. "Advances and challenges in explaining fuel spray impingement: How much of single droplet impact research is useful?" In: *Prog. Energ. Combust.* 36 (2010), pp. 554–580. DOI: 10.1016/j.pecs.2010.01.002.

169. Nakouzi, E., Goldstein, R. E., and Steinbock, O. "Do Dissolving Objects Converge to a Universal Shape?" In: *Langmuir* 31.14 (2015), pp. 4145–4150. DOI: 10.1021/la503562z.

170. O'Leary, M. H. "Carbon isotope fractionation in plants". In: *Phytochemistry* 20.4 (1981), pp. 553–567. DOI: 10.1016/0031-9422(81)85134-5.

171. Parmentier, J., Terrapon, V., and Gilet, T. "Drop impact on thin film: Mixing, thickness variations, and ejections". In: *Phys. Rev. Fluids* 8 (2023). DOI: 10.1103/PhysRevFluids.8.053603.

172. Parmentier, J. et al. "A drop does not fall in a straight line: a rationale for the width of stalagmites". In: *Proc. R. Soc. A* 475 (2019). DOI: 10.1098/rspa.2019.0556.

173. Ploumhans, P. et al. "Vortex Methods for Direct Numerical Simulation of three-dimensional bluff body flows: Application to the sphere at Re = 300, 500, and 1000". In: *J. Comput. Phys* 178 (2002), pp. 427–463. DOI: 10.1006/jcph.2002.7035.

174. Plummer, L. N., Wigley, T. M. L., and Parkhurst, D. L. "The Kinetics of calcite dissolution in CO_2-water systems at 5 °C to 60 °C and 0.0 atm to 1.0 atm CO_2". In: *Am. J. Sci.* 278 (1978), pp. 179–216.

175. Quarteroni, A. and Valli, A. *Numerical approximation of partial different equations*. Vol. 23. Springer Link, Jan. 1994.

176. Raman, K. A. et al. "Dynamics of simultaneously impinging drops on a dry surface: Role of impact velocity and air inertia". In: *J. Colloid Interf. Sci.* 486 (2017), pp. 265–278. DOI: 10.1103/PhysRevFluids.5.023602.

177. Ray, B., Biswas, G., and Sharma, A. "Regimes during liquid drop impact on a liquid pool". In: *J. Fluid Mech.* 768 (2015), pp. 492–523. DOI: 10.1017/jfm.2015.108.

178. Redon, C., Brochard-Wyart, F., and Rondelez, F. "Dynamics of dewetting". In: *Phys. Rev. Lett.* 66 (1991). DOI: 10.1103/PhysRevLett.66.715.

179. Rein, M. "Phenomena of liquid drop impact on solid and liquid surfaces". In: *Fluid Dyn. Res.* 12 (1993), pp. 61–93. DOI: 10.1016/0169-5983(93)90106-K.

180. Reynolds, O. "IV. On the theory of lubrication and its application to Mr. Beauchamp Tower's experiments, including an experimental determination of the viscosity of olive oil". In: *Phil. Trans. R. Soc.* 177 (1886), pp. 157–234. DOI: 10.1098/rstl.1886.0005.

181. Reyssat, E. "Gouttes, films et jets : quand les écoulements modèlent les interfaces". PhD thesis. Université Paris-Diderot - Paris VII, 2007. URL: https://tel.archives-ouvertes.fr/tel-00169432.

182. Reyssat, E. et al. "Shape and instability of free-falling liquid globules". In: *Europhys. Lett.* 80 (2007). DOI: 10.1209/0295-5075/80/34005.

183. Rioboo, R., Marengo, M., and Tropea, C. "Time evolution of liquid drop impact onto solid, dry surfaces". In: *Exp. Fluids* 33 (2002), pp. 112–124. DOI: 10.1007/s00348-002-0431-x.

184. Rioboo, R., Tropea, C., and Marengo, M. "Outcomes from a drop impact on solid surfaces". In: *Atomization Spray* 11 (2001), pp. 155–165. DOI: 10.1615/AtomizSpr.v11.i2.40.

185. Rioboo, R. et al. "Experimental investigation of splash and crown formation during single drop impact on wetted surfaces". In: *Exp. Fluids* 35 (2003), pp. 648–652. DOI: 10.1007/s00348-003-0719-5.

186. Rodriguez, I. et al. "Direct numerical simulation of the flow over a sphere at Re = 3700". In: *J. Fluid Mech.* 679 (2011), pp. 263–287. DOI: 10.1017/jfm.2011.136.

187. Roisman, I. V., Horvat, K., and Tropea, C. "Spray impact: Rim transverse instability initiating fingering and splash, and description of a secondary spray". In: *Phys. Fluids* 18 (2006). DOI: 10.1063/1.2364187.

188. Roisman, I. V. and Tropea, C. "Impact of a drop onto a wetted wall: description of crown formation and propagation". In: *J. Fluid Mech.* 472 (2002), pp. 373–397. DOI: 10.1017/jfm.2019.117.

189. Romanov, D. and Dreybrodt, W. "Regular stalagmites: the theory behind their shape". In: *Acta Carsol.* 37.2 (2008), pp. 175–184. DOI: 10.3986/ac.v37i2-3.145.

190. Romanov, D., Kaufmann, G., and Dreybrodt, W. "Modeling stalagmite growth by first principles of chemistry and physics of calcite precipitation". In: *Geochim. Cosmochim. Ac.* 72 (2008), pp. 423–437. DOI: 10.1016/j.gca.2007.09.038.

191. Rossi, C. and Lozano, R. "Hydrochemical controls on aragonite versus calcite precipitation in cave dripwaters". In: *Geochim. Cosmochim. Ac.* 192 (2016), pp. 70–96. DOI: 10.1016/j.gca.2016.07.021.

192. Royne, A., Dalby, K. N., and Hassenkam, T. "Repulsive hydration forces between calcite surfaces and their effect on the brittle strength of calcite-bearing rocks". In: *Geophys. Res. Lett.* 42 (2015), pp. 4786–4794. DOI: 10.1002/2015GL064365.

193. Schopf, T. J. M. *Paleoceanography*. Harvard University Press, 1980. DOI: 10.4159/harvard.9780674432888.

194. Seiwert, J. et al. "Drainage on a rough surface". In: *Europhys. Lett.* 94 (2011). DOI: 10.1209/0295-5075/94/16002.

195. Sherwin, C. M. and Baldini, J. U. L. "Cave air and Hydrological controls on prior calcite precipitation and stalagmite growth rates: Implications for palaeoclimate reconstructions using speleothems". In: *Geochim. Cosmochim. Ac.* 75 (2011), pp. 3915–3929. DOI: 10.1016/j.gca.2011.04.020.

196. Short, M. B., Baygents, J. C., and Goldstein, R. E. "Stalactite growth as a free-boundary problem". In: *Phys. Fluids* 17 (2005). DOI: 10.1063/1.2006027.

197. Short, M. B. et al. "Stalactite growth as a free-boundary problem: A Geometric law and its platonic ideal". In: *Phys. Rev. Lett.* 94 (2005). DOI: 10.1103/physrevlett.94.018501.

198. Simpson, J. E. "Gravity currents in the laboratory, atmosphere, and ocean". In: *Ann. Rev. Fluid Mech.* 14 (1982), pp. 213–234. DOI: 10.1146/annurev.fl.14.010182.001241.

199. Sly, M. K. et al. "Low-temperature rheology of calcite". In: *Geophys. J. Int.* 221 (2020), pp. 129–141. DOI: 10.1093/gji/ggz577.

200. Smith, C. et al. "Reconstructing regional climates from multiple stalagmite records". In: *Int. J. Climatol.* 26 (2006), pp. 1417–1424. DOI: 10.1002/joc.1329.

201. Song, J.-W. and Fan, L.-W. "Temperature dependence of the contact angle of water: A review of research progress, theoretical understanding, and implications for boiling heat transfer". In: *Adv. Colloid Interfac. Sci.* 288 (2021). DOI: 10.1016/j.cis.2020.102339.

202. Soto, D. et al. "The force of impacting rain". In: *Soft Matter* 10 (2014). DOI: 10.1039/c4sm00513a.

203. Spence, D. A. and Sharp, P. "Self-similar solutions for elastohydrodynamic cavity flow". In: *Proc. R. Soc. Lond. A* 400 (1985), pp. 289–313. DOI: 10.1098/rspa.1985.0081.

204. Spötl, C. et al. "Thermoelasticity of ice explains widespread damage in dripstone caves during glacial periods". In: *Sci. Rep.* 13 (2023), pp. 2155–2158. DOI: 10.1038/s41598-023-34499-9.

205. Stegner, M. A. and Spanbauer, T. L. "North American pollen records provide evidence for macroscale ecological changes in the Anthropocene". In: *Proc. Natl. Acad. Sci. U.S.A.* 120.43 (2023). DOI: 10.1073/pnas.2306815120.

206. Stevens, C. S., Latka, A., and Nagel, S. R. "Droplet impact: Viscosity and wettability effects on splashing". In: *Journal of Colloid and Interface Science* 553 (2019), pp. 22–30. DOI: 10.1016/j.jcis.2019.05.101.

207. Strullu-Derrien, C., Servais, T., and Kenrick, P. "Insights into palaeobotany". In: *Bot. Lett.* 170.2 (2023), pp. 157–164. DOI: 10.1080/23818107.2023.2200293.

208. Strutt, J. W. "I. Notes on the theory of lubrication". In: *London Edinburgh Dublin Philos. Mag. J. Sci.* 35.205 (1918), pp. 1–12. DOI: 10.1080/14786440108635730.

209. Strutt[5], J. W. "VI. On the capillary phenomena of jets". In: *London Edinburgh Dublin Philos. Mag. J. Sci.* 29 (1879), pp. 71–97. DOI: 10.1098/rspl.1879.0015.

210. Sykes, T. C. et al. "Surface jets and internal mixing during the coalescence of impacting and sessile droplets". In: *Phys. Rev. Fluids* 5 (2020). DOI: 10.1103/PhysRevFluids.5.023602.

[5]Lord Rayleigh, O.M. F.R.S. (Order of Merit Fellow of the Royal Society)

211. Tan, M. et al. "Applications of stalagmite laminae to paleoclimate reconstructions: Comparison with dendrochronology/climatology". In: *Quaternary Sci. Rev.* 25 (2006). DOI: 10.1016/j.quascirev.2006.01.034.

212. Taniguchi, M. and Lindsey, J. S. "Database of Absorption and Fluorescence Spectra of >300 Common Compounds for use in PhotochemCAD". In: *Photochem Photobiol* 94 (2018), pp. 290–327. DOI: 10.1111/php.12860.

213. Taylor, R. E. *Radiocarbon dating: An Archaeological perspective*. New York: Academic Press, Elsevier, 1987.

214. The Engineering ToolBox. *Evaporation from a Water Surface.* 2004. URL: https://www.engineeringtoolbox.com/evaporation-water-surface-d_690.html (visited on 09/26/2023).

215. Tisato, N. et al. "Microbial mediation of complex subterranean mineral structures". In: *Sci. Rep.* 5 (2015). DOI: 10.1038/srep15525.

216. Usdowski, E. "Reactions and equilibria in the systems CO_2 and H_2O and $CaCO_3 - CO_2 - H_2O$ ($0\,°C - 50\,°C$) - A Review". In: *N. Jb. Miner. Abh.* 144.2 (1982), pp. 148–171. DOI: 10.1127/njma/144/1982/148.

217. Varanasi, K. K. et al. "Hierarchical superhydrophobic surfaces resist water droplet impact". In: *Tech. Proc. NSTI Conf.* (2009).

218. Verheyden, S. et al. "Late-glacial and Holocene climate reconstruction as inferred from a stalagmite - Grotte du Père Noël, Han-sur-Lesse, Belgium". In: *Geol. Belg.* 17.1 (2014), pp. 83–89.

219. Verheyden, S. et al. "Mg, Sr and Sr isotope geochemistry of a Belgian Holocene speleothem: implications for paleoclimate reconstructions". In: *Chem. Geol.* 169 (2000), pp. 131–144. DOI: 10.1016/S0009-2541(00)00299-0.

220. Verheyden, S. et al. "Paleoclimate reconstruction in the Levant region from the geochemistry of a Holocene stalagmite from the Jeita cave, Lebanon". In: *Quat. Res.* 70 (2008), pp. 368–381. DOI: 10.1016/j.yqres.2008.05.004.

221. Vernay, C. et al. "Drop impact experiment as a model experiment to investigate the role of oil-in-water emulsions in controlling the drop size distribution of an agricultural spray". In: *Atomization Spray* 26.8 (2016). DOI: 10.1615/AtomizSpr.2015013630.

222. Vesipa, R., Camporeale, C., and Ridolfi, L. "Thin-film-induced morphological instabilities over calcite surfaces". In: *Proc. R. Soc. A* 471 (2015). DOI: 10.1098/rspa.2015.0031.

223. Villermaux, E. and Bossa, B. "Drop framgentation on impact". In: *J. Fluid Mech.* 668 (2011), pp. 412–435. DOI: 10.1017/S002211201000474X.

224. Villermaux, E. and Bossa, B. "Single-drop fragmentation determines size distribution of raindrops". In: *Nat. Phys.* 5 (2009), pp. 697–702. DOI: 10.1038/NPHYS1340.

225. Wagner, G. A. *Age determination of young rocks and artifacts*. Berlin: Springer, 1995.

226. Walentowitz, A. et al. "Long-term trajectories of non-native vegetation on islands globally". In: *Ecol. Lett.* 26 (2023), pp. 729–741. DOI: 10.1111/ele.14196.

227. Wang, A.-B. and Chen, C.-C. "Splashing impact of a single drop onto very thin liquid films". In: *Phys. Fluids* 12 (2000), pp. 2155–2158. DOI: 10.1063/1.1287511.

228. Wang, Y. et al. "Millennial- and orbital-scale changes in the East Asian monsoon over the past 224,000 years". In: *Nature* 451 (2008), pp. 1090–1093. DOI: 10.1038/nature06692.

229. Weiss, D. A. and Yarin, A. L. "Single drop impact onto liquid films: Neck distortion, jetting, tiny bubble entrainment, and crown formation". In: *J. Fluid Mech.* 385 (1999), pp. 229–254. DOI: 10.1017/S002211209800411X.

230. White, W. B. *Geomorphology and Hydrology of Karst Terrains*. New York: Oxford University Press, 1988. ISBN: 978-0195044447.

231. White, W. B., Culver, D. C., and Pipan, T. *Encyclopedia of Caves*. Third Edition. Academic Press, Elsevier, 2019. ISBN: 978-0-12-814124-3. DOI: 10.1016/C2017-0-01162-X.

232. Wilson, S. K. and D'Ambrosio, H.-M. "Evaporation of sessile droplets". In: *Annu. Rev. Fluid Mech.* 55 (2023), pp. 481–509. DOI: 10.1146/annurev-fluid-031822-013213.

233. Worthington, A. M. "On impact with a liquid surface". In: *Proc. R. Soc. Lond.* 34 (1883), pp. 217–230. DOI: 10.1098/rspl.1882.0035.

234. Wu, Y., Wang, Q., and Zhao, C. Y. "A comparative study of the immiscibility effect on liquid drop impacting onto very thin films". In: *Exp. Fluids* 62 (2021). DOI: 10.1007/s00348-021-03232-5.

235. Yarin, A. L. "Drop Impact Dynamics: Splashing, Spreading, Receding, Bouncing". In: *Annu. Rev. Fluid Mech.* 38 (2006). DOI: 10.1146/annurev.fluid.38.050304.092144.

236. Yarin, A. L. and Weiss, D. A. "Impact of drops on solid surfaces: self-similar capillary waves, and splashing as a new type of kinematic discontinuity". In: *J. Fluid Mech.* 283 (1995), pp. 141–173. DOI: 10.1017/S0022112095002266.

237. Yun, G., Kim, D., and Choi, H. "Vortical structures behind a sphere at subcritical Reynolds numbers". In: *Phys. Fluids* 18 (2006). DOI: 10.1063/1.2166454.

238. Zhang, B. et al. "Short-term oscillation and falling dynamics for a water drop dripping in quiescent air". In: *Phys. Rev. Fluids* 4 (12 2019). DOI: 10.1103/PhysRevFluids.4.123604.

239. Zhang, L. V. et al. "Wavelength selection in the crown splash". In: *Phys. Fluids* 22 (2010). DOI: 10.1063/1.35267435.

240. Zheng, Z. et al. "Fluid drainage from the edge of a porous reservoir". In: *J. Fluid Mech.* 718 (2013), pp. 558–568. DOI: 10.1017/jfm.2012.630.

241. Zimoch, P. J., Neufeld, J. A., and Vella, D. "Leakage from inclined porous reservoirs". In: *J. Fluid Mech.* 673 (2011), pp. 395–405. DOI: 10.1017/S0022112011000723.

PUBLICATIONS

The present dissertation includes publications in peer-reviewed journals, as well as oral and poster communications, all listed below. For direct hyperlinks, please refer to the PDF version.

Research articles

Parmentier J., Lejeune S., Maréchal M., Bourges F., Genty D., Terrapon V., Maréchal J.-C. and Gilet T. "A drop does not fall in a straight line: a rationale for stalagmite width". In: *Proc. R. Soc. A* 475 (2019) DOI: 10.1098/rspa.2019.0556.

Parmentier J., Terrapon V. and Gilet T. "Drop impact on a thin film: mixing, thickness variations and ejections". In: *Phys. Rev. Fluids* 8 (2023), pp. DOI: 10.1103/PhysRevFluids.8.053603

Parmentier J., Terrapon V. and Gilet T. "Gravity-driven drainage of a thin film over a stalagmite of variable shape". *To be submitted.*

Communications as contributed speaker

Parmentier J., Lejeune S., Maréchal M., Bourges F., Genty D., Terrapon V., Maréchal J.-C. and Gilet T. *A drop does not fall in a straight line: a rationale for stalagmite width* (2019). **Droplets IV**, Durham, UK. Poster.

Parmentier J., Terrapon V. and Gilet T. *A drop does not fall in a straight line: a rationale for the width of stalagmites* (2020+1). **24ᵉ Rencontre du Non-Linéaire**, remote. Presentation slides.

Parmentier J., Terrapon V. and Gilet T. *A drop does not fall in a straight line: a rationale for the width of stalagmites* (2021). **Soft Matter seminar** from GRASP FRS-FNRS contact group, remote. Presentation slides.

Parmentier J., Terrapon V. and Gilet T. *Drop impact on thin film: mixing, thickness variations and ejections* (2021). **Droplets V**, remote. Presentation slides.

Parmentier J., Terrapon V. and Gilet T. *A drop does not fall in a straight line: a rationale for the width of stalagmites* (2020+1). **ICTAM 2020+1**, remote. Video presentation.

Parmentier J., Terrapon V. and Gilet T. *Drop impact on thin film: mixing, thickness variations and ejections* (2021). **Fluids and Complexity II**, Nice, France. Presentation slides.

Parmentier J., Terrapon V. and Gilet T. *Drop impact on thin film: mixing, thickness variations and ejections* (2022). **25ᵉ Rencontre du Non-Linéaire**, Paris, France. Poster.

Parmentier J., Terrapon V. and Gilet T. , *Drainage of a thin film* (2023). **Fluid Meeting**, gathering of research groups from Department of Aerospace and Mechanical Engineering, Liège, Belgium. Presentation slides.

Miscellaneous

New York Times press article from Nov. 2019. *How stalagmites get their shape.*

Le Monde Science et Médecine brief from Dec. 2019.

La Croix press article from Jan. 2020. *Pourquoi les stalagmites ont-elles des formes différentes ?*

Réjouisciences vulgarised scientific photography contest from 2020. La preuve par l'Image.

APS Physics press article from May 2023. *Drops Wear Different "Crowns".*

Il Nuovo Saggiatore selection from Vol. 39, No. 3-4, p. 90 (2023). *Le Differenti Corone Delle Gocce.*